RUSSIAN ACADEMY OF SCIENCES
SCIENTIFIC COUNCIL FOR DIRECT ENERGY CONVERSION
SCIENTIFIC COUNCIL FOR FLUID MECHANICS
SCIENTIFIC COUNCIL FOR LOW TEMPERATURE PLASMA PHYSICS

THE 10TH INTERNATIONAL WORKSHOP ON MAGNETO-PLASMA AERODYNAMICS

MOSCOW
MARCH 22-24, 2011

Organized by Joint Institute for High Temperatures of RAS
In co-operation and sponsorship by:

RAS RFBR EOARD / ISTC

UDK 533.6.011:(533.95:537.84)

Proceedings the 10th Workshop on Magneto-Plasma Aerodynamics.
Ed. V.A.Bityurin, Moscow, JIHT RAS, 2011, pp.368

© Joint Institute for High Temperatures of Russian Academy of Sciences, 2011
ISBN 5-201-09558-5

ACKNOWLEDGMENTS

The Local Committee of the 10th International Workshop on Magneto-Plasma-Aerodynamics for Aerospace Applications expresses their approximation to all participants who have contributed to the success of the Workshop. The Committee gratefully acknowledges the collaboration and the financial support provided by the following organizations:

Joint Institute for High Temperatures of Russian Academy of Sciences (JIHT RAS)
International Science and Technology Center (ISTC)
European Office of Aerospace Research and Development (EOARD)
Russian Academy of Sciences (RAS)
Russian Foundation for Basic Research (RFBR)
International Liaison Group on MHD Energy Conversion (ILG MHD)

Program Committee

Aleksandrov A.F. (Russia)
Alferov V.I. (Russia)
Batenin V.M. (Russia)
Levin V.A. (Russia)
Bityurin V.A. – Chairman (Russia)
Bobashev S.V. (Russia)
Borghi C. (Italy)
Chernyi G.G. (Russia)
Giordano D. (The Netherlands)
Ishikawa M. (Japan)
Khodataev K.V. (Russia)
Kuznetsova T. N. – Science Secretary
Laux C. (France)
Lineberry J. (USA)
Macheret S. (USA)
Miles R. (USA)
Tishkoff J. (USA)
Vatazhin A.B. (Russia)

Local Committee

Bityurin V. A. – Chairman
Kuznetsova T. N. – Science Secretary
Bocharova E. A.
Klimov A. I.
Kolesnichenko Yu. F.
Leonov S. B.
Semenova T. M.
Son E.E

Contents

SESSION 1. Electrical Discharge in High Speed Air Flows – 1

1.1. Physics of the surface dielectric barrier discharge (Invited) **13**

Soloviev V.R.

1.2. Bluff Body Aerodynamic Wake Structure Control by a High Frequency Dielectric Barier Discharge **22**

..... **22**

Moralev I.A., Kazansky P.N., Chertov D.S., Klimov A.I., Bityurin V.A., Borisov I.A.

1.3. Plasma destruction of toluene impurities in N2: O2 mixture by pulse-periodical discharge **29**

Trushkin A.N., Kochetov V.I.

1.4. The kinetic processes initiated by the pulse nanosecond discharge in hot air **35**

Popov N. A.

SESSION 2. Electrical Discharge in High Speed Air Flows – 2

2.1. Kinetic Simulation of Radio Frequency Discharge inFluence on the Plasma Layer Near Surface in Supersonic Gas Flow **50**

Schweigert I.V.

2.2. Electron Beam and Gas Discharge Ionization of a Hypersonic Flow in a Magnetic Field **51**

Devjatkov V.N., Koval N.N., Fomichev V.P. and Schevchenko A.B.

2.3. Initiation Long Discharge in Supersonic Air Flow **58**

Golub V.V., Saveliev A.S., Sechenov V.A., Son E.E.

2.4. Simulation of Dynamics and Structure of Plasma Microjets **60**

Naidis G.V.

2.5. Microwave Energy Deposition In Discharge Plasma Structures **64**

Vedenin P., Afanas'ev S., Bityurin V., Brovkin V.

SESSION 3. Electrical Discharge – 1

3.1. Dielectric Barrier Discharge For Mixing Enhancement in the Wake of a Circular Cylinder **69**

Benard N., Cordier L., and Moreau E.

3.2. Supersonic Flow Control under Spark Discharge **71**

Tereshonok D.A., Son E.E.

2.2. Energy Characteristics and Relaxation of a "Plasma Sheet"..... **75**

Znamenskaya I.A., Ivanov I.E., Koroteeva E.Yu., Mursenkova I.V., Orlov D.M.

3.4. Experimental Researches of Fast-Flying Bodies Interaction with Laser-Induced Spark Plasma 76

Nikolayeva V.I., Pashchina A.S., Sakhonchik A.N.

3.5. Plasma Decay in Air Excited by Pulsed Nanosecond Discharge **81**

Aleksandrov N.L., Anokhin E.M., Kindysheva S.V., Kirpichnikov A.A., Kosarev I.N., Nudnova M.N., Starikovskaia S.M., Starikovskiy A.Yu.

SESSION 4. Shock Wave Propagation in Gas-Plasma Systems

4.1. Formation of Separation Zones during the Interaction of a Shock Wave with a Thin Temperature Wake **88**

Georgievsky P.Yu., Levin V.A., Sutyrin O.G.

4.2. The Impact of Electric Discharge on Self-oscillating Shock Waves When Supersonic Jet Impinging on the Finite Obstacle of Various Permeability **92**

Fomin V.M., Lomanovich K.A., Postnikov B.V.

4.3. Influence of Dust Concentration on Shock Wave Splitting in Discharge Plasma in Different Gases . 95

Baryshnikov A.S., Basargin I.V., Chistyakova M.V.

4.4. The Buffet Control by Local Energy and Momentum Release in the Vicinity of λ Shock **100**

Starodubtsev M.A.

4.5. Ion-Acoustic Shock Wave in Plasma (Abnormal Streaming, Detonation of Explosives) **101**

Serov Yu.L.

SESSION 5. Electrical Discharge - 2

5.1. On Fireball Generation by Microwave Resonance in Photonic Wire Grids **108**

Geert C. Dijkhuis

5.2. Gas Discharge Processes in Stratosphere and Mesosphere during a Thunder-Storm **109**

Khodotaev Kirill V.

5.3. On Possible Nature of Ball Lightning as of an Object of Plasma Assisted Combustion **110**

Bychkov V.L.

5.4. Some Features of High-Voltage Discharge within a Stream of the Water Anode Erosion's Products **118**

Astafiev A.M., Emelin S.E. and Kudryavtsev A.A.

5.5. New Method of Electric Power Extraction from High-Speed Plasma Flow **126**

Klimov A., Polyakov L., Tolkunov B.

5.6. Probability Law of MW Discharge Ignition **134**

Melnichenko D.

SESSION 6. Plasma Assisted Ignition and Combustion Control in High Speed Gas and Air Flows - 1

6.1. Distribution of H2O Temperature and Concentration in Zone of Plasma-Assisted High-Speed Combustion **135**

Leonov S. B., Firsov A. A., Shurupov M. A., Yarantsev D. A., Bolshov M.A., Kuritsyn Yu. A., Liger V.V., Mironenko V.R.

6.2. Nonequilibrum Plasma Accompanying the Ignition of Methane-Oxygen Mixtures **141**

Artem'ev K.V., Berezhetskaya N.K., Davydov A.M., Kazantsev S.Yu., Kononov I.G., Kossyi I.A., Malykh N.I., Popov N.A. 1, Taktakishvili M.I., Tarasova N.M., Firsov K.N., Filimonova E.A., Shakarov M.R.

6.3. Programmable Microwave Discharge as the Way of Combustion Stabilization o f Liquid Alcohol, Injected into Transonic Air Stream **142**

Gusev I.N., Karachev A.A., Kopyl P.V., Shibkov V.M., Shibkova L.V., Surkont O.S.

6.4. Fast Deflagration Waves and DDT-Processes Accompanying the Electric-Discharge Ignition of CH4:O2 Mixtures in the Closed Volumes..... **145**

Berezhetskaya N.K., Gritsinin S.I., Davydov A.M., Kossyi I.A., Popov N.A., Tarasova N.M., Firsov K.N.

SESSION 7. Plasma Assisted Ignition and Combustion Control in High Speed Gas and Air Flows - 2

7.1. Advanced Turbulent Combustion Modeling. Application to Supersonic Combustion (Invited)..... 152

V. Sabelnikov & C. Fureby

7.2. Time measurement of Induction Reaction H2 + O2 in the Detonation Wave Formation in a Stoichiometric Mixture at the Pressure within the Range of 1.1 2.3 atm..... 172

Kozlov P.V., Romanenko Yu.V., Losev S.A.

7.3. Electrical Discharge Effect on the Multistage in Flammation and Combustion: a Chemical Kinetics Mechanism and Practical Application..... 177

Bityurin V.A. and Filimonova E.A.

7.4. Flow Structure analysis by Means of Image Processing..... 181

Leonov S. B., Firsov A. A., Shurupov M. A.

SESSION 8. Plasma Aerodynamics

8.1. Simulation of Heat Transfer to the Space Vehicle EXPERT Using Inductively Heated Plasmatron 184

Kolesnikov A.F., Gordeev A.N., Vasilevskii S.A.

8.2. Structures of the Single Electrode RF Gas Discharge In Swirling Air Flow 185

Makaryan V.G. 1, Molevich N.E., Porfiriev D.P., Zavershinsky I.P

8.3. Oscillation frequencies of an unsteady vortex ring..... 189

Shugaev F.V., Solenaya O.A.

8.4. Study of a Longitudinal Plasmoid Created by Capacity Coupled HF Discharge in Swirl Airflow ... 193

Klimov A., Bitiurin V., Tolkunov B., Moralev I, Boytsov A.

8.5. About Some Features of Radio-Waves Propagation Through Extended Nonuniform Plasma..... 210

Nikolayeva V.I., Pashchina A.S., Sidorenko M.K.

8.6. Thermal Calculation of Magnetoplasma Engine Based on Fusion Power..... 216

Romadanov I.V., Ryzhkov S.V.

SESSION 9 MHD&PA Flow/Flight Control – 1

9.1. Experimental Activities on the MHD Interaction in a Hypersonic Argon and Nitrogen Flows **217**

Andrea Cristofolini, Gabriele Neretti, Carlo Angelo Borghi

9.2. Heat Flux Mitigation by the Magnetic Field in MHD Re-Entry Flow..... **226**

Bityurin V.A., Bocharov A.N.

9.3. The Experimental Study of The Electrical Discharge over the Flat Plate in a Hypersonic Air Flow at the Magnetic Field **237**

Fomichev V. P., Yadrenkin M. A., Podzin V. E., Shevchenko A. B.

9.4. Supersonic Air Flow around Body at near Surface Gas Discharge..... **239**

Erofeev A.V., Lapushkina T.A., Poniaev S.A.

9.5. Formation of the Shock Wave on a Wedge in the Hypersonic Air Flow at the Local MHD-Interaction..... **245**

Fomichev V. P., Yadrenkin M. A., Podzin V. E., Shevchenko A. B.

SESSION 10 MHD&PA flow/flight control - 2

10.1. Numerical Simulation of a Flow within Induced Magnetic and Electric Fields..... **247**

Goncharov A.E., Korotaeva T. A., Shashkin A. P.

10.2. Gas-Dynamic Equipments at the Ioffe Institute of Russian Academy of Sciences **249**

Bobashev S.V., Erofeev A.V., Krasovskaya I.V., Sakharov V.A., Stepanova Z.A., Tumakaev G.K.

10.3. Investigation of Miniature Magneto-Plasma Compressors as a Basic Part for Perspective Plasma Actuators for Supersonic Flows **250**

Mashek I.Ch., Lashkov V.A., Anisimov Yu.I., Kolesnichenko Yu.F., Brovkin V.G.

10.4. Numerical Simulation of Supersonic Ionized Gas Flow about Bodies: the Wall Heat Flux **255**

Bobashev S.V., Golovachev Yu.P. Chernyshev A.S., Schmidt A. A.

10.5. Experiments with Corona Discharge over Liquids with Additions of Metallic Micro Particles..... **256**

Bychkov V.L., Volkov S.A., Chernikov V.A. Kostiuk A.A.

SESSION 11. Electrical Discharge - 3

11.1. Experimental Investigation on the Energy Transfer in a DBD Plasma Actuator f or Airflow Control **261**

Andrea Cristofolini, Gabriele Neretti, Carlo Angelo Borghi

11.2. Determination of the Velocity Profile in a DBD Plasma Flow by Means of Schlieren Imaging..... **270**

Andrea Cristofolini, Gabriele Neretti, Carlo Angelo Borghi

11.3. Plasma Actuator Based on a Sectioned Dielectric Barrier Corona Discharge **276**

Akishev Yu., Grushin M., Trushkin N., Petryakov A.

11.4. Methods and Results of Plasma Spectral Studies in the Steady-State Ar-Al-H2O Discharge **277**

Bityurin VA, Klimov AI, Grigorenko A.V., Efimov A.V., Kutuzov D., Chinnov V.F.

11.5. Plasmoid with Strong Magnetic Field **282**

Vlasov Alexander N.

SESSION 12. Related problems

12.1. Plasma-Assisted Reaction of Heterogeneous Al-H2O Mixture in High-Speed Swirl Flow..... **294**

Klimov A., Bityurin V., Chinnov V., Grigorenko A., Efimov A.V., Kutuzov D.S., Tolkunov B.N., Polyakov L.B.

12.2. Two Approaches to the Condensation Model of Aluminum Oxide in Water Steam. **302**

Bityurin V.A., Filimonova E.A., Dobrovolskaya A.S., Alekseev Yu.V.

12.3. Analysis of Thermal Radiation in Combustion Chamber of Al-H2 MHD Generator. **306**

Bityurin V.A., Galaktionov A.V., Ivanov P.P.

12.4. Study of Kerosene Combustion Stimulated by Discharges in Supersonic Flow. **313**

Velikodny V.Yu., Bykov A.A., Dyrenkov V.V., Krikunova A.I., Popov V.V., Tolkunov B.N.

12.5. Energetics of ball lightning. **315**

Nikitin A.I.

POSTER SESSION

1. Effect of Ambient Air Pressure on Initiation of MW Discharge by Laser Radiation. **326**

Afanas'ev S., Brovkin V., Kolesnichenko Yu. and Mashek I.

2. Influence of Electrical Discharge in External Magnetic on Swirling Flow Parameters. **333**

Klementyeva I.B., Moralev I.A., Bityurin V.A., Klimov A.I.

3. Spatial Symmetry of Converging Shock Waves in Hard-Sphere Model: Carnahan-Starling Equation of State. **337**

Konyukhov A.V., Likhachev A.P., Fortov V.E.

3. Hypersonic MHD Flow over Rotation Body at Finite Magnetic Reynolds Numbers. **342**

Gubanov E.V., Likhachev A.P., Medin S.A.

4. Observation of the structure of charged macroscopic particles on the metal surface (analog dusty plasma). **349**

Baranov D.S.

6. Experimental Study of Emulsified Fuel Rheological Properties. **354**

Velikodny V.Yu., Bykov A.A., Krikunova A.I.

7. On the Three Interpretations for the Theoretical Existence of the Shock Wave Discontinuity in the Eulerian Substance. **354**

Belokogne Valentine A.V.

8. The general and peculiar in the microfusion flying machine (MFFM) feasibility. **356**

Belokogne Valentine A.V.

9. The Reality For The Laboratory Imitation Of The Stellar Elements Synthesis By The Very Advanced Inertial Fusion Around 2017-2020 Years. **357**

Belokogne Valentine A.V.

10. The Non-Paradoxical "Forbidden" Arising of the Subshock Isothermal in the One-Dimensional (Cp/Cv ≡ 3) Plasmas By Means of the Thermodynamic Input of the "Photon Steam".. ..... **359**

Belokogne Valentine A.V.

11. On hot High Beta Plasma Flows Near Magnetized Bodies in Rarefied Plasmas: Governing Parameters and Shape of the Velocity Distribution Function **361**

Gubchenko Vladimir M.

12. Numerical Simulation of Micro-Engine Based on the Capillary Discharge System. **362**

Kuzenov V.V., 1)Ryzhkov S.V.

Index of Autors..... **363**

1.1. PHYSICS OF SURFACE DIELECTRIC BARRIER DISCHARGE

V. Soloviev
Moscow Institute of Physics and Technology
vicsol@mail.cnt.ru

Abstract. This talk is devoted to analysis of experimental, theoretical and numerical modeling data shedding light on the physics of surface dielectric barrier discharge (SDBD) and the body force generation due to discharge action on the flow.
First, the physics for streamer and diffusive form of a single microdischarge evolution is considered. The spatial distributions of charged particle densities and electric field have been discussed both for electrical current generation phase and relaxation phase between microdischarges.
The model of a set of microdischarges forming SDBD at sinusoidal alternating voltage is considered phenomenologically. The main feature of SDBD physics at negative electrode polarity governing the easy start of consequent microdischarges is the existence of a gap between the exposed electrode edge and the negative surface charge layer, which is filled by the positive surface charge. The electric field inside this gap remains rather high even when microdischarge ends off and relaxes, so a small increase of applied voltage becomes enough to restore the air breakdown condition and start a new microdischarge. Qualitative coincidence between theoretical predictions and experimental observations for body force dependence on voltage at different dielectric thicknesses and its permittivities has been demonstrated by phenomenological physical model of SDBD. Accordingly, the volumetric force is primarily induced by the negative going voltage half-cycle. The origin of the force is the accumulation of volumetric negative charge carried by negative long-lived O_2^- and O_3^- ions. This accumulation is proportional to the third power of discharge length giving a strong force dependence on applied voltage.
The directions of further SDBD investigation and actuator performance improvement are discussed.

Introduction

Intense analysis of boundary-layer and separation flow control using surface dielectric barrier discharge (SDBD) actuators continues during last few years [1-4]. SDBD has a complex structure and evolves as a streamer and/or diffusive discharge depending on applied voltage polarity and its waveform. It consists of a set of tens microdischarges repeating each half cycle of alternating applied voltage. Because of this complexity, the main gap in theoretical and numerical predictions of the SDBD aerodynamic performance is a lack of adequate physical and numerical modeling of the SDBD evolution in air. This did not allow for correct estimations of momentum and heat sources induced by SDBD, which are commonly substituted into Navier-Stokes equations for simulation of aerodynamic effects generated by actuator.

The SDBD plasma model developed by Boeuf et al [5,6] simulates the body force production by a set of microdischarges for a ramp voltage of positive and negative polarity. In the advanced model version accounting for oxygen negative ion formation [6] the obtained results are correct for negative applied voltage. For positive going voltage, when the discharge evolves in a streamer form, the results are wrong, because authors do not account for an air photoionization by UV radiation from discharge region, which is shown to be the main mechanism for streamer formation [7]. Without this process the calculated streamer length is an order of magnitude less then its experimental value.

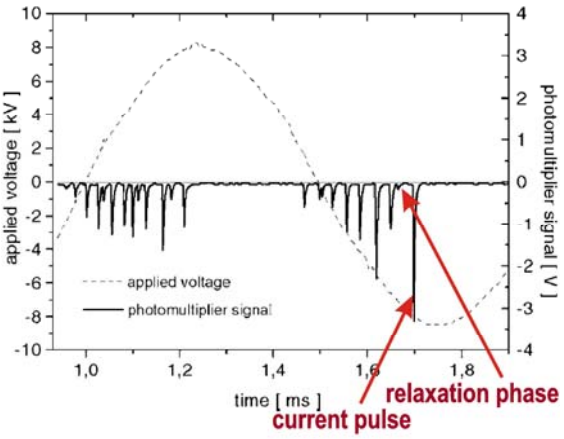

Fig. 1. *Photodetection of microdischarges in atmospheric air for 1 kHz applied sinusoidal voltage [11].*

Our recently developed model [7-10] simulates the building up and relaxation of a single microdischarge only. This model has been validated using available experimental data on a discharge length and charge density distribution along the dielectric surface, but the obtained data are not enough for momentum and heat source predictions for practical DBD-plasma actuator. In practical case the actuator induced action on a flow is due to a set of tens consequent microdischarges developed during each half-period of alternating applied voltage (Fig. 1). Numerical modeling of this bulk of microdischarges is extremely time-consuming problem and it is not solved yet, except for a case of negative ramp voltage [6].

In this paper we try to estimate the integral value of momentum source induced by SDBD using a phenomenological model of discharge action on the quiescent air based on existing experimental data and achieved understanding of SDBD physics [6,10]. According to available experimental data summarized in [2] the actuator performance for commonly used SDBD layout and sinusoidal applied voltage waveform is saturated with the increase of voltage amplitude. The primary objective of this paper is to get analytical phenomenological model of the body force in order to understand the main reason of actuator saturation effect, to recognize the main trends of body force dependence on applied voltage parameters and dielectric material properties and to see the possibilities of improving the SDBD actuator performance.

1. Physics of a single microdischarge

According to experimental data [11] and numerical modeling the SDBD at alternating applied voltage takes a form of a set of microdischarges (Fig.1). For each microdischarge the current pulse in external circuit is generated in a time of the order of few tens nanosecond, and the duration of relaxation phase between microdischarges is three orders of magnitude greater.

1.1 Microdischarge at positive electrode polarity

Both numerous experimental observations and numerical modeling have shown that the microdischarge properties are quite different for positive and negative going voltage half-cycle.

For positive electrode polarity the discharge evolves in a streamer form, which is characterized by a high electron-ion density at the level of 10^{15} cm^{-3} and a longer discharge length. According to numerical simulation [10] streamer head parameters do not vary notably after the streamer formation – the electron density contours for the streamer nose practically coincide for different time instants as shown in Fig. 2.

Because of high electron density the electric field is small inside a streamer body and gets a high value only in front of the streamer head (Fig. 3).

Streamer breakdown in atmospheric air has a threshold nature. If the applied voltage is below a certain level, then the streamer is not formed and the discharge just starts to glow near the electrode edge and rapidly decays. Experimentally observed streamer length for positive electrode polarity increases with applied voltage [11]. For $d \approx 1$ mm and $\varepsilon \approx 5-10$ its minimal value is around 10 mm under the near breakdown condition corresponding to $V \approx 4$ kV in atmospheric air.

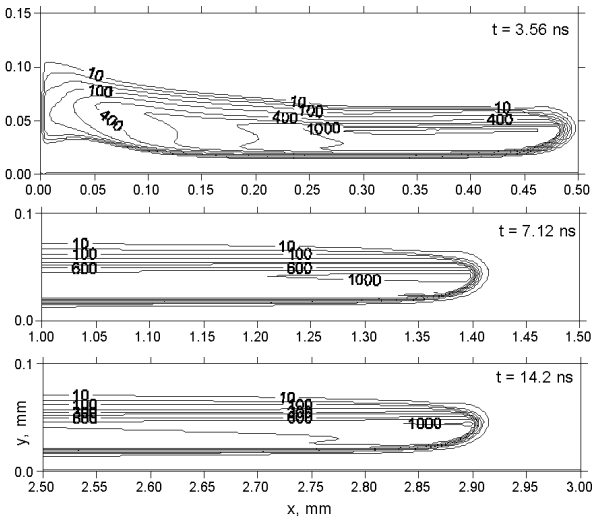

Fig. 2. *Streamer evolution predicted by numerical model [10]; electron density n_e/n_0 contours for V = 4.2 kV, d = 1 mm, ε = 8; $n_0 = 0.82\times10^{12}$ cm^{-3}*

The bottom boundary of a streamer body does not tough the dielectric surface (see Fig.2). Nevertheless, the dielectric surface is effectively charged positively until the surface charge density reaches its saturation level $\sigma_0 = \dfrac{\varepsilon V}{4\pi d}$ corresponding to exposed electrode potential *V*. The surface charging is due to a strong drift flux of ions, caused by the electric field in a gap between streamer body and dielectric surface. This field remains high for notable distance from the streamer head (Fig. 3) and could induce air fluorescence not

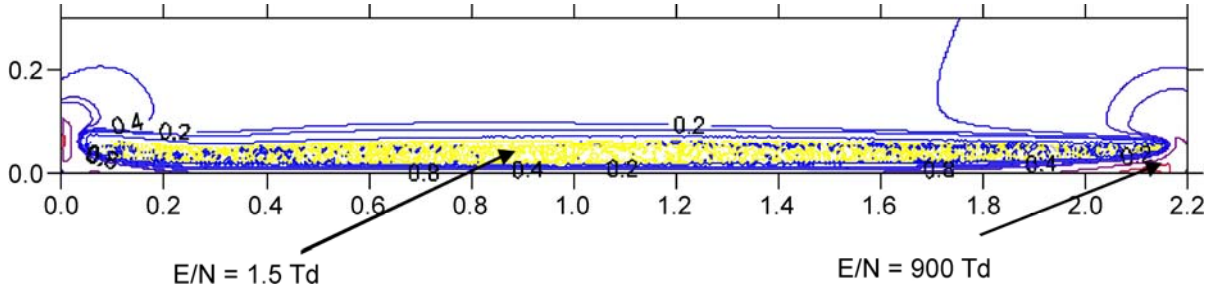

Fig. 3. *Calculated electric field contours E/E_0 for streamer formation phase [10] ; V = 4.2kV, d = 1 mm, ε = 8; E_0 = 40.35 kV/cm.*

only in the head but in the gap as well.

1.2 Microdischarge at negative electrode polarity

For negative exposed electrode polarity the discharge has a form, which is similar to glow discharge [10]. The following scenario of discharge evolution takes place. First, a small cathode region is formed near the electrode edge. This region is characterized by electron-ion density of the order of 10^{15} cm^{-3} with severe charge separation caused by a high electric field. Strong ionization occurs here. The born ions drift to the electrode edge, whereas electrons drift to dielectric surface. The electrons seed the dielectric surface and create a negative surface charge, which shields the *y*-component of external electric field and slows down the electron motion to the dielectric surface. The electron density contours for discharge evolution are shown in Fig. 4.

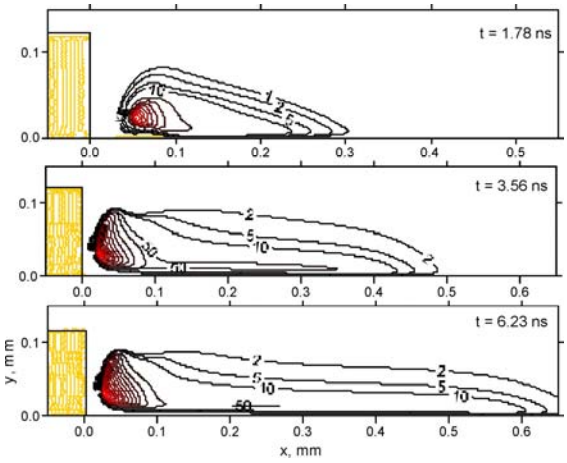

Fig. 4. *Electron density n_e/n_0 contours evolution at V = - 4.5kV, d = 1 mm, ε = 8; rectangular region denotes the exposed electrode.*

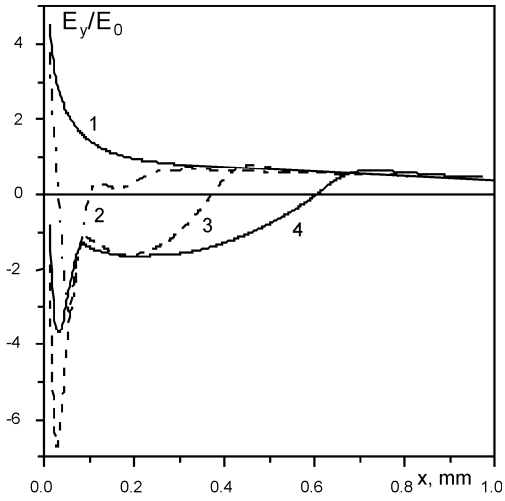

Fig. 5. *Instantaneous distributions of $E_y(x)$ on the dielectric surface: (1) – t = 0, (2) – 1.8 ns, (3) – 3.6 ns, (4) – 7.1 ns; V = - 4.5 kV, d = 1 mm, ε = 8.*

At the second stage of discharge evolution a near-surface layer is formed. Initially, the E_y component is positive on the dielectric surface for all $x > 0$ (curve 1 in Fig. 5) representing the E_y component of external *E*-field for a zero surface charge value. The drift flux of electrons is negative, i.e. directed toward a surface, in this case. The increase of negative surface-charge density continues until E_y changes its sign. Then the drift electron flux becomes positive and high enough to compensate the negative electron diffusion flux toward the surface, so the balance electron flux to the surface becomes equal to zero.

Figures 5 and 6 show temporal evolutions of electric field normal component E_y on the dielectric surface and the surface charge density at a constant voltage *V* = - 4.5 kV. The E_y component becomes negative over the surface part with high enough charge and ultimately tends to an asymptotic value corresponding to zero flux of electrons to the dielectric surface. The instantaneous distributions of $E_y(x)$ (Fig. 5) correlate with the surface charge density distributions $s(x)$ shown in Fig. 6.

Another feature of the surface charge building up on the dielectric surface is the existence of a gap between the electrode edge and the negative surface charge layer. The sufficient for discharge burning electron-ion breeding takes place along a critical *E*-field line, which has a finite length. The end of this critical line on the dielectric surface corresponds to the starting point of the surface charge layer. Initially this gap is uncharged (curve 2 in Fig. 6), but later it is filled by positive charge (curves 3, 4 in Fig. 6). This occurs because the formed cathode region with positive ion surplus creates a strong electric field directed toward the surface (pikes of negative electric field on curves 2, 3 and 4 in Fig. 5). Positive ion drift flux from the cathode region is directed to the surface due to this *E*-field and fills

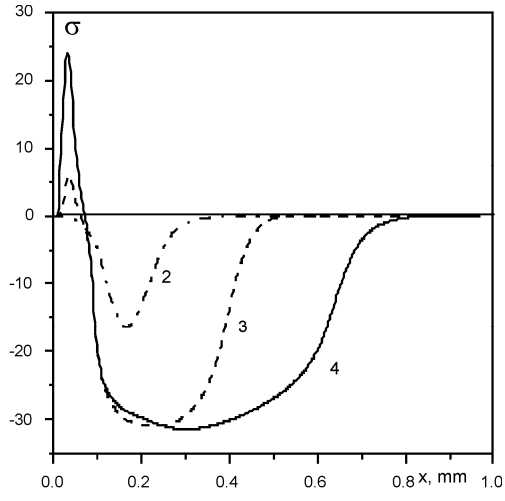

Fig. 6. *Instantaneous distributions of the surface charge density $\sigma(x)$ in units of nC/cm^2: (2) – 1.8 ns, (3) – 3.6 ns, (4) – 7.1 ns; V = - 4.5 kV, d = 1 mm, ε = 8.*

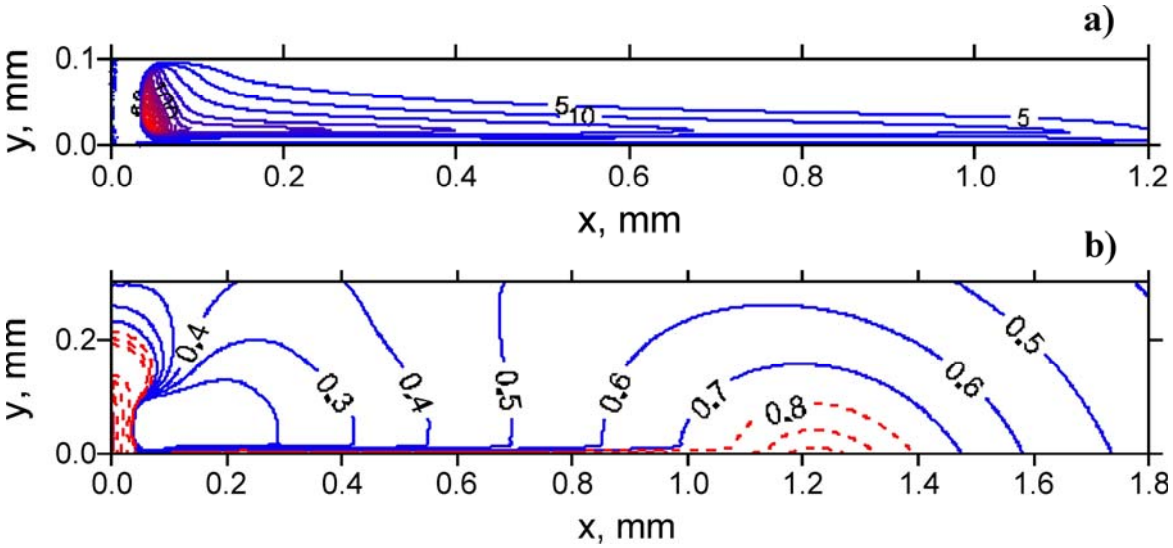

Fig. 7 *Electron density n_e/n_0 (a) and electric field E/E_0 (b) contours for t = 16 ns; V = -5 kV, d = 1 mm, ε = 8; dashed lines correspond to E-field values greater than a threshold of air breakdown.*

the gap by positive ion charge. The positive charge grows up until the cathode region starts to decay (curves 4 in Figs. 5 and 6).

The gap formation between the electrode edge and the negative surface charge layer will be shown to be extremely important for dynamics of microdischarge repetition at alternating voltage.

Electron concentration above the dielectric surface is not as great as in the case of the streamer microdischarge relevant for positive electrode polarity and takes a value around 10^{13} cm^{-3}. Accordingly, the electric field value inside the main part of discharge volume is much greater that inside a streamer body. This otherness is a reason of quite different body force values induced by a single microdischarge at positive and negative exposed electrode polarity.

The electric field spatial distribution also has some features. Negative surface charge layer forms an additional contribution to electric field like an '*E*-field bubble' at a moving leading edge of the layer. An example of this '*E*-field bubble' production is shown in Fig. 7 for a case of SDBD microdischarge progress at applied voltage *V* = -5 kV, *d* = 1 mm, ε = 8 [10,12]. The main air ionization occurs inside a near-cathode region at $x \approx 0.05$ mm and the distribution of electrons spreads to $x \approx 1.2$ mm along a surface. As shown in Fig. 7, the negatively charged 'needle' formed by electrons seeding the dielectric surface creates an additional electric field with hemi-cylindrical contours centered at the top of this 'needle' at $x \approx 1.2$. The dashed lines in electric field contour lines in Fig. 7 correspond to *E*-field values greater or equal to a threshold of air breakdown. Accordingly, additional ionization and gas excitation occurs inside a hemi-cylinder with 0.1 mm radius. This hemi-cylinder moves in *x*-direction following the front edge of electron population of the dielectric surface.

2. Time resolved measurements of the body force

The momentum source due to charged particles collisions with neutral gas molecules (body force) is estimated as [5]

$$\vec{F} = e(n_i - n_- - n_e)\vec{E}, \qquad (1)$$

where n_e, n_-, and n_i = electron, negative ion and positive ion concentrations, e = electron charge. The analysis of kinetic processes carried out in Ref. [7, 8] has shown that positive ions are primarily represented by O_4^+, O_2^+ ions coming after a fast conversion of N_4^+, N_2^+ ions in charge-exchange collisions with O_2 molecules. Positive ions O_4^+, O_2^+ are close to equilibrium; accordingly, in the first approximation we can combine them into one type of effective positive ion.

At the stage of microdischarge generation (current pulse phase in Fig. 1) negative ions are mainly O^- ions [7,8], but at relaxation phase between microdischarges the type of negative ion changes onto O_2^-, O_3^- ions because of both a rapid conversion of O^- ions into O_2^-, O_3^- ions and additional production of O_2^- ions in three-body electron attachment process. Thus, the main time of SDBD evolution negative ions are represented by long-lived O_2^-, O_3^- ions, which disappear either due to recombination with positive ions or drifting to dielectric surface.

According to Eq. (1) the body force is proportional to volumetric charge. Because of three orders of magnitude difference between microdischarge current generation phase and relaxation phase the main contribution into body force occurs at relaxation phase. Microdischarge building up phase primarily serves as a plasma generator.

Numerical simulation [10] has shown that the body force induced at the relaxation phase of a single microdischarge is approximately an order of magnitude greater for a case of negative going voltage, than for a case of positive going one. This happens because the average over the volume electric field at relaxation phase is much greater in the case of negative electrode potential.

The volumetric charge at relaxation phase is due to heavy positive or negative ions, because the electrons either rapidly recombine with positive ions in dissociative recombination process or leave the volume because of their high mobility.

There are two possible versions of the body force generation. The first one implies that volumetric charge totally disappears during the relaxation phase between microdischarges. In this case the body force averaged over the microdischarge cycle should be constant and should exist simultaneously with the set of microdischarges. Another scenario implies that volumetric charge does not vanish between microdischarges and increases in a set of microdischarges due to accumulation. In this case the body force increases in time, gets maximum at the end of microdischarge series, and remains non-zero after the end of microdischarge series.

The correct numerical simulation of a set of microdischarges has been done only for negative ramp voltage [6] (see Introduction). Accordingly, only experimental data could shed a light what version of body force production is realized in the case of alternating voltage.

In the first and very impressive experiment for time resolved body force measurements authors have mounted SDBD on a torsional pendulum and registered the pendulum shifting due to SDBD action using laser interferometer [13,14]. The results of pendulum angular velocity dependence on time are shown in Fig. 8 with schematic visualization of microdischarge series.

Body force (plasma force in Fig. 8) is proportional to $\frac{dV_\omega}{dt}$. The data presented in Fig. 8 show the following.

1. Body force is approximately the same for negative and positive going voltage half-cycle, forward and back stroke, respectively.
2. It is positive, i.e. directed downstream from the exposed electrode edge, both for positive and negative voltage half-cycle.
3. The force action is shifted regarding a set of microdischarges.

The second outcome means that the body force is due to positive ion surplus for positive going voltage half-cycle and due to negative ion surplus for negative one. The third result implies that the force is due to **accumulated** charge. The conclusion, that the accumulated volumetric charge is responsible for body force production has been confirmed by numerical simulation [6] for negative ramp voltage.

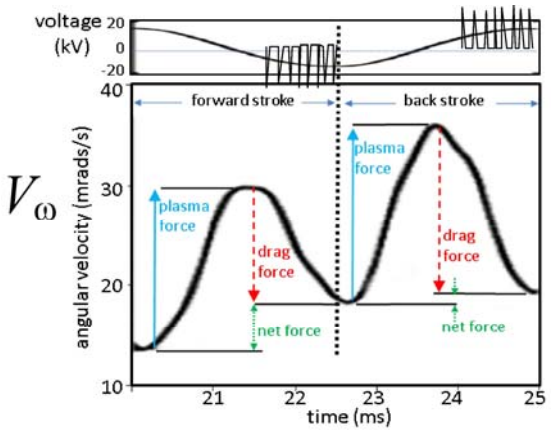

Fig. 8. *Torsional pendulum angular velocity versus time under the SDBD action [14].*

Another experimental data for time resolved body force evaluation were obtained by Pitot tube pressure measurements [12]. According to these data the body force produced during a negative going voltage half-cycle is an order of magnitude greater than for positive going voltage half-cycle, and the force action is not shifted regarding the microdischarge series. The controversial experimental data mean that additional efforts are needed to clarify the production of the body force.

3. Simplified analytical model of the body force

The aforementioned experimental findings for body force measurements and achieved understanding of SDBD physics based on available numerical models made it possible to develop a phenomenological model of the body force induced by SDBD driven by sinusoidal voltage [15]. To estimate an integral force value per unit electrode length the following assumptions were made

1. Ignore the body force produced by positive voltage half-cycle.
2. Assume that body force is due to accumulated volumetric charge of negative ions.
3. Assume that all microdischarges in the series are similar and produce the same amount of charged particles (electron-ion pairs).

The scheme of volumetric negative charge accumulation is shown in Fig.9 for negative going voltage half-cycle. Consider the evolution of some arbitrary microdischarge located somewhere in the middle of the series. Denote the length of the surface charge layer created in previous microdischarges as $l(t)$ and its potential as V_s. For negative electrode polarity the main amount of electron-ion pairs in microdischarge burning process is produced in a cathode layer. Electrons leave the cathode layer and drift along the dielectric surface because the normal component of electric field is zero due to screening by surface charge layer. On their drift way to the end of surface charge layer in longitudinal electric field E_{xl} electrons could be attached to O_2 molecules and create O_2^- ions or reach the dielectric surface and increase the surface charge layer length. The created O_2^- ions drift along the dielectric surface much slower, because the mobility of negative ions K_n is approximately two orders of magnitude less than electron mobility.

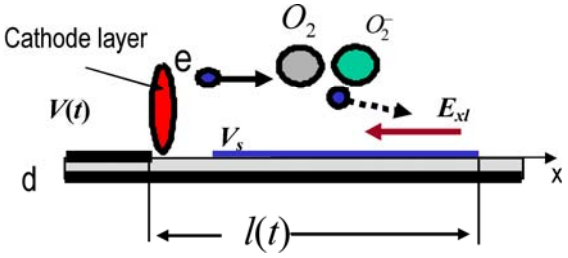

Fig. 9. *The scheme of negative ion production and drifting along the surface charge layer.*

The negative ion residence time inside a volume is

$$\Delta\tau_n \approx \frac{l(t)}{K_n E_{xl}(t)}, \qquad (2)$$

and this value is much greater than the time between microdischarges $\Delta\tau_{md}$: $\Delta\tau_n >> \Delta\tau_{md}$. This means that negative charge accumulation occurs.

The probability of negative ion formation is

$$p_n(t) \approx \frac{\nu_{at} l(t)}{K_e E_{xl}(t)}, \qquad (3)$$

where ν_{at} = frequency of electron attachment to O_2 molecule in the process $e + 2O_2 \rightarrow O_2^- + O_2$, K_e = electron mobility.

The length of the surface charge layer comes from capacitance relation

$$C \approx \frac{\varepsilon l(t)}{4\pi d}, \quad q(t) \approx C(t)V_s(t) \approx \Delta q N_{md}(t),$$

$$l(t) \approx \frac{4\pi d \Delta q N_{md}(t)}{\varepsilon V_s(t)}, \qquad (4)$$

where d = distance between electrodes, ε = relative dielectric permittivity, $q(t)$ = total charge of electrons produced in all microdischarges to time instant t, Δq = total charge of electrons produced during a single microdischarge, $N_{md}(t)$ = number of microdischarges has been passed to time instant t.

Total charge of negative ions produced during a single microdischarge is

$$\Delta q_n \approx \Delta q \cdot p_n(t), \qquad (5)$$

and accumulated to the time instant t negative charge may be estimated as

$$q_n(t) \approx \frac{1}{3} N_{md}(t) \cdot \Delta q \cdot p_n(t). \qquad (6)$$

The time averaged force due to accumulated negative charge is equal to

$$\overline{F} \approx \frac{1}{T_v} \int_0^{T_v} q_n(t) E_{xl}(t) dt, \qquad (7)$$

here T_v = voltage period, $f_v = \frac{1}{T_v}$ is the voltage frequency. After the substitution of expressions (6), (5) and (3) for $q_n(t)$, Δq_n and $p_n(t)$ into Eq.(7) and integration we get

$$\overline{F} \approx \frac{\nu_{at} l^2 N_{md} f_v \Delta q}{3 K_e K_n E_{xl}}, \text{ for } f_v \Delta\tau_n << 1. \qquad (8)$$

Estimation of l, N_{md}, Δq and E_{xl} has been done in Ref. [15]. Substitution of these values into Eq. (8) finally gives the following analytical expression for average force per unit electrode length

$$\overline{F}(\text{N/m}) \approx 2.6 \cdot 10^{-8} \frac{f_v(\text{kHz})}{d(\text{cm})} V_0^{\,4}(\text{kV}) \left(1 - \frac{V_{bd}}{V_0}\right)^4 \qquad (9)$$

where V_0 = voltage amplitude, V_{bd} = breakdown voltage.

Comparison of the body force calculated using Eq. (9) with experimental data from Ref. [2] is shown in Fig. 10. The obtained theoretical predictions show qualitative agreement with experimental results for different dielectrics and their thicknesses. Experimental data in Fig. 10a demonstrate weak dependence of the body force versus dielectric relative permittivity ε. In expressions (8) and (9) there is no dependence on ε at all. This disagreement and discrepancy between predicted and observed force dependence on voltage for near breakdown voltages can be

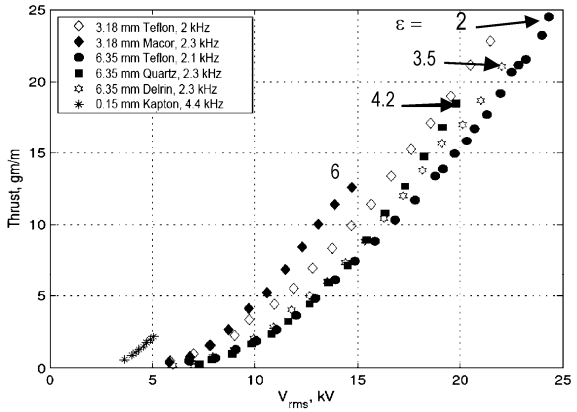

Fig. 10a *Experimental data [2] for integrated body force per unit electrode length dependence on applied voltage.*

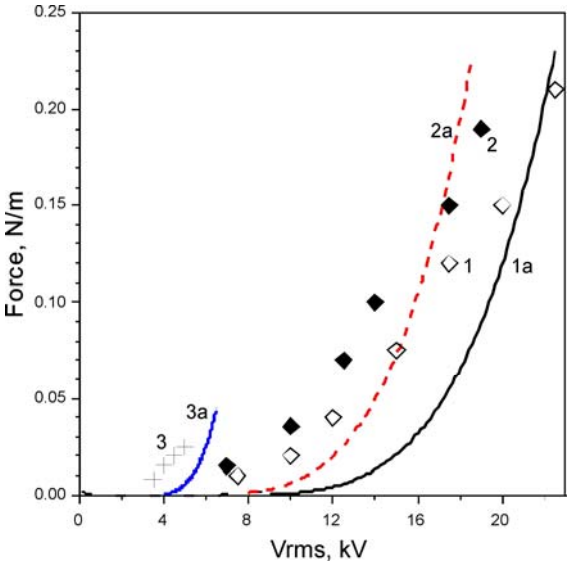

Fig. 10b *Theoretical estimations of average force per unit electrode lenght (lines) against experimental data [2] (symbols) for 1,1a – teflon (ε =2), d = 6.35mm, fv=2.1kHz; 2,2a – teflon, d = 3.18 mm, fv=2 kHz; 3,3a – Kapton (ε =3.9), d = 0.15 mm, fv=4.4kHz.*

attributed to the inaccuracy of the breakdown voltage estimation. In simplified analytical approximation of electric field near the electrode edge used in Ref.[15] to estimate the breakdown voltage V_{bd} this electric field did not depend on ε. Accurate numerical calculation of the electric field near the electrode edge shows that this approximation is correct for rough estimations, but weak dependence on ε still exists and should give a weak dependence V_{bd} on ε. This correction could improve the coincidence between theoretical predictions and experiment.

4. Discussion

Analytical estimation of the integral force per unit length of exposed electrode has been done on the basis of hypothesis, that the body force induced by SDBD plasma is mainly due to negative ion accumulation inside a volume above the dielectric. Predicted force dependences on applied voltage, dielectric thickness and its relative permittivity qualitatively coincide with experimental observation. This coincidence validates our hypothesis, i.e. the main contribution into body force is produced during negative going voltage half-cycle and this contribution is governed by accumulated volumetric charge of negative ions.

According to developed analytical model [15], the breakdown condition for ignition of regular microdischarge is achieved by a small increase of applied voltage $\delta V << V_0$. This occurs because of aforementioned gap existence between the electrode edge and the negative surface charge layer. The electric field inside this gap remains high even after the end of microdischarge. Accordingly, a small voltage increase restores the breakdown condition and ignites the next microdischarge.

Microdischarge starts to decay and comes to relaxation phase when the breakdown condition is violated. This happens due to electric field screening by a new portion of negative charge Δq produced in a microdischarge. At the beginning of microdischarge series the main part of this charge is transported by electrons to dielectric surface and creates the surface charge layer and a small part is converted into negative O_2^- ions and supplements the volumetric charge. Accordingly, the screening role of the surface charge is much greater, than that one of the volumetric charge.

With the increase of voltage amplitude the volumetric charge of negative ions sharply increases because of elevation of discharge length *l*. The greater the *l* value – the higher the negative ion formation probability and the bigger the negative ion residence time in the volume. When the screening effect of volumetric charge becomes comparable with that one from surface charge the saturation effect arises. The force stops to grow with increasing voltage. In this case the set of microdischarges ends off before the voltage reaches its amplitude value – less part of the voltage cycle contributes into force production.

Saturation effect is accompanied by violation of discharge spatial homogeneity – spark breakdowns occur regularly along the exposed electrode. The reason of this phenomenon is a breakdown between the volumetric negative charge cloud and electrode, when the positive going voltage half-cycle comes.

Saturation effect is shifted to higher voltages if one reduces the capacitance of dielectric layer, i.e. increases the dielectric thickness and decreases the dielectric relative permittivity [2]. It is seen in Fig. 10a – the last points on the curves correspond to

saturation of the force. According to these data it is clear, that we can not feather significantly improve the actuator performance varying voltage frequency, dielectric thickness and its relative permittivity using standard SDBD layout.

To improve the actuator performance we have to suppress the saturation effect. Accounting for that saturation is mainly due to electric field screening by the surface charge, and the body force is due to volumetric charge, it looks promising to use dielectric possessing a property of small conductivity. This could decrease the screening action of the surface charge layer and permit to increase the volumetric charge to get a greater force value. The dielectric conductivity σ_d should have a value, which supplies a characteristic time of surface charge reduction $\tau_{RC} = RC$ approximately equal to a half of voltage period

$$\tau_{RC} \approx \frac{1}{2 f_v}. \qquad (10)$$

The resistance $R = \frac{d}{\sigma_d S}$, the capacitance $C = \frac{\varepsilon S}{4\pi d}$, so $\tau_{RC} = RC = \frac{\varepsilon}{4\pi\sigma_d}$, and

$$\sigma_d \approx \frac{\varepsilon f_v}{2\pi}. \qquad (11)$$

The idea to use a "conducting" dielectric for surface charge depletion has been proposed and tested by Princeton team two years ago[16]. They used linen based phenolic with $\sigma_d \approx 10^{-9}$ Ohm^{-1} m^{-1} supplying $\tau_{RC} \approx 10^{-2}$ s for $\varepsilon \approx 1$, but needed much smaller time $\tau_{RC} \approx 10^{-4}$ s, because they tried to reduce a surface charge between nanosecond pulses of voltage with repetition rate 10 kHz. The used dielectric had too small conductivity and they did not succeed in actuator improvement in that experiment. To get a positive result with linen based phenolic we have to use sinusoidal voltage with $f_v \approx 100$ Hz.

5. Summary

Numerical simulation of a set of microdischarges relevant for SDBD evolution at alternating voltage is too time consuming and has not been done yet. Accordingly, there is still no accurate numerical model for simulation of momentum and heat sources in SDBD induced plasma, which is necessary for improvement of SDBD actuator performance. Nevertheless, the performed theoretical and numerical modeling of a single microdischarge together with experimental findings made it possible to develop a simplified analytical model of the body force induced by SDBD driven by alternating voltage.

The developed phenomenological model of the body force generation concludes that

- The main contribution into momentum source occurs at negative going voltage half-cycle
- Body force is primarily due to accumulation of volumetric negative charge
- To improve the SDBD actuator performance one has to increase the volumetric charge of negative ions
- This could be achieved by artificial increasing of the discharge length or by using the dielectric possessing a small conductivity to deplete a surface charge
- Further investigation of this problem could be promising for actuator improvement

The developed phenomenological model sheds a light on the main physics of body force generation and the ways how to improve the actuator performance, but it can not replace an accurate numerical simulation of sets of microdischarges at alternating voltage. This problem is still important, because its solution gives not only integral force value, but spatial distributions of momentum and heat sources.

Available experimental data for time resolved measurements of the body force are controversial and need additional validation.

References

1. Corke, T.C., Post, M.L., Orlov D.M., "Single dielectric barrier discharge plasma enhanced aerodynamics: physics, modeling and applications", *Exp.Fluids*, **46**, 2009, pp.1-26.
2. Thomas, F.O., Corke T.C., Iqbal M., Kozlov A., Schatzman D., "Optimization of Dielectric Barrier Discharge Plasma Actuators for Active Aerodynamic Flow Control", *AIAA J.*, **47**, 2009, pp. 2169-2178.
3. Moreau, E. "Airflow control by non-thermal plasma actuators", *J. Phys. D: Appl. Phys*., **40**, 2007, pp. 605-636.
4. Enloe, C.L., McHarg, M.G., and McLaughlin, Th.E. "Time-correlated force production measurements of the dielectric barrier discharge plasma aerodynamic actuator", *J.Appl.Phys*., **103**, 2008, 073302.
5. Boeuf J.P., Lagmich Y., Unfer Th., Callegary Th., Pichford L.C, "Electrodynamic force in dielectric barrier discharge plasma actuators", *J. Phys. D: Appl. Phys*., **40**, 2007, 652-662.
6. Boeuf J.P., Lagmich Y., Callegary Th., Pichford L.C., UnferTh., "New insights in the physics of DBD plasma actuators for flow control ", AIAA Paper 2008-1376, 2008.

7. Soloviev, V.R., Krivtsov, V.M, Konchakov, A.M., Malmuth, N.D, "Surface Barrier Discharge Simulation in Air for Constant Applied Voltage", 46th AIAA Aerospace Sciences Meeting, Jan.2008,Reno, Nevada, AIAA Paper 2008-1378, 2008.
8. Soloviev, V.R., Konchakov, A.M., Krivtsov, V.M, Aleksandrov, N.L. "Numerical Simulation of a Surface Barrier Discharge in Air", *Plasma Physics Reports*, **34**, 2008, pp. 594-608.
9. Soloviev, V.R., Krivtsov, V.M "Features of a Surface Barrier Discharge Modeling", 47th AIAA Aerospace Sciences Meeting, Jan.2009, Orlando, Florida, AIAA Paper 2009-0842, 2009.
10. Soloviev, V.R., Krivtsov, V.M. "Surface barrier discharge modeling for aerodynamic applications" *J. Phys. D: Appl. Phys*, **42**, 2009, 125208(13pp).
11. Gibalov, V.I., Pietsch, G.J. "The Development of Dielectric Barrier Discharges in Gas Gaps and on Surfaces", *J. Phys. D: Appl. Phys.*, **33**, 2000, pp. 2618-2636.
12. Leonov, S., Opaits, D., Miles, R., Soloviev, V., "Time-resolved measurements of plasma-induced momentum in air and nitrogen under dielectric barrier discharge actuation", *Physics of Plasmas* **17**, 2010, 113505
13. Enloe, C.L., McHarg, M.G., Font G.I. and McLaughlin, Th.E., "Plasma-induced force and self-induced drag in the dielectric barrier discharge aerodynamic plasma actuator" , 47th AIAA Aerospace Sciences Meeting, Jan.2009, Orlando, Florida, AIAA Paper 2009-1622, 2009.
14. Font, G.I., Enloe, C.L., and McLaughlin, Th.E., "Effect of volumetric momentum addition on the total force production of a plasma actuator", 39th AIAA Fluid Dynamics Conf., June 2009, San Antonio, Texas, AIAA Paper 2009-4285, 2009.
15. Soloviev, V.R., Krivtsov, V.M "Phenomenological Model of Body Force Induced by Surface Dielectric Barrier Discharge", 49th AIAA Aerospace Sciences Meeting, Jan.2011, Orlando, Florida, AIAA Paper 2011-157, 2011.
16. Opaits, D., Zaidi, S., Shneider, M., Miles, R., Likhanskii, A., Macheret. S., "Improving Thrust by Suppressing Charge Build-up in Pulsed DBD Plasma Actuators", 47th AIAA Aerospace Sciences Meeting, Jan. 2009, Orlando, Florida, AIAA Paper 2009-487, 2009

1.2. BLUFF BODY AERODYNAMIC WAKE STRUCTURE CONTROL BY A HIGH FREQUENCY DIELECTRIC BARRIER DISCHARGE

Moralev I.A., Kazansky P.N., Chertov D.S., Klimov A.I., Bityurin V.A., Borisov I.A.
[1] Joint Institute for High Temperatures RAS,
Izhorskaya 13, bld..2, Moscow, 125412, Russia
E-mail: ivmoralev@gmail.com

Abstract. In recent work, flow control in two cases is studied: leading edge stall on the wing model at high attack angle and unsteady boundary layer separation on the circular cylinder. Discharge used for flow control is a dielectric barrier type capacity coupled HF discharge (CHFD), with typical parameters: HF frequency F_{HF}~350 kHz, modulation frequency F_M=10-10^4 Hz, mean HF power N_{HF}< 20W/cm span.

Airflow parameters are the followings: airflow velocity up to 140m/s, Re < $6x10^5$.

Wake structure behind models is studied with PIV, shadow methods, flow visualization and pressure measurements. Vortex shedding triggering is obtained when forcing at Sh~0.3 for a cylindrical model.

Pressure measurements in the model's wake are performed. Drag decrease of about 40% is measured *for a wing model* at M~0.3, Re~$3x10^5$ and HF plasma on. This result is obtained at post-stall angles of attack (AoA). It is revealed, that HF plasma actuator effectiveness drops significantly at stall attack angle and Re > $4x10^5$. This result should be connected with a boundary layer turbulisation near the leading edge of a wing model.

This work follows our previous ones [1,2].

Nomenclature

HF	= high frequency
DBD	= dielectric barrier discharge
SHFD	= surface HF discharge
f_{HF}	= HF frequency
F_M	= modulation frequency
T_i	= pulse duration
I_{HF}	= HF electric discharge current
U_{HF}	= HF electric discharge voltage
N_{HF}	= pulse power input in plasma
M	=Mach number
V_{af}	= airflow velocity
P_0	= stagnation pressure
P_{st}	= static pressure
T_g	= gas temperature
T_R	=rotation temperature
Sh	= Strouchal's number
α	=attack angle of actuator

I. Introduction

Surface discharge flow separation control is a task of a great interest today.

It is well known that efficiency of flow control near a body by a chord-wise dielectric barrier discharge (DBD) is decreased considerably at high airflow velocity (V_{af}>10m/s). The reason is physical limitations on the DBD induced momentum, while pressure gradients in the external flow increases with velocity increase [3,4].

However, attempts are recently made to use the surface discharges for boundary layer control, referring to other mechanisms of discharge –flow action.

Several works were devoted to flow separation control at velocities up to 240 m/s by high-current nanosecond discharges [5,6]. Authors argue the discharge in these cases acts rather as a pulsing heat release source than a flow momentum generator.

The problem of a boundary layer flow turbulization and generation of a longitudinal vorticity by means of DBD was studied in [7].

Surface high frequency discharge was proposed in [8,9] for separation control on a flat plate and cone drag reduction. It was shown, that at definite angles of attack and discharge regimes, significant change in pressure distribution behind the plate can be achieved.

Main goal of our current work is to study the separation process and wake structure behind the bluff body with transversal SHFD, operating near the separation point.

Cylinder was chosen for this study as an aerodynamic body with well-known flow structure in the wake for a variety of regimes [10]. Low-speed flow around the cylinder with the DBD discharge actuators was studied in [11-13]. Wake structure at pulse-periodic discharge operation was studied in [11], actuator orientation effects – in [12]. In [13], vortex shedding was synchronized along the length by means of co-flow DBD. However, all authors implies that it is ionic wind, induced by the discharge, that leads to effects obtained.

In the works [14-16], a keen study of the cylinder wake excitation by a single DBD pulse initiated at different phases of natural shedding

cycle was performed. Measurements were performed by a high-speed PIV system, with simultaneous measurements of drag and lift force oscillations. Most dramatic changes were obtained for discharge initiation at the moment of separation point upstream motion. It was obtained, that vortex shedding can be disturbed for time period comparable to 6 cycles. This led to a 200% lift oscillations amplitude increase. Authors argued their results from the position of momentum addition, however, they obtained a closed separation region at the discharge location.

Since the flow separation control around a wing is of significant practical importance, it was widely studied up to date. However, most authors, both working with conventional and with nanosecond DBD at velocities up to 20 meters per second, report an effective stall control at large attack angles at discharge positioned near the leading edge of the model. Several studies, concerning flap aerodynamics improvement by conventional DBD can be found in [17-19]. It is also known, that at $Re<10^5$, leading-edge stall mainly takes place due to laminar boundary layer separation. Boundary layer turbulization leads to separation delay due to a higher stability of the turbulent boundary layer. It is shown, that nanosecond discharge operation near the leading edge leads to significant (up to $2\text{-}4^0$) stall delay at high attack angles.

Unsteady forcing seems to be an essential feature of any DBD, therefore several studies were focused on forcing frequency optimization. Starikovskii et. al. [20] reported a maximum efficiency of nanosecond discharge at Sh~1, Samimi et. al. [17] found frequency ranges for conventional discharge forcing. Furthermore, in vortex street formation along the shear layer behind the flap was obtained, synchronized to the actuator forcing.

In spite of the wide use of the surface DBD discharges of any frequency range in the aerodynamic studies, up to the moment there is no clear understanding of the prevailing mechanism of the discharge action, especially at high oncoming flow velocities.

II. Experimental setup

Low-velocity (<20m/s) experiments were cared in the aerodynamic channel with 100x100x300 test section, operating in a continuous regime. Flow velocity can be changed by controlling the blower motor. Large-scale flow turbulence after the blower was quenched by honeycomb. However, turbulence level remained high enough (~several percents).

For high-speed experiments (<140 m/s), aerodynamic system was supplied from high pressure tanks. Experiment duration was about 5 - 30s, depending on the airflow velocity.

Cylindrical model (fig.1a) was manufactured of a 40mm diameter quartz tube. Dielectric thickness was ~2mm. Discharge was organized in a spanwise direction. Electrodes were manufactured of aluminum foil 200 μm thickness, the inner one was covered by epoxy or silicon resin to avoid arcing in the discharge gap.

NACA 23012 airfoil model 8cm x 10cm (chord x span) was manufactured from Nylon-6. Model was positioned in the test section at a desirable attack angle using rotating windows. The electrodes were arranged near the model's leading edge (fig.1b), with wiring connected to the mounting points of the model. Flow blockage was up to 30% at 20^0 attack angle and 10% at 0^0 attack angle.

Discharge was created by "RF switch" generator, loaded with the model through the air-core resonant transformer with resonance frequency ~350 kHz. Output voltage measured was up to 20 kV, the peak discharge power- 1 kW. The generator was operating in the pulse-periodic regime, creating RF pulses with 30-100 us duration and repetition frequency up to 10 kHz. Typical RF pulse is shown on fig.2. Rise time was about 5 - 10 us. Pulse shape changed with discharge power due to resonant frequency shift during the pulse. These changes weren't controlled in the experiments.

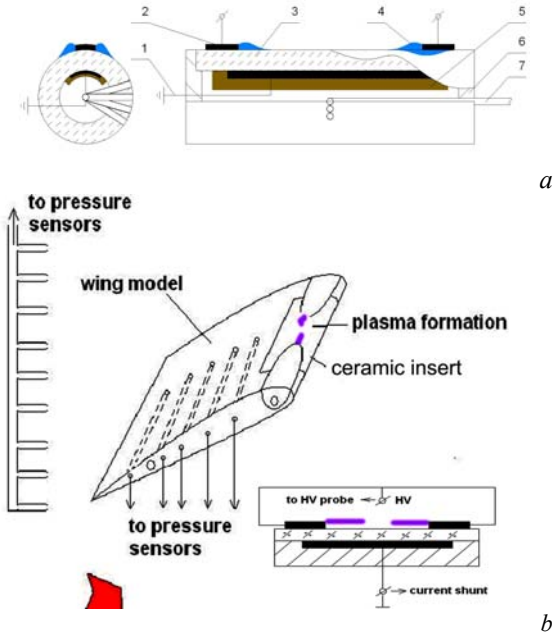

Fig.1. *Model schemes. 1-ground lead, 2-exposed electrode, 3- quartz body, 4-discharge, 5- epoxy layer, 6-pressure tubes, 7- fastening bolt.*

Discharge voltage was measured with Tektronix P6014A HV probe, discharge current was measured in the ground lead with Tektronix AC current shunt. Stray current was negligible due to significant discharge capacity. Electrical power

input was calculated by digital multiplication of current and voltage signals via TDS 2014B oscilloscope with ~10% error. Alternatively, energy release over the pulse was measured by an integration on the capacity

Wake structure was studied by an array of 14 0.7mm Pitot tubes, positioned 0.5-5 diameters downstream from the model, in the middle of its span. The pressure was measured by a 16-channel pressure scanner Esterline 9116 with 500 Hz time resolution.

Shadow pictures of the flow were taken by excimer KrF laser (248nm) with 20ns pulse length. Direct shadow method with a divergent beam was used. Pictures were acquired by digital camera from the white-sheet paper used as wavelength convertor (UV to blue).

PIV data were acquired by a LaVision PIV system, based on 200mJ NdYAG laser and a 2048x2048 pix camera. Frames were acquired at frame rate ~7Hz, with further averaging of 50-140 images. Accuracy of a single measurement was about 2% (for 20 m/s), while averaging error was several times higher, velocity field resolution was about 1.5mm.

Diagnostic equipment was synchronized with the discharge pulses through the frequency divider and delay generator, allowing phase-locked acquisition of data.

Flow smoke visualization was also performed. Ammoniac smoke was injected in the rear point of the cylinder, tangentially to model's surface.

III. Results and discussion

A. Circular cylinder.

As described earlier, SHFD ignition on the cylinder surface can impact the separation process on the cylinder surface, charge the properties of the flow in the wake and reduce aerodynamic drag [2,21-23].

PIV images of the near wake behind the cylinder are presented on fig2. In this experiment discharge was operating on the frequency 130Hz. Phase-locked imaging was performed with a 1ms step. Discharge was located at ~80deg, with discharge channels propagating counter wise versa along the axis. Consequent stages of flow reaction on the discharge pulse can be described as follows.

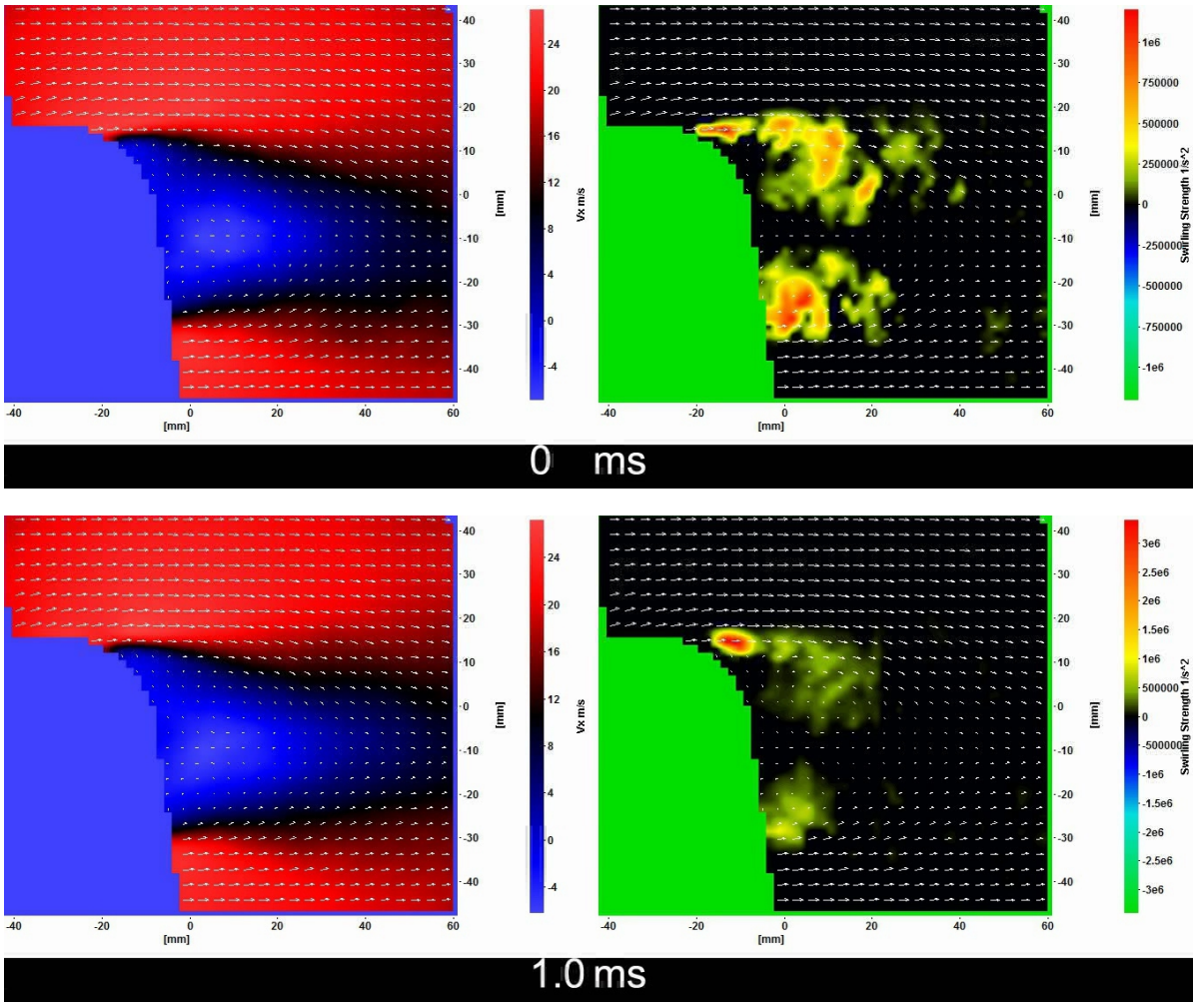

Fig.2. *Velocity x-component (a) and vorticity (b) distributions in the wake behind a cylinder. V=20m/s, Re=60k, Sh=0.3*

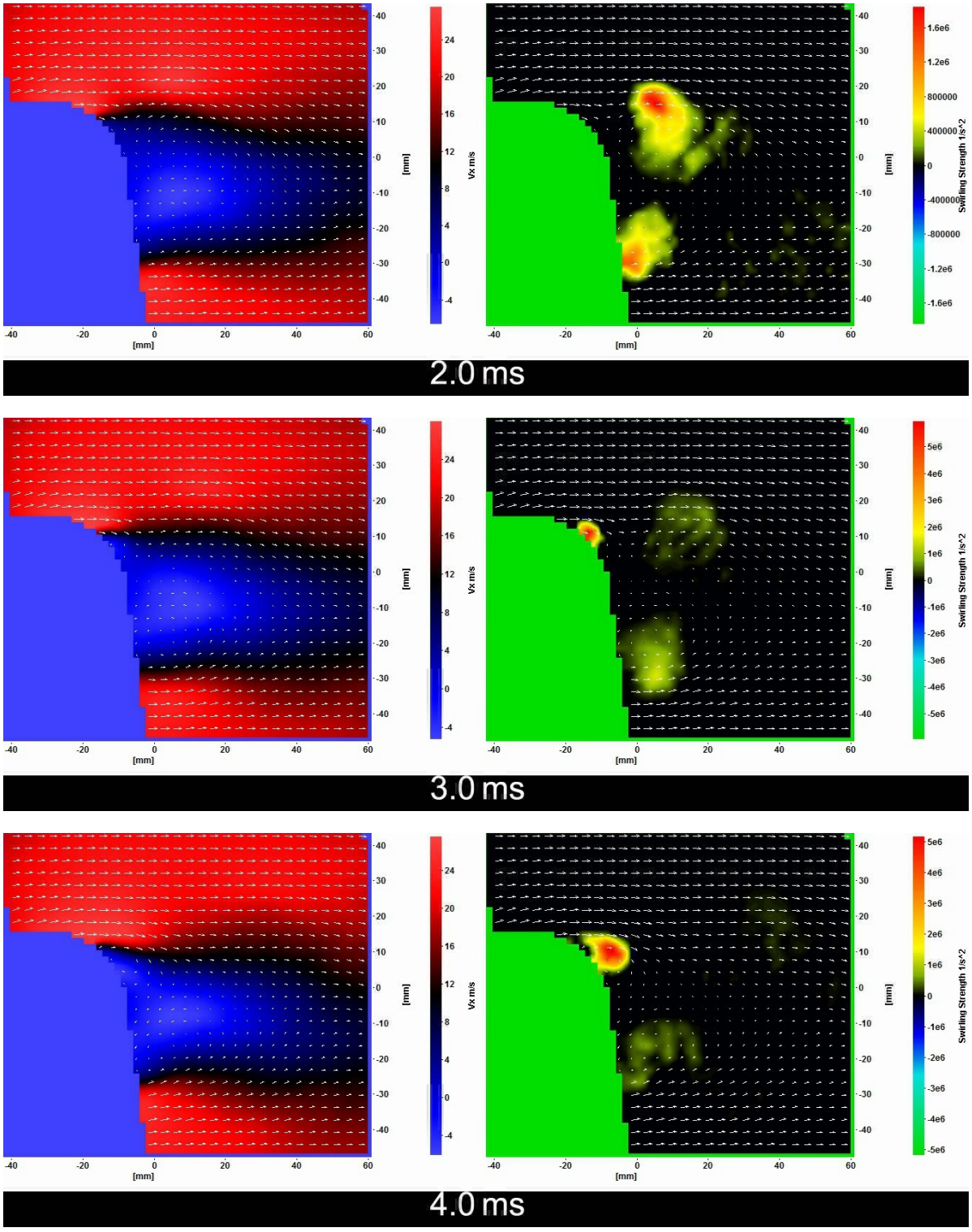

Fig.2 (Cont.). *Velocity x-component (a) and vorticity (b) distributions in the wake behind a cylinder. V=20m/s, Re=60k, Sh=0.3*

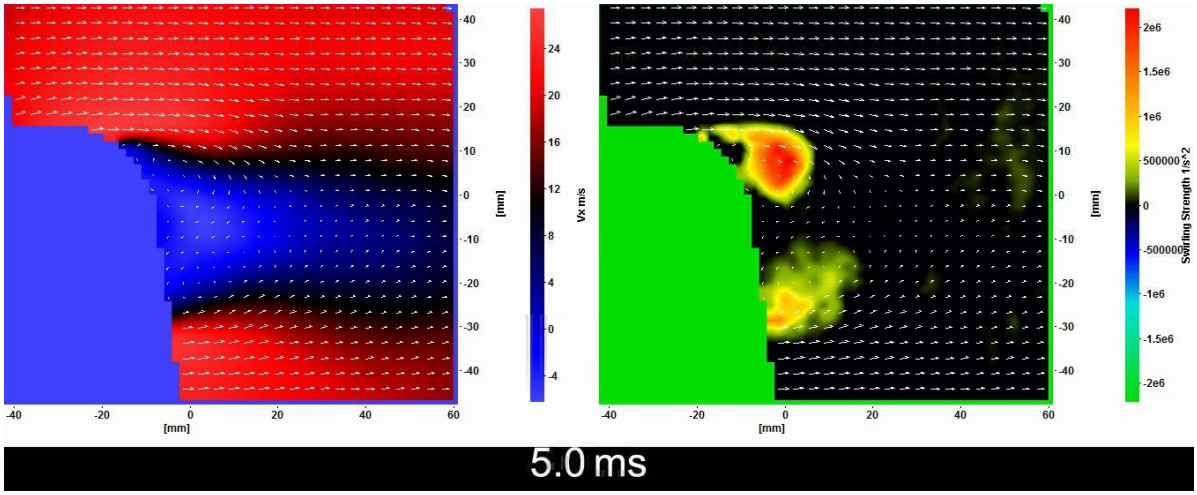

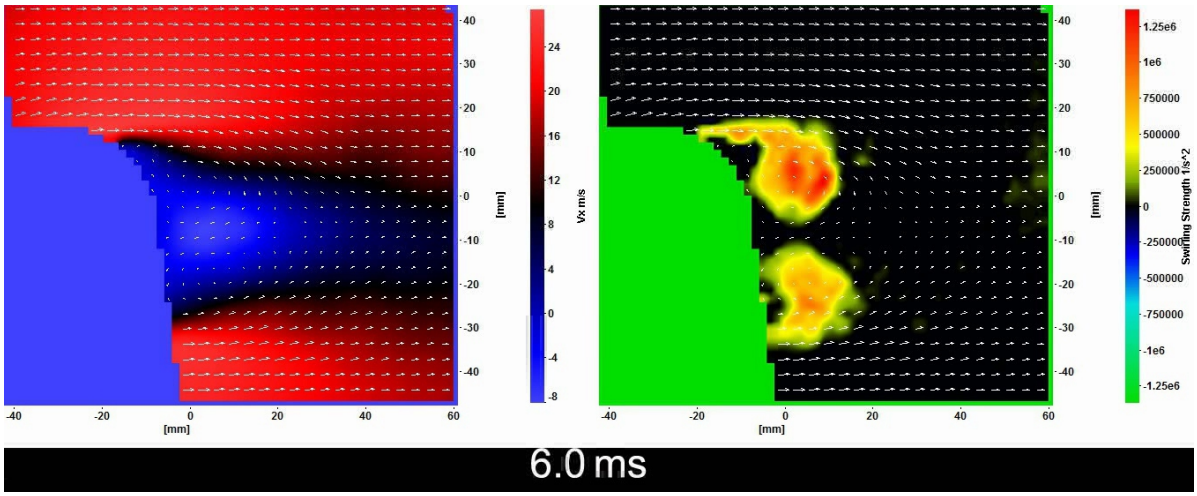

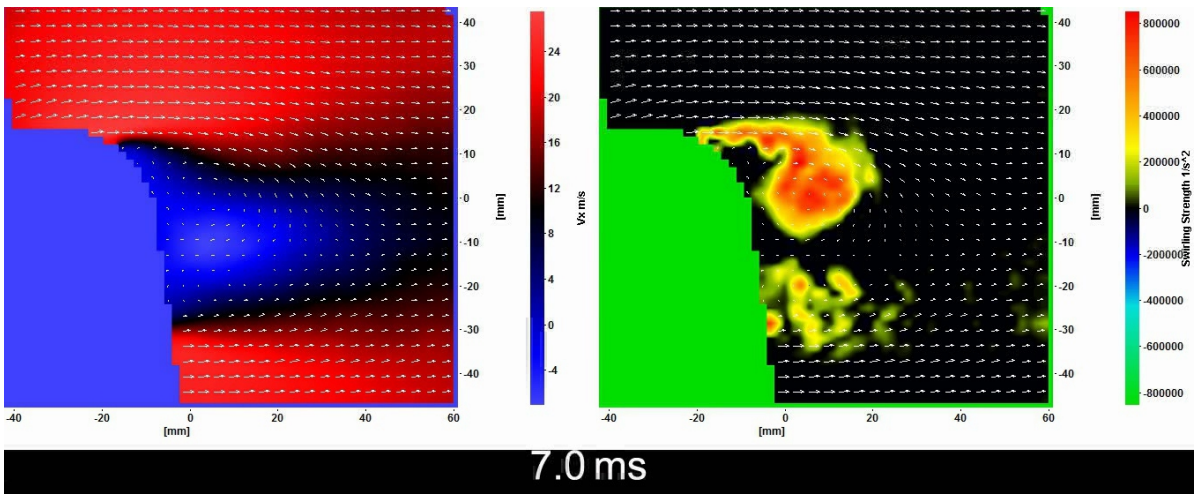

Fig.2 (Cont.). *Velocity x-component (a) and vorticity (b) distributions in the wake behind a cylinder. V=20m/s, Re=60k, Sh=0.3*

First, at t~1ms, a kink at the shear layer is formed. This kink cuts off the main vortex being shed from the source of vorticity. During this process, the separation point moves downstream and reaches the position ~140 deg at t~2ms from the pulse moment. At t~3ms, a new vortex is formed, and grows during the rest of a period. One can see smaller vortex structures in a shear layer, that further run into main one.

Special study was performed in terms to separate the influence of the ions-induced velocity and thermal influence of the discharge. PIV data were acquired for three different discharge propagation directions: co-flow, counter-flow and spanwise. No qualitative difference in vortex shedding process was obtained for these cases. In both cases, the orientation of vorticity vector in the vortex core correspond to the one in the boundary layer.

Flow visualization images are shown for comparison on fig.3. One can see large-scale vortices creation in the near wake, locked to the discharge pulse.

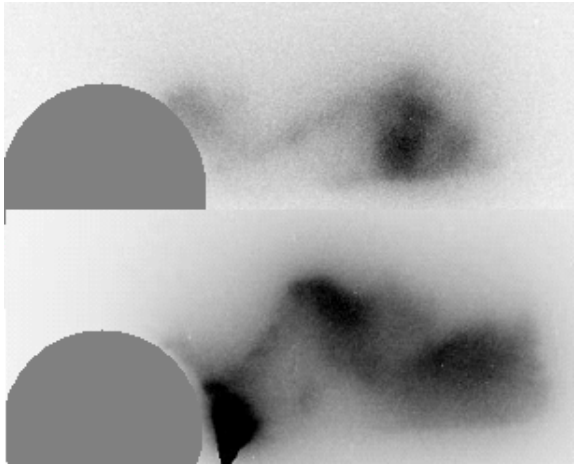

Fig3. *Flow patterns at different delays after the discharge pulse 1-300us, 2-600us. V=20м/с, F_m=1kHz (Sh~2).*

B. Leading edge separation on a wing model

Leading edge separation on a wing model was studied at V=20m/s in our previous work. However, flow velocities of a practical interest are significantly higher. Therefore, we extended our study to the range Re<4x10^4 and V<140m/s. Experiments were cared for two attack angles: 11^0 and 15°.

Drag decrease at both attack angles was obtained up to the oncoming flow velocities V<80m/s. Drag decrease due to separation point shift up to 10-50% was obtained at discharge on. At flow velocities 80<V<140m/s, model drag is decreased only at supercritical attack angles $\alpha>\alpha^*$. At AoA=11° and V=140m/s the drag increases at discharge on. Drag coefficient based on a total pressure losses is plotted at fig.4 vs Re number. At Re~400k an abrupt decrease of the drag coefficient in a reference case is obtained. This should happen because of flow turbulization prior to separation point.

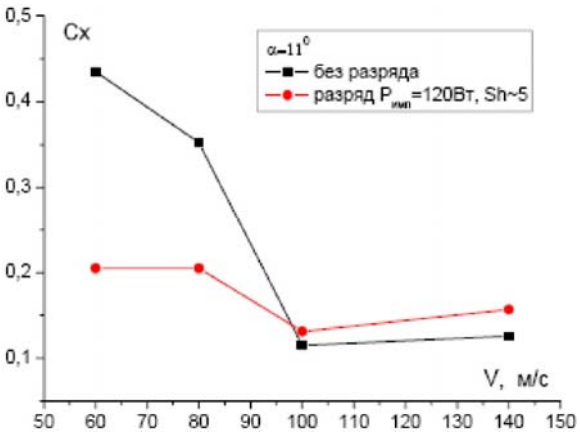

Fig.4. *Drag coefficient of the airfoil model vs flow velocity.*

IV. Conclusions

- PIV visualization images were obtained for the flow around a cylinder at Re~60k.
- Vortex triggering is obtained in the near wake. After the discharge, a separation point shift occurs, followed with the new vortex formation.
- Vortex formation length and diameter are reduced.
- SHFD at the wing leading edge is capable of stall control up to Re<400k, i.e. up to boundary layer transition.

References

1. V.A. Bityurin, A.N. Bocharov, A.I. Klimov, I.A. Moralev, and B.N. Tolkunov, "Surface HF Plasma Actuator in Airflow," *40th AIAA Plasmadynamics and Lasers Conference 22 - 25 June 2009, San Antonio, Texas*, 2009, pp. AIAA 2009-4073.
2. A.I. Klimov, V.A. Bityurin, I.A. Moralev, B.N. Tolkunov, K. Zhirnov, and V. Kutlaliev, "Surface HF Plasma Aerodynamic Actuator," *46th AIAA Aerospace Sciences Meeting and Exhibit 7 - 10 January 2008, Reno, Nevada*, 2008, pp. AIAA 2008-1411.
3. A.V. Likhanskii, M.N. Shneider, D.F. Opaits, R.B. Miles, and S.O. Macheret, "Limitations of the DBD effects on the external flow," *48th AIAA Aerospace Sciences Meeting Including the New Horizons Forum and Aerospace Exposition 4 - 7 January 2010, Orlando, Florida*, 2010.
4. D.F. Opaits, M.R. Edwards, S.H. Zaidi, M.N.

Shneider, R.B. Miles, and S.O. Macheret, "Surface plasma induced wall jets," *48th AIAA Aerospace Sciences Meeting Including the New Horizons Forum and Aerospace Exposition 4 - 7 January 2010, Orlando, Florida*, 2010.
5. G. Correale, I.B. Popov, A.E. Rakitin, A.Y. Starikovskiy, S.J. Hulshoff, and L.L.M. Veldhuis, "Flow Separation Control on Airfoil With Pulsed Nanosecond Discharge Actuator," *49th AIAA Aerospace Sciences Meeting including the New Horizons Forum and Aerospace Exposition. 4 - 7 January 2011. Orlando, Florida.*, 2011.
6. D.V. Roupassov, a a Nikipelov, M.M. Nudnova, and a Y. Starikovskii, "Flow Separation Control by Plasma Actuator with Nanosecond Pulsed-Periodic Discharge," *AIAA Journal*, vol. 47, Jan. 2009, pp. 168-185.
7. R.E. Hanson, P. Lavoie, and A.M. Naguib, "Effect of Plasma Actuator Excitation for Controlling Bypass Transition in Boundary Layers," *48th AIAA Aerospace Sciences Meeting Including the New Horizons Forum and Aerospace Exposition 4 - 7 January 2010, Orlando, Florida*, 2010, pp. AIAA 2010-1091.
8. V.A. Bityurin, A.N. Bocharov, A.I. Klimov, I.A. Moralev, and B.N. Tolkunov, "Surface HF Plasma Actuator in Airflow," *40th AIAA Plasmadynamics and Lasers Conference 22 - 25 June 2009, San Antonio, Texas*, 2009, pp. AIAA 2009-4073.
9. A.I. Klimov, V.A. Bityurin, I.A. Moralev, B.N. Tolkunov, K. Zhirnov, and V. Kutlaliev, "Surface HF Plasma Aerodynamic Actuator," *46th AIAA Aerospace Sciences Meeting and Exhibit 7 - 10 January 2008, Reno, Nevada*, 2008, pp. AIAA 2008-1411.
10. C.H.K. Williamson, "VORTEX DYNAMICS IN THE CYLINDER WAKE," *New York*, 1996.
11. F.O. Thomas, A. Kozlov, and T.C. Corke, "Plasma Actuators for Cylinder Flow Control and Noise Reduction," *AIAA Journal*, vol. 46, Aug. 2008, pp. 1921-1931.
12. S. Yamada, S. Koui, I. Hitoshi, H. Shinji, and M. Motosuke, "Flow Behavior behind a Circular Cylinder by DBD Plasma Actuators in Low Reynolds Number," *48th AIAA Aerospace Sciences Meeting Including the New Horizons Forum and Aerospace Exposition 4 - 7 January 2010, Orlando, Florida*, 2010, pp. AIAA 2010-549.
13. T. McLaughlin, M. Munska, J. Vaeth, and T. Dauwalte, "Plasma-Based Actuators for Cylinder Wake Vortex Control," *2nd AIAA Flow Control Conference, Portland, Oregon, June 28-1, 2004*, 2004, pp. AIAA-2004-2129.
14. T.N. Jukes and K.-so Choi, "Long Lasting Modifications to Vortex Shedding Using a Short Plasma Excitation," *Physical Review Letters*, vol. 102, 2009, p. 254501.
15. T.N. Jukes and K.-so Choi, "Flow control around a circular cylinder using pulsed dielectric barrier discharge surface plasma," *Physics of Fluids*, vol. 21, 2009, p. 084103.
16. T.N. Jukes and K.-so Choi, "Control of unsteady flow separation over a circular cylinder using dielectric-barrier-discharge surface plasma," *Physics of Fluids*, vol. 21, 2009, p. 094106.
17. J. Little and M. Samimy, "High-Lift Airfoil Separation with Dielectric Barrier Discharge Plasma Actuation," *AIAA Journal*, vol. 48, Dec. 2010, pp. 2884-2898.
18. J. Little and M. Samimy, "Control of Separation from the Flap of a High-Lift Airfoil with DBD Plasma Actuation," *48th AIAA Aerospace Sciences Meeting Including the New Horizons Forum and Aerospace Exposition 4 - 7 January 2010, Orlando, Florida*, 2010, pp. AIAA 2010-1088.
19. J. Little *and* M. Samimy, "Control of Separation from the Flap of a High-Lift Airfoil with DBD Plasma Actuation," *48th AIAA Aerospace Sciences Meeting Including the New Horizons Forum and Aerospace Exposition 4 - 7 January 2010, Orlando, Florida*, 2010, pp. AIAA 2010-1088.
20. D.V. *Roupassov*, a a Nikipelov, M.M. Nudnova, and a Y. Starikovskii, "Flow Separation Control by Plasma Actuator with Nanosecond Pulsed-Periodic Discharge," *47th AIAA Aerospace Sciences Meeting Including The New Horizons Forum and Aerospace Exposition 5 - 8 January 2009, Orlando, Florida*, 2009, pp. 168-185.
21. A.I. Klimov, I.A. Moralev, V.A. Bityurin, P.N. Kazansky, and D.A. Chertov, "Flow Around Wing Model with a Surface HF Discharge," *49th AIAA Aerospace Sciences Meeting including the New Horizons Forum and Aerospace Exposition. 4 - 7 January 2011. Orlando, Florida.*, 2011.
22. I.A. Moralev, V.A. Bityurin, P.N. Kasansky, A.I. Klimov, and D.A. Chertov, "Flow Control around Wing Model by HF DBD Discharge," *The 9th Iternational Workshop on Magneto-plasma Aerodynamics*, 2010.
23. I.A. Moralev, V.A. Bityurin, P.N. Kasansky, A.I. Klimov, and D.A. Chertov, "Flow Control around Cylinder by HF DBD Discharge," *The 9th Iternational Workshop on Magneto-plasma Aerodynamics*, 2010, pp. 7-11.

1.3. PLASMA DESTRUCTION OF TOLUENE IMPURITIES IN N_2: O_2 MIXTURE BY PULSE-PERIODICAL DISCHARGE

A.N. Trushkin, I.V. Kochetov
State Research Center of Russian Federation, Troitsk Institute for Innovation and Thermonuclear Research (TRINITI), Troitsk, Moscow region, Russia

Abstract. The kinetic model of toluene destruction in a nonequilibrium low-temperature plasma of a pulsed-periodic discharge in a gas mixture of N_2: O_2 are presented. The results of numerical simulation of plasmachemical processes of toluene destruction are presented, the main mechanisms of toluene removal at various oxygen concentrations are established, the primary intermediate and final products of toluene destruction are identified. It is shown that metastable electronic - excited nitrogen molecule $N_2(A^3\Sigma^+_u)$ and $N_2(a`^1\Sigma^-_u)$ have an essential contribution to the C_7H_8 removal in the N_2: O_2 gas mixture as a result of direct interaction with C_7H_8 molecules and due to their contribution to the production of the oxygen atoms and hydroxyl radical OH. Dynamics of plasmachemical toluene destruction was analyzed, the existence of three successive stages in this process was revealed. These stages differ from each other as the time duration and intensity of the C_7H_8 destruction. Different basic mechanism of toluene destruction corresponds to each time stage. A comparison between a numerical results and experimental data as on the degree of toluene destruction and on the composition and concentration of intermediate and final products of C_7H_8 decomposition was conducted. There is a reasonable correspondence each other.

Introduction

Toluene vapors (C_7H_8) are one of the most widespread air pollutants of industrial premises in the textile and chemical industry, which have a negative impact on human health. These vapors enter into the atmosphere through the air emissions and have a significant contribution to environmental pollution. A characteristic feature of these air flows is the relatively low concentrations of toluene vapor, which, however, several orders of magnitude greater than the health standards established. In this case, the use of traditional methods of gas purification (thermal incineration, catalytic oxidation, the use of absorption and adsorption methods) is ineffective and economically unprofitable. This situation stimulates the search for new, more effective methods of purification of gas emissions with low pollutant concentration. Non-thermal plasma methods of gas purification are currently investigated actively in all developed countries. These methods are based on the creation of the reactive and environmentally friendly particles at high concentrations in polluted gas using a gas discharge without significant heating of the gas flow treated. Chemically active particles produced are then reacted with the pollutant molecules and produce destruction of the contaminants. The toluene vapor is a very popular subject for laboratory research, which tested the effectiveness of the non-thermal plasma technology for air purification from pollutants, because a toluene molecules are the most difficult to destroy. However, it should be noted that despite the large number of experimental studies on the toluene destruction the kinetics of plasma-chemical destruction of C_7H_8 is currently far from the necessary level, which is required to determine the optimal conditions for the cleaning process. The results of numerical simulation of plasmachemical processes of toluene destruction are presented, the main mechanisms of toluene removal are established, the primary intermediate and final products of toluene destruction are identified in this paper.

Model description

The model developed consists of two interconnected units: discharge stage, describing the generation of nonequilibrium low-temperature plasma, reactive particles production and plasma-chemical processes in an external electric field and postdischarge stage, in which the plasma-chemical processes occur in the absence of an electric field. Discharge stage is modeled by a periodic sequence of voltage pulses, the repetition period is much greater than their duration. Gas discharge in molecular gases at atmospheric pressure is often highly nonuniform in space and nonstationary in time plasma formation (streamer, spark). In this case, the complete self-consistent description of the discharge should be based on the nonstationary three-dimensional model of discharge and chemical processes. The streamer propagation should be described together with plasma chemical reactions in its channel in this model. A large number of reactions occurs in a nonequilibrium low-temperature plasma at atmospheric pressure depends on the plasma gas composition. Comprehensive description of the plasma reactor, taking into account both of the above factors

(inhomogeneity and nonstationarity of plasma and a large number of plasma chemical reactions) is currently not possible, and therefore the numerical simulations of real plasma devices have been made under various simplifying assumptions. In this paper numerical calculations were performed for the experimental conditions of [1], which studied the toluene removal in an unipolar pulse-periodic barrier discharge in a N_2: O_2 gas mixture at atmospheric pressure. The choice of [1] as a basis for verification of the plasma-chemical model developed was due to the fact that in this paper in addition to determining of the toluene decomposition degree was recorded a number of intermediate by-products of toluene destruction. In the experiment the repetition rate of unipolar voltage pulses ranged from f = 0-200 Hz. Current pulse duration at half amplitude was equal to 50 ns. Gas energy density was varied by changing the current pulse repetition frequency at a fixed gas flow rate and was in the range of Q = 0 – 400 J/L. The oxygen content in the gas mixture was varied within 0-10%. Experiments were performed at two initial toluene concentrations: 100 and 400 ppm. In [1] does not describe the discharge spatial structure, but it is well known from the literature [2] that the dielectric barrier discharge (DBD) in a N_2: O_2 gas mixture transits from a spatially uniform mode to the multi-channel (microdischarge) mode at excess oxygen concentration ~ 450 ppm. Kinetic model of toluene destruction in pure nitrogen, the results of numerical calculations with using this model and their comparison with experimental data were presented in our previous study [3]. In this paper, this model is included as part of the mechanism of toluene conversion in a N_2: O_2 gas mixture. Typical radius of an individual microdischarge at atmospheric pressure is equal to 100 μm, the distance between the individual microdischarges in electrode gap filled is equal of 1 mm. A rough estimations show that under the experimental conditions chosen the lifetime of free radicals, electronically excited atoms and molecules and other reactive particles produced in the discharge is less than 100 μs. The exception is ozone, which has no appreciable effect on the toluene removal due to the low values of the reactions rate coefficients with toluene and the intermediate by - products toluene destruction, $k = 10^{-18} - 10^{-22}$ cm^3 s^{-1}. During this time the active particles produced in the microdischarge do not have time to diffuse significantly from the MD channel into the surrounding gas and plasma-chemical reactions take place in the MD channel mainly. The energy deposition localized in narrow plasma channels leads to a high concentrations of chemically active species and, in principle, can lead to nonlinear radical termination reactions. Nonlinear radical termination reactions are undesirable for plasma gas processing as it leads to an increase in energy costs and reduced energy efficiency of the plasma gas treatment. However, a rough estimations using typical concentrations of O, H, N atoms, OH radicals and electronically excited N_2 and O_2 molecules in the microdischarge channel show that the nonlinear radical termination is small compared to radical loss in reactions with toluene at the toluene concentration equal to 100 and 400 ppm.

In modeling of the plasmachemical processes of toluene destruction was assumed that gas portion is exposed to a sequence of current pulses during reactor residence time. The number of current pulses, which affects the gas portion, depends on its repetition frequency. Activated gas medium of each microdischarge has time to react during the time between current pulses (t> 5 ms) and uniformly mixed due to the diffusion with neighboring microdischarges. Thus, a homogeneous gas mixture with composition changed will be in the in the whole reactor volume by the beginning of the next current pulse. Then this gas mixture is exposed to the next current pulse, etc. A homogeneous model to describe of the discharge development and the active particles generation in a N_2: O_2 gas mixture was used in this paper. This model was developed on basis of known models of nonequilibrium plasma in atmospheric air [4, 5] and includes more than 100 elementary processes involving electrons, positive and negative ions, radicals, molecules and atoms in the ground and excited states. The excitation of rotational, vibrational and electronic levels, as well as ionization and dissociation of N_2, O_2 and H_2O molecules by electron impact (H_2O molecules in the gas mixture are the result of plasma chemical reactions) is taken into account in the model. Electrons loss are due to the electron-ion recombination and attachment (dissociative and three body) to electronegative molecules. The results of experimental studies in recent years [6-8] indicate that the main contribution to active particles production in pulsed corona and dielectric barrier discharge does not occur in the streamer head but in the secondary streamer channel. In this channel is carried out the main energy input in gas at reduced electric field E / N = 70 -100 Td. In this paper the kinetic Boltzmann equation for the function of the electron energy distribution was solved numerically at a reduced electric field E / N = 70 -100 Td to determine the rate coefficients of processes occurring in the discharge by collisions with electrons. These processes lead to the chemically active species production.

The kinetic model of plasma-chemical toluene removal during the pause between current pulses (post-discharge stage) includes more than 300 reactions involving 90 components, consisting of both initial molecules and by- products molecules produced in discharge. Radicals, atoms and molecules of nitrogen and oxygen in the ground and excited states, the products of toluene

decomposition and oxidation are taken into account. The reactions involved in plasma-chemical process of toluene removing and their rate coefficients were chosen using published data. A significant number of reactions and their rate coefficients have been taken in accordance with the recommendations of NIST [9]. It should be noted that some stages in the plasma chemical toluene decomposition to the final products (CO_2 and H_2O) are currently hypothetical and are the subject of heated discussions. This mainly concerns the decay stages of toluene decomposition products containing aromatic ring. The dicarbonyl mechanism of the aromatic peroxide complex decay was selected in this study, favored by most researchers [10, 11]. Numerical calculations were performed using the Chemical Workbench code [12, 13]. This code allows the simultaneous solution of equations of chemical and ion-molecular kinetics, the kinetic Boltzmann equation for the function of electron energy distribution and the equation for the translational gas temperature. Cross sections for electron interaction with N_2 and O_2 molecules were taken from [14, 15] respectively.

Numerical simulation results and comparison with experimental data

Fig. 1 shows a comparison of numerical results with experimental data [1] on the degree of toluene removal depending on the energy density in the N_2: O_2 gas mixture at the three initial oxygen concentration [O_2] = 0% (pure nitrogen), 1.5% and 10% and initial toluene concentration equal to 400 ppm.

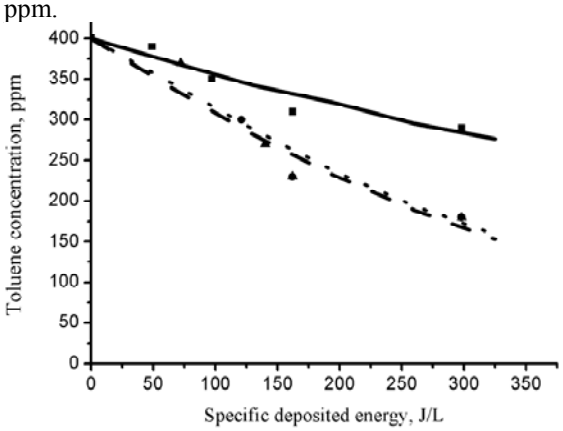

Fig. 1. *Dependence of the toluene concentration at the plasma reactor exit vs the specific energy for various oxygen contents in the gas mixture. Initial toluene concentration [C_7H_8] $_0$ = 400 ppm, gas temperature T = 323 K. Markers - experiment [1]:* ■- 0% O_2, ●-1.5% O_2, ▲- 10% O_2; line - modeling results.

It is seen that the simulation results reproduce the experimental data with good accuracy. It should be noted, however, that the value of reduced electric field in the secondary streamer channel should be increased from 70 Td (pure nitrogen and [O_2] = 1.5%) to 80 Td at [O_2] = 10% to achieve agreement between simulation results and experimental data on the degree of toluene removal. The main generation of the chemically active species is in this channel according to our model. The oxygen presence in the gas mixture is significantly reduced the energy cost of one toluene molecule removal from 1120 eV / molecule in pure nitrogen to 350 eV / molecule at [O_2] = 1.5% and 10%.

In Fig. 2 (a-e) are presented the temporal dynamics of the main channels of the toluene destruction (a-c), the contribution of each channel in the total number of toluene removed (d) and the dynamics of the C_7H_8 concentration (e) in the post-discharge stage of the second current pulse in the N_2: O_2 gas mixture at the oxygen concentration [O_2] = 1.5%. It is evident that there are several characteristic stages in the toluene destruction dynamics. These stages differ from each other as the time duration and C_7H_8 destruction intensity. The analysis of Fig. 2 (a-e) points out that various basic mechanisms of toluene destruction correspond to each time-stage.

The most fast C_7H_8 removal mechanism acting on the characteristic times $<2\times10^{-6}$ s due to the interaction of toluene molecules with metastable nitrogen molecules N_2 ($A^3\Sigma$) and N_2 ($a'^1\Sigma$):

$$N_2(A) + C_6H_5CH_3 \rightarrow C_6H_5 + CH_3 + N_2 \quad (1)$$

$$N_2(A) + C_6H_5CH_3 \rightarrow C_6H_5CH_2 + H + N_2 \quad (2)$$

$$N_2(A) + C_6H_5CH_3 \rightarrow C_6H_4CH_3 + H + N_2 \quad (3)$$

$$N_2(a') + C_6H_5CH_3 \rightarrow C_5H_6 + C_2H_2 + N_2 \quad (4)$$

This channel contributed about 22% of the total C_7H_8 removal at the oxygen concentration [O_2] = 1.5% in gas mixture.

The basic mechanisms of toluene destruction due to the reactions of toluene molecules with oxygen atoms and hydroxyl radicals OH at times of 2×10^{-6} - 10^{-3} s:

$$O + C_6H_5CH_3 \rightarrow C_6H_5CH_2 + OH \quad (5)$$

$$OH + C_6H_5CH_3 + N_2 \rightarrow C_6H_5CH_3OH + N_2 \quad (6)$$

$$OH + C_6H_5CH_3 \rightarrow C_6H_5CH_2 + H_2O \quad (7)$$

The reactions (5-7) rates are much less than the reactions rates of C_7H_8 molecules with $N_2(A^3\Sigma^+_u)$ and $N_2(a`^1\Sigma^-_u)$ molecules, but the long duration of this stage leads to the fact that the number of toluene removed for $2 \cdot 10^{-6}$ - 10^{-3} s stage reaches of 27% for channel (5) and 32% for the channels (6,7).

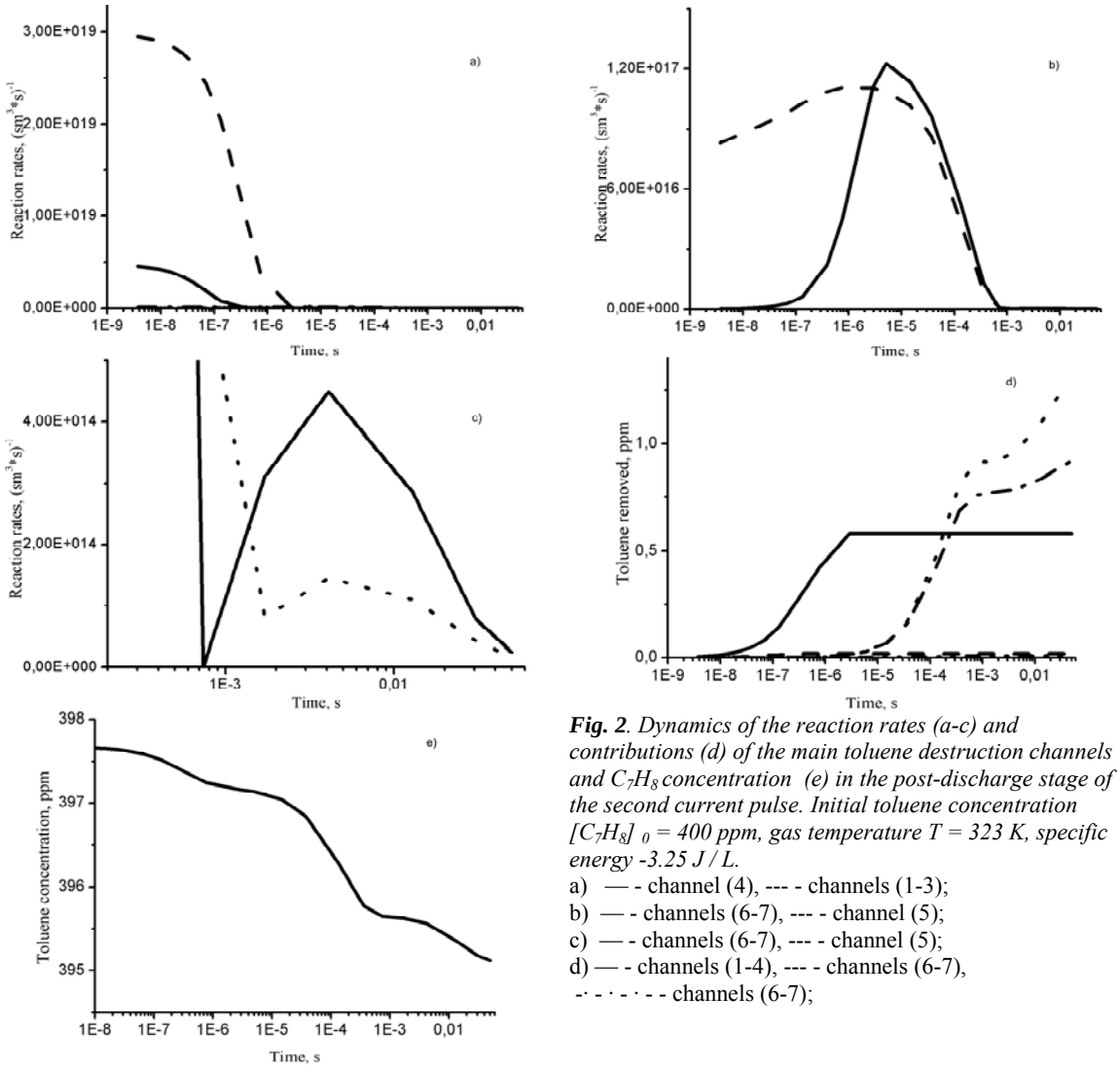

***Fig. 2**. Dynamics of the reaction rates (a-c) and contributions (d) of the main toluene destruction channels and C_7H_8 concentration (e) in the post-discharge stage of the second current pulse. Initial toluene concentration $[C_7H_8]_0$ = 400 ppm, gas temperature T = 323 K, specific energy -3.25 J / L.*

a) — - channel (4), --- - channels (1-3);
b) — - channels (6-7), --- - channel (5);
c) — - channels (6-7), --- - channel (5);
d) — - channels (1-4), --- - channels (6-7),
-· - · - · - - channels (6-7);

The main channel of the toluene destruction is due mainly to the interaction of C_7H_8 molecules with the hydroxyl radical OH at later times 10^{-3} - 5 • 10^{-2} s. The intensity of this channel is even lower than in the previous stage due to low OH concentration, but the long duration of its operation leads to ~ 13% of the total removal of C_7H_8 The channel (5) leads to 6% toluene destruction at this stage.

In Fig. 3 are shown the results of numerical simulations that demonstrate the contribution of the main channels of the toluene destruction depending on the oxygen concentration $[O_2]$ in the gas mixture at the second current pulse.

The results presented show that the metastable electronically excited nitrogen molecule $N_2(A^3\Sigma^+_u)$ and $N_2(a`^1\Sigma^-_u)$ have a significant contribution to the direct toluene destruction at the content of $[O_2]$ <5%. In addition, analysis of the production channels of the O atoms and the hydroxyl radical OH which have a main contribution to the C_7H_8 removal at $[O_2]$> 0.05% shows that the main production of these active particles at $[O_2]$ <5% occurs in the post-discharge stage involving $N_2(A^3\Sigma^+_u)$ and $N_2(a`^1\Sigma^-_u)$.

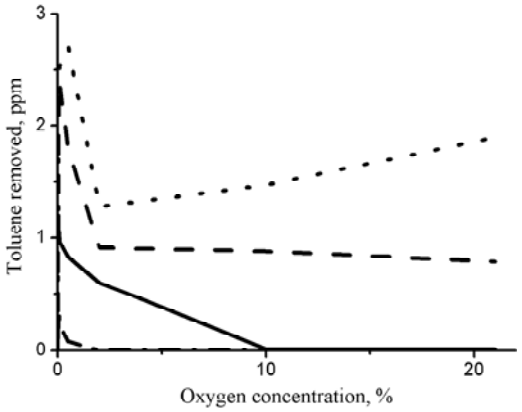

***Fig. 3**.Ccontribution of the main toluene destruction channels in the post-discharge stage of the second current pulse depending on the O_2 concentration. Initial toluene concentration $[C_7H_8]_0$ = 400 ppm, gas temperature T = 323 K, specific energy -3.25 J / L.*

— - N_2, - - - - - O, ····· - OH, — ·- H

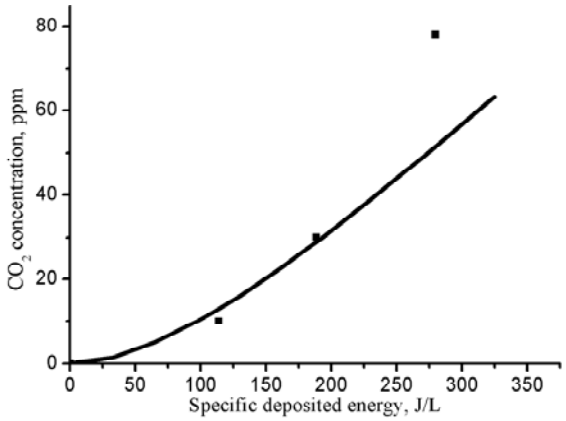

***Fig.4**. Dependence of CO_2 concentration at the plasma reactor exit vs the specific energy. Gas mixture N_2:O_2, $[O_2]$ = 1.5% , initial toluene concentration $[C_7H_8]_0$ = 400 ppm, gas temperature T = 323 K. Line - modeling results, markers ■ - experiment [1].*

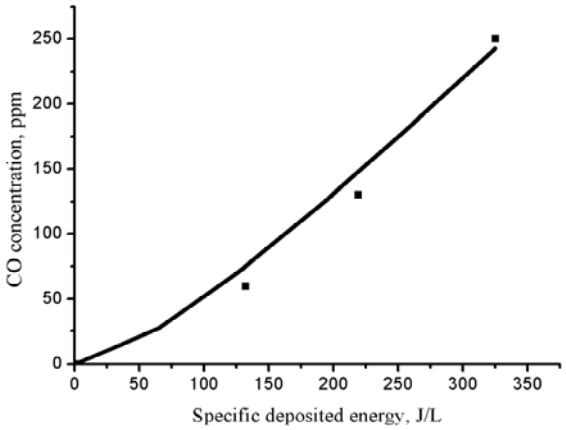

***Fig.5.** Dependence of CO concentration at the plasma reactor exit vs the specific energy. Gas mixture N_2:O_2, $[O_2]$ = 1.5% , initial toluene concentration $[C_7H_8]_0$ = 400 ppm, gas temperature T = 323 K. Line - modeling results, markers ■ - experiment [1].*

The presence of molecular oxygen in the N_2: O_2 gas mixture has a significant influence on the composition of intermediate and final products of plasma chemical toluene conversion. First of all, it should be noted that the oxygen addition to nitrogen leads to complete disappearance of such environmentally hazardous final product toluene decomposition in pure nitrogen as hydrogen cyanide HCN.

Fig. 4 - 6 show the kinetic curves of the production of some by-products which were recorded in the experiment [1]. Carbon dioxide, CO_2, along with water is the end product of a full plasma oxidation of any hydrocarbons. For such complex molecules as C_7H_8 full plasma-oxidation proceeds through a long reaction chain. The primary active particles, producing in the discharge stage, and active particles, which appear in the gas treated in the post-discharge stage are involved in these reactions. As can be seen from Fig. 4, a reasonably good agreement between the results of numerical simulation with experimental data is observed. The model predicts the production of a wide spectrum of intermediate species of toluene degradation, part of which was recorded in [1]. Comparison of numerical results with experimental data on the composition and concentration of some intermediate species was carried out in Fig. (5 - 7). It is clear from the results presented that the results of numerical simulation are in a reasonable agreement with the experimental data. This situation indicates that the plasma-chemical model developed describes adequately the process of toluene conversion in the N_2: O_2 gas mixture.

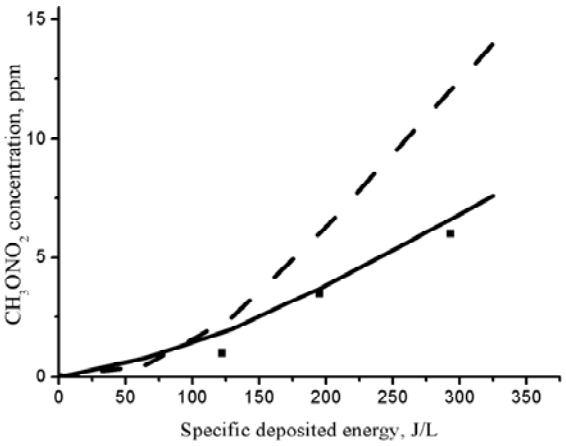

***Fig.6.** Dependence of $CH3ONO_2$ concentration at the plasma reactor exit vs the specific energy. Gas mixture N_2:O_2, initial toluene concentration $[C_7H_8]_0$ = 400 ppm, gas temperature T = 323 K. Markers ■ - experiment [1] at $[O_2]$ = 1.5%. Line - modeling results: — $[O_2]$ = 1.5%, - - - $[O_2]$ = 10%.*

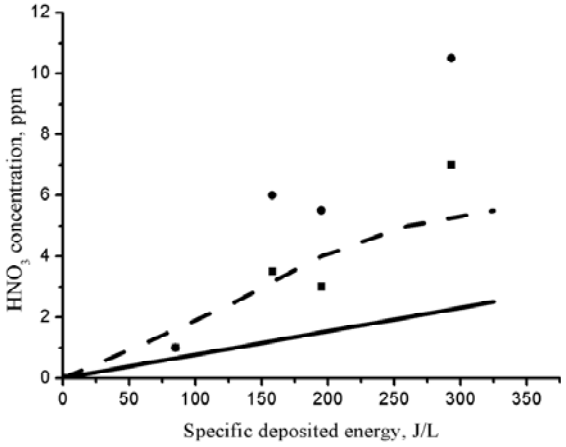

***Fig.7.** Dependence of HNO_3 concentration at the plasma reactor exit vs the specific energy. Gas mixture N_2:O_2, initial toluene concentration $[C_7H_8]_0$ = 400 ppm, gas temperature T = 323 K. Markers - experiment [1]: ■ - $[O_2]$ = 1.5% , ●-.$[O_2]$ = 10%. Line - modeling results: — $[O_2]$ = 1.5%, - - - $[O_2]$ = 10%.*

Conclusions

1. A kinetic model of the plasmachemical toluene destruction in a non-equilibrium low-temperature plasma in N_2: O_2 gas mixture was developed. The results of numerical simulation are in good qualitative and quantitative agreement with available experimental data as for the effectiveness of plasma-chemical toluene removal and composition of the final products of C_7H_8 conversion.

2. The oxygen presence in the plasma-forming gas leads to a change in the main channels of the toluene destruction and increases the toluene removal efficiency compared with pure nitrogen. Metastable nitrogen molecule $N_2(A^3\Sigma^+_u)$ and $N_2(a`^1\Sigma^-_u)$ have a significant contribution to the C_7H_8 removal in the N_2: O_2 gas mixture both through direct interaction with C_7H_8 molecules and due to contribution to oxygen atoms and hydroxyl radical OH production.

3. The composition of intermediate and final products of plasma chemical toluene decomposition varies considerably in the presence of oxygen in the plasma-forming gas in comparison with pure nitrogen.

References

1. Blin-Simiand N., Jorand F., Magne L., Pasquiers S., Postel C., Vacher J.-R. Plasma Reactivity and Plasma-Surface Interactions During Treatment of Toluene by a Dielectric Barrier Discharge. - Plasma Chem. Plasma Process, (2008), **28**, pp. 429-466.
2. Brandenburg R., Maiorov V.A., Golubovskii Yu.B., Wagner H.E., Behnke J., and Behnke J.F. Diffuse barrier discharges in nitrogen with small admixtures of oxygen: discharge mechanism and transition to the filamentary regime. - J. Phys. D: Appl. Phys., (2005), **38**, p. 287-2197.
3. Trushkin A.N., Kochetov I.V. Model of toluene admixture destruction in dielectric barrier discharge in nitrogen at atmospheric pressure.- Abstract collection of III Int. Conf. "Aeroengines of XXI century", (2010), Moscow, CIAM, pp.1391-93.
4. Kossyi I.A, Kostinskii A.Y., Matveev A.A., Silakov V.P. Kinetic scheme of the non-equilibrium discharge in nitrogen - oxygen mixtures. - Plasma Sources Sci. Techn., (1992), **1**, 207.
5. Akishev Yu.S., Derugin A.A., Karalnik V.B., Kochetov I.V., Napartovich A.P., Trushkin N.I. Experimental study and numerical modeling of DC glow discharge at atmospheric pressure. - Plasma Phys. Rep., (1994), **20**, pp. 571- 584.
6. Ono R. and Oda R. Spatial distribution of ozone density in pulsed corona discharges observed by two-dimensional laser absorption method. - J. Phys D: Appl. Phys., (2004), **37**, pp. 730-735.
7. Ono R. and R Oda. Measurement of gas temperature and OH density in the afterglow of pulsed positive corona discharge - J. Phys D: Appl. Phys., (2008), **41**, 035204 (11pp).
8. Eichwald O., Ducasse O., Dubois D., Abahazem A., Merbahi N., Benhenni M. and Yousfi M. Experimental analysis and modelling of positive streamer in air: towards an estimation of O and N radical production- J. Phys D: Appl. Phys., (2008), **41**, 234002 (11pp).
9. W. Mallard, F. Westley, J. Herron, R. Hampson, D. Frizzell. - NIST Chemical kinetics database (version 2Q98), (1998).
10. 10. Wagner V., Jenkin M.E., Saunders S.V., Stanton J., Wirtz K., and Pilling M.J. Modelling of the photooxidation of toluene: conceptual ideas for validating detailed mechanisms. - Atmos. Chem. Phys., (2003), **3**, pp. 89-106.
11. E.G. Alvarez, Viidanoja J., Muniz A. Experimental Confirmation of the Dicarbonyl Route in the Photooxidation of Toluene and Benzene. - Environ. Sci. Technol., (2007), **41**, pp. 8362-69.
12. KINTECH. Kinetic technologies. Chemical Workbench (http//www.kintech.ru).
13. Deminsky M., Chorkov V., Belov G., et al. Chemical Workbench—integrated environment for materials science. – Computational Materials Science, (2003), **28**, p. 169.
14. Phelps A. V. and Pitchford L.C. 26-th report. JILA Information Center Report, Boulder. (1985).
15. Ionin A.A., Kochetov I.V., Napartovich A.P., Yuryshev N.N. Physics and engineering of singlet delta oxygen production in low-temperature Plasma. –J. Phys. D: Appl. Phys., (2007), **40**, R25.

1.4. THE KINETIC PROCESSES INITIATED BY THE PULSE NANOSECOND DISCHARGE IN HOT AIR

N. A. Popov
Skobel'tsyn Research Institute of Nuclear Physics, Moscow State University,
Moscow, 119992 Russia
e-mail: NPopov@mics.msu.su

Abstract. The effect of various radicals and excited particles on the induction delay time reduction is discussed when analyzing the ignition of combustible mixtures under nonequilibrium conditions. A review is made of experimental and theoretical investigations of the effect of hydrogen and oxygen atoms, electronically excited $O_2(a^1\Delta_g)$ molecules on the induction times and on shift of the ignition temperature limits of hydrogen-oxygen mixtures. The addition of oxygen and hydrogen atoms to a combustible mixture may cause a significant reduction of the induction times and the lowering of the ignition temperature limit of combustible mixtures. However, the latter effect is observed only in the vicinity of the ignition limit. In the region of relatively low initial temperatures, the shift of the ignition limit is largely associated with the heating of mixture owing to recombination of atomic particles being added. In so doing, the nonequilibrium pattern of the impact hardly shows up.

Molecules of singlet delta oxygen (SDO) $O_2(a^1\Delta_g)$ may be involved in both chain initiation reactions and chain branching reactions. A kinetic model describing the impact of the admixture of SDO molecules $O_2(a^1\Delta_g)$ on the evolution of the composition of hydrogen-oxygen mixtures was worked out. There was shown in the framework of this model the possibility of describing all the main experimental data on the dynamics of quenching of singlet oxygen in $H_2 : O_2$ gas mixtures in the temperature range of T_0 = 300 - 1050 K. Most of the acts of interaction between singlet oxygen molecules and atomic hydrogen $O_2(a^1\Delta_g) + H$ lead to quenching of $O_2(a^1\Delta_g)$. Efficiency of this interaction channel is more than 80% and fraction of the reaction $H + O_2(a^1\Delta_g) \rightarrow OH + O(^3P)$ was only in 10-20%. The impact of the admixture of SDO molecules on the ignition of $H_2 : O_2$ mixtures was investigated. The dominant process determining the degree of impact of $O_2(a^1\Delta_g)$ is its deactivation by molecules of HO_2. As a result, in $H_2 : O_2$ mixtures of high pressure, where the density of produced HO_2 molecules can be high enough, the effect of singlet oxygen on the ignition time of these mixtures turns out to be relatively weak. This effect becomes even less noticeable if admixtures of atomic oxygen are present in the mixture. The last case is typical when the electric discharge systems are used for production of singlet oxygen. Presence of even small (10^{-4}) initial concentration of atomic oxygen reduces the effect of $O_2(a^1\Delta_g)$ admixtures on the processes of ignition only to additional heating of the mixture in the process of SDO deactivation

Introduction

Considerable recent attention has been given to the problem of fast ignition of combustible gas mixtures, which is motivated by a possibility of applying the obtained results in the design of engines and various plasmachemical systems. It is common knowledge that, in most cases of practical importance, the ignition of combustible mixtures is achieved by increasing their temperature to values exceeding the ignition temperature. The effect of an additional nonequilibrium excitation can be twofold: (i) a shorter induction period of a combustible mixture; (ii) a lower ignition temperature T_g^*, i.e., the ignition of a mixture at initial temperatures below T_g^*. In this case, the effect of the nonequilibrium excitation might be reckoned as substantial if the ignition temperature of the mixture is reduced by the value that considerably exceeds its heating due to relaxation of the excitation energy.

In recent years, several methods have been proposed for nonequilibrium initiation of the combustion in gas flows. Takita et al. [1] reported a significant increase in the velocity of combustion wave as a result of direct injection of arc DC discharge plasma into a gas mixture. Besides, the feasibility of initiating the combustion by pulsed high-current DC discharges [2-8], by RF and microwave discharges [9-13], and by electron beams [14, 15] is being investigated. A review of some recent works on the ignition of combustible gas mixtures by means of electric discharges and on the stabilization of the combustion is given by Starikovskaia [3].

An analysis of kinetic processes which are initiated by electric discharges and affect the ignition of combustible gas mixtures is rather complicated, because the discharge is accompanied by excitation of various degrees of freedom of the mixture molecules. The same problems complicate a comparative analysis of different types of electric-discharge systems. Depending on a value of the reduced electric field E/N in a particular discharge, different species of chemically active particles dominate the mixture. At large values of E/N in the discharge, most of the discharge energy goes into ionization and dissociation of molecules in the mixture [16, 17]. At relatively low values of E/N, there take place an effective excitation of the

electronic states $O_2(a^1\Delta_g)$, $O_2(b^1\Sigma_g^+)$ [18, 19] and vibrational degrees of freedom of molecules [16, 17].

Apparently, we must first analyze the effect of different chemically active particles on the characteristics of the ignition process. It is only after this that it will be possible to identify a set of particles and their ratios which have an optimal effect on ignition. It is only then that it will be possible to formulate the problem of determining the characteristics of electric discharges which enable one to produce the desired chemically active particles in optimal ratios.

1. The Effect of Hydrogen and Oxygen Atoms on the Ignition of $H_2 : O_2$ Mixtures

A number of papers are available at present, which deal with the investigation of additions of chemically active radicals on the shift of temperature ignition limits [20 - 26] and on the times of induction [14, 15, 27–29] in hydrogen-containing and hydrocarbon mixtures. These investigations involved the use of UV radiation, electric discharge, electron beam etc. for obtaining the initial concentration of chemically active particles.

Nalbandyan [21] investigated the effect of UV photolysis on the ignition temperature of a stoichiometric hydrogen-oxygen mixture at pressure P = 2 to 30 torr. The experiments were performed in a quartz tube 2.7 cm in diameter, whose walls were treated with hydrofluoric acid. The radiation source was provided by a DC discharge in hydrogen, and the intensity of radiation was adjusted by varying the discharge current I = 0.1 - 1 A. A quartz membrane was used to identify a spectral region $\lambda \leq 175$ nm corresponding to Schumann–Runge continuum of absorption of oxygen.

The possibility was demonstrated of some lowering of the temperature ignition limit ΔT_g^* of $H_2 : O_2$ mixtures. For example, at P = 20 torr, the maximal value of ΔT_g^* was 27 K at the radiating discharge current of 1 A. The intensity of the UV radiation source in the range of $\lambda \leq 175$ nm was determined by the number of water molecules formed as a result of photolysis of $H_2 : O_2$ mixtures at room temperature. It was assumed that two atoms of oxygen are formed upon absorption of each radiation quantum and, with time, are converted to H_2O.

Nalbandyan [21] further investigated the effectiveness of chain chemical reactions depending on the initial gas temperature. This effectiveness is characterized by the chain length ϕ which was determined as the ratio of the rate of production of water molecules at a given gas temperature to the rate of production at T_0 = 300 K,

$$\phi = \frac{dH_2O}{dt} \Big/ \left(\frac{dH_2O}{dt}\right)_{T=300}$$

As was already noted, the latter rate is defined by the intensity of the source of UV radiation. The experimental data of [21], as well as the results of calculation of the dependence of chain length ϕon the gas temperature under the effect of radiation of discharge with current I = 150 mA, are given in Fig.1. One can see in the figure that the chain pattern of the process starts showing up only in the region of temperatures close to the ignition limit. At low temperatures, the production of radicals as a result of UV photolysis leads only to heating of the mixture.

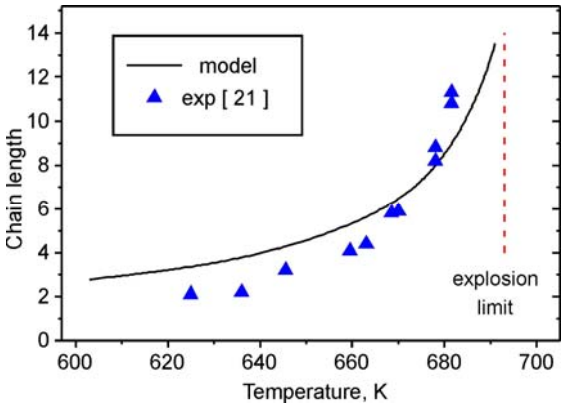

Fig. 1. *The chain length in a mixture of $H_2 : O_2$ = 2 : 1 at P = 20 torr and discharge current I = 150 mA as a function of the initial temperature of gas: the points indicate the experiment of [21], the curve - calculation, and the dashed curve - the temperature limit of autoignition for the conditions of [21].*

The absorption of radiation by oxygen in the region of Schumann-Runge continuum is accompanied by dissociation of O_2, with one of the atoms being formed in the excited $O(^1D)$ state [30],

$$O_2(X^3\Sigma_g^-) + h\omega \rightarrow O(^3P) + O(^1D).$$

This results in a rapid production of H and OH radicals during the quenching of $O(^1D)$ atoms by hydrogen [31],

$$O(^1D) + H_2 \rightarrow H + OH \qquad k = 1.1\cdot10^{-10}\ \text{см}^3/\text{с}.$$

The results of the impact of UV radiation were simulated by introducing a source of atomic oxygen ($O(^3P) + O(^1D)$) of intensity $\nu_{O2}\cdot[O_2]$. The calculation results given in Fig. 1 correspond to the value $\nu_{O2} = 4.5\cdot10^{-5}\ s^{-1}$ and, as one can see, agree with the experimental data. The existing differences

may be associated with the fact that, under conditions being considered (P = 20 torr), an important part is played by heterogeneous reactions on the discharge tube surface [32]. These processes are not known well enough at present. In order to increase the importance of the part played by the volumetric reactions, it is necessary to make a transition to higher pressures. However, problems arise in this case, which are associated with the nonuniformity of absorption of radiation by oxygen in the Schumann- Runge continuum.

Many experiments on the initiation of ignition of combustible mixtures by means of UV photolysis were conducted by using the focused laser radiation [22-24]. Most frequently in these experiments, a breakdown a fast gas heating occur on the focus of the laser beam with the resulting formation of a high-temperature region, where the combustion is then initiated. In this case, the probability for the ignition depends substantially on characteristic dimensions of this high-temperature region, since a critical question is of whether the mixture has time to ignite during its cooling by heat conduction. Such experiments with laser radiation have much in common with the combustion initiation by spark electric discharges [33].

Lavid et al. [24] used the focused radiation of an ArF laser (λ = 193 nm) for igniting atmospheric-pressure H_2 : O_2 mixtures. During the pulse, most of the energy of absorbed photons is spent for dissociation of oxygen molecules rather than for gas heating,

$$O_2(X^3\Sigma_g^-) + h\omega \rightarrow O(^3P) + O(^3P).$$

In this case, the temperature of mixture turns out to be below the limit of ignition, and reactions involving $O(^3P)$ and H atoms, OH radicals, and other play an important part in the initiation of combustion. The transverse dimension of the excitation zone in the focused laser beam was relatively small ($R \approx$0.4 mm [24]). Therefore, similar to [22, 23], the probability of ignition was affected both by the diffusion "departure" of radicals from the excitation zone and by the rate of cooling down of this region due to heat conduction. Figure 2 gives the minimal values of the initial concentration of $O(^3P)$ atoms, required for the ignition of a stoichiometric H_2 : O_2 mixture at P = 1 atm, as a function of the initial gas temperature. Note that both the calculation (curves) and experimental (symbols) results [24] indicate that very significant (in excess of 10^{16} cm^{-3}) concentrations of oxygen atoms are required for the ignition of this mixture at temperatures below the ignition limit. In view of the small size of the excitation zone, the temperature limit of ignition of the mixture under consideration is higher than 880 K [33]. The results of calculations performed within a uniform 0-D model [47] (curve 1) lie markedly below the experimental data. As was already mentioned, this is indicative of the important part played by diffusion and heat conduction processes in determining the ignition temperature.

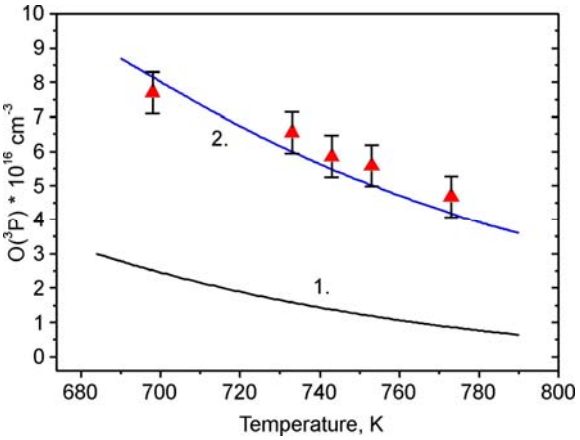

Fig. 2. *The minimal initial concentration of $O(^3P)$ atoms required for the ignition of a stoichiometric H_2 : O_2 mixture at P = 1 atm as a function of gas temperature: the symbols indicate the experiment of [24], and the curve indicates the calculation by the 0-D model (curve 1) and by the 1-D model (curve 2).*

To analyse the effect of diffusive and thermal conductivity processes on determination of ignition temperature in H_2 : O_2 mixtures the comparison of calculation results executed in the frame of uniform (0-D) model and one dimensional (1-D) axisymmetric model has been performed. In the latter the corresponding diffusive terms for all considered components have been inserted in the balance equation. The values of diffusive coefficients D_k and their dependences on temperature were estimated using the data [36]. Apart from the thermal conductivity term was included in the equation for temperature. In the calculation of thermal conductivity coefficient λ_{ef} of multicomponent mixture the following expression has been used:

$$\lambda_{ef} = 0.5 \cdot \left(\sum_k \lambda_k X_k + \left(\sum_k \frac{X_k}{\lambda_k} \right)^{-1} \right), \quad [36]$$

where the X_k is the mole fraction of main components, and λ_k are the corresponding values of thermal conductivity coefficients.

In calculations in the frame of one dimensional (1-D) model the initial distribution of $O(^3P)$ atom density and gas temperature were assumed as Gaussian with R_0 = 0.4 mm [24]. Then,

under consideration of this simulation the values of temperature and atom concentrations at laser channel axis are given.

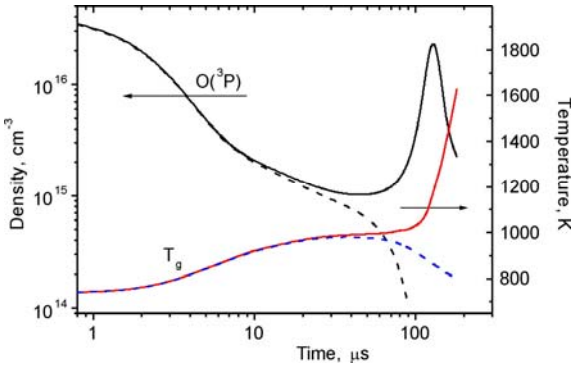

Figure 3. *Temporal dynamics of the temperature and the density of atoms O(^{3}P) at the axis for a stoichiometric H_2 : O_2 mixture at P = 1 atm, T_0 = 740 K and initial concentrations: $[O]_0 = 5.6 \cdot 10^{16}$ cm^{-3} (solid lines) u $[O]_0 = 5.5 \cdot 10^{16}$ cm^{-3} (dashed lines).*

As example, in Figure 3 the simulation results (in frame of 1-D model) of the time dependence of O atom concentration and temperature at laser channel axis in mixture of H_2 : O_2 = 2 : 1 at P =1 atm and T_0 = 740 K with two different initial O(^{3}P) concentrations ($[O]_0 = 5.6 \cdot 10^{16}$ cm^{-3} and $[O]_0 = 5.5 \cdot 10^{16}$cm^{-3}) are demonstrated. As one can see in spite of very small change of $[O]_0$, in first case the ignition of mixture occurs, but in the second one does not take place. This example is evidence that in calculations described above the accuracy of determination of O(^{3}P) concentration needed for mixture ignition is rather high.

The minimal atom concentrations $[O(^3P)]_{min}$, needed for ignition of H_2 : O_2 mixture in the range of T_0 = 690 - 790 K are presented in Figure 2. Apparently, the 0-D model (curve 1) and 1-D model (curve 2) obtained results differ from each other in 3-5 times. That difference increases with gas temperature. The 1-D model results (curve 2) agree with experimental data [24]. The shown calculation results were executed in conditions of stoichiometric mixture of H_2 : O_2 = 2 : 1. Similar results were obtained for other $[H_2]/[O_2]$ values as well (in the work [24] that ratio was varied from 0.4 to 4).

The experimental investigation of kinetic mechanisms of the effect of radical's initial density on the ignition time requires the development of a rather uniform and extended excitation region. Such experiments were described by Chou and Zukowski [25], who investigated the pulsed UV photolysis of stoichiometric H_2 : O_2, H_2 : air, and CH_4 : O_2 mixtures with additions of molecules of ammonia NH_3. The initial temperature of mixture was 300 K, with pressure P = 1 atm. The radiation of ArF laser on wavelength λ = 193 nm, which is effectively absorbed by NH_3 molecules, was used for production of radicals [30],

$NH_3 + h\omega \rightarrow NH_2 + H.$

The power of laser radiation was sufficient for decomposition of all available molecules of ammonia. This provided for spatially uniform production of radicals of preassigned initial concentration equal to the concentration of NH_3. Chou and Zukowski [25] assumed that the reactivity of the NH_2 radicals being formed is relatively low; therefore, the main result of the impact of UV radiation on the characteristics of ignition is the production of atomic hydrogen with concentration $[H]_0 = [NH_3]$.

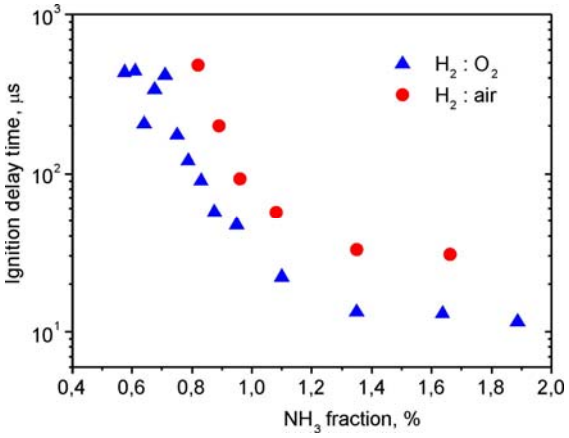

Fig. 4. *The induction period for stoichiometric mixtures of H_2 : O_2 and H_2 : air excited by a pulsed source of UV radiation as a function of the initial fraction of NH3 molecules in the mixture: P_0 = 1 atm, T_0 = 300 K; the symbols indicate the experiment of [25].*

Figure 4 gives the ignition times of stoichiometric mixtures of H_2 : O_2 and H_2 : air at P = 1 atm and T_0 = 300 K as a function of the fraction of NH_3 in the mixture [25]. The ignition of a $2 \cdot H_2$: O_2 mixture could be experimentally accomplished for a fraction of ammonia molecules of 0.6 - 0.7%. The calculation results indicate that initial concentrations of hydrogen atoms $[H]_0/M = [NH_3]/M \geq 2\%$, are required for the ignition of the mixture under consideration. This is three times higher than the experimentally obtained values. The reason for discrepancy between the calculation and experimental data may be as follows. Indeed, NH_2 radicals formed as a result of UV photolysis of ammonia hardly react with O_2 and H_2 molecules. However, a fairly fast reaction of NH_2 with O(^{3}P) atoms may occur, which causes the emergence of additional channels of production of hydrogen radicals H and OH, as well as nitrogen oxides [34],

$NH_2 + O \rightarrow NH + OH$;

$NH_2 + O \rightarrow HNO + H$;

$NH + O_2 \rightarrow NO + OH$;

$NH + O_2 \rightarrow NO_2 + H$.

The latter is especially important because it is known [20, 33 and 35] that nitrogen oxides cause a significant reduction of the induction times and the ignition temperature limit of high-pressure hydrogen-oxygen and hydrogen-air mixtures. Therefore, Chou and Zukowski [25] managed to accomplish the ignition of hydrogen-oxygen mixtures (with additions of ammonia) at atmospheric pressure and T_0 = 300 K as a result of their nonequilibrium excitation by ArF laser radiation. However, the use of NH_3 additions results in a significant complication of the ignition kinetics of H_2 : O_2 mixtures, which makes the interpretation of the results quite difficult.

Starikovskaia et al. [28] investigated the effect of pulsed UV photolysis, caused by the ArF laser radiation, on the induction times of O_2 : N_2O : H_2 : Ar = 3 : 11 : 32 : 54 mixture. The absorbed energy was W = 2 to 4 mJ/cm^3, with P_0 = 0.3 - 0.7 atm and T_0 = 850 - 1300 K. The measurements were performed in a shock tube behind reflected shock wave. The induction times were determined by the dynamics of radiation intensity of OH* excited state. In the mixture under investigation, the radiation at λ= 193 nm is largely absorbed by N_2O molecules [30],

$N_2O + h\omega \rightarrow N_2 + O(^1D)$.

Therefore, the impact of the ArF laser pulse leads to the production of excited atoms whose concentration under the conditions of [28] reaches a value of $[O(^1D)]/[M] = (1 \pm 0.5)\cdot 10^{-3}$. The results of such impact are given in Fig. 5 which shows the dependences of the induction times for the given mixture on the initial temperature, experimentally obtained both in the mode of autoignition (symbols) and in view of UV photolysis (points). One can see in Fig. 5 that the use of UV radiation makes for a significant reduction of the induction times and for the lowering of the ignition temperature limit by 100 - 150 K. At the same time, the laser pulse proper is capable of gas heating by no more than 5 - 10 K.

Starikovskaia et al. [28] used unfocused laser radiation to accomplish a fairly uniform excitation of combustible mixture. The concentration of excited atoms being formed was determined by the results of measurements of absorbed energy. Additions of $O(^1D)$ make it possible to significantly reduce the induction times. The simulation results of [28] agree with the experimental data (Fig. 5); however, the required additions of $O(^1D)$ atoms $[O(^1D)]/[M] = 3\cdot 10^{-4}$ turn out to be approximately three times less than the measured values.

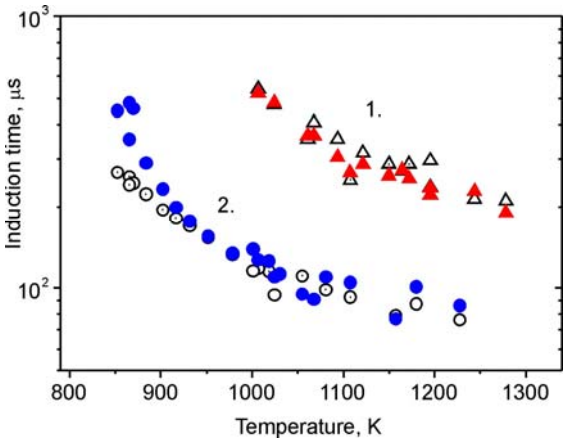

Fig. 5. *The time of induction for a mixture of O_2 : N_2O : H_2 : Ar = 3 : 11 : 32 : 54 (P = 0.3–0.6 atm) as a function of initial temperature: (1) autoignition, (2) impact of UV radiation; solid symbols - experiment, hollow symbols - calculation [28].*

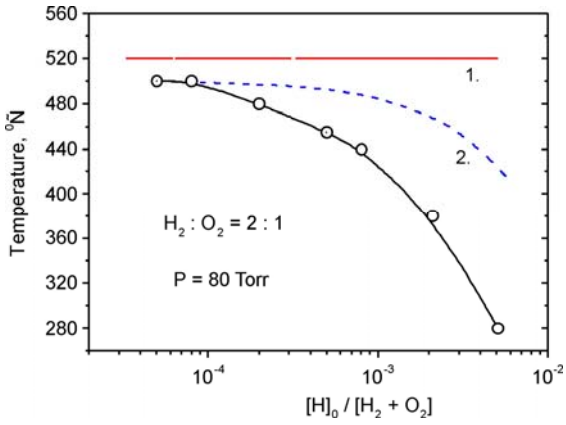

Fig. 6. *The ignition temperature of a mixture of H_2 : O_2 = 2 : 1 as a function of the fraction of hydrogen atoms at P = 80 torr. The points indicate calculation [26], curve 1 - temperature limit of ignition for the given conditions [33], and curve 2 - variation of the ignition temperature because of autoheating of the mixture as a result of recombination of hydrogen atoms.*

Seleznev et al. [26] performed numerical investigations of the effect of hydrogen and oxygen atoms additions on the ignition temperature of a stoichiometric H_2 : O_2 mixture in a wide range of pressures (P = 1 to 10^4 torr). Given by way of example in Fig. 6 are the results of calculation of the shift of ignition limits as a function of the initial fraction of hydrogen atoms at P = 80 torr (points) [26]. Note that the experimentally obtained value of the ignition temperature of unexcited mixture (curve *1*) given in [33] somewhat exceeds the calculated values. Also given in Fig. 6 for

comparison are our estimates of the variation of ignition temperature because of heating of the mixture as a result of recombination of hydrogen atoms H_0. One can see that additions of hydrogen atoms in excess of $3 \cdot 10^{-3}$ are required for a more significant (over 200 K) reduction of the ignition temperature limit. In so doing (according to the data of [26]), the effect of heating of the mixture is of significant importance because it leads to an increase in the effectiveness of chain chemical reactions (see Fig. 1) initiated by additions of H.

A fairly uniform excitation of a mixture may be accomplished by using short-pulse high-current discharges [37] which propagate in the form of a fast ionization wave (FIW). Owing to the high values of reduced field E/N, which may be realized under these conditions, the most part of electron energy is delivered for the ionization and dissociation of mixture molecules.

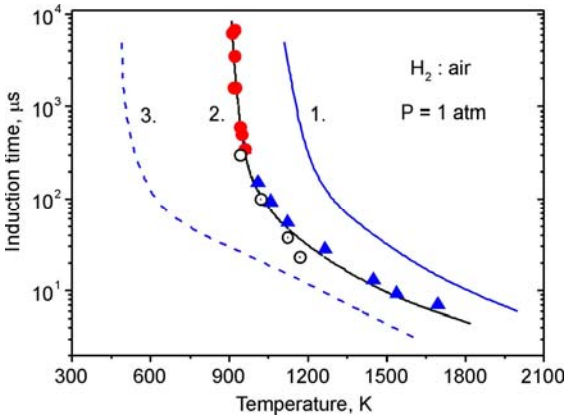

Fig. 7. *The temperature dependence of the time of induction of a stoichiometric mixture of H_2 : air, P = 1 atm. Curves 1 and 2 indicate autoignition, curve 3 - additional excitation by a high-current discharge; symbols, experiment [35, 38]; curves 1 and 3, calculation [29].*

Starikovskii [29] gives the results of theoretical investigations of the induction times dependence on the initial temperature for stoichiometric H_2 : O_2, H_2 : air, and CH_4 : air mixtures. Comparison is made of the ignition delay times of these mixtures with and without a pulsed high-current discharge impact. Figure 7 gives the results of calculations of [29] for a stoichiometric H_2 : air mixture at P = 1 atm. Under these conditions, according to [29], the use of additional discharge excitation makes it possible to reduce the ignition temperature in the vicinity of the ignition limit by 500 - 600 K. Also given in this figure are the experimental data on the induction times of this mixture borrowed from [35, 38]. These data differ very significantly from the calculation results of [29] for the times of autoignition. Therefore, it is difficult to make the final inference about the degree of temperature ignition limit reduction of using the numerical simulation results of [29].

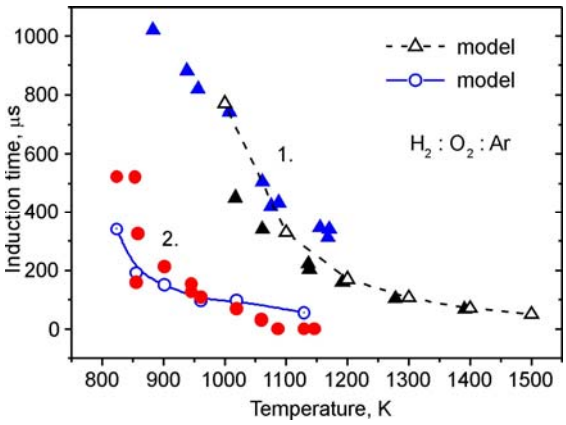

Fig. 8. *The time of induction for a stoichiometric mixture of H_2 : O_2 : Ar = 12 : 6 : 82 (P = 0.3–0.6 atm) as a function of initial temperature: (1) autoignition, (2) in view of the impact of discharge; solid symbols, experiment [4]; hollow symbols, calculation [4].*

Bozhenkov et al. [4] performed experimental investigations of the effect of a fast ionization wave on the induction times of H_2 : O_2 : Ar = 12 : 6 : 82 mixture in the temperature range of T_0 = 800 - 1400 K (P_0 = 0.25 - 0.75 atm). The discharge input energy did not exceed 30 - 50 mJ/cm^3. The measurement results given in Fig. 8 indicate that the use of this discharge enables one to reduce the ignition temperature by 200 - 250 K. Bozhenkov et al. [4] used the results of measurements of the dynamics of electric field $E(t)$ for the numerical simulation of the discharge impact and for the determination of the hydrogen and oxygen atoms density produced in the discharge. The obtained concentrations of atoms were used as the initial conditions in calculating the ignition delay time of the considering mixture. The results of simulation of autoignition and of the effect of discharge on the induction time agree with the experimental data (Fig. 8).

Note that Bozhenkov et al. [4] described the production of hydrogen and oxygen atoms in the discharge in view of only the dissociation of H_2 and O_2 molecules by electron impact. However, in a mixture with more than 80% Ar (H_2 : O_2 : Ar = 12 : 6 : 82) at high E/N values, a very significant additional channel of dissociation is provided by the processes of quenching of metastable electronically excited atoms of $Ar^* = Ar(^3P_0, {}^3P_2)$, for example [39],

$$Ar^* + O_2 \rightarrow Ar + O(^3P) + O(^1D, {}^1S).$$

The inclusion of these reactions must more than double the initial atom concentration and reduces the predicted induction delay times accordingly. In

this case, agreement with the experimental data may be impaired.

Therefore, the addition of oxygen and hydrogen atoms to a combustible mixture enables one to significantly reduce the induction times and the ignition temperature of mixtures. However, in the zone of relatively low initial temperatures, the shift of the ignition limit is largely associated with the heating of mixture due to the recombination of the atomic particles being added. In so doing, the nonequilibrium character of the impact hardly shows up. Therefore, it is of interest to search for other forms of nonequilibrium excitation (for example, the introduction of non-equilibrium concentrations of electronically- and vibrationally excited particles).

2. The Effect of $O_2(A^1\Delta_G)$ on the Ignition Delay Time and the Flame Propagation Velocity in Hydrogen-Oxygen Mixtures

Investigations have been continued recently of the processes which define the initiation of combustion and detonation in combustible mixtures in the presence of excited oxygen molecules $O_2(a^1\Delta_g)$ [40-46]. In [41, 42], it was suggested (apparently for the first time) to use reactions involving $O_2(a^1\Delta_g)$ for explaining the observed increase in the rate of flame propagation in H_2 : O_2 mixtures after the impact of electric discharge. This phenomenon was experimentally investigated by Basevich and Kogarko [40, 41] who used a glow discharge (I = 5 to 85 mA) for exciting a flow of molecular oxygen. After the discharge, molecular hydrogen was added to the flow. The resultant mixture contained 7% H_2 + 93% O_2 and the products of impact of the discharge, namely, atoms of $O(^3P)$ and molecules of ozone and singlet oxygen $O_2(a^1\Delta_g)$ and $O_2(b^1\Sigma_g^+)$ (mixture pressure P_0 = 50 torr, T_0 = 293 K). This mixture was ignited by a pulsed spark discharge with subsequent measurement of the normal rate of flame propagation and of the axial profile of gas temperature.

In the case of discharge currents higher than 17 mA, the velocity of combustion wave almost doubled. In so doing, the gas temperature in the discharge increased by no more than 5 - 10 K. The measurement results of [41] are given in Fig. 9. For current I = 17 mA, the characteristic time during which the discharge has a significant effect on the flame velocity is approximately 0.2 s. Note that the pause increase is accompanied by a significant variation of the content of active particles before the front of combustion wave with an almost unchanged concentration of stable products (ozone and nitrogen oxides).

The characteristic time of loss of $O(^3P)$ atoms is defined by their conversion to ozone and amounts to several milliseconds under conditions of [41]. The quenching of $O_2(a^1\Delta_g)$ largely occurs on O_2 molecules and in reactions with ozone with a characteristic time of 0.15 s, which is comparable with the measured time of impact of discharge [41]. The calculation results of [42] supported the assumption that the effect of glow discharge in oxygen on the flame propagation velocity is most likely associated with the involvement in combustion of the molecules of $O_2(a^1\Delta_g)$ produced in the discharge.

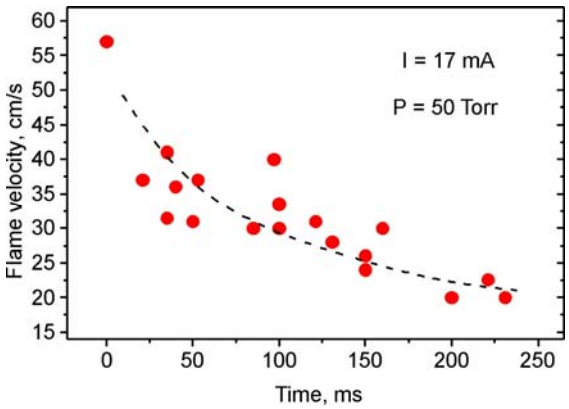

Fig. 9. *Flame propagation velocity vs. the duration of a pause between the end of the discharge and the ignition time of a 7% H_2 : 93% O_2 mixture at P = 50 Torr and discharge current I = 17 mA [41].*

In papers [44-46], the results from theoretical research of the impact of $O_2(a^1\Delta_g)$ on the ignition delay time of H_2 : O_2 : $O_2(a^1\Delta_g)$ mixtures are presented. There was shown a possibility of a sufficient reduction in the temperature threshold of ignition and in the induction times of hydrogen-oxygen mixtures when the fraction of singlet oxygen (SDO) is $[O_2(a^1\Delta_g)/O_2] \geq 1\%$. One of the important processes that determine the efficiency of the impact of SDO on the ignition of combustive mixtures is the following:

$$O_2(a^1\Delta_g) + H_2 \rightarrow OH + OH. \qquad (1)$$

This process can result in a sufficiently more rapid production of chemically active particles by the adding of SDO. The rate of reaction (1) sufficiently increases with the rise of gas temperature. The corresponding dependence $k_1(T)$ got in [45] is shown in Fig. 10 (curve 1).

Along with this, quenching of $O_2(a^1\Delta_g)$ by molecules of hydrogen is also possible:

$$O_2(a^1\Delta_g) + H_2 \rightarrow O_2 + H_2. \qquad (2)$$

The rate of reaction (2) at T = 300 K was measured in several experiments (see review [48]). The results from calculations of the dependence of the rate of this reaction on temperature are given in

[49]. The approach adopted in this work is based on assumptions that the spin ban on the transition $O_2(a^1\Delta_g) \rightarrow O_2(X^3\Sigma_g^-)$ is withdrawn by taking into account spin-orbit interaction inside the O_2 molecule, the kinetic energy of relative motion is a lot more than the potential energy of interaction of molecules and the transition probability is small.

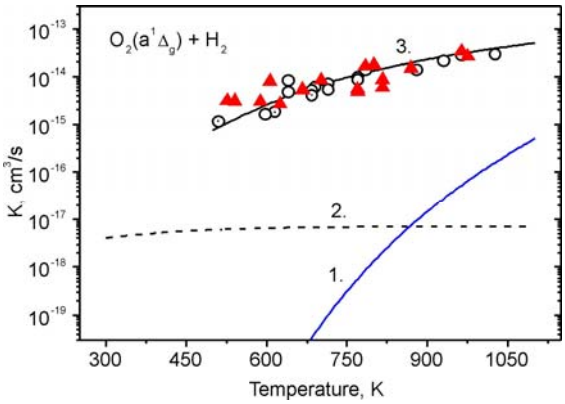

Figure 10. *Dependences of reaction rate coefficients on the temperature: 1 - $O_2(a^1\Delta_g) + H_2 \rightarrow 2{\cdot}OH$ [45]; 2 - $O_2(a^1\Delta_g) + H_2 \rightarrow O_2 + H_2$ [49]; 3 - experimental data [50].*

The last two conditions allow us to apply perturbation theory. The results from calculation of the dependence $k_2(T)$ [49] are shown in Fig. 10 (curve 2). Also here (curve 3), the results of measuring the effective quenching rate of $O_2(a^1\Delta_g)$ got in paper [50] are also presented in the temperature range T = 500 - 1000 K. In this paper the temporal dynamics of $O_2(a^1\Delta_g)$ quenching in a $H_2 : O_2$ mixture (with the fraction of hydrogen less than 2-3%) was measured. In [50], the main mechanism of SDO quenching was associated with reaction (2). As it is seen from Fig. 10, the experimentally obtained rates of $O_2(a^1\Delta_g)$ losses far exceed both the rate of reaction $k_1(T)$ [45] and the rate of SDO deactivation $k_2(T)$ [49]. One of the reasons for such difference can be the fact that the analysis of experimental results [50] does not take into account the specifics of considered mixture in which the chain chemical reactions can proceed in the temperature range of T_0 = 500 - 1000 K. As a result, particles that are actively involved in the SDO deactivation are produced, for example, H and HO_2. Therefore, a further numerical analysis of experimental results [50] is necessary to determine the possible reasons for the high rate of $O_2(a^1\Delta_g)$ losses under these conditions.

Another important process for the combustion problems is the following:

$$H + O_2(a^1\Delta_g) \rightarrow OH + O(^3P). \qquad (3)$$

This reaction was investigated experimentally in [51, 52] in the temperature ranges of T = 300 - 431 K and T = 520 - 930 K, correspondingly. The total rate of processes (3) and (4) was measured in these papers:

$$H + O_2(a^1\Delta_g) \rightarrow H + O_2, \qquad (4)$$

and, according to paper [52], reaction (3) is dominant. However, it was shown in more recent studies [53] that $k_3 / (k_3 + k_4) \leq 0.1$ in the temperature range of T = 300 - 437 K. Thus, the

Table 1. The reactions with the $O_2(a^1\Delta_g)$, $O_2(b^1\Sigma_g^+)$ participation in $H_2 : O_2$ mixtures

No	Reaction	Rate coefficient, cm^3/s	Reference
1.	$O_2(a^1\Delta_g) + H_2 \rightarrow OH + OH$	$2.8{\cdot}10^{-9}{\cdot}exp(-17906/T)$	[45]
2.	$O_2(a^1\Delta_g) + H_2 \rightarrow O_2 + H_2$	$4.5{\cdot}10^{-18}{\cdot}(T/300)^{0.5}$	[49]
3.	$O_2(a^1\Delta_g) + H \rightarrow O(^3P) + OH$	$\alpha \cdot 6.5{\cdot}10^{-11}{\cdot}exp(-2530/T)$	[47*]
4.	$O_2(a^1\Delta_g) + H \rightarrow O_2 + H$	$(1-\alpha){\cdot}6.5{\cdot}10^{-11}{\cdot}exp(-2530/T)$	[47*]
5.	$O_2(a^1\Delta_g) + HO_2 \rightarrow O_2 + HO_2^*$	$2.0{\cdot}10^{-11}$	[55]
6.	$O_2(a^1\Delta_g) + O_2 \rightarrow O_2 + O_2$	$2.2{\cdot}10^{-18}$	[48]
7.	$O_2(a^1\Delta_g) + O_2(a^1\Delta_g) \rightarrow O_2(b^1\Sigma_g^+) + O_2$	$2.4{\cdot}10^{-17}$	[48]
8.	$O_2(b^1\Sigma_g^+) + H_2 \rightarrow O_2(a^1\Delta_g) + H_2$	$1.0{\cdot}10^{-12}$	[48]
9.	$O_2(b^1\Sigma_g^+) + N_2 \rightarrow O_2(a^1\Delta_g) + N_2$	$4.9{\cdot}10^{-15}{\cdot}exp(-253/T)$	[48]
10.	$O_2(b^1\Sigma_g^+) + O_2 \rightarrow O_2(a^1\Delta_g) + O_2$	$4.0{\cdot}10^{-17}$	[48]

[*] The coefficient $\alpha \cong 0.2$ is determined in the given work (see below).

ratio between the reaction rates k_3 : k_4 remains unknown.

In [53, 54], the following process was involved to explain the experimental results concerning the dynamics of the concentration of atomic hydrogen when $O_2(a^1\Delta_g)$ molecules were added to a mixture of H : H_2 : O_2 :

$$O_2(a^1\Delta_g) + HO_2 \rightarrow O_2 + HO_2^* \qquad (5)$$

The rate of this reaction is $k_5 = 2.0 \cdot 10^{-12}$ cm^3/s, according to [53, 54]. In paper [55], higher rates of SDO quenching by HO_2 molecules were reported which amounted to $k_5 = 3.0 \cdot 10^{-11}$ cm^3/s. Consequently, reaction (5) can also effect the dynamics of $O_2(a^1\Delta_g)$ and the ignition time of H_2 : O_2 : $O_2(a^1\Delta_g)$ mixtures.

In [47], a model of ignition of hydrogen-oxygen mixtures is described. In this section, the system of reactions [47] was supplemented by processes involving singlet oxygen molecules $O_2(a^1\Delta_g)$ and $O_2(b^1\Sigma_g^+)$. These processes are given in Table 1. The aim of this investigation is to analyze the results from the named experiments and to explain the discrepancy of obtained there data. Based on this analysis, the recommendations concerning the rates of the main processes involving $O_2(a^1\Delta_g)$ (1-5) will be provided which will make it possible to estimate the impact of SDO molecules on the induction time and ignition threshold shift for H_2 : O_2 mixtures.

In all the further considered experiments (except in cases explicitly stated) studies were carried out in a flow reactor with a system of flows mixing. The $O_2(a^1\Delta_g)$ molecules were produced, typically, in a microwave discharge (in oxygen or O_2 : Ar or O_2 : He mixtures). The $O(^3P)$ atoms, which are also produced in the discharge, were removed in reactions with mercury oxide HgO, which coated the walls of the tube. Hydrogen atoms were produced in a microwave discharge in argon (or helium) with the admixture of H_2.

In [51], the quenching of the $O_2(a^1\Delta_g)$ molecules by atomic hydrogen was studied in a mixture of H_2 : O_2 : Ar at P = 0.3 - 0.9 torr. The experiments were conducted both in the presence of $O(^3P)$ atoms and with the removal of them. After mixing the flows of excited hydrogen and oxygen, dynamics of the variation of O, H, and also OH and $O_2(a^1\Delta_g)$ densities was studied using the electron-paramagnetic-resonance (EPR) spectrometer. Based on these data, the rate of $O_2(a^1\Delta_g)$ deactivation by the hydrogen atoms ($k_3 + k_4$) was determined at T = 300 - 431 K. To reduce the probability of heterogeneous losses of active particles, the tube walls were covered with orthoboric acid. As a result, it was achieved that the reactions at the surface had practically no effect on the dynamics of the main studied components and this was verified experimentally.

As an example, Fig. 11 shows the results from calculating the dynamics of the main components of the mixture which has the following initial composition: Ar = $9.1 \cdot 10^{15}$ cm^{-3}, O_2 = $5.3 \cdot 10^{15}$ cm^{-3}, $H_2 = 7.4 \cdot 10^{14}$ cm^{-3}, $H = 4.4 \cdot 10^{14}$ cm^{-3}, $O_2(a^1\Delta_g) = 5.5 \cdot 10^{14}$ cm^{-3}, T_0 = 300 K. Under these conditions the main losses of SDO molecules occur in the reactions with H atoms, the decay of $O_2(a^1\Delta_g)$ being monoexponential [51]. It is therefore necessary that the hydrogen number density H(t) varies only slightly in time. As it is seen from results of calculations presented in Fig. 11, this condition is fulfilled.

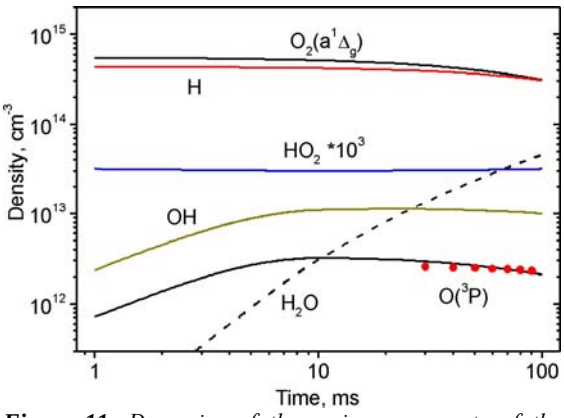

Figure 11. *Dynamics of the main components of the mixture H_2 : O_2 : $O_2(a^1\Delta_g)$: Ar at T = 300 K and at the ratio of reaction rates k_3 : k_4 = 2 : 8. Dots correspond to the calculated values of $2.17 \cdot [O(^3P)]$ at $O_2(a^1\Delta_g)$ = 0. The initial concentrations of components are: Ar = $9.1 \cdot 10^{15}$ cm^{-3}; $O_2 = 5.3 \cdot 10^{15}$ cm^{-3}; $H_2 = 7.4 \cdot 10^{14}$ cm^{-3}; H = $4.4 \cdot 10^{14}$ cm^{-3} and $O_2(a^1\Delta_g) = 5.5 \cdot 10^{14}$ cm^{-3}.*

In [53], another mechanism of SDO quenching associated with reaction (5) was proposed to explain the experimental results [51]:

$$O_2(a^1\Delta_g) + HO_2 \rightarrow O_2 + HO_2.$$

According to the calculations given in Fig. 11, the number density of $HO_2(t)$ within the considered time interval remains practically constant, being $\cong 3 \cdot 10^{10}$ cm^{-3} total. In this case, the frequency of $O_2(a^1\Delta_g)$ quenching in the reaction (5) does not exceed $\nu_a \leq 0.6$ s^{-1}, which is much lower than the experimentally observed value for these conditions $\nu_a \cong 8$ c^{-1} [51]. So, the proposed in [53] mechanism of $O_2(a^1\Delta_g)$ quenching is enabled in conditions of experiment [51].

It was also shown in [51] that the concentration of atomic oxygen is increased under these conditions by adding molecules of $O_2(a^1\Delta_g)$. These data can be used to determine the fractions of reaction channels (3) and (4). According to [51], the addition of $O_2(a^1\Delta_g)$ molecules with number

density $5{,}5\cdot10^{14}$ cm^{-3} to the studied mixture increases the concentration of atomic oxygen by a factor of 2,17. To receive in the calculations the value of $\xi = [O(^3P)]/[O(^3P)]_0 = 2.17$, it is necessary that the ratio of reaction rates $k_3 : k_4$ was about 2 : 8 (see Fig. 12). It is good to mention that taking into account the uncertainty associated with the heterogeneous recombination of atomic oxygen on the walls of the tube has practically no effect on the value of ξ (in the frequency range $\nu_{get} = 2 - 20\ s^{-1}$).

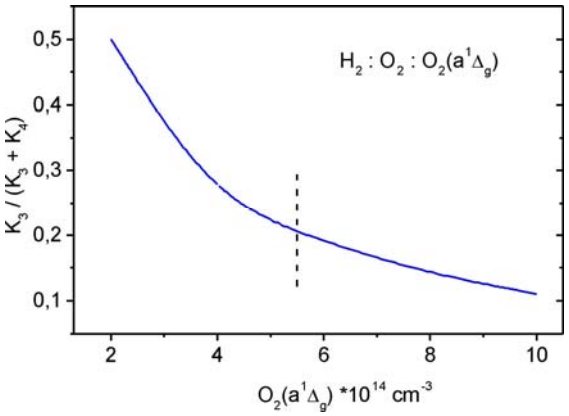

Figure 12. *Relative fraction of the reaction (3) ($k_3/(k_3 + k_4)$) versus the concentration of admixed $O_2(a^1\Delta_g)$ molecules for the conditions of Fig. 11. Dashed curve corresponds to the measured in [51] concentration $O_2(a^1\Delta_g) = 5.5\cdot10^{14}$ cm^{-3}.*

The reaction $H + O_2(a^1\Delta_g) \rightarrow OH + O$ was also studied in [53] under the conditions T = 295 - 423 K, P = 0.5 - 7 torr. Here, as in [51], the mixing of hydrogen and oxygen flows excited by microwave discharges took place. The densities of O and H atoms were measured by the absorption of diagnostic radiation having wavelengths $\lambda = 130.5$ nm and $\lambda = 121.6$ nm, correspondingly. To determine the number density of OH radicals, there was used the laser-induced fluorescence (LIF) technique for the transition $OH(X^2\Pi,\ v = 0) \rightarrow OH(A^2\Sigma,\ v' = 0)$ ($\lambda = 308.2$ nm). The content of $O_2(a^1\Delta_g)$ was determined by the value and dynamics of the photo ionization current occurring as the radiation of Ar lamp ($\lambda = 106.7$ nm) was absorbed by SDO molecules.

Figure 13 shows the experimental data [53] and the calculation results of the temporal dynamics of some components produced in a mixture of He = $3.3\cdot10^{16}$ cm^{-3}, $O_2 = 6.0\cdot10^{15}$ $cm^{-3}$and H = $5.0\cdot10^{11}$ cm^{-3} at T = 300 K. The main reactions determining the change of density of H and $O(^3P)$ atoms and OH and HO_2 molecules in this case are the following:

It should be noted that, in order to agree the results of calculations with the experimental data on the OH(t) dynamics, the rate of reaction (7) was taken equal to $k_7 = 3.8\cdot10^{-11}$ cm^3/s [53] which is 1.7 times less than recommended in [56]. Studies [53, 54] and [56] were performed using identical method and even with the same diagnostics (absorption of UV radiation and LIF). One of the reasons for the pointed out difference in results can be the errors in determining the absolute values of the number density of atomic H. As shown by our calculations, a decrease of the absolute values of $[H]_0$ concentration by approximately 22 - 25% allows to agree data on the value of k_7, i.e. to describe measured in [53] dynamics of OH(t) at a value of $k_7 = 6.6\cdot10^{-11}$ cm^3/s [56].

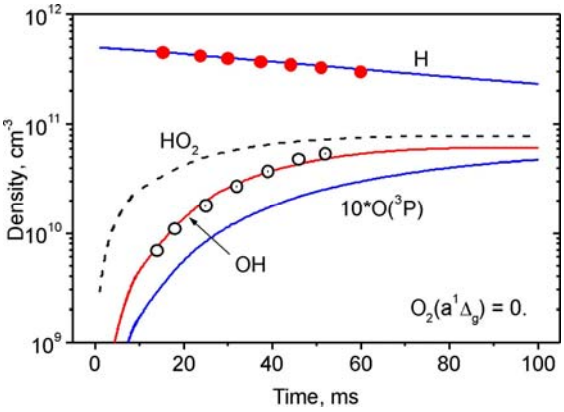

Figure 13. *Temporal dynamics of the main components of the mixture He = $3.3\cdot10^{16}$ cm^{-3}, $O_2 = 6.0\cdot10^{15}$ cm^{-3}, H = $5.0\cdot10^{11}$ cm^{-3}, $O_2(a^1\Delta_g) = 0$ at T = 300 K. Signs correspond to the experimental data [53].*

(6) $H + O_2 + M \rightarrow HO_2 + M$,

(7) $H + HO_2 \rightarrow OH + OH$,

(8) $OH + OH \rightarrow O + H_2O$,

(9) $O + HO_2 \rightarrow OH + O_2$,

(10) $O + OH \rightarrow H + O_2$.

Adding of $O_2(a^1\Delta_g)$ molecules to the mixture results in a sufficient increase in the concentration of produced $O(^3P)$ atoms, but it decreases OH concentration and the rate of hydrogen atoms losses [53, 54]. To explain such dynamics H(t), we should assume the possibility of losses of HO_2 molecules in the reaction involving $O_2(a^1\Delta_g)$. The production of hydrogen atoms should also take place in this reaction.

It is well-known that HO_2 molecules are produced in a highly excited state in the process (6):

$H + O_2 + M \rightarrow HO_2^* + M$.

In this paper, the reaction of dissociation of produced in (6) HO_2^* molecules was additionally considered to explain the results [53, 54].

$O_2(a^1\Delta_g) + HO_2^* \rightarrow H + 2{\cdot}O_2.$ (11)

Additionally, the possible quenching of HO_2^* molecules was taken into account [54]:

$HO_2^* + He \rightarrow HO_2 + He \qquad k = 1.7{\cdot}10^{-12}$ cm^3/s.

The results from the comparison between calculated and experimental profiles of the main considered components are given in Fig. 14. The initial conditions were taken the same as in Fig. 13 but the addition of $O_2(a^1\Delta_g) = 2.6{\cdot}10^{14}$ cm^{-3} was taken into account. The presented calculated curves were obtained at $k_{11} = 5.0{\cdot}10^{-10}$ cm^3/s. Just as in [51], the production of $O(^3P)$ atoms in these conditions is determined by the reaction (3):

$H + O_2(a^1\Delta_g) \rightarrow O(^3P) + OH,$

which allows to determine the fraction of this channel $\alpha = k_3/(k_3 + k_4)$. The presented in Fig. 14 simulation results were obtained at $\alpha = 10\%$. It is good to mention that taking into account the possible errors in determining $[H]_0$ (mentioned above), i.e. decreasing of the initial number density of H by 25%, results in an increase of α up to 16 - 17%, which is close to the values obtained in the processing of experimental data [51].

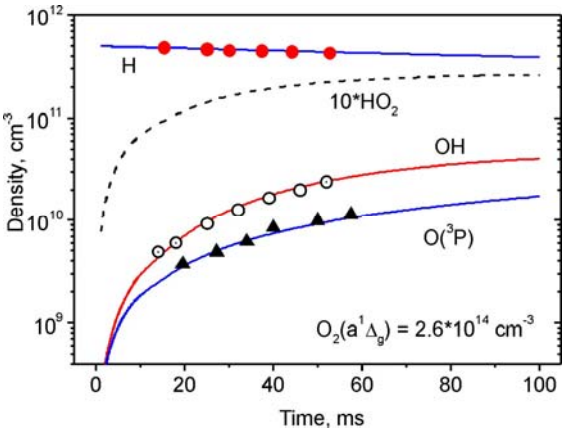

Figure 14. *Temporal dynamics of the main components of the mixture for the conditions of Fig.* ***13*** *at $O_2(a^1\Delta_g) = 2.6{\cdot}10^{14}$ cm^{-3}. Signs correspond to the experimental data*

It is noted in [53] that the time profiles of $O(^3P)$ concentration change with increasing pressure of the mixture in the range of P = 0.1 - 7 torr. This may indicate that the factor α depends on pressure. However, other explanations of this phenomenon are possible (for example, reduction of the characteristic diffusion time and, correspondingly, the rate of heterogeneous losses of $O(^3P)$ with increasing pressure). Since the experimental data on the dependence of the concentration of atomic oxygen on pressure is not given in [53], then it is difficult to make a final conclusion on the causes of this phenomenon.

Thus, a comparative analysis of experimental results [51] and [53, 54] allows making the following conclusions. In [51], due to the low pressure of mixture, the degree of conversion of atomic hydrogen to HO_2 is low during the considered times. Therefore, the main contribution to the $O_2(a^1\Delta_g)$ quenching occurs due to the reactions with atomic H, and quenching by HO_2 can be neglected. In [53, 54] (due to higher pressure), atomic hydrogen is quickly converted to HO_2 and the reactions between SDO molecules and HO_2 became dominant (HO_2 can be produced in both the ground and excited states). The results from numerical simulations of data [51] and [53] concerning the production of atomic oxygen $O(^3P)$ point out that the fraction of reaction (3) is $\alpha = 15$ - 20%, the value of α changing slightly in the temperature range T = 295 - 420 K.
[53].

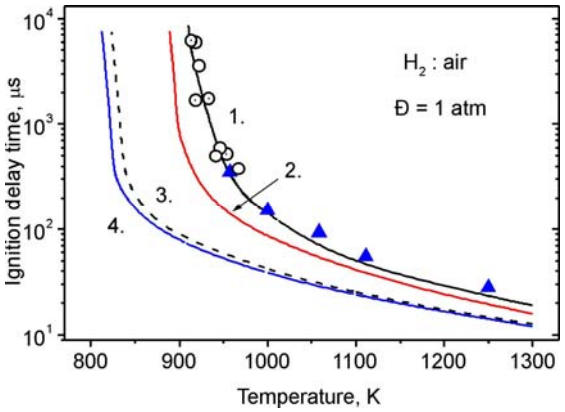

Figure 15. *Dependences of the ignition time of a stoichiometric H_2 : air mixture on the initial temperature ($\alpha = 0.2$) at P = 1 atm and at the various admixtures of $O_2(a^1\Delta_g)$ and $O(^3P)$. Signs correspond to the experimental data [35, 38], curves correspond to the results of calculations without admixtures (curve 1) and with the admixtures of 1% $[O_2(a^1\Delta_g)]/[O_2]$ (curve 2); 0.1% $[O(^3P)]/[O_2]$ (curve 3) and 1% $[O_2(a^1\Delta_g)]/[O_2]$ + 0.1% $[O(^3P)]/[O_2]$ (curve 4).*

Effect of $O_2(a^1\Delta_g)$ admixtures on the ignition of H_2 : O_2 mixtures

Here we analyze the effect of the obtained data on the rates of reactions involving singlet oxygen (3-5) on the ignition of hydrogen-oxygen mixtures. The calculations of the dependence of the ignition times of these mixtures on temperature were performed for different proportions of the processes involving $O_2(a^1\Delta_g)$. The rate constant of reaction (1) was taken similar as in [45] (Table 1) while the fraction of reaction (3) $\alpha = k_3 / (k_3 + k_4)$ was varied from 0.1 to 1. Figure 15 presents the results of calculations of ignition times of

stoichiometric H_2 : air mixture (in the case of α = 0.2) at P = 1 atm and at different initial concentrations of singlet oxygen $O_2(a^1\Delta_g)$ and $O(^3P)$ atoms. All results were compared with curve 1 obtained at concentrations $[O_2(a^1\Delta_g)]_0 = [O(^3P)]_0 = 0$. Curve 2 corresponds to the initial ratio $[O_2(a^1\Delta_g)]/[O_2]_0$ = 1%. As can be seen, the addition of 1% $O_2(a^1\Delta_g)$ does not lead to a sufficient decrease in the temperature threshold of ignition which distinguishes the obtained results from those given in papers [44, 45].

Figure 16 shows calculations of the temporal dynamics of concentrations of the main components and the temperature of the H_2 : air mixture at P = 1 atm, $[O_2(a^1\Delta_g)]/[O_2]_0$ = 1%, T_0 = 900 K. Number density of HO_2 molecules is (1 - 6)·10^{14} cm^{-3} over times of t = 100 - 700 μs which leads to a rapid quenching of $O_2(a^1\Delta_g)$ molecules by these particles. During the ignition time ($\tau_{ind} \cong$ 740 μs) the concentration of singlet oxygen is reduced by more than 100 times. Let us note some increase in the concentration of $O_2(a^1\Delta_g)$ molecules over times of 720 - 780 μs which is associated with the intensification of the process: O + OH → H + $O_2(a^1\Delta_g)$ (the rate constant k(T) was taken from [44]). In addition, the rate of SDO quenching by the HO_2 molecules decreases over these times as their density falls.

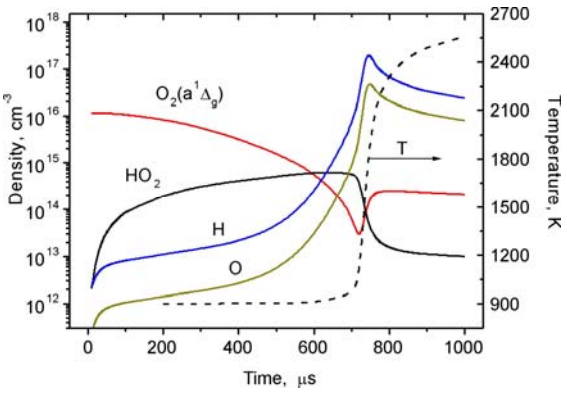

Figure 16. *Temporal dynamics of the temperature and the concentrations of some components of a stoichiometric mixture of H_2 : air at P = 1 atm, T_0 = 900 K and $[O_2(a^1\Delta_g)]/[O_2]_0$ = 1 %.*

Thus, as follows from the calculations presented in Fig. 15, a relatively small effect of admixtures of $O_2(a^1\Delta_g)$ molecules on the ignition of hydrogen-oxygen mixtures occurs due to the rapid quenching of SDO by HO_2 molecules. These molecules are actively produced in H_2 : O_2 mixtures under considered conditions.

One of the main studied now sources of singlet oxygen is an electrical discharge [18], which allows to achieve a sufficiently high degree of excitation of $[O_2(a^1\Delta_g)]/[O_2]$. This is confirmed by experimental results ([18-19] etc.) obtained for different types of discharges. However, as SDO is generated in electric discharge, a great deal of energy can be expended for the dissociation of O_2. In this case it is necessary to consider the total effect (admixtures of $O_2(a^1\Delta_g)$ and atomic oxygen) on the ignition of combustible mixtures.

An example of such a calculation is presented in Fig. 15 (curves 3 and 4) which shows the dependences of ignition times of H_2 : air mixture on initial temperature with admixtures of $[O(^3P)]/[O_2]$ = 0.1% (curve 3) and with the joint effect of 1% $O_2(a^1\Delta_g)$ and 0.1% $O(^3P)$ (curve 4). Adding to the H_2 : air mixture 0.1% of oxygen atoms results in the sufficient decrease in the induction time and in the temperature threshold of ignition of considered mixture. Additional admixing of another 1% $O_2(a^1\Delta_g)$ to this mixture does not give noticeable improvement in ignition characteristics, as is evident from comparison of curves 3 and 4. That is, in presence of even a small initial concentration of atomic particles in a mixture, the effect of SDO admixtures is reduced compared with the unexcited mixture. The reason for this is that the addition of $[O(^3P)]_0$ atoms leads to reducing the role of reaction (1) as a process of chain initiation. The contribution of the reaction of chain branching (3) is also small at the given temperatures [47]. Therefore, under considered conditions, the effect of admixtures of singlet oxygen is reduced only to additional heating of the mixture in the process of its deactivation.

CONCLUSIONS

The results of our analysis lead to the following conclusions. The addition of oxygen and hydrogen atoms to a combustible mixture may result in a significant reduction of the induction delay time of H_2 : O_2 mixtures. Such reduction may be attained with a relative concentration of additions exceeding 10^{-3}. The introduction of atomic particles provides a further possibility of reducing the ignition temperature of mixtures. However, this effect shows up only in the vicinity of the ignition limit. In the zone of relatively low initial temperatures, the shift of the ignition limit is largely associated with the heating of mixture owing to recombination of atomic particles being added. In so doing, the nonequilibrium character of the impact hardly shows up.

A kinetic model describing the effect of the admixtures of molecules of singlet delta oxygen $O_2(a^1\Delta_g)$ on the evolution of the hydrogen-oxygen mixtures was worked out. The dynamics of SDO quenching in H_2 : O_2 mixtures was calculated for the experimental conditions [51-54] in the temperature range of T_0 = 300 - 1050 K. The possibility of describing the entire set of the

experimental data [51-54] in the framework of the model was illustrated.

The effect of admixtures of singlet oxygen molecules $O_2(a^1\Delta_g)$ on ignition of H_2 : O_2 mixtures was studied. The SDO molecules can also participate both in the reactions of chain initiation ($O_2(a^1\Delta_g) + H_2 \rightarrow OH + OH$), and in the reactions of chain branching ($O_2(a^1\Delta_g) + H \rightarrow OH + O$). By comparing the results of calculations with experimental data, the following conclusions on the rates of these processes can be drawn. Most of the acts of interaction of SDO molecules with atomic hydrogen $O_2(a^1\Delta_g) + H$ leads to quenching of $O_2(a^1\Delta_g)$ molecules (reaction 4). Share of this channel is more than 80% and the reaction of chain branching is observed only in 15 - 20% of cases. It is not possible to determine the rate constant of the process $O_2(a^1\Delta_g) + H_2 \rightarrow OH + OH$ (1) on the basis of available experimental data. So, the values of $k_1(T)$ still remain undetermined.

An important process that determines the effect of SDO molecules on the ignition characteristics of hydrogen-oxygen mixtures is its deactivation by HO_2 molecules. According to [55, 57], this reaction is very effective. As a result, in H_2 : O_2 mixtures at high pressure, where the concentration of produced HO_2 molecules can be high enough, the effect of singlet oxygen on the ignition times of these mixtures is relatively weak. This effect becomes even less noticeable if the mixture contains admixtures of atomic oxygen. The last case is typical when the electric discharge systems are used for production of singlet oxygen. Presence of even small (10^{-4}) initial concentration of atomic oxygen or ozone reduces the effect of $O_2(a^1\Delta_g)$ admixtures on the processes of ignition only to additional heating of the mixture in the process of SDO deactivation

ACKNOWLEDGMENTS

This work was partially supported by Russian Agency of Technologies and Innovations (Contract no 02.740.11.5108), the International Science and Technology Center (project no. 3833p) and Grant for Support of Leading Scientific Schools (Grant no. 3322.2010.2).

REFERENCES

1. *Takita K., Moriwaki A., Kitagawa T., Masuya G.* Ignition and flame-holding of H_2 and CH_4 in high temperature airflow by plasma torch // Combustion and Flame. 2003. V. 132. P. 679-689.
2. *Starikovskii A.Yu*. Plasma supported combustion // Proc. Combustion Institute. 2005. V. 30. P. 2405-2417.
3. *Starikovskaia S.M*. Plasma assisted ignition and combustion // J. Phys. D: Appl. Phys. 2006. V. 39. R265-R299.
4. *Bozhenkov S.A., Starikovskaia S.M., Starikovskii A.Yu*. Nanosecond gas discharge ignition of H_2 and CH_4 - containing mixtures // Combustion and Flame. 2003. V. 133. No 1-2. P. 133-146.
5. *Pancheshnyi S.V., Lacoste D.A., Bourdon A., Laux C.O*. Ignition of propane-air mixture by a repetitively pulsed nanosecond discharge // IEEE Trans. Plasma Sci. 2006. V. 34. № 6. P. 2478-2487.
6. *Leonov S.B., Biturin V.A., Yarantsev D.A.* Plasma-induced ignition and plasma-assisted combustion in high speed flow (Issue «Non-equilubrium processes») // TORUS PRESS. 2005. V. 2. P. 104-115.
7. *Brown M.S., Forlines R.A., Ganguly B.N.* Dynamics of hydrocarbon-based pulsed DC discharge for ignition application // 44th AIAA Aerospace Sciences Meeting and Exhibition (9-12 January, 2006, Reno). AIAA 2006-0611.
8. *Lou G., Bao A., Nishihara M., Keshav S., Utkin Yu.G., Rich J.W., Lempert W.R., Adamovich I.V.* Ignition of premixed hydrocarbon-air flows by repetitively pulsed, nanosecond pulse duration plasma // Proc. Combustion Institute. 2007. V. 31. P. 3327-3334.
9. *Chintala N., Bao A., Lou G., Adamovich I.* Measured of combustion efficiency in nonequilibrium RF plasma-ignited flows // Combustion and Flame. 2006. V. 144. P. 744-756.
10. *Shibkov V.M., Chernikov A.P., Ershov A.P. et al.* Ignition of the supersonic propane-air mixture with the help of the surface microwave discharge // The 5th Workshop on Magnetoplasma Aerodynamics for Aerospace Applications. Moscow. 2003. P. 162-165.
11. *Berezhetskaya N.K., Gritsinin S.I., Kop'ev V.A., Kossyi I.A., Popov N.A., Silakov V.P., Van Wie D.M.* Microwave discharge as a method for igniting combustion in gas mixtures // 43th AIAA Aerospace Sciences Meeting and Exhibit. 2005. Reno. AIAA 2005-0991.
12. *Esakov I.I., Grachev L.P., Bychkov V.L., VanWie D.M.* Investigations of undercritical MW discharge with volumetrically-developed streamer structure in propane-air supersonic stream // 44th AIAA Aerospace Sciences Meeting and Exhibition (9-12 January, 2006, Reno). AIAA 2006-0790.
13. *Ikeda Y., Nishiyama A., Kaneko M.* Microwave enhanced ignition process for fuel mixture at elevated pressure of 1 MPa // 47-th AIAA Aerospace Sci. Meeting and Exhibit (January, 2009, Orlando). AIAA 2009-223.

14. *Gerasimov G.Ya.* Ignition of hydrogen-air mixtures exposed to ionizing radiation // Khim. Vys. Energ. 2002. V. 36. No 6. P. 408-412.
15. *Pushkarev A.I., Remnev G.E.* Initiation of hydrogen oxidation by pulsed electron beams // Physics of Combustion & Explosion. 2005. V. 41. No. P. 46-51.
16. *Raizer Yu. P.* Gas Discharge Physics. Berlin: Springer. 1991.
17. *Rusanov V.D., Fridman A.A.* Physics of Chemically Active Plasma, Moscow: Nauka, 1984.
18. *Ionin A.A., Klimachev Yu.M.,Kotkov A.A., Kochetov I.V., Napartovich A.P., Seleznev L.V., Hager G.D.* // Non-self-sustained electric discharge in oxygen gas mixtures: singlet delta oxygen production // J. Phys. D: Appl.Phys. 2003. V. 36. P. 982-989.
19. *Vasiljeva A.N., Klopovsky K.S., Kovalev A.S., Lopaev D.V., Mankelevich Y.A., Popov N.A., Rakhimov A.T., Rakhimova T.V.* // On the possibility of $O_2(^1\Delta_g)$ production by a non-self-sustained discharge for oxygen-iodine laser pumping // J.Phys. D: Appl.Phys. 2004. V. 37. P. 2455-2468.
20. *Semenov N.N.* Chain Reactions. Moscow: Nauka, 1986 (in Russian).
21. *Nalbandyan A.B.* Photochemical Oxidation of Hydrogen // J. Phys. Chem. 1946. V. 20. No 11. P. 1259-1272 (in Russian).
22. *Lavid M., Stevens J.G.* Photochemical ignition of premixed hydrogen/oxygen mixtures with excimer lasers // Combustion Flame. 1985. V. 60. P. 195-202.
23. *Lucas D., Dunn-Rankin D., Hom K., Brown N.J.* Ignition by excimer laser photolysis of ozone // Combustion Flame. 1987. V. 69. P. 171-184.
24. *Lavid M., Nachshon Y., Gulati S.K., Stevens J.G.* Photochemical ignition of premixed hydrogen/oxygen mixtures with ArF laser // Combust. Sci. & Tech. 1994. V. 96. P. 231-245.
25. *Chou M-S., Zukowski T.J.* Ignition of $H_2/O_2/NH_3$, $H_2/Air/NH_3$ and $CH_4/O_2/NH_3$ mixtures by excimer-laser photolysis of NH_3 // Combustion Flame. 1991. V. 87. P. 191-202.
26. *Seleznev A.A., Aleinikov A.Yu., Yaroshenko V.V.* Effect of radiolysis on displacement of explosion limit for hydrogen/oxygen gas mixtures // Chem. Phys. 1999. V. 18. No 5. P. 65-71.
27. *Baratov A.N., Shebeko Yu.N. Korol'chenko A.Ya.* Influence of active centers produced by an external source on the induction period of self-ignition hydrogen/oxygen gas mixtures // Kinetics and Catalysis. 1986. V. 27. No 2. P. 482-485.
28. *Starikovskaia S.M., Anikin N.B., Kosarev I.N., Popov N.A., Starikovskii A.Yu.* Analysis of Ignition by Nonequilibrium Sources. Ignition of Homological Series of Hydrocarbons by Volume Nanosecond Discharge // 44th AIAA Aerospace Sciences Meeting and Exhibition (9-12 January, 2006, Reno). AIAA 2006-0616.
29. *Starikovskii A.Yu.* Ignition initiation by pulsed high-current discharge in gas // Phys. Combustion & Explosion. 2003. V. 39. N 6. P. 12-19.
30. *Okabe H.* Photochemistry of small molecules // J. Willey & Sons Inc., NY. 1978.
31. *Baulch D.L., Cox R.A., Hampson R.F., Kerr J.A.* Kinetic and photochemical data for atmospheric chemistry // J. Phys. Chem. Ref. Data. 1984. V. 13. No 4. P. 1259.
32. *Klopovsky K.S., Lopaev D.V., Popov N.A., Rakhimov A.T., Rakhimova T.V.* // Heterogeneous quenching of $O_2(^1\Delta_g)$ molecules in H_2 : O_2 mixtures // J. Phys. D: Appl. Phys. 1999. V. 32. P. 3003-3012.
33. *Lewis B., van Elbe G.* Combustion, Flame and Explosions in Gases. New York: Academic Press. 1961.
34. *Baulch D.L., Cobos C.J., Cox R.A. et al* Summary table of evaluated kinetic data for combustion modelling // Combust. Flame. 1994. V. 98. No 1. P. 59-79.
35. *Slack M., Grillo A.* Investigation of hydrogen-air ignition sensitized by nitric oxide and nitrogen dioxide // NASA Report CR-2896. 1977.
36. *Warnatz J., Maas U., Dibble R.W.* Combustion: physical and chemical fundamentals, modeling and simulations, experiments, pollutant formation. Berlin: Springer. 2001.
37. *Starikovskaia S.M., Kukaev E.N., Kuksin A.Yu., Nudnova M.M., Starikovskii A.Yu.* Analysis of spatial uniformity of the combustion of a gaseous mixture initiated by a nanosecond discharge // Combustion & Flame. 2004. V. 139. P. 177-187.
38. *Schultz E., Shepherd J.* Validation of detailed reaction mechanisms for detonation simulation // California Institute of Technology Graduate Aeronautical Laboratories Technical Report FM 99-5. 2000. 230p.
39. *Delacroix G. Fereira K.M., Rikar A. Metastable Atoms and Molecules in Ionized Gases* // in: Principles of laser plasma, G. Bekefi Ed. Jonn Willey & Sons Inc. NY. 1976.
40. *Basevich V.Ya., Kogarko S.M.* Mechanism governing the effect of glow-discharge products on the velocity of hydrogen/oxygen flames in combustion peninsula // Kinetics & Catalysis. 1965. V. 6. No 1. P. 23 (in Russian).
41. *Basevich V.Ya., Kogarko S.M.* Mechanism governing the effect of glow-discharge products on the velocity of hydrogen/oxygen flames in

combustion peninsula // Kinetics & Catalysis. 1966. V. 7. No 3. P. 393-400 (in Russian).
42. *Basevich V.Ya., Belyaev A.A.* Calculation of acceleration of hydrogen/oxygen flame on additions of singlet oxygen // Chem. Phys. 1989. V. 8. No 8. P. 1124-1127.
43. *Klopovsky K.S., Lopaev D.V., Popov N.A., Rakhimov A.T., Rakhimova T.V.* // Heterogeneous quenching of $O_2(^1\Delta_g)$ molecules in H_2 : O_2 mixtures // J. Phys. D: Appl. Phys. 1999. V. 32. P. 3003-3012.
44. *Starik A.M., Titova N.S.* Initiation of combustion and detonation in combustible mixtures at excitation of molecular hydrogen to the $O_2(a^1\Delta_g)$ state // Chem. Phys. 2001. V. 20. P. 17-25.
45. *Starik A.M., Titova N.S.* On kinetic mechanisms for combustion initiation in hydrogen/oxygen mixtures at excitation of electron degrees of freedom of oxygen molecules by laser radiation // JTP 2003. V. 73. No. 3. P. 59-68.
46. *Starik A.M., Titova N.S.* On kinetics of detonation initiation in supersonic flows of H_2 + O_2 (air) mixtures at excitation of O_2 molecules by resonance laser radiatiation // Kinetics & Catalysis. 2003. V. 44. No 1. P. 35-46.
47. *Popov N. A.* The effect of nonequilibrium excitation on the ignition of hydrogen-oxygen mixtures // High Temp. 2007. V. 45. P. 261.
48. *Morozov I.I., Temchin S.M.* Kinetics of reactions of singlet oxygen in gaseous phase // Plas. Chem. No 16. Moscow: Energoizdat. 1989. P. 39-67.
49. *Kustarev V. G.* Recommended data for the rate constants of singlet oxygen $O_2(^1\Delta_g)$ deactivation in gas phase // Itogi nauki i tekhniki. Kinet. Catal. 1991 (Moscow, VINITI) V. 24. P. 71.
50. *Borrell P., Richards D.S.* Quenching of singlet molecular oxygen $O_2(a^1\Delta_g)$ by H_2, D_2, HCl, and HBr // J. Chem. Soc. Faraday Trans. II. 1989. V 85. P. 1401-1411.
51. *Cupitt L.T., Takacs G.A., Glass G.P.* Reaction of hydrogen atoms and $O_2(^1\Delta_g)$ // Intern. J. Chem. Kinet. 1982. V. 14. P. 487-497.
52. *Basevich V.Ya., Vedeneev V.I.* Rate constant for reaction H + $O_2(a^1\Delta_g)$ = OH + O // Chem. Phys. 1985. V. 4. P. 1102-1106.
53. *Hack W., Kurzke H.* Kinetic study of the elementary chemical reaction H + $O_2(^1\Delta_g)$ = OH + $O(^3P)$ in gas phase // J. Phys. Chem. 1986. V. 90. P. 1900.
54. *Hack W., Kurzke H.* The production of H atoms in the energy-transfer reaction of $O_2(^1\Delta_g)$ with HO_2 (X^2A') // Chem. Phys. Lett. 1984. V. 104. P. 93.
55. *Podolske J. R., Johnston H. S.* Rate of the resonant energy-transfer reaction between $O_2(^1\Delta_g)$ and HOO // J. Phys. Chem. 1983. V. 83. P. 626.
56. *Sridharau U. C., Qiu L. X., Kaufman F.* Kinetics and product channels of the reaction of HO_2 with O and H atoms at 296 K // J. Phys. Chem. 1982. V. 86. P. 4569.
57. *Becker K. H., Fink E. H., Langen P., Schurath U.* Near infrared emission bands of the HO_2 radical // J. Chem. Phys. 1974. V. 60. P. 4623.

2.1. KINETIC SIMULATION OF RADIO FREQUENCY DISCHARGE INFLUENCE ON THE PLASMA LAYER NEAR SURFACE IN SUPERSONIC GAS FLOW

I.V. Schweigert
Institute of Theoretical and Applied Mechanics,
Novosibirsk 630090, Russia

It is known that the supersonic flight vehicles at high altitudes is surrounded by plasma layer. The density of electrons in this layer is high enough to block the vehicle communication channels. The aim of this study is understand the mechanism of influence of RF discharge on the external plasma layer.

Low pressure radio frequency (RF) discharge near the surface is studied with using the two dimensional Particle-in-cell Monte Carlo simulations. The kinetics of electrons in nitrogen includes elastic scattering and excitation of rotation, vibration, metastable states and ionization. The supersonic flow near the surface is set with a model function. The external ionization is assumed to be constant within layer.

In RF discharge the electron density is diluted in the electrode sheath during the cathode part of rf-cycle. We varied the RF frequency and applied voltage and study the dynamics and size of the electrode sheath. Our purpose is to reduce locally the electron concentration near the surface.

We consider the kilovolt applied voltages and gas pressure lower than 100 mTorr. In this case the electron and ion distribution functions demonstrate non-local dependence from the electrical field. We pay special attention to set accurately the boundary conditions on the dielectric surface. The electrical potential on the dielectric surface around the electrodes is calculated from the balance equation of the local electron and ion currents on the surface.

2.2. ELECTRON BEAM AND GAS DISCHARGE IONIZATION OF A HYPERSONIC FLOW IN A MAGNETIC FIELD

V.N. Devjatkov, N.N. Koval, V.P. Fomichev*, and A.B. Shevchenko*
Institute of High Current Electronic SB RAS, 2/3 Akademichesky Ave., Tomsk, 634055, Russia
Fax: +7(3822) 492-410, Phone: +7(3822) 491-713, E-mail: vlad@opee.hcei.tsc.ru
*Khristianovich Institute of Theoretical and Applied Mechanics, 4/1 Institutskaya St., Novosibirsk, 630090, Russia, Fax: +7(383) 330-72-68, E-mail: fomichev@itam.nsc.ru

Abstract. The paper considers methods of creating and maintaining nonequilibrium conductivity of supersonic and hypersonic air flows that can be used in their MHD control. The flow is characterized by a relatively high pressure (a few torr) and is produced in a strong magnetic field (a few tesla). The methods of ionization considered in the paper are ionization with an electron beam of energy up to 10–15 keV (either injected into the region of a strong magnetic field, or produced directly in a magnetic field) and with electric discharges initiated length- and crosswise magnetic field lines.

Introduction

The advance of magnetohydrodynamic (MHD) technologies in magnetoplasma aerodynamics is impossible without producing and maintaining nonequilibrium conductivity of supersonic and hypersonic air flows with full-scale flight parameters and a magnetic field up to a few tesla. Among rather accessible and efficient tools of gas ionization, electron beams [1] and electric discharges [2] hold promise. These technologies are distinguished by a relatively high gas pressure (a few torr) and strong magnetic field (a few tesla), and this complicates the generation of an electron beam and the initiation of an electric discharge with required parameters (the current density is fractions of ampere per square centimeter and the electron energy is a few kiloelectron volts). In experiments, the desired current pulse duration is no less than 100 μs; an indispensible condition of ionization is the homogeneity of the ionization region. All the above factors are the main troubles in the development of methods for electron beam and gas discharge ionization of hypersonic flows in a magnetic field. Moreover, electron beam ionization requires small losses of the beam propagating lengthwise magnetic field lines.

An electric discharge for ionization of a hypersonic flow can also be realized lengthwise a magnetic field. In this case, the discharge renders the flow conductivity irrespective of the induced electric current ($V \times B$). In electron beam or gas discharge ionization of hypersonic flows along a magnetic field, the MHD current kept by the induced electric current is non-self-sustained and depends on the level of external ionization. Figure 1 shows schematic of a typical experimental arrangement. An ionizing electric discharge can be initiated crosswise the flow and magnetic field. In this case, an external magnetic field can be applied to the MHD electrodes and the discharge in the external and induced electric field is a self-sustained discharge in which the ionization current directly participates in the development of MHD effects [3, 4].

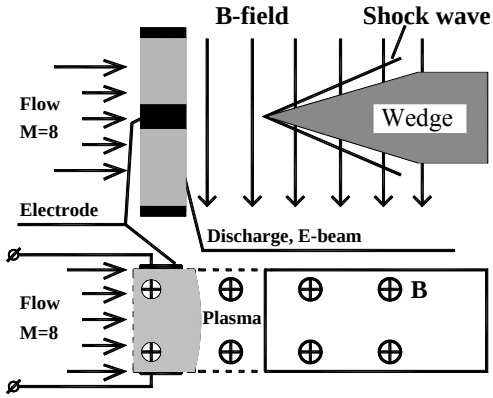

Fig. 1. *Experimental arrangement for electron beam and gas discharge ionization of a hypersonic flow in a magnetic field.*

Electron beam ionization

Preliminary experiments on ionization of a hypersonic flow with an electron beam produced by a thermionic-cathode electron gun show that the main problem is in the necessity to reject the electron beam injection into the gas flow through a foil window. This is because efficient gas ionization requires a relatively low electron energy (up to 20 keV) in the flow, whereas transport of the beam through the foil window with small losses requires that the electron energy reaches ~ 100 keV. Moreover, fracture of the foil window at the instant of electron injection through it and hence failure of the gun cathode is highly probable. The abandonment of the foil necessitated the use of plasma emission cathodes with grid stabilization of the emission surface to provide the generation of electron beams of required duration and long-term operation of the cathode at increased pressures. The use of this cathode for

ionization of a hypersonic air flow is possible if the acceleration gap escapes breakdown as the pressure in the chamber is increased during the passage of the air flow; an electron beam is too difficult to produce at a working pressure characteristic of hypersonic flows. Therefore, the plasma-cathode electron gun was preconditioned at a pressure no greater than p = $3 \cdot 10^{-3}$ Torr produced in the vacuum chamber at the stage preceding the passage of a hypersonic air flow with a pressure of several torr in the gas discharge channel.

An electron beam with a cross section of several square centimeters propagating along magnetic field lines in the region of a hypersonic flow can be obtained by either injecting the electron beam from the place of its generation into the increasing magnetic field or generating the beam directly in the strong longitudinal magnetic field. In the first case, the position of the plasma cathode outside the strong magnetic field simplifies the problem of electron beam formation (homogenous gas discharge plasma emitting the electron beam is rather easily available; the acceleration gap of the electron source is removed as far as possible from the region of the hypersonic flow of increased pressure). However, the injection of a broad electron beam into a strong magnetic field can be hard to realize. In the second case, it is necessary to provide the ignition and rather homogeneous operation of the discharge producing emission plasma in a strong magnetic field. Moreover, the acceleration gap of the electron gun, in this case, is located in the strong magnetic field and is much closer to the region of the hypersonic air flow; this also complicates the formation of a homogeneous electron beam of long duration.

Experiments on electron beam injection into a magnetic filed

Figure 2 shows schematically the setup for experiments on MHD control of hypersonic flows and the plasma-cathode electron gun with grid stabilization of the plasma emission boundary. This design was used to determine whether it is feasible to employ a plasma cathode in the electron source for ionization of hypersonic flows.

The electrode system of the plasma gun consists of two coupled discharge systems. The discharge initiating system is used to ignite a cathode spot at Mg cathode *1*. The amplitude of the auxiliary discharge current is 10–15 A at a pulse duration of ~25 μs. The main arc discharge with a discharge pulse duration of 100 μs and controllable amplitude of 20– 200 A is ignited between the electrodes *1* and *2*. The pulsed discharge current is measured with Rogowski coils Id1 and Id2. The surface of the electrode *2* from which electrons are emitted is a rectangle of dimensions 20 × 60 mm tightly covered with a fine stainless steel grid of mesh size 0.3 × 0.3 mm. Accelerating electrode *3* is a diaphragm with a hole of diameter 80 mm.

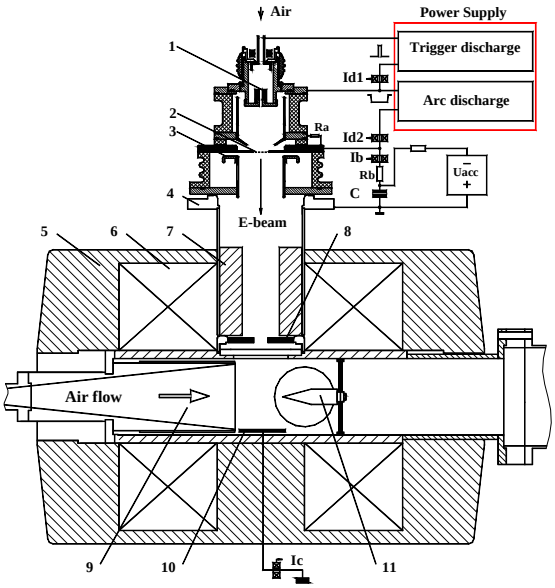

Fig.2. *Setup for experiments on MHD control of a hypersonic air flow with the plasma-cathode electron gun placed atop.*

Electrons are extracted from the plasma produced by the main discharge as an accelerating voltage is applied between the electrodes *2* and *3*; the electrodes are connected to a 3-μF capacitive store charged with a dc voltage source Uacc. As the acceleration gap is broken down, the current limits the ballast resistance Rb to ~ 1 Ohm. The beam electrons accelerated in the acceleration gap pass through drift tube *4* and enter the magnetic field B = (0.1 ÷ 0.2) T produced by solenoid *6* with magnetic circuits *5* and additional magnetic inserts *7* changing the magnetic field configuration in the region of electron beam injection. Part of the electron beam passes into the working volume of the setup through diaphragm *8* (20 × 60 mm) and arrives at collector *10* arranged at the bottom of the working chamber. The collector current is measured with a Rogowski coil Ic. In the operating mode, the hypersonic flow (air at a pressure of ~10 Torr forced out by the second gas – He) passes through nozzle *9*, is ionized by the electron beam, and gets into the region in which model (wedge) *11* and additional electrodes (not shown in Fig. 2.) for MHD control of the flow can be arranged. The working chamber of the setup, the additional volume into which the hypersonic flow is released, and the volume of the electron source are pumped down to a limiting pressure p = (1–3)· 10^{-3} Torr with an oil-vapor booster pump. For stabilization of the discharge operation and electron beam emission, an additional small portion of gas (air) was leaked in the electron

source. The additional gas supply changed almost not at all the pressure in the vacuum chamber (the pressure varied within < 5%). For synchronization of the electron beam pulse, hypersonic flow in the setup, and video cameras for visualization of the flow, the power supply units of the electron gun are equipped with an external synchronization input port. The synchronization signal is produced by a signal of a detector located in the gas line at the instant of passage of the air flow. The instant at which a pulse of the electron beam current is generated is determined by the instant at which the main discharge of the plasma emitter is ignited and is within ~ 15 μs after the arrival of the synchronization pulse. In preliminary adjustment and conditioning of the electron gun, its power supply units are started by a built-in generator with a pulse repetition frequency of 1 Hz.

The electrons are extracted from the plasma cathode under the conditions of intense gas ionization in the space of electron beam transport and attendant self-consistent creation of a plasma anode. Figure 3 shows typical waveforms taken in the adjustment mode of the electron gun (with ultimate vacuum and with no magnetic field). In this mode, the collector current reaches its maximum value ranging to over 60 A.

Fig.3. *Characteristic waveforms of the currents of the electron gun with no magnetic field: 1 – synchronization pulse, 2 – pulse of the main discharge current Id2 (200 A/div), 3 – total beam current Ib (80 A/div), 4 – collector current Ic (60 A/div) for p = 1.7 · 10^{-3} Torr, Uacc = 10 kV, B = 0 T. The time scale is 25 μs/div.*

As the magnetic field is applied, both the dimension and the amplitude of the beam current passed into the working chamber decrease. The injection of the electron beam into the increasing magnetic field along its lines is possible only in the central part of the axially symmetric magnetic system (when the electron beam enters the field at a small angle to the magnetic field lines). For injection of a broad ribbon beam, the magnetic system of the setup was added with ferromagnetic inserts such that the beam was injected into a plane-parallel gap between the elements of the magnetic system. Figure 4 shows waveforms of the currents taken with this configuration at B = 0.17 T.

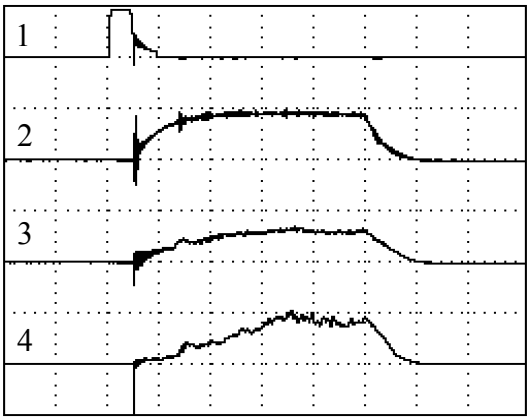

Fig.4. *Characteristic waveforms of the currents with a magnetic field: 1 – synchronization pulse, 2 – pulse of the main discharge current Id2 (200 A/div), 3 – total beam current Ib (200 A/div), 4 – collector current Ic (2 A/div) for p = 1.7 · 10^{-3} Torr, Uacc = 10 kV, and B = 0.17 T. The time scale is 25 μs/div.*

Figure 5 shows the magnetic system with inserts from the side of electron beam injection into the working chamber and glow of the air ionized by the electron beam.

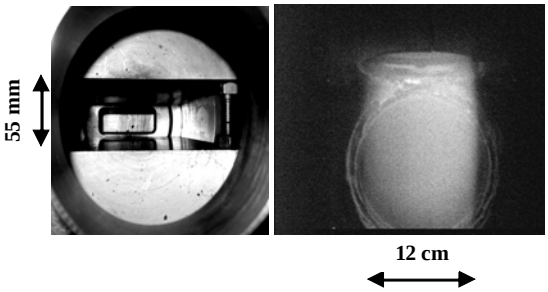

Fig.5. *Modified magnetic system and glow of the gas ionized by the electron beam in the working chamber for p = 1.7 · 10^{-3} Torr, B = 0.17 T, Uacc = 10 kV, and Ic ~ 2 A.*

The experiments on the generation of an electron beam in the presence of a hypersonic flow confirm that ionization of the flow with the plasma-cathode electron gun is feasible. Although the pressure in the hypersonic flow is 1–20 Torr, the pressure in the channel through which the electron beam passes is likely to have no chance to increase during the electron beam current pulse. After conditioning, the breakdown of the acceleration gap of the electron gun due to the increase in pressure occurs much later than the end of the electron beam current pulse. In the experiments, the time between the end of the beam current pulse and the breakdown of the acceleration gap is from 2 to 5 ms. With the

preconditioned electron gun, the probability of an operating current pulse with no breakdown of the acceleration gap is no less than 80%.

Figure 6 shows waveforms of the currents taken in the experiments on ionization of a hypersonic flow with electron beam injection into a magnetic field.

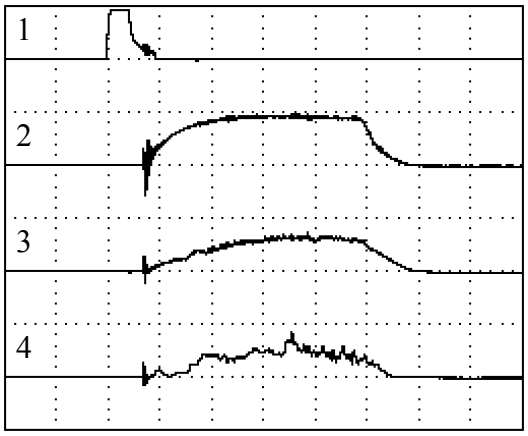

Fig.6. *Waveforms of the currents for electron beam injection into a magnetic field B = 0.17 T: 1 – synchronization pulse, 2 – pulse of the main discharge current Id2 (200 A/div), 3 – total beam current Ib (200 A/div), 4 – collector current Ic (2 A/div) for p = 1.7 · 10^{-3} Torr and Uacc = 10 kV. The time scale is 25 μs/div.*

In the experiments, intense glow in the working chamber was observed, and this points to efficient electron beam ionization of the gas flow. The maximum current at the collector (with a magnetic field B = 0.17 T in the presence of the hypersonic flow) decreases from 2 to 1 A. However, it should be noted with intense ionization of the gas near the collector, high ionization currents can flow toward the collector and hence the actual electron beam current can be much higher than that measured with the Rogowski coil. With a higher-pressure flow, the current that takes the path through the collector can also decrease due to partial scattering of the electron beam.

A photo of the glow of the ionized hypersonic flow (along the flow direction) is shown in Fig.7. The bright glow at the bottom of the figure corresponds to the position of the nozzle.

Increasing the magnetic field causes more intense gas ionization in the region of electron beam transport. This changes somewhat the operating mode of the plasma cathode. The beam current increases due to secondary ion-electron emission from the cathode of the electron source and can exceed the discharge current of the plasma cathode; the beam current measured at the collector with a magnetic field B = 0.34 T decreases to 0.1–0.2 A (Fig. 8). It should be noted that during the pulse rise time, the current measured at the collector has a resultant ion component. Further increasing the

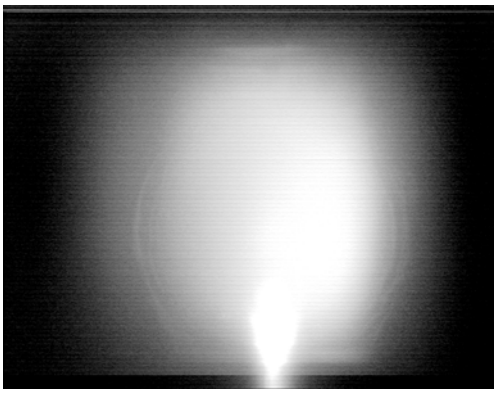

Fig.7. *Glow of the hypersonic flow ionized by the electron beam for B = 0.17 T, Uacc = 10 kV, and Ic ~ 1 A.*

magnetic field also decreases the dimension of the beam injected into the working chamber and the beam as a filament enters the chamber thus breaking the required geometry of the ionization region. Therefore, further studies were toward the design of a plasma cathode to be placed directly in the magnetic field.

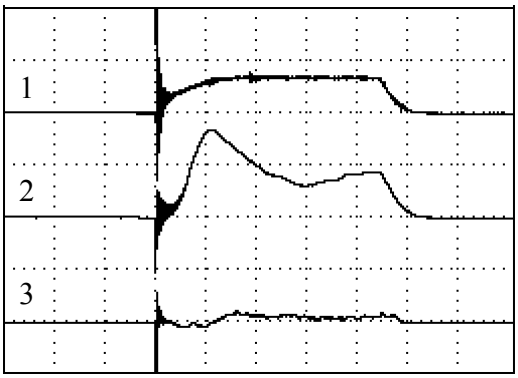

Fig.8. *Waveforms of the currents for electron beam injection into a magnetic field B = 0.34 T: 1 – pulse of the main discharge current Id2 (80 A/div), 2 – total beam current Ib (80 A/div), 3 – collector current Ic (0.5 A/div) for p=1.7·10^{-3} Torr, Uacc = 12 kV. The time scale is 25 μs/div.*

Electron beam generation in a magnetic field

Arc-discharge plasma cathodes, as a rule, use an electrode system with an anode of rather large area. With no external magnetic field in the region of discharge operation, the discharge is homogenous over the entire inner surface of the hollow anode. Part of the anode surface facing the acceleration gap serves as an emission electrode. This surface can be a fine metal grid that limits the plasma emission surface. In this case, the electron beam extraction through the grid meshes can be rather uniform over the entire surface.

Application of a magnetic field greatly impairs the homogeneity of the arc discharge at

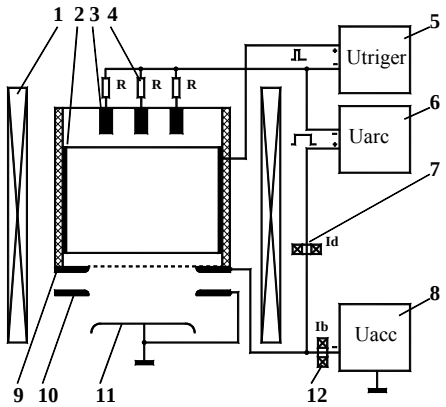

Fig.9. *Electrode system and power supply circuit of the discharges in the multi-arc plasma emitter in a magnetic field: 1 – solenoid, 2 – trigger electrode, 3 – cathode, 4 – ballast resistor, 5 – power supply of the auxiliary discharge, 6 – power supply of the arc discharges, 7 – discharge current sensor (Id), 8 – power supply of the acceleration gap, 9 – emission electrode, 10 – accelerating electrode, 11 – collector, 12 – beam current sensor (Ib).*

the emission electrode. The discharge starts operating as a "filament" of increased current density in a local surface patch of the emission electrode, and this can limit the total maximum current of the extracted electron beam. To overcome this problem and to provide the generation of emission plasma over the whole region of beam extraction, the discharge system operated in a magnetic field must ensure several arc discharges.

Figure 9 shows a block diagram of the electrode system of an electron source with three arc channels. The discharge gaps were powered by one channel of power supply unit *6* with the use of ballast resistors *4*. The discharge chamber was placed in a about 0.05-T longitudinal magnetic field of solenoid *1*. Arc discharges were initiated by applying a high-voltage initiation pulse (of voltage 10–12 kV and current up to 10 A) from pulsed voltage source *5* to additional electrode *2*. In the discharge system, a Penning discharge is first ignited for which electrodes *3* and *9* are cathodes and electrode *2* is an anode. The voltage for the auxiliary discharge is applied 10 μs earlier than that from power supply *6* of the arc discharges and remains applied till the end of the formation of a current pulse of the main arc discharges between the cathodes *3* and the electrode *9* which has an emission hole of 2 × 6 cm tightly covered with a grid of mesh size 0.3 × 0.3 mm.

Although this initiation and power supply system of the arc discharges fails to ensure reliable simultaneous ignition and operation of even three arc discharges, the system allowed experiments on the electron beam generation with the plasma cathode placed in a magnetic field using the single-channel power supply unit of the arc discharges.

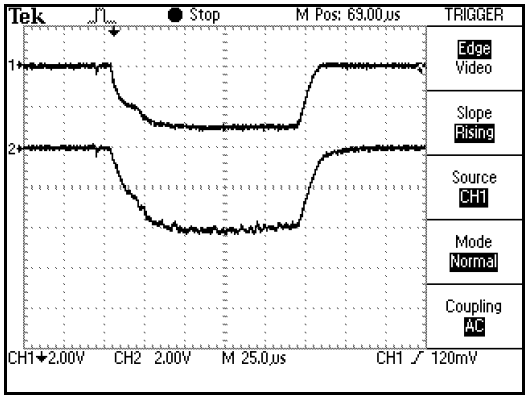

Fig. 10. *Waveforms of the currents: 1 – total arc discharge current Id, 2 – total current in the acceleration gap Ib for $p = 2 \cdot 10^{-3}$ Torr, U = 10 kV. The scale is 40 A/div, 25 μs/div.*

In this discharge system, gas leak-in was not used and the pressure in the vacuum chamber was controlled in the range $p = (1–3) \times 10^{-3}$ Torr by varying the efficiency of the pumping system through varying the number of revolutions of the turbomolecular pump.

Figure 10 shows waveforms of the total arc discharge current Id and total beam current Ib (current in the acceleration gap of the electron gun). The total beam current exceeds the total arc discharge current because the former contains both the ion component and the electron component produced in secondary ion-electron emission from the emission electrode and grid [5].

As the discharge current is increased (Id ≥ 100 A), the total beam current no longer replicates the form of the discharge current (Fig. 11) and breakdowns of the acceleration gap can be escaped only by decreasing the operating pressure. The sufficiently high electron beam amplitude obtained in the experiments allows us to hope that the further increase in magnetic field will ensure a

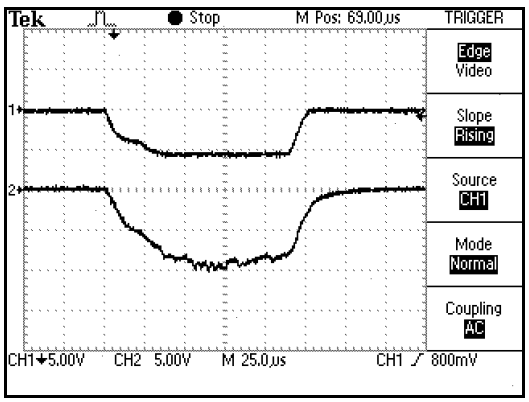

Fig. 11. *Waveforms of the currents: 1 – total arc discharge current Id, 2 – total current in the acceleration gap Ib for $p = 1 \cdot 10^{-3}$ Torr, Uacc = 10 kV. The scale is 100 A/div, 25 μs/div.*

current sufficient for ionization of hypersonic flows.

Gas discharge ionization

Discharge lengthwise the field

An electric discharge along a magnetic field was used for external ionization of the flow in a circuit similar to that used for electron beam ionization and shown in Fig. 1. The MHD electrodes were located upstream of the model. The dimensions of the electrodes were 1.5 × 25 mm^2. The air flow at a static pressure of 0.5 Torr has a velocity of 2000 m/s; the Mach number of the flow was M = 10. A current pulse of duration 120 μs was applied from the high-voltage source to the electrodes whose axis was perpendicular to the flow (Fig. 1). The discharge with no flow at a pressure of 0.5 Torr in a magnetic field B = 0.85 T is clearly seen in the photo in Fig. 12.

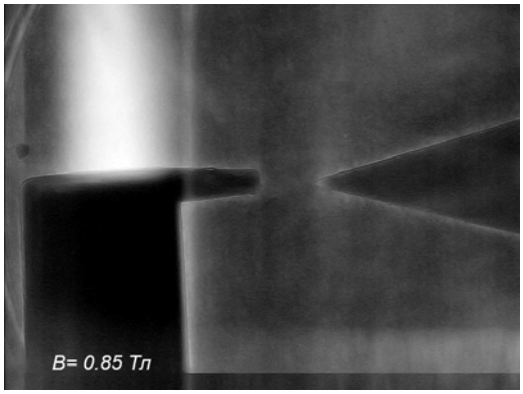

Fig. 12. *Photo of the discharge with no flow, B = 0.85 T.*

In the flow, the discharge region moves along the flow with respect to the MHD electrodes (Fig.13).

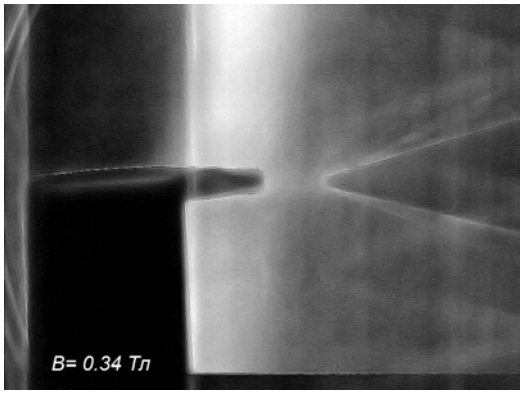

Fig. 13. *Photo of the ionizing discharge in the flow and in the magnetic field B = 0.34 T.*

In these experiments, the MHD electrodes were short-circuited. The current to be measured was the short-circuit current induced by the MHD interaction in the flow. Oblique shock waves formed at the wedge in wedge flow are seen in Fig. 13. The experiments reveal pulsations of the MHD current at a relatively constant ionization current [2]. Figure 14 shows waveforms of the ionization current (curve *1*) and MHD current (curve *2*). It is seen that the pulsations of the MHD current are not associated with the variation in the ionization current and result from certain processes occurring in the MHD discharge region. This effect calls for further research.

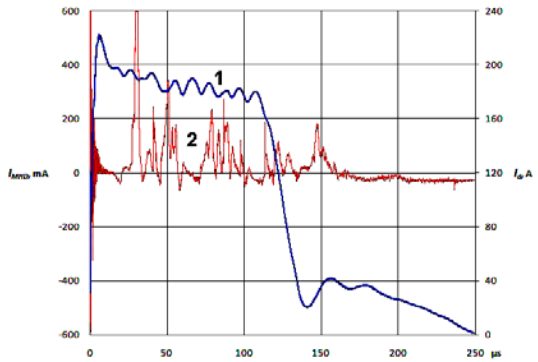

Fig. 14. *Waveforms of the ionization current (1) and MHD current (2) at B = 0.85 T. The scale is 50 μs/div, 40A/div (1), 0.2A/div (2).*

Discharge crosswise the filed

Experiments on an external electric discharge crosswise the magnetic field were also performed according to the arrangement shown in Fig. 1. The relative position of the electrodes and model is shown in Fig. 15.

Fig. 15. *Relative position of the electrodes and model: 1 – electrodes, 2 – model (wedge).*

The ionized and flow-heated gas with no magnetic field can be seen in Fig. 16.

In the magnetic field between the electrodes, the MHD interaction region is localized, and this results in retardation and heating of the flow and in an increase in the slope of the oblique shock wave generated by the wedge in the hypersonic flow

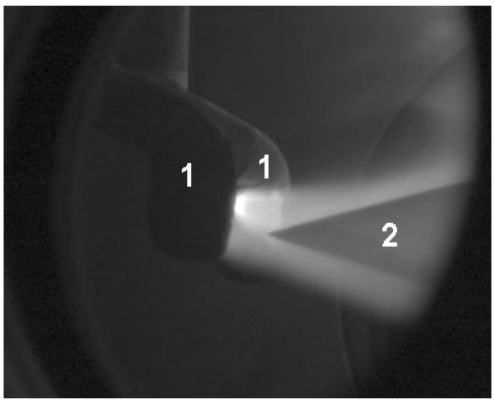

Fig. 16. *Photo of the discharge and flow.*

with M = 8 [6]. The experiments demonstrate a rather high efficiency and a relative simplicity of the MHD control of the flow [2, 4]. However, the experiments also disclose a danger of the discharge constriction in the MHD interaction region with its attendant loss in MHD control efficiency, Fig. 17 [2].

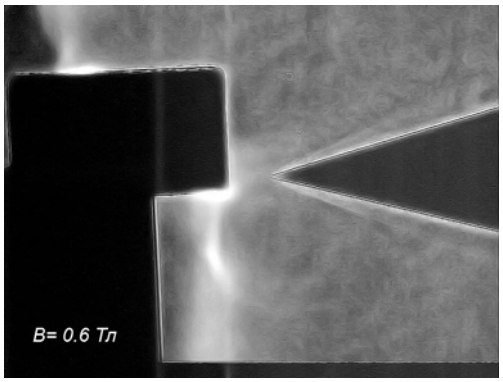

Fig. 17. *Photo of the contracted discharge and flow with M=10 at B = 0.6 T.*

Conclusion

1. The studies demonstrate the feasibility to use a plasma emission cathode with grid stabilization of the emission plasma boundary and a plasma anode for ionization of a hypersonic air flow of pressure ~10 Torr in a magnetic field of 0.17 T on the test bench pumped down to a limiting pressure $p = 1.0^{-3}$ Torr.
2. In the experiments on the multi-arc electron source with a plasma cathode, an electron beam current up to 200 A was obtained at a pressure $p=1\cdot 10^{-3}$ Torr, duration of the electron beam current pulse of 100 μs, and accelerating voltage up to 10 kV in a magnetic field of 0.05 T.
3. The advantage of electron beam ionization of hypersonic flows is in the relative independence of the ionization from MHD interaction and in the possibility to control the parameters over a wide range.
4. Electric discharges hold promise for external ionization of hypersonic flows in a magnetic field; however, this method has to do with the secondary effects of MHD interaction.

Thus, despite the feasibility of an ionization region in a hypersonic gas flow in a strong magnetic field with the studied methods, certain effort is still to be taken to provide uniform electric conductivity at a level sufficient for reliable experimental research on MHD control of the flow.

The work was supported by the interdisciplinary integration project IM80 of SB RAS.

References

1. V.N. Devjatkov, N.N. Koval, V.P. Fomichev, A.B. Schevchenko. Generation of electron beam for ionization of hypersonic air flow. // Proceedings of 16th International Symposium on High-Current Electronics. Tomsk. – 2010. – PP.19-22.
2. V.P. Fomichev, T.A. Korotaeva, A.P. Shashkin, M.A. Yadrenkin. Investigation of the MHD-interaction in a supersonic flow // Proceedings of the 17th International Conference on MHD energy conversion, Shonan Village Center, Kanagawa, Japan, 14-17 September 2009, 13p.
3. V.M. Fomin, V.P. Fomichev, T.A. Korotaeva, A.A. Maslov, A.A. Pavlov, Al.A. Pavlov, S.S. Pravdin, A.P. Shashkin, V.I. Yakovlev, N.D. Malmuth, P. Smereczniak and J. S. Silkey. Initiation of nonequilibrium conductivity of a hypersonic flow and MHD-interaction // AIAA 2007-1376, 45th AIAA Aerospace Sciences Meeting and Exhibit, Reno, Nevada, 2007.
4. V.P. Fomichev, V.E. Podzin, A.B. Shevchenko, M.A. Yadrenkin. Investigation of the air flow around a wedge at M=6 under the local MHD-influence // The 9th international workshop on magneto-plasma aerodynamics, Abstracts, Moscow, April 13-15, 2010. PP. 83-86.
5. S.V. Grigoryev, V.N. Devyatkov, N.N. Koval, A.D. Teresov. Effect of Intensified Emission During the Generation of a Submillisecond Low-Energy Electron Beam in in the diode with the grid plasma cathode and plasma Anode. Rus. Tech. Phys. Letters 36/4, 2010. PP. 23-31.
6. T.A. Korotaeva, V.P. Fomichev, A.P. Shashkin and M.A. Yadrenkin. Investigation of Magnetohydrodynamic Interaction in a supersonic Air Flow at M=8. Technical Physics, 2011,Vol. 56, NO. 3, PP. 327-334.

2.3. LONG SPARK DISCHARGE INITIATION IN SUPERSONIC AIRFLOW

Golub V.V.[1], Saveliev A.S.[2], Sechenov V.A.[2], Son E.E.[1]
[1]Joint Institute for High Temperatures RAS, Moscow
[2]Moscow Institute of Physics and Technology, Dolgoprudny

The investigation of the pulse-periodic initiation of long spark discharge on the surface of aerodynamic model, streamlined by supersonic airflow with Mach number M=2, with the frequency of 10 kHz order and with submicrosecond duration was carried out. NACA64A212 wing profile was chosen as aerodynamic model with chord length 10 cm, wing span 15 cm and thickness 12 mm, the material of model was fused silica. The slot was provided on the airfoil upper surface for discharge device placement. Discharge device is straight device, that consists of big amount of electrodes, separated by dielectric layer. Each of electrodes is made from kovar, it has 3 mm x 2 mm dimensions, and the electrodes are separated by teflon tape of 50 μm thickness. The discharge device is aligned perpendicular to airfoil chord, i.e. perpendicular to streamlines of incoming flow. The high voltage was applied to outside segments (electrodes) by high voltage wires from the capacitor box, charged through the ballast resistor by high voltage supply Spellman SL15P2000 up to 10 kV voltage value, that is close to breakdown value. Capacitor box consists of a set of ceramic capacitors K15-5 of 4.7 nF capacity each. The electrical and temporal characteristics were registered by LeCroy Wave Runner 104 Xi oscilloscope and Tektronix 6015A high voltage probe. And during two seconds of test run the start time, breakdown voltage, remanent voltage of each discharge were possible to register.

The experiments on electrical discharge initiation in airflow were carried out on the atmospheric-vacuum supersonic wind tunnel ST-4. The working chamber of ST-4 is equipped with transparent windows of optical glass for flow visualization. The shadow and schlieren visualization were applied as the diagnostics of unsteady gasdynamics processes that occurs after electrical breakdown. The optical diagnostics was developed on the base of schlieren device IAB-451, high speed digital videocamera Photron FASTAM SA4, xenon arc lamp XBO 150w/1. All the diagnostics system allowed to obtain the photographs of flow with the exposition time not less than 1 μs, acquisition speed $2 \cdot 10^4$ fps, $4 \cdot 10^4$ frames during one test run. Synchronization signal from the videocamera, that corresponds to frames exposition, was applied on one of oscilloscope channels. Due to this synchronization the certain moment of time after discharge breakdown and its energy can be assigned to each frame of photoregistration.

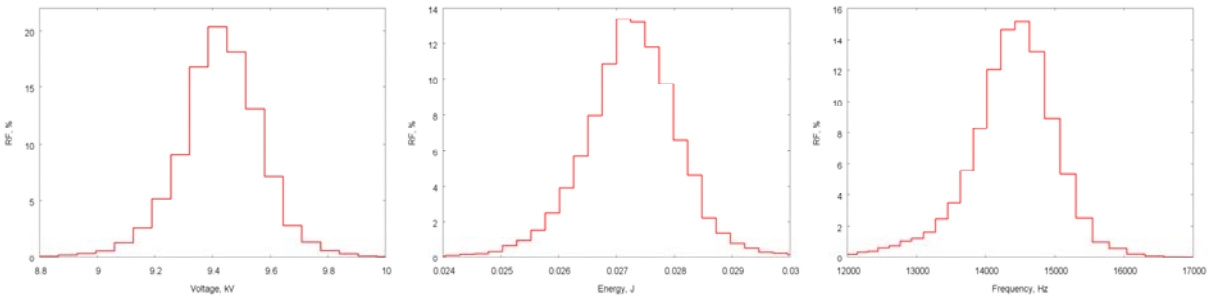

Fig. 1. *The histograms of breakdown voltage, energy and frequency of discharge.*

Fig. 2. *The photograph (reversed image) of separate discharge with 100 mJ energy and length of 10 cm. The supersonic airflow goes from top to bottom.*

The experiment has shown that breakdown voltage, remanent voltage on the capacitor and, correspondingly, the energy of each discharge vary in range of 10% of average values. This fact is presented on the Fig. 1, where spark length is 10 cm, total value of capacity of capacitor box is 612 pF. On the Fig. 2 the reversed image of spark discharge (top view) with the energy of 100 mJ is presented.

This circumstance has allowed making the averaging of shadow pictures of airflow around the airfoil. And the evolution of unsteady disturbance of the supersonic flow above the airfoil surface, that consists of cylindrical shock wave and vortex, that spread downstream along the airfoil surface, was obtained. The obtained time-resolved pictures of the processe have shown that unsteady flow caused by discharge has influence on the flow separation point position during the time, that is comparable with time of flight (30-50 μs). The obtained pictures have allowed determining the dependence between the Mach number of shock wave, caused by electrical discharge, in relation to coming airflow and the energy of discharge, stored in capacitor box, in range of 20 mJ - 200 mJ.

2.4. SIMULATION OF DYNAMICS AND STRUCTURE OF PLASMA MICROJETS

G.V. Naidis
Joint Institute for High Temperatures RAS, 125412 Moscow, Russia, gnaidis@mail.ru

Abstract: Results of simulation of streamer propagation along helium jets in ambient air are presented. Two-dimensional axially symmetric streamer model, accounting for variation of helium-air mixture composition inside the jet, is used. Obtained distributions of plasma parameters have a ring-shaped structure, typical for plasma bullets. The effect of voltage polarity on the calculated plasma bullet parameters is similar to that observed in experiments. Calculated radial profiles of emitting nitrogen molecules agree with experimental data.

1. Introduction

Cold atmospheric-pressure plasma jets, formed by barrier discharges in a gas flow (usually helium, argon or their mixtures) in thin dielectric tubes and injected into ambient air, are actively studied as an effective source for production of non-thermal plasmas. High-speed photographs have revealed that the jets are typically composed of bullet-like plasma volumes traveling with velocities in the range 10^6-10^8 cm/s, like ionization waves – streamers (e.g. [1-3]).

Although plasma bullets are similar to streamers, some specific features of plasma bullets propagating in a jet column differ from those of streamers in a free space (in uniform gas). In particular, experiments [1] have revealed ring-shaped profiles of plasma bullet radiation intensity [1,3] and of the density of metastable helium atoms [2]. Simulations [4] of streamer propagation in a helium jet injected into ambient air, in assumption that a sharp boundary exists between helium (inside the jet) and air (outside the jet), have showed that streamer structures of two types can be formed: one with maximums of electric field and electron density at the jet axis and another with maximums of these parameters near the boundary separating helium and surrounding air. The latter structure is similar to observed ring-shaped structures of plasma bullets.

In experiments [5,6] the effect of applied voltage polarity has been studied. It has been shown that the propagation length and the width of plasma bullets for positive voltage pulses are typically larger that those for negative polarity.

In the given work, the plasma bullet dynamics is simulated, in the framework of standard two-dimensional streamer model, with account of mixing of helium jet with surrounding air. Results of simulations show that plasma bullets have a ring-shaped structure, the calculated ring radius decreasing with growth of the distance from the tube end. The effect of voltage polarity on the calculated plasma bullet parameters is similar to that observed in experiments. A comparison of calculated plasma bullet characteristics with experimental data [3,5] is presented.

2. The model

The plasma bullet (streamer) is assumed to propagate along z the axis of symmetry, coinciding with the jet axis. For simulation of streamer dynamics a two-dimensional (axially symmetric) model is used, analogous to that described in [4]. It includes an equation for the electric field (Poisson equation) and balance equations for species densities. Transport of charged species is described in the framework of fluid (drift-diffusion) approximation, the values of kinetic and transport coefficients are taken as functions of the local electric field. Besides equations for charged species, the model includes balance equations for excited helium atoms He*, excimer molecules He_2*, and excited nitrogen molecules $N_2(C^3\Pi)$.

The kinetic scheme used for evaluation of the source terms in the balance equations includes direct and stepwise ionization of neutral species by electron impact, excitation of He* by electrons, three-body conversion of He* to He_2*, Penning process of ionization of air molecules in collisions with He* and He_2*, electron-ion recombination, excitation of $N_2(C^3\Pi)$ by electron impact and its quenching due to radiation and in collisions with neutral species. The kinetic and transport parameters for electrons in helium-air mixtures are governed by the values of reduced electric field E/n (where n is the gas density) and molar fraction of air X_{air}. For evaluation of these parameters versus E/n and X_{air} the BOLSIG+ code [7] has been used.

The mixture composition along the jet is obtained by solving the system of continuity, momentum and mass diffusion equations.

Under conditions of experiments with plasma jets, the electric field outside dielectric tube is governed by the electrode system, the volume and surface charges generated by barrier discharge inside the tube (at $z < 0$), and the volume charges of

streamers (at $z > 0$). The sum of contributions of the electrode system and the charges inside the tube forms the electric field that is external for streamer propagation in the region $z > 0$. This field may have a complex spatial structure and vary with time. To simplify the problem of streamer simulation, in our approach, as in [4], the external field (that is, the field in the absence of volume charges inside streamers, at $z > 0$), assumed to be constant in time, is evaluated as that produced by a charged sphere; its surface is placed at $z = 0$. The sphere radius is chosen larger than the jet radius but much smaller than the length of streamer propagation, so as the spatial structure of the external field to be more or less similar to that typical for experiments with plasma jets. The total electric field is calculated as superposition of the external field and the field of volume charges produced by propagating streamer.

3. Results

In figure 1 the calculated radial distributions of the air molar fraction at various axial positions z are given, for conditions of experiment [3]: for helium jet injected from a tube with internal diameter of 3 mm at gas flow rate of 7 *l*/min. These data are used at simulation of streamer propagating in electric field produced, as described above, by a sphere with radius R_{sph} = 0.5 cm, charged to positive potential U = 7 kV.

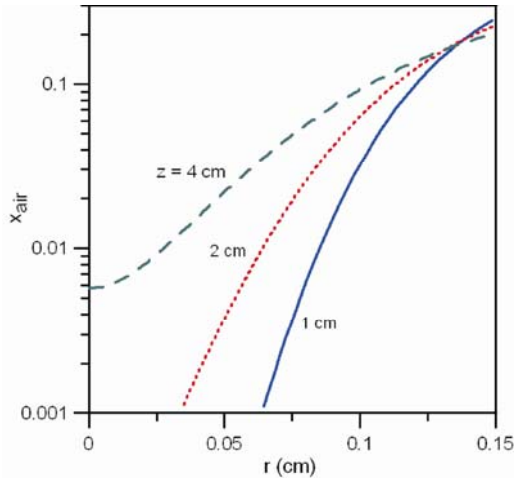

Figure 1. *Radial distributions of air molar fraction at various axial positions, for conditions of experiment [3]*

The distributions of electric field along the symmetry axis at several time moments during streamer propagation are given in figure 2. The line at $t = 0$ shows the external electric field (e.g. the field of the charged sphere). The position of electric field maximum, the streamer front, moves along the jet with a mean velocity about 10^7 cm/s.

The radial structure of the streamer is shown in figure 3 where the radial profiles of the electron number density are presented at axial positions z = 1, 2 and 4 cm, just after arrival of the streamer front. The maximums of the number density are shifted from the axis to some distance, nearly the same for the both parameters, that decreases with growth of z. Figure 1 shows that this distance nearly corresponds to the position where the air molar fraction is equal to 10^{-2}. Like in [4], the streamer tends to expand to the width that is limited by the surface separating the regions with high and low ionization rates.

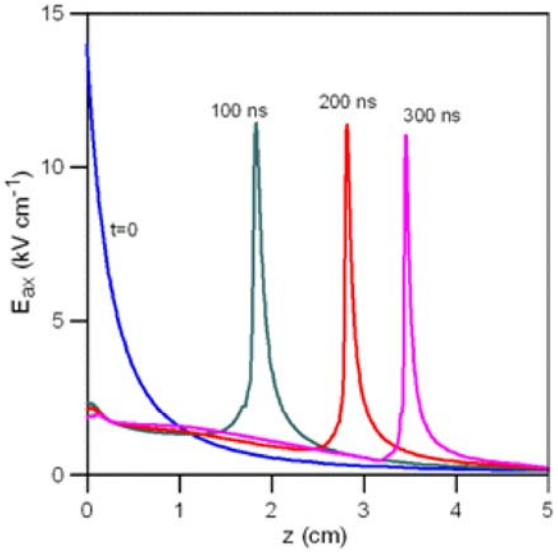

Figure 2. *Profiles of electric field along the symmetry axis at various time moments*

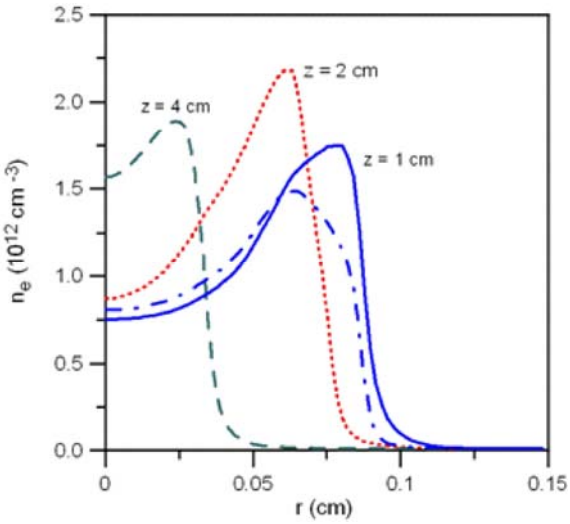

Figure 3. *Radial distributions of the number density of electrons at various axial positions, for time moments 50 ns (z = 1 cm), 130 ns (2 cm) and 430 ns (4 cm). Dot-dashed line shows the data for z = 1 cm obtained without account of Penning reaction.*

In several papers (e.g. [3,8]) an assumption on the leading role of Penning process in plasma bullet dynamics is made. To check this assumption, we have performed simulations setting rate constants for Penning reactions equal to zero. Corresponding distribution of the number density of electrons at z = 1 cm is shown in figure 3 (dot-dashed line). It is seen that Penning process does have a quantitative effect on streamer parameters, though the patterns of streamer structure in both cases, with and without account of this reaction, are nearly the same.

A comparison of calculated radial distributions of the normalized $N_2(C^3\Pi)$ number density with the data obtained in [3] is given in figure 4. Both positions of the maximums and the widths of the calculated distributions agree with the measured data.

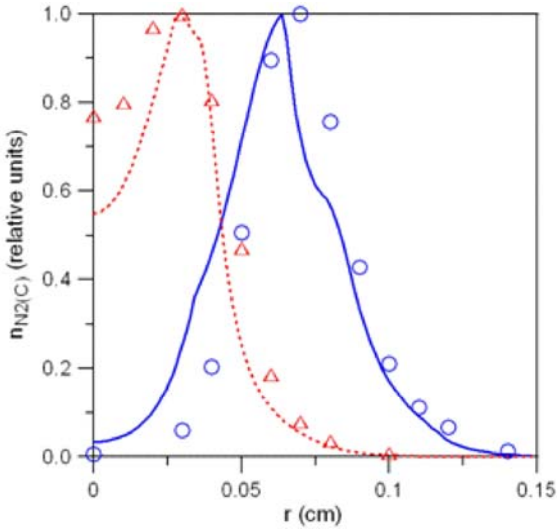

Figure 4. *Radial distributions of normalized $N_2(C^3\Pi)$ number density. Symbols – experiment [3], lines – simulation, for z = 2 cm (circles, solid line) and 4 cm (triangles, dotted line).*

To study the effect of voltage polarity, we have performed simulations for conditions of experiment [5]: for the jet of helium with admixture of 1% of oxygen (in our simulations oxygen was substituted with air), injected from a tube with internal diameter of 1 mm at gas flow rate of 1 *l*/min. The calculated, for these conditions, radial distributions of the air molar fraction are given in figure 5. These data are used at simulation of streamers propagating in electric field produced by a sphere with radius R_{sph} = 0.25 cm, charged to potentials U = – 6 kV or 6 kV.

The distributions of absolute value of electric field along the symmetry axis both for positive and negative streamers are given in Figure 6. The maximum field values (in streamer heads) for positive streamers are much higher than those for negative streamers. Contrary, the electric field in channels of negative streamers is much higher than that in positive streamers. (Note that the similar polarity effect was revealed in previous simulations of streamers in air [9,10]).

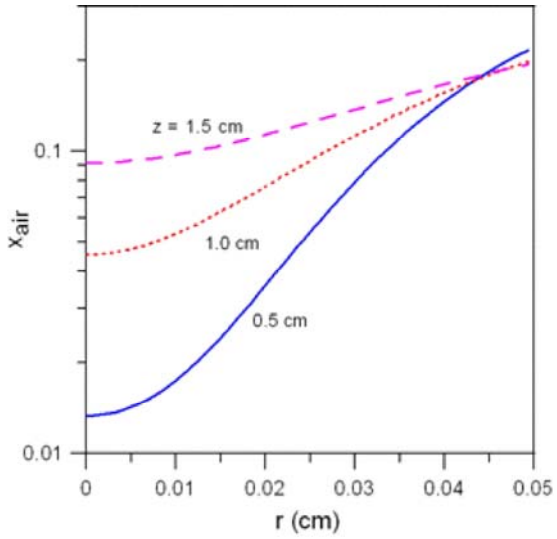

Figure 5. *Radial distributions of air molar fraction at various axial positions, for conditions of experiment [5]*

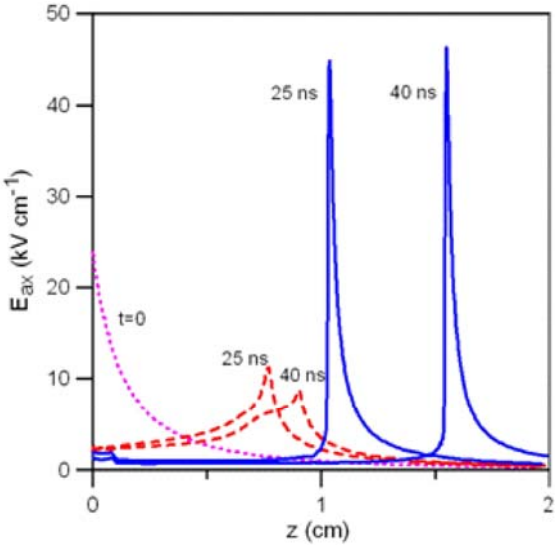

Figure 6. *Profiles of electric field along the symmetry axis at various time moments for positive (solid) and negative (dashed) streamers.*

The radial profiles of electron number density at two axial positions are shown in figure 7. Both negative and positive streamers initially (at small z) have a ring-shaped structure. With increase of z the ring radius decreases (as in the case shown in figure

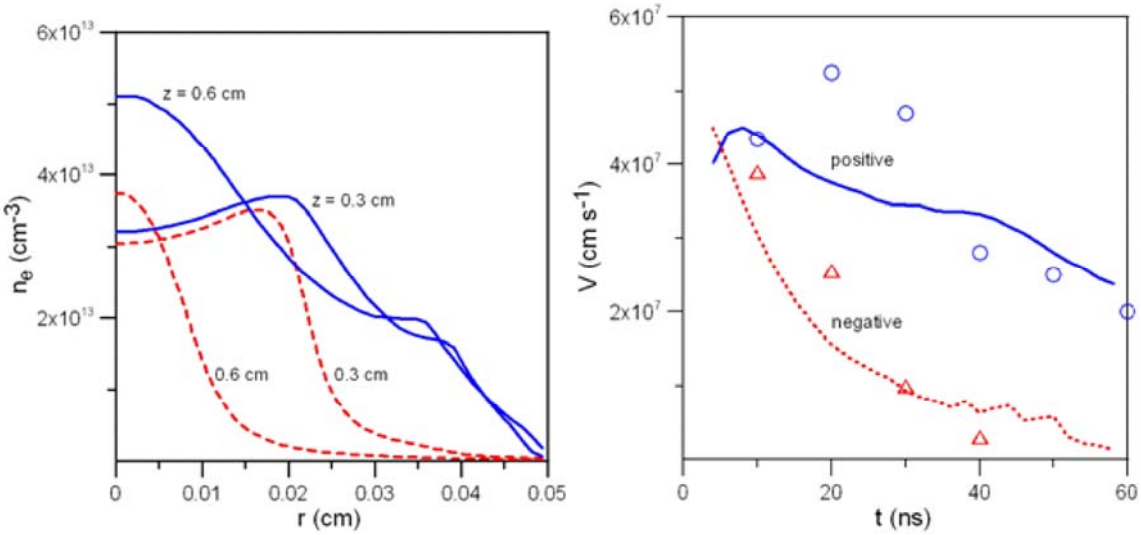

Figure 7. *Radial distributions of the number density of electrons at various axial positions for positive (solid) and negative (dashed) streamers.*

Figure 8. *Streamer propagation velocity. Symbols – experiment [5], lines – simulation.*

3), and at z = 0.6 cm the electron density is maximal at the axis. The width of positive streamer channel is larger than of negative one, especially at larger z. This result is in line with observations [5,6].

The calculated streamer propagation velocity V versus time is shown in figure 8. Experimental data [5] are also shown. It is seen that the character of variation of calculated V values with time is similar to the observed one. Initially the velocities of positive and negative streamers are nearly equal, however the time dependences of positive and negative streamer velocities are quite different. While the velocity of positive streamer changes with time rather slowly, for negative streamers a steep decrease with time takes place. As a result, the propagation length for positive streamers is substantially higher than that for negative streamers.

References

1. N. Mericam-Bourdet, M. Laroussi, A. Begum, E. Karakas, J. Phys. D: Appl. Phys. **42,** 055297 (2009).
2. K. Urabe, T. Morita, K. Tachibana, B.N. Ganguly, J. Phys. D: Appl. Phys. **43,** 095201 (2010).
3. Y. Sakiyama, D.B. Graves, J. Jarrige, M. Laroussi, Appl. Phys. Lett. **96,** 041501 (2010).
4. G.V. Naidis, J. Phys. D: Appl. Phys. **43,** 402001 (2010).
5. C. Jiang, M.T. Chen, M.A. Gundersen, J. Phys. D: Appl. Phys. **42,** 232002 (2009).
6. Z. Xiong, X. Lu, Y. Xian, Z. Jiang, Y. Pan, J. Appl. Phys. **108,** 103303 (2010).
7. G.J.M. Hagelaar, L.C. Pitchford, Plasma Sources Sci. Technol. **14,** 722 (2005).
8. E. Karakas, M. Koklu, M. Laroussi, J. Phys. D: Appl. Phys. **43** 155202 (2010).
9. N.Yu. Babaeva, G.V. Naidis, IEEE Trans. Plasma Sci. **25,** 375 (1997).
10. A. Luque, V. Ratushnaya, U. Ebert, J. Phys. D: Appl. Phys. **41**, 234005 (2008).

2.5. MICROWAVE ENERGY ABSORPTION BY PLASMA STRUCTURES

P. Vedenin, S. Afanas'ev, V. Bityurin, V. Brovkin
Joint Institute for High Temperatures RAS, Moscow
Izhorskaya 13, bld..2, Moscow, 125412, Russia

Abstract— A regular dipole type plasma structure evolution at focal region of MW linearly polarized quasi-Gaussian beam was observed experimentally in air at pressure P ~ 100 Torr. The magnetron type MW source (F=13GHz) with impulse power up to 700kW and 10mks pulse duration was used. This type of plasma structure consists of thin plasma channels (plasmoids) oriented parallel to the external electric field. A model of a microwave streamer based on analytical relations was developed, which describes the evolution of plasmoid both during its elongation along the external electric field and after its stop. The simple analytical relations that allow the power released in a plasma channel to be estimated on the fly were derived. Almost the entire energy contribution is shown to be made after the termination of the streamer elongation.

1. Introduction

A characteristic feature of a nonequilibrium high-pressure microwave discharge ($\nu >> \omega, \nu$– is the transport electron collision frequency and ω – is the circular frequency of the field) is its spatial inhomogeneity. It is in this range of parameters that the diversity of diffusion "unsmeared" plasma configurations shows up most vividly.

By now, dipole type plasma structures, which align in the field of linearly polarized electromagnetic waves and consist of thin plasma channels (plasmoids) oriented parallel to the external electric field, have been most extensively studied experimentally and theoretically (see references in [1]). One channel, several channels, or a spatially regular multiplasmoid structure is formed, depending on the discharge ignition conditions.

The plasma dipole, which is the main element of a plasma structure and affects noticeably the interference pattern of the electromagnetic field in the discharge region, results from the development of a microwave streamer. The latter comprises two ionization waves traveling in two mutually opposite directions along the external electric field. The uncompensated space charges of opposite signs that emerge during the oscillatory motion of electrons relative to a stationary (in a period $T = 2\pi\omega^{-1}$) ion background are located symmetrically relative to the streamer center. These charges are concentrated mainly at the ionization wave fronts in regions of enhanced field and maximum plasma density gradients.

2. Experiment

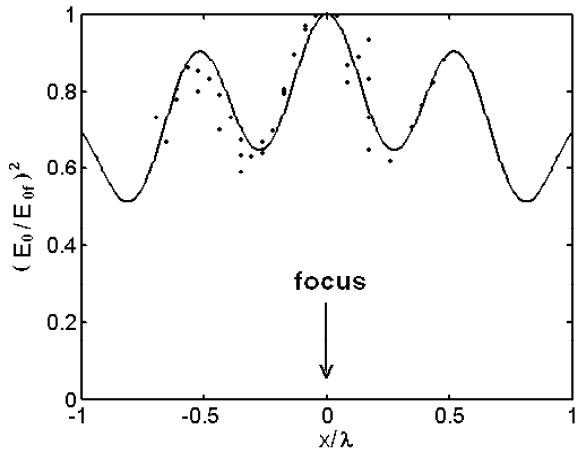

Fig. 1. *Longitudinal distribution of dimensionless intensity on the wave beam axis. The dots represent the results of the experimental investigation; solid line is the result of approximation.*

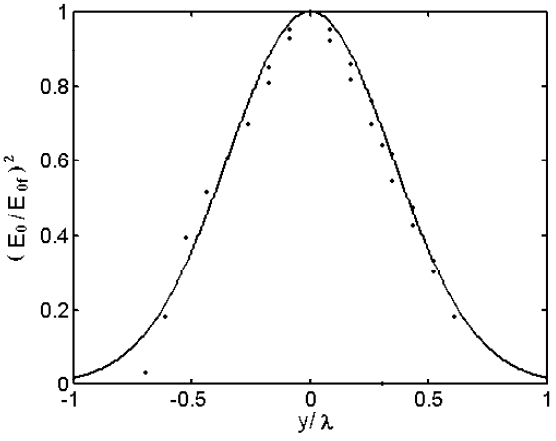

Fig. 2. *Transverse distribution of dimensionless intensity in the focus plane. The dots represent the results of the experimental investigation; solid line is the result of approximation.*

Our experimental setup consists of a magnetron and a focusing system. A pulse regime magnetron operates at 13 GHz with maximum output power of 700 kW and duration up to 10 μs.. An antenna forms a linearly polarized MW beam and directs it into vacuum chamber. A reflector compresses the beam radius down to 0.7 λ (λ is wave length) at the waist. The typical interference pattern is formed along the chamber axis. The discharge chamber of 70 cm external diameter and 100 cm length can be pumped out up to ~1 Torr. The intensity of a microwave field distribution we measured by MW probe (the open end of the half rigid cable). The results at focal area are shown on Fig. 1, 2. Our study carried out over pressure range P=70 – 100 Torr. For stable discharge ignition in air we applied a laser light. Laser radiation is produced by a pulsed Nd:YAG laser (LF 117) at the second harmonic (532nm) with pulse duration about 15 ns. The system of mirrors allows introduce the laser beam into the chamber along the electric field vector of MW wave in a desirable point. The plasma images are recorded by camera type of Sony and high speed camera type of Sensicam. The

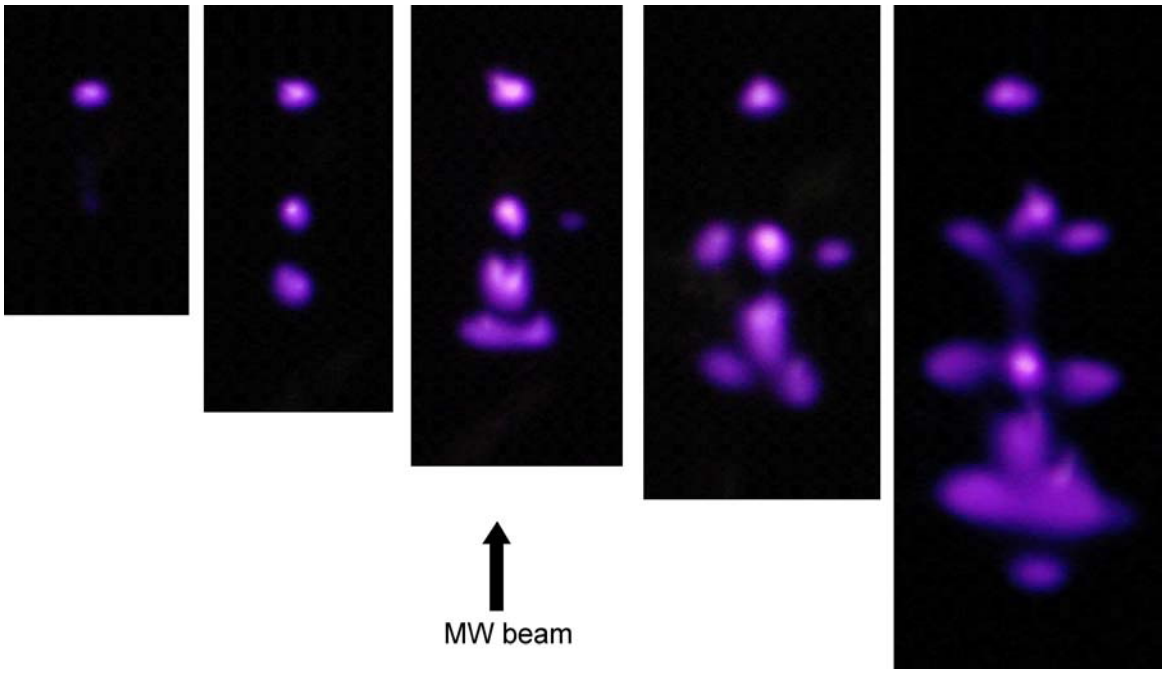

Fig. 3. *Time- integral images of MW discharge (kB-plane) in air at P=75 Torr .*

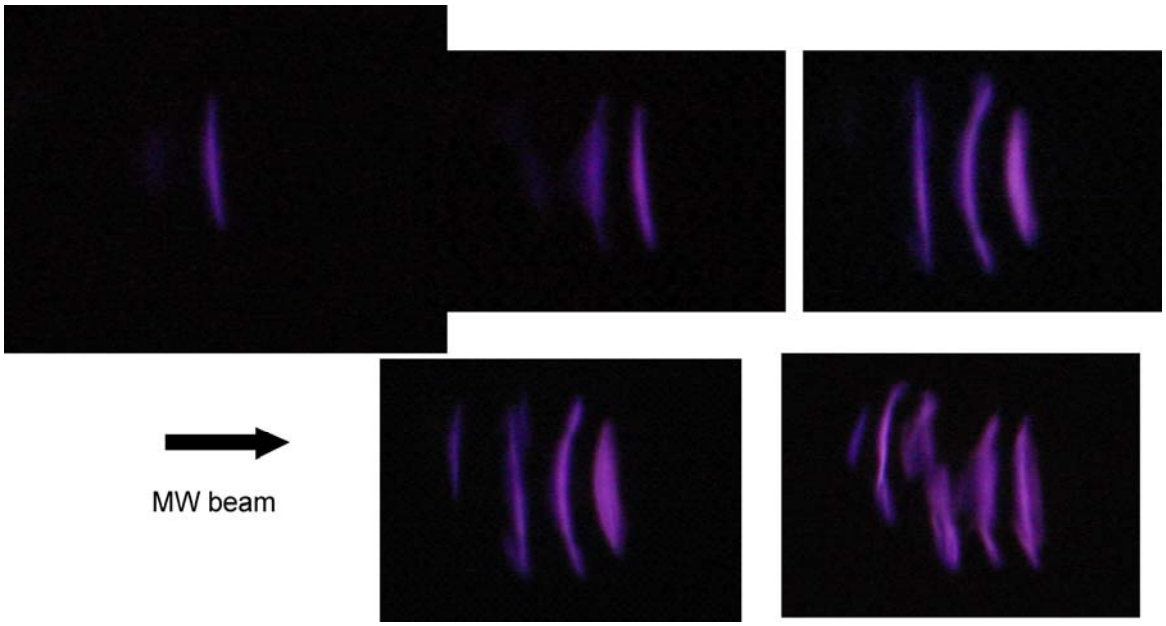

Fig. 4. *Time- integral images of MW discharge (kE- plane) in air at P=75*

typical time - integral images of MW discharge across (**kB**-plane) and along (**kE**- plane) electric field vector on different forming stages are shown on Fig. 3, 4.

3. The electrodynamic model of a microwave streamer

A theoretical analysis of a microwave discharge is usually performed by assuming that the changes in the Fourier components of the electric and magnetic fields, the excess space charge, current densities and the mean plasma parameters are insignificant in the period of high frequency oscillations.

The microwave streamer elongates along the *z* axis and is a dipole whose excess unlike charges $\mathrm{Re}\left\{Q^{\pm}(t)\exp(-i\omega t)\right\}$ located symmetrically relative to the *z* = 0 plane are connected by a plasma channel. The following assumptions underlie the model.

(1) The charge is concentrated at the longitudinal ionization wave front in a region whose maximum linear size is much smaller than the half length *l*(*t*) of the streamer and is distributed uniformly in the head volume.

(2) The current flows along a cylindrical channel of effective radius $r_{ch}(t)$ and length $2l_{ch}(t)$ uniformly filled with plasma with $l_{ch*} = l_{ch}/l = const$.

(3) The skin depth exceeds channel radius

$$\Lambda = \frac{\omega_p^2}{\omega\nu}\frac{\kappa^2}{4} < 1, \qquad (1)$$

where $\omega_p^2 = e^2 N_e/\varepsilon_0 m$, $\kappa = kr_{ch}$, $k = 2\pi/\lambda$. Hence, the field amplitude distribution in the channel is uniform $|\mathbf{E}(\mathbf{r})| = |E_c|$

$$E_c = \frac{E_{0c}}{1+\dfrac{\Lambda(A+iB)}{1-i\vartheta}}, \qquad (2)$$

where E_{0c} is an external field A, B are the form factors, $\vartheta = \omega/\nu$. Everywhere below, we will assume the condition $\vartheta < 1$ to be met. The expressions for form factors in the case $2l_{ch} \le 0.5\lambda$ are

$$A = \frac{4s}{3} + O\left(\left(\frac{\kappa}{s}\right)^2\right),$$

$$B = 2\left(\frac{1}{s^2} - \ln\frac{2s}{\kappa}\right) - \left(\frac{s}{2}\right)^2 + O\left(\left(\frac{\kappa}{s}\right)^2\right),$$

$s = kl_{ch}$.

(4) The dynamics of the scales $l(t)$ and $r_{ch}(t)$ is described by the equations

$$V_z = \xi\frac{\nu_{ih}^{eff}(|E_h|)}{\nu_{ic0}^{eff}(E_{0c})}l), \quad \xi \cong 2\cdot 10^6, \text{ s}^{-1}. \qquad (3)$$

$$r_{ch} = r_{ch0}\left(\frac{l}{l_0}\right)^b, \quad b = \frac{\ln(\hat{r}_{ch}/r_{ch0})}{\ln(\hat{l}/l_0)} \qquad (4)$$

where $\nu_i^{eff} = \nu_i - \nu_a$, ν_i and ν_a are the direct ionization and attachment frequencies, $|E_h|$ is the maximum field amplitude, r_{ch0} and l_0 are the radius and longitudinal scale of the plasma cloud by the end of the stage of development of the electron avalanche in the external field E_{0c}, $\hat{r}_{ch}$, $\hat{l}$ are the maximum values of the scales $l(t)$ and $r_{ch}(t)$.

The maximum field amplitude is described by the formula

$$|E_h(r=0,z=l)| = |E_c|\left|1+\frac{i\Lambda\Psi_h(r=0,z=l)}{1-i\vartheta}\right|, \qquad (5)$$

where

$$\Psi_h = \frac{\Psi_{Qh}}{(kl)^2} - (\Psi_{Ic} - \Psi_{Ih}),$$

$$\Psi_{Qh} = 2\Psi_{Qc} - \Psi_{Qh}^{+} + \Psi_{Qh}^{-},$$

$$\Psi_{Ic} = \Psi_{Iz}(r=0, z=0),$$

$$\Psi_{Ih} = \Psi_{Iz}(r=0, z=l),$$

$$\Psi_{Iz}(r=0, z) = \frac{-2i}{(kr_{ch})^2}$$

$$\int_{-kl_{ch}}^{kl_{ch}} d\eta\left(\exp\left(i\sqrt{(kr_{ch})^2+(\eta-kz)^2}\right) - \exp(i|\eta-kz|)\right)$$

$$\Psi_{Qc} = \left(\frac{l}{l_{ch}}\right)^2 \left(1 - ikl_{ch}\right)\exp\left(ikl_{ch}\right),$$

$$\Psi_{Qh}^{-} \cong -\left(\frac{l}{l_{ch}+l}\right)^2 \left(1 - ik\left(l_{ch}+l\right)\right)\exp\left(ik\left(l_{ch}+l\right)\right)$$

The form factor Ψ_{Qh}^{+} characterizes the influence of the charge Q^{+} concentrated near the amplitude maximum $\left|E_h\left(r=0, z=l\right)\right|$. The model parameter increases Ψ_{Qh}^{+} with decreasing head sizes. The value Ψ_{Qh}^{+} is chosen so as to provide the possibility of elongation to the length $2\hat{l}$.

The kinetic block of the model in air includes the system of processes that describe the change in the concentration of the main neutral and charged components of the nitrogen–oxygen mixture and the vibrational excitation of the gas. Nine types of positive and negative ions are taken into account: O_2^+, O_4^+, N_2^+, N_4^+, NO^+, O^-, O_2^-, O_3^-, O_4^-. The system of ion-molecular reactions [2] was taken as the basis.

The formula to estimate the total power released in the plasmoid is

$$W_J \cong \frac{W_0}{\pi}\frac{2kl_{ch}\Lambda}{\left(1+\Lambda A\right)^2 + \left(\Lambda B - \vartheta\right)^2}, \qquad (6)$$

where $W_0 = \lambda^2 S_0$, $S_0 = c\varepsilon_0 E_{0c}^2/2$. Since the field amplitude in the channel decreases with increasing parameter Λ at fixed sizes l_{ch} and r_{ch}, the function $W_J\left(\Lambda\right)$ has a maximum,

$$W_{Jm}\left(l_{ch}, r_{ch}\right) = \frac{W_0}{\pi}\frac{kl_{ch}}{A - \vartheta B + \sqrt{\left(1+\vartheta^2\right)\left(A^2+B^2\right)}}, \qquad (7)$$

and its maximum value takes place when

$$\Lambda = \Lambda_m\left(l_{ch}, r_{ch}\right) = \sqrt{\left(1+\vartheta^2\right)/\left(A^2+B^2\right)}.$$

The fraction of the wave beam energy transferred to the plasmoid is

$$\eta = \frac{\int_0^t dtW}{S_0 \pi r_f^2 t}, \qquad (8)$$

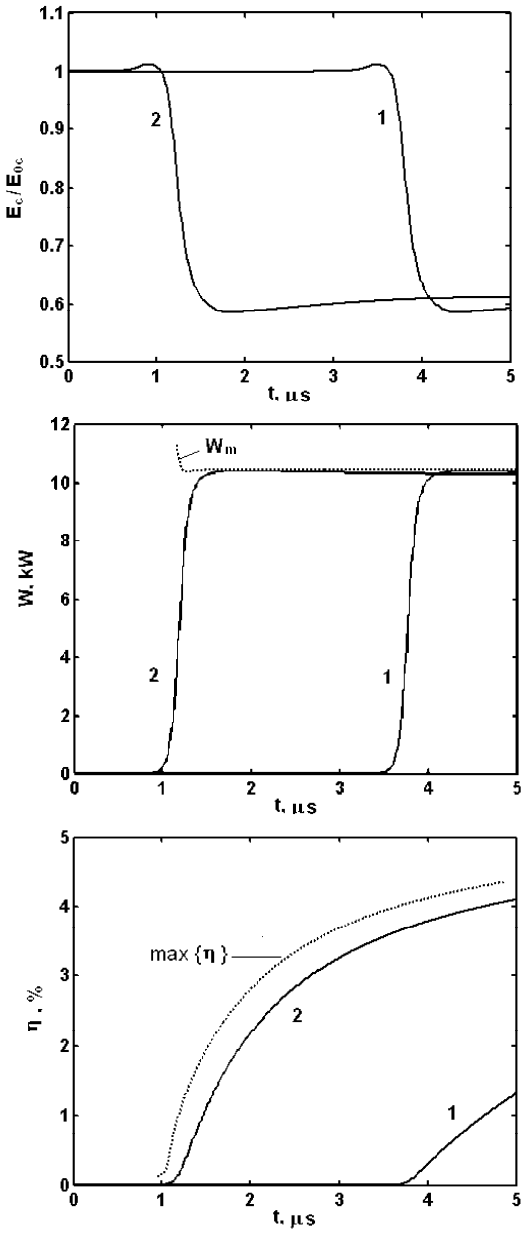

Fig. 5. *Dynamics of the functions* $\left|E_c/E_{0c}\right|$, W_J, η *in air for the conditions:* $P_0 = 75$ *Torr,* $\lambda = 2.3$ *cm,* $E_{0c} = 1.1E_{br}$, $N_{e0} = 10$ *(1) and* 10^{10} *(2)* cm^{-3}.

where r_f is the effective radius of the wave beam at the focus. It is easy to verify that under conditions when $2l_{ch} \le 0.5\lambda$ and $r_f \approx 0.7\lambda$, the released power and the energy absorption efficiency are limited from above by

$$\hat{W}_J = \frac{3W_0}{8\pi},\ \hat{\eta} = \frac{3}{8}\left(\frac{\lambda}{\pi r_f}\right)^2 \approx 0.077. \qquad (9)$$

4. Calculation results

Fig. 5. Presents the dynamics of the basic integral streamer characteristics in air for the conditions: pressure $P_0 = 75$ Torr, wavelength $\lambda = 2.3$ cm, external field amplitude $E_{0c} = 1.1E_{br}$ (E_{br} is the breakdown value of the field amplitude), initial electron number density $N_{e0} = 10$ cm^{-3} and 10^{10} cm^{-3}. In our calculations, we used final plasmoid sizes $2\hat{l} = 0.5\lambda$, $\hat{r}_{ch} = 7\,\hat{l}$. The invariable (throughout the entire calculation) relative length of the plasma channel ($l_{ch*} = l_{ch}/l$) is 0.9.

The decrease in amplitude $|E_c|$ related to the growth of the space charge leads to a slowdown of the electron production processes and, hence, to a decrease in derivative $d|E_c|/dt$. The level of the released power rises almost abruptly: as our calculations showed, the characteristic time in air is $\Delta t \sim \left(\nu_{i0}\left(E_{0c}\right)\right)^{-1}$. The function $\Lambda(t)$ continues to increase as long as the production of electrons during ionization dominates over recombination. After a noticeable ionization wave deceleration due to the decrease in function $|E_h|$, the final stage of plasmoid evolution begins, at which quasi-stationary levels of the field amplitude $|E_c|$, parameter Λ and the released power W_J are established. The quasi-stationary values of the integral characteristics are virtually independent of the intermediate states of the streamer.

A distinctive feature of the evolution of a microwave streamer in air is a quasi-equilibrium state of the plasmoid, in which the associative ionization involving the metastable electron_excited $N_2(A^3\Sigma_u^+)$ and $N_2(a'^1\Sigma_u^-)$ molecules plays a significant role.

As the value of initial electron number density decreases, the duration of the initial plasma cloud nucleation stage increases; hence, the energy absorption efficiency η decreases.

5. Results

1. Regular multiplasmoid structure evolution at focal region of MW linearly polarized quasi-Gaussian wave beam was observed experimentally in air at pressure P ~ 100 Torr.
2. Almost the entire energy contribution is made after the termination of the streamer elongation. A state characterized by a slight change in the electric field amplitude in the channel and the released power is established at this stage of evolution of the plasmoid.
3. Preionization substantially increases the fraction of the wave beam energy transferred to the plasmoid (efficiency).
4. The fraction of the wave beam energy transferred to the plasmoid does not exceed a few percent

References

1. V.A. Bityurin, P.V. Vedenin, Journal of Experimental and Theoretical Physics, 2010, Vol. 111, No. 3, pp. 512–521.
2. I. A. Kossyi, A. Y. Kostinsky, A. A. Matveev, and V. P. Silakov, Plasma Sources Sci. Technol. 1992, 1, p. 201.

3.1. DIELECTRIC BARRIER DISCHARGE FOR MIXING ENHANCEMENT IN THE WAKE OF A CIRCULAR CYLINDER

N. Benard[1], L. Cordier[1], and E. Moreau[1],

[1] Institut Pprime, CNRS, Université de Poitiers, ENSMA
Dpt Fluides, Thermique, Combustion
Bld Marie et Pierre Curie, Téléport 2, 86962 Futuroscope Cedex, France

Abstract. The flow dynamic past a bluff body is rich in instability phenomena that develop in well-defined flow regimes [1]. Each of these instabilities can compose a control objective. Most of the studies target mitigation or total elimination of the vortex street formed in the near wake of circular cylinder placed in cross-flow. This can significantly reduce the radiated noise, affect the drag and inhibit structural vibrations. However, a second approach consists of improving the turbulent mixing in the wake of the cylinder with objective of increasing heat exchange or turbulent transfer. This later objective is at the centre of the present study.

A circular cylinder is placed in an open wind-tunnel for freestream velocity of 15.6 m/s (Re_D=40000, i.e. subcritical regime). The circular cylinder has an outer diameter of 40 mm and a span of 300 mm. Two plasma actuators are flush mounted on opposite sides of the cylinder surface, the cylinder thickness being the dielectric material (PMMA, thickness of 2 mm). These actuators are two dielectric barrier discharges operated in phase. The control strategy is based on wake flow modification by imparting small amplitude velocity perturbations in the attached upper and lower regions, upstream the separation points. Actuations by ac sinusoidal forcing and burst modulation (duty-cycle of 50%) are compared for different forcing frequencies (voltage amplitude maintained at 18 kV). This parametric study provides the mean drag changes incurred by the cylinder, this drag being measured by a force balance. The results indicate that actuation systematically promotes a drag increase, but burst modulation appears as an effective strategy to reach larger increase in the drag (Figure 1). This increase is especially verified for burst actuation performed at modulating frequency equal to twice the frequency of the natural vortex shedding in the upper or lower free shear layers (a natural vortex shedding at roughly 75 Hz is expected). This demonstrates that the produced maximal velocity due to colliding particles in the ionized region is not the key point for this control process. Burst modulation that produces reduced mean electric wind velocity is clearly more effective to increase turbulent quantities, this even by using low duty-cycle of about few percents (not shown here).

The next step was to investigate the velocity field by a time-resolved PIV system for the most effective control strategies observed in the parametric study (Figure 2). A particular attention was paid to the extraction of the coherent flow structures embedded in the global turbulent flow field. Two methodologies are used to describe the changes in the flow fields. A proper orthogonal decomposition [2] is performed to accurately extract the most energetic flow structures (Hussein-Reynolds decomposition). This decomposition is based on energy hierarchy of flow scales and suggests slightly stronger flow structures in the near wake region under actuation. As illustrated in figures 2 and 3, these structures are formed closer to the suction base of the cylinder that corroborate a drag increase.

In a second approach, the flow dynamic is analyzed by dynamic mode decomposition [3] (data

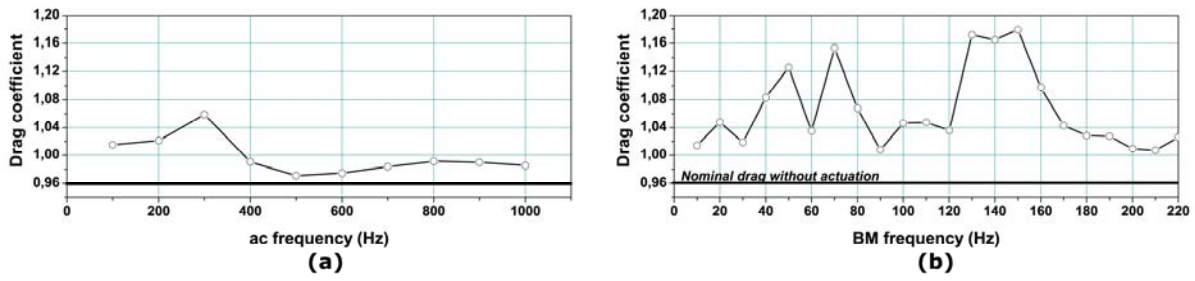

Figure 1: *Drag coefficient for (a) ac sinusoidal forcing and (b) burst modulation (duty-cycle of 50%)*

processing under progress). This decomposition can rank the flow structures by growth rate and highlight the occurrence of transient events, identify the prevalent frequencies as well as stable and unstable structures. This post-processing is supported by intermittent cancellations of the vortex shedding observed in the baseline flow. These transient regimes do no longer exist under plasma actuation (vortex shedding regularization).

It is expected that the proper orthogonal and dynamic mode decompositions will provide relevant and complete quantification of physical mechanisms related to the vortex shedding regularization and amplification promoted by the two opposite regions of ionized air by high local electric field.

References

1. Williamson, C.H.K., 1996, 'Vortex dynamics in the cylinder wake', Ann. Rev. Fluid Mech., Vol. 28.
2. Bergmann M. and Cordier L., 2008, 'Optimal control of the cylinder wake in the laminar regime by trust-region methods and pod reduced-order models', J. Comp. Phys., Vol. 227.
3. Schmid, P.J., 2010, 'Dynamic mode decomposition of numerical and experimental data', J. fluid Mech., Vol. 656.

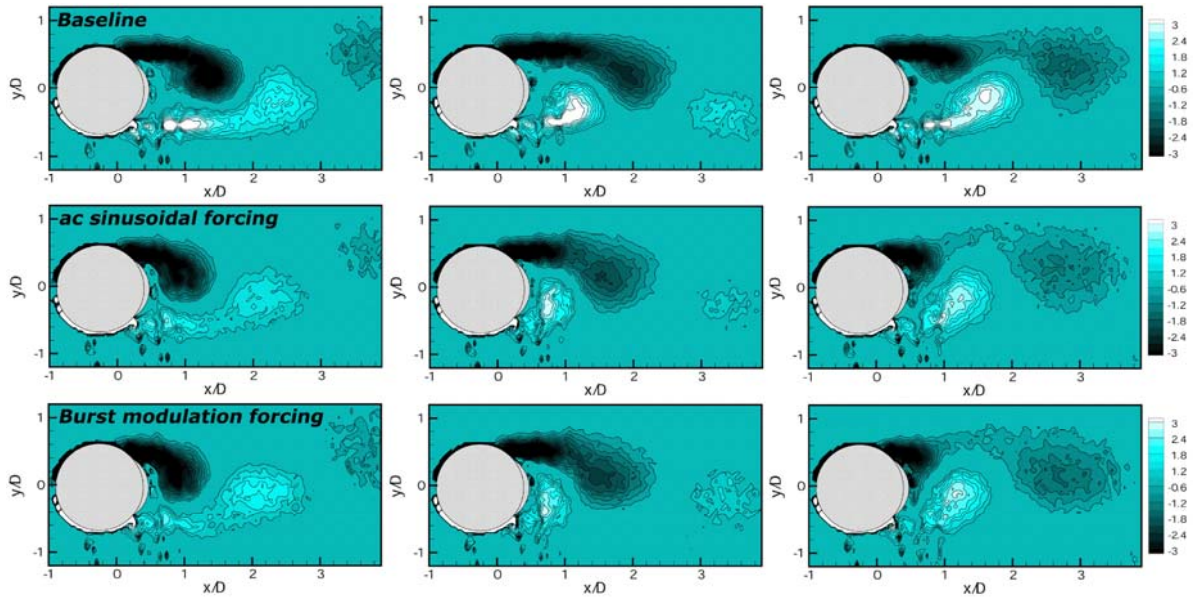

Figure 2: *Iso-values of normalized vorticity for phase-angles of 0, 120 and 240° (POD filtering on coherent contribution; ac forcing at 300 Hz and burst modulation at 150 Hz)*

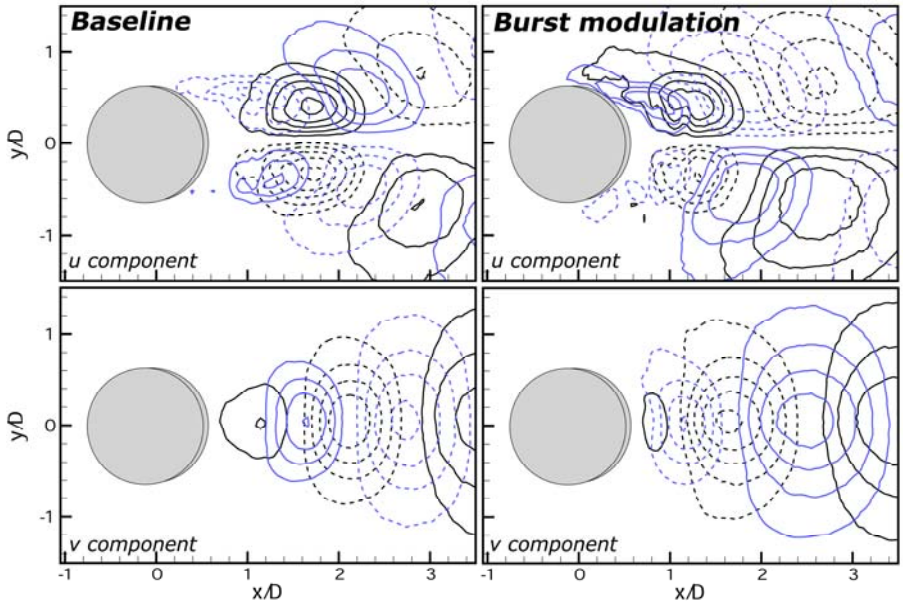

Figure 3: *First (black lines) and second (blue lines) POD eigen-modes.*

3.2. SUPERSONIC FLOW CONTROL UNDER SPARK DISCHARGE

E.E. Son, D.V. Tereshonok
Joint Institute for High Temperatures of Russian Academy of Sciences, Moscow, Russia
Moscow Institute of Physics and Technology, Dolgoprudny, Russia
dimon_ter@mail.ru

Abstract. The present work shows the results of the numerical simulation that have been made for the displacement of a separation point to downstream under the initiation of the spark discharge on the wing surface. Has been obtained a good agreement of numerical simulation and experiment for the location of a separation point under thermal effect on supersonic flow with Much number M=2 around profile NACA64A212.

Nomenclature

$\mathbf{V}$ = velocity vector
t = time
V_y = vertical velocity component
V_x = longitudinal velocity component
η = dynamic viscosity
ν = kinematic viscosity
p = pressure
ρ = density
C_p = heat capacity
T = temperature
λ = heat conductivity
Q = heat power
$\ddot{\sigma}$ = viscous stress tensor
h = enthalpy
R = gas constant
M = Much number
α = angle of attack

1. Introduction

It's known that under high Reynolds number the flow structure loses stability and changes from laminar flow to turbulent. This phenomena determines an aerodynamic characteristics of aircraft. Under some conditions the pressure gradient appears nearly the aircraft surface and causes gas flow to move upstream in the opposite direction of the main flow. The separated flow is determined by the momentum, angle of attack and geometry of an aerodynamic body. The separated flow causes negative phenomena in aerodynamics such as decrease of a lift force and increase a drug force. Under the circumstances a maneuverability and a controllability are worse. Therefore the displacement of the flow separation region to downstream has row of advantages. At the present time the plasma and thermal flow control are given with consideration [1, 2].

Some experimenters used corona discharge for the flow control. For example H. Velkoff and J. Ketchman in 1968 [3] demonstrated that the application of an electric field produced by a dc corona discharge can be used for the control of separation point on a flat plate. But the velocity of the incident flow was $V = 0.4$ m/s. G. Artana *et al.* [4] placed a dc corona discharge at the leading edge of a flat plate and show boundary layer flow control under incident flow $V = 17.5$ m/s. Soetomo [5] investigated a drag reduction in case of ac and dc corona discharges along a flat plate with incident velocities up to $V = 2$ m/s.

In the middle of the 1990s several groups used dielectric barrier discharge (DBD) for flow control [6-8]. As a corona discharge DBD induces airflow - ionic wind of several meters per second.

Therefore a airflow with velocity more than $V = 100$ m/s couldn't be controlled by ionic wind.

Ionic wind flow control alternative is a thermal influence. Usage of a nanosecond dielectric barrier discharge [9] and a spark discharge [10] demonstrated an ability to control a separated flow.

2. Numerical simulation

The experiment [10] that was made by Saveliev *et al* is a foundation of a presented numerical simulation. Numerical simulation has been made for profile NACA64A212 with chord length 10 cm and attack angle $\alpha = 8^0$. Under this angle a separation point is placed at distance 17-20 mm from trailing edge. Spark discharge area is placed at distance 40 mm from trailing edge, has sizes shown by Fig.1 and extended along wing span. Discharge time is approximately 100 ns.

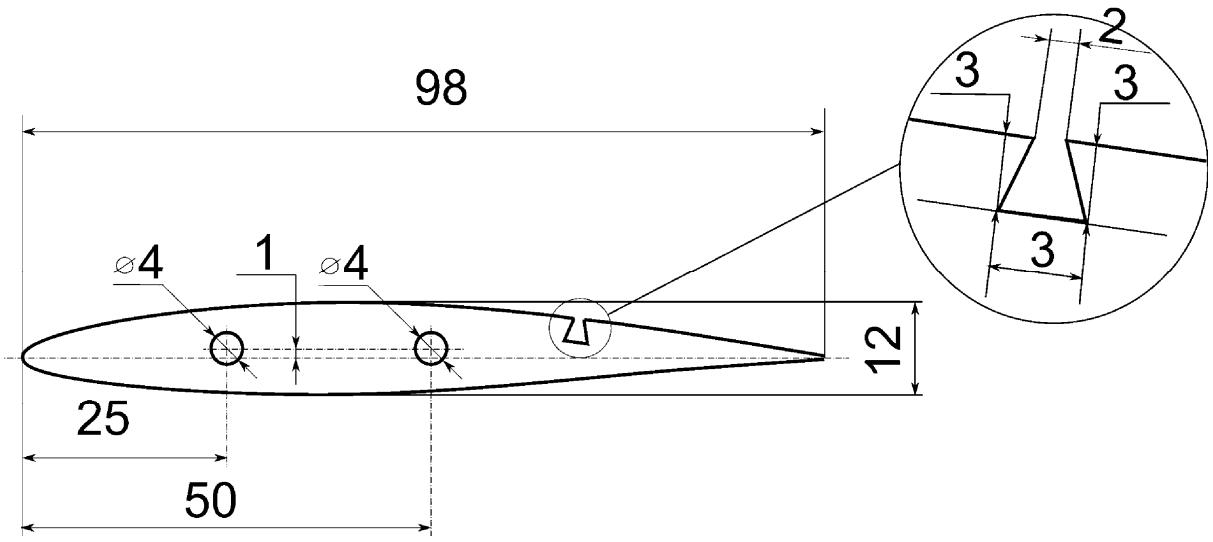

Fig.1. *Size (in mm) of profile NACA64A212 for experiment.*

Initial temperature and pressure $T_0 = 160\text{K}$, $p_0 = 0.15$ *atm*. Heat power: $Q = 10^{10} \div 5 \cdot 10^{10} \dfrac{\text{J}}{\text{m}^3 \cdot \text{s}}$, if *t*<100 ns, else $Q = 0$. Airflow velocity: $V_x = 520$ m/s and $V_y = 0$, Much number: $M = 2$. Size of calculation area is two-dimensional rectangular region with size 20X15 cm.

Current set of equations that have been solved numerically are presented below (1).

$$\frac{\partial \rho}{\partial t} + \nabla \cdot (\rho \mathbf{V}) = 0$$

$$\rho \left[\frac{\partial \mathbf{V}}{\partial t} + (\mathbf{V} \cdot \nabla)\mathbf{V} \right] = -\nabla p + \nabla \cdot \ddot{\sigma}$$

$$\rho \frac{dh}{dt} = \frac{dp}{dt} + \ddot{\sigma} : \nabla \mathbf{V} + \nabla \cdot (\lambda \nabla T)$$

$$p = \rho R T \qquad (1)$$

$$h = C_V T + p/\rho$$

$$\lambda = 2.37 \cdot 10^{-2} \cdot \left(\frac{T}{273} \right)^{0.5} \frac{\text{Watt}}{\text{m} \cdot \text{K}}$$

$$\eta = 18 \cdot 10^{-6} \cdot \left(\frac{T}{273} \right)^{0.5} \text{Pa} \cdot \text{s}$$

For the numerical simulation package GasDynamicsTool (GDT) has been used with constant time and space steps: $\tau = 10^{-8}$ s, $h = 10^{-4}$ m. GDT has first order in space and time of accuracy. Results of position of separation point vs different angle of attack without discharge for numerical simulation and experiment is presented by Fig.2. It is good illustration of a verification of GDT.

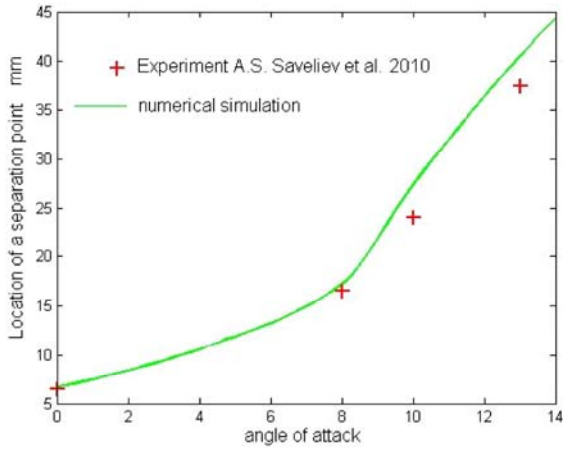

Fig.2. *Position of separation point vs angle of attack.*

Fig.3 and Fig.4 show nonstationary evolution a thermal disturbance propagation and separation point position under spark discharge. Fig.3 shows a good qualitative agreement of a thermal disturbance through time. And Fig.4 shows a good numerical agreement displacement of a separation point through time. One of main results

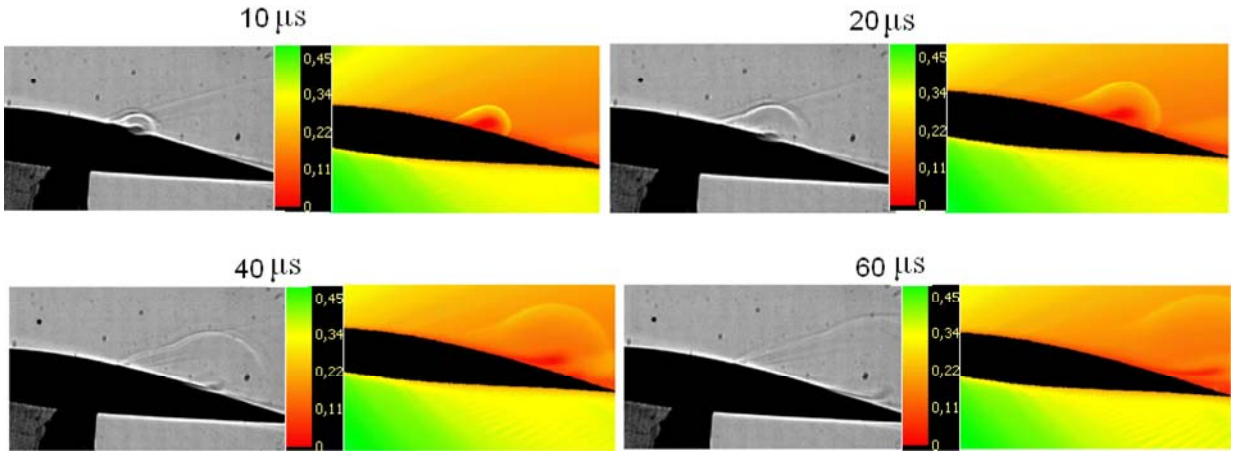

Fig.3. *Thermal disturbance propagation through time.*

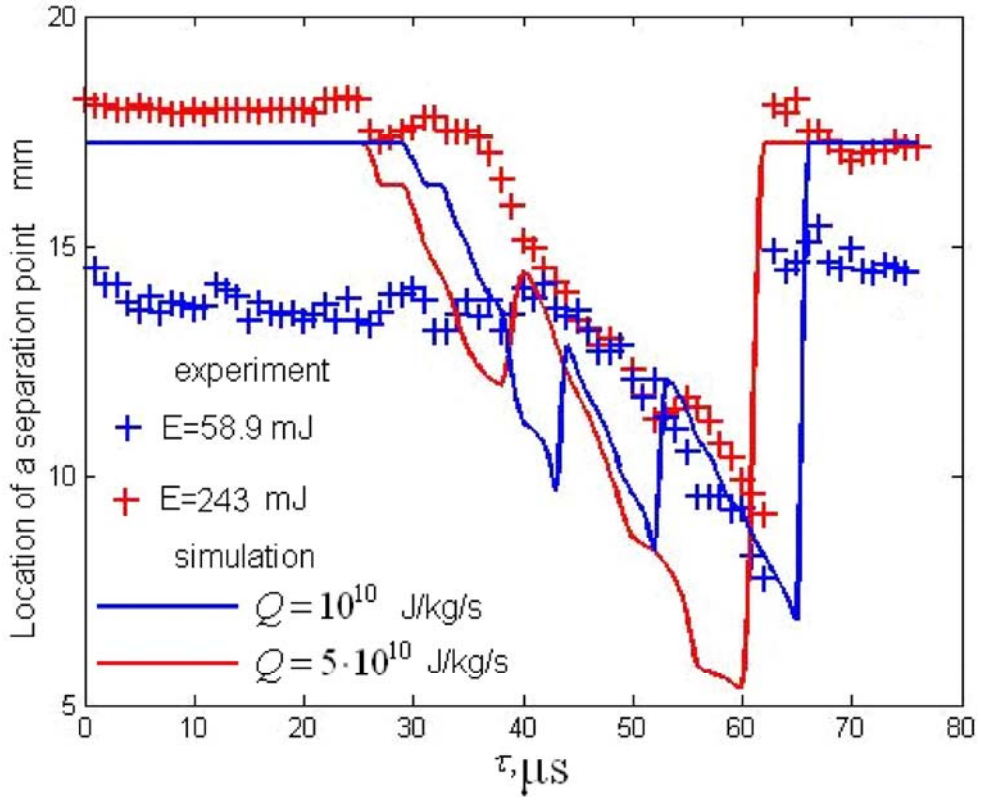

Fig.4. *Position of separation point vs time under different discharge power .*

of the numerical simulation is presented by Fig.4 where velocity of separation point displacement doesn't depend on source power in some range.

3. Conclusions

Numerical simulations for the supersonic flow (M=2) control by impulse thermal source has been made. A satisfactory fit between the experiment and the numerical simulation has been obtained.

Disturbance from an impulse thermal source interacts with a detachable area. In the issue turbulent area is divided on several parts which move downstream.

A displacement velocity and a final position of a separation point don't depend on source power in some range.

References

1. El-Khabiry S., Colver G. Drag reduction by a dc corona discharge along an electrically conductive flat plate for small Reynolds number flow // Phys. Fluids, 1997, Vol. 9, P. 587.
2. Post M., Corke T. Separation Control using Plasma Actuators - Stationary & Oscillating Airfoils // 42nd AIAA Aerospace Sciences Meeting and Exhibit, Reno, Nevada, 2004, AIAA-2004-0841.
3. Velkoff H. and Ketchman J. Effect of an electrostatic field on boundary layer transition // AIAA J. 1968, Vol.16, P. 1381.
4. Artana G., D'Adamo J., L´eger L., Moreau E. and Touchard G. Flow control with electrohydrodynamic actuator// AIAA J., 2002, Vol. 20040, P. 1773.
5. Soetomo F. The influence of high voltage discharge on flat plate drag at low Reynolds number air flow // MS Thesis Iowa State University 1992.
6. Roth J., Sherman D. and Wilkinson S. AIAA Meeting (Reno, USA, January 1998) 1998 AIAA-98-0328.
7. Shcherbakov Y., Isanov N., Baryshev N., Frolovskij V. and Syssoev V. // 31st AIAA Plasmadynamics and Lasers Conference, Denver, CO, 2000, AIAA-2000-2670.
8. Zavialov I., Opaits D., Roupassov D., Starikovskaia A. and Saddoughi S. Boundary layer control for naca-0015 airfoil in subsonic regime// Proc. 15th ICMHD,Moscow, Russia, 2005, P. 186.
9. Roupassov D.V., Nikipelov A.A., Nudnova M.M., Starikovskii A.Yu. Flow separation control by plasma actuator with nanosecond pulse periodic discharge// 46th AIAA Aerospace Sciences Meeting and Exhibit, Reno, Nevada, 2008, AIAA-2008-1367.
10. Golub V.V., Saveliev A.S., Sechenov V.A., Son E.E. and Tereshonok D.V. Plasma Aerodynamics in a Supersonic Gas Flow// High Temperature, 2010, Vol. 48, No. 6, P. 903.

3.3. ENERGY CHARACTERISTICS AND RELAXATION OF A "PLASMA SHEET".

Znamenskaya I.A., Ivanov I.E., Koroteeva E.Yu., Mursenkova I.V., Orlov D.M.
Moscow state University, Molecular Physics Department.

The energy characteristics of a distributed high-current sliding surface discharge ("plasma sheet") are investigated experimentally and numerically. Gas-dynamical aspects of the interaction between a non-equilibrium near-wall region created by the initiation of the pulsed discharge of planar configuration and a flow with a plane shock wave in a channel are considered. The inverse problem is solved, concerning the restoration of spatial energy distribution and the amount of electric energy converted into heat. On the basic of the solution of the inverse problem the behaviour of parameters in the relaxation zone is examined.

The "plasma sheet" as a system of bright parallel channels, 30x100 mm^2 in area, is developed in a thin near-wall layer of gas on the interface of gaseous and solid dielectrics. The investigation of the dynamics of perturbations from the discharge has shown [1] that after less that 1 μs approximately 40±10% of the total discharge energy is converted directly into heat. Then, during the relaxation of molecular excited states the translational temperature of the near-wall gas is increased; this process is accompanied by the energy dissipation due to the transport phenomena. The propagation of a plane shock wave along the "plasma sheet" is considered 40-500 μs after the energy release, when the main gas-dynamical disturbances weaken and the non-equilibrium "relaxing zone" of a heated gas is formed in the vicinity of the surface. The influence of the non-equilibrium near-wall zone on the shock wave dynamics reveals in the appearance of the precursor wave and also in the enhancement of inhomogeneities by the shock wave and in spatial turbulization of the upstream flow. The investigation of the flow structure near the channel surface allows to evaluate the thermodynamic parameters of the medium at fixed time periods after the discharge and to follow the temperature evolution in the primary energy deposition zone. The analysis of the flow patterns arising after the interaction of the shock wave with the discharge under different initial conditions suggests that the evolution of the relaxing plasma in the post-discharge period is significantly governed by the turbulent convective processes.

The work was supported by the Russian Foundation for Basic Research grant № 11-07-93959-ЮАР_а.

3.4. EXPERIMENTAL RESEARCHES OF FAST-FLYING BODIES INTERACTION WITH LASER-INDUCED SPARK PLASMA

V.I.Nikolayeva[1], A.S.Pashchina[2], A.N.Sakhonchik[1]
[1]Joint Stock Company "GSKB "Almaz-Antei", 80-A, Leningradsky prospect, Moscow, Russia, 125178
[2]Joint Institute for High Temperatures RAS, Moscow, 125412, Russia

Abstract. Experimental results of fast-flying bodies interaction with extended plasma object, created by laser-induced spark, are presented. EPO's formation was carried out by the teamwork of two laser systems including specially developed giant-pulse CO_2-lasers and stationary CO_2-laser KS-10 created in OKB "Raduga". Giant-pulse CO_2-lasers has provided spark ignition on a route site of 45 m. Stationary laser KS-10 in a pulse-periodic mode provided discharge channel development till the demanded geometrical sizes and spark maintenance during the model interaction with EPO's site. Processing of experimental data shows essential deflection of model's trajectory in laser-induced spark plasma and presence of the model's trajectory fracture on a site where interaction with plasma takes place.

The majority of plasma aerodynamics experimental researches are spent in the conditions of gas flow organizing in the vicinity of immobile explored object. Such experimental simulation is quite full matched flight conditions for the cases when plasma is formed by means of onboard generators. In this case plasma parameters essentially depend on parameters of an incident gas flow. Simulation of body's flight conditions through stationary plasma area created by means of exterior generators can be reached in ballistic experiment.

The aeroballistic method, in essence, is a method of the flight experiment which problems are: extended or local plasma area formation, running flying vehicles models through plasma area, and registration of models parameters before, during and after interaction with plasma area. Comparison of models parameters in two conditions (with and without plasma area interaction) determines plasma area influence on body's flight dynamics.

Selection of the extended plasma area formation method

Interaction duration of the flying vehicle model with plasma area is one of parameters that determine degree of plasma area influence on flight dynamics. Necessary interaction duration for appreciable influence on flight dynamics may be provided by various methods. One of them is plasma area formation (for example, by MW radiation focusing) in the vicinity of fast flying body and its accompanying during the necessary time interval. However, for space and time requirements of aeroballistic experiment extended plasma area formation along ballistic route, which dimensions provides necessary for explored object interaction duration, is more suitable.

Laser-induced spark in air can be considered as one of suitable methods of EPO formation for aeroballistic experiment conditions. This method have been used in researches of fast-flying bodies interaction with extended plasma object (EPO), held by employees of Scientific Research Institute of Radio Device Instruments (the supervisor of studies R.F.Avramenko) in 1992 … 93 on OKB "Raduga" stand, Raduzhny town [1, 2].

CO_2 lasers on wavelength $\lambda=10,6$ microns, characterized by lower break threshold in air in comparison with smaller wavelength lasers, have been used for EPO formation. In particular, the power density of spark break for CO_2 laser wavelength of $\lambda=10,6$ microns makes about $W \geq 2 \cdot 10^9$ W/cm^2 in enough transparent atmosphere, and for Nd laser wavelength $\lambda=1,06$ microns enlarges to $W \geq 10^{11}$ W/cm^2. Dust presence in air causes CO_2 laser break threshold value lowering for order.

Laser spark ignition in air can be realized by so called giant-pulse lasers, characterized by short radiation pulse (about few tens of nanoseconds). Few tens of Joules radiation energy can provide more than *1 GW* of radiation power. Low beam divergence and great aperture are providing optical break at distances of few hundred of meters. Spark length is approximately equal to half of focus length of optical system. Laser-induced spark is represented by local break centers located along optical caustic. Distance between local sparks is determined by laser power parameters and beam divergence. Laser-induced spark lifetime in giant-pulse mode, however, does not exceed *100 mcs*, that is insufficient for plasma interaction with model, taking into account model's inertance. That's why for spark evolution and maintenance (increasing of discharge duration, decreasing of distance between local sparks) feeding by radiation on the same wavelength but with essentially greater pulse energy is needed.

Really available length of laser-induced spark is approximately equal to half of focus distance of optical system. In general the focus distance range is determined by radiation pulse

power. So, focus length increase (because of laser beam divergence) causes focal spot diameter increase, that, in turn, results in power density and laser spark length decrease. On the other hand, focus length diminishing at invariable aperture causes optical radiation cone angle increase that leads to waist of space boundaries where the power density exceeds threshold, i.e. to laser spark length diminishing. Taking into account maximal values of interaction duration of plasma and model and power parameters of laser systems, optimal focus length value was selected to be one hundred meters. Thus real achievable and maximal possible optical spark length can reach *40 m*. For characteristic models velocity value *1 km/s* interaction duration can reach *40 ms* that is enough for model's flight dynamics influence.

However, laser pulse duration has limitation, caused by plasma front formation, moving towards laser radiation with high speed *(v~100 km/s*, so called light-detonation wave effect). Plasma front shields up to 80% of power preventing penetration of radiation deep into channel. Specified effect influence on laser spark channel evolution can be essentially weakening by laser functioning in pulse-periodic mode. Thus, laser pulse duration value is selected from condition, when plasma front path length is less than laser spark length L, i.e

$$\tau_p<0,1L/v,$$

where τ_p – laser pulse duration; L – laser spark length, equal to *40 m*; v – plasma front velocity, *100 km/s*.

Laser pulse duration cannot exceed *40 mcs* for specified parameters. That's why for laser spark maintaining during needed time interval *40 ms* it is necessary to realize laser system functioning in pulse periodic mode.

Used in experiments [1, 2] laser KS-10 OKB "Raduga" provided pulse sequence of *30 mcs* duration at pulse repetitive frequency of *100 Hz*. During model's flight throughout EPO area (*~40 ms*), energy of four pulses will released in the spark region. As in time between pulses practically full recombination of plasma takes place, there is a necessity of giant short pulse for each long pulse of KS-10 laser.

Thus EPO's formation was carried out by the teamwork of two laser systems including specially developed giant-pulse CO_2-lasers and pulsing CO_2-laser KS-10 created in OKB "Raduga". Giant-pulse CO_2-lasers has provided spark ignition on a route site that approximately equal to half of optical system focal length. Laser KS-10 in a pulse-periodic mode provided discharge channel development till the demanded geometrical sizes and spark maintenance during the model interaction with EPO's site (*40 ms* for the model velocity of *1 km/s*). Algorithm of two laser systems teamwork is presented on fig.1.

Three independent units of giant-pulse CO_2-lasers with surface discharge preionization mounted in car box body have been used in experiments. Main parameters of giant-pulse laser are:

- Gas mixtures CO_2:N_2:He – 1:1:5; 1:1:6, 2:1:7; 1:2:7; 1:2:6;
- Operation pressure – 1 atm;
- Operation volume – 18 liters;
- Input voltage – 70 kV;
- Peak pulsed voltage on plasma electrodes – 70 kV;
- Peak pulsed discharge voltage – 280 kV;
- Pulse radiation energy – up to 300 J;
- Power density – up to 10^{11} W/cm^2
- Radiation wavelength - λ=10,6 microns;
- Output beam diameter – 160 mm;
- Pulse radiation duration- τ=0,05…5 mcs;
- Beam divergence - $5\cdot10^{-4}$ rad;
- Operation mode – monopulse.

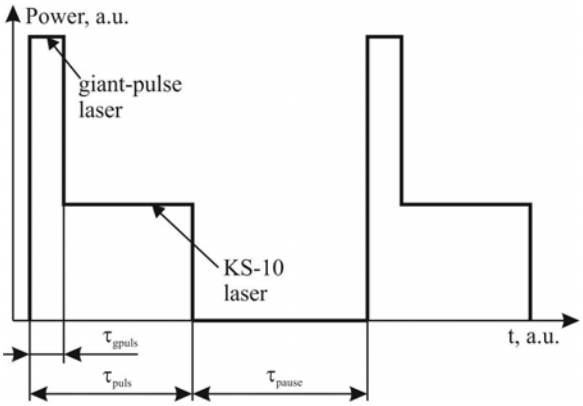

Fig.1. *Algorithm of two laser systems teamwork.*

KS-10 stand is ionizing CO_2 laser of atmospheric pressure and closed cycle, operating in pulse and pulse-periodic modes. Main parameters of KS-10 stand are:

- Pulse radiation energy – 1,5…2 kJ;
- Pulse radiation duration – 25…40 mcs;
- Pulse repetitive rate – up to 125 Hz,
- Radiation aperture – 20x40 cm^2;
- Beam divergence – 0,7…1,5·10^{-3} rad (depending on operation mode);
- Radiation wavelength - λ=10,6 microns;
- Operation mode – monopulse, pulse-periodic;
- Functioning duration in pulse-periodic mode – up to 1 s.

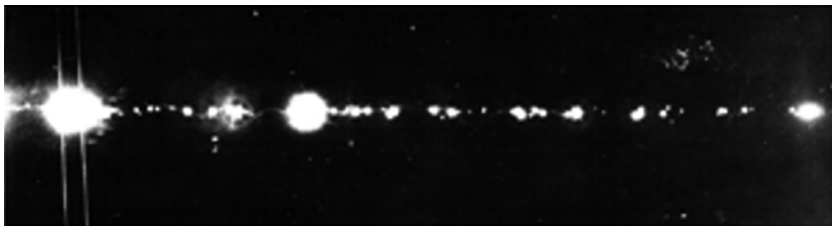

Fig.2. *Extended plasma area formed by laser-induced spark.*

Teamwork of two laser systems provided EPO formation with length of 45 m and focal spot diameter of 50 mm (fig.2). Distance between local sparks varied from 200 mm to 7000 mm depending on KS-10 laser pulse energy. Thus, most frequently observed distance between sparks was 300…400 mm.

Research technique

The stand represents plurality of the equipment, allowing making aeroballistic experiment on laser spark influence on models flight dynamics in field requirements (fig.3). Stand included next systems:

- EPO's formation complex, including mobile setup with 3 units of giant-pulse lasers, stationary KS-10 laser, focusing system and synchronization system;
- Powder ballistic unit of 60,5 mm caliber;
- Models catcher;
- Measuring velocity system on the trajectory sites – before and after plasma contact area (chorographical targets);
- Film recording system, including speed cameras (1000…4000 frames/sec);
- Device of shadow photographing;
- Paper targets;
- Automated management system of experiment.

Disposition of stand main parts were correlated with EPO position and model's flight trajectory such as to provide maximal interaction duration within model and EPO. Ballistic unit placed on 20 m distance from EPO, and the angle between ballistic unit and EPO axes was about 21′.

Measuring of laser's KS-10 radiation energy was made by a flow lattice bolometer of 500x700 type terminated to oscilloscope. Laser spark geometrical parameters registration (space position, sizes) was made by single frame speed cam photographing (RFK-5 type).

Flying vehicle model represents cylindrical body with nose needle. Design of one model's variant is presented on fig.4. Parameters of model variant (MA-3 [2]) are:

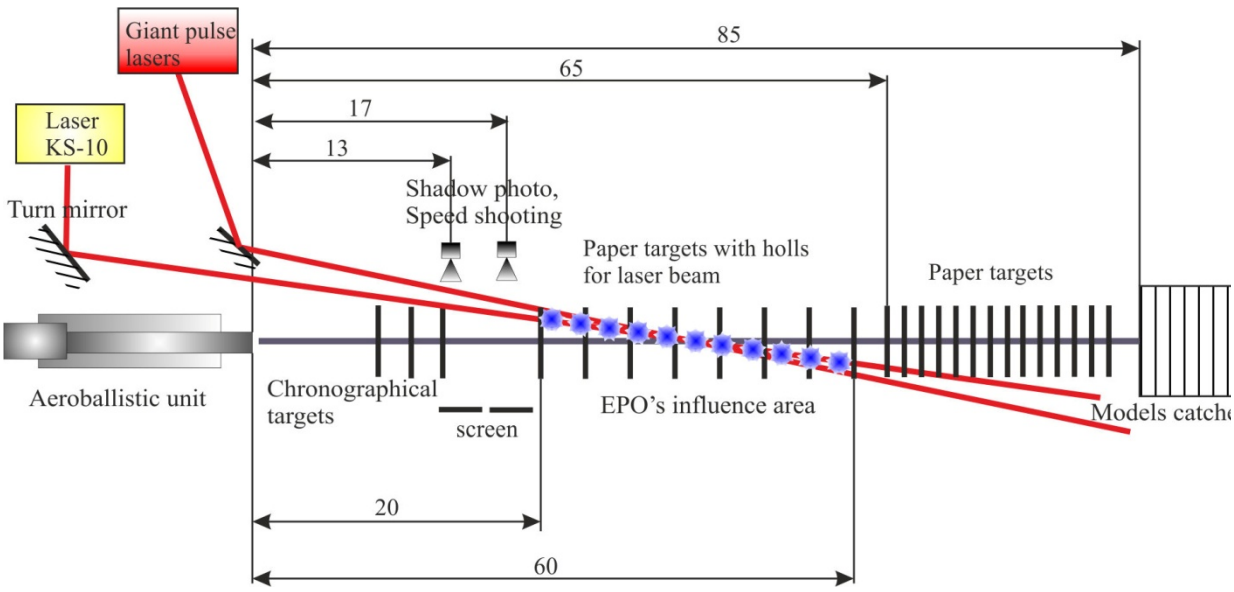

Fig.3. *Principal stand schematics (distances specified in meters).*

- mass m=0,48 kg;
- relative coordinate of barycenter X_T=56%;
- moment of inertia relatively transverse axis, passed through barycenter $J_z=0{,}96\cdot10^{-3}$ kg·m^2.

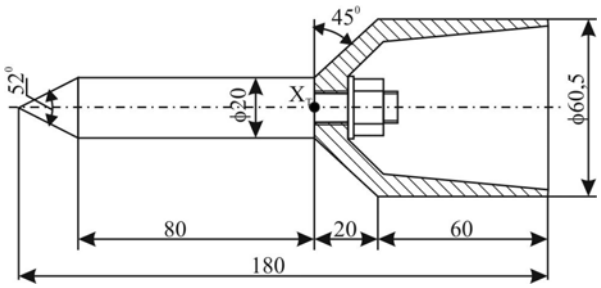

Fig.4. *Model design.*

Model's aerodynamics parameters in operational Mach numbers range M=2,8…3,5 are constant practically, that simplifies experimental results analyses. For the model integrity control and the fact of model trajectory and laser-induced spark crossing the shadow photographing was spent. The example of a shadow photo of the model flow pattern in the presence of plasma formations is presented on fig.5.

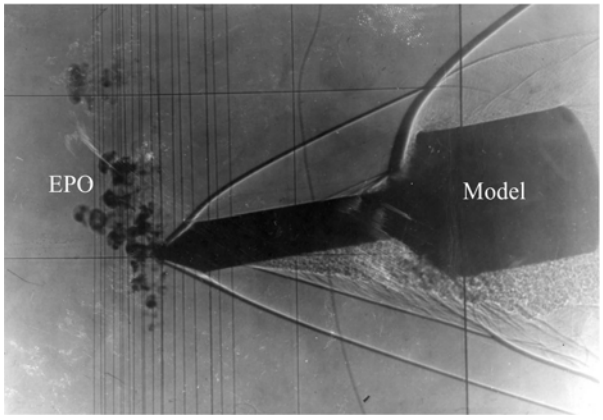

Fig.5. *Model's shadow streamline pattern with EPO presence.*

Aeroballistic experiments have been spent in requirements of atmospheric pressure $p_0=1\cdot10^5$ *Pa*, temperature $T_0=265...300$ *K* and model's average velocity *v=1000 m/s*. KS-10 laser operation mode – pulse-periodic, pulse repetitive frequency – 100 Hz, duration of operation – 3 s.

Models deflection from trajectory that registered without plasma area influence was the criterion of laser spark influence. For the purpose of reliable definition of the fact of interaction within model and laser spark, transparent for laser radiation polyethylene segments were "sewed" on paper targets with holes for laser beam. This is allowed to fix laser beam position in aeroballistic frame. Photo of targets mounted out of (a) and in spark zone (b) are presented on fig.6.

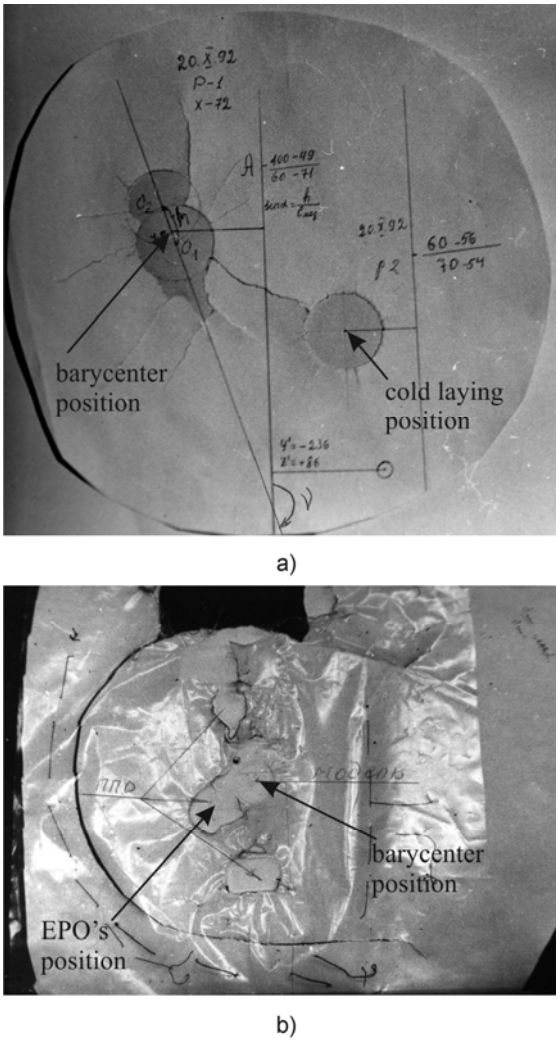

Fig.6. *Photos of targets, mounted out of (a) and in (b) the EPO's interaction area.*

Decoding of target holes allows determining models barycenter coordinates, spatial attack angle and precession angle.

Cold laying position by the use of shoot down tube is pointed on each target before every shoot. In requirements of stationary ballistic stand cold laying position coordinates (Y_0, Z_0) and model's barycenter coordinates (Y_g, Z_g) in target plane are determined independently in the stand frame, and after that the deviation values $Y=Y_g-Y_0$ and $Z=Z_g-Z_0$ are determined. In field requirements the axes $0Y_g$ and $0Z_g$ runs through cold laying position. In obtained frame the barycenter coordinates of model, i.e. deviation values Y, Z from cold laying position, and attack angle α are determined.

Processing observed data permits to determine parameters of technical scattering:

medial hit point coordinates Y_1, Z_1 and mean-square deviations S_y, S_z:

$$Y_1 = \frac{1}{n}\sum_{i=1}^{n} Y_i, \; Z_1 = \frac{1}{n}\sum_{i=1}^{n} Z_i$$

$$S_y = \sqrt{\frac{1}{n-1}\sum_{i=1}^{n}(Y_i - Y_1)^2},$$

$$S_z = \sqrt{\frac{1}{n-1}\sum_{i=1}^{n}(Z_i - Z_1)^2}$$

where $Y_i=Y_g-Y_0$; $Z_i=Z_g-Z_0$ – model's deflection in *i-th* shoot from *n* shoot series.

Research results

Experimental data were processed according to statistical methods which have allowed defining regression model. Statistical parameters of regression permitted to conclude with 95% probability about linear approximation model reliability that in turn confirms absence of model probable deformations, which are capable to cause additional component of aerodynamics forces modifying trajectory.

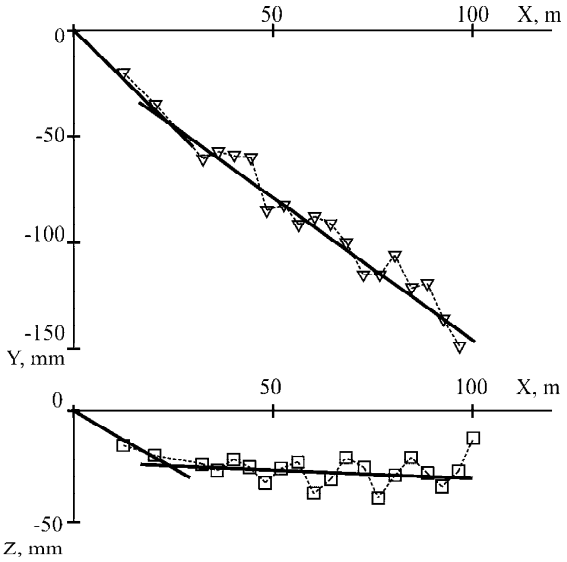

Fig.7. *Example of model's barycenter coordinates along ballistic route and piecewise linear approximation (solid straight lines).*

Gained in regression analyses mean-square coordinates deviations without EPO influence are: 12…25 mm along Y-axis and 5…70 mm along Z-axis. In condition of EPO influence mean-square coordinates deviation values increase is observed. For spent experiments series [2] their values were: 7…90 mm along Y-axis and 12…130 mm along Z-axis. This is exceeding technical scattering parameters and may be the proof of scattering rising caused by EPO influence.

For better convergence of experimental values, attempts of piecewise linear approximation were undertaken. Diagrams of calculations on this procedure for one of shoots are given on fig.7.

The straight lines gained at keeping the criterion of the regression residual quadrates sum minimum are shows models' trajectory fracture on a site where interaction with laser spark takes place. Value of the model total deviation angle after EPO's interaction is $\Delta\varphi=3{,}2\ldots7{,}9^0$.

Conclusion

Thus, experimental results permits to conclude about possibility of fast flying body's trajectory parameters change by plasma formations influence, in viewed case by laser-induced spark. Trajectory fracture in contact area confirms essential EPO's influence on models flight dynamics. Obviously, increasing of contact time interval is necessary for EPO's influence magnification that was limited by laser spark length. That's why it is interesting organization of experiment, when plasma object accompanies flying body during necessary time interval.

References

1. Experimental researches of flying vehicles models motion in laser-induced spark plasma. Scientific report on theme 750-1200. № Б-17/130. Vladimir: OKB «Raduga», 1992, 54 p. (in Russian).
2. Investigations of flying vehicles models interaction with extended plasma formations. Scientific report. № 98/93. Faustovo: GosNIPAS, 1993, 39 p. (in Russian).

3.5. PLASMA DECAY IN AIR EXCITED BY HIGH-VOLTAGE NANOSECOND DISCHARGE

N.L. Aleksandrov
MIPT, Dolgoprudny, Russia, e-mail: nick_aleksandrov@mail.ru
E.M. Anokhin
MIPT, Dolgoprudny, Russia, e-mail: anohin@neq.mipt.ru
S.V. Kindysheva
MIPT, Dolgoprudny, Russia, e-mail: yuki@neq.mipt.ru
A.A. Kirpichnikov
MIPT, Dolgoprudny, Russia, e-mail: master_artyom@rambler.ru
I.N. Kosarev
MIPT, Dolgoprudny, Russia, e-mail: ilyakosarev@gmail.com
M.M. Nudnova
MIPT, Dolgoprudny, Russia, e-mail: maryia.mik@gmail.com
S.M. Starikovskaia
Ecole Politecnique, Palaiseau Cedex, France, e-mail: star.svet@gmail.com
A. Yu. Starikovskii
Princeton University, Princeton, USA, e-mail: astariko@princeton.edu

Abstract. Plasma decay in air after a high-voltage nanosecond discharge has been studied experimentally and numerically at room temperature for pressures between 1 and 10 Torr. Time-resolved electron density was measured by a microwave interferometer for initial electron densities in the range $(2 - 3)\times10^{12}$ cm^{-3}. Discharge non-uniformity was investigated by optical methods. The balance equations for charged particles and electron temperature were numerically solved to describe the temporal evolution of the densities of electrons and ions in the discharge afterglow. It was shown that the loss of electrons is governed by dissociative and three-body recombination with O_2^+ ions under the conditions considered. Good agreement between the calculated and measured electron density histories could be obtained only when increasing the rate of three-body recombination by an order of magnitude and when changing the dependence of the recombination rate on electron temperature. This could testify that the well-known mechanism of three-body recombination of atomic ions changes in the case of molecular ions.

1. Introduction

High-voltage nanosecond discharge produced by a fast ionization wave in a gas is characterized by high propagation velocity (10^9 - 2×10^{10} cm/s), high uniformity and repeatability of the parameters from pulse to pulse [1, 2]. This discharge can be initiated in a large volume (40 l or even more) [3], but it is more frequently studied in long shielded dielectric tubes with electrodes at their ends.

The high-voltage nanosecond discharge has attracted considerable attention owing to its ability to deposit energy in the excitation of high levels and ionization of neutral particles as well as in the dissociation of molecules. Therefore, this discharge shows promise for the control of plasma-chemical reactions [4], for plasma assisted ignition and combustion [5-9] and for high speed aerodynamics [10, 11]. For applications, it is important to know the properties of discharge plasma not only in the discharge, but also in its afterglow.

There is reason to believe that the decay of the high-voltage nanosecond discharge differs quantitatively from the decay of plasma generated by quasi-steady discharges at not-too-high overvoltages. Indeed, positive ions produced in the high-voltage nanosecond discharge are simple and have no time to transform into complex ones. Hence it is expected that, at the beginning of the plasma decay, the ion composition differs noticeably from that of long-lived plasma in which the ion composition is dominated by complex ions at room gas temperature. On the other hand, active neutral particles (excited molecules, atoms and radicals) that could affect the rate of plasma decay have no time to accumulate in the volume in the active phase of the nanosecond discharge. Thus description of electron density decay of the discharge under consideration could be noticeably simpler than that of plasma decay after discharges of long duration.

The purpose of this paper was to study experimentally and numerically peculiarities of plasma decay after the high-voltage nanosecond discharge in air for pressures between 1 and 10 Torr. Time-resolved electron density was measured by microwave interferometer in room temperature air with initial electron densities in the range 2×10^{12} – 3×10^{12} cm^{-3}. A kinetic scheme was suggested to describe recombination processes in the afterglow and time variation of the densities of charged

particles was calculated under the conditions considered. A comparison between the calculated results and measurements revealed the dominant mechanisms of electron loss and explained the pressure dependence of the rate of plasma decay.

2. Experiment

The experimental setup is represented schematically in figure 1 and has been described in detail elsewhere [12, 13]. Discharge was initiated in a quartz tube of inner diameter 47 mm and outer diameter 48.5 mm, the metallic electrodes being at the ends of the tube. The high-voltage electrode was a cone of angle 60 degrees at its vertex. The low-voltage electrode was an earthed ring placed at a distance of 20 cm from the opposite electrode.

Observations were made for gas pressures between 1 and 10 Torr. Pulses of amplitude 11 kV in cable, duration 25 ns at half-height and rise time 5 ns were supplied to the electrodes from a high-voltage generator. The energy input did not exceed 0.1 mJ cm^{-3}.

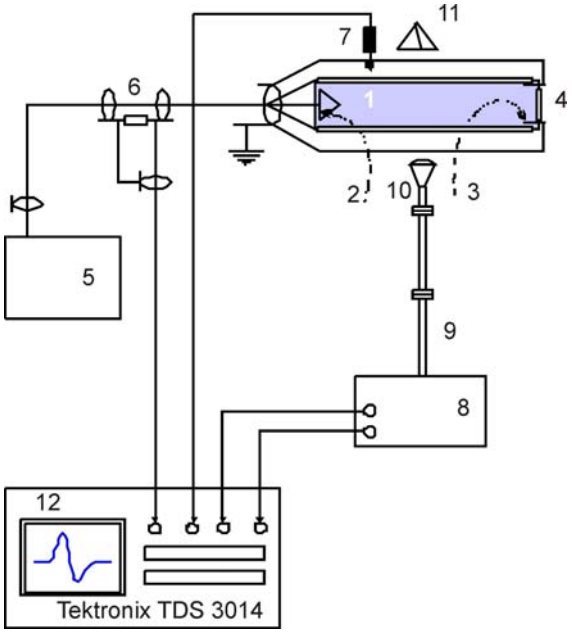

Figure 1. *A schematic diagram of the experimental setup: (1) quartz discharge tube, (2) high-voltage electrode, (3) low-voltage electrode, (4) CaF_2 window, (5) high-voltage generator, (6) back-current shunt, (7) capacitive gauge, (8) main block of the interferometer, (9) wave guide, (10) horn antenna, (11) reflector and (12) oscillograph.*

Time-resolved electron density was measured in the afterglow using a two-channel microwave interferometer. It involved the main block, waveguide, horn antenna, and reflector. A reference wave of frequency 9.4×10^{10} Hz (a wavelength of 3 mm) was produced by the generator in the main block of the interferometer. The reference wave extended along the 1.5 m waveguide to the horn antenna with teflon lens to form a parallel probing beam. Its diameter was much lower than the diameter of the discharge tube. The probing signal passed twice through the plasma and returned to the antenna and waveguide to interfere with the reference signal. Due to capacitors placed in series, signals were transferred from the detectors to the interferometer only when the shift between phases of the reference and probing waves and, consequently, wave pattern in the waveguide varied with time. Signals did not exist if plasma had not been generated in the space under consideration or if the plasma properties did not vary in time.

In the simplest case of a plane uniform plasma layer, the phase shift of the probing signal, $\Delta\Phi(t)$, is related to the electron density $n_e(t)$ in a linear way [14]

$$n_e(t) = \frac{2\varepsilon_0 mc}{e^2}\frac{\omega\Delta\Phi(t)}{l}, \qquad (1)$$

where m is the electron mass, ε_0 is the permittivity of vacuum, c is the light speed in vacuum, e is the elementary charge, ω is the angle frequency and l is the path length of the beam through the plasma. In (1), it was assumed that $\nu_m << \omega$, where ν_m is the frequency of electron momentum relaxation in collisions with other particles. This inequality was satisfied in the pressure range studied. In the case of non-uniform plasma, such measurements provided electron density averaged over the diameter of the discharge tube.

To analyze the spatial uniformity of the discharge plasma and of the initial electron density in the discharge afterglow, photographs of the discharge were taken with nanosecond resolution. The emission intensity was registered with a PicoStar HR 12 (La Vision) ICCD camera in the 350 – 800 nm wavelength range. The gate time of the ICCD camera was set to 300 ns. The radial distribution of electron density was extracted from the measured distributions of emission intensity.

3. Experimental results

Figure 2 and 3 show the electron density histories measured in air at 2.5 and 8 Torr, respectively. It follows from the measurements that the rate of plasma decay decreases with decreasing pressure. The electron density decreased over the first microsecond by a factor of three at 8 Torr and by a factor of two at 2.5 Torr. The decrease in electron density started at t = 0.3 μs for 8 Torr and only at t = 0.6 μs for 2.5 Torr. In the latter case, the instant at which the electron density started decreasing was more pronounced.

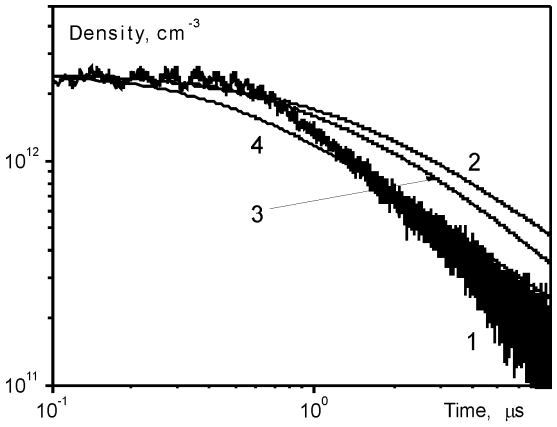

Figure 2. *The evolution in time of the electron density in the air afterglow for 2.5 Torr. Curve 1 corresponds to measurements. Calculations were carried out (curve 2) with the three-body coefficient, $k_3 = aT_e^{-n}$, from [15], (curve 3) with the value of a increased by an order of magnitude, n being the same, and (curve 4) with the value of a increased by an order of magnitude and n = 2.*

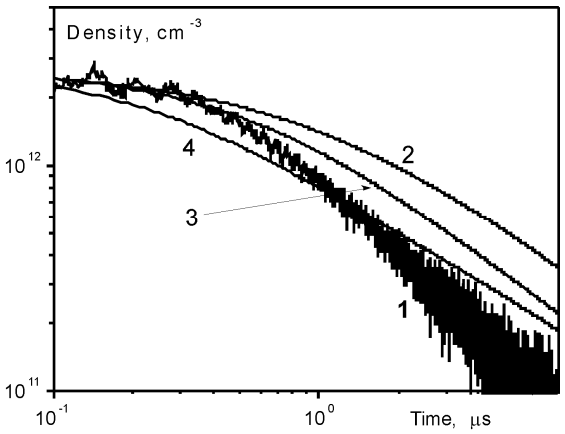

Figure 3. *The evolution in time of the electron density in the air afterglow for 8 Torr. The notation is similar to that in figure 2.*

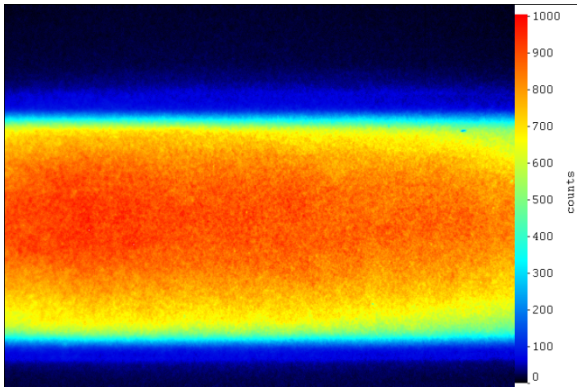

Figure 4. *ICCD image of the discharge in air for 2.5 Torr.*

Figure 4 shows an ICCD image of the discharge in air for 2 Tor. The corresponding radial distribution of the emission intensity is shown in figure 5. This distribution was extracted using the inverse Abelian transformation. The emission from the discharge turned out to be non-uniform. Its maximum was at a distance of ≈ 10 mm from the axis of the discharge tube, rather than directly on the axis.

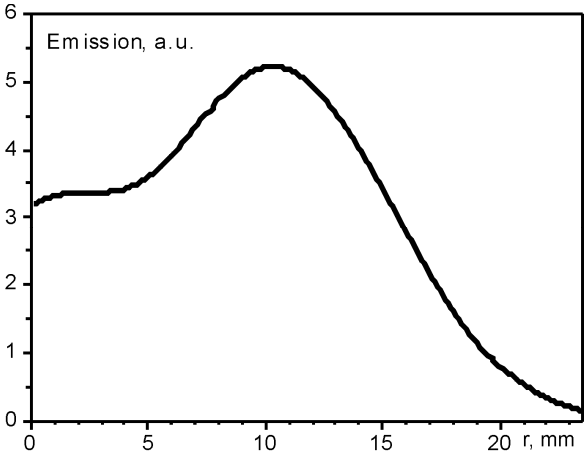

Figure 5. *The radial profile of emission intensity from the discharge for 2 Torr.*

4. Kinetic model

To simulate the loss of charged particles in the afterglow of the nanosecond pulsed discharge, we solved numerically a system of balance equations for electrons and ions. We neglected the loss of charged particles due to ambipolar diffusion; this effect could be important under the conditions considered only for $t > 10^{-2}$ s, the time that is several orders of magnitude longer than the characteristic time of plasma decay in our experiment.

Table 1 shows reactions taken into account in the simulation and the references for their rate constants. The kinetic scheme used in this work considered the loss of electrons due to recombination with simple positive ions produced in the discharge and the possibility of formation of complex positive ions in the discharge afterglow. This effect could be important because the rate of recombination of complex ions is an order of magnitude higher than that of recombination for simple ions. In addition, we considered three-body electron attachment to O_2 molecules, the process that could be important at not-too-high electron energies and sufficiently high gas pressures.

The rates of electron processes depend on the electron average energy that reaches several eV in the discharge phase. In the discharge afterglow, electrons are cooled (thermalized) in elastic and inelastic collisions with cold molecules. In addition,

during this phase electrons could be heated due to electron-ion recombination in which low-energy electrons are lost more efficiently. As a result, the average electron energy becomes somewhat higher [17]. Under the conditions considered the rate of electron thermalization and the rate of electron loss were of the same order of magnitude. Therefore, it was necessary to calculate the densities of charge particles and the average electron energy when simulating the plasma decay.

Table 1. *Reactions considered in the kinetic model.*

No	Reaction	Reference
(R1)	$e + N_2^+ \rightarrow N + N$	[15]
(R2)	$e + O_2^+ \rightarrow O + O$	[15]
(R3)	$e + N_4^+ \rightarrow N_2 + N_2(C)$	[15]
(R4)	$e + O_4^+ \rightarrow O_2 + O_2$	[16]
(R5)	$e + O_2^+N_2 \rightarrow O_2 + N_2$	[15]
(R6)	$e + A_2^+ + e \rightarrow A + A + e$	see the text
(R7)	$N_2^+ + O_2 \rightarrow N_2 + O_2^+$	[15]
(R8)	$N_2^+ + 2N_2 \rightarrow N_4^+ + N_2$	[15]
(R9)	$O_2^+ + 2O_2 \rightarrow O_4^+ + O_2$	[15]
(R10)	$O_2^+ + 2N_2 \rightarrow O_2^+N_2 + N_2$	[15]
(R11)	$N_4^+ + O_2 \rightarrow 2N_2 + O_2^+$	[15]
(R12)	$O_2^+N_2 + N_2 \rightarrow O_2^+ + 2N_2$	[15]
(R13)	$O_2^+N_2 + O_2 \rightarrow O_4^+ + N_2$	[15]
(R14)	$e + 2O_2 \rightarrow O_2^- + O_2$	[15]

In our simulation, it was assumed that the electron energy distribution is a Maxwellian one. This assumption was satisfied because, under the conditions studied, the frequency of electron-electron collisions, ν_{ee}, was much larger than the frequency of electron energy relaxation in collisions with molecules, ν_ε. In this case, the equation for the evolution of the electron temperature in the discharge afterglow is expressed as

$$\frac{dT_e}{dt} = -\nu_\varepsilon (T_e - T) - \frac{2}{3} T_e^2 \left(\frac{dk_3}{dT_e} n_e n_i + \frac{dk_2}{dT_e} n_i \right) \quad (2)$$

where T_e is the electron temperature, T is the gas temperature, k_3 is the rate constant of three-body electron-ion recombination (reaction (R6)) and k_2 is the rate constant of two-body dissociative electron-ion recombination.

The initial value of T_e was assumed to be in the range 1 – 10 eV corresponding to the mean electron energy in the discharge. The calculated results are not sensitive to this magnitude because the rate of electron thermalization decreases sharply with decreasing electron energy. Indeed, hot electrons quickly lose their energy in the inelastic collisions with excitation of electronic states of N_2 and O_2 molecules; however, when the electron energy decreases below the energy threshold of these processes, electrons relatively slowly get cold in the elastic and inelastic collisions with excitation of vibrational and rotational levels of molecules.

The frequency ν_ε was calculated as a function of T_e from the expression

$$\nu_\varepsilon = \frac{2ewE}{3k_B(T_e - T)}, \quad (3)$$

where k_B is the Boltzmann constant and w is the electron drift velocity in air in a steady external electric field E heating electrons up to the average energy $3k_BT_e/2$. The electron drift velocity and average energy were calculated as a function of the reduced electron energy E/N (N is the gas number density) from a numerical solution of the electron Boltzmann equation in the two-term approximation for the spherical harmonic expansion [18]. To obtain a Maxwellian electron energy distribution, the calculations were carried out at sufficiently high ionization degree taking into account electron-electron collisions. The Boltzmann equation for electrons was solved using the code EEDF [19].

In (2), we neglected the heating of electrons in superelastic collisions with electronically and vibrationally excited molecules. Under the conditions studied the vibrational temperature of molecules and the density of electronically excited molecules were low because of a small energy input in the discharge. As a result, the time of electron impact quenching of the excited molecules was longer than 10 μs and, consequently, then the lifetime of the plasma. For the same reason, we neglected associative ionization of the molecules in collisions between electronically excited particles and the decomposition of complex ions in collisions with atoms and excited particles.

5. Calculation results

We simulated the discharge afterglow taking into account the radial non-uniformity of the plasma. It was assumed that the plasma density at a given point is proportional to the emission intensity at this point. The initial radial distribution of the electron density n_e was assumed to be similar to the distribution of emission intensity. The initial distribution of n_e was normalized using the average electron density measured with the microwave interferometer. The plasma decay was simulated separately for various cylindrical layers located at different distances from the tube axis. At each instant, the electron density was averaged over the tube diameter and the obtained average values of n_e were compared with experimental data. It was shown that the difference between the calculations

when taking into account the plasma non-uniformity and those when assuming plasma uniformity did not exceed 10%.

Figures 2 and 3 compare the electron density history calculated from the electron and ion balance equations taking into account the plasma non-uniformity and measured history in air afterglow for 2.5 and 8 Torr, respectively. The calculation based on the traditional set of rate constants from [15] agreed qualitatively with the measured electron density history in the plasma afterglow. In particular, the rate of plasma decay increased with time, in agreement with the observations. This was associated with the cooling of electrons (see figure 6); the cooling led to an increase in the rates of electron-ion recombination because these rates are decreasing functions of T_e. However, the quantitative difference between the calculation and measurements of n_e reached a factor of 2 – 3, much higher than the experimental error of the electron density measurements that was around 20-30%.

To understand the difference between the calculation and measurements, we analyzed the kinetic scheme and rate constants used. It turned out that all rate constants were taken from measurements, with the exception of the rate of three-body electron-ion recombination (reaction (R6)). The rate of this reaction has been measured only at $T_e = T > 1500$ K and only for atomic ions [20]. It is generally assumed that, at not-too-high temperatures, the rate of three-body recombination is independent of ion species and varies with T_e as $k_3 = aT_e^{-n}$, where $n = 4.5$.

It was shown in a model calculation [21] that the values of a and n can change drastically when atomic ions are replaced by molecular ones. This is associated with the mechanism of three-body recombination that proceeds in many stages [20]. In the first stage, the free electron is captured by the ion in a three-body collision to form a neutral particle in a highly excited Rydberg state. Then, the weekly bonded electron loses its energy diffusively due to collisions with free electrons and due to radiation transitions. The process is finished when the electron descends to a sufficiently low energetic level of the neutral particle. It was shown in [21] that, in the case of molecular ions, the quenching rate for highly excited states of neutral particles could be drastically increased because of dissociation of highly excited molecular states. According to the calculation [21], the value of a could be increased by an order of magnitude and the value of n could be around 2-2.5.

Our calculations showed that the dominant ion species under the conditions studied is O_2^+. To take into account the effect suggested in [21], we repeated the simulation of the plasma decay when, for three-body recombination with O_2^+ ions, (i) the value of a was increased by an order of magnitude as compared with that given in [15] and (ii) it was assumed that $n = 2$. The results of such a simulation are also shown in figures 2 and 3. The increase in a led to some reduction in the difference between measured and calculated electron densities. However, this difference remained considerable. With the additional replacement of $n = 4.5$ by $n = 2$, we obtained good agreement between the measurement and calculation. In this case, the difference between them was within the experimental error of the electron density measurements. The observed increase in the rate of plasma decay with increasing gas pressure is associated with more efficient electron thermalization at high pressures. The higher is the pressure, the lower is the electron temperature. Hence the rate of electron-ion recombination is higher.

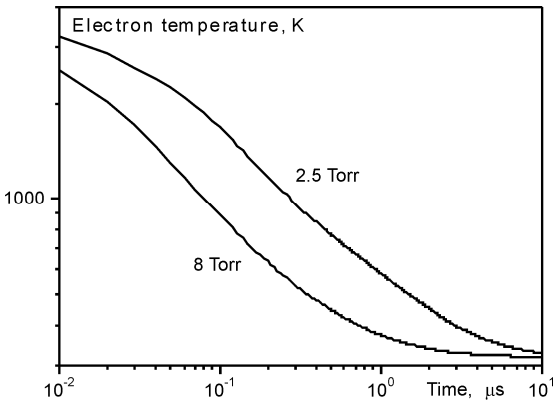

Figure 6. *The evolution in time of the electron temperature at various air pressures.*

Thus, it may be concluded that the rate of three-body recombination for O_2^+ ions is much higher than that for atomic ions and that the T_e-dependence of the recombination rate is weaker for O_2^+ ions.

Figures 7 and 8 show the calculated evolution in time of the ion composition in air for 2.5 and 8 Torr, respectively. For comparison purposes, the temporal evolution of the electron density is also given there. It is clear that the slow electron thermalization in air affects noticeably not only the evolution of the electron density, but also the evolution of the ion densities as well. At low times, when the value of T_e was high and electron-ion recombination was slow, the dominant ion species was N_2^+. These ions were lost via charge exchange in collisions with O_2 molecules (reaction (R7)) and via conversion to complex N_4^+ ions (reaction (R8)). Although the rate of recombination for complex ions is high, this process is not important because of fast charge exchange in collisions with O_2 molecules (reaction (R11)). As a result, the ion composition was dominated by O_2^+ ions during the plasma decay. The rate of

conversion of these ions to form complex O_4^+ ions is much lower than the rate of conversion of N_2^+ ions to N_4^+ ions [15]. Therefore, O_4^+ ions had no time to be formed in the discharge afterglow. Thus, it was expected that electron recombination with O_2^+ ions governed the plasma decay under the conditions considered.

Figure 9 shows the evolution in time of the frequencies of the main processes of electron loss in the discharge afterglow at 2 Torr. It follows from the calculation that, when increasing the rate of three-body recombination and assuming $n = 2$, this process controls the plasma decay in our case. Two-body dissociative recombination with O_2^+ ions is also important; however, its role is not crucial. Recombination with complex ions and electron attachment to O_2 molecules could be neglected.

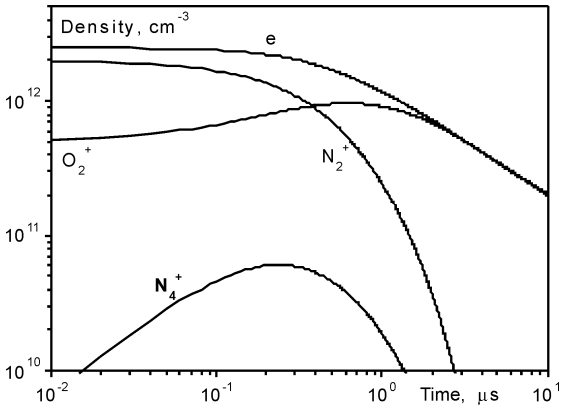

Figure 7. *The evolution in time of the ion and electron densities for 2.5 Torr. The calculations correspond to the assumptions for curve 4 in figure 2.*

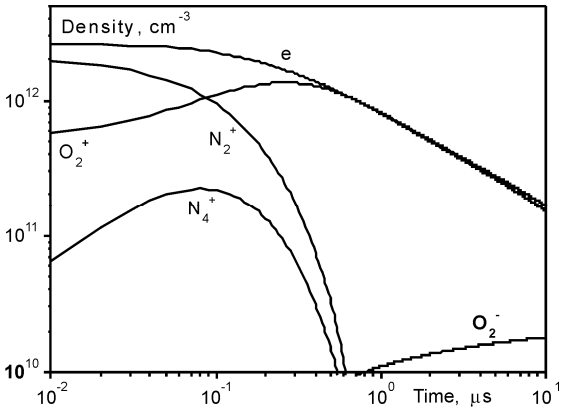

Figure 8. *The evolution in time of the ion and electron densities for 8 Torr. The calculations correspond to the assumptions for curve 4 in figure 3.*

In our previous work [22], we studied the plasma decay after a high-voltage nanosecond discharge in pure N_2, CO_2 and H_2O. The conditions were similar to those in this work. We obtained good agreement between measured and calculated electron density histories in these gases without changing the rate of three-body electron-ion recombination. We carried out additional simulation of the plasma decay in N_2, CO_2 and H_2O with changing the values of a and n for the rate of three-body electron-ion recombination in these gases by analogy with this work. It turned out that the change in the rate of this process does not affect noticeably the simulation results under the conditions of the experiment [22]. This is explained by the fact that in this case complex ions had time to be formed and the plasma decay was governed by fast recombination with these ions, rather than by three-body recombination. In air, this does not occur because of low rate of formation of O_4^+ ions. By analogy with plasma decay in air, the important role of three-body recombination could be expected for the plasma decay in pure oxygen.

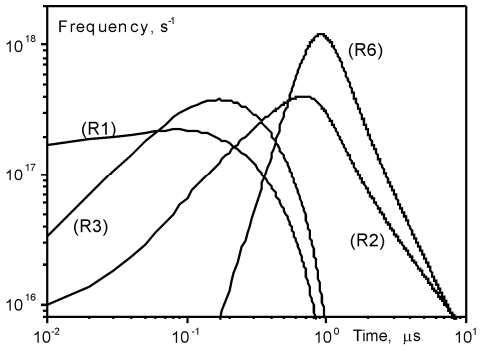

Figure 9. *The evolution in time of the frequencies for the main processes of electron loss for 2 Torr. The calculations correspond to the assumptions for curve 4 in figure 2.*

6. Conclusions

1. Using a microwave interferometer, the evolution in time of the electron density was measured in the afterglow of a high-voltage nanosecond discharge in air at 1-10 Torr. It was shown that the rate of the plasma decay increases with gas pressure.
2. A kinetic model was developed to describe the plasma decay under the conditions studied taking into account the finite rate electron thermalization. The electron densities that were calculated using the recombination rate constants available in the literature differ greatly, by a factor of 2 – 3, from the measured electron densities.
3. A hypothesis was proposed that the rate of three-body recombination for O_2^+ ions is an order of magnitude higher than that for atomic ions and that the T_e-dependence of recombination rate is weaker for molecular ions. This agrees with the calculation [21] carried out for a model molecular system. The simulation based on the proposed hypothesis agrees well with the measured electron density histories. It may be concluded that the mechanism of three-

body recombination of molecular ions differs noticeably from the well-known mechanism of this process for atomic ions.

4. Radial uniformity of the discharge was studied with optical methods. Although the discharge plasma was radially non-uniform, the consideration of this effect did not influence noticeably the results of simulation of the plasma decay.

References

1. Vasilyak L.M., S.V. Kostyuchenko S.V., Kudryavtsev N.N. and I.V. Filyugin I.V., "High-speed ionization waves at an electric breakdown", *Phys.—Usp,* Vol. 163, 1994, pp. 247–68.
2. Starikovskaia S.M., Anikin N.B., Pancheshnyi S.V., Zatsepin D.V. and Starikovskii A.Yu., "Pulsed breakdown at high overvoltage: development, propagation and energy branching" *Plasma Sources Sci. Technol.,* Vol. 10, 2001, pp. 344–55.
3. Starikovskaia S.M., Starikovskii A.Yu. and Zatsepin D.V., "Development of a spatially uniform fast ionization wave in a large discharges volume" *J. Phys. D: Appl.Phys.,* Vol. 31**,** 1998, pp. 1118–24.
4. Ganguly B.N. and Parish J.W., "Absolute H atom density measurement in pure methane pulsed discharge", *Appl. Phys. Lett.,* Vol. 84**,** 2004, pp. 4953–5.
5. Kof L.M. and Starikovskii A.Yu. 1996 "Oxygen-hydrogen mixtures ignition under the high-voltage ionization wave conditions at high temperatures" *26th Int. Symp. On Combustion. Abstracts of Work-in-Progress Papers*, Napoli: The Combustion Institute Publications, p. 406.
6. Bozhenkov S.A., Starikovskaia S.M. and Starikovskii A.Yu., "Nanosecond gas discharge ignition of H_2 – and CH_4 -containing mixtures", *Combust. Flame,* Vol. 133, 2003, pp. 133–46.
7. Starikovskii A.Yu., Anikin N.B., Kosarev I.N., Mintoussov E.I., Starikovskaia S.M. and Zhukov V.P. "Plasma-assisted combustion", *Pure Appl. Chem.*, Vol. 78, 2006, pp. 1265-94.
8. Lou G., Bao A., Nishihara M., Keshav S., Utkin Y.G. and Adamovich I.V. 2006 "Ignition of premixed hydrocarbon-air flows by repetitively pulsed, nanosecond pulse duration introduction plasma", AIAA-2006-1215, January 2006.
9. Pancheshnyi S.V., Lacoste D.A., Bourdon A. and Laux C.O., "Ignition of propane—air mixtures by a repetitively pulsed nanosecond discharge", *IEEE Trans. Plasma Science,* Vol. 34**,** 2006, pp. 2478–87.
10. Sidorenko A.A., Zanin B.Yu., Postnikov B.V., Budovsky A.D., Starikovskii A.Yu., Roupassov D.V., Zavialov I.N., Malmuth N.D., Smereczniak P. and Silkey J.S. 2007 "Pulsed discharge actuators for rectangular wing separation control", AIAA-2007-633, January 2007.
11. Likhanskii A., Shneider M., Macheret S. and Miles R. "Optimization of dielectric barrier discharge plasma actuators driven by repetitive nanosecond pulses", AIAA-2007-941, January 2007.
12. Anikin N. B., Starikovskaia S. M. and Starikovskii A.Yu., "Oxidation of saturated hydrocarbons under the effect of nanosecond pulsed space discharge" *J. Phys. D: Appl. Phys.,* Vol. 39, 2006**,** pp. 3244–52.
13. Anikin N.B., Starikovskaia S.M. and Starikovskii A.Yu., "Study of the oxidation of alkanes in their mixtures with oxygen and air under the action of a pulsed volume nanosecond discharge" *Plasma Phys. Rep.,* Vol. 30, 2004, pp. 1028–42.
14. Heald M.A. and Wharton C.B., *"Plasma Diagnostics with Microwaves"*, Wiley, New York, 1965.
15. Kossyi I.A., Kostinsky A.Yu., Matveyev A.A. and Silakov V.P., "Kinetic scheme of the non-equilibrium discharge in nitrogen–oxygen mixtures", *Plasma Source Sci. Technol.,* Vol. 1, 1992 , pp. 207–20.
16. Florescu-Mitchell A.I., Mitchell J.B.A., Phys. Rep., "Dissociative Recombination", Vol. 430, 2006, 277-374.
17. Bychkov V. L., Eletskii A. V. "Electron-beam high-pressure plasma" In: *Chemistry of plasma, ed. B M Smirnov* No. 12, p 119 Moscow, Energoatomizdat, 1985.
18. Shkarofsky I.P., Johnston T.W. and Bachynski M.P., "*The Particle Kinetics of Plasmas",* Addison-Wesley, Reading, MA, 1966.
19. Dyatko N.A., Kochetov I.V., Napartovich A.P., Sukharev A.G., "EEDF: the software package for calculations of the electron energy distribution function in gas mixtures", http://www.lxcat.laplace.univ-tlse.fr/software/EEDF/
20. Biberman L.M., Vorobiev V.S., Yakubov I.T., "Kinetics of non-equilibrium plasma" Nauka, Moscow, 1982.
21. Collins C.B., "Collisional-dissociative recombination of electrons with molecular ions", Phys. Rev., Vol. 140, 1965, pp. A1850-57.
22. Aleksandrov N.L., Kindysheva S.V., Kirpichnikov A.A., Kosarev I.N., Starikovskaia S.M. and Starikovskii A.Yu. "Plasma decay in N_2, CO_2 and H_2O excited by high-voltage nanosecond discharge*", J. Phys. D: Appl. Phys.*, Vol. 40, 2007, pp. 4493-4502

4.1. FORMATION OF SEPARATION ZONES DURING THE INTERACTION OF SHOCK WAVE WITH THIN TEMPERATURE WAKE

P.Yu. Georgievsky, O.G. Sutyrin
Institute of Mechanics of Moscow State University,
1 Michurinsky prospect, Moscow 119192, Russia
V.A. Levin
Institute of Automation and Control Processes of Russian Academy of Sciences,
5 Radio street, Vladivostok 690041, Russia

The interaction of plane shock wave and bow shock wave with thin high temperature wake was investigated. The technique of block embedded grids was used to improve the accuracy of numerical simulation in the vicinity of the temperature layer. The mechanism of front separation zones formation in the presence of the upstream energy deposition was determined.

The effect of formation of front separation zones for supersonic flows past bodies in the presence of localized upstream energy deposition was considered as the basic reason for wave drag reduction [1–2]. The existence of isobaric front separation zones is acceptable from classic gasdynamic point of view for "wake-type" upstream flow inhomogeneity of any nature [3]. In particular for thin high temperature wakes the efficiency of the wave drag reduction theoretically is infinitely high because static pressure inside the front separation zone is determined by dynamic pressure inside the temperature wake but not by the temperature wake thickness (the conception of "thermal spike" [4] or "air spike" [5]). However the serious possible problem was pulsing and shift instabilities of front separation zones, which had been noticed during numerical simulations for small energy deposition regions [6-7] and thin temperature filaments [8].

In the present paper the interaction of plane shock wave and bow shock wave with thin high temperature wake was investigated. The gasdynamic effects of the interaction are critically important for understanding of the mechanism of front separation zones formation. Euler equations and the "energy source" model [6-7] were used for numerical simulation. The explicit MacCormack scheme of the second order accuracy with coordinates and time was applied. The technique of block embedded grids was used to improve the accuracy of numerical simulation in the vicinity of the temperature layer.

Interaction of the plane shock with high temperature layers and "precursor" formation effect

The interaction of the plane shock with high temperature region (quarter plane) was investigated in [9]. The formulation of this problem was free from linear scale parameter, so that the solution should be self-similar two-dimensional one (it was good test for numerical simulation accuracy).

The complicated unsteady flow structure known as "precursor" was observed (Fig. 1). Two points of shock intersection could be identified (A – the inter-

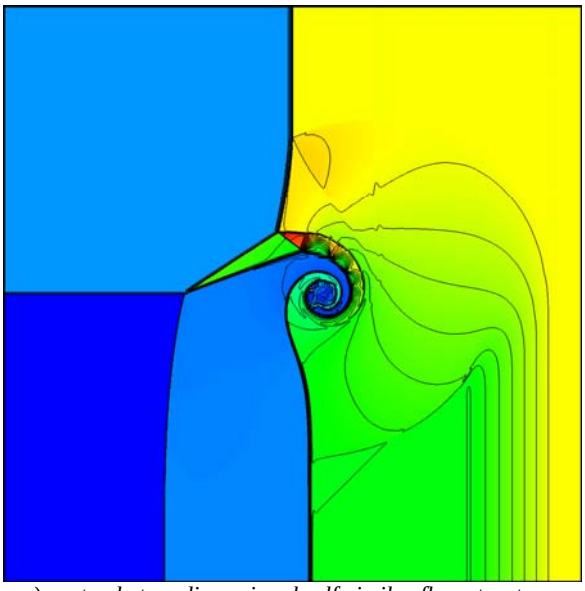

a) unsteady two-dimensional self-similar flow structure;

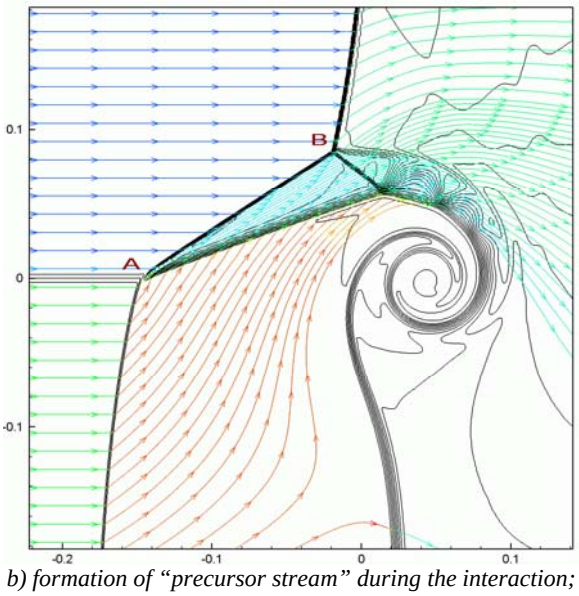

b) formation of "precursor stream" during the interaction;

Fig. 1 *The interaction of the plane shock with high temperature region (quarter plane).*

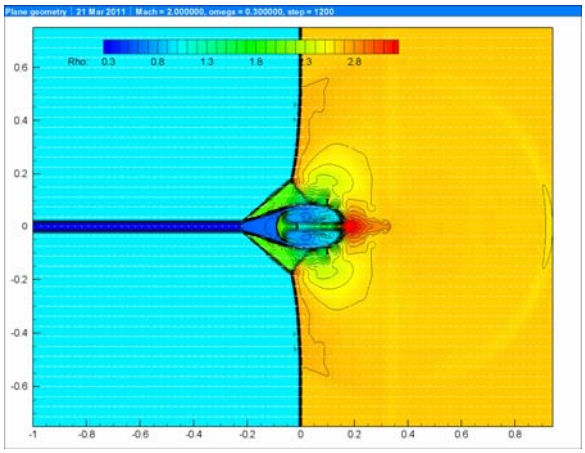

a) $t=t_1$

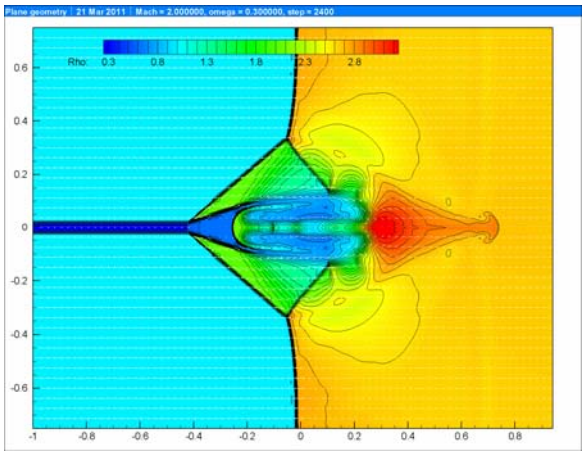

b) $t=2t_1$

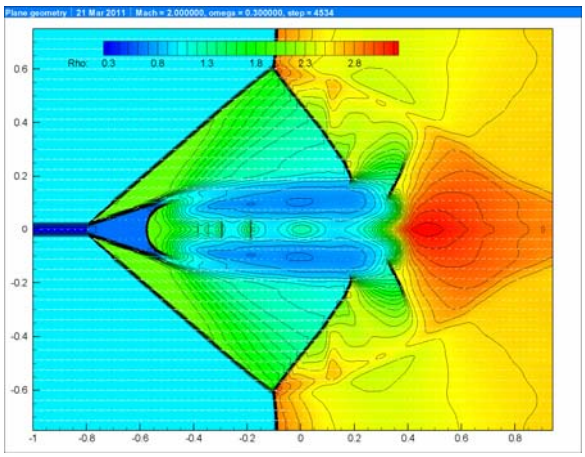

c) $t=4t_1$

Fig. 2 *The interaction of plane shock wave with thin temperature layer (illustration of asymptotical self-similarity effect).*

section point of the leading shock, the oblique shock and two tangential discontinuities, B – the intersection point of the initial shock, the oblique shock, the internal shock and the origin of tangential discontinuity). The leading shock inside the hot domain, as well as the initial shock near the triple points A and B are distorted (to satisfy gasdynamics conditions for shock intersection). It is very important, that the formation of self-similar stream and vortex was observed. The high enthalpy stream was consisted of gas particles coming through the plane oblique shock and the internal shock. It was bounded by the tangential surfaces from both sides. The "swirl" effect of the stream could be explained by pressure difference on the "inner" and "outer" tangential surfaces. The stream turning was provided by the combination of the internal Prandtl-Meyer fans. The flow field is just constant within x/t, y/t variables because of self-similarity of the problem (it was controlled during the simulation). The effect of formation of swirling stream is the unsteady self-similar analogue of the steady Edney IV shock interaction phenomena.

The interaction of the plane shock with thin high temperature layer was examined. The technique of block embedded grids was used to improve the accuracy of numerical simulation in the vicinity of the temperature layer. Actually for this problem only one length-scale parameter exists – the temperature layer thickness. The time scale $l_\infty \left(p_\infty / \rho_\infty \right)^{-1/2}$ is proportional to the length scale. So the term "thin layer" was used to accent that physical calculation time was large enough and the layer was thin in the comparison with precursor size. This situation was described in [4] as asymptotical self-similarity.

The effect of the asymptotical self-similarity is illustrated in Fig.2. For very small time moments (or thick temperature layers) two symmetrical precursors were formed (each precursor look as in Fig.1). Then because of the interaction of two separate symmetrical swirling streams and vortexes the mushroom structure was appeared (Fig.2a). The next result of the interaction was the formation of counter-flow stream in the vicinity of the symmetry axes (Fig.2b). Finally the separation zone was appeared on the symmetry axes where the regulation of mass balance was taken place: the major gas portion was involved by the counter-flow stream whereas the minor gas portion – by the cocurrent flow stream (Fig.2c). The velocity of the leading shock, which was moved upstream inside the temperature layer, was just constant during all the observation time. So the basic conclusion, formulated in [4] concerning asymptotical self-similarity, was absolutely right despite the space resolution during the numerical simulation due to objective reasons was not enough to observe flow structures like in Fig.2.

The mechanism of front separation zones formation in the presence of the upstream energy deposition

The analyze of the interaction of the plane shock with the temperature layer could be used for better understanding of the mechanism of front separation zones formation in the presence of the upstream energy deposition.

If the energy source is powered on in the uniform supersonic upstream flow, then the high temperature cloud appears. The elongation of the cloud is

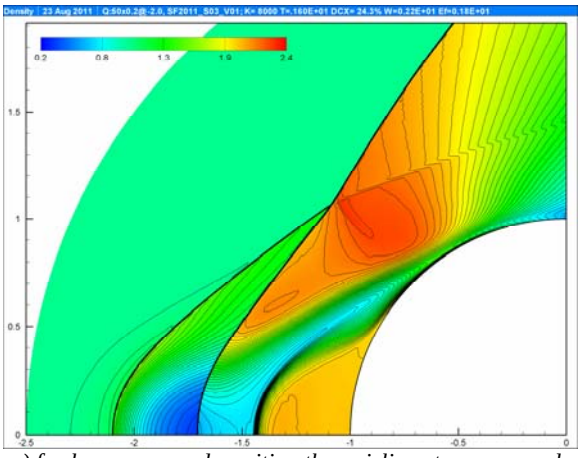

a) for large energy deposition the swirling stream spreads over the lateral surface of the body

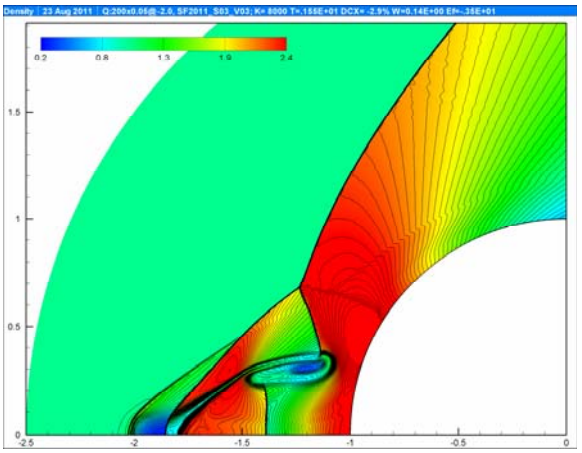

b) for small energy deposition region swirling stream was captured by the front separation zone

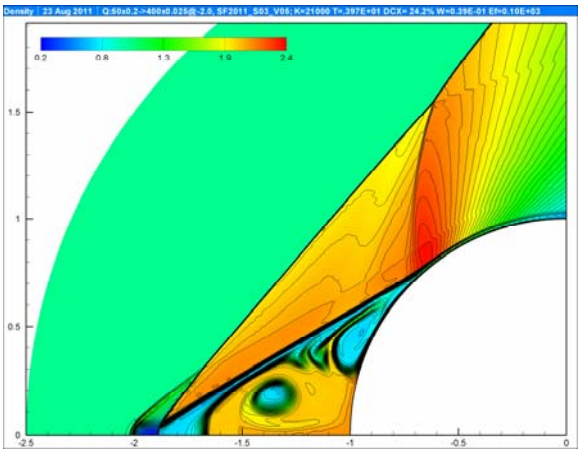

c) formation of steady front separation zone during quasi-stationary transformation of the energy deposition region

***Fig. 3** Front separation zones formation in the presence of the upstream energy deposition as the result of the interaction of high temperature wake with shock layer.*

provided by the drifting effect of the upstream flow and by the acceleration effect conditioned by the pressure gradient [2]. At the time moment when the cloud reaches the bow shock ahead of the body the process of the interaction was started. Locally in the vicinity of the of the symmetry axes the bow shock is plane so that local similarity is taking place (the only scale is the temperature wake thickness). The above described precursor structure appears. Appearing of the precursor structure during the high temperature wake – the bow shock interaction was noticed in [4] as the basic reason for formation of front separation regions for blunt bodies. According to [4] only pulsing regimes were realizable in numerical experiments.

Actually the precursor scale for the initial stage of the interaction is determined by the temperature wake thickness. In Fig.3a-b flow structures are presented for the same time moment for temperature wakes of different thickness (energy deposition regions of different sizes). For enough thick temperature wake the precursor was "young" (physical time is proportional to the temperature wake thickness) and the swirling stream spreads over the lateral surface of the body (Fig.3a). Finally the steady front separation zone was appeared. But for the same time moment and thin temperature wake the precursor was "old" so that swirling stream was captured by the front separation zone and the circulating flow was appeared (Fig.3b). For the last case the inflow of additional gas into the separation zone was the reason for appearing of periodical transversal pulsations.

To eliminate the transversal pulsations the process of quasi-stationary transformation of the energy deposition region was proposed [6-7]. It was found that the numerical solution depends on the process history. On the first stage the numerical simulation was carried out for enough large energy deposition region and the formation of steady isobaric front separation zone was observed (Fig.3a). Then the time marching procedure was started from this solution. The energy deposition region geometry was transformed to small size during the numerical simulation. Now this procedure was applied to found steady isobaric front separation zone for the energy deposition region of very small size (Fig.3c).

Conclusions

The interaction of plane shock wave with thin high temperature wake was investigated. The technique of block embedded grids was used to improve the accuracy of numerical simulation in the vicinity of the temperature layer. The effect of asymptotical self-similarity and the effect formation of counter flow stream where observed. The mechanism of front separation zones formation in the presence of the upstream energy deposition was determined as the result of the interaction of high temperature wake with shock layer. The appearing of transversal pulsations of front separation zones is the result of capturing the "precursor" swirling stream by the front separation zone. The method of quasi-stationary transformation of the energy deposition region from large size to small size could be applied to found steady front separation regions in numerical experiments.

Acknowledgments

These investigations were financially supported by Russian Foundation for Basic Researches (grant 11-01-00052), Ministry of Education and Sciences of Russian Federation (grant NSh-8424.2010.1) and Russian Academy of Sciences (as Part of Special Program for Support of Fundamental Researches).

References

1. Georgievsky P.Yu., Levin V.A. Supersonic Flow over Bodies in the Presence of External Energy Input // Pis'ma v Zhurnal Tekhnicheskoi Fiziki. 1988. Vol. 14, No. 8. P. 684–687.
2. Georgievskii P.Yu., Levin V.A. Control of the Flow past Bodies Using Localized Energy Addition to the Supersonic Oncoming Flow // Fluid Dynamics. 2003 Vol. 38. No. 5. P. 154–167.
3. Guvernyuk S.V., Savinov K.G. Isobaric Separation Structures in Supersonic Flows with a Localized Inhomogeneity // Doklady Physics. 2007. Vol. 52. No. 3. P. 151–155.
4. Artem'ev V.I., Bergel'son V.I., Nemchinov I.V., Orlova T.I., Smirnov V.A., Khazins V.M. Change of Regime in Supersonic Flow past an Obstacle Preceded by a Thin Channel of Reduced Density // Fluid Dynamics. 1989. Vol. 24. No. 5. P. 779–784.
5. Myrabo L., Raizer Y. Laser-Induced Air Spike for Advanced Transatmospheric Vehicles // AIAA Paper 1994–2451, 1994.
6. Georgievsky P.Yu., Levin V.A. Hysteresis Effect and Stability Problem for Flow-over-Body Control Realized by Local Energy Deposition // Proc. of the 15th International Conference on MHD Energy Conversion and the 6th International Workshop on Magneto-Plasma Aerodynamics / Ed. V.A. Bityurin. Moscow. IVTAN. 2005. Vol. 3. P. 751–757.
7. P.Yu. Georgievsky, V.A. Levin, R.R. Gadelev, O.G. Sutyrin Control of Front Separation Regions for Supersonic Flows over Blunt and Streamlined Bodies by Upstream Energy Deposition // Proc. 7th International Workshop on Magneto-Plasma Aerodynamics / Ed. V.A. Bityurin, Moscow, JIHT RAS, 2007. P. 79–86.
8. Azarova O.A., Grudnitsky V.G., Kolesnichenko Yu. F. Some Gas Dynamic Aspects of Flow Control by MW Energy Deposition // Proc. of the 15th International Conference on MHD Energy Conversion and the 6th International Workshop on Magneto-Plasma Aerodynamics. Ed. V.A.Bityurin, Moscow, IVTAN, 2005, pp. 152–163.
9. Georgievskii P.Yu. , Levin V.A., Sutyrin O.G. Two-Dimensional Self-Similar Flows Generated by the Interaction Between a Shock and Low-Density Gas Regions // Fluid Dynamics. 2010 Vol. 45. No. 2. P. 281–288.

4.2. THE IMPACT OF ELECTRIC DISCHARGE ON SELF-OSCILLATING SHOCK WAVES WHEN SUPERSONIC JET IMPINGING ON THE FINITE OBSTACLE OF VARIOUS PERMEABILITY

V.M. Fomin, B.V. Postnikov, and K.A. Lomanovich
Khristianovich Institute of Theoretical and Applied Mechanics
4/1 Institutskaya str., Novosibirsk 630090, Russia

Abstract. Experimental data on the suppression, with a peripheral electric discharge, of intense shock-wave-front self-oscillations emerging during impingement of supersonic jets onto permeable and impermeable flat finite-sized obstacles are reported.

Supersonic off-design jets, either free or impinging onto flat obstacles, feature rather an intricate gas-dynamics. This circumstance is related, first of all, with the involvement in observed phenomena of a specific system of shocks, large gradients of determining parameters, and a wide range of sub- and supersonic flow velocities. In impact jets, instabilities leading to intense self-oscillations of shock-wave fronts often develop. The self-oscillations emerge at certain values of flow quantities and at certain geometric characteristics of the nozzle-obstacle system. An unsteady regime with self-oscillations was observed both in under- and overexpanded jets. Self-oscillations may arise if the obstacle is located

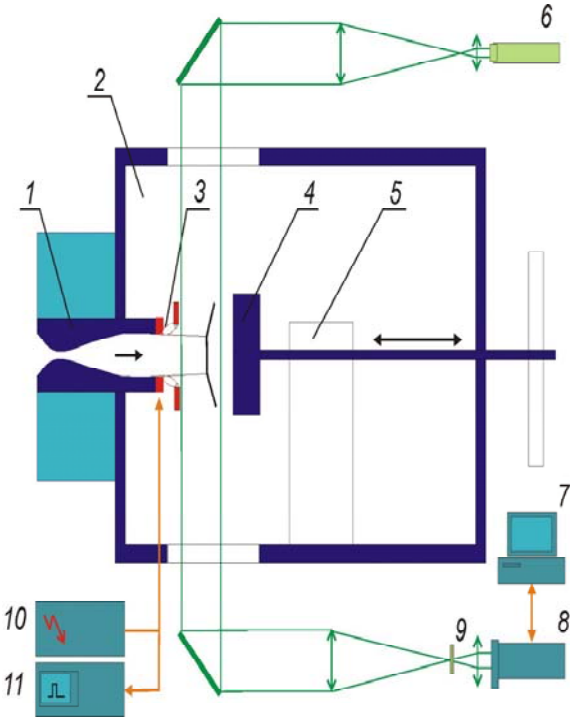

Fig.1. *Experimental arrangement. 1 – supersonic nozzle; 2 – test section; 3 – discharge initiation zone, electrodes; 4 – obstacle; 5 – pylon; 6 – laser; 7 – PC; 8 – camera; 9 – adaptive visualizing transparent; 10 – power supply; 11 – oscilloscope*

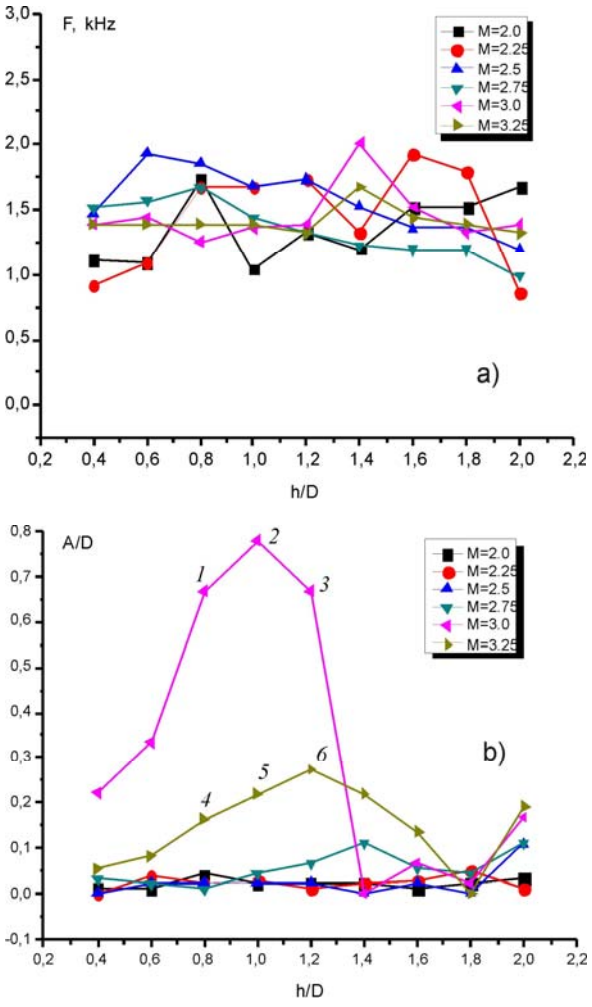

Fig.2. *The frequency F (a) and the relative amplitude A/D (b) of bow shock wave oscillations for an impermeable obstacle of relative diameter d/D=1.2. The numerals 1–6 denote regimes with discharge initiation.*

in jet within the first barrel or in subsequent barrels. From the practical point of view, it is the possibility of reduction or complete suppression of intense self-oscillations in jet flows that is of significance, along with the possibility to exercise control over the amplitude-frequency characteristics of such oscillations. Recent developments in magnetoplasma control methods for high-speed gas flows allow a new strategy to be adhered in this field.

Investigations of supersonic jets interacting with finite or infinite obstacles have been the subject matter of many studies performed since the sixties [1-3]. Nonetheless, the physics and mechanics of processes leading to emergence of intense self-oscillations of jet flows still remain understood scantily. Studies are known in which attempts were made to exercise an influence on the internal characteristics of sub- or supersonic jets using electric discharges [4, 5]. The authors of [6, 7] showed that initiation of a peripheral electric discharge in a supersonic air or methane jet impinging onto a flat impermeable or permeable obstacle had an effect on the oscillation frequency of shock-wave fronts. The present work was performed to examine this influence in more detail, with primary emphasis placed on the possibility of suppression of intense self-oscillations.

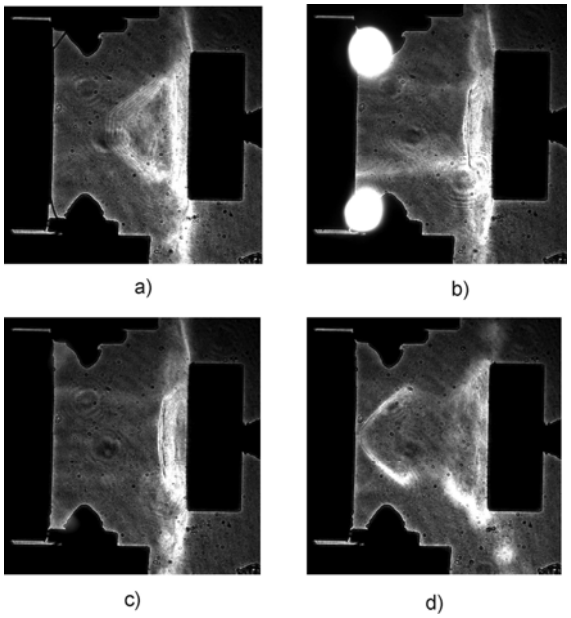

Fig.3. *Visualization of the suppression of shock-wave front self-oscillations with a peripheral electric discharge. Impermeable obstacle: M=3.0, d/D=1.2, h/D=1.2.a) regime with intense self-oscillations; b) suppression of self-oscillations with initiated discharge; c) regime without self-oscillations; d) recovery of the regime with intense self-oscillations.*

The experimental facility was an intermittent supersonic wind tunnel in which air exhaust was organized into an vacuum tank (Fig.1). The blowdown time of the wind tunnel was about one minute. The atmospheric air from the room in which the experimental setup was installed could freely enter a shaped Laval nozzle; this enabled a substantial reduction of flow perturbations at the nozzle inlet. At the nozzle outlet, near the nozzle lip, two electrode assemblies were provided, installed so that the burning discharge, a low-pressure arc, did not obstruct the supersonic stream. In the experiments, a three-electrode arrangement was used which involved two rod electrodes located at the nozzle lip and a central copper ring electrode through which a stream could pass. The discharge was initiated by a short circuit organized in the discharge gap. A typical voltage applied to either of the two initiated gaps was 30 V, the current becoming established at 50-70 A. As the stream approached the cylindrical obstacle, it decelerated, and oscillating shock-wave fronts were produced in it. Flow visualization tests of the supersonic impact jets were performed using a shadow instrument provided with an adaptive visualizing transparent (AVT) [8]. As the photodetector, a high-speed PCO 1200hs camera with a shooting rate of 10 thousand frames per second was used. In linear-pixel-array mode, the shooting rate could be increased to 24 thousand frames per second. According to gained visualization data, the emerging large-amplitude oscillations were periodic oscillations, or self-oscillations.

Gas-dynamic regimes with large-amplitude oscillations of shock-wave fronts for an impermeable obstacle of diameter d/D are illustrated in Fig. 2. This figure shows the frequency F and the relative amplitude A/D of the oscillations versus the nozzle exit-to-obstacle separation h/D (here, d is the obstacle diameter, and D is the nozzle outlet diameter). Under the amplitude A, we understand the distance to which the shock-wave front departs from its stationary position, since in our experiments regimes with non-periodic oscillations were also observed. The oscillation frequencies fall into the range 1 to 2 kHz. Simultaneously, in experiments with Mach 3.0 and M=3.25 nozzles much greater oscillation amplitudes were obtained (regime with intense oscillations). Experiments with a peripheral electric discharge were therefore carried out on Mach 3.0 and Mach 3.25 nozzles. In the latter cases, the jet was an overexpanded jet displaying a slight convergence of its boundaries towards the symmetry axis. Figure 3 shows four schlieren pictures that illustrate the evolution of the shock-wave pattern of flow during discharge initiation at the periphery of the oscillating jet. It is seen that discharge initiation allows one to suppress the

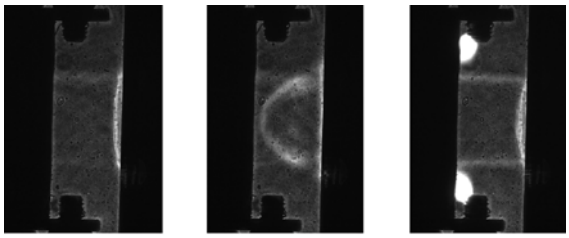

Fig.4. *Suppression of self-oscillations with an initiated electric discharge, obstacle ϕ=30 ppi. Regime with self-oscillations: a) minimal departure of the normal compression shock, b) maximal departure of the normal compression shock. Suppression of self-oscillations with an electric discharge: c) steady flow.*

regime with self-oscillations. The flow responds to the ignited discharge in a time shorter than 50 ms. In some cases, even faster responses were observed, produced within a time of 1 ms. After the discharge is quenched, the oscillations recover with a certain delay (Fig. 3c). The duration of the delay, up to 200 ms, was much greater than the response time of the flow to discharge initiation.

Similar results in terms of suppression of intense self-oscillations were obtained with obstacles prepared from a high-porosity cellular material (HPSM). This bulk material was obtained by replication, with powder metallurgy methods, of the highly porous structure of a mesh-cellular polymer, for instance, foamed polyurethane [9]. In the experiments, an HPSM obstacle prepared from nickel with relative diameter d/D=2.8 was used. The obstacle was installed on a ring pylon. Obstacles having the following porosities were examined: ϕ=10, 20, and 30 pores per inch (ppi). A self-oscillatory regime was obtained on an obstacle with ϕ=30 ppi installed at the relative distance from Mach 3.25 nozzle h/D=0.4. The relative amplitude and frequency of obtained self-oscillations were A/D=0.47 and F=1.3 kHz. At positions remote farther from the nozzle or at lower values of ϕ no self-oscillations were observed. A specific feature of the jet flows impinging onto HPSM obstacles was close position of normal shocks to the obstacle front face. The discharge gap geometry and power supply characteristics were as described above. On discharge initiation, suppression of the self-oscillatory process was achieved, with emergence of a steady flow pattern (see Fig. 4).

To summarize, in our experiments we proved it possible to suppress, using a peripheral electric discharge, intense self-oscillations of a supersonic jet impinging onto impermeable or HPSM obstacles.

References

1. A.G. Golubkov, B.K. Koz'menko, V.A. Ostapenko, and A.V. Solotchin, On the interaction of supersonic underexpanded jets with a flat finite obstacle // Izv. SO AN SSSR, ser. Tekhn. Nauki, No.13. Iss. 3, 1972, p. 52.
2. V.G. Dulov and G.A. Luk'yanov, Gas-Dynamics of Discharged Flows, Novosibirsk, Nauka, 1984, 230 p.
3. V.N. Glaznev, V.I. Zapryagaev, V.N. Uskov, et al., Jet and Unsteady Flows in Gas Dynamics, Novosibirsk, SB RAS, 2000, 200 p.
4. Y.G. Utkin, S. Keshav, J.-H. Kim, et al. Development and use of localized arc filament plasma actuators for high-speed flow control, J. Phys. D: Applied Phys., Vol. 40, No. 3, 2007, P. 685.
5. M. Kearney-Fischer, J.-H. Kim, and M. Samimy, Flow control of a high Reynolds number Mach 1.3 heated jet using plasma actuators, AIAA Paper 2010-4418.
6. V.M. Fomin, K.A. Lomanovich, and B.V. Postnikov. Discharge Plasma Effect on Shock Wave Pattern in a Pyrolytic Reactor, AIAA Paper 2010-4887.
7. V.M. Fomin, B.V. Postnikov, and K.A. Lomanovich, Effect of the Electric Discharge on Nonstationary Processes during Supersonic Air and Methane Jet Flow over a Flat Obstacle, High Temperature, No. 2, 2011.
8. V.M. Boiko, A.M. Orishich, A.A. Pavlov, and V.V. Pikalov, Optical Diagnostics in Aerophysical Experiment, Novosibirsk, 2009, 450 p.
9. V.N. Antsiferov, A.M. Makarov, and A.A. Ostroushko, Problems of current interest in powder materials science. Pt. VII. High-porous permeable cellular materials as promising catalyst carriers, Ekaterinburg, UD RAS, 2006, 227 p.

4.3. INFLUENCE OF DUST CONCENTRATION ON SHOCK WAVE SPLITTING IN DISCHARGE PLASMA IN DIFFERENT GASES

A.S.Baryshnikov, I.V.Basargin, M.V.Chistyakova
Ioffe Physico-Technical Institute of RAS,
26 Politechnicheskaya, S.Petersburg, 194021, E-mail: al.bar@mail.ioffe.ru

1. Installation.

1.1 Description of the installation.

Experiments were conducted on the electric discharge shock tube of Ioffe Institute. It consists of cylindrical camera (1) with an inside diameter of 300 mm and with a height of 400 mm, supplied with receiver (length of 1000 mm, the diameter of 200 mm) and with electromagnetic shock tube (EMST) (2). Installation was pumped out to P≈0,05 Tor by pump (12) through gate (11). Gas inlet was achieved through gate (13), and its pressure was controlled by manometers (14). The glow discharge in the camera was created between the conical copper electrodes water-cooled: by anode (5), with the diameter of 30 mm, and by cathode (b), with the diameter of 50 mm. The anode was introduced into the camera by means of the vacuum seal through the flange from organic glass. The distance between the electrodes was equally to 65 mm. The nourishment of camera was achieved from the powerful, adjustable, high-voltage source with the use of ballast resistance. The value of voltage could vary from 1 kV to 10 kV, current - from 0,25 to 2,5 A. The current strength was controlled on the ammeter.

The maximum speed of shock wave - to 1,6 km/s, pressure in the camera 4000 PA. In the experiments the time profiles of the signal from the end of piezoelectric pickup streamlined with the incident shock wave were obtained. They correspond to the distribution of pressure behind the wave.

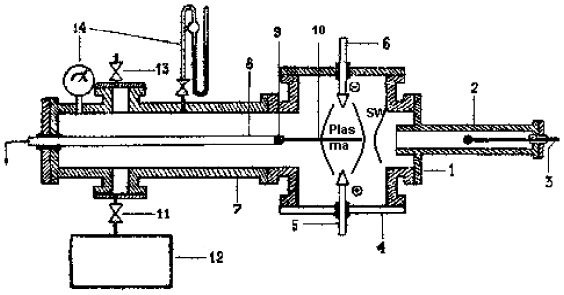

Fig.1. *Installation diagram. 1- camera; 2- electromagnetic shock tube, 3- central electrode (EMST); 4- flanges from organic glass, 5- the anode, 6- cathode; 7- receiver; 8 - rod; 9- piezoelectric pickup; 10- quartz rod; 11- gate of evacuation; 12- pump; 13- gate of gas inlet; 14- manometers.*

Experiments were conducted in the transonic regimes of shock wave propagation. Such regimes with difficulty yield to numerical simulation, those more in the plasma, and at the same time precisely these regimes are interesting for the practice. The experimental form of the distribution of pressure after shock wave in the plasma differs significantly from form in the gas without the plasma. “Two-wave” form in the plasma makes it possible to hope for reductions in the expenditures of energy of the motion of gas for an increase in the entropy in the shock wave, as this occurs in the case of the mechanical method of splitting wave, for example on the conical surfaces.

1.1. Modernization of installation.

It is necessary to note that before beginning studies for increasing the accuracy of measurement was accomplished the extensive work on the modernization of the system of the registration of signal in schlieren system. Usually the use of the Foucault’s knife and the photoelectric pickup has small signal-to-noise ratio with the presence of electrical interference. The application of prism instead of the Foucault’s knife and the operational amplifier significantly improved use of schlieren of system. Prism divides light ray into two rays. Light modulation with shock wave leads to an increase of the intensity of light in one ray and its decrease in other. Output electrical signals from two photoelectric receivers are united at the entrance of operational amplifier that gives the doubling of the value of useful signal and the considerable weakening of cophasal interferences to 80-100 decibel. The accomplished work considerably improved the accuracy of the measurement of the impact velocity wave.

In addition, a new, modern Board recording system, increasing the number of points of registration on the order. As a result of processing the results do not permit smoothing. This allowed to significantly greater attention averaging values in different experiments, each point of registration. Moreover, accomplished work made this averaging as rational processing because at smoothing there is no sense in averaging. Accomplished work significantly improved measurement accuracy. At present it is 1 to 2%.

2. Dustiness.

In the work the influence of dustiness only on the waveform in the positive column of discharge with different concentrations of dustiness was studied.

Carbonic dust was used as the dust. Dust possesses exceptional dryness and dispersiveness. As show photographs from the electron microscope, specks have sizes, compared with the sizes of nanos-particle. The diameter of specks is 150 nm.

2.1. Small dustiness.

The study of waveform from the piezoelectric pickup was conducted in accordance with the plan of studies in air and in nitrogen with concentration of dust, which varied in the environment of concentration of approximately 20 mg to the cubic meter. In this case the luminous flux of the laser, which controlled the dustiness of working volume, decreased in transit through working volume by 4%.

With the first shot of shock wave the dust rises into the atmosphere, and then, the concentration of dust in practice is supported by constant due to the intensive convective motions of gas, that one can see well on the motion of the separate large particles of the dust with the observation of the discharge through the window.

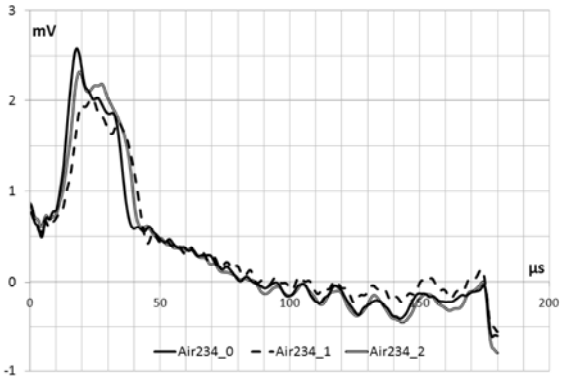

a)

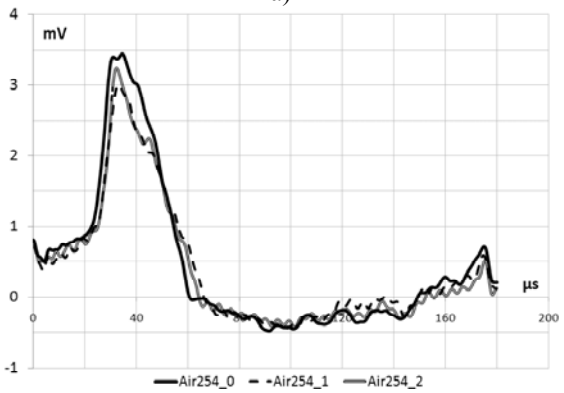

b)

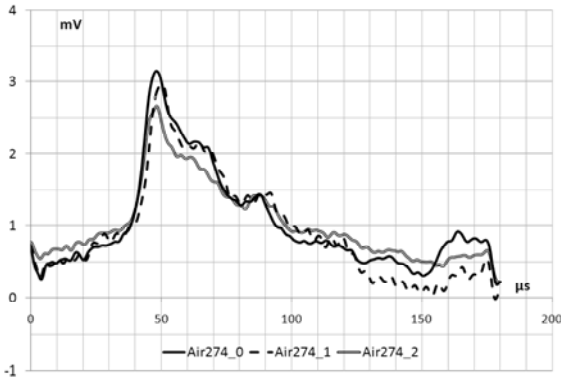

b)

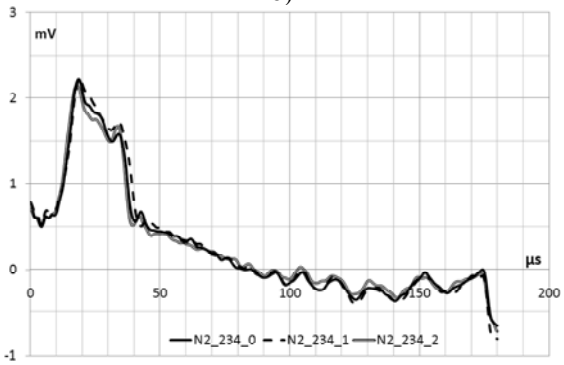

d)

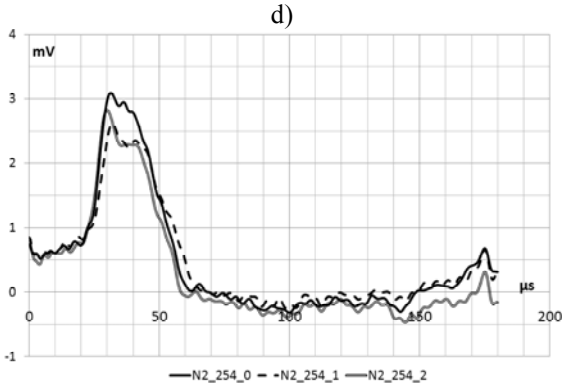

e)

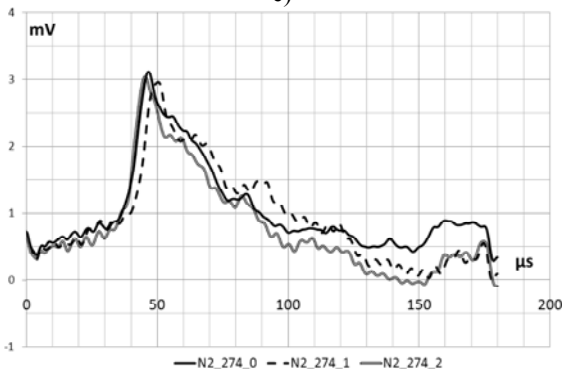

f)

Fig.2. *a) - f). Weak influence of dustiness on the form of the distribution of pressure behind the shock wave in the plasma of the glow discharge for the small concentration of dust (20mg in m^3) for air (Air) and nitrogen (N_2). 2- maximum dustiness (20mg in m^3), 1- dustiness is two times lower, 0 - without the dust. 234 - point 20 mm prior to center, 254 - center of discharge, 274 -20 mm after center. The initial velocity of shock wave at the output from the electric discharge shock tube of 1,6 km/s.*

Studies showed that for the presented concentrations the signals from piezoelectric pickup differed not more than to 3% from each other, which indicates the very small influence of dustiness in this range of concentrations on the distribution of pressure behind the shock wave in the plasma of air and nitrogen (Fig.2).

Bearing in mind the theoretical works [3,4], and also work [5], in which it was indicated the significant role of the dustiness of the atmosphere to the appearance of the studied effect, and in order to explain nature of the studied effect, besides the studies indicated investigation of influence of the dustiness in the considerably larger concentration (10 times) in the argon plasma were conducted also. Argon was selected in order to exclude chemical reactions with the dust in the plasma. First studies in the argon plasma for the small concentration of dust were carried out at the same concentration, as for air and nitrogen, and then - for the concentration 10 times of greater.

2.2. High dustiness - preliminary results.

The dustiness of the atmosphere was controlled by the absorption of laser beam in the positive column of discharge. In the experiments for the small concentration it was absorbed by 4% of emission of laser, and for the high concentration - 31%. Thus, in the last experiments the concentration of dust was increased almost 10 times in comparison with the concentration of dust in the first experiments. Measurements, as in the case air and nitrogen, were carried out at a distance by 20 mm after the center of discharge, 20 mm before the center and in the center of discharge.

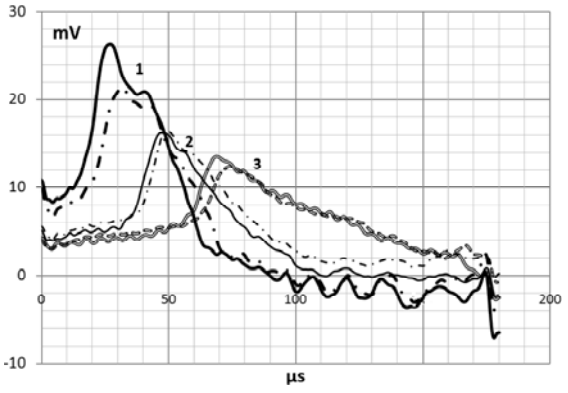

Fig.3. *The influence of dustiness on the form of the distribution of pressure behind the shock wave in argon with the concentration of dust 200 mg in m^3 - is ten times higher than in Fig.2. 1- point 20 mm prior to center (the maximum speed of shock wave), 2- the center of discharge, 3- of 20 mm after center. The initial velocity of shock wave at the output from the electric discharge shock tube as in Fig.2 - 1,6 km/s.*

The comparison of experimental results in the case "small" and "large" dustiness shows that, conditionally speaking "small" dustiness, which in reality composes 4% of absorption of the radiant flux of laser beam, practically does not influence waveform both in air and in nitrogen (Fig.2).

At the same time the dustiness, conditionally named "large" dustiness, and which composes only 31% of absorption of the radiant flux of laser beam, influences waveform from the piezoelectric pickup.

However, this influence strongly depends on the speed at the point, at which were conducted the tests. At a distance 20 mm of the center of the discharge, when the speed of the motion of shock wave in the discharge is maximum, influence, both in the amplitude of second wave and on the distance from the forerunner to the second wave, exceeds the frame of 10%. Thus, this influence can be considered significant. It is here necessary to note that with "small" dustiness of 20 mg/m^3 its influence on the waveform in argon is considerably below at all three points exactly as for air and for nitrogen (see Fig.2).

In the Center and at a distance of 20 mm behind the center impact of dust at large concentrations
(200 mg/m^3) in the form of signal is much smaller and is approximately 3%. Due to the symmetry of the discharge, the dustiness is also symmetrical and cause of separating, apparently, is the speed of shock wave. As experiments show, shock wave speed when passing discharge is reduced. At 20 mm from the Centre of speed is approximately 1.5 km/s, in the Center-1.3 km/s, and at a distance of 20 mm for Centre-1.1 km/s. Thus, when the speed is reduced of 30% dustiness influence decreases in 3 times (in the center of the discharge the dustiness can be significantly reduced). There is a strong dependence of dustiness effect on shock wave speed.

2.3. High dustiness - refined results

The next step consisted in conducting experiments in the upgraded installation with increased measurement precision by increasing the registration point to order, and at the expense of averaging at each point registration number experiments. In this study there was an averaging of 10 experiments. The measurement results are presented in Fig. 4-6. Experiments carried out under the same conditions. Dustiness was high (200 mg/m3), because at such mass concentration of dust effect of dust was observed in the pressure distribution behind shock wave in preliminary experiments.

Experiments were also conducted in the upgraded installation and in dusty air, nitrogen and argon without the ignition of glow discharge. Influence of made virtually no. For example, distribution of pressure in the air in the middle of discharge is presented (Fig. 4).

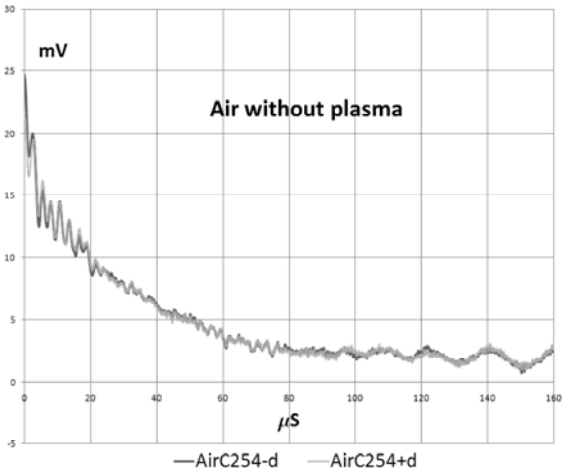

Fig.4 *The effect of dustiness of the atmosphere without discharge on the pressure distribution behind shock wave in the air at the point where the discharge center should be (-d-without the dust, + d- with dust 200 mg/m^3)*

Initial shock wave speed on the output from electromagnetic shock tube was 1.6 km/s. The fine carbon dust which was used for dusty plasma has low energy electron affinity with electron. Perhaps this is the reason why there was no electrization of dust. There is a uniform distribution of dust for space in free convection flows.

Main results in plasma in glow discharge are two facts unexplained now. The first fact; the impact of dust on the pressure distribution behind shock wave in the air is minimal (Fig. 5) and is limited to only a small effect on the pressure distribution only at high speeds shock wave. Amplitude secondary wave in the air a bit increases (Fig. 5). The upper part of the secondary waves in air also changes its form (Fig. 5).

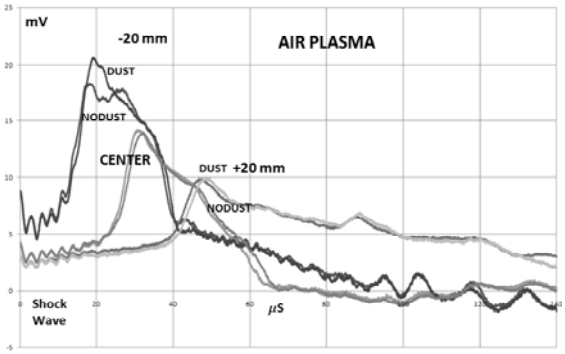

Fig. 5. *The impact of dust on secondary wave in air plasma.*

The second fact: under the same initial conditions in argon plasma influence is pronounced. Dustiness of argon plasma leads, unlike air plasma, to significantly increase of amplitudes of secondary wave (Fig. 6).

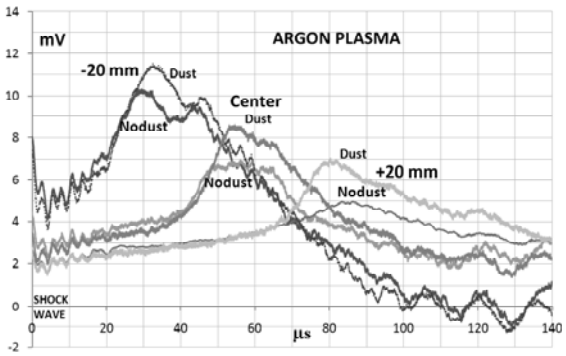

Fig. 6. *The impact of dust on secondary wave in argon plasma.*

In addition, primary wave also varies. In contrast to secondary wave primary wave becomes smaller than wave dust-free under the same conditions (Fig. 7). This behavior of primary wave is usual for shock waves in dusty gas. Apparently, the second wave has a different nature than the primary.

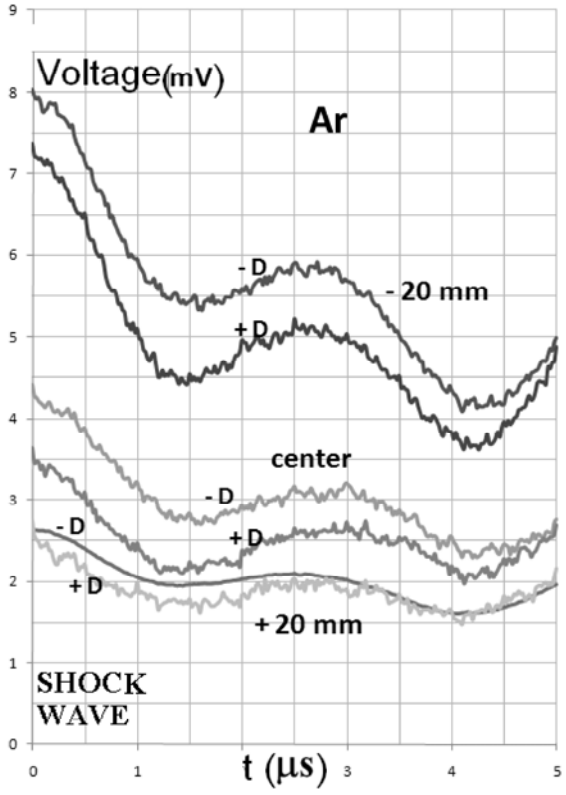

Puc. 7. *The impact of dust on first wave in argon plasma. +D – dust, -D – no dust.*

Calming primary wave in dusty gas [8] take the place for dusty gas, for which there is a dispersion of shock wave in dusty environments. Dispersion increases with increasing Mach. The same is true for argon, because the speed of the shock wave is the same as for air and nitrogen, but

the speed of sound is less due to high molecular weight of argon.

2. Conclusion.

The influence of carbon dust on the pressure distribution behind shock wave in atmosphere of air and argon in plasma of glow discharge and without plasma is investigated. Increasing the natural dustiness in 10 times, as in the air and argon, influence of dustiness on pressure distribution behind shock wave in the atmosphere without plasma practically is not observed. Influence of dustiness evident in argon plasma of glow discharge (in the case of increasing of natural level of dust in 10 times).

The influence of dustiness in plasma of glow discharge in air is not essential. The same behavior is observed in nitrogen. In argon plasma dustiness leads to a substantial increase of amplitude of secondary wave. Preliminary experiments have shown that the impact of dustiness strongly depends on the speed of shock wave. For stronger shocks influence of dustiness is greater. More precise studies have shown that such behavior is more common for plasma air than for argon plasma.

The difference in influence of dust in argon in the air can be attributed to the fact that molecular gas in plasma is greater than the speed of sound in argon plasma, due to the high molecular weight of argon. Thus, shockwave Mach number is increasing, but for high Mach numbers effect dispersion of Shockwave in the dusty atmosphere is well known, at which the intensity of the shock wave compression reduces and the amplitude of the shock wave increases [8].

Referances

1. Klimov A.I., Bityurin V., Kharitonov A., at.el., Shock Wave Propagation through Non-Equilibrium Cluster Plasma, AIAA Paper 2002-7978, 40th AIAA Aerospace Science Meeting & Exhibit, Reno NV, P.8 Anatoly Klimov.
2. Akishev YU.S., Deryugin A.A., Karalnik V.B., Kochetov I.V., Napartovich A.P., Trushkin N.I. Experimental study and the numerical simulation of the glow discharge of the direct current of atmospheric pressure. Physics of plasma. 1994. V.20. №6. P.571-584. [in Russian]
3. Velikodnyy V.YU., Bityurin V.A. Propagation and the structure of shock wave front in the ion plasma with the presence of the negatively charged nanos-particle (clusters, specks). Applied physics, 2002, №5, P.90-98. [in Russian]
4. Popel S.I., Golub A.P., Loseva T.V., Binkhem R., Benkadda S. Formation of shock-wave structures in the dust plasma. Physics of plasma. 2001. V.27. №.6. P.483-490. [in Russian]
5. Zobnin A.V., Usachev A.D., Petrov O. F, Fortov V.E. Dust-acoustic instability in the plasma of induction gas discharge. Journal of Experimental and Theoretical Phisics, 2002, V. 122, N. 3 (9), P. 500-512. [in Russian]
6. Baryshnikov A.S., Basargin I.V., Chistyakova M.V. Influence of moistening the atmosphere and its dustiness on the effect of the destruction of shock wave in the plasma of the glow discharge. Letters into the Journal of Technical Physics, 2008, V.33, N.10, P.54-57. [in Russian]
7. Baryshnikov A.S., Basargin I.V., Chistyakova M.V. Experimental and theoretical study of splitting effect of shock wave in glow discharge in dry, dusted and humid air and nitrogen. The 7th Workshop on Magneto-Plasma-Aerodynamics in Aerospace Applications, Moscow, 17-19 April, 2007, IVTAN, P. 174-178
8. Van Donger M. Shock Wave Science and Technology Reference Library. Multiphase Flows I. Springer, Berlin Heidelberg, New York. 2007. V. 1. Part II. P. 135-186.

4.4. THE BUFFET CONTROL BY LOCAL ENERGY AND MOMENTUM RELEASE IN THE VICINITY OF λ SHOCK.

M.A. Starodubtsev
Central Aerohydrodynamic Institute, Zhukovsky

In transonic airflow strong boundary layer – breakdown shock wave can lead to periodic shock motion along wing surface. This phenomenon is known as transonic buffet and can be observed in a set of aerodynamic branches. At the same time with investigation of airflow self-oscillations properties active and passive buffet control methods develop. One of the possible methods of active transonic flow control is the electric discharge on a wing surface acting simultaneously as thermal energy source and/or momentum source.

In the present investigation 2-dimensional transonic unsteady transonic flow with heat release and momentum input is under of consideration. The numerical solution of URANS equations have been carried out using 2D solver based upon finite volume method with 2nd order time and space integration scheme and global time step strategy. SST turbulence model taking into account additional turbulence production near reattachment zone was used in consideration. Set of source positions and forms were modeled in simulations to find optimal way of buffet control.

4.5. ION – ACOUSTIC SHOCK WAVE IN PLASMA (ABNORMAL STREAMING, DETONATION OF EXPLOSIVES)

Yu.L. Serov
Ioffe Institute RAS, 26 Polytechnicheskaya,
194021 St.-Petersburg, Russia,
E-mail: yuserov@mail.ioffe.ru

Introduction

In some conditions at high-speed movement the streaming of a body by plasma isn't described by the equations of dynamics of neutral gases. Our experiments spent since 1980 on ballistic installation of PTI of the Russian Academy of Sciences at speeds of a throwing of 700 - 2500 m/s and pressure $10^0 \div 10^2$ Torr have shown it. Authors had been registered for the first time not thermal plasma effects at a streamlining of a high-speed supersonic body by gas-discharge plasma [1-3]. In plasma the considerable off-design increase of standoff distance of a bow shock wave from a body and its easing was in certain cases revealed. There is also a decrease in thermal streams on a body surface in plasma. It is shown experimentally and theoretically in ref. [3,4] that observable anomalies are connected with nonlinear properties of plasma and formation of ion-acoustic soliton bunch in dense collisional plasma in the field of a shock wave. This bunch interacting with medium in the running flow, exists in a range of ionic Mach-numbers of $1 < M_i \leq 1{,}63$. Such soliton bunch is found out for the first time in ballistic experiments [5]. In fig. 1 examples of oscillograms of radiation from a supersonic body in plasma of glow discharge are shown. Soliton bunch is observed on oscillograms on forward front of a head shock wave. Model position was defined on a signal from interception of a laser beam (the bottom oscillogram in fig. 1a). The ion-acoustic shock wave is formed as a result of interaction of charged and neutral component of plasma in the field of ion-acoustic soliton bunch. It changes character of propagation of a shock wave in plasma. The ion-acoustic shock wave determines characteristic features of the various effects connected with propagation of shock waves in plasma.

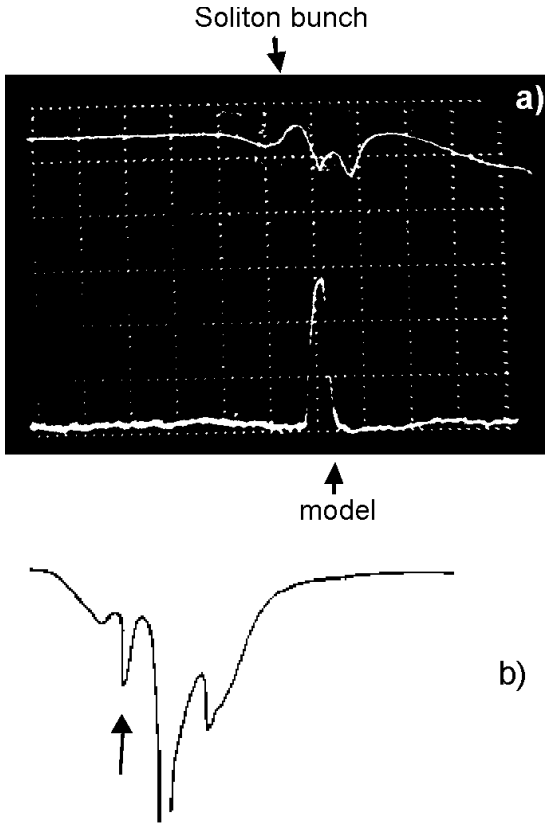

Fig.1. *Ballistic apparatus; signal of radiation from multiplier, sphere.*
The soliton package on a front of the bow shock: a) helium, glow discharge plasma, P = 40 Torr, V = 2160 m/s; b) xenon, P = 40 Torr, V = 2260 m/s, M_i= 1,3.

Theoretical model. The physical model of observable anomalies in dense collisional plasma is considered in ref. [6-8]. The solution of the dynamic equations of three-component plasma accounted for nonlinearity and dispersion has shown that, indeed, the soliton bunch is formed in the field of plasma shock wave and the "Houston's horse" effect is realized. This model is in a good agreement with the results of high-speed ballistic experiments and other experiments on instability of shock waves in plasma [1-6]. According to our model, the equations of a shock wave in dense three-component plasma can be reduced to the nonlinear equation for potential. In the extreme case, if we neglect collisions between ions and neutral particles and utilize the nonlinearity of the equation for the electric field, it leads to the well-known Sagdeev equation:

$$2D\psi'' = -\frac{d\phi(\psi)}{d\psi} \qquad (1)$$

$$\phi(\psi) \equiv 1 - \exp\psi + M_i^2[1-(1-2M_i^{-2}\psi)^{1/2}]$$

,

$$\psi \le \psi_*; \qquad \psi_* \equiv 0{,}5M_i^2,$$

Where D is the Debye radius, M_i is the ionic Mach-number. The Debye radius characterizes dispersive properties of plasma. This equation has the soliton solution in the field of ionic Mach-numbers $1 < M_i \le 1{,}6$, ($M_i = V/V_{is}$, where V is speed of a shock wave, $V_{is} = \sqrt{T_e/m_i}$ is speed of an ionic sound). Equation, which serves as a better approximation and includes an elastic ion-neutral collisions, electronic heat conductivity, ionic viscosity, nonlinearity and dispersion is derived and analyzed in [6]:

$$-V''' 2D^2 V_{is}^2 (1-Vc^{-1})^2 + V''\eta c\rho\omega^{-1} (1-Vc^{-1})^2 + V'[(c-V)^2 - V^2_{is}] - V\omega V(c-V)(V-V_n) \approx 0$$

$$V\omega \equiv V_{in}[1 - V_n(\xi) V^{-1}] + \varkappa^{-1} V_{is}^2 \kappa n\omega \quad (2)$$

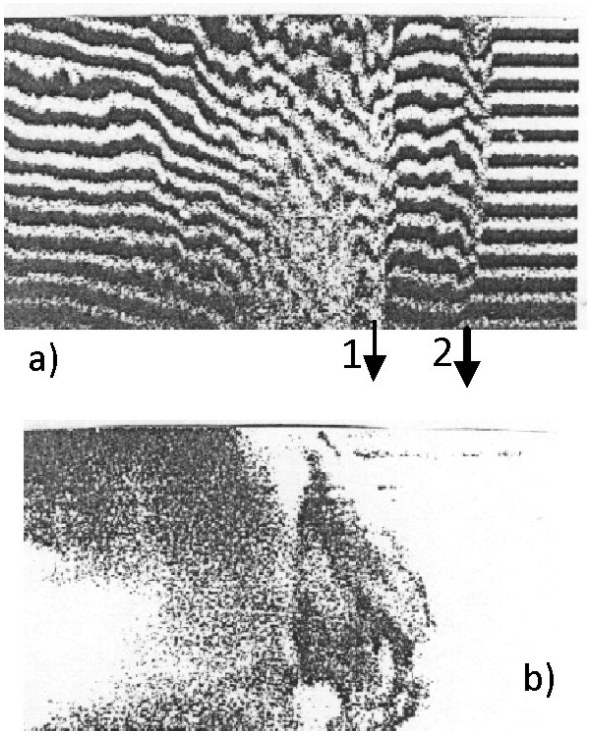

Fig. 2. *Interferograms of a shock wave in xenon [13]; a) M = 25, Mi ≈1,5; 1 - front of a gas-dynamic shock wave, 2 - front of an ion-acoustic shock wave in precursor; b) destruction of the wave front and transition to multyflow movement at M_i≈ 1,6; M=27,1.*

In the given problem stationary perturbation in weakly ionized not isothermal plasma was investigated. The fields depend on ζ= x – ct, where x, t , coordinates and time, c is speed of moving of a shock wave, n is concentration, indexes i, e, n correspond to ions, electrons and to neutral particles, æ is a factor of electronic heat conductivity, η is factor of dynamic viscosity. In the equation (2) members nonlinear on Vc^{-1}, an elastic ion-neutral impacts, electronic heat conductivity, ionic viscosity and a dispersion are considered. If we take into account the collisions, the equation has a solution similar to those of Sagdeev equation. In fact, even strong dissipation does not destroy sharp resonant effect. Analytical estimations and numerical analysis [7] have shown that specific ion-acoustic shock wave is formed in a shock wave precursor. The analysis of the equation (2) has confirmed the existence of soliton bunch in dense collisional plasma in the field of a shock wave when shock wave speed is in resonant range $1 < M_i \le \sqrt{3}$, which is similar to data of ballistic experiments. Ion- acoustic soliton bunch, arising at $M_i > 1$, leads to development of instability of a shock wave. With increase of ionic Mach number both the amplitude of a bunch grows and the factor of ionization in bunch increases. The analysis [7] has shown, that at critical value of ionic Mach-number $M_i \approx \sqrt{3}$ there is an explosive instability. The finite increment in speed of neutral component shock wave leads to infinite increase of soliton bunch amplitude of ionic component. When ionic Mach-number approaches its critical value, the ionization factor comes to $\alpha \approx 1$. The strongest interaction between charged and neutral components takes place in this area of highly-ionized bunch. It is the moment of the greatest instability, which is followed by the collapse of the soliton bunch and destruction of the shock wave (see fig. 2).

Ballistic experiment

Abnormal (resonant) streamlining of sphere in plasma. Experiments in a ballistic apparatus have shown that in a range of 700 ÷1200 m/s the streaming of sphere without the shock wave is observed. The maximum speed of a sound in the field of glow discharge is $V_s \approx 680$ m/s. In fig. 3 the shadow photo of a streamlining of sphere by plasma at speed of V = 850 m/s is shown. The shock wave is observed only in area out of the discharge. In the field of the discharge full dissipation of a bow shock wave has occurred, and it isn't visualized even on plasma border in the discharge. Bow shock wave starts to appear before a body only at speed of 1150 m/s. The abnormal streamlining with the increased standoff distance of a bow shock wave in air plasma ($T_e \approx 1 \div 1{,}3$eV) is realized in a range of speeds from V = 1200 m/s to V = 2800÷3400 m/s [1-4]. The top border for an abnormal streamlining at $T_e \approx 1 \div 1{,}3$ eV is speed V =3100 ÷3400 m/s (M = 9÷10). Relative change of a standoff distance in air plasma is shown in fig.4. If to extrapolate this dependence on area of the high speeds within an error limit the abnormal streamlining disappears at

speeds of 3100÷3400 m/s. Speed of V = 3000÷3200 m/s corresponds to border of ranges V =1,63Vis at T_e ≈1eV for ions N_2^+, C_2^+, CO^+, NO^+. These ions can exist in plasma of air and determine the most high-speed resonant ranges. At this speed corresponding to a collapse of ion-acoustic soliton bunch, the abnormal streamlining disappears. The shadow photo of streamlining of sphere by xenon plasma (T_e=2,2 ± 0,3 eV), and also the schedule of change of a relative standoff distance in xenon plasma is shown in fig.5. Figures near to experimental points indicate the shot number. The schedule generalizes experimental results in various series of experiments. The border of an abnormal streamlining in xenon plasma also corresponds to value of M_i ≈ 1,6 (V = 2100÷ 2150 m/s).

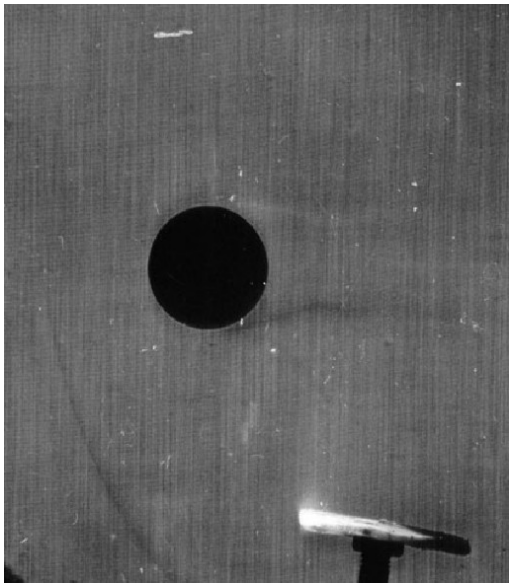

Fig.3. *Supersonic streamlining of a spherical body without a shock wave in the field of plasma (top part of a shadow photo); air, glow discharge, V=850 m/s, M > 1,25.*

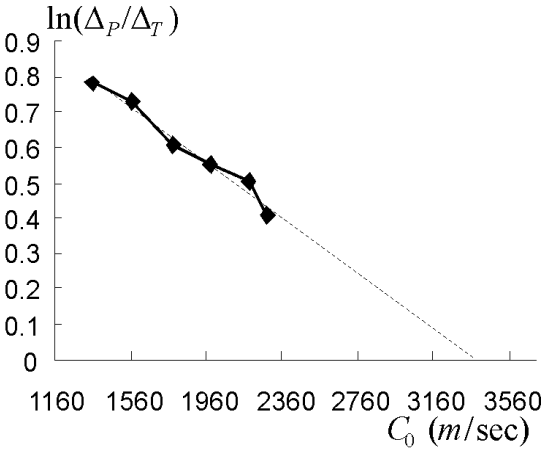

Fig.4. *Change of a relative standoff distance of a bow shock wave in air plasma depending on speed of spherical model; Δ_p is a standoff distance in plasma, Δ_T is a standoff distance in heat air.*

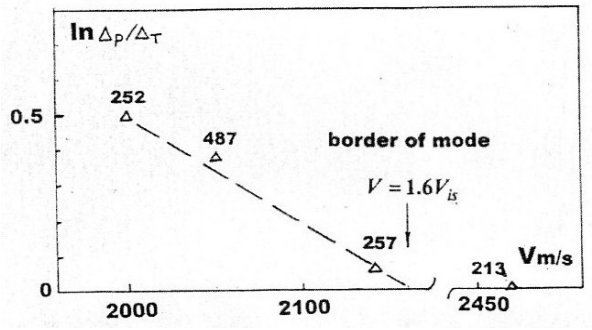

Fig. 5. *Change of a relative standoff distance of a bow shock wave in the xenon plasma depending on speed of spherical model; Δ_p is a standoff distance in plasma, Δ_T is a standoff distance in heat gas.*

Not resonant (conventional) streamlining of sphere at high-speed movement in nitrogen plasma. It has been above noticed that the abnormal streamlining is observed only in resonant ranges of speeds where an ion-acoustic soliton bunch exists. Low-speed resonant ranges of speeds are realized at movement in air plasma and the abnormal streamlining in all investigated range of speeds 700-2400 m/s is observed. Speed ranges of an abnormal streamlining are connected with atomic and molecular structure of medium in a running flow. In plasma there are various ions and electron groups, formed at collisions of the second kind**.** Therefore the set of speeds of an ionic sound exists in plasma. Low-speed resonant ranges in air plasma are determined by small speeds of an ionic sound. These ranges are connected with a low metastable term of a molecule of oxygen O* (0,98 eV) and heavy ions of oxides of nitrogen. However, in other gases resonant ranges and an abnormal streamlining can be realized only at much higher speeds. These speeds are determined by more high energy of metastable terms of ionized gas. In fig.7 the streamlining example in the experiments executed on a ballistic apparatus at high speed of movement (V = 2km/s) in decaying plasma of the impulse discharge in nitrogen is resulted. There are no low metastable terms in nitrogen. Therefore the abnormal streamlining in nitrogen can be observed only at higher speeds, than in air plasma. Experiments were spent on ballistic apparatus of PTI together with employees of I.A. Kossyi (IGPRAS), developed the impulse discharge device. The usual streamlining of sphere by nitrogen plasma is observed in the shadow photos (fig.6) received through 10^2 ÷ 10^3 μs after an impulse of a current. The streamlining of sphere in nitric plasma (b) doesn't differ from a streamlining in nitrogen (a). Most low-speed resonant ranges which can be realized in decaying plasma of nitrogen are resulted in table 1. These ranges are

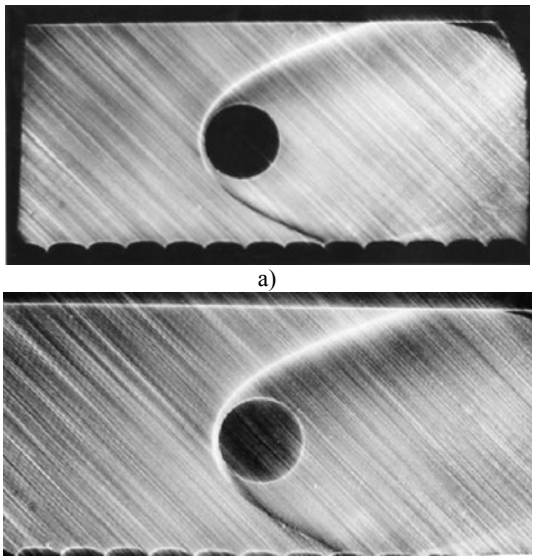

a)

b)

Fig. 6. *A conventional streamlining in nitrogen (a) and nitric plasma (b); the pulse discharge, afterglow, V = 2km/s.*

connected with ions of nitrogen and electrons, formed at collisions of the second kind with atoms of nitrogen in the lowest metastable state N* (2,38eV).

$$N^* (2{,}38eV) + e = N + e (2{,}38eV)$$

Thus low-speed resonant ranges in nitric plasma (Table 1) are connected with electron group e (2,38eV) and ions N^+, N_2^+, N_3^+, N_4^+. Most low-speed resonant range of an abnormal streamlining is caused by ions N_4^+ and begins at speed of a shock wave of V ≈ 2 km/s.

Table 1

ion	Soliton bunch	Resonance range $\Delta C = V_{is} \div 1{,}63V_{is}$ km/s
N^+	N^* (2,38eV), N^+	4 ÷ 6,5
N_2^+	N^* (2,38eV), N_2^+	2,84 ÷ 4,6
N_3^+	N^* (2,38eV), N_3^+	2,32 ÷ 3,3
N_4^+	N^* (2,38eV), N_4^+	2,02 ÷ 3,3

Shadow pictures of streamlining by the nitric plasma, resulted in fig. 6, are received at speed of V = 2 km/s on border out of limits of resonant ranges and consequently correspond to a conventional streamlining of a body by usual gas. But in air plasma at the same speed V = 2 km/s the abnormal streamlining is observed. The executed experiments have demonstrated that it shouldn't search the anomaly in a streamlining by plasma at any, even the high speeds which experimental installation allows to reproduce. Especially it concerns to low-speed modeling by means of a nozzle. In such experiments the usual streamlining similar to a streamlining by the gas medium is realized only.

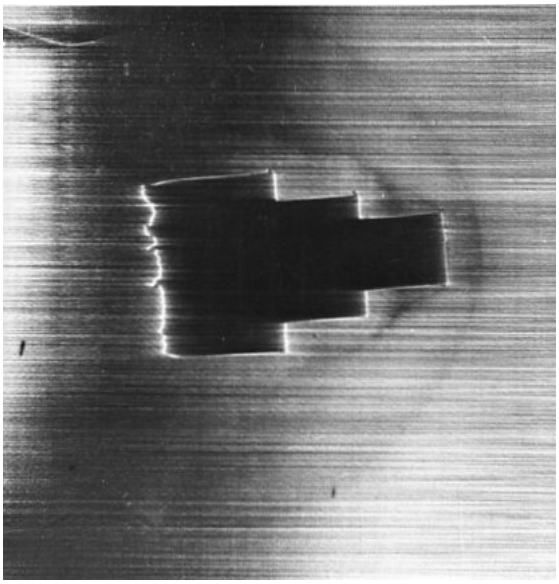

Fig. 7. *A conventional streamlining in air (a) and ion-acoustic bow shock wave in air plasma (b); glow discharge, V = 2 km/s.*

Resonant streamlining of a step body at high-speed movement in air plasma.

Interaction of charged and neutral plasma component in area of soliton bunch leads to occurrence of specific “an ion-acoustic shock wave of a neutral component“. As a result of ion-acoustic interaction at movement in plasma there is ion-acoustic "Houston's horse" effect [7]. The effect of occurrence of an ion-acoustic shock wave of a neutral component is well observed at ionizational instability of shock waves [6] (fig.2). The ionic-sound shock wave arises also in ballistic experiment.

Shadow photos of a streamlining of a step body with ledges by air (a) and plasma of the glow discharge (b) are shown in fig.7. Experiments show basic difference in a streamlining of a body by air and plasma. It concerns a corner of a spread of a shock wave from body ledges. In the first case the divergence corner increases and a convergence of shock waves from various ledges are observed behind a body. It is connected with that circumstance that behind the each shock wave the temperature of a neutral components increases. Speed of a sound thus increases and the Mach-number decreases. It also leads to increase of a divergence corner of a shock wave. The ion-acoustic shock wave which speed is determined by electronic temperature otherwise behaves. The electronic temperature behind a shock wave decreases. It leads to reduction of speed of an ionic sound. The ionic Mach-number which determines a

streamlining in resonant ranges of speeds thus increases. The divergence corner of a shock wave as a result decreases. Thus, behind a shock wave the Mach- number M decreases, and the ionic Mach-numbe Mi increases. It leads to differences of streamlining in gas and plasma. Thus, it appears that the body streamlining in a resonant range in plasma is caused by occurrence of special jump of density in a neutral component. This jump has arisen owing to formation of ion-acoustic soliton bunch in which there is a strong interaction of charged and neutral components. This jump of density is a component of an ion-acoustic shock wave. It it is conditionally possible to name "an ionic-sound shock wave of a neutral component". In this case the spatial scale is centimeters. Really it is certainly not the shock wave, which has width of front of some lengths free path.

Ion-acoustic resonances at explosive decomposition of powerful and initiating explosives on the basis of nitro - compaunds

Speeds and limits of propagation of detonation waves were measured in various gas mixtures by many researchers. From the point of view of nonlinear resonant plasma dynamics speed limit of a detonation is the maximum phase speed of ion-acoustic soliton bunch arising in plasma of decomposition products of explosive. This speed determines speed limit of propagation of a shock wave in dispersive medium. On reaching of this speed the soliton bunch and the generated ion-acoustic shock wave overturn. We will compare the speeds of a detonation with the speeds of soliton bunches which can be formed in products of reaction of decomposition of the most powerful known explosives. We will consider also some special features of formation of soliton bunches at detonation of azides which are the initiating explosives. Such consideration allows to understand the detailed physical mechanisms determining the nature and high-speed borders of a detonation of various explosives, and also propagation of shock waves in complex reacting gas- plasma mixtures. In ref. [14] some well-known explosives on the basis of nitro – compounds including trotyl, nitroglycerine, nitromethane, nitroglycol have been investigated. It has been shown that heat of explosion determines the population of power terms of atoms and the molecules formed in products of decomposition of explosives. At increase in heat of explosion the higher power terms of atoms and molecules are populated . Energy of electrons and phase speed ion-acoustic soliton bunch as a result grows. Is of interest to find the metastable terms which determin the maximum known speeds of a detonation of existing powerful explosives. In table 1 results of comparison of speeds of a detonation of some especially powerful explosives on the basis of nitro-compounds with phase speeds of soliton bunches arising in the field of front of a wave are presented. In the table similar results of comparison of speeds of a detonation with phase speeds of soliton bunches for silver azide and cadmium azide also are resulted.

Oktogen $(CH_2)_4N_4(NO_2)_4$. Heat-resistant brisant explosive [14-16]. Colourless crystal substance. It possesses high sensitivity to blow. Heat of explosion is 5,7 MJ /kg. Speed of detonation is D = 9100 m/s at density of 1,84 g/cm³. This speed corresponds to the top border of a range of existence of soliton bunch which has arisen in a range of speeds of $\Delta C = V_{is} \div 1{,}63\ V_{is}$ for the account of ions of atomic nitrogen and electrons, connected with population of metastable term NO $\Rightarrow$ (4,7eV). These electrons, participating in formation of soliton bunches, are formed at collisions of the second kind in reactions

$$NO \Rightarrow (4{,}7eV) + e \rightarrow NO + e\ (4{,}7eV).$$

Arising soliton bunch we will designate as follows:

$[NO \Rightarrow (4{,}7eV), N^+]$. Speed of this bunch lies in a range of $\Delta C = 4600 \div 9150$ m/s. The top border of a range determines the speed of detonation (Table 1).

Benzothreefuroxane. $C_6N_6O_6$. Heat of explosion is 5.86 MJ /kg. Density is 1.901 g/cm^3. It has a very high temperature at the detonation: nearby 4700 K. In the products of detonation of explosives C-N-O, not containing hydrogen the presence of NO and O_2 is typically. The composition of explosion products of 1 mole: 2.93 mole of N_2, 1.56 mole of CO_2, 2.87 mole of CO and 1.57 mole of soot. Speed of detonation is D = 7500 m/s at density of 1.54 g/cm^3, D = 8620 m/s at density of 1,9 g/cm^3. Its use in detonators, solid fuels, explosive mixtures is supposed. The registered speeds of a detonation of benzothreefuroxane can be associated with soliton bunches which have formed due to different near metastable terms and ions C^+ , O^+ (Table 1).

Hexanitrobenzene $C_6(NO_2)_6$. Heat of explosion is 6,99 MJ /kg. Speed of detonation is D =9450 m/s at density of 1,9 g/cm^3. The zero oxygen balance. Very high heat of decomposition. High fugacity makes hexanitrobenzene promising component of rocket fuels. Detonation velocity D = 9450 m/s coincides with the maximum phase velocity of the bunch associated with metastable terms of oxygen (Table 1).

Dinitrodiazenofuroksan $C_4N_8O_8$. 4,4'-Dinitro-3-3'-diazenofuroksan (1). This is a new powerful

explosive. At density of a monocrystal is 2.002 g/cm^3 diazenofuroksan has a detonation velocity D = 10000 m/s, which is a record now. The speed of detonation diazenofuroksan exceeds the speed of detonation hexanitrobenzene at the same density of more than 500 m/s. Speed of detonation D=10000 m/s coincides with the maximum phase speed of the only bunch associated with term [NO □ (4,7eV) (Table 1). Thus it appears that the detonation of various explosives, including oktogen [NO ⇒ (4,7eV), N^+], benzotrifuroksan [NO ⇒ (4,7eV)), O^+], dinitrodiazenofuroksan [NO ⇒ (4,7eV), C^+], may be associated to population of the same metastable term of NO ⇒ (4,7eV).

Silver azide . For crystals of silver azide speed of a detonation is D= 4400 m/s [18]. This speed coincides with the maximal phase speed of a soliton bunch ΔC = 2700 ÷ 4400 m/s formed for the account of high populated resonant term of atom of silver Ag_{res} ⇒ (3,67 eV) and heavy ions of nitrogen N_4^+. Electrons, participating in formation of a soliton bunch, are formed at collisions of the second kind in reaction

Ag_{res} ⇒ (3,67 eV) + e → Ag + e (3,67eV).

In plasma the heavy ions of nitrogen are formed as a result of reaction $N_2^+ + N_2 \rightarrow N_4^+$. It is known also that in afterglow of nitric plasma the charged heavy particles are formed as a result of reaction of associative ionization

$N_2^* + N_2^* \rightarrow N_4^+ + e$.

In the field of front of a strong shock wave the heavy ions are formed in a precursor due to absorption of advanced radiation and the subsequent collisions.

Cadmium azide $Cd(N_3)_2$. Heat of explosion is 2,3-2,6 MJ/kg, speed of a detonation is 4200 m/s at density of 3,2 g/cm^3 [18]. It is sensitive to blow and a friction. The soliton bunch in a range of ΔC =2600 ÷ 4220 m/s in this case is generated in the same way, as at explosive decomposition of silver azide. The soliton bunch is formed due to resonant term of cadmium atom and heavy ions o f nitrogen (Table 1).

Lead azide $Pb(N_3)_2$ It is the crystal substance, which has two basic crystal forms with various density. It is applied as initiating explosive, has high sensitivity and very small critical diameter. It is most often applied in caps-detonators. Heat of explosion of lead azide is about 1,536 MJ/kg, speed of a detonation is about 4800m/s. Speed of a detonation is D = 4630 m/s at 3.0 g/sm³, D=5300 m/s at 4.1 g/sm ³.

Copper azide $Cu(N_3)_2$, solid explosive substance. Copper azide is extremely explosive, has no practical application because of high sensitivity to

Table 2.

Compound	Heat of explosion (MJ/kg)	Speed of detonation m/s	Soliton bunch	Phase speed of a soliton bunch m/s
Oktogen $(CH_2)_4N_4(NO_2)_4$,	5,526	9150	NO □ (4,7eV), N^+	4600 ÷ 9150
Benzothree-furoxan $C_6N_6O_6$	5,86	8620 7500	N □ (3,58 eV), C^+ NO □ (4,7eV), O^+ N □ (3,58 eV), O^+	5300 ÷ 8600 5300 ÷ 8600 4550 ÷ 7500
Hexanitrobenzene $C_6(NO_2)_6$	6,99	9450	O □ (4,19 eV), C^+	5750 ÷ 9400
Dinitrodiazeno-furoxan $C_4N_8O_8$	-	10000	NO □ (4,7eV), C^+	6100 ÷ 10000
Silver azide AgN_3	-	4400	Ag_{res} □ (3,67 eV), N_4^+	2700 ÷ 4400
Cadmium azide $Cd(N_3)_2$	2,33-2,61	4200	Cd_{res} □ (3,96 eV), N_4^+	2600 ÷ 4220
Lead azide $Pb(N_3)_2$		4800 4630 5300	Pb^*_{res} (1,31eV), N^+ N^* (2,38 eV), N_2^+ N^* (3,58 eV), N_2^+ N_2 (6,17), N_4^+	3000 ÷ 4850 2840 ÷ 4650 2840 ÷ 4650 3250 ÷ 5300
Copper azide $Cu(N_3)_2$		5000	Cu^*_{res} (1,39eV), N^+	3070 ÷ 5000

any initial impulse and possibility of spontaneous explosion.

It can detonate spontaneously in dry conditions, without the visible reasons. Speed of a detonation is D = 5000 m/s. The soliton bunch formed during detonation due to the resonant term of copper Cu^{*}_{res} (1,39eV) and ions of atomic nitrogen [Table 2].

Conclusion

The conducted ballistic research has shown that:

- an abnormal streamlining of high-speed bodies has resonant character;
- an abnormal streamlining is determined by atomic - molecular structure of medium and is due to the formation of ion-acoustic shock wave;
- density discontinuity in a bow shock wave is a component of an ion-acoustic shock wave at abnormal streamlining.

Analysis of experimental data on detonation showed that:

- the abnormal streamlining and a detonation of explosives have the general nature;
- - the detonation of explosives is a special case of propagation of a shock wave in plasma;
- detonation is the result of the formation of ion-acoustic shock waves in a plasma formed in the decomposition products of explosives;
- speed limits of detonation of explosives associated with the emergence of nonlinear dynamic plasma resonances in gaseous decomposition products;
- forward front of a detonation of the condensed explosives is an ion-acoustic soliton bunch;
- speed of a detonation coincides with the maximum phase speed of ion-acoustic soliton bunch in dispersive gas-plasma medium formed in products of explosive decomposition;
- the detonation of the most powerful known explosives is connected with population of a metastable power term of molecule NO $\Rightarrow$ (4,7eV);
- speed of a detonation of metal azides is caused mainly by population of the bottom resonant terms of metal atoms and formation of ions of nitrogen.

References

1. Р.Ф. Авраменко, А.И. Климов, Ю.Л. Серов и др.” Эффект аномального обтекания тел плазмой “ // Открытие № 007. Приоритет 17.09.80. Зарегистрировано 25.12.86 в Гос.реестре открытий СССР.
2. Г.И.Мишин, Ю.Л.Серов, И.П.Явор. Обтекание сферы при сверхзвуковом движении в газоразрядной плазме // Письма в ЖТФ, т.17, в.11,(1991), с.65-71.
3. Yu.L. Serov Experimental Investigation of a Supersonic Sphere Motion in Plasma on Ballistic Apparatus // Proc.2nd Weakly Ionized Gases Workshop, Norfolk, USA, 24-25 April,1998, AIAA, 1998, pp.32-45.
4. Pavlov V.A., Serov Yu.L. Supersonic Motion of a Body in Weakly Ionized Plasma: Phenomena of Trans-Ion- Acoustic Plasma Dynamics // 3rd Weakly Ionized Gases Workshop, Norfolk, USA, 1999 / AIAA-99-4852.
5. Ю.Л.Серов, И.П. Явор. Волны заряда в ионизованном газе перед гиперзвуковым телом // ЖТФ т.66, в.11, 1996, с.181-186.
6. Yu.L. Serov. Ion-Acoustic Model of Instability of Strong Shock Waves. J. Actual Problems of Aviation and Aerospace Sistems.Kazan-Daytona Beach. №2(18), 2004, pp..49-55.
7. V.A.Pavlov. Ion-Acoustic "Houston's Horse" Effect. Plasma Physics Reports, 2000, V.26, No.6, pp.507- 511.
8. V.A. Pavlov. Weakly Ionized Plasma in a Supersonic Plasma Flow. Plasma Physics Reports, v.28, №6,2002, pp.479-483.
9. F.V. Shugaev. Report MSU №277(1979), theme 29/79.
10. A.A. Radcig, B.M. Smirnov. Handbook on atomic and molecular physics. M.: Atomizdat,1980.
11. Yu.L. Serov. Interaction of shock waves with plasma: detonation of explosives on the basis of nitro- compounds (nitroglycerine, nitroglycol, trotyl). Proc. 8th International Workshop on Magneto-Plasma Aerodynamics. Moscow, Russia, March 31-April 2, 2009, pp.343-347.
12. T. Urbanski – Chemistry and Technology of Explosives Vol. 1 – Pergamon Press. Oxford. 1964.
13. Encyclopedia of explosives and related items./ Basil T. Fedoroff & Oliver E. Sheffield.Vol. 2 – Piccatiny Arsenal Dover, New Jersey, USA – 1962. B45.
14. Dobratz B.M. LLNL Explosives Handbook Properties of Chemical Explosives and Explosive Simulants –LLNL University of California, Livermore, California – (UCRL – 52997, 1985).
15. Багал Л.И. "Химия и технология инициирующих взрывчатых веществ" М. 1975.

5.1. ON FIREBALL GENERATION BY MICROWAVE RESONANCE IN PHOTONIC WIRE GRIDS

Geert C. Dijkhuis, Convectron N.V.
Rotterdam, the Netherlands, icblchair@kpnmail.nl

The author's text in ref. 1 treats ball lightning and similar artificial fireballs as charged eigenstates in photonic vortex plasma. Here we focus on accidental fireball generation as observed repeatedly during early ruby laser tests at Philips Laboratories in Eindhoven. An open induction coil as in Fig. 1 formed these atmospheric fireballs upon discharge of high voltage from a capacitor bank. Remarkably, the copper wiring emerged without ero-sive or other damage from such fireball generation. Treating its spiralling wiring scheme as a perfect lens for incident microwaves we find

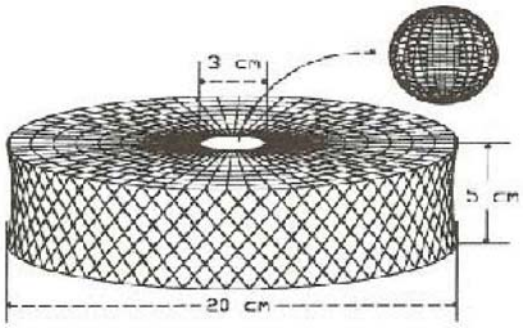

Figure. 1. *High-voltage pulse on open induction coil generates an atmospheric fireball.*

exponential growth of voltages above breakdown threshold values in air. From Maxwell theory Veselago had derived solutions for materials with negative refractive index. Negative permittivities and permeabilities underlying this unusual electromagnetic response exist separately in natural materials, but not in combination. Modern meta-materials demonstrate photonic response at frequencies ranging from microwaves to light. A diamond-type lattice of air channels drilled in dielectric material made the first photonic crystal now called yablonovite after its inventor. Microwave transmission tests by Pendry demonstrate photonic response of thin wires stacked in cubic grids [2]. We propose demonstration tests for photonic plasma generation using wire-based and lens-shaped electrodes as in Fig. 1. For wake flow in cubic wire grids the lattice unit in Fig. 2 models vorticity as a 3D version of Von Karman's universal vortex rows [1]. Vortex tubes in Fig. 2 have right-handed stacking helicity allowing coherent propagation of one helical surface mode. Paschen's law initiates high-voltage breakdown in tenuous vortex cores, turning wake flow into vortex plasma. Cavitation in cool, dense discharge plasma fosters photonic response at equal cross sections for ionization and scattering. Pendry's photonic cylinder and crescent lenses achieve perfect magnification through stratified refractive indices [3]. Our helical vortex plasma has quaternion potentials with stratified space charge for atmospheric fireballs in free space, in external fields and in ducted solutions.

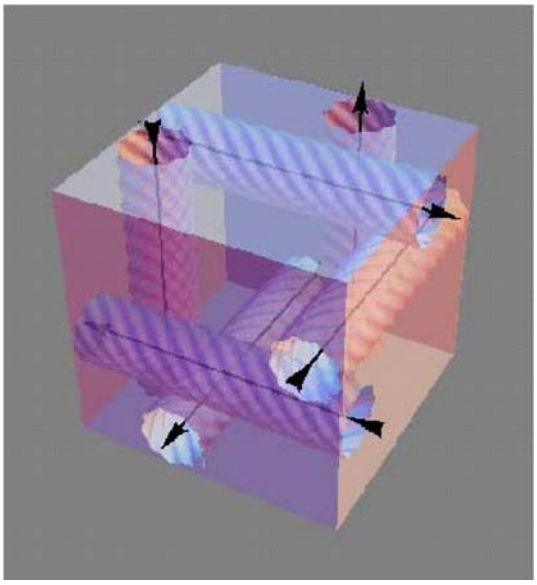

Figure. 2. *Right-handed lattice unit shows coherent propagation transverse surface wave in vortex plasma.*

1. G.C. Dijkhuis, *Ball lightning as thermodynamic limit of the periodic system*, in: The Atmosphere and Ionosphere. Eds. V.L. Bychkov, G.V. Golubkov and A.I. Nikitin, Springer, pp. 331-355, 2010. 2 J.B. Pendry et al., *Low frequency plasmons in thin-wire structures*, J. Phys.: Condens. Matter 10, pp. 47854809, 1998. 3 J. B. Pendry, *Perfect cylindrical lenses*, Optics Express 11, pp. 755-760, 2003.

5.2. GAS-DISCHARGE PROCESSES IN A STRATOSPHERE AND MESOSPHERE DURING A THUNDER-STORM

Kirill V.Khodataev
FSUE "Moscow Radiotechnical institute of the Russian Academy of Sciences".
Moscow, Russia
K.V.K@home.ptt.ru

Overall aim of researches of the discharges observed in a Overall aim of researches of the discharges observed in a stratosphere and mesosphere during strong thunder-storms, conducted in the world, is working out of the self-fitted closed theory of high-altitude discharges in a stratosphere and mesosphere, being based on known properties of laboratory gas discharges.

For an explanation of the observable phenomena, which have obtained the names "elves" and "sprites", representation about initiating role of electromagnetic field of powerful lightning discharges and streamer mechanism of the filament plasma formations development is usually used. In the known literature the separate parties of the phenomenon without the quantitative description of process in details and as a whole have been discussed.

But there are many the opened questions yet:

- how the ionization processes initiation occur in "elves"
- why there are large-scale formations on their bottom border, so named - "sprites"
- why all process occurs for time exceeding duration of lightning discharges, etc.

For decision of formulated task first of all it has been found out:

- distribution of electric conductivity on height from troposphere to an ionosphere
- spatial-temporal distribution of a thunder-storm cloud electric field before lightning
- evolution of an electromagnetic field after lightning.

The obtained data have allowed to clarify the all picture of the phenomenon "elves - sprites" at quantitative level, having revealed the mechanism of "elves" initiation, formation of "sprites" and their transition in the streamer stage, having constructed the elementary model, suitable for the further specifications and complications.

5.3. ON POSSIBLE NATURE OF BALL LIGHTNING AS OF AN OBJECT OF PLASMA ASSISTED COMBUSTION

Bychkov V.L.
M.V. Lomonosov Moscow state university, Physical department.
119991 Vorobievy gory, Moscow, Russia bychvl@orc.ru

Abstracn. Creation of natural ball lightning as the result of plasma assisted combustion processes has been considered. Basing on successful experiments in discharges at plasma influence on different materials a theoretical model of ball lightning creation in the result of linear lightning impact on earth components or melting inorganic subjects (with cavities filled with organic dust and water molecules) with creation in the heated area of the an oxide reservoir filled by a metallic or metalloid powder, at that the reservoir is covered by an oxide cover preventing metallic powder from fast ignition, has been proposed. The theory is capable to explain an observation of ball lightning with a diameter of 1.5 m , which left near a place of its destruction about of 400 kg of glassy slag peaces.

Preliminary consideration

We start to discuss a model of BL which appears at an impact of the linear lightning to some melting and evaporating material. It can be formed at the impact of some high power discharge created between the high voltage electric power transmission line and the earth surface.

Let us consider the simplest model of the ball lightning [1] which helps to understand main features of BL phenomenon described above. Following [2,3] we consider that at hit of usual linear lightning into the earth (or some melting object) takes place a creation of so called a cavern in earth or a fulgurite region. In particular BL can be originated in the fulgurite area and take a form of it. At average lightning parameters it transfers to the earth about 10^{10} J [4] creating high pressure up to several hundreds of atmospheres in the cavity. After which ejection of a modified material part takes place. At that at constructing of the model we take into account that BL can be heavy, hot and high energy content object.

So during the lightning discharge process into the earth takes place creation of the region with high temperature where processes of the soil destruction takes, they include chemical reactions of the soil components – silica (SiO_2),), atoms and molecules of the dissociated organic macromolecules including C and H_2.

At the theory constructing we also take into the account that the linear lightning is charged unipolarly, i.e. it has charges of one sign (non-compensated) in it. So at transmission of energy into the soil it also transmits the electric charge which flows from the area of the impact.

We have seen above that all these processes were observed at combustion experiments and the constructing theory already has the experimental grounding/

BL model with an oxide cover and metallic core

Under the impact of the linear lightning inside the cavern creation of a region takes place where at high temperature reactions of metal reduction from silica, SiO_2 [2,3,5,6] or their mixture at destruction of organic components of a soil occur:

$$SiO_2 + 2C \rightarrow Si + 2CO \ ;$$
$$SiO_2 + 2H_2 \rightarrow Si + 2H_2O$$

Here C – atoms of carbon, H_2 – molecules of hydrogen, H_2O -water molecules.

So in this region gas pressure and temperature rise in the result of which appear metallic particles and gases. This process is analogous to the creation process of powders at electric explosion of wires when the pressure rises to tens or hundreds atmospheres, or to the industrial creation of powders at recovery of oxides at high temperatures [5, 6].

The hot region becomes unipolarly electrically charged due to the charge transferred from the linear lightning to it.

Since the soil conductivity in dry conditions around the hot region is very small so electric processes develop inside the hot region. The electric charge has time to move to the outer boundary of the hot region over the metallic particles during a time before an ejection of the hot metal from the cavern taking place during gasdynamic times. There the oxidizing processes acceleration under an impact of the electrical charges and their fields [6] take place, and the oxide film of SiO_2 is created. This oxide film is charged. The oxide film strongly decelerates metal oxidation due to decrease of oxygen penetration inside the region. These films have rather high tensile strength. This cover can withstand pressure of charges on the surface or gases appearing inside

the object. (For example, the limit of tensile strength for Al_2O_3 is $\sigma = 21$ MPa [6] , the thickness of typical alumina film is ~0.2 μm and of SiO_2 is σ = 40-60 MPa in the quartz glass state [7], however below we will consider an additional mechanism, which due to polarization helps to create a force withstanding the pressure of charges on the surface).

In the result of these processes appearance of, as if, a reservoir is realized: the oxide cover is from above and the metallic powder particles are inside it. A slow combustion takes place inside the reservoir (using small amount of penetrating oxygen through the cover or captured inside). It ensures an illumination of the ball.

After that the ejection of these charged reservoir – a ball from the earth under an influence of pressure takes place. Charged heavy object – the ball lightning appears in air. It does not fall down due to the Coulomb repulsion from the charged surface of the Earth.

Due to the large charge of the object a plasma layer originates on its surface [5]. The surface layer heats up the ball surface [8]. Oxygen diffusion into the reservoir sharply increases at the surface layer heating [6], oxidation and release of gases takes place in different chemical reaction such as [5,6]

$$Si + O_2 \rightarrow SiO_2 ; \quad SiO_2 + Si \rightarrow 2SiO .$$

Pressure rises inside the object. Cracks appear in the cover. Oxygen freely penetrates inside the object. The combustion takes place, and the object explodes and tears apart.

Application to the Khabarovsk Case

On the basis of the proposed model let us make estimations for described above observation case in the Khabarovsk city [9].

«The ball lightning (BL) was observed on August, 24th, 1978, at 23 o'clock 20 minutes in Khabarovsk during a strong rain. There was the sharp whistle reminding work of the jet engine and accompanied by a strong crash. It became light as day. Then over a cinema building … there appeared a fireball of bright orange color in diameter about of 1.5 m. From it sparks were strewed. Then BL has started to descend, it has passed to the earth surface through branches of trees, for an instant it has flashed over a site of soil and again has risen upwards. Strong explosion was heard, it became dark and silent. In total BL existed about one minute. BL was observed by many eyewitnesses including one of authors of the article [9]. At distances up to 100 m electrical wiring has been put out of action. Despite the water considerable quantity on the soil and the torrential rain, in the zone in diameter of ~1,5 m and depth of 20-25 cm the soil was charred and fused. The total volume of the zone filled with the slag, was about of 0,4 m^3. The slag consisted not of a continuous crust but of many pieces of the irregular form. They were of 5-6 cm in the average size, and they were mutually alloyed with each other. In total there was revealed over a thousand of such pieces.

Near the place where there was a BL flash, a vegetative cover did not renew…. On the data obtained by the meteorites Committee of the USSR AN, a ground after the influence of BL on it represented not completely melted a slag-type soil and glass with a fluid-type structure. This formation contained of the numerous rests of minerals, basically quartz and epidote in different degree changed by heating. For separate samples of the slag a presence of pores and cavities, and also the glass-type inclusions similar to the opaque smalt, both on the surface, and in the material was typical. One can assume that the slag was formed as the result of fast heating of the ground to the temperature close to the temperature of its fusion, and the heating had the uniform volumetric character. The initial ground represented the typical sandy loam on the basis of the quartz sand.» Estimations of released by BL energy made by the authors of [9] taking into account heating of the ground and the evaporation of the moisture being in it had appeared to be $W \approx 1.1 \cdot 10^9$ J.

Let us suppose that in this case BL was created at the linear lightning stroke into earth, then it moved over the ground. BL explosion took place at the initial stage of its existence and all its internal content fell on earth and combusted there. So we consider BL as a ball which radius is 0.75 m and it is filled with the hot Si powder.

Chemical energy.

Let us determine the mass of BL substance – Si powder. For this purpose we consider that the pieces of the slag left on earth consisted of a quartz glass with density $\rho = 2.65 \cdot 10^3$ kg/m^3 [7], for simplicity of estimates we consider them balls with the radius r_{SiO2}=3 cm. Then 1000 such pieces of SiO_2 have the weigh $m_{SiO2} \approx$ 300 kg and a corresponding mass of Si is $m_{Si} \approx$ 140 kg. Accepting a radius of the ball lightning as R=0.75 m one obtains a density of BL content as $\rho_{Si} \approx 80$kg/m^3, i.e. it is a very low-density material.

The energy W_{ch} released at its oxidation is

$$W_{ch} = m_{Si} \cdot \Delta Q \qquad (1)$$

where ΔQ is the oxidation enthalpy of Si, at typical combustion temperature T=2000K it is $\Delta Q = 8.8 \cdot 10^6$ J/kg as it follows from [10]. So the chemical energy released at its combustion was about $W_{ch} \approx 1.2 \cdot 10^9$J, i.e. it is close to the estimates of [9] given above.

Process time.

Let us estimate the charge leakage time from the surface of the created object in the soil. Charge leakage equals to a current from the object surface, which in case of a sphere equals to

$$\frac{dq}{dt} = -\sigma E \cdot 4\pi R^2 =$$

$$-4\pi R^2 \sigma\, q/(4\pi R^2 \varepsilon\varepsilon_0) = -\sigma/\varepsilon\varepsilon_0 \cdot q$$

Where q is a charge of the sphere, E is the electric field strength near the sphere, R is its radius, σ is electric conductivity of a medium around a sphere, ε is its dielectric permittivity, and ε_0 is dielectric permittivity of vacuum. Analysis of soils [11], show that the leakage process time greatly varies from $0.3 \div 3\cdot10^3$ s in case of dry soils to $\cdot10^{-7}$- 10^{-6} s in case of humid soils. So the whole process of BL formation has to take place in the dry soils.

BL cover.

At BL theoretical modeling of one of the key questions is connected with the BL construction stability. Estimates show that there are two impacts connected with charge inside the sphere. One of them is the pressure P_C created by the Coulomb action of charges inside the ball, leading to its stretching, a formulae describing this has a form [12]

$$P_C = \frac{k \cdot q^2}{8 \cdot \pi \cdot R^4}$$

Where R is the radius of the ball, q its charge, $k = 1/(4 \cdot \pi \cdot \varepsilon \cdot \varepsilon_0)$.

The second impact is caused by the polarization of charges acting the dielectric cover [12 Sec. 3.3.1]. Let inside the spherical shell of some dielectric material a core with the non-compensated charge q is located. This charge generates an electric field in the place, where the shell is located, $E_{sh} = q/(4\cdot\pi\varepsilon\varepsilon_0 R_{sh}^2)$ (R_{sh} is the inner radius of the shell). In such a field the polarization of the shell takes place: on its inner surface positive charges will appear, and on the outer surface – negative ones. Under the total polarization of the shell's material in the strong electric field the surface density of charges σ_{ch} may be assumed to be equal to N_s, which is the number of SiO_2 molecules on the unit of the shell surface. The distance γ between the silica molecules can be estimated as $\gamma = \left(\rho_{SiO_2} / m_{SiO_2}\right)^{-1/3}$ where ρ_{SiO_2} and m_{SiO_2} are the density of the silica and the mass of the silica molecule, $\gamma = 3\cdot10^{-10}$ m, and hence $N_s = (\gamma)^{-2} = 10^{19}$ m^{-2} and the surface density of charges is $\sigma_{ch} = N_s \cdot e = 1.6$ C/m^2. The dipole moment of the surface unit of the thickness a is $D = \sigma_{ch} \cdot a = 1.6\, a$ C/m. Therefore, the force f_{cp}, attracting a unit of the surface towards the charge q, is equal to

$$f_{cp} = D \cdot \mathrm{grad} E = -2Dq/4\cdot\pi\cdot\varepsilon\varepsilon_0\cdot R^3 = -2DE/R. \quad (2)$$

By multiplying f_{cp} by an area of the inner surface of the shell $S = 4\pi\cdot R^2$, we can find a force, shrinking the shell towards the center:

$$F_{cp} = f_{cp}\cdot 4\pi\cdot R^2 = 2\sigma_{ch} a \cdot q/(\varepsilon\varepsilon_0 \cdot R). \quad (3)$$

The corresponding formula for the pressure has a form

$$P_{cp} = \frac{2 \cdot \sigma_{ch} \cdot k \cdot a \cdot q}{R^3}.$$

Now we can write a condition of BL surface stability accounting that its surface represents a thing layer of SiO_2:

$$P_{cover} + P_{atm} + \frac{2 \cdot \sigma_{ch} \cdot k \cdot a \cdot q}{R^3} = \frac{k \cdot q^2}{8 \cdot \pi \cdot R^4} + P_{gas}, \quad (4)$$

here P_{atm} is the atmospheric pressure, P_{cover} is the pressure which can keep the cover layer due to its tensile strength, P_{gas} is the pressure of gases captured inside BL at its formation and appearing in chemical reactions during its lifetime. The layer thickness a in the general case decreases with temperature $a = a_0 (T/T_0)^{-\alpha}$, where $\alpha>0$.

Estimates show that in case of chemical reactions absence inside the ball in wide range of parameters from (4) one has (4)

$$R \approx \frac{q}{16 \cdot \sigma_{ch} \cdot a}. \quad (5)$$

One can see that in frames of this model BL size rises with increase of its charge, at that the increase of the surface unit charge and the increase of the surface layer thickness act against this, since they lead to BL surface compression. At heating of the surface accompanying with the decrease of BL cover thickness its radius increases, i.e. BL explodes.

For example, at the cover SiO_2 layer of a =0.4 mm thickness and $\sigma_{ch} \sim 1.6$ C/ m^2 one gets $R \approx 1$ m at $q\cdot = 10^{-2}$ C/m^2. However, this value is only a tentative estimate obtained at many simplifying suppositions.

There is no indication in (4) on the presence of some substance inside BL captured during its formation. Evidently, in case when a linear lightning stroke melts metallic, oxide, amorphous (glass, plastics) objects and unipolarly charges them, an appearance of rupture of the melt (a liquid) takes place. In the result of them bubbles or

large caverns filled by vapors of melted material and precipitated gases dissolved in the liquid appear, they simplify the process of the charged bubble appearance. This process can be realized also in melts of SiO_2 so it can explain usual appearance of BL at lightning strokes.

BL lifetime.

BL lifetime is determined by the time of the metallic powder material combustion. We could not find necessary data for Si combustion from the literature, so we use the data for the combustion of Al powder in conditions of low concentrations of oxygen in the volume [5]. The radial combustion velocity of Al powder is V_{com}= 5-10 mm/s. So the estimate for BL lifetime can be $\tau_{BL} \sim R_{sph} / V_{com} \sim$ 75-150 s, which well fits to the observed lifetime of the large BL [13-15].

Let us estimate the maximal lifetime of BL. Since in this model it is represented by the unipolarly charged sphere then charges from air in a form of oppositely to sphere charged ions will move to its surface. So the maximal time of sphere's discharging is connected with the recombination of the atmospheric ions with the charges on the sphere. Let us write down an equation describing the process of the charge q on the sphere decrease, when the ions come to the sphere through an area $4\pi R^2$:

$$\frac{dq}{dt} = -4\pi R^2 w N_i e = -4\pi R^2 b_i E \cdot N_i e = -4\pi R^2 b_i \cdot N_i e q/(4\pi R^2 \varepsilon \varepsilon_0) = -b_i \cdot N_i e q / \varepsilon \varepsilon_0 \quad , \quad (6)$$

here w - is a drift velocity of ions, e- elementary charge, b_i – a mobility of ions, N_i – their concentration. A solution of (6) gives the typical time τ of the charge decrease:

$$\tau = \varepsilon \varepsilon_0 /(b_i e N_i) . \quad (7)$$

Accounting that in the atmospheric air charged particles are mainly produced by the background ionization with a rate S and disappear through ion-ion recombination with a rate constant α_r one obtains that the average number of the ions in air is

$$N_i \approx \sqrt{S/\alpha_r} . \quad (8)$$

Inserting (8) into (7) one obtains the following formula for the typical time of the sphere charge decrease (maximal value of its lifetime)

$$\tau = \varepsilon \varepsilon_0 / b_i \cdot \sqrt{\alpha_r / S} . \quad (9)$$

The average value of the ion mobility is b_i= 2.8 10^{-4} m^2/(V s) [16], the ion-ion recombination coefficient at room temperature in air is $\alpha_r = 2\ 10^{-6}$ cm^3/s [16], and S = 4 cm^{-3} s^{-1} (S changes with respect to location on earth) [16]. Inserting these values into (9) one obtains the maximal BL lifetime $\tau \approx 1.4 \cdot 10^2$ s, which well fits to the observed lifetime of BL.

Electric properties.

In order to explain the BL motion in air we accept the following mechanism of levitation. For levitation this ball has to satisfy to the balance of forces of BL attraction to earth by gravitation and image forces and a repulsion in the electric field of earth (and environment). The uncompensated charge of BL defines the levitation capability of the charged ball. For example in the external field of earth E_{ext} the balance of the indicated forces acting the charged ball has a form [12]

$$q \cdot E_{ext} = m \cdot g + \frac{q^2}{16\pi x^2 \varepsilon \varepsilon_0} , \quad (10)$$

where q is the charge of the ball, g is acceleration of free fall, x is a distance between the BL and the earth surface (we consider that the charge of the ball coincides with the sign of earth charge). For using of (10) one should know a value of E_{ext} and x in considering conditions. For estimates let us accept x=10 m equal to the height of a not tall tree. The external electric field value under the cloud can be estimated as the field under the charged sphere

$$E_{ext} = \frac{q_{cl}}{4\pi H^2 \varepsilon \varepsilon_0} ,$$

here H is the height of the cloud over earth and q_{cl} is the charge of the cloud. Usually q_{cl}~ 10 C. (in this situation we accept that negative charge has already gone to earth with lightnings, and the cloud left positive. We consider heavy rainy conditions with the level H=500 m. At these parameters one gets the following value of the external electric field over earth $E_{ext} \approx 3.6 \cdot 10^5$ V/m.

The electrical charge of the ball of the mass $m_{Si} \approx$ 140 kg. obtained with a help of the equation (2) is $q \approx 9.8 \cdot 10^{-3}$ C.

Knowing the BL charge one can calculate its electrostatic energy W_{el} [12]

$$W_{el} = \frac{q^2}{2 \cdot 4\pi \cdot \varepsilon \varepsilon_0 R_{sph}} , \quad (11)$$

which appears to be rather high, $W_{el} \approx 6 \cdot 10^5$ J, but it is considerably smaller than BL chemical energy.

Concerning the electrostatic properties of BL one can calculate an electric field strength E_{surf} on BL surface

$$E_{surf} = \frac{q}{4\pi R_{sph}^2 \varepsilon \varepsilon_0}. \qquad (12)$$

This equation gives $E_{surf} = 1.6\cdot10^8$ V/m. This is a large value and it is greater than the breakdown value of air $E_{br}\sim3\cdot10^6$ V/m.

Electric field distribution.

An electric field strength distribution of the charged ball over the radial direction at plasma absence is decreasing as

$$E_0(r) = E_{surf}(R/r)^2,$$

and in the region between the ball surface $r = R$ and the distance at which the air breakdown takes place $r = r(E=E_{br})$ an appearance of a plasma has to be realized in the result of ionization, attachment, recombination and other elementary processes [16,17] action. In this case there has to appear a plasma region which impacts the electric field of the charged ball decreasing it.

According to [16-18] at appearance of the charge q in the spatially homogeneous plasma with temperature of electrons T_e and ions T_i there appears a field over the charge:

$$E(r) = \frac{q}{4\pi\varepsilon\varepsilon_0 \cdot r} e^{-r/r_D}\left(\frac{1}{r} + \frac{1}{r_D}\right), \qquad (13)$$

where $r_D^2 = \left(\varepsilon\varepsilon_0 \cdot k_B / e^2\right)\cdot\left(\frac{N_e}{T_e} + \frac{Z_i \cdot N_i}{T_i}\right)^{-1}$,

k_B- Boltzmann constant, N_e, N_i concentrations of electrons and ions, Z_i - ion multiplicity. Debye radius is r_D is reduced to

$$r_D = \left(\frac{\varepsilon\varepsilon_0 T_i}{e^2 N_e}\right)^{1/2}$$

at $Z_i = 1$, $T_e >> T_i$, $N_e = N_i$. From (6) it is easily seen that at presence of plasma the field is greatly decreased. This plasma is characterized by electron temperature $T_e > 1.5$ eV and ion temperature $T_i > 0.5$ eV concentrations of electrons $N_e > 10^{16}$ cm^{-3} [16-17]. According to [16-18] electrons and ions of the plasma create a layer in the region between E_{surf} and E_{br} with the local fields directed oppositely to the electric field of the sphere and decrease the initial field of the sphere to the level below the breakdown field value. After that the plasma decays and the initial electric field E_{surf} is restored. After that the whole process repeats The distance at which the local field decreases, the Debye radius, is $r_D \sim 5.0\cdot10^{-6}$ cm, and the time of the initial field switching off is about of the time of the plasma frequency

$$\tau_p = \omega_p^{-1} = (4\pi e^2 N_e / m)^{-1} \sim 7\cdot10^{-13}\ \text{s}$$

(here m is the electron mass).

Analysis of elementary processes shows that the ionization times and creation of electrons prove to be of the order of $\tau_i \sim 1/\nu_i = 1/(N\cdot k_i) \sim 1/(3.0\cdot10^{19}\cdot10^{-11}) = 3.0\cdot10^{-9}$ s, where N-concentration of molecules in air, k_i is rate constant of ionization, $k_i \sim 10^{-11}$ cm^3/s [16-17].

Charges disappearance is characterized by the recombination time $\tau_r \sim 1/(N_{e0}\cdot\alpha_r)$, where N_{e0} is the concentration of electrons in the plasma, and α_r is the coefficient of charges recombination $\alpha_r \sim 2.6\cdot10^{-8}$ cm^3/s [16-18], i.e. the recombination time at $Ne_0 \sim 1.0\cdot10^{16}$ cm^3 is $\tau_r \sim 3\cdot10^{-9}$ s .

So the longest time corresponds to the plasma decay.

From the consideration of the problem the electric field distribution over the radial coordinate r in case of the plasma realization is the following:

$$R < r < R + r_D,\ E(r) = \frac{q}{4\pi\varepsilon\varepsilon_0 \cdot r^2} e^{-r/r_D}; \qquad (14a)$$

$$r_D < r \le r(E=E_{br}) \quad E(r)=0; \qquad (14b)$$

$$r > r(E=E_{br}) \quad E(r) = E_{surf}(R/r)^2. \qquad (14c)$$

The frequency of the electric field pulses is $\nu \sim 10^9$ s^{-1} in the area between $r = R$ and $r = r(E=E_{br})$, further the field acts in a usual way. Presence of such a pulsed field can explain a luminescence of lamps with cut wires.

Luminescence.

At burning combusting metallic particles emit radiation that ensures the luminescence of BL. Let us calculate a mass of these particles material necessary to ensure the radiation by burning inside BL. For this purpose we apply the following equation describing the radiation of the solid particles

$$\sigma_{SB} \cdot T^4 \cdot 4\pi \cdot R^2 \cdot \tau_{BL} = m \cdot \Delta Q,$$

where σ_{SB} is the constant of Stephan-Boltzmann, m is the mass of burnt metallic particles and τ_{BL} is the BL lifetime. For the considering case we get $m \approx 44$ kg, or the mass of the burnt particles is much smaller than those of the hole metallic particles

inside the BL, $m << m_{Si}$. So the BL can irradiate light, at that it has enough of the metallic material for a following explosion.

Considering the layer $R < r < R + r_D$ we can calculate an effect of the electric field near the surface and the plasma in the thin Debye layer on a heating of the BL surface, accepting that all the released discharge energy goes to the heating of the surface. In this case the temperature of the surface is determined by the discharge the surface and the radiation cooling of the surface, or

$$\sigma_{SB} \cdot T^4 \cdot 4\pi \cdot R_{sp}^2 \cdot \approx \overline{J} \cdot \overline{E} \cdot 4\pi \cdot R_{sp}^2 \cdot r_D = , \quad (15)$$
$$= e \cdot \overline{N}_e \cdot \overline{w}_{dr} \cdot \overline{E} \cdot 4\pi \cdot R_{sp}^2 \cdot r_D$$

where $\overline{\overline{J}}$, $\overline{\overline{E}}$, $\overline{\overline{N}}_e$, $\overline{\overline{w}}_{dr}$ are averaged over the time of the current density, electric field strength, concentration of electrons and the electrons drift velocity values in the Debye layer over the ball, respectively, e-is the elementary electric charge.
$\overline{\overline{Y}}$ means:

$$\overline{Y} = \frac{1}{t_2 - t_1} \int_{t_1}^{t_2} Y \, dt \cdot$$

At that the main rise of the temperature takes place during the plasma decay in the recombination. From (15) one gets an estimate of the surface temperature without accounting of the combustion processes in the ball

$$T = (e \cdot \overline{\overline{N}}_e \cdot \overline{\overline{w}}_{dr} \cdot \overline{\overline{E}} \cdot r_D / \sigma_{SB})^{1/4} . \quad (16)$$

For the considering case when the electric field changes from $3 \cdot 10^6$ to $\sim 10^0$ V/m during $6 \cdot 10^{-9}$ s , electron concentration changes from 10^{16} to $\sim 10^0$ cm^{-3}, and the drift velocity - from $2 \cdot 10^7$ to $2 \cdot 10^5$ cm/s the formula (16) gives $T \approx 860$ K.

So the oxide cover will not be burnt through by the discharge on its surface but an addition of energy from the internal part of the ball can lead to its melting. This process realizes an additional luminescence of the BL surface. This can also cause burns of people and combustible materials ignition with origination of fires at contacts with BL.

Some remarks.

BL model presented in this section considers BL as an object which can be hollow, can contain charged metallic particles inside it - a metallic core inside the oxide cover. This cover prevents metal particles inside the cover from immediate burning in oxygen of air. The lifetime is limited by slow combustion of metal particles inside the object. The object' internal substance can represent a powder. The powder is charged, its motion inside the cover can lead to mechanical effects on BL motion and form. So this object is alike a soft flexible cushion that can penetrate through holes. Its main energy is connected with the metal oxidation, but it also possesses rather large amount of electrical energy.

Presence of electric charges in this object represents its essential feature, since it determines its capability to fly and to realize harmful impact on different electrical devices and people. Undertaking analysis of the Khabarovsk case has shown that can be heavy and high energy containing object. Due to its weight it can realize mechanical damages. From this approach we see that the surface charge is limited by the surface features and values of charges can be very high. So BL represents a unique joint of chemical electrical and mechanical features and it requires additional experiments, collection and analysis of observation data and field investigations to places of its impact with earth, objects and people.

Appearance of BL with tails and tape or tube-type form described above can be easily explained by this model as BL origination in long narrow fulgurite cavities. Presence of charged metallic powders inside of them can lead to curving of their form and a possibility of their turning into a ring or sphere in case of the multiple turning.

From the point of view of realized experiments the presented model shows productivity of experiments with Si and oxides, it also explains successes of experiments of [19] connected with combustion of metal particles. In particular it explains appearance of a shell cover in experiments [19]. It also shows that there is a necessity to involve a non-compensated charge in experiments with metallic subjects, which represents a challenging problem. Impact of BL to window glasses in frames of this model is, most probably, connected with the polarization and melting of glass and its stretching in melted state. For the detailed analysis of this phenomenon there is nowadays a shortage of both observation and experimental information. In particular there is a necessity of experiments undertaking at high electric fields and high temperatures.

Let us roughly estimate a velocity of the ball that can be ejected from the Earth after transfer of energy from a linear lightning to earth. For this let us use Bernoulli equation

$$P_{\text{int}} = \rho \cdot v^2 / 2 \quad (18)$$

where P_{int} – is pressure of gases in the fulgurite area, ρ- is a density of a soil ejected into air and v - is a velocity of the ball. Let us suppose that a part of percent of linear lightning energy went in increase of pressure, then $P_{int} \sim 10^{-4} E_{light} / V$, where E_{light} - is energy of linear lightning and V- is the volume in the Earth impacted by the lightning,

which is ~10^{-2} m^3, the density of soil $\rho \sim 4 \cdot 10^3$ kg/m^3. From (18) follows that the velocity of the ejected object can be v~(1-2) 10^2 m/s.

So the observer due to inertia of his perception will not see the moment when BL appears from the Earth in the sky, for him its appearance can seem as if BL has appeared from "nowhere". If it has such a velocity then it can rise rather high and far from a place of its origination, and only after that it will descend and participate in the levitation process, or it will be falling over a curved trajectory.

BL can also appear at impact of the linear lightning or inter-cloud discharges into air crafts. The last ones can detach some metallic pieces from the aircraft surface, melt and ignite them. In this case BL can appear near aircrafts.

BL can be also produced during geotectonic processes in the Earth, in volcanoes and at earthquakes, when there can be realized high temperatures and electric currents in the Earth crust. The ejection of burning charged object into the atmosphere is analogous to BL considered by us above. From this point of view BL could appear at Tunguska event, as it is considered in some hypothesizes of this phenomenon [20].

BL appearing in atmosphere high in the sky and near airplanes can be considered as UFO. But extreme long duration of glowing subjects in the atmosphere are sooner connected with optical illusions [21].

Difficulties of BL science development is connected with experimental realization of observation events. It is well understood that the BL problem will be considered as solved only after experimental modeling of this object having all indicated in Section 1 features.

Nowadays there are problems with copying of BL impact on window glasses. Especially it is true with their penetration through glasses without clearly detected traces. Available information on BL glasses impact is insufficient for understanding of physical and chemical processes that take place at BL interaction with glasses.

There are difficulties with experimental modeling of magnetic impact of BL on metallic subjects. There are left only two descriptions of such events and no analysis of metals influenced by BL. So we do not definitely know what to model.

It is also difficult to imagine how to model BL impact on golden rings and bracelets. We understand that we can use high frequency electric fields, but what else have we to foresee in experiments in order to realize disappearance of these subjects?

Generally speaking there is a shortage of detailed observations how these effects are realized by nature. So we have to continue collection of detailed descriptions of BL unusual events and analyze approaches to their experimental modeling.

New investigations are to be undertaken in modeling of BL appearance and creation of luminescent objects on a base of burning metals inside oxide covers. We have to understand and realize mechanisms of BL explosions. It is difficult to model BL levitation, though we understand how to charge a ball by Van-der –Graaf accelerators. This can be another type of experiments. We have to continue experiments with combusting powders and jets, especially creation them in charged and excited states and so on.

References

1. Bychkov, V. L. Ball Lightning as an Object with Metallic Powder Core and Oxide Cover. Proceedings 11-th Intern. Sympos. On Ball Lightning and 4rd Intern. Sympos. On Unconventional Plasmas. Kaliningrad, June 21-27, 2010. P.34-41.
2. Abrahamson, J., Dinniss, J.: Ball lightning caused by oxidation of nanoparticle networks from normal lightning strikes on soil. Nature. **403**, 519-521 (2000)
3. Abrahamson, J. Ball lightning from atmospheric discharges via metal nanosphere oxidation. Phil.Trans. Roy. Soc. 2002. V.360. P.61-88.
4. Bazelyan, E.M., Raizer, Yu.P. Phisics of lightning and lightning protection. Fizmatlit Publishers. Moscow. 2001.
5. Greenwood, N.N., Ernshaw, A. Chemistry of elements. . BINOM. Moscow. 2008.
6. Pokhil, P.F., Belyaev, A.F., Frolov, Yu.V., et al. Combustion of powder - type metals in active media. Nauka Publishers. Moscow. 1972.
7. Reference book. Physics values. Eds. I.S. Grigoriev, E.Z. Meilikhov. Energoatomizdat publishers. Moscow.1991.
8. Bychkov, V. L.: Unipolarly charged ball lightning. Khim. Fiz. **25**, N. 3. 63-71 (2006).
9. Dmitriev, M.T., Bakhtin, B.I., Martynov, B.I.: Thermal factor of ball lightning. Zhur. Tech. Fiz. **51,** N. 12. 2567–2572 (1981).
10. Gorskyi, V.V., Nosatenko, P.Ya. Mathematical modeling of thermal and mass exchange processes at aero-thermal-chemical destruction of composite heat protecting materials on silica base. Nauchnyi mir Publishers. Moscow. 2008.
11. Nerpin, S.V., Chudnovskyi, A.F.: Soil Physics. Nauka Publishers. Moscow. 1967.
12. Bychkov, V., Nikitin, A., and Dijkhuis, G. Modern State of Ball Lightning Investigations. The Atmosphere and Ionospher: Dynamics, Processes and Monitoring. Eds. V. Bychkov, G. Golubkov, A. Nikitin. Springer. 2010 (P. 201-373.)
13. Singer, S.: The Nature of Ball Lightning. Plenum, New York (1971)
14. Barry, J.D.: Ball Lightning and Bead Lightning. Plenum, New York (1980)

15. Grigorjev, A.I.: Ball Lightning. YarGU publishers, Yaroslavl (2006)
16. Smirnov, B.M. Physics of low ionized gas. Nauka Publishers. Moscow. 1978.
17. Raizer, Yu.P.: Physics of gaseous discharge. Nauka, Moscow (1992)
18. Aleksandrov, A.F., Bogdankevich, L.S., Rukhadze, A.A. Basics of plasma electrodynamics. Vysshaya shkola. Moscow. 1988.
19. Emelin, S.E., Semenov, V.S., Bychkov, V.L., Belisheva, N.K., Kovshyk, A.P.: Some objects formed in the interaction of electrical discharges with metals and polymers. Tech. Phys. 42, N.3. 269-277 (1997)
20. Olkhovatov, A. Tunguska phenomenon of 1908. BINOM. Laboratorya znanii. Moscow. 2008.
21. Menzel, D.H. Flying Saucers. Harward University Press. Harward. 1960.

5.4. SOME FEATURES OF HIGH-VOLTAGE DISCHARGE WITHIN A STREAM OF THE WATER ANODE EROSION'S PRODUCTS

Astafiev A.M., Emelin S.E., Kudryavtsev A.A., Pirozerski A.L..
Faculty of Physics, Saint-Petersburg State University, Russia

Abstract. In our study of the Gatchina's discharge the essential feature, which connected with the uniformity of a current distribution on the water anode surface with the density of about 10^{-1} A/cm^2 at the current values of order of tens of amperes, has been found out. In the present work to explain this phenomenon we studied the high-voltage DC discharge with a carbon cathode and water anode at varying its conductivity. It was found out that the anode spots are separated from the plasma volume by faint or dark layer and possess different structures as circles, rings, spokes and combinations thereof, depending on the current and the conductivity of the water. It has been observed that at the current level, exceeding the maximum current of the corona discharge by about two orders of magnitude, the smooth increase in the interelectrode distance to the limit resulted in a significant increase in the size of the dark zone and the appearance of instability. One kind of the instability manifested itself in an unexpected appearance and movement of the luminous anode structures, as well as the appearance of the torch from their center. Another one revealed itself via the reconnection of a curved plasma column. Propagation of the streamers in both cases was characterized by low velocity and down field direction only. Video frames to illustrate the observed phenomena are presented.

1. Introduction

Gatchina's discharge [1, 2, 3] is one of the most interesting experiments that gives a possibility to model some properties of the ball lightning on the base of non-ideal dust chemical plasma. It is a discharge between the surface of a low conductive solution and a metal or carbon central electrode isolated from the water via a fused silica tube. Previously [4], we showed that under initial voltage of a storage capacitor ~ 5 kV and a current attaining at maximum of a magnitude about tens ampere a characteristic feature of the discharge is a setting in of a uniform current distribution with a low density (~ 10^{-1} A/cm^2) over the electrolytic anode surface, while at a sufficient decrease of the current a transition to a non-uniform distribution with a three order of magnitude greater current density occurs. In this paper we point out differences between the discharge regimes of opposite polarity and indicate nature of the current distribution peculiarity with the help of an additional experiment.

2. Gatchina's discharge at different polarities

Experiments were carried out using installation described in [4]. A carbon rod was used as the central electrode, and the vessel was filled either by mains water with addition of NaCl or by distillated water with addition of nitric acid. In the latter case this implies the absence in the solution of components capable to form dust particles in the discharge and to cause an intensive visible radiation at relatively low electron temperatures characteristic for the afterglow.

Fig. 1 shows time dependencies of the current and of relative optic radiation intensity of the discharge under different polarities of low conductive NaCl solution. As may be seen from the figure, in the case of electrolyte anode the radiation

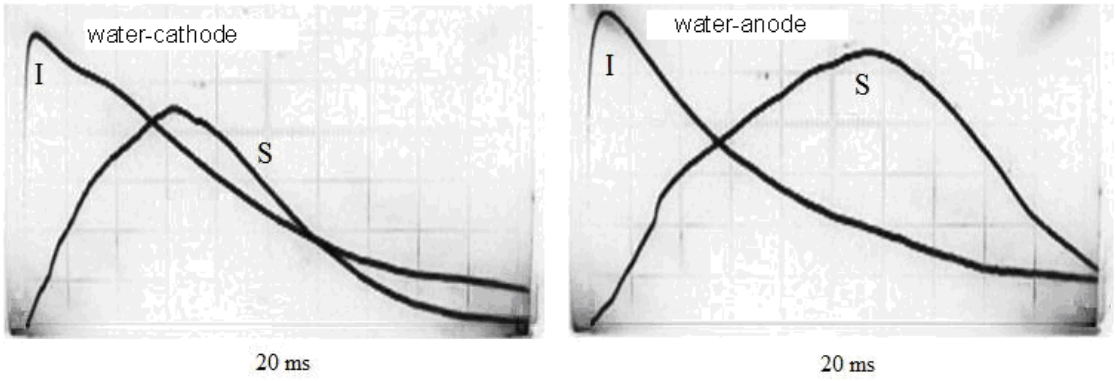

Fig. 1. *The current (I) and relative optic radiation intensity (S) of the discharge in the cases of the electrolytic cathode and electrolytic anode (NaCl).*

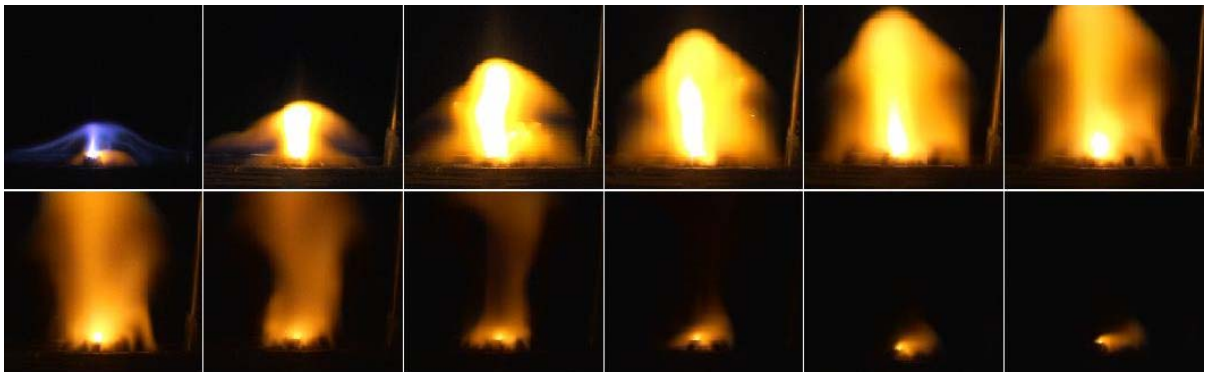

Fig. 2. *Discharge images of low luminosity taken with 20 ms intervals in the case of the electrolytic cathode (NaCl).*

intensity reaches a maximum sufficiently later than in the case of electrolytic cathode.

From videorecording data (Fig. 2) it has been found that the discharge current distribution over the surface of the electrolytic cathode is rather different than that in the case of the electrolytic anode described in [4]. A conjunction of the volume discharge to the solution-cathode occurs via a great number of spots, the current density in them being several orders of magnitude greater than in the case of the uniform discharge distribution over the anode. Measured spectral characteristics showed that due to a high current density at the conjunction spots to the solution surface an ejection of the dissolved substance into the discharge occurs just after the discharge beginning that results in more rapid catalytic decomposition of the chemically active mixture and in a shorter duration of the afterglow.

A significant difference of the discharge at different polarities manifests itself in the erosional ejections dynamics which can be easily traced via a videogram of spectral images. Fig. 3 shows the spectral images of the discharge visible radiation at the short-wave area of the visible range, where spectral images corresponding to Ca II (393,367 nm and 396,847 nm) and Ca I (422,673 nm) are more prominent. In the case of the electrolytic cathode more lines are excited but all they decay rapidly with the current decrease. This indirectly points to (integrally) a lower density of the cathode current at the case of the normal polarity (i.e. at positive

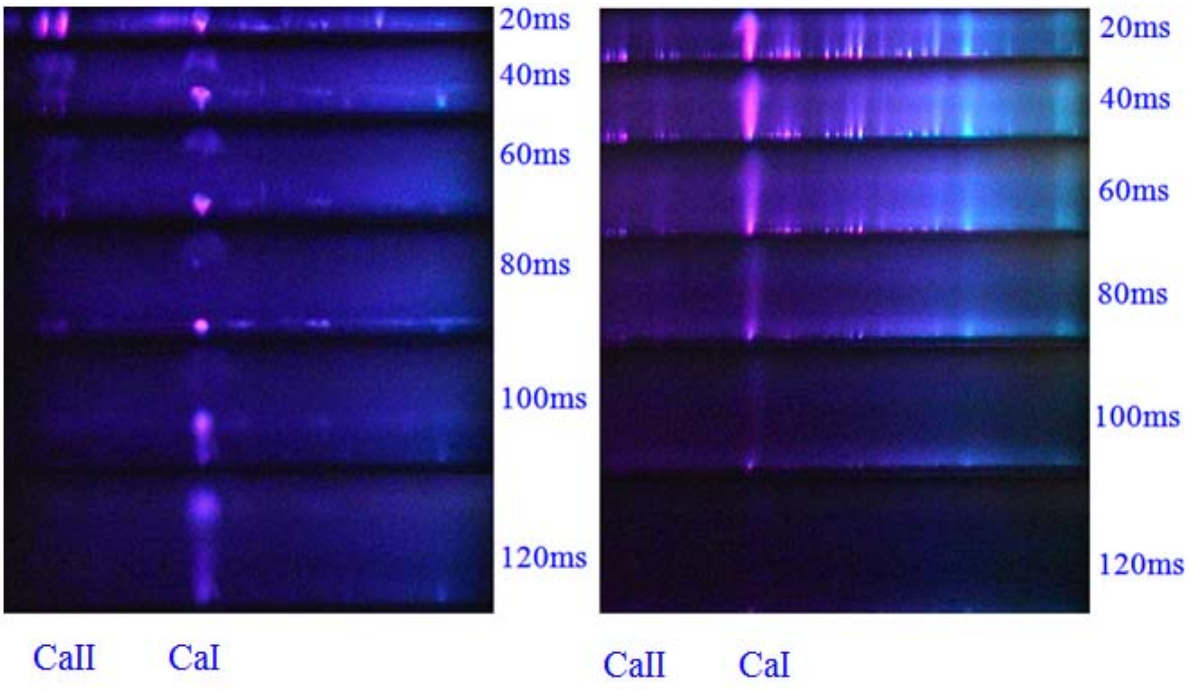

Fig. 3. *Spectral images at bands Ca I and Ca II for the NaCl solution and the carbon electrode. On the left – for the case of the electrolyte anode, on the right – for the electrolyte cathode.*

potential of the solution). On the Fig. 3 an erosional ejection radiation arising approximately at the moment of the transition to a non-uniform current distribution on the 80-th millisecond can be apparently seen, which forms a flying up object and is absent at the reverse polarity. We think that this intensification of the radiation can be explained, on the one hand, by the appearance of a droplet phase in the solution inflow to the plasma at increasing of the current density by three orders of magnitude, and, on the other hand, by explosion processes at the central electrode related with accumulation of hydrogen due to the ionic current. In the case of a positive temperature dependence of cathode material saturation by hydrogen, a cathode cooling occurring with the current decreasing should lead to a local over-saturation by hydrogen, to an explosion and to appearance of hydrogen saturated dust particles in the plasma that gives qualitatively different properties to the generated autonomous plasma formation.

For a more detailed study of the influence on the discharge of the dust component arising from an erosion of the central carbon electrode a weak solution of nitric acid in the distillated water was used.

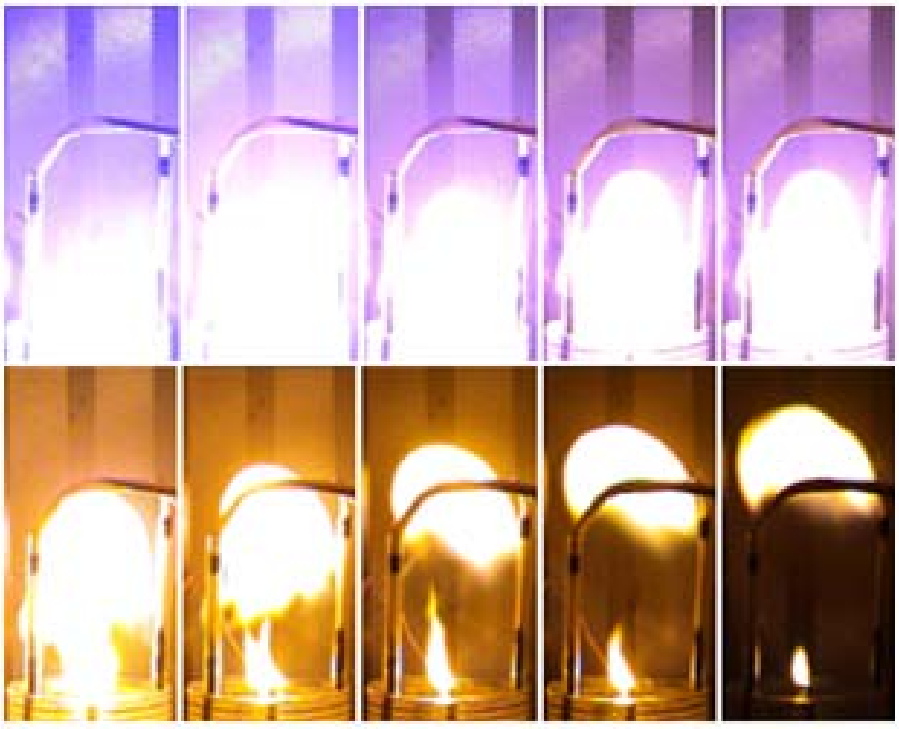

Fig. 4. *Images of the discharge taken with the interval 20ms in the case of electrolytic anode at the initial storage capacitor voltage 5 kV (HNO_3).*

Fig. 5. *Images of the discharge taken with the interval 20ms in the case of electrolytic cathode at the initial storage capacitor voltage 5 kV (HNO_3).*

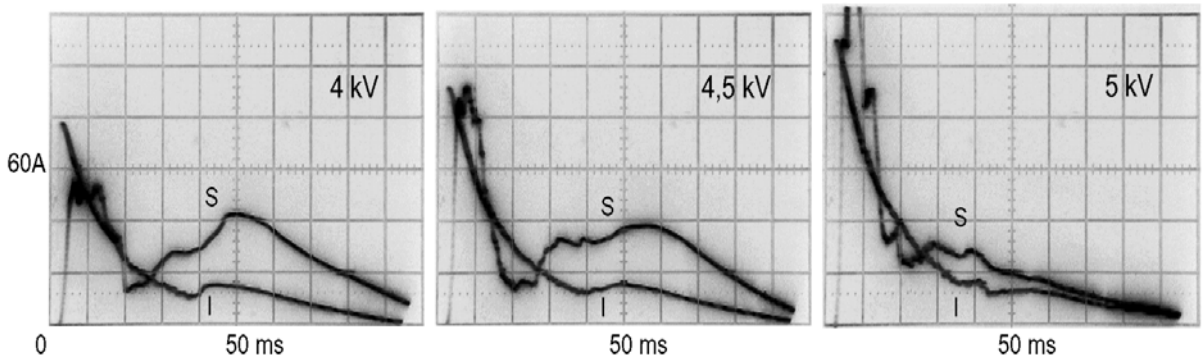

Fig. 6. *Current (I) and intensity of optical radiation (S) of the discharge in the case of electrolytic cathode on the base of HNO_3 at different initial capacitor storage voltages.*

Figures 4 and 5 represent a videorecording of the discharge at different polarities. The discharge with the electrolytic cathode on the base of HNO_3 similarly to the case when a NaCl solution was used has a shorter lifetime of the afterglow relative to the case of the electrolytic anode.

With increasing of the initial storage capacitor voltage this difference intensifies, the radiation maximum at reverse polarity disappears (Fig. 6), and the object practically is not forming.

On the base of the videorecording data the following differences in behavior of the erosional jet from the central electrode depending on the discharge polarity can be noted. At the normal polarity of the water electrode the erosional particles which have a positive charge form a relatively thin upward directed jet. On the stage of a vortex formation under influence of the aerodynamic deceleration the substance of the cathode jet flows around the chemically active substance volume and forms an "envelope". At opposite polarity, the dust particles under influence of the electric field get into interior of the chemical plasma volume which results in a more rapid decay of the plasma.

So, the comparison of Gatchina's discharge characteristics at different polarity revealed some of its features, the common nature of them, by our opinion, consists, firstly, in low mobility of hydrated charge carriers, and secondly, in a short deactivation time of the chemically active substance, created from water by the discharge. The former determines the existence of a special form of the glow erosional discharge characterized by a significantly (about three orders of magnitude) lower current density at the anode [5-7]. The later necessitates some techniques for a compulsory formation of the autonomous object complicating related physical conditions because the self-structuring processes is longer than self-decay of the water-based chemically active plasma.

3. Discharge of a small current

To study of a contact area of the discharge with water electrode the experiment with high-voltage discharge within a range of currents characteristic for a glow discharge has been carried out. Distilled, tap water or water with addition of baking soda poured in a glass jar of 19 cm in diameter and 17 cm in depth served as high-voltage electrode. The carbon rod 0.8 cm in diameter fixed on a dielectric rod with possibility of moving relative to the water surface was the grounded electrode. The source of DC voltage up to 25 kV with possibility of the polarity switch and the maximum current up to 200 mA has been connected through the limiting resistor 40 – 540 kOhm to the coal anode which has been isolated by a glass tube and lowered in water. Images were taken by means of videocamera SONY HDR-HC9 operating at DV-mode with a speed of 50 or 200 fields per second and resolution of 720x576 pixel.

Approach of a carbon electrode to a water surface up to characteristic distance [7] led at first to occurrence of a corona discharge with a depression on the water caused the action of an ionic wind and then to a streamer breakdown similar to [1] and to setting up of the discharge. On Fig. 7 images of discharges including the area of contact with water at different conductivities are presented. It is clearly visible that various ordered structures in the form of circles, rings, wheel spokes and their combination have been formed at the water. At the greatest concentration of a solution-cathode the yellow torch at its surface was present when the anode was both carbon and aluminium. At a current 150 mA the diameter of the anode spot at the surface of distilled water was more than 3 cm and it corresponds to average density of a current ~ 20 mA/cm^2. However the luminescence of the spot had a bright external border.

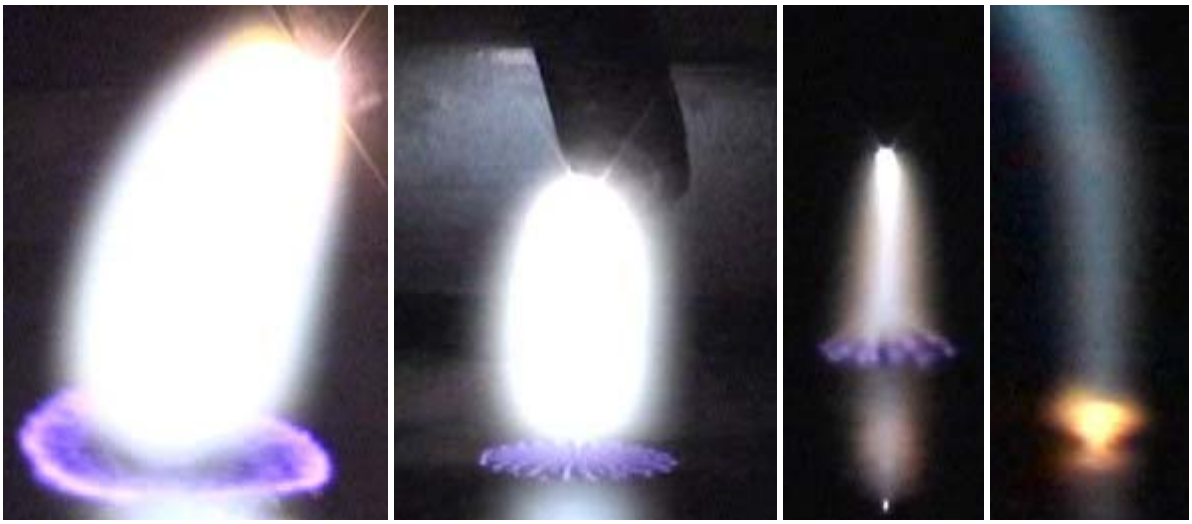

Fig. 7. *Discharge images (from left to right):*
- the anode – distilled water, coal cathode;
- the anode – tap water, coal cathode;
- the cathode – tap water, coal anode;
- the cathode – water with baking soda addition, aluminium anode.

Depression on a water surface at the spot was greatest for the anode on the basis of the distilled water, also as well as in the case of a corona dischage it point out to presence of a stream of gas. Intensity of the luminescence of a plasma column above the water anode rose sharply at some distance from the water surface which increased with moving off of the carbon cathode up to some limit (Fig. 8). When magnitude of the current was of order of tens milliampers and more, further

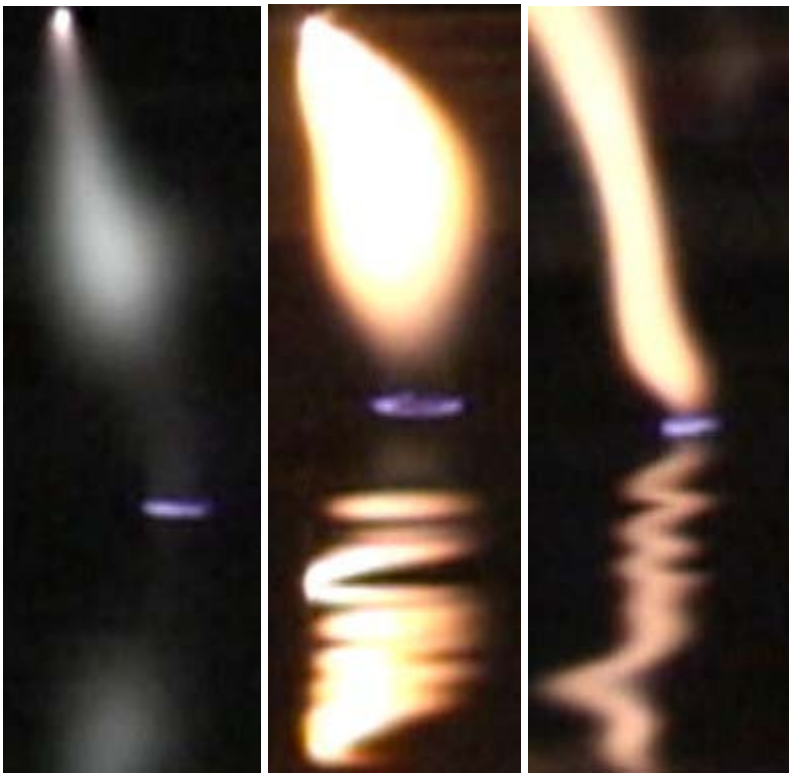

Fig. 8. *Limiting height of dark area at a current of 15 mA and voltage of 12,5 kV (at the left) and at more voltage and current (the rest).*

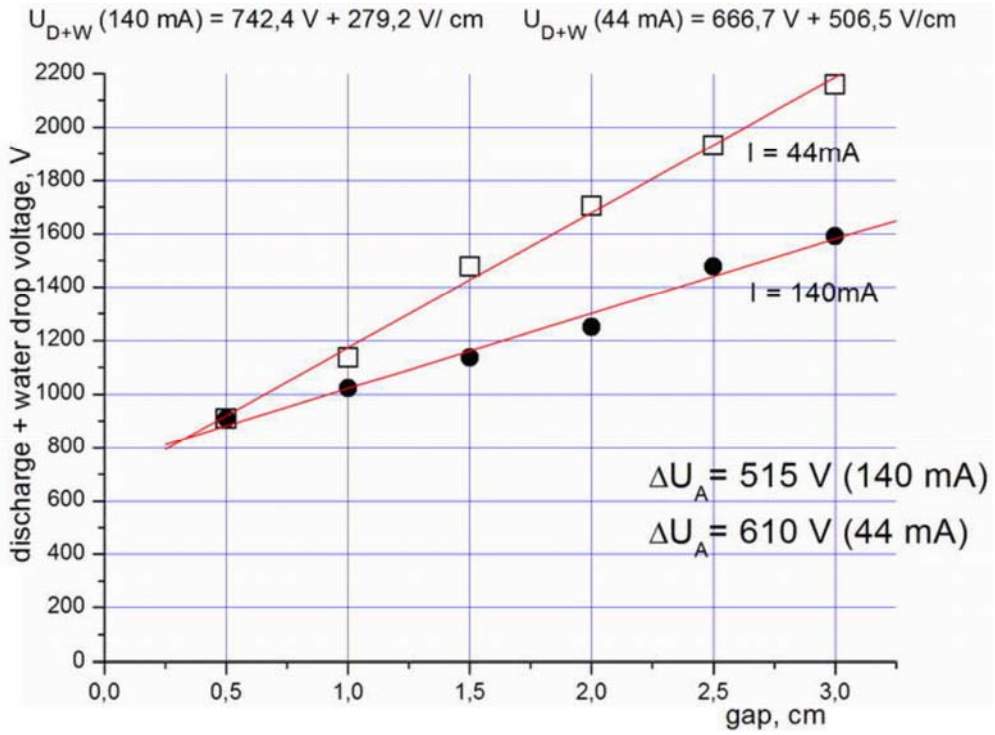

Fig. 9. *Dependence of the total voltage drop at the water and the discharge on the gap distance for two values of the current: 44 mA and 140 mA.ΔU_A – the anode drop extrapolated to a zero gap.*

increase in the interelectrode distance led to formation of the plasma column.

For comparison of strength of electric field in a regular part of the discharge and in thin near-surface area the dependence of voltage at the anode having been at the jar's bottom on the height of the carbon cathode above the water surface was measured in a range from 0,5cm to 3 cm for two values of a current: 140 mA and 44 mA (Fig. 9). The voltage drop on water was defined when the cathode had been dipped in water and proved to be 227.3 V for the big current and 57 V for the small one. Then the anode drop ΔU_A extrapolated to a zero gap, was 515 V and 610 V accordingly. If to consider a thickness of dark area at the big current equal to ~ 2mm the voltage drop on it will 571 V that coincides with the minimum magnitude of interelectrode voltage drop in Gatchina's discharge [4]. The field strength in it is about ~ 2.85 kV/cm that is 10 times more than in a regular part of a plasma column.

For the chosen voltage there was the optimum value of a current corresponding to the greatest height of area in which the luminescence is very weak despite the current value being two order of magnitude greater than the maximum current of a corona discharge at the same voltage (Fig. 8 on the left).

Further increase in the interelectrode distance led to occurrence of instability of a picture of the discharge, character of which depended on current and voltage values. In the optimum mode the anode spot started moving under the influence of a steam jet and new spots could arise on smaller distance from the bright cathode part of a plasma column. At such secondary breakdown the field strength is many times lower than at primary breakdown, nevertheless the torches which were not crossing completely a dark area could develop from the centers of spots. Different spots with torches co-existed some time (Fig. 10 on the left). At higher currents the torches appearing from new anode spots created a flashover of the gap and formed shorter plasma column (Fig. 10 on the right). The coexistence of anode spots was limited by time of development of the new plasma column and degradation of the old one. At further growth of the current the time of such secondary breakdown decreased but remained two orders of magnitude more than time of primary breakdown [3], the electric strength being lowered 10 times.

On Fig. 11 an example of the oscillogram of a discharge current break-off at lengthening of a plasma column (under the rectifier voltage of 15 kV and 290 kOhm limiting resistor) is represented. The first stage — a relaxation of the self-maintained discharge was characterised by growth of excess of its voltage drop above the voltage drop at the limiting resistor and by smooth reduction of a current. At the second stage the magnitude of the current (less than 1 mA) was determined by a relaxation of plasma as source of electrons and the

Fig. 10. *Torches not resulting (at the left) and resulting in flashover (on the right).*

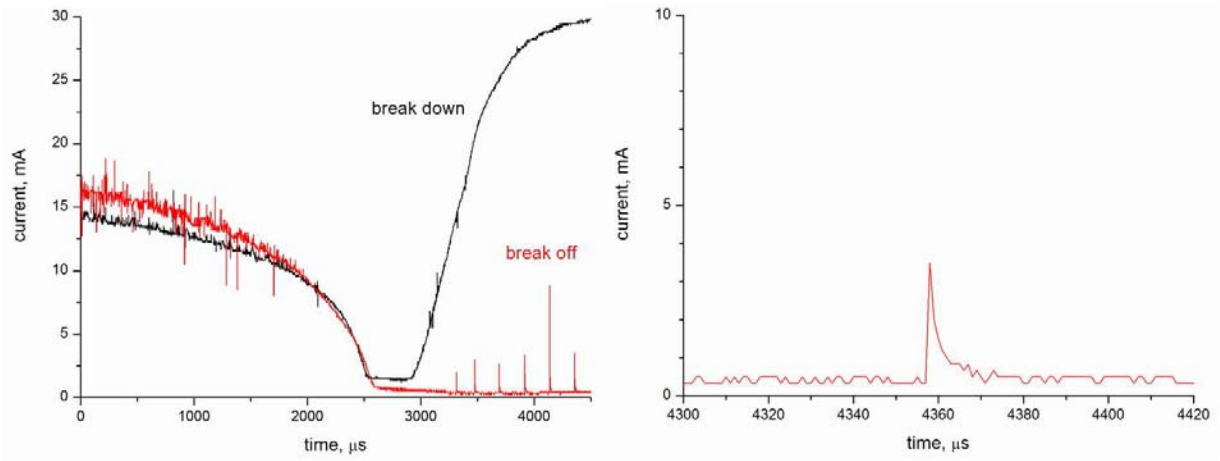

Fig. 11. *At the left – examples of oscillograms of the current for two possible variants of a non-stationary phase of the discharge: resulting in transition to the semi-self-maintained discharge and resulting in breakdown by shorter way. On the right — the characteristic form of current impulses.*

electric field strength. The characteristic form of the current impulses (Fig. 11 on the right) corresponds to the avalanche nature of the semi-self-maintained discharge. The voltage increase at a part of the relaxing plasma close to a cathode can prove to be sufficient for increase of a current of the semi-self-maintained discharge by shorter way and an avalanche formation (Fig. 10 on the right). In case of the breakdown beginning actually after the end of the stage of the self-maintained discharge, as it takes place at the oscillogram (Fig. 11 at the left), it is possible to find breakdown parameters. The current at the initial stage is ~ 1 mA, its duration – about 0.4 ms, a total time up to a current setting up – about 1 ms, so speed of a streamer movement is ~ 100 m/s.

Besides breakdowns from the water surface, the breakdowns between different parts of the curved plasma column were observed also (Fig. 12). They developed so slowly that change of a

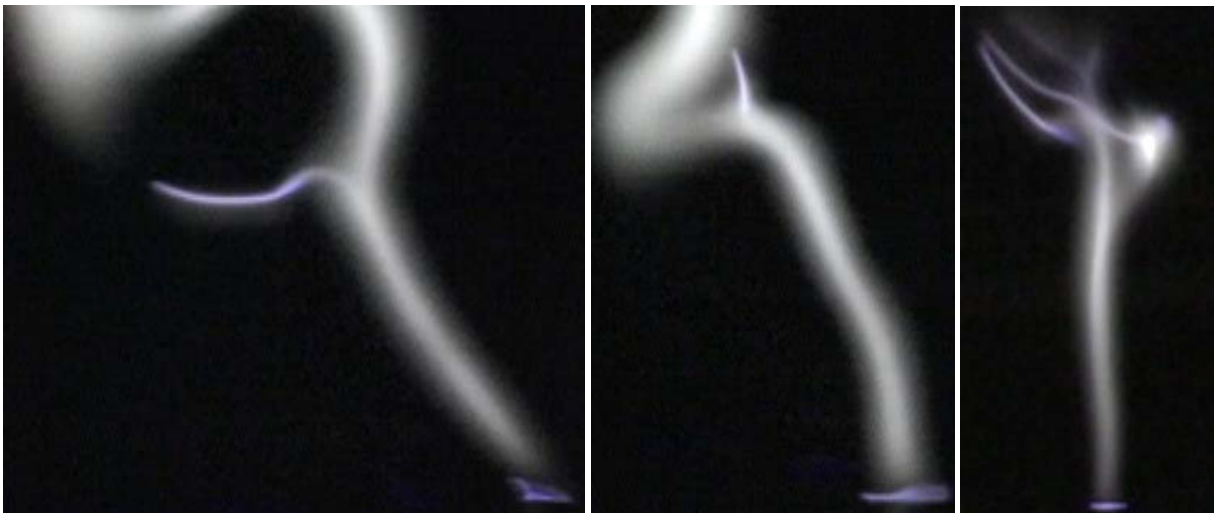

Fig. 12. *Development of breakdowns at the arched parts of a plasma column and a group of the not completed streamers (on the right).*

column configuration often leaved them not finished. "Slow" streamers extended exclusively in the electric field direction.

4. Conclusions

From the obtained experimental results it is possible to conclude that in the Gatchina's discharge at the water surface the dark plasma layer exists limited from above by chemically active plasma. It represents not self-sustained zone of the discharge which arises under the influence of evaporated water and receives electrons from the top plasma layer. The low temperature of steam in it leads to a steady hydrating of charges, decrease of their mobility and suppression of radiation. The discharge expansion on the water surface after streamer stages is connected with formation of a layer of chemically active plasma and points out that not self-sustained zone of the discharge is in a saturation mode. In case of opposite polarity on the water surface the glow discharge is set up, the normal current density of which repeatedly exceeds average one in a cathode spot. It leads to parting of a cathode layer into group of separate cathode spots and to entering of the dissolved substance into the plasma due to a droplet phase at the erosional stream.

References

1. Egorov A.I., Stepanov S.I., Shabanov G.D. *Laboratory demonstration of ball lightning*. UFN. 2004. V.174. No.1. P.99–101.
2. Emelin S.E., Pirozerski A.L., Vassiliev N.N. *Dust-gas fireball as special form of electric erosive discharge afterglow*. Proceedings of ISBL-06, 16-19 August 2006, Eindhoven, The Netherlands. Preprint: http://arxiv.org/abs/physics/0604115
3. S.E. Emelin, A.L. Pirozerski, *Some questions on the dense energy plasma-chemical fireball*, Chemical Physics V.25 N.3 (2006) P.82–88.
4. Emelin S.E., Astafiev A.M., Pirozerski A.L. *Investigation of space-time structure of the discharge with an electrolytic anode and face-type, air half-space directed cathode (Gatchina's discharge)*. Proceedings of ISBL-08, 16-19 July 7, 2008. Kaliningrad, Russia. P. 42.
5. QiangWang, Ivanka Koleva, Vincent M. Donnelly and Demetre J. Economou. *Spatially resolved diagnostics of an atmospheric pressure direct current helium microplasma*. J. Phys. D: Appl. Phys. **38** (2005) 1690–1697.
6. QiangWang, Florian Doll, Vincent M. Donnelly, Demetre J Economou, Nader Sadeghi and Gerhard F. Franz. *Experimental and theoretical study of the effect of gas flow on gas temperature in an atmospheric pressure microplasma*. J. Phys. D: Appl. Phys. **40** (2007) 4202–4211.
7. Peter Bruggeman and Christophe Leys. *Non-thermal plasmas in and in contact with liquids.* J. Phys. D: Appl. Phys. **42** (2009) 053001 (28pp).

5.5.NEW METHOD OF ELECTRIC POWER EXTRACTION FROM HIGH-SPEED PLASMA FLOW

Klimov A., Polyakov L., Tolkunov B.
Joint Institute for High Temperatures of Russian Academy of Sciences, Moscow, Russia

klimov@ihed.ras.ru

Abstract. New conception of electric power extraction from charged plasma creation in high-speed airflow is considered in this work. It is revealed that strong electric charge separation in plasma formation in high-speed airflow is possible. It is demonstrated that a charged plasma formation can control of airflow near body in some regimes also. The series of recent plasma aerodynamics observations are discussed from the point of view of charged plasma effects involved. The common physical approach is proposed to treat and understand such phenomena. This approach is based on detailed evaluation of the ion current effects, which are more pronounced in regions of space charged formed by convection, diffusion of charged particle in external electric field

Nomenclature

HF = high frequency
PA = plasma aerodynamic
PG = plasma generator
AC = alternative current
DC =direct current
LP = longitudinal plasmoid
F_i = pulse repetitive frequency
I_d = electric discharge current
M = Mach number
V_{af} = airflow velocity
N_d = power input in plasma
P_{st} = static pressure
T_g = gas temperature
φ = electric potential

It was revealed that there is charged (non-neutral) plasma interaction with high-speed airflow in some plasma aerodynamic experiment [1-10]:

- DC discharge plasma near conical model N with needle in supersonic airflow at Mach number 4, (P_{st}~40 Torr) [1-3], fig.1,
- Combined discharge plasma (DC+ electron beam) near spherical model at Mach number 2, (Pst~20 Torr) [4-6], fig.3,
- Charged DC plasma near plate model [4-6],
- DBD discharge plasma near wing model [9],
- and others.

Remind that it is possible to obtain AC electric current rectification in surface discharge plasma near model N in high-speed airflow, fig.2, [1]. It was revealed that this electric current rectification is connected with ion mass difference and their mobility of charged particles (light electrons and heavy ions) in high-speed airflow namely at external electric field namely. Analyzing the figure 2 one can see that there are two different regimes of ion transportation (drift) by external electric field in high speed flow:

1. Ion counter-flow to airflow direction.
2. Ion co-flow to airflow direction

The electric current is switched off in the regime #1 at definite airflow velocity V_{af}. Note that simulation of this experiment proves this result [6].

It is interesting to note that that drag force depends on direction of external electric field, fig.1. Maximal drag decrease is realized at AC current namely.

Dependence of drag decrease on electric field direction is studied in combined discharge (electron beam+ DC discharge) also [4-6], fig.3. One can see that drag's decrease of spherical model depends on electric current direction.

There are the simulations [6], which confirm that some of the obtained experimental results may be explained by different electrode arrangement on the model's surface and different electric field orientation.

Note that there is a very large mass difference between cluster ions and electrons in cluster plasma. So, charge separation by external electric field in high speed airflow may be effective in cluster plasmoid also. Our experiment proves this conclusion. Motion of a cluster plasmoid in the external electric field is shown in fig. 4, 5. One can see that this charged plasmoid is stopped by electric field directed along its motion and it accelerates in the field of opposite direction.

The phenomenon of charge separation in plasma formation in high-speed airflow by external electric field is studied in [4-6,10] in detail.

Experimental set up #1 used in this work with three- electrode configuration is shown in fig.6. DC arc plasma generator (PG) is used in this set up.

Parameters of this PG are the followings:

- Electric DC current 30-40 Amp
- DC voltage 110-140 V
- Plasma temperature 4000-6000K
- Plasma jet velocity <1 m/s
- Working gas water vapour

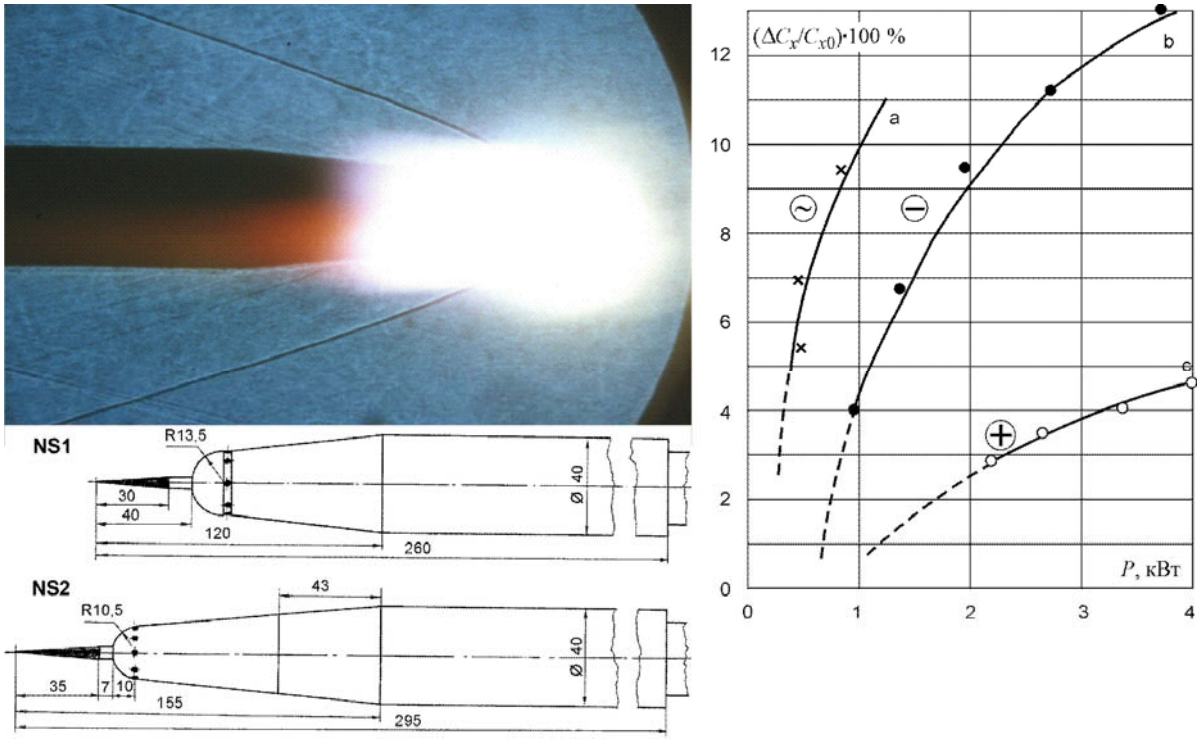

Figure1. Model NS1 (NS2). Drag coefficient dependence on electric power input in plasma and electric field direction. *Mach number 4, P_{st}~40 Torr. DC discharge, I_{DC}~1 Amp, (+)- needle electrode-anode, (-)-needle electrode-cathode, (~)-AC current*

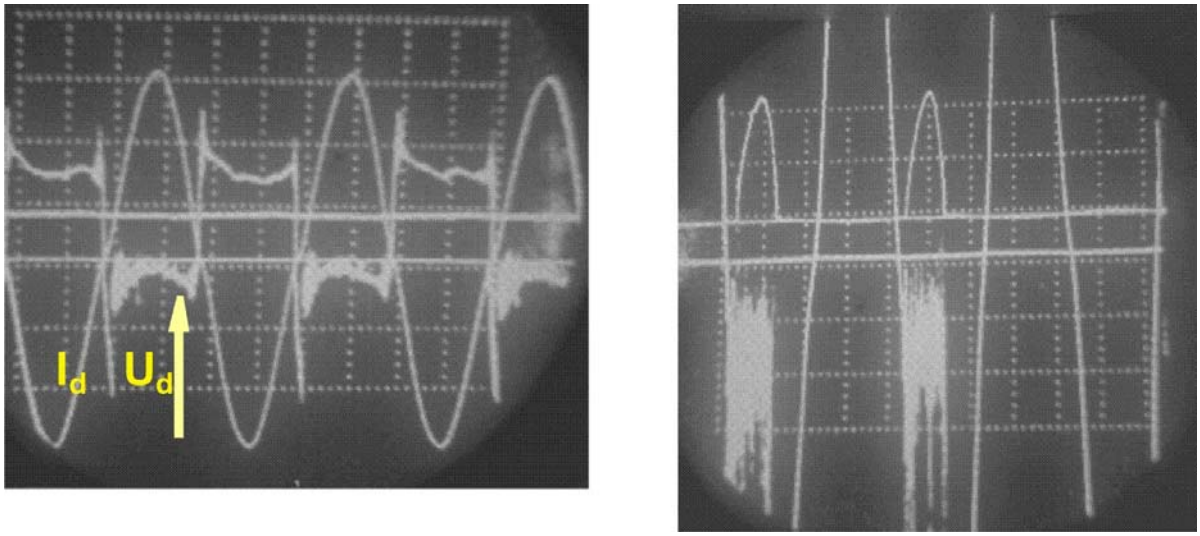

Figure 2. AC discharge near model NS1. *Right- airflow off, left- supersonic airflow on and ion counter-flow. Mach number 4, P_{st}~40 Torr, 5ms/div*

Third ring electrode is used to separate of charged particles. External electric potential of third electrode is varied from φ_1= – 4kV up to φ_2=+4 kV. Voltage probe Tektronix-2048 measures an electric potential of plasma jet. Distances between PG, ring electrode and voltage probe are varied in experiment. The typical voltage signals of charged plasma jet are shown in the fig.7. One can see that there is considerable difference between two regimes of separator operation at the φ_1= – 4kV and the φ_2=+4 kV. The measured negative potential of plasma jet is about φ^*= – (3÷4) kV at ring electrode potential φ_1= – 4kV. The positive measured potential of plasma jet is about φ^*= + (0,5 ÷1) kV at ring electrode potential φ_2=+4kV. There are the different shapes signals also.

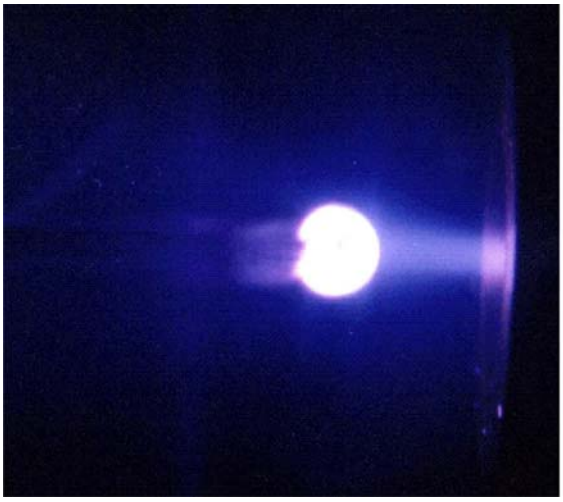

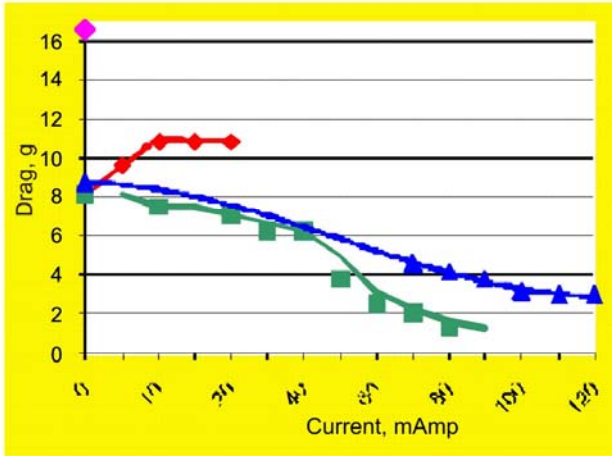

Figure 3. Spherical model with combined discharge plasma (DC+ EB). *Drag coefficient dependence on DS electric current and electric field direction: red-ion counter-flow, blue – ion co-flow + EB, green- ion co-flow + EB off. M~ 1,6; P_{st}= 15 Torr, I_{EB}~ 10 mA, I_d=200 mA, D= 10mm*

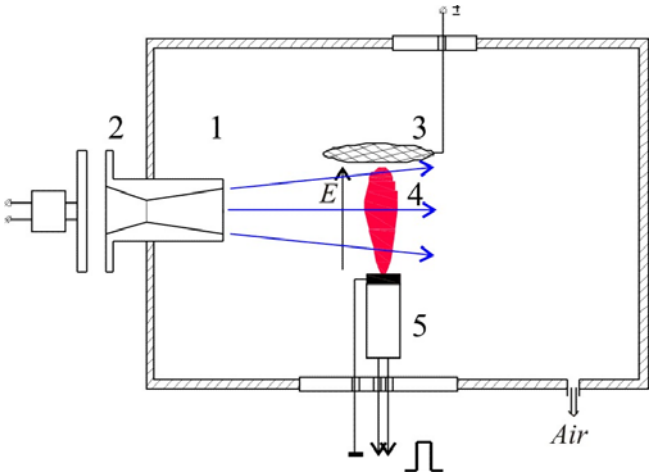

Figure 4. Scheme of experiment with charged cluster plasmoid. *1- working vacuum section, 2- nozzle with valve, 3- grid electrode, 4- charged cluster plasmoid, 5- plasma generator*

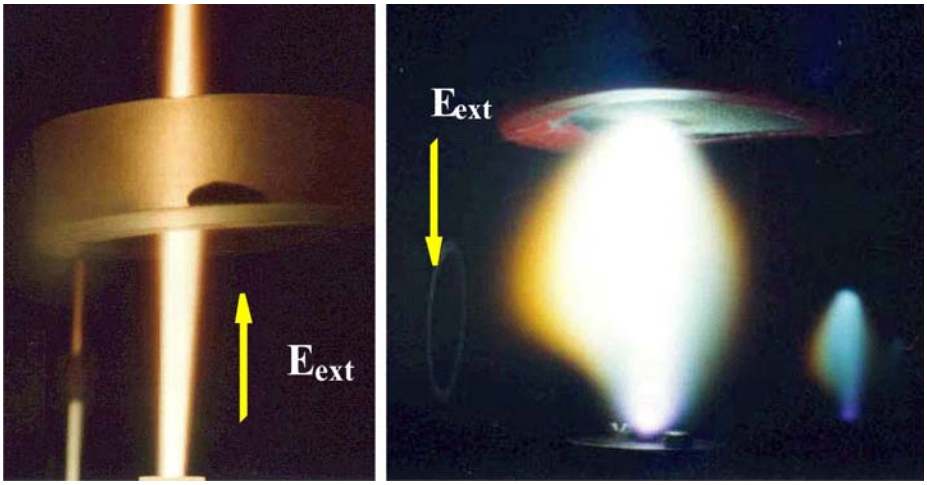

Figure 5. Charged cluster plasmoid in an external electric field. *Plasma generator parameters:*
I_p~100 Amp, pulse duration T_p=1-10 ms, pulsed power N_p~10^5 W, pulse repetitive frequency F_p<50Hz. External electric field ~1kV/cm

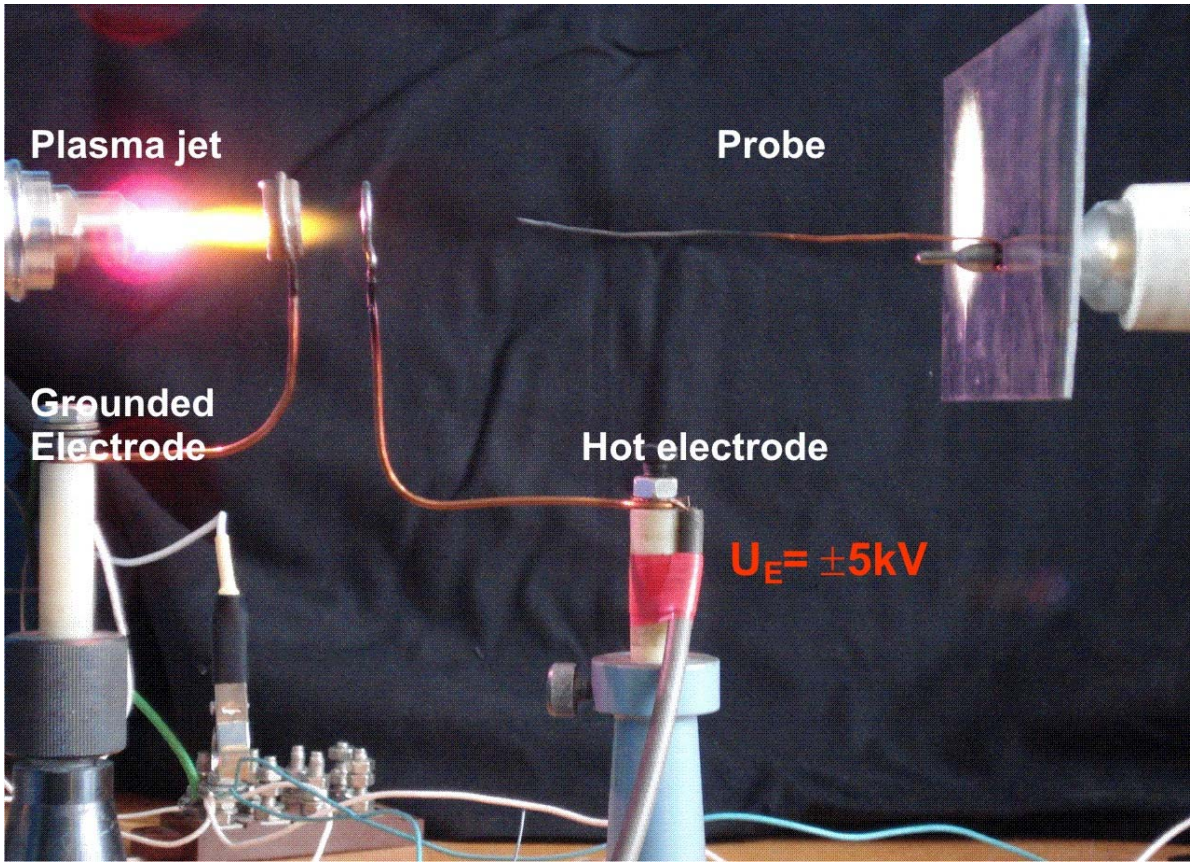

Figure 6. Experimental setup #1

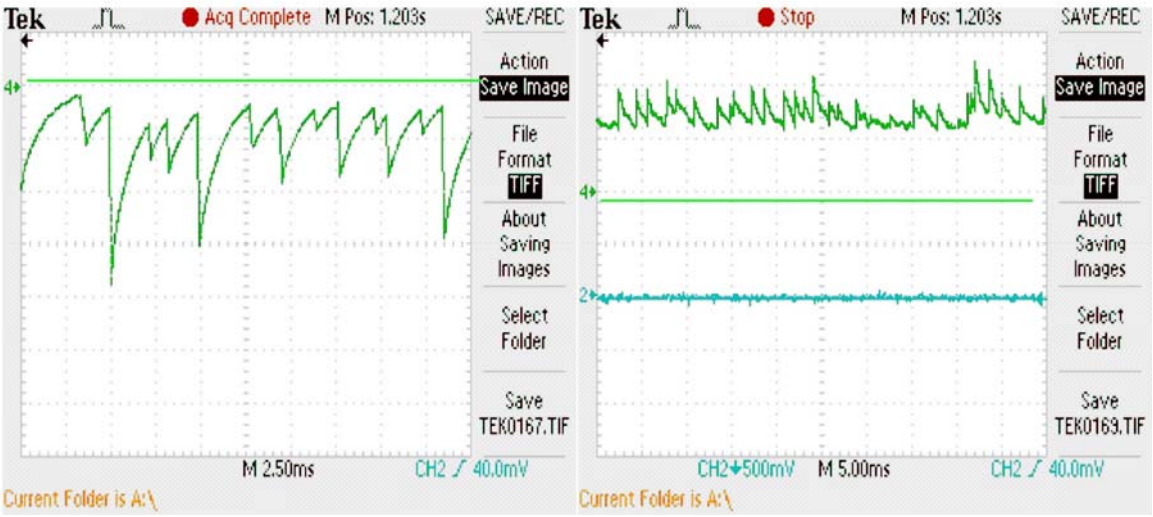

Figure 7. The typical probe's signals of plasma jet at different external electric potential φ. *Left picture-* $\varphi_1 = -4kV$. *Right-* $\varphi_1 = -4kV$. K_{V1}=1:1000, K_{V2}=1:500

Another experimental set up #2 with tree-electrode configuration is shown in the fig.8. this set up consists of three-electrode configuration (1, 2), subsonic nozzle, electric probe (3). Three-electrode configuration is arranged on the dielectric plate (PMMA). Needle electrode (plasma jet electrode) is located above this plate. Another grounded electrode is placed on plate surface. Distance between them is varied from 1mm up to10 mm. Transverse electric discharge is created in airflow by these electrodes. Top needle electrode can be anode or cathode.

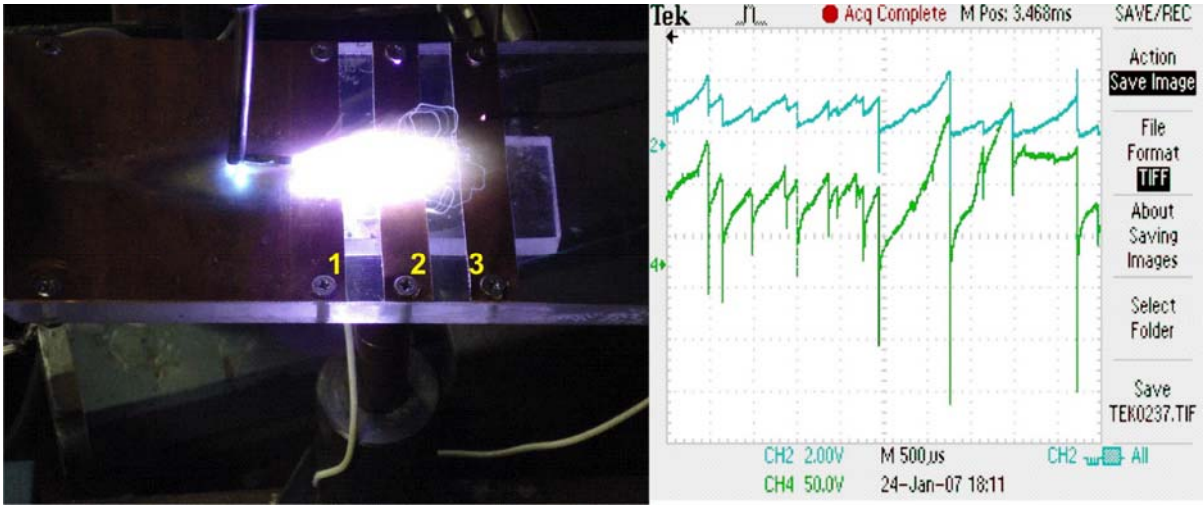

Figure 8.Transverse electric discharge created by three-electrode configuration in airflow - left. *1- main electrodes (needle+ grounded plate), 2- third electrode- separator, 3- probe electrode, Electrode voltage signal (top) and probe signal (down) – right.* I_{DC}*~ 1 Amp,* P_{st}*~1 Bar, M< 0.1,* U_3*=-3kV, K(*U_2*)= 1:1000, K(probe)=1:1*

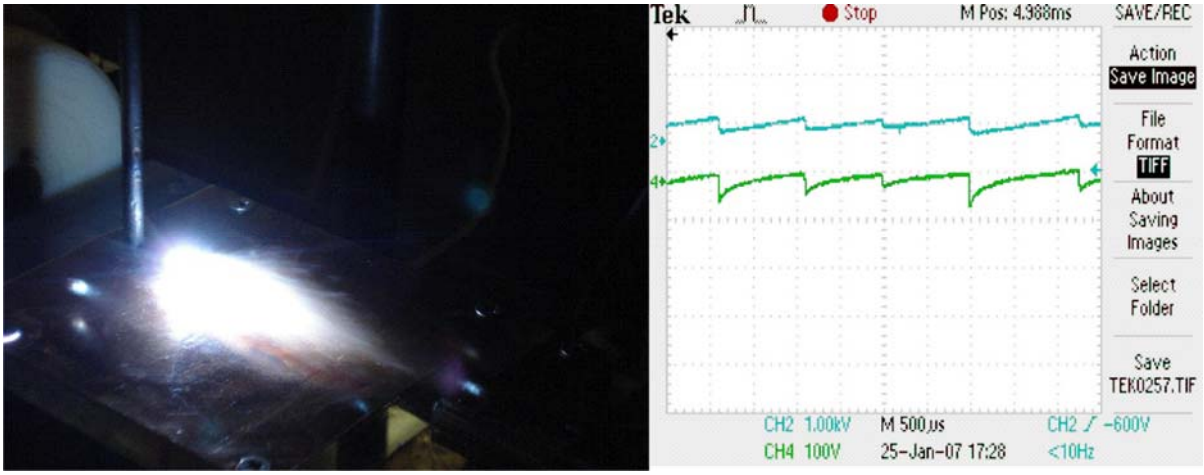

Figure 9.Transverse electric discharge created by three-electrode configuration in airflow - left. Electrode voltage signal (top) and probe signal (down) – right. I_{DC}*~ 1 Amp,* P_{st}*~1 Bar, M< 0.1,* U_3*=+3kV, K(*U_2*)= 1:1, K(probe)=1:1*

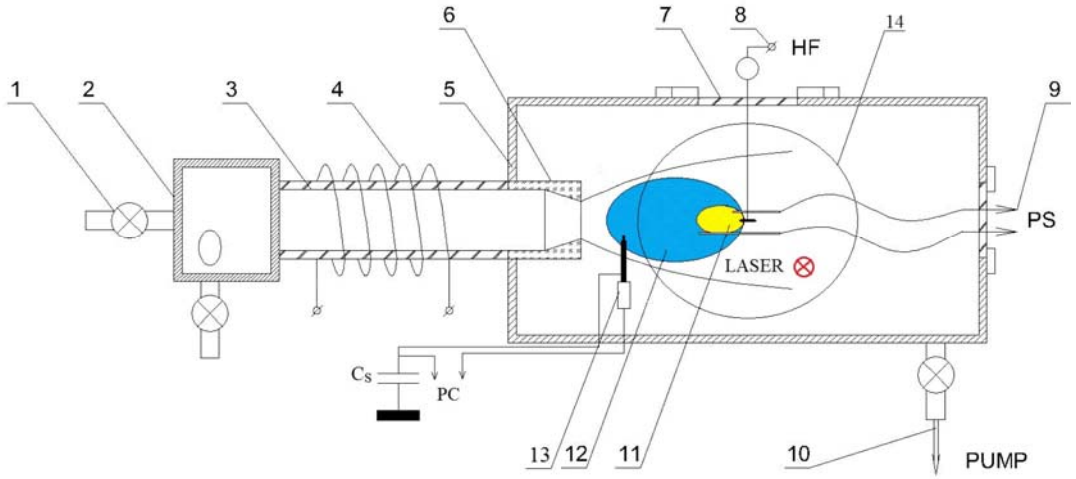

Figure 10. Scheme of the blow-down experimental set up SWT-2. *1,2-swirl generator; 3-preheater, 4- electric heater, 5-test section, 6- conical nozzle, 7- dielectric window,8-HF electrode,9-presure sensors,10- vacuum pump,11-constricted white plasmoid, 12- blue plasma halo, 13- ballast resistance, 14-optical window*

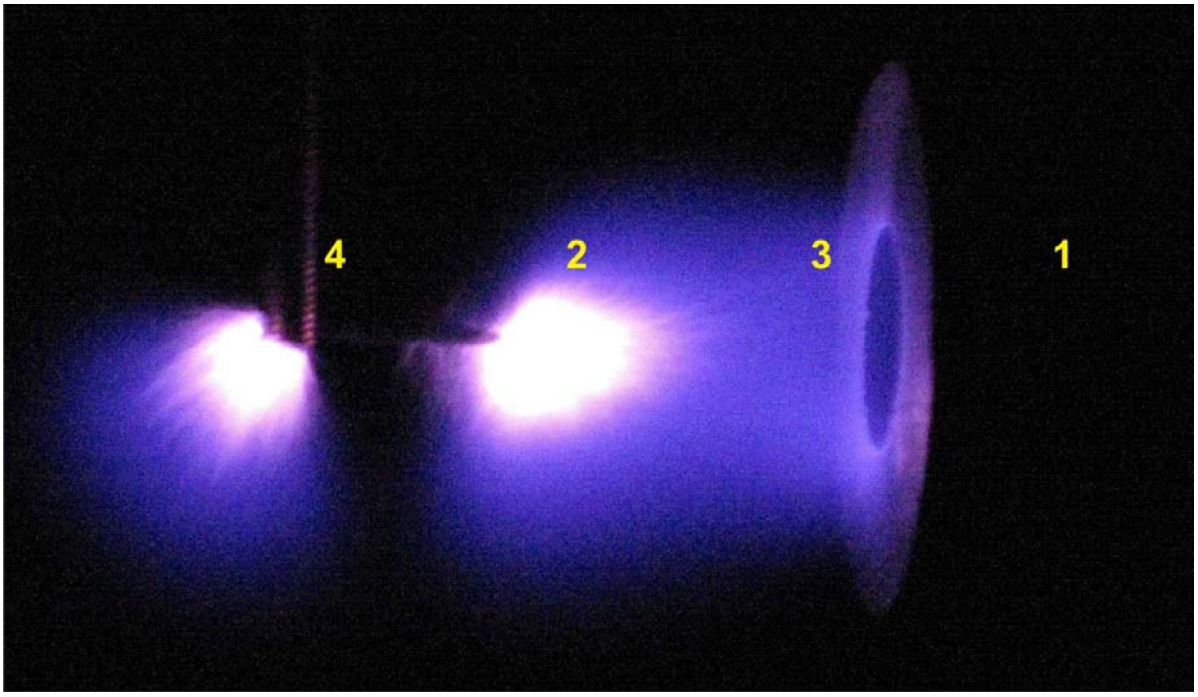

Figure 11. Typical pictures of plasma formation created by CHFD in high-speed swirl flow. *SWT-2. Longitudinal charged HF plasmoid with blue plasma halo at P_{st}~300Torr, V_{ax}~90m/s. 1-nozzle, 2- white constricted plasmoid, 3- blue plasma halo,4- needle electrode*

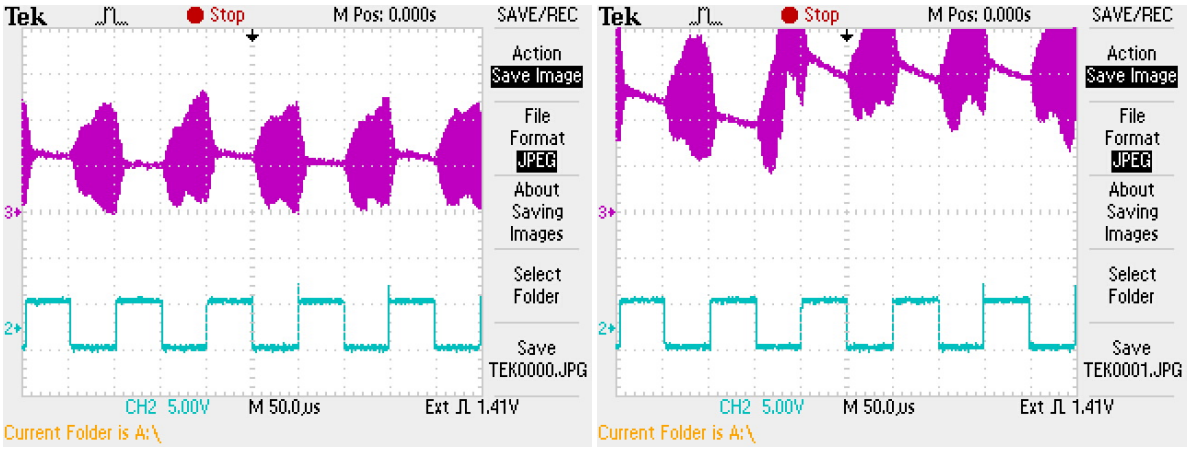

Figure 12. Typical HF plasmoid's electric potential at different experimental conditions. *SWT-2. Left.- longitudinal charged HF plasmoid with blue halo at P_{st}~300Torr, V_{ax}~90m/s*
Right.- longitudinal charged HF plasmoid with blue halo at P_{st}~300Torr, V_{ax}~140m/s

Experimental conditions are the following:

- Electric DC current ≤ 1Amp
- Voltage U_2 between power electrodes 1,2 ≤ 6kV
- Static pressure ~1Bar
- Airflow velocity ≤ 30m/s
- Third electrode voltage $-4kV<U_3<+4kV$

The typical pictures of this electric discharge at different values of U_2 and U_3 are shown in the fig. 9. One can see that different plasma structures are created in airflow at different values of U_3 and U_2. There is bright arc plasma and thin streamers (filamentary discharge) simultaneously in high-speed airflow at the following conditions:

– needle electrode is anode and third electrode has positive potential (separator for electrons).

On another hand there is only arc plasma in airflow at the following conditions:

– needle electrode is anode and third electrode has negative potential (separator for electrons).

This result is predicted by our simulation. There is considerable charge separation of a plasma jet by the three electrode configuration and electric breakdown between charge plasma formation and the grounded electrode in first regime. It is

interesting to note that the typical dimension of charge separation region is very small about 1-2 cm in this experiment. Filamentary plasma formation ("streamer") creation in airflow is recorded by electric probe also, fig. 16. One can see that there is sharp negative pulses with amplitudes of about several kV connected with "streamer" creation.

Study of a longitudinal plasmoid (LP) created by capacity coupled HF discharge (CHFD) in high-speed swirl airflow is carried out in the work [8]. The experimental set up SWT-2 used in this work is shown in the figures 10, 11. Swirl generator (1) is connected with vacuum chamber by conical nozzle (2).

The conical nozzle has the following dimensions and parameters:

- Contraction angle 60^O
- Outer diameter 20 mm

The experimental conditions are the followings:

- Mach number of axial flow $M_x<0.3$
- Mach number of tangential flow $M_t<0.3$
- Testing gas Airflow
- Flow static pressure P_{st} ~100 Torr

The HF plasma generator has the following parameters:

- Pulsed HF power N_{HF}=200W
- HF frequency F_{HF} =1.2 MHz; 13.6 MHz
- Operation regime continuous, and pulse repetitive
- Modulation frequency $F_M<20$kHz
- Pulse duration $T_i=50\div500\mu$s

The typical picture of a longitudinal plasmoid (LP) created by CHFD in *swirl high-speed airflow* is shown in the fig.11. One can see that there is a compact homogeneous constricted white plasmoid (2) and extended blue plasma halo (3) in swirl flow at the large swirl parameter S~1.

It is revealed that it is possible to create of a positive charged plasmoid in *high-speed swirl airflow* at high HF power input in plasma $N_{HF}>800$W and high velocity about $V_{ax}\sim V_\tau>70$m/s, fig.12. Bright white spherical plasmoid ~10mm diameter is created near needle HF electrode in this regime. External blue plasma halo 30mm diameter is created around this plasmoid. Electric potential of this plasma halo measured by electric high voltage probe Tektronix. The typical value of this electric potential is about $\varphi\sim+1$-3 kV, fig.12. This value is depended on value N_{HF}, pulse repetition frequency F_i and airflow velocity $V_{ax}\sim V_\tau$. The maximal value $\varphi\sim+3$kV is measured at maximal value $N_{HF}\sim$ 800W, maximal pulse repetition frequency F_i ~10 kHz and optimal airflow velocity $V_{ax}\sim V\sim$ 80-150 m/s. It is not clear why measured plasmoid's potential is positive? This question will be cleared in future experiment.

Note that it possible to create *DC power supply* by this plasma-vortex convertor, fig.10. The possible design of this plasma-gas dynamic convertor is very simple. It consists of ballast resistance (13) and capacity storage C_s. Main question is efficiency of this plasma-vortex convertor in this regime. This question is studied now in detail. Now this value is about 10-30% of mechanical power of incoming swirl flow.

Conclusion

1. New conception of electric power extraction from charged plasma formation created by HF discharge in high-speed swirl airflow is considered in this work.
2. It is revealed that a strong electric charge separation in plasma formation in high-speed airflow is possible.
3. A number of plasma aerodynamic experiments are discussed from the point of view of charged plasma effects involved. Our approach is based on detailed evaluation of the ion current effects, which are more pronounced in the regions of space charge separation formed by convection, diffusion of charged particle in external electric field

References

1. Beaulieu W., Byturin V., Klimov A., et. al., Plasma Aerodynamic WT Tests with 1/6 Scale Model. Proc. of the Workshop on Magneto-Plasma-Aerodynamics in aerospace applications, Moscow, March 24-25, 1999, IVTAN, P.44
2. Ershov A.P., Klimov A.I., Timofeev I.B. et. al., Flow Around Body and Characteristics of AC/DC Discharges in Plasma Aerodynamic Experiment. Proc. 2nd WIG Workshop. Norfolk. April 24-25. 1998, P.59.
3. Гридин А.Ю., Ефимов Б.Г., Забродин А.В., Климов А.И. и др., Расчетно-экспериментальное исследование сверхзвукового обтекания затупленного тела с иглой при наличии электрического разряда в его головной части. Препринт ИПМ № 19,1995, С.31
4. Bityurin V., Bocharov A., Klimov A., Leonov S., Analysis of Non-Thermal Plasma Aerodynamics Effects, In: 44rd AIAA Aerospace Sciences and Exhibit, Jan 9-12 2006, Reno, NV. AIAA Paper 2006-1209, P.8
5. Klimov A., Byturin V., Non-Thermal Plasma Aerodynamics Effects, 43th AIAA Aerospace Sciences Meeting & Exhibit. AIAA 2005-0978, 10-13 January 2005, Reno/ NV, p.9

6. Bityurin V., Bocharov A., et.al., Numerical Simulation of the Discharge in Supersonic Flow Around a Sphere, AIAA 2007-0223 Paper, 45th AIAA Aerospace Sciences Meeting & Exhibit, 8-11 January 2007, Reno, NV, p.14
7. Klimov A., Bityurin V., Serov Yu., Non-Thermal Approach in Plasma Aerodynamics, 39th AIAA Aerospace Sciences Meeting & Exhibit. AIAA 2001-0348, 8-11 January 2001, Reno/ NV, p.10
8. Klimov A., Moralev I., et.al., Study of a Longitudinal Plasmoid Created by Capacity Coupled HF Discharge in Vortex Flow, AIAA Paper 2009-1046, Proc. 478th AIAA Conf., Orlando FV, 5-8 Jan 2009, P.11
9. Klimov A., Strategy of Plasma Aerodynamic Researches Today, Proc. EUCASS, 2009, P.16
10. Klimov A., Byturin V., Kuznetsov A., Sukovatkin N., Vystavkin N, Van Wie D.M., Plasma-Assisted Combustion, 33rd AIAA Plasma dynamics and Lasers Conference, 11-14 June 2002, Maui, Hawaii, P.10

5.6. PROBABILITY LAW OF MW DISCHARGE IGNITION

Melnichenko D.M
MRTI RAS

The obtained experimental results on powerful MW discharge ignition (breakdown) are compared with theoretical Boltsman's probability function. It is revealed a good correlation between these results. Possible physical explanation of this correlation is discussed in this work.

6.1. DISTRIBUTION OF H2O TEMPERATURE AND CONCENTRATION IN ZONE OF PLASMA-ASSISTED HIGH-SPEED COMBUSTION.

Sergey B. Leonov, Aleksander A. Firsov, Michail A. Shurupov, Dmitry A. Yarantsev
Joint Institute for High Temperature RAS, Moscow, 125412 Russia,
d.yaran@rambler.ru

M.A. Bolshov, Yu. A. Kuritsyn, V.V. Liger, V.R. Mironenko
Institute for Spectroscopy RAS, Troitsk, Moscow reg, 142190, Russia

Abstract. The paper is focused on study of particular mechanisms of plasma impact on high-speed combustion. A tunable diode laser absorption spectroscopy (TDLAS) technique and appropriate instrumentation was developed for the measurement of temperature and water vapor concentrations in reacted gases. The technique is based on the detection of the spectra of H_2O absorption lines with different energies of low levels. Spectra were recorded using fast frequency scanning of a single distributed feedback (DFB) laser. Under conditions of high level of flow disturbances an optimal technique for fitting the experimental spectra was developed based on presentation of the transient absorption spectra as 2D images in the first step of data processing. In the most cases the high signal-to-noise ratio enabled the reconstruction of the temporal behavior of temperature with a resolution of ~1ms. The validated TDLAS technique was applied for detection of temperature and H2O concentration in the combustion zone of a supersonic (M = 2) air-fuel flow. Direct wall-injected hydrogen and ethylene were used as the fuels. The combustion process was initiated and sustained by near-surface electric discharge. The data of DLAS measurements have proved the idea of two-stage mechanism of plasma-assisted combustion.

Introduction.

This study is motivated by our previous experimental results [1] and also by experimental results and modeling of other groups [2-4]. It was expected that the main heat release due to combustion will be within the region of the plasma-fuel interaction. Experiments demonstrated that the main pressure rise was observed far downstream of the electrodes line, with bright luminosity is being observed from discharge region, Fig. 1.

One more result has been recently obtained by group of TRINITY [6]. 1-D simulation of the ethylene/air mixture ignition by the glow discharge and heating at three different initial temperatures predicted two-stage pattern of plasma ignition. Calculated evolution of the gas temperature during ignition is shown on the Fig. 2.

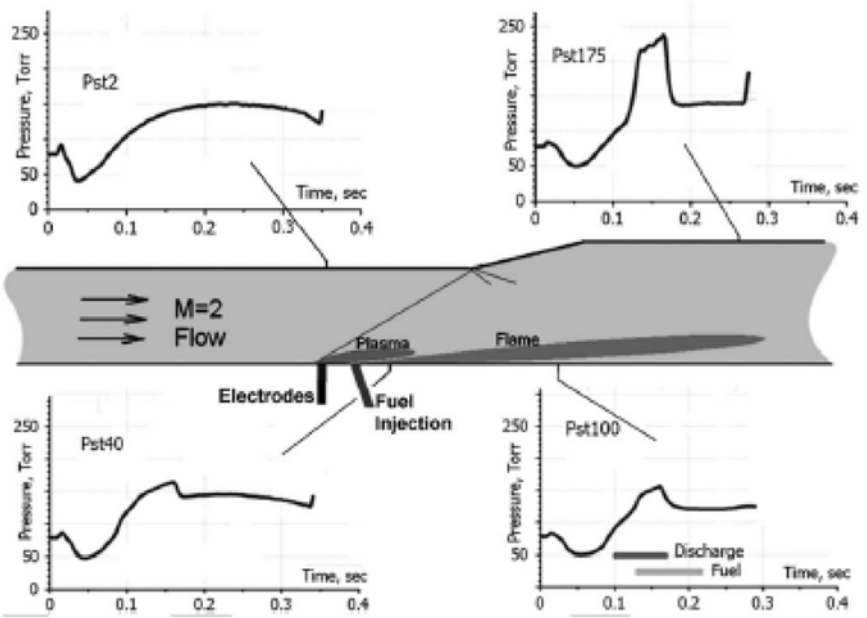

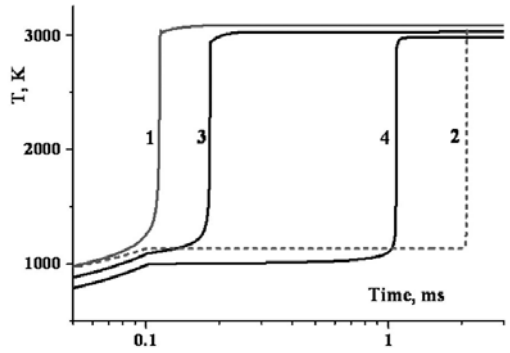

Fig.2. *Calculated evolution of gas temperature at three different initial temperatures: 1,2 – 800K; 3 – 700K; 4 – 600K. 1,3,4 – Plasma-induced ignition. 2 – heating-induced ignition*

Main idea pushed forward by this paper is that the plasma assistance for combustion enhancement occurs on sophisticated multistage manner. Under some conditions the multistage combustion is observed without plasma of electrical discharge; see [2-3] for example. But at the plasma assisted combustion the kinetic mechanism of ignition looks to be principally multistage process (at least, two stages), as it is pointed in some last publications, for example in [5-7]. The idea may be briefly described as follows: in case of hydrocarbon fueling and low temperature, flame stabilization by non-equilibrium plasma occurs by means of a two-step process. During the first step the plasma induces active radicals production and so called "preflame" (or fuel reforming in terms of Stanford's team), which may be simplified as production of H2, CH2O, and CO. In spite of bright luminescence, this zone does not experience significant temperature and pressure increase. This "preflame" or "cool flame" [2-4] appears as a source of active chemical species that initiates (under favorable conditions) the second step of normal "hot" combustion, characterized by high temperature and pressure rise. Now this idea is promoted as one of the most important features of plasma method for the combustion enhancement.

To prove this idea experimentally some additional diagnostic technique possessing high temporal and space resolution is needed. A tunable diode laser absorption spectroscopy (TDLAS) was developed and applied to measure spatial distribution of the H_2O temperature and concentration.

Pulsed wind tunnel PWT-50H of JIHT has been described earlier in details, for example in [5-6]. The hydrogen and ethylene fuels are injected directly into the supersonic air flow M=2 from the combustion section wall. Combustors cross-section is 72*72 mm^2. Experimental conditions are: static pressure Pst = 100-150 Torr, air flow rate mair = 0.6-0.9 kg/s, fuel mass flow-rate in the range mfuel = 0.05-2 g/s for hydrogen and mfuel = 0.1-4 g/s for ethylene, discharge power Wpl = 1-10kW, test duration <0.5 s.

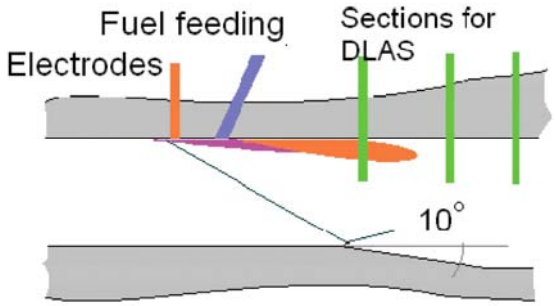

Fig.3. *Main scheme of the test section arrangement*

The facility is equipped with pressure scanner (16 sensors), a schlieren system (1000 fps, t_{exp}=100 ns), devices for optical and spectroscopic observations, current-voltage sensors, laser-absorption spectroscopy of water vapor, station of chemical analysis of exhaust gases, etc. The fuel was injected through 5 circular (d=3,5mm) orifices all in a row across the span and inclined at 25 degrees from the normal in the upstream direction, Fig.3. The row of injectors is 15 mm downstream from the row of electrodes, just downstream of the ceramic block; each injector is inline with an electrode in the configuration that includes 5 electrodes. The fuel mass flow rate was balanced between the orifices using a fuel plenum. Fuel injection was started 20 ms after discharge initiation and was switched off after completion of the discharge. Typically, the fuel injection continued 10-20 ms after the discharge to observe whether the flame was held or extinguished.

The discharge appears in the form of oscillating plasma filaments as it is shown in Fig.4a, b. Initial electrical breakdown occurs not far from the electrodes location. The individual filaments are blown down due to main flow at velocity a bit less than the core value. The frequency of oscillations depends on flow speed, inter-electrodes gap, and parameters of power supply. In the most cases this value was F=10-30kHz under the experimental conditions. The regulation of power release in a range W_{pl}= 3-17kW was performed by means of electrical current change Ipl=2-20A. If the current is increased by a factor of 10, the voltage is decreased, but only by a factor of 5. It is resulted in rise of the power in about 2 times. Such a method leads to some variation in the reduced electric field E/N. Usually it is mentioned that nonequilibrium plasma (characterized by higher level of E/N) occurs more effective in terms of fast fuel ignition. In our particular case it should be considered two main factors of successful fuel ignition and

flameholding: (1) the discharge power; and (2) length of the discharge filaments (reflects a time of interaction). All other factors appeared as much less important. Special experimental series shown a generation of sequence of active zones of reacting gas moved downstream from the place of immediate plasma-fuel interaction that is well seen in Fig.4.

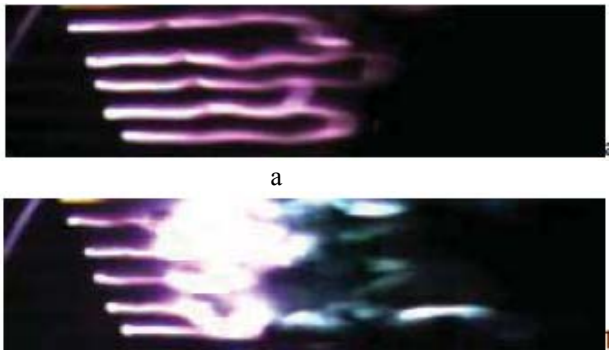

a

b

Fig.4. *Discharge appearance. a – discharge in flow; b – discharge at the ethylene injection.*

At low current, the discharge is unstable, while at high current, electrode erosion is significant. Temperature measurements based on optical emission spectroscopy of the N2 second-positive system (i.e., $C^3\Pi_u \rightarrow B^3G_g$ emission) yield a rotational temperature of Tg=3500±300 K, independently of the power release from the discharge under conditions of this experiment.

The basic effect: plasma-based flameholding in high-speed flow can be found in publications [5-7] Ignition and flameholding were realized for H2 and C2H4 fuelling on a plane wall by using a transversal electrical discharge at relatively low power deposition (<2% of flow enthalpy). The power threshold for a hydrogen flameholding was measured to be Wpl<3kW; with ethylene fuelling it was measured to be Wpl≥4kW. The combustion efficiency was estimated and it is found sufficiently high, about 0.9, for both hydrogen and ethylene. The ignition effect of the gas discharge was compared for different levels of the power, power density, and reduced electrical field (characterizing the departure from equilibrium for the discharge). Here it was found that the effectiveness of the flameholding is determined primarily by the level of power deposition, and secondarily by the power density. In this experiment the effect of reduced electrical field was not an important factor. In comparison with hydrogen fuelling, a main difference with ethylene fuelling was that thermal choking was not observed, even at the maximum discharge power of Wpl>10 kW. Furthermore, the completeness of the ethylene combustion decreases with increased fuel mass flow rate.

Schlieren images in Fig.5 and wall pressure distributions in Fig.6 for ethylene combustion illustrate details of plasma-fuel-flow interaction.

One can conclude that the combustion zone locates not in immediate vicinity of the zone of discharge and the fuel feeding.

Tunable diode laser (DL) absorption spectroscopy (TDLAS) is a widely used spectroscopic technique for the detection of various parameters of heated zones. This technique provides remote, nonperturbing measurements of the parameters of a hot zone with time resolution in the μs-ms range depending on the specific experimental conditions. The technique is usually based on the measurements of the ratio of the absorption line intensities of a test molecule. If Boltzmann distribution of the energy levels is established, the ratio of the line intensities depends only on the kinetic temperature of the object. The technically easiest and most straightforward version of TDLAS is the detection of direct absorption. It works well in the case of high signal-to-noise ratio (SNR). For weak lines the well developed wavelength modulation (WM) technique can be

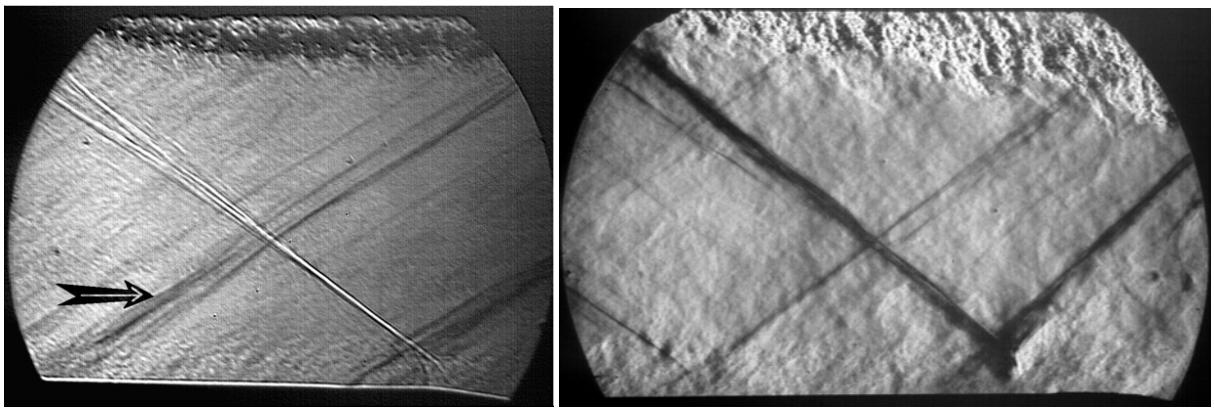

Fig.5. *Schlieren pictures of ethylene combustion. Left – discharge inflow; right – ethylene combustion*

applied for reducing low-frequency noise (flicker noise) in the baseline and correcting for nonspecific absorption.

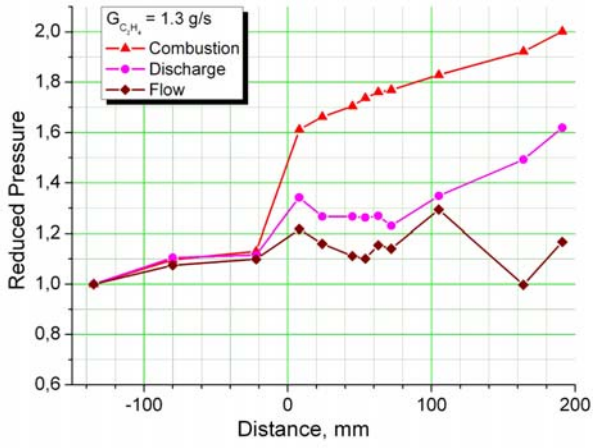

Fig.6. *Evolution of wall pressure. Ethylene injection G=1.3g/s, discharge power Wpl=8.4kW. X=0 – electrodes line.*

An original differential registration scheme was developed to reduce baseline fluctuations and amplitude modulation of the DL intensity not connected with water vapor absorption. An optimal model of the experimental spectra fitting was found in laboratory experiments with stable temperature and pressure. The best coincidence of T and P values measured by TDLAS and by thermocouple and pressure sensor was obtained using the multi-line spectrum fitting model. The parameters of the probed medium are obtained as a result of experimental spectra fitting. In most cases the individual absorption lines are fitted using Voigt profiles. This approach does not require the exact mechanism of line broadening. The temperature is inferred from the ratio of the integrals (or amplitudes) of the selected lines using the ratio calculated from spectroscopic databases. The alternative is the fitting of a whole spectral interval, which includes the selected lines. In this case the spectroscopic parameters of the lines from the databases are used. One should correctly account for different mechanisms and fit experimental line profiles using selected models of line broadening.

Molecular water was used as a test molecule. Water vapor is one of the major combustion products and key indicators of the extent of combustion and is therefore widely used as a tracer of combustion processes in mixed gas flows. Initially, the optimal TDLAS strategy was developed in laboratory experiments with stable conditions in an evacuated cell filled with the air. The optimized and validated version of the TDLAS technique was then applied to the measurement of the temperature, total gas pressure, and H2O concentration in a plasma-assisted supersonic combustion flow. The selection of the specific spectral lines was dictated by several reasons: the energies of low levels should be different, the lines should be reasonably resolved and the spectral interval should be free from lines of other gas components. The following H2O absorption lines were selected: 7189.344 cm-1 (E" = 142 cm-1), 7189.541 cm^{-1} (E" = 1255 cm^{-1}), 7189.715 cm^{-1} (E" = 2005 cm^{-1}). All lines could be recorded in a single scan of the DL wavelength across a $\Delta\lambda\sim$ 1 cm^{-1} spectral interval.

The optical scheme was modified for the actual experimental conditions of the test section. The results of the preliminary experiments have shown that DL beam transport to the test chamber of the aerodynamic tunnel using a free-space approach was absolutely unsuitable. Firstly, the strong acoustic vibrations of the facility caused

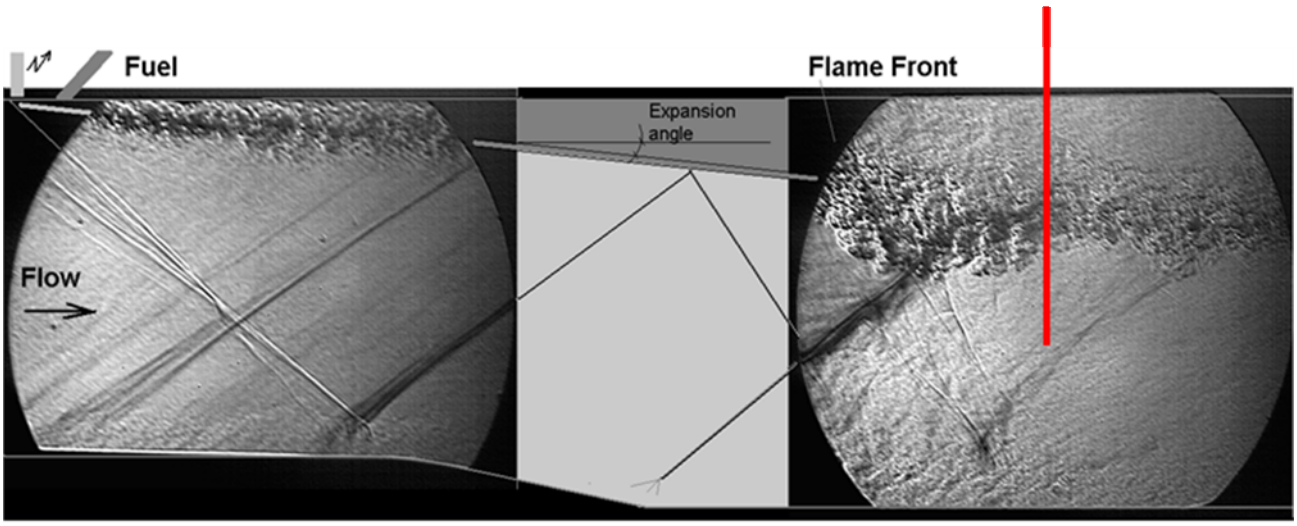

Fig.7. *Typical schlieren pictures of ethylene combustion. Combination of images from two windows. DLAS measurements was made for different sections of the flow, the red line in Fig.6 shows a sample section.*

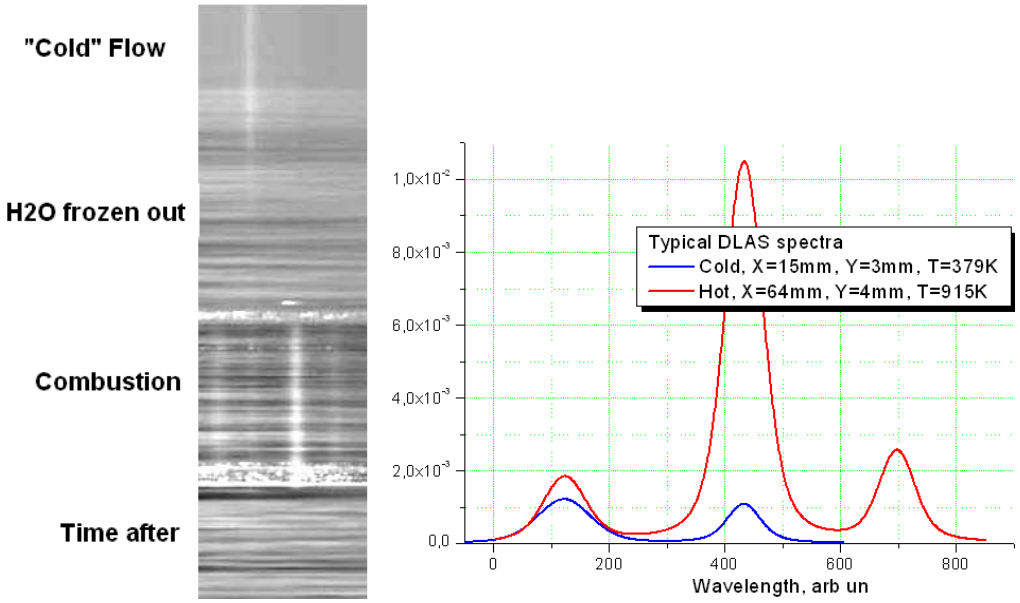

Fig.8. *Sample of real spectral dynamics. Typical absorption spectra of water vapors for two zones of flowfield (b).*

serious problems in reproducibly coupling the DL beam to the focusing optics. Secondly, the absorption of the DL by the water vapor of laboratory atmosphere dramatically increased the absorption signal of the "room temperature" line 7189.344 cm^{-1}. In addition, strong electric noise of the pulsed plasma facility increased the instability of the DL drivers and, hence, the instability of DL operation. All these reasons dictated the location of the sensitive electronics (drivers, optical block with DL, recording system) in a separate room away from the facility and transporting the DL beam to the chamber by a fiber.

DLAS measurements was made for different sections of the flow, the red line in Fig.7 shows a sample section.

Distribution of H2O temperature and concentration. The DLAS measurements were fulfilled in typical operation modes: plasma power was W_{pl}=8kW, hydrogen mass flow rate was G_{H2}=0.3g/s, and the ethylene G_{C2H4}=0.8g/s. The typical absorption spectra are shown in Fig.8b for "cold" and "hot" conditions. They were averaged over 30 scans. In some cases a high signal-to-noise ratio enabled spectral fitting with fewer averaged scans. In reality the fluctuations of gas parameters is observed strong, especially in vicinity of fuel injection place. Figures 8a give some impression on the combustion dynamics: it is a 2D image of DLAS spectra before combustion and after it.

The temperature distribution along the combustor for hydrogen obtained as a result of such fitting is shown in Fig.9. Each point in the figure was obtained in individual run of the facility. The values of the temperature inferred from both slopes coincide reasonably well. The water vapor partial pressure measured in a parallel way is presented in Fig.10. The uncertainty of the temperature evaluation associated with the experimental errors and fitting procedure was estimated as σ = 40 K.

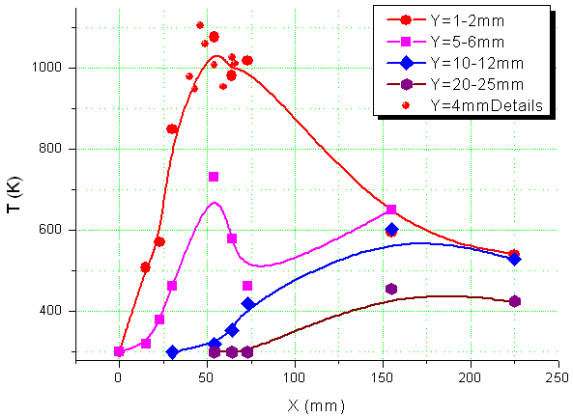

Fig.9 *Temperature distribution for H_2 combustion measured by DLAS. X axis is along the flow direction. Y is the distance from the wall.*

To explain the above observations, we propose the following two-zone (it reflects the two-stage ignition process) scheme of the plasma assisted flameholding. Zone 1, in which the "cold" combustion takes place accompanied by plasma-induced fuel conversion and relatively small power release. Note, that the combustion layer in this zone is rather thin. It is actually the shear layer, where the mixing is additionally promoted by the plasma filaments. Despite of high gas temperature here a total heat release is not big. Zone 2, in which the combustion is completed or almost completed with

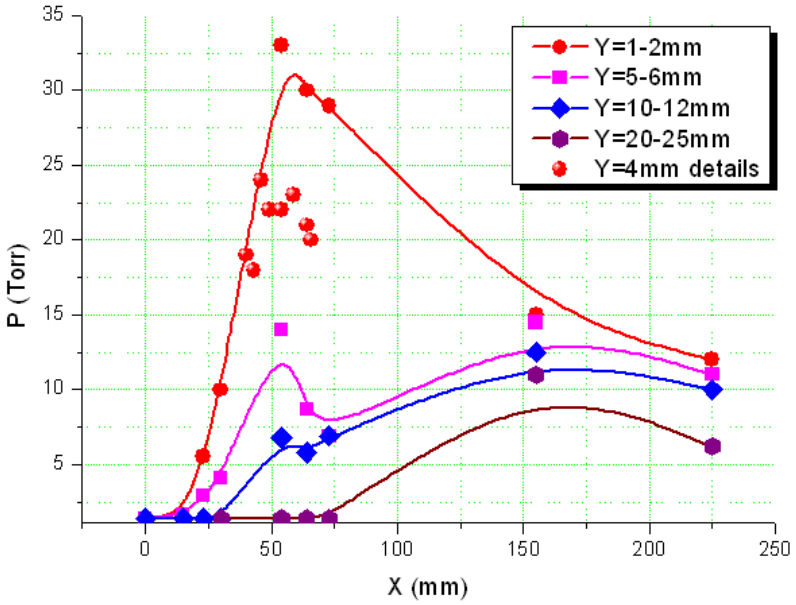

Fig.10. *Water vapor partial pressure in plasma assisted combustor for hydrogen.*

high energy release. Intensive mixing limits the gas temperature elevation. We emphasize that the plasma is the key element of this scheme: it launches the cold combustion inside of the first zone by generating high amount of active species. The lengths of the first zone in our tests were measured by the schlieren and schlieren-streak technique in the range of from 50mm to 150mm. It corresponds to the induction time range τ_{ind}=0.1- 0.3ms.

The combustion completeness was estimated based on three independent methods. The first method includes sampling measurements of chemical composition of exhaust gases, namely, the concentrations of CO2, CO, NOx, CxHy, and O2. In the second method the measurements of the water vapor concentration in zone of combustion and downstream by means of laser absorption spectroscopy are utilized for estimation. The third method compares the experimental data and the results of the 3D Navier-Stokes simulation. All three methods gave the value of combustion completeness higher then η=0.9.

Acknowledgments

The experimental study is supported through EOARD-ISTC project #3057p (special thanks to Dr. Julian Tishkoff and Dr. Campbell Carter). Some part of this work was also supported by the Russian Academy of Science (Program #9, Project 9.2 and OFN-10, Project 4.6).

References.

1. Leonov S. B., Yarantsev D. A., Napartovich A. P., Kochetov I. V. "Plasma-Assisted Combustion of Gaseous Fuel in Supersonic Duct", Plasma Science, IEEE Transactions on Plasma Science, 2006, Volume: 34, Issue: 6, pp.2514-2525
2. Basevich, V. Ya. Chemical kinetics in the combustion processes. In: "Handbook of heat and mass transfer". V. 4 (Ed. N.Cheremisinoff), Houston: Gulf. 1990, p. 769
3. Sokolik A. S., "Self-ignition and combustion in gases", *UFN (rus)*, XXIII, issue 3, 1940, pp.209-250
4. Kim W., Mungal M. G., and Cappelli M. A., "Formation and Role of Cool Flames in Plasma-assisted Premixed Combustion," *Appl. Phys. Lett.*, vol. 92, 051503, Feb. 2008.
5. Leonov S.B., Carter C., Yarantsev D.A. "Experiments on Electrically Controlled Flameholding on a Plane Wall in Supersonic Airflow", Journal of Propulsion and Power, 2009, vol.25, no.2, pp.289-298
6. Sergey Leonov, Dmitry Yarantsev, Vladimir Sabelnikov, Electrically Driven Combustion near Plane Wall in M>1 Duct, 3rd EUCASS Proceedings, July 2009, Versailles, France
7. Leonov S. B., Sabelnikov V.A., Yarantsev D. A., Napartovich A. P., Kochetov I. V. "Plasma-Induced Ethylene Ignition and Flameholding in Confined Supersonic Air Flow at Low Temperatures", Plasma Science, IEEE Transactions on Plasma Science, 2011, February, accepted for publishing.

6.2. NONEQUILIBRUM PLASMA ACCOMPANYING THE IGNITION OF METHANE-OXYGEN MIXTURES

K.V. Artem'ev, N.K. Berezhetskaya, A.M.Davydov, S.Yu.Kazantsev, I.G.Kononov, I.A. Kossyi, N.I.Malykh, N.A.Popov[1], M.I.Taktakishvili, N.M. Tarasova, K.N.Firsov, E.A.Filimonova[2], M.R.Shakarov[3]

A.M. Prokhorov General Physics Institute, Russian Academy of Sciences, Moscow, Russia
[1]D.V. Skobeltsyn Institute of Nuclear Physics, Moscow State University, Moscow, Russia
[2]OIVT Russian Academy of Sciences, Moscow, Russia
[3]Moscow Institute of Electronic Technology, Moscow, Russia

The problem of plasma production in processes of ignition of combustible gas mixtures has been much investigated in both experimental and theoretical works. The presence of charged particles in flames is a well-known fact established early in the last century. In the forties, flame conductivities have been studied in some detail. It has been shown that the conductivity value is several orders greater than values calculated assuming equilibrium ionization. Such "overequilibrium" ionization is also known as "chemical" ionization. Considerable progress in research on chemical ionization was achieved in the 1960-70s. As a result, a considerable amount of experimental and theoretical data was gathered, for the greater part, on hydrocarbon flames. When analyzing the current state of the problem, we have to note that the investigations concern only a limited range of phenomena (in most cases, shock waves and steady-state flames) and diagnostic methods (usually, probes). For a number of hydrocarbons, adequate kinetic schemes are as yet unavailable to explain experimental values of the electron density of the plasma accompanying oxidation processes in chemically active gases.

The experiments described in this work were stimulated by a series of investigations carried out at the GPI with the aim to reveal peculiarities of the ignition process initiated in combustible gas mixtures by high-power electric discharges locally in small volumes (which are much less than the reactor volume). As initiators in our experiments, we used high-current gliding surface discharges, microwave discharges, laser sparks on solid target surfaces and laser sparks in space inside the reactor.

We present results of measurements of the electron density in the plasma accompanying the ignition of stoichiometric methane-oxygen mixtures in closed volumes. To initiate the ignition, we used discharges of a different type: high-current gliding surface discharges produced by a multielectrode system, microwave discharges ('microwave arc'), and laser sparks from a focused HF laser. The electron density n_e was measured with the help of two microwave interferometers (wavelengths λ_1 = 0.2 cm and λ_2 = 0.8 cm). A series of measurements was performed with a single Langmuir probe.

The experiments have revealed certain peculiar features of the spatiotemporal behavior of the chemically ionized nonequilibrium plasma. The results afford a basis for further experimentation. It is proposed to use microwaves to exert influence upon the ionized component of the flame and, through it, upon the combustion process, when irradiating different zones of the flame with relatively strong microwaves, where these waves will be absorbed by the ionized medium.

6.3. PROGRAMMABLE MICROWAVE DISCHARGE AS THE WAY OF COMBUSTION STABILIZATION OF LIQUID ALCOHOL, INJECTED INTO TRANSONIC AIR STREAM

I.N.Gusev, A.A.Karachev, P.V.Kopyl, V.M.Shibkov, L.V.Shibkova, O.S.Surkont
Faculty of Physics, Moscow State University, 119991, Moscow, Russia,
shibkov <shibkov@phys.msu.ru>

One of the major practical problems arising by development of the hypersonic direct-flow air-breathing engine is reduction of its longitudinal size. For this purpose it is necessary to apply new unconventional ways of maintenance of fast volumetric ignition and control of process of combustion of hydrocarbon fuel in conditions of a high-speed stream. One of new decisions of the given problem is use of various types of gas discharges. For stationary combustion of hydrocarbon-air mixture at use of non-stationary low-temperature plasma it is necessary to optimize a mode of initiation of the pulsed discharge, i.e. the value of energy put into plasma, pulse duration and frequency of following of the microwave pulses. It can be carried out at creation of the discharge in a mode of a programmable pulse [1]. In a programmable pulse mode gas breakdown and creation of plasma is carried out with the help of a short powerful pulse, or a train of short powerful pulses, and maintenance of the formed plasma and energy input occurs during the long low-power pulse following with some time delay after the first pulse, or after a pack of short powerful pulses.

In the report the combined discharge created in a programmable mode in a high-speed air stream is considered. Influence of low temperature plasma of a programmable microwave discharge on efficiency of combustion of liquid hydrocarbon fuel, injected in a drop phase into transonic (flow Mach number of $M \approx 1$) air stream is investigated. These researches are a first step to revealing an opportunity of application of a programmable discharge in hypersonic aerodynamics. The programmable discharge represents a combination of the self-sustained pulse-periodic microwave discharge and the non-self-sustained transversal electrode discharge created on a surface of a dielectric plate. Thus surface microwave discharge serves for the several purposes. First, it facilitates initiation of the direct current discharge. Second, effective energy contribution to plasma takes place under conditions of the microwave discharge. It leads to effective creation of the active radicals, excited and charged particles, and also to intensive volumetric illumination of gas flow by ultra-violet radiation. These factors can result in fast ignition of a gas mixture. The direct current discharge serves for the contribution of a thermal energy to gas and stabilization of combustion of a high speed stream of hydrocarbon fuel. Without use of the microwave discharge the electrode direct current discharge could not exists in a free high-speed air stream.

In the work the programmable discharge was created in a mode when the low-power pulse is switched during time, equal to duration of a pack of short powerful pulses. The number of microwave pulses N in a train was possible to change from 1 up to 100, frequency of recurrence of pulses $f = 50$ Hz. The microwave source is a pulsed magnetron generator with parameters: the wavelength is $\lambda = 2.4$ cm, the pulse duration is $\tau = 20$ μs, the pulsed microwave power is $W = 50$ kW, and the period-to-pulse duration ratio is $Q = 1000$. As a direct current source for creation of the transversal electrode discharge the power supply with a voltage up to 5 kV was used. The discharge current could change from 1 up to 20 A. In experiments duration of a programmable pulse changed from 0.8 up to 1.2 s. At the first stage technical alcohol was used as liquid hydrocarbon fuel. The delay time of injection of liquid alcohol changed from 0.2 up to 0.3 s.

For optimization of process of combustion of liquid hydrocarbon fuel in a high-speed air stream it is necessary to carry out full diagnostics of the investigated phenomenon. With this purpose in laboratory the automated diagnostic complex consisting from optical refracting gauges, photo electronic multipliers, pulse shadow installation, system for measurement of conductivity of a flame, electric probes, thermocouples, gauges of pressure, a two-wire line, digital monochromaters, spectroscopes, oscillographs, photo and video cameras has been created.

Under conditions of the programmable discharge stabilization of plasma-stimulated combustion of alcohol, injected in drop phase (as a spray) in transonic ($M \sim 1$) air stream is realized. Measurements of parameters of plasma and gas in conditions of stationary combustion of alcohol have been carried out. It was shown, that at ignition of liquid hydrocarbon fuel sharply change common view and characteristics of the discharge (the volt-

Fig. 1

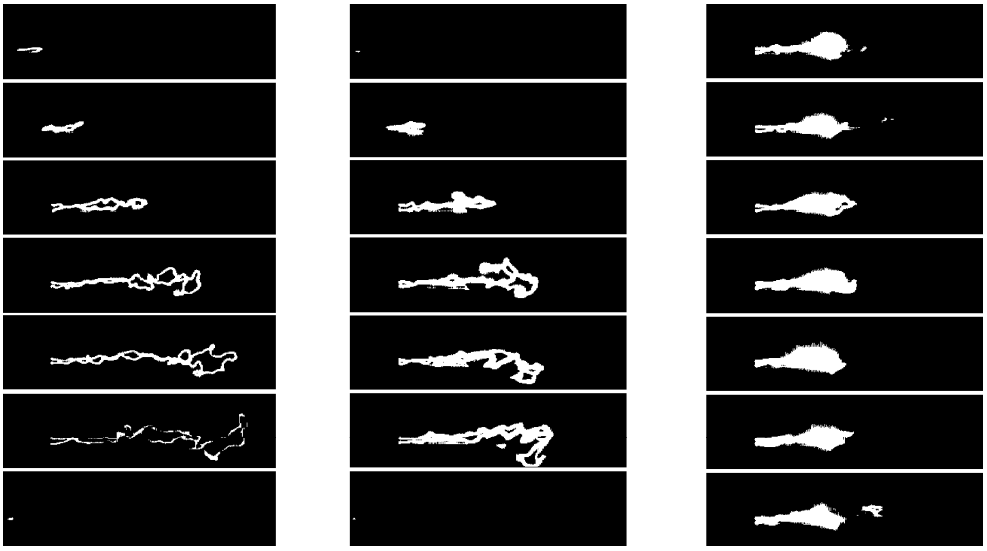

Fig. 2

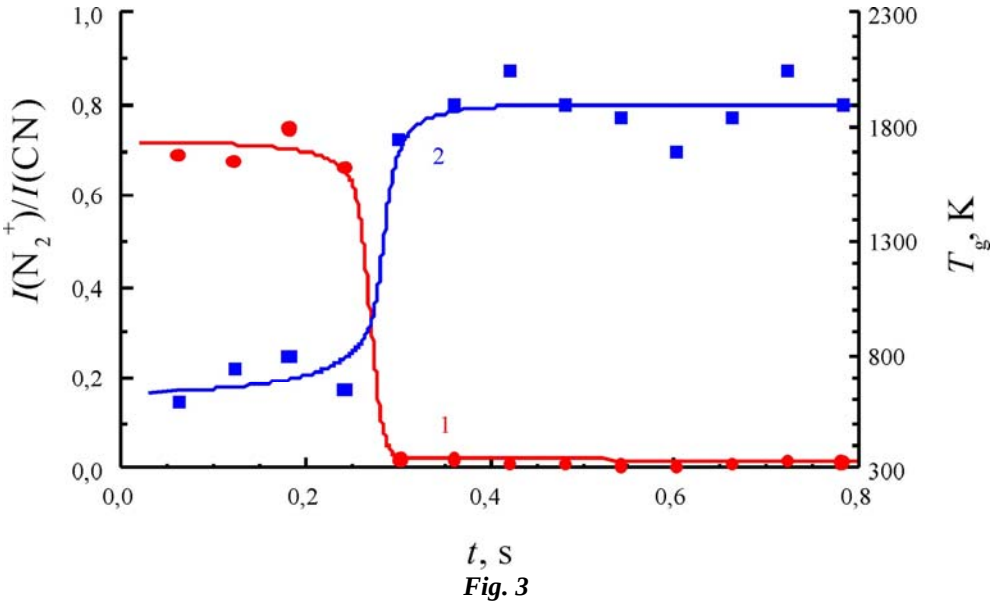

Fig. 3

ampere characteristic of the discharge, time dependences of a discharge current and it is especial voltage on a discharge gap, a spectrum of radiation and integrated intensity of a luminescence of a flame, the thermal stream, registered by thermocouple located on distance of 15 cm downwards on an air stream).

The general view of process of combustion is submitted in Fig. 1. The stream is propagated from left to right. The separate

fragments of dynamics of development of process of ignition and combustion of liquid alcohol are submitted in Fig. 2. An exposition time of one fragment is 4 μs, frequency of shooting is f = 5000 Hz/s. At the left – the discharge in an air stream, in the middle – transient of ignition, on the right – combustion stabilization. It was shown, that at injection of alcohol intensity of the thermal streams registered by the thermocouple sharply grows. Process of stabilization of liquid hydrocarbon fuel combustion can be observed on change of a time dependences of a pulse of a discharge current and especially a pulse of a voltage on a discharge gap. Fluctuations of amplitude of a voltage sharply decrease at combustion stabilization. Completeness of combustion of liquid alcohol reaches of 80 % depending on microwave power. Combustion occurs at a flame temperature ~2000 K (look Fig. 3). Integrated intensity of a flame luminescence increases only on 25-30 % at combustion whereas intensity of a hydroxyl luminescence grows in 30 times. The same results are received at high-speed combustion others liquid hydrocarbon fuels (kerosene, gasoline).

1. A.S.Zarin, A.A.Kuzovnikov, V.M.Shibkov. Freely localized microwave discharge in air. Moscow: Oil and gas. 1996.

6.4. FAST DEFLAGRATION WAVES AND DDT-PROCESSES ACCOMPANYING THE IGNITION OF CH_4:O_2 MIXTURES IN THE CLOSED VOLUMES

N.K. Berezhetskaya, S.I.Gritsinin, A.M.Davydov, I.A. Kossyi, N.A. Popov[1], N.M. Tarasova, K.N. Firsov, S.Yu. Kazantsev, I.G. Kononov
A.M. Prokhorov General Physics Institute, Russian Academy of Sciences, Moscow
kossyi@fpl.gpi.ru
[1]D.V. Skobeltsyn Institute of Nuclear Physics, Moscow State University, Moscow

Introduction

In the present work, we continue investigations [1-7] and employ a CO_2-laser for initiating combustion. In the present experiment, the combustion initiation process begins with local heating of a gas mixture, and thus we exclude a number of factors accompanying electric discharges (for example, reactions with the participation of charge particles and also ultraviolet radiation exciting the ambient gas).

Besides, a special feature of this type of initiation in the reactor free space is the absence of electrodes and other requisite components for electric discharge operation. This, in turn, substantially affects the characteristics of gas-dynamical processes accompanying the propagation of combustion waves when such methods of combustion initiation are used.

Experimental Layout. Results of measurements

The experimental layout is shown in Fig. 1. A cylindrical quartz chamber (3) with inner radius D = 44 cm and length L = 25-30 cm was preliminarily evacuated to a pressure $p \le 0.1$ Torr and then filled with a combustible gas mixture. Experiments were carried out in gas mixtures of the following composition: CH_4:O_2:SF_6 = 3:6:1 (3:6:2) with a total pressure of p = 150 (165) Torr. The ends of the chamber were closed with flanges, of which one was a blind metallic flange. The other flange had a BaF_2 window, through which the laser beam passed into the chamber. In front of the window, we placed different circular diaphragms and calibrated filters to attenuate the beam intensity.

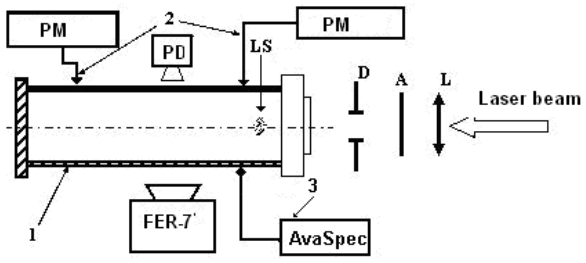

Fig. 1. *Experimental layout:*
1 reactor chamber (quartz tube); *2* fibers; *AvaSpec* spectrograph; *PD* photodiode; *FER-7* streak camera; *PM* photomultiplier; *LS* the region of combustion initiation by the laser beam; *D* circular diaphragm; *A* calibrated beam attenuators; *L* BaF_2 (NaCl) lens.

We used a pulsed electric-discharge CO_2-laser [8] with lasing line λ = 10.6 μm (P2O). The pulse energy was estimated as ε = 60 J; from the pulse shape typical of TEA CO_2-lasers, the radiation pulse duration was estimated as $\tau_{0,1} \approx 3$ μs [9]. The radiation energy distribution within the cross-sectional area of the diaphragm was nearly uniform.

Addition of a small portion (15-30 Torr) of SiF_6 to a combustible gas mixture resulted in its heating. Analysis [9] shows that, under our experimental conditions, the time during which the energy stored in vibrational degrees of freedom of SiF_6 molecules transforms into heat is shorter than 1 μs. Consequently, the laser energy absorbed by the gas during the pulse is totally transformed into heat by the end of the laser pulse, by which time thermal equilibrium is established. To determine the temperature distribution along the chamber axis, which is formed by the end of the laser pulse ($\tau_{las} \approx 3$ μs), we used the method described in [9]. Essentially, this method is as follows: two gas cells with absorption lengths of 19 mm and 29 mm were irradiated with a CO_2-laser, and for these cells we measured the dependences of their transmission on the energy density of the laser radiation incident on the cell. We filled the cells with SF_6:CH_4:O_2 = 15:45:90 and SF_6:CH_4:N_2 = 30:45:90 mixtures. We carried out a particular experiment to check on whether a combustible mixture SF_6:CH_4:O_2 in our measurements might be changed for a SF_6:CH_4:N_2 mixture. It was shown that, at a partial pressure of N_2 or O_2 up to 200 Torr, the transmission of SF_6:N_2 and SF_6:O_2 mixtures did not differ from the transmission of SF_6 (at the same pressure as it was in the mixture). Measurements of the transmission of cells with the given absorption lengths yield the dependence of the CO_2-laser energy absorbed by a 10-mm thick gas-mixture layer on the energy density of incident radiation. To construct the

temperature distribution along the length of the chamber, the entire gas volume along the axis was divided into 10-mm thick layers, and the energy absorbed by each layer was computed. Thus, by analogy to [8], we calculated the gas temperature in the layer. Data on the temperature dependence of heat capacity were borrowed from [10]; heat-exchange processes between gas layers and chambers walls were ignored because the laser pulse action is short enough ($\tau_{las} \approx 3$ μs).

To analyze the dynamics of ignition and combustion of combustible mixtures, we used an FD-25k photodiode and FER-7 streak camera which provided the streak images of the reactor radiation; its slit was oriented along the axis of the cylindrical chamber (Z axis).To analyze the gas glow and the time evolution of glow intensity in different cross sections along the quartz, we used an AVANTES AvaSpec-2048 spectrographs and an FEU-106 photomultiplier. The gas radiation from the quartz tube was transmitted into the spectrograph and photomultiplier through fibers.

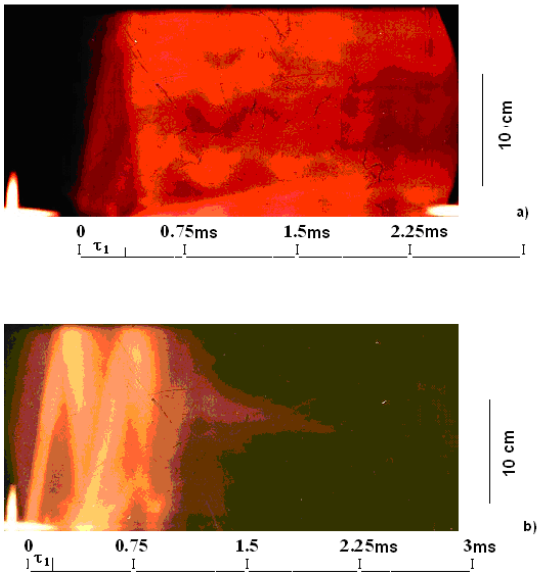

Fig. 2. *Streak images of radiation recorded by the FER-7 streak camera. The horizontal axis is temporal, the vertical axis is spatial (axial). The energy density of incident laser radiation: (a) $W_1 \cong 1.6$ J/cm^2; b) $W_1 \cong 2.5$J/cm^2.*

Figure 2 shows typical streak images of radiation from the reactor recorded by the FER-7 streak camera for the case where ignition is not accompanied by detonation and for the case where ignition is accompanied by detonation and explosion of the chamber. A mixture CH_4:O_2:SF_6 = 45:90:15 torr was ignited on its heating by the CO_2-laser. The horizontal axis in the photographs is temporal, whereas the vertical axis is spatial.

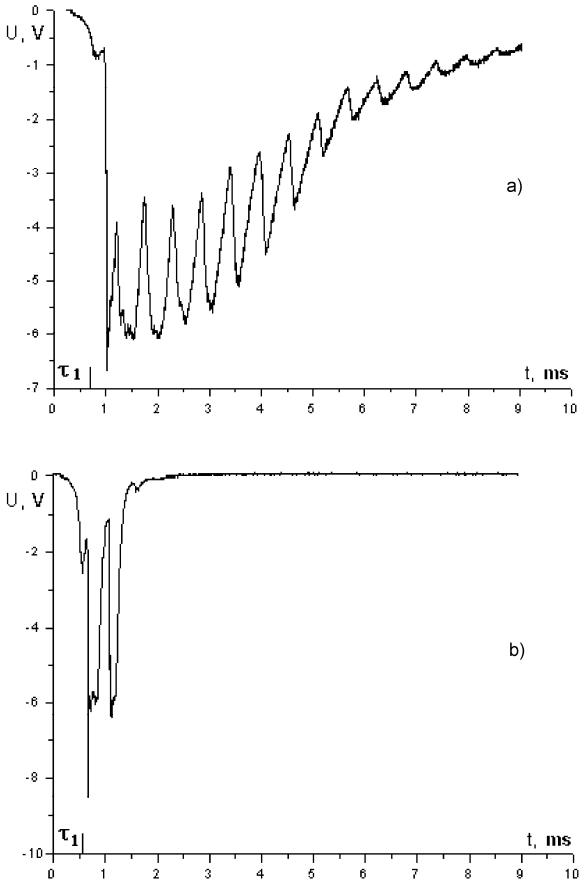

Fig. 3. *Oscillograms of photomultiplier signals: (a) $W_1 \cong 1.6$ J/cm^2; b) $W_1 \cong 2.5$ J/cm^2.*

Characteristic temporal and spatial scales are indicated in the figures.

Figure 3 shows typical oscillograms of the photomultiplier signals for these two cases, respectively.

Figure 4a illustrates a typical radiation spectrum (integrated over the burning time) measured in the wavelength range $400 \le \lambda \le 800$. The spectrum has a quasi-continuous component and emission lines. Most bright in the spectrum are the radiation lines identified with a sodium doublet and atomic potassium. The spectral interval does not include the radiation band of electronically excited molecule $\mathrm{OH}\left(A^2\Sigma^+\right)$ (the edge is near $\lambda \cong$ 306 nm) which contributes substantially into integral over spectrum measured by the FER-7 (Fig. 2) and photomultiplier (Fig. 3) (see [7]). Radiation sources that form the quasi-continuous component of the spectrum are not identified. However, an analysis shows that the spectrum on its certain regions is very close to Planckian and can be used to determine the gas temperature by the method described in [11]. In this method, we treat the measured spectrum in the coordinates $x \to \ln\left(I\lambda^4\right)$ and $y \to 1{,}4388 \cdot 10^8 / \lambda$ as

shown in Fig. 4b. The dependence obtained allows us to identify continuum in the spectrum with Planckian and infer the average temperature over the gas combustion time: $T_g \approx 4000$K.

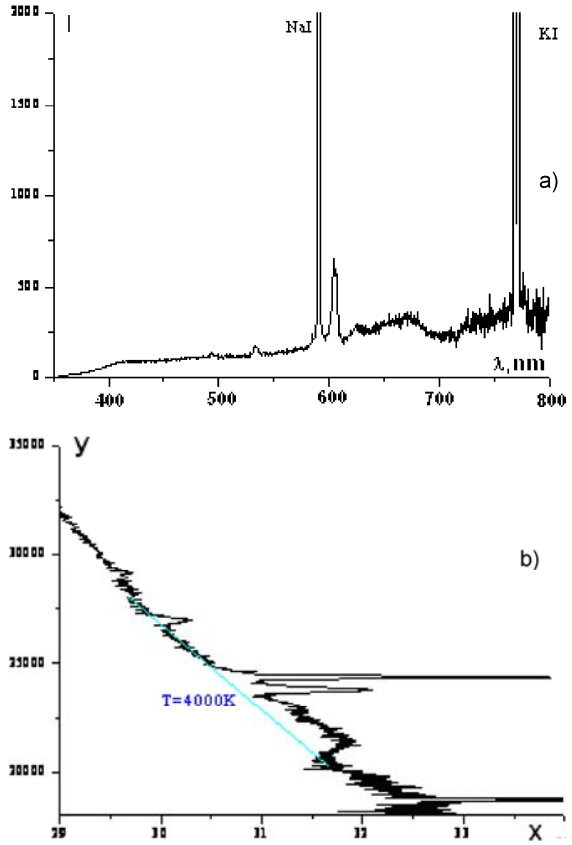

Fig. 4. *Spectral characteristics of the flame.*
(a) Typical radiation spectrum of a burning methane-oxygen mixture (integrated over the burning time).
(b) Quasi-continuous spectrum plotted in coordinates $x \to \ln\left(I_\lambda \lambda^4\right)$ *and* $y \to 1{,}4388 \cdot 10^8 / \lambda$. $T_g \cong 4000K$

Figure 5 shows the gas temperature distribution along the axis of the cylindrical chamber, which is formed immediately after the end of the CO_2-laser pulse, at the stage preceding the ignition of the three-component working gas mixture. The temperature distribution is calculated for two values of the energy density of the incident laser radiation which ensured reproducible initiation of combustion at W_{in} = 1.6 J/cm^2 or detonation of the combustible mixture at W_{in} = 2.5 J/cm^2 (the diameter of the diaphragm placed in front of the input window was 29 mm). It can be seen from Fig. 5 that the laser radiation provides heating of the gas at a considerable distance from the input window of the chamber. It is particularly remarkable that the induction time in our experiment ($t_{ind} \approx 600$ μs) is rather short (its value is substantially smaller that the literature data on induction times of stoichiometric methane-oxygen mixtures where the initial gas temperatures during CO_2-laser-heating correspond to the maximal values in distributions in Fig. 5).

It has been found experimentally that, depending on the diameter of a diaphragm limiting the cross-sectional dimension of the inherent laser beam, there exist always two threshold values of the laser-heating energy density (W_{1thr} and W_{2thr}) such that exceeding these thresholds leads to either "nonexplosive" ignition of the combustible mixture or ignition followed by explosion of the chamber (detonation regime). As in [12], the threshold for initiation of combustion of a combustible mixture depends on the initiation energy, i.e., when the diaphragm diameter was increased, the value of

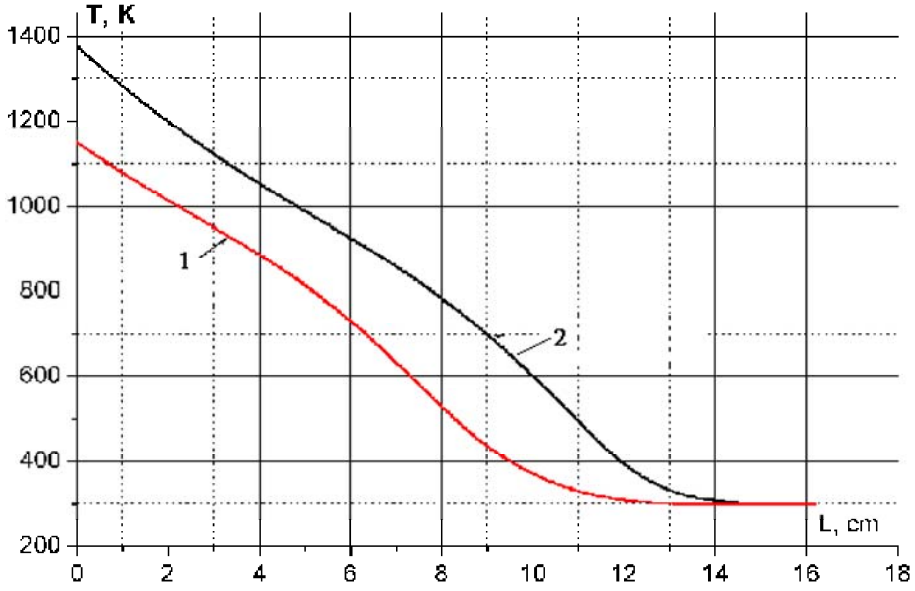

Fig. 5. *Gas temperature distribution along the axis of the cylindrical chamber, which is formed immediately after the end of the laser pulse, for two values of the energy density of the incident CO_2-laser beam:*
(1) $W_1 \cong 1.6$ *J/cm*^{2}*; (2)* $W_1 \cong 2.5$ *J/cm*^{2}.

W_{1thr} decreased approximately in inversed proportion to the diaphragm area.

Discussion of Experimental Results

Our experiment have shown that the initiation of combustion of a CH_4+O_2+SF_6 mixture inside a closed volume by CO_2-laser due to local gas heating demonstrates features peculiar to previous experiments with different types of initiators, such as high-current gliding surface discharges [1,2], microwave discharges [3,4], surface laser sparks and laser sparks in the reactor space [5-7]. Fast heating of a small volume (which is much less than the chamber volume) near the focal spot of the laser beam to 1200 – 1400 K is followed by a radiation wave with a relatively low intensity (the "primary wave") propagating inward from the initiator. The wave velocity is on the order of 10^5 cm/s, which far exceeds deflagration wave velocities in a stoichiometric $CH_4 + O_2$ mixture excited by low-power sparks (it is easy to show that the visible velocity of a combustion wave in a methane-oxygen mixture, where its propagation is determined by the heat-conduction and diffusion mechanisms, may not exceed values of order 4×10^3 cm/s).

In a time sufficient for the primary wave to run though the length of the reactor chamber, a bright burst is observed almost simultaneously throughout the reactor volume. Such a burst is characteristic of the processes of fast ("explosive") combustion and is indicative of branching chain reactions coming to play.

A time interval $\tau_1$during which we observe the primary wave preceding the volume combustion in the reactor is indicated in Figs. 2, 3. The axial propagation velocity of this wave in the present experiment was determined from the slope of its bright front in high-speed photographs like these in Fig. 2.

In [13], numerical work was made of combustion initiation of a methane-oxygen mixture ($\varphi = 1.5$) at $P_0 = 1.65$ atm in a tube 32 mm in length and 5 mm in radius. Formulation of the problem was closely related to conditions of our experiment, and the results of calculations agree qualitatively with data of measurements. In particular, the calculations predict the formation of a fast combustion wave (its velocity approaching $V = 2 \times 10^4$ cm/s) which is associated with active gas-dynamic processes initiated by heat release in the closed volume. It should be noted that in the calculations [13], the initial gas temperature in the combustion region was taken to be equal to 4000 K. As mentioned above, however, the temperature value in the present experiments was $T_0 \leq 1400$ K. Induction times observed in our experiments, $\tau_{ind} \leq$ 500-600 μs are rather short for methane-oxygen mixtures (for a stoichiometric $CH_4 : O_2$ mixture at $T_0 \leq 1400$ K and P = 200 Torr, the ignition time is more than 6 ms). However, at given conditions of the present experiment one should take into account the presence of SF_6 in the combustible mixture and possible dissociation of these molecules by CO_2-laser radiation. In [14], the induction time was measured for a $CH_4 : O_2 : SF_6 = 7 : 14 : 1$ mixture at P = 100 Torr, excited by two successive pulses of a CO_2 laser. The first pulse provided heating of the mixture, whereas the second provided its combustion. It was shown that, at initial temperature $T_0 = 1400$ - 1430 K, the induction time of this mixture was 200 – 600 μs (depending on the temperature to which the gas was heated by the first pulse). These results compare well with the results of our measurements. The induction time was defined as a time interval between the end of the second pulse and a burst of radiation detected by a photomuliplier from the region the second pulse initiated combustion. Furthermore, from comparison of the induction times for second pulses in which the radiation energy density was the same but the action time was different, the author has made the inference that the combustion of this mixture may be affected by chemically active particles produced by laser radiation.

One is the most interesting results, which was first obtained in the present experiment and did not made itself so evident in previous studies [1-7] with various systems of electric-discharge initiation, is transition to the detonation regime at a maximum energy of laser radiation. This transition is evidenced by a substantially shorter duration and higher intensity of radiation from the reactor (see Figs. 2b, 3b), and by breakage of the reactor chamber (a quartz cylinder). Detonation occurring at moderate energy release in the initiation region (< 60 J) and at such a short axial length of the cylindrical chamber (L = 20 – 30 cm), in which combustion is initiated near one of its ends, seems a rather unusual and not readily achievable phenomenon. There is reason to interpret it as an effect of transformation of a deflagration wave into a detonation wave (*Deflagration-to-Detonation Transition, DDT*). Investigations of this phenomenon are of interest to the combustion physics, in particular, to the problem of shortening the length of the pre-detonation zone which is all-important in the development of pulse detonation propulsion [15,16].

The physics of the phenomenon of transition of combustion to the detonation mode is the subject of a considerable literature, including theoretical investigations (see, e.g., [17-22]) and experiments (see, e.g., [23,24]). Models presented in [17-22] are based on the assumption of definite mechanisms responsible for the acceleration of a combustion wave to velocities higher than the velocity of sound and for the transition of the combustion wave to detonation.

A number of mechanisms of acceleration of deflagration waves whose initial velocities are much less than the velocity of sound velocities were considered in the literature. Of these mechanisms, noteworthy are the following: first, the mechanism of the formation of a fast combustion wave in a gas with nonuniform temperature. This model proposed by Ya.B. Zel'dovich et al. [17] and then used as the basis for numerical calculations [18] predicts the formation of combustion waves with properties peculiar to "phase" waves, which at a certain distribution of the gas temperature, can accelerate to supersonic velocities. In [20, 21], where acceleration of deflagration waves a cylindrical chamber was dealt with, the authors considered the acceleration mechanism related to the processes occurring in the wall layer, which involve an increase of the frontal zone of the combustion wave and its resulting acceleration. And, lastly, in [19,22], the authors have pointed to the important role of shock waves formed in the region of combustion initiation, because their reflection from the walls and multiple interaction with the region of initiation will result in acceleration of a deflagration wave even to velocities higher than the velocity of sound.

So far as we know, experiments for studying the DDT process based on the Zel'dovich model [17] have never been conducted. It is possible that such experiments are absent because they pose a serious problem: it is essential that a gas-temperature profile with prescribed parameters should be formed in a combustible gas mixture. From this point of view, the scheme described in the present work may be regarded as one of few feasible solutions of the difficult experimental problem. The axial gradient of the initial temperature here may be varied over rather wide limits by varying the content of SF_6 absorbing CO_2-laser radiation. However, in the present experiment, we used only the one composition of the working gas with its associated initial temperature distribution shown in Fig.5. Based on this distribution, the phase velocity of a deflagration wave, which can be estimated as $v_{def} \approx \frac{\partial Z}{\partial \tau_{ind}}$ (where Z is the axial coordinate, and τ_{ind} is the induction time at a given T(Z)), is on the order of $v_{def} \approx 10^2$ cm/s, which value is considerably smaller than the experimental value.

It should be noted that, in the Zel'dovich model [17], we are dealing with the temperature gradient, but strictly speaking, the gradient of the induction time of combustible mixtures should be considered. This gradient can be formed by not only the gas temperature profile but also by the density profile of chemically active particles. It is just this case which has been realized in our experiments, because the action of high-power CO_2-laser radiation on methane-oxygen mixtures with SF_6 additions produces not only heating of theses mixtures but also the effective dissociation of SF_6 molecules, thereby increasing the concentration of chemically active radicals CH_3, CH_2.

The most closely corresponding to the experiments described in this paper (and also in [1-7]) is the mechanism of deflagration wave acceleration considered in [19,22] and related to strong gas-dynamic perturbations accompanying the electric-discharge initiation of combustion of gas mixtures. Understanding the obvious necessity of obtaining the experimental data to refine the acceleration mechanism for deflagration waves, we emphasize that the fact is certain that high velocities of combustion waves were obtained at rather short (a few centimeters to ten centimeters) distances from the region of electric-discharge initiation of combustion in both the present and previous experiments [1-7]. When these experiments are compared, it becomes clear that the combustion initiation with the use of the CO_2-laser allowed maximal deflagration-wave velocities (~ 10^5 cm/) to be obtained at minimal distances (~ 1 – 2 cm) from the region of local energy release provided the combustion. The result of the present experiment, i.e., the reliably achieved excitation of detonation waves, is consistent with the effect underlying the DDT model, specifically, the acceleration of an initially slow deflagration wave up to supersonic velocities.

In conclusion, we note that low-intensity glow wave preceding the volume combustion may only tentatively be defined as deflagration waves. It is our opinion that a more adequate definition for these waves was given in [1-7], namely, "incomplete combustion" waves – that is the waves propagating along the reactor chamber at the initial stage, when chain branching reactions processes have not yet come into play (the first stage of the two-stage combustion). Even at this stage, however, the temperature behind the front of the incomplete combustion wave is as high as 1500 – 2000 K [25]. This temperature is considerably smaller than the burnout temperature of a stoichiometric methane-oxygen mixture but appears to be sufficient to initiate the DDP process.

Conclusion

The ignition of a three-component gas mixture (CH_4:O_2:SF_6) by CO_2-laser radiation was realized in the experiment under conditions excluding spark generation. As in the previous experiments with high-power electric-discharge initiation, a fast "incomplete combustion" wave was observed, which propagated inward from the region initiation, thereby promoting combustion of the gas mixture throughout the reactor volume. This wave is "deflagration" in character and possesses velocities

exceeding the velocity of sound. At a maximum energy density in the laser beam in our experiments, the fast incomplete combustion wave was transformed into a detonation wave (DDT process), which is evidenced particularly by explosion and breakage of the reactor. Thus the experiment has demonstrated the feasibility of DDT process at energy release in the initiation region as small 60 J and at distances from the region of initiation as small as ≤ 20 cm.

This work was supported in part by the Russian Foundation for Basic Research (project no. 11-02-00465) and the Presidium of the RAS (program 09P "Fundamental Problems of the Mechanics of Interaction in Technological and Natural Systems).

References

1. I.A.Kossyi, V.P.Silakov, N.M.Tarasova. Combustion of Methane-Oxygen-CFC Mixtures Initiated by a High-Current Slipping Surface Discharge // Plasma Physics Reports, vol. 27, No 8, 2001, pp. 715-725.
2. [2] S.I.Gritsinin, I.A.Kossyi, M.A.Misakyan, V.P.Silakov, N.M.Tarasova and S.M.Temchin. Features of Gaseous Mixtures Combustion Initiated by High-Current Slipping Surface Discharge // Journal of Thermophysics and Heat Transfer, vol. 16, No 3, 2002, pp. 450-454.
3. N.K.Berezhetskaya, S.I.Gritsinin, V.A.Kop'ev, I.A.Kossyi, N.A.Popov, V.P.Silakov and D. Van Wie. Microwave Discharge as a Method for Igniting Combustion in Gas Mixtures // 43rd AIAA Aerospace Sciences Meeting, Report AIAA – 2005 – 0991, Reno, Nevada, 2005.
4. N.K.Berezhetskaya, S.I.Gritsinin, V.A.Kop'ev and D. Van Wie. Long-Lived Plasmoid Generated by Surface Microwave Discharges in Chemically Active Gases // Plasma Physics Reports, v. 31, No 10, 2005, pp. 886-890.
5. I.A.Kossyi, V.P.Silakov, N.M.Tarasova and D. Van Wie. Long-Lived Plasmoids Generated by Surface Laser Sparks in Combustible Gas Mixtures // Plasma Physics Reports, v. 32, No 4, 2006, pp. 349-351.
6. S.Yu.Kazantsev, I.G.Kononov, I.A.Kossyi, N.M.Tarasova and K.N.Firsov. Ignition of Gaseous Methane-Oxygen Mixture in Closed Volume by a Freely Localized Spark Generation by HF-Laser // "Nonequilibrium Phenomena. Plasma, Combustion, Atmosphere", NEPCAP-2009, Ed. by G.D.Rey, S.M.Frolov, A.M.Starik, Torus Press, Moscow, 2009, pp. 208-209.
7. S.Yu.Kazantsev, I.G.Kononov, I.A.Kossyi, N.M.Tarasova and K.N.Firsov. Ignition of Combustible Gas Mixture by a Laser Spark Excited in the Reactor Volume // Plasma Physics Reports, v. 35, No 3, 2009, pp. 251-257.
8. Belevtsev A.A., Firsov K.N., Kazantsev S.Yu. and Kononov I.G. // Quantum Electron., **36**, 2006, pp. 646-652.
9. Belevtsev A.A., Firsov K.N., Kazantsev S.Yu., Kononov I.G. // Appl. Phys. B: **82**, 2006, pp. 455-462.
10. [10] Babichev A.P., Babushkuna N.A., Bratkovskii A.M. // Physical Quantities: Reference Book, Moscow, Energoizdat Publ., 1991 (in Russisn).
11. V.A.Kop'ev, I.A.Kossyi, A.N.Magunov and N.M.Tarasova. Thermometry Based on the Intensity Distribution in a Thermal-Radiation Spectrum // Instruments of Experimental Techniques, v. 49, No 4, 2006, p. 573.
12. Bratov V.A., Isakov L.M., Petrov Yu.V. // Doklady Akademii Nauk (DAN), 422, 2008, pp. 612-614, in Russian.
13. Babushenko D.I., Gouskov O.V., Kopchenov V.I., Smirnov V.V., Stelmach O.M., Titova N.S., Starik A.M. Some physical and gasdynamic aspects of combustion initiation by powerful electric discharge // In Nonequilibrium process: Plasma, combustion, and atmospheric phenomena. Eds. G.D. Roy, S.M. Frolov, A.M. Starik. Moscow: Torus Press. pp. 294-301.
14. *Hill R.A.* Ignition-delay times in laser initiated combustion // Applied Optics. 1981. V. 20. pp. 2239-2243.
15. Liberman M. Introduction to physics and chemistry of combustion. Springer-Verlag, 2008, 360p.
16. Roy G.D., Frolov S.M., Borisov A.A., Netzer D.W. Pulse detonation propulsion: challenges, current status, and future perspective // Prog. Energy Combustion Sci., 2004, v. 30, pp. 545-672.
17. Ya. B. Zel'dovich, V.B.Librovich, G.M.Makhviladze and G.I.Sivashinskii. On the onset of detonation in a nonuniformly heated gas // Zhurnal Prikladnoi Mekhaniki I Tekhnicheskoi Fiziki, vol. 11, No 2, pp. 76-84, 1970.
18. Kapila A.K., Schwendeman D.W., Quirk J.J., Hawa T. Mechanisms of detonation formation due to temperature gradient // Combustion Theory and Modelling. 2002, V. 6(4), pp. 553-594.
19. D.A.Kessler, V.N.Gamezo, E.S.Oran. Simulations of flame acceleration and deflagration-to-detonation transitions in methane-air system // Combustion and Flame, 157, (2010), pp. 2063-2077.
20. Kuznetsov M., Alekseev V., Matsukov I., Dorofeev S. DDT in a smooth tube filled with

a hydrogen-oxygen mixture // Shock Waves, 2005, v. 14(3), pp. 205-215.
21. Liberman M.A., Kuznetsov M., Ivanov A., Matsukov I. Formation of the preheated zone ahead of a propagation flame and the mechanism underlying the deflagration-to-detonation transition // Physics Letters, 2009, v. A373, pp. 501-510.
22. O.V. Gus'kov, V.I. Kopchenov, N,S. Titova, A.M. Starik. Peculiarities of the Formation and Propagation of a Combustion Wave in a Model Chamber at Initiation of Combustion of a Gas Mixture by Laser Spark. Numerical Analysis // Aero-engines of XXI Century [Electronic Resource]: Proc. of Conf. – Electron. Dan. – Moscow: TsIAM, 2010, pp. 1452-1454 (in Russian).
23. Rakitin A.E., Starikovskii A.Yu. Experimental investigation of gradient mechanism of detonation initiation // 22nd International Colloquium on the Dynamics of Explosions and Reactive Systems (27-31 July, 2009, Minsk).
24. Smirnov N.N., Tyurnikov M.V. Experimental investigation of deflagration to detonation transition in hydrocarbon-air gaseous mixtures // Comb. Flame, 1995, v. 100, pp. 661-668.
25. N.K.Berezhetskaya, S.I.Gritsinin, V.A.Kop'ev, I.A.Kossyi, P.S.Kuleshov, N.A.Popov, A.M.Starik and N.M.Tarasova. Ignition of a Combustible Gas Mixture by a High Current Electric Discharge in a Closed Volume // Plasma Physics Reports, vol. 35, No 6, 2009, pp. 471-483.

7.1. ADVANCED TURBULENT COMBUSTION MODELING. APPLICATION TO SUPERSONIC COMBUSTION

V. Sabelnikov*[†] *& C. Fureby*[‡]*,
[†]ONERA, The French Aerospace Lab, F-91761 Palaiseau, France
[‡]Defense Security Systems Technology, The Swedish Defense Research Agency – FOI,
SE 147 25. Tumba Stockholm, Sweden

Abstract. In this work we propose a novel model for Large Eddy Simulations (LES) of premixed, non-premixed and partially premixed turbulent flames. The development is motivated by the need for more accurate and versatile LES combustion models that can be used to simulate a range of engineering applications such as airbreathing engines, IC-engines in order to assist in developing improved combustion devices. The model is based on the finite chemistry approach in which species transport equations are solved with chemistry represented by a (typically reduced) reaction mechanism. Provided that the filtered reaction rates are modeled sufficiently accurately this approach has the advantage of being able to represent also different types of flames under different conditions. The modeling of the filtered reaction rate provides the challenge: As most of the chemical activity, and thus also most of the exothermicity occurs on the subgrid scales, this model needs to be based on the properties of fine-scale turbulence and mixing and Arrhenius chemistry. The model developed here makes use of the similarities with the mathematical treatment of multi-phase flows together with the knowledge of fine-scale turbulence and chemistry obtained by Direct Numerical Simulation (DNS) and experiments. In the model developed, equations are proposed for the fine-structure composition and volume fraction that are solved together with the LES equations for the resolved scales. If subgrid convection can be neglected the proposed model simplifies to the well-known Partially Stirred Reactor (PaSR) model. To validate the proposed LES model comparisons are made with experimental data for an axisymmetric dump combustor.

1. Introduction

Predictive modeling of turbulent combustion is becoming increasingly important for the development of air-, land- and marine gas turbines, airbreathing engines, IC-engines and for studies of e.g. ammunition and waste destruction as well as fire spread. Reynolds Averaged Navier-Stokes (RANS) based combustion models, [1], have been successful in predicting some gross features of combustion, such as combustor exit temperatures, whereas they are unable to predict transient phenomena such as combustion instabilities, cycle-to-cycle variations, self-ignition and emission formation. Large Eddy Simulation (LES), [2-3], based combustion models is a promising alternative, [4-6], that can provide accurate data for improvement of combustion devices. The idea of LES is to compute the large (energetic) scales of the flow, affected by the boundary conditions, whilst modeling the small (less energetic) scales of the flow. For non-reactive flows this translates into providing closure models for the subgrid transport terms, [2, 4], whilst for reacting flows also the filtered mixing and (highly non-linear) reaction rate terms requires proper modeling, [4-6], as the reaction zone is not often well resolved on the grid.

To overcome these difficulties several methods have been developed, such as (i) *Flamelet Progress Variable (LES-FPV) models*, including G-equation, [7], and flame surface density, [8-9], models in which the reactions are assumed to take place in thin layers, separating the reactant mixture from the product mixture, wrinkled by the turbulence; (ii) *Probability Density Function models* (LES-PDF), [10], employing presumed shape or transported probability density functions to model the filtered reaction rates; (iii) *Finite Rate Chemistry models* (FRC-LES) including the Thickened Flame Model (LES-TFM), [11], Partially Stirred Reactor (LES-PaSR) model, [12], as well as the Eddy Dissipation Concept (LES-EDC) model, [13], using different mathematical and phenomenological models for the filtered reaction rates; (iv) *Conditional Moment Closure* (LES-CMC) models, [14], in which the species equations are conditionally averaged on a few variables on which the reaction rates are critically known to depend on, and (v) *Linear Eddy Models* (LES-LEM), [15], using a grid-within-the-grid approach to solve 1D species equations with full resolution. All these models have features that limit their usefulness in different ways, and thus it is desirable to develop more versatile LES combustion models.

This paper proposes a novel LES finite rate chemistry model for turbulent combustion. The idea of this model is based on the ideas of Chomiak, [16-17], which in turn are based on the non-reactive experimental data of Batchelor & Townsend, [18], indicating that at high Reynolds (Re) numbers turbulent fine structure is not uniformly distributed but concentrated into small isolated regions, whose entire volume is a small fraction of the total volume. This has more recently been verified by Direct Numerical Simulations (DNS) in non-reactive, [19], as well as reactive, [20], flows. Later, Magnussen, [13, 21], starting from the Chomiak model, developed the well-known EDC model. The core of the model proposed here is the use of mathematical treatment of multi-phase flows for the modeling of

the high-intensity fine-scale structures embedded in an environ-ment of low-intensity turbulence, with slower mixing. The proposed model framework incorporates the PaSR model, [12], as limiting case when subgrid convection is neglected, and thus the model will be referred to as the Expended PaSR (EPaSR) model. Here, we develop the EPaSR model and test it against experimental data for an axisymmetric premixed dump combustor. To compare the proposed model with conventional LES combustion model comparisons are also shown with a few ordinary LES-FPV and LES-FRC models. The LES-EPaSR (and PaSR) model reproduces the experimental data well and typically shows improved agreement with the reference data than the conventional LES-FPV and FRC models.

1.1 A conceptual representation of turbulent combustion

To develop successful physically-based subgrid Turbulence Chemistry Interaction (TCI) models for LES-FRC we have to take into account that the spatial and temporal distributions of velocity gradients have a major impact on the spatial and temporal structure of the chemical reactions regions in turbulent flows. As was observed first (in non-reactive case) by Batchelor & Townsend, [18], velocity gradients are highly intermittent, which means that the fine structures, possessing most of the small-scale turbulence, are distributed non-uniformly in space, with the intermittency increasing with increasing Reynolds (Re) number. This picture of small-scale turbulence is quite different from the Kolmogorov 1941 turbulences theory, [22 - 23]. In this K41 turbulence theory, the fine-structures, and associated quantities such as dissipation and acceleration, are distributed quasi-uniformly in space and in time. The spatial and temporal statistics of fine-structures in the K41 theory is determined solely by the Kolmogorov length and time scales, i.e. $\ell_K = (\nu^3/\varepsilon)^{1/4}$ and $\tau_K = (\nu/\varepsilon)^{1/2}$, respectively, [22-23], in which ε is the mean dissipation. The experimental study of Kuo & Corrsin, [24], suggests that fine-structure regions consist of topological structures such as vortex sheets, ribbons and tubes folded in regions of the flow. More recently, DNS, e.g. [19-20], provided support to this view, revealing how high intensity vortices merge in complex shaped filaments that are embedded into sheets or arcs of low(er) intensity vorticity.

The intermittency is also apparent by long-range spatio-temporal correlations (comparable with integral length and time scales, ℓ_I and τ_I, respectively) of quantities such as dissipation and acceleration. Kolmogorov, [25], and Oboukhov, [26], proposed 1962 a modified theory of small-scale turbulence, where intermittency is taken into account, following the well-known remark of Landau, [27]. The most exciting result of the K62 theory is that the spatial and temporal statistics of the fine-structures is determined not solely by ℓ_K and τ_K, as was supposed in the K41 theory, but also by ℓ_I and τ_I. This interrelation of the Kolmogov and larger scales (up to integral scales) can be illustrated by considering a tubular region in a turbulent flow with length ℓ_I and diameter ℓ_K ($<<\ell_I$). This tubular region is thus subjected to the stretch produced by the velocity gradient of larger vortices, ν'/ℓ_I, where ν' represents the fluctuating velocity. Since the velocity is correlated to a length of order ℓ_I, it may be assumed that the characteristic time scale of this stretch is of order ℓ_I/ν', being applied over a length of order ℓ_I. This situation is similar to Burgers vortices, and time of life of this tube will be of the order of integral time scale ℓ_I/ν'. A more detailed discussion of intermittency in high Re turbulent flows may be found in Monin & Yaglom, [28], Frisch, [29], Tsinober, [30], and other review papers, [31-32].

Recent DNS of combustion (at moderate Re numbers), e.g. [20], show a similar organization of the flow with the fine-structure vortices at the flame being essentially parallel to the flame whereas those behind the flame are predominantly perpendicular to the flame. Regions of high exothermicity and volumetric expansion are found in tubular structures distributed among the fine-structure vortices whereas regions of low exothermicity may be distributed more randomly. [16-17]. Thus we can conclude that the geometry of heat release zones (more generally, zones, where the chemistry reactions take place) and their spatial and temporal distributions are highly correlated with fine turbulent structures. From physical viewpoint this conclusion is not surprising as these small-scale structures contain the molecular fluxes on which the mixing and chemical reactions, are so heavily depending on. The consequences of the last conclusion are very important for the formulation of TCI models. If the spectrum of life-times of the fine structures can vary from the Kolmogorov scale to the integral scale the micromixing times that inevitably must enter any subgrid TCI model have also to respect this wide range of scales. The proposed model that will be described next is formulated upon the cartoon sketched above.

2. LES combustion modeling using a multi-phase analogy

The reactive flow equations are the balance equations of mass, momentum and energy describing convection, diffusion and chemical reactions, [4-6, 10]. In LES, [2], all variables are decomposed into resolved and unresolved (subgrid) components by a

spatial filter such that $f = \tilde{f} + f''$, where $\tilde{f} = \overline{\rho f} / \bar{\rho}$ is the Favre filtered variable. Filtering the reactive flow equations yields,

$$\begin{cases} \partial_t(\bar{\rho}) + \nabla\cdot(\bar{\rho}\tilde{\mathbf{v}}) = 0, \\ \partial_t(\bar{\rho}\tilde{Y}_i) + \nabla\cdot(\bar{\rho}\tilde{\mathbf{v}}\tilde{Y}_i) = \nabla\cdot(\overline{\mathbf{j}_i} - \mathbf{b}_i) + \overline{w}_i, \\ \partial_t(\bar{\rho}\tilde{\mathbf{v}}) + \nabla\cdot(\bar{\rho}\tilde{\mathbf{v}}\otimes\tilde{\mathbf{v}}) = -\nabla\bar{p} + \nabla\cdot(\bar{\mathbf{S}} - \mathbf{B}), \\ \partial_t(\bar{\rho}\tilde{h}_S) + \nabla\cdot(\bar{\rho}\tilde{\mathbf{v}}\tilde{h}_S) = \bar{\mathbf{S}}\cdot\nabla\tilde{\mathbf{v}} + \partial_t(\bar{p}) + \\ \qquad \nabla\bar{p}\cdot\tilde{\mathbf{v}} + \nabla\cdot(\bar{\mathbf{h}} - \mathbf{b}_h) + \bar{\rho}\bar{\sigma} + \Sigma_{i=1}^{N}(\overline{w}_i h_{f,i}^{\theta}). \end{cases} \quad (1)$$

Here, ρ is the density, **v** the velocity, p the pressure, **S** the viscous stress tensor, $h_S = \Sigma_i Y_i \int_{T_0}^{T} C_{p,i} dT$ the sensible enthalpy, T the temperature, **h** the heat flux vector, Y_i the species mass-fraction, $\dot{w}_i$ the species reaction rate, $\mathbf{j}_i$ the species mass-flux, $h_{f,i}^{\theta}$ the species formation enthalpies and σ the radiative heat loss which will be neglected. The subgrid flow physics is concealed in the subgrid stress tensor $\mathbf{B} = \bar{\rho}(\mathbf{v}\tilde{\otimes}\mathbf{v} - \tilde{\mathbf{v}}\otimes\tilde{\mathbf{v}})$ and flux vectors $\mathbf{b}_i = \bar{\rho}(\widetilde{\mathbf{v}Y_i} - \tilde{\mathbf{v}}\tilde{Y}_i)$ and $\mathbf{b}_h = \bar{\rho}(\widetilde{\mathbf{v}h} - \tilde{\mathbf{v}}\tilde{h})$, which results from filtering the convective terms. Following [6] we postulate that the gas mixture behaves as a linear viscous fluid with Fourier heat conduction and Fickian species diffusion so that $\overline{\mathbf{j}_i} \approx D_i\nabla\tilde{Y}_i$, $\bar{p} \approx \bar{\rho}R\tilde{T}$, $\bar{\mathbf{S}} \approx 2\mu\tilde{\mathbf{D}}_D$, $\bar{\mathbf{h}} \approx \kappa\nabla\tilde{T}$, respectively. Here, $D_i = \mu/Sc_i$ is the species diffusivities, R the composition dependent gas constant, μ the viscosity, $\tilde{\mathbf{D}}_D = \frac{1}{2}(\nabla\tilde{\mathbf{v}} + \nabla\tilde{\mathbf{v}}^T) - \frac{1}{3}(\nabla\cdot\tilde{\mathbf{v}})\mathbf{I}$ the deviatoric part of the rate of strain tensor, $\kappa = \mu/\mathrm{Pr}$ the thermal diffusivity, in which Sc_i and Pr are the Schmidt and Prandtl numbers, respectively. Finally, the filtered reactions rates are defined as $\overline{\dot{w}_i} = M_i\Sigma_{j=1}^{M} P_{ij}\overline{\dot{w}_j}$, in which M_i is the molar mass of specie i, P_{ij} the stoichiometric matrix and $\dot{w}_j = \rho^{\Sigma_{i=1}^{N}P_{ij}} T^{\beta_j} k_j \Pi_{i=1}^{N} Y_i^{P_{ij}}$ the reaction rate of the j^{th} reaction step, with k_j being the Arrhenius rate.

2.1 Subgrid flow modelling

To close the LES equations (1) we need to provide models for **B**, $\mathbf{b}_i$, $\mathbf{b}_E$ and $\overline{\dot{w}_i}$, and considering first the subgrid stress tensor and flux vectors, these are not unique to reactive flows and closure models can be acquired from the plethora of subgrid models for non-reactive flows, [2-3]. Here, we use the Mixed Model (MM), [33], with

$\mathbf{B} = \bar{\rho}(\tilde{\mathbf{v}}\widetilde{\otimes}\tilde{\mathbf{v}} - \tilde{\mathbf{v}}\otimes\tilde{\mathbf{v}}) - 2\mu_k\tilde{\mathbf{D}}_D$,

$\mathbf{b}_i = \bar{\rho}(\widetilde{\tilde{\mathbf{v}}\tilde{Y}_i} - \tilde{\mathbf{v}}\tilde{\tilde{Y}}_i) - \frac{\mu_k}{Sc_t}\nabla\tilde{Y}_i$ and

$\mathbf{b}_h = \bar{\rho}(\widetilde{\tilde{\mathbf{v}}\tilde{h}_S} - \tilde{\mathbf{v}}\tilde{\tilde{h}}_S) - \frac{\mu_k}{\mathrm{Pr}_t}\nabla\tilde{h}_S$, in which the subgrid viscosity, $\mu_k = c_k\Delta k^{1/2}$, is provided by an equation for the subgrid kinetic energy, k, [33], and where Sc_t and Pr_t are the turbulent Schmidt and Prandtl numbers. The model coefficients are calculated under the assumption of an infinite inertial sub-range, [2]. To reduce the computational cost we use *wall-modeled* LES, in which a model is used to handle the near-wall flow physics, [34]. This model is based on replacing the viscosity ($\mu + \mu_k$), and thermal and species diffusivities ($\mu/\mathrm{Pr} + \mu_k/\mathrm{Pr}_T$) and ($\mu/Sc_i + \mu_k/Sc_T$), respectively) in the first grid point at the wall, with values consistent with the logarithmic law of the wall.

2.2 A multi-phase framework for subgrid combustion modelling

Considering next the filtered reaction rates $\overline{\dot{w}_i}$, incorporating the turbulence chemistry interactions, being notoriously difficult to model because of their non-linear nature, [1]. Using the phenomenological models, [16-17, 35], based on experimental data, and DNS results, [19-20], a cartoon of turbulent mixing and combustion may be drawn. In this, turbulent reacting flows may be viewed as a muddle of vortex structures of different topological character, sheets, ribbons and tubes, in which the tubes and ribbons carry most of the high-intensity vorticity and dissipation. This implies that the fine-structure regions, denoted by (*), are embedded in a surrounding fluid, here denoted by (^{0}), will be responsible for most of the molecular mixing, chemical reactions (if the temperature is sufficiently high) and heat release. This cartoon is similar to that of the Eddy Dissipation Concept (EDC), [13, 21, 36], but here a different strategy, based on an analogy with modeling multiphase flows, will be used to model the filtered reaction rates $\overline{\dot{w}_i}$.

For the derivation of the proposed model we let $\mathbf{\Psi} = [Y_i, h_S]$ be the composition space that satisfies the equation $\partial_t(\rho\psi_i) + \nabla\cdot(\rho\mathbf{v}\psi_i) = \nabla\cdot\mathbf{k}_i + \dot{\omega}_i$, in which $\psi_i = Y_i$, $\mathbf{k}_i = \mathbf{j}_i$ and $\dot{\omega}_i = \dot{w}_i$ for 1<i<N, where N denotes the number of species in the species

equation (1_3) whereas $\psi_{N+1}=h_s$, $\mathbf{k}_{N+1}=\mathbf{h}$, and $\dot{\omega}_{N+1}=\overline{\mathbf{S}}\cdot\nabla\widetilde{\mathbf{v}}+\partial_t\overline{p}+\nabla\overline{p}\cdot\widetilde{\mathbf{v}}+\Sigma_{i=1}^{N}(\overline{\dot{w}_i}h_{f,i}^{\theta})$ are the terms associated with the energy equation (1_4). As for the theory of multi-phase flows, e.g. [37], a phase indicator function, denoted I_α, with $\alpha=1$ in the fine structures (*) and $\alpha=0$ in the surroundings (^{0}) is next introduced to differentiate between these regions so that the local balance equations for the composition space becomes,

$$\begin{aligned}\partial_t(\rho_\alpha\psi_{i,\alpha}I_\alpha)+\nabla\cdot(\rho_\alpha\psi_{i,\alpha}I_\alpha\mathbf{v})=\\ \nabla\cdot(\mathbf{k}_{i,\alpha}I_\alpha)+\omega_{i,\alpha}I_\alpha+\mathrm{M}_{i,\alpha},\end{aligned}\qquad(2)$$

in which $\mathrm{M}_{i,\alpha}$ denote the exchange terms at the immaterial surface separating the fine structures and $\alpha=0$ in the surroundings. By summing over α in (2), provided that the exchange terms satisfies $\Sigma_{\alpha=0}^{1}(\mathrm{M}_{i,\alpha})=0$, the composition space equations are recovered. Although achievable, velocity differences between the fine-structures and surroundings are not included. In the framework of LES the species mass fraction equations are filtered over space to obtain equations for the large energetic scales of motion. If we take the filtering to correspond to a box-filter, covering the cell volume, ΔV, as often done in LES, [2], the volume fraction of phase α is,

$$\begin{aligned}&\gamma_\alpha=\tfrac{1}{\Delta V}\textstyle\int_{\Delta V}I_\alpha(\mathbf{x},t)dV=\Delta V_\alpha/\Delta V=\bar{I}_\alpha\\ &\text{with }\Sigma_{\alpha=0}^{1}\gamma_\alpha=1,\end{aligned}\qquad(3)$$

so that for products $I_\alpha\psi_{i,\alpha}$ and $\rho_\alpha\psi_{i,\alpha}I_\alpha$ it can easily be shown that $(\psi_{i,\alpha})_\alpha=\overline{\psi_{i,\alpha}I_\alpha}/\bar{I}_\alpha$ and $\overline{\rho_\alpha\psi_{i,\alpha}I_\alpha}=\gamma_\alpha(\overline{\rho_\alpha\psi_{i,\alpha}})_\alpha=\gamma_\alpha(\overline{\rho}_\alpha)_\alpha(\widetilde{\psi}_{i,\alpha})_\alpha$. Filtering the equations (2) then yields,

$$\begin{aligned}\partial_t(\gamma_\alpha(\overline{\rho}_\alpha)_\alpha(\widetilde{\psi}_{i,\alpha})_\alpha)+\nabla\cdot(\gamma_\alpha(\overline{\rho}_\alpha)_\alpha(\widetilde{\psi}_{i,\alpha})_\alpha\widetilde{\mathbf{v}})=\\ \nabla\cdot(\gamma_\alpha(\overline{\mathbf{k}}_{i,\alpha})_\alpha-\gamma_\alpha\mathbf{b}_i)+\gamma_\alpha(\overline{\omega}_{i,\alpha})_\alpha+\overline{\mathrm{M}}_{i,\alpha},\end{aligned}\qquad(4)$$

in which $\gamma_\alpha\mathbf{b}_i=\overline{\rho_\alpha\psi_{i,\alpha}I_\alpha\mathbf{v}}-\gamma_\alpha(\overline{\rho}_\alpha)_\alpha(\widetilde{\psi}_{i,\alpha})_\alpha\widetilde{\mathbf{v}}$ denotes the subgrid transport term, which will typically be modeled by a conventional subgrid viscosity model. Summing over the filtered equations (4) results in that the filtered exchange terms satisfy $\Sigma_{\alpha=0}^{1}(\overline{\mathrm{M}}_{i,\alpha})=0$ so that the LES composition space equations (1_2) and (1_4) are recovered. Returning next to the old notions, with (*) denoting the fine structures and (^{0}) the surroundings, such that $\psi_i^*=(\widetilde{\psi}_{i,1})_1$ and $\psi_i^0=(\widetilde{\psi}_{i,2})_2$, and $\widetilde{\psi}_i=\gamma^*\psi_i^*+\gamma^0\psi_i^0=\gamma^*\psi_i^*+(1-\gamma^*)\psi_i^0$, we then obtain the set of equations,

$$\begin{cases}\partial_t(\gamma^*\rho^*\psi_i^*)+\nabla\cdot(\gamma^*\rho^*\psi_i^*\widetilde{\mathbf{v}})=\\ \quad\nabla\cdot(\gamma^*(\overline{\mathbf{k}}_i-\mathbf{b}_i))+\gamma^*\overline{\omega}_i^*+\overline{\mathrm{M}}_i^*,\\ \partial_t(\gamma^0\rho^0\psi_i^0)+\nabla\cdot(\gamma^0\rho^0\psi_i^0\widetilde{\mathbf{v}})=\\ \quad\nabla\cdot(\gamma^0(\overline{\mathbf{k}}_i-\mathbf{b}_i))+\gamma^0\overline{\omega}_i^0+\overline{\mathrm{M}}_i^0.\end{cases}\qquad(5)$$

The above equations can be solved together for ψ_i^* and ψ_i^0 after which the LES quantity $\widetilde{\psi}_i$ can be constructed from $\widetilde{\psi}_i=\gamma^*\psi_i^*+(1-\gamma^*)\psi_i^0$ once the fine structure volume fraction, γ^*, is known. A more convenient and straightforward approach is however to solve the balance equations for the fine structure fractions, ψ_i^*, (5_1) together with the LES balance equations for $\widetilde{\psi}_i$, or more precise-ly the LES species equations (1_2) and energy equation (1_4).

Noticing that $\overline{\omega}_i=\gamma^*\overline{\omega}_i^*+(1-\gamma^*)\overline{\omega}_i^0$, and more specifically that $\overline{w}_i=\gamma^*\overline{w}_i^*+(1-\gamma^*)\overline{w}_i^0$, and taking advantage of the theoretical, [16-17], experimental, [35], and computational, [20], observations that (fast exothermal) reactions mainly occur in the fine structures, (1_2) becomes,

$$\partial_t(\overline{\rho}\widetilde{Y}_i)+\nabla\cdot(\overline{\rho}\widetilde{Y}_i\widetilde{\mathbf{v}})=\nabla\cdot(\overline{\mathbf{j}}_i-\mathbf{b}_i)+\gamma^*\overline{w}_i^*,\qquad(6)$$

emphasizing the importance of the volume fraction of the fine structures. Equation (6) further implies that the reaction rate can be expressed as $\overline{w}_i=\int_{\Psi}\wp(\mathbf{\Psi})w_i(\mathbf{\Psi})d\mathbf{\Psi}\approx\gamma^*\overline{w}_i^0+(1-\gamma^*)\overline{w}_i^0\approx\gamma^*\overline{w}_i^*$, in which $\wp(\mathbf{\Psi})$ is hence a probability density function of the form $\wp(\mathbf{\Psi})=\gamma^*\delta(\mathbf{\Psi}-\mathbf{\Psi}^*)+(1-\gamma^*)\delta(\mathbf{\Psi}-\mathbf{\Psi}^0)$. Moreover, by summing over the N species equations in (5) and taking specifically into account that $\Sigma_{i=1}^{N}(\psi_i^*)=\Sigma_{i=1}^{N}(\psi_i^0)=1$ and $\Sigma_{i=1}^{N}(\overline{\omega}_i^*)=\Sigma_{i=1}^{N}(\overline{\omega}_i^0)=0$, it immediately follows that,

$$\begin{aligned}&\partial_t(\gamma^*\rho^*)+\nabla\cdot(\gamma^*\rho^*\widetilde{\mathbf{v}})=\Sigma_{i=1}^{N}(\overline{\mathrm{M}}_i^*)\\ &\text{and}\\ &\partial_t(\gamma^0\rho^0)+\nabla\cdot(\gamma^0\rho^0\widetilde{\mathbf{v}})=\Sigma_{i=1}^{N}(\overline{\mathrm{M}}_i^0),\end{aligned}\qquad(7)$$

the sum of which must satisfy the continuity equation (1_1). This constraint subsequently results in

that $\dot{m} = \Sigma_i(\overline{\mathrm{M}}_i^*) = -\Sigma_i(\overline{\mathrm{M}}_i^0)$, where we denoted by $\dot{m}$ the exchange rate of mass between the fine structures and the surroundings. This exchange rate of mass between the fine structures and surroundings is a key quantity for accurate predictions of species mixing and reactions.

2.3 Subgrid combustion modelling

To provide a closure of the exchange rate of mass, $\dot{m}$, through the immaterial surface separating the fine structures and surroundings, we suppose that if there is a dynamic equilibrium state between the fine structures and the surroundings, which is characterized by the value γ_{eq}^* (which is to be discussed later), then mass exchange rate between the fine structures and the surroundings is equal to zero, i.e. $\dot{m}(\gamma_{eq}^*) = 0$. For this equilibrium state, the surface separating the surroundings and fine structures can be considered material. Developing $\dot{m}$ in the vicinity of γ_{eq}^*, whilst retaining only the first-order linear term, assumed proportional to $(\gamma^* - \gamma_{eq}^*)$, results in that,

$$\dot{m} = -\overline{\rho}(\gamma^* - \gamma_{eq}^*)/\tau^*, \tag{8}$$

where τ^* is the fine structure residence time, and where the term $\overline{\rho}/\tau^*$ follows from dimensional considerations. The hypothesis underlying (8) refers to high Re-number flows, in which combustion takes place in concentrated regions, whose entire volume is a small fraction of the total volume. The application of this approach for lower Re-numbers, i.e. in the flamelet regime, is not straightforward. We conclude from (8), that if $\dot{m} > 0$, $\gamma^* < \gamma_{eq}^*$, then the exchange rate of mass is directed from the surroundings to the fine structures. Otherwise, if $\dot{m} < 0$, $\gamma^* > \gamma_{eq}^*$, then the exchange rate of mass is directed from the fine structures to the surroundings. We also note, that this mass exchange rate is due to convection through the interface separating fine structures and surroundings. Using the closure model (8), γ^* can be obtained from (7_1),

$$\partial_t(\gamma^*\rho^*) + \nabla\cdot(\gamma^*\rho^*\tilde{\mathbf{v}}) = -\overline{\rho}(\gamma^* - \gamma_{eq}^*)/\tau^*. \tag{9}$$

Next we consider the necessary modeling of the exchange terms $\overline{\mathrm{M}}_i^*$ and $\overline{\mathrm{M}}_i^0$ in equation (5). As follows from the core physical considerations, $\overline{\mathrm{M}}_i^*$ and $\overline{\mathrm{M}}_i^0$ contain two kinds of terms. The first type of term, here denoted by $\overline{\Theta}_i^*$ and $\overline{\Theta}_i^0$, is due to the exchange rate of mass between the fine structures and the surroundings (through the surface separating the fine structures and surroundings) as discussed above. If the exchange rate of mass is absent (i.e. in the dynamic equilibrium state, when the surface separating the fine structures and surroundings can be considered as material one), $\dot{m} = 0,$ as there is no transport through the interface between the fine structures and the surroundings, these two terms both turn to zero. The second type of term, here denoted by $\overline{\Omega}_i^*$ and $\overline{\Omega}_i^0$, is due to molecular diffusion through the interface between the fine structures and surroundings. Indeed, even if the exchange rate of mass is absent (i.e. in dynamic equilibrium), i.e. $\dot{m} = 0,$ there is exchange through the interface due to molecular diffusion. If $\psi_i^* = \psi_i^0$, these terms however turn to zero, since in this case there is no molecular diffusion. Based on the above physical considerations we propose to model these exchange terms as,

$$\begin{aligned}
&\overline{\mathrm{M}}_i^* = \overline{\Theta}_i^* + \overline{\Omega}_i^*, && \overline{\mathrm{M}}_i^0 = \overline{\Theta}_i^0 + \overline{\Omega}_i^0,\\
&\overline{\Omega}_i^* = -\gamma^*\overline{\rho}(\psi_i^* - \psi_l^0)/\tau^*, && \overline{\Omega}_i^0 = -\overline{\Omega}_i^* = -\gamma^*\overline{\rho}(\psi_l^0 - \psi_i^*)/\tau^*,\\
&\overline{\Theta}_i^* = \tfrac{1}{2}(\dot{m} + |\dot{m}|)\psi_l^0 + \tfrac{1}{2}(\dot{m} - |\dot{m}|)\psi_i^*, && \overline{\Theta}_i^0 = -\overline{\Theta}_i^*,
\end{aligned} \tag{10}$$

thereby satisfying $\Sigma_{\alpha=0}^1(\overline{\mathrm{M}}_{i,\alpha}) = 0$ (in fact, separately for both two types of terms, $\Sigma_{\alpha=0}^1(\overline{\Theta}_{i,\alpha}) = 0$ and $\Sigma_{\alpha=0}^1(\overline{\Omega}_{i,\alpha}) = 0$, as has to be). We note, that in correspondence with the underlying physics, if mass exchange is directed from the surroundings to the fine structures, $\dot{m} > 0$, one obtain from (10) that $\overline{\Theta}_i^* = \dot{m}\psi_i^0$ and $\overline{\Theta}_i^0 = -\overline{\Theta}_i^* = -\dot{m}\psi_i^0$. Similarly, if the mass exchange is directed from the fine structures to the surroundings, i.e. for $\dot{m} < 0$, one has that $\overline{\Theta}_i^* = \dot{m}\psi_i^*$ and $\overline{\Theta}_i^0 = -\overline{\Theta}_i^* = -\dot{m}\psi_i^*$.

By assuming that the convective and diffusive terms in (5_1) can be neglected we have that $\gamma^*\overline{\dot{\omega}}_i^* + \overline{\mathrm{M}}_i^* = 0$. Summing in this relation over i∈[1,…, N], and taking into account that $\Sigma_i(\overline{\dot{\omega}}_i^*) = 0$, as follows from the law of mass action, it follows that $\Sigma_i(\overline{\mathrm{M}}_i^*) = 0$, which, by the definition of $\dot{m}$ as $\dot{m} = \Sigma_i(\overline{\mathrm{M}}_i^*)$, results in that $\dot{m} = 0$. By using the linear model introduced in (8) this results in that $\gamma^* = \gamma_{eq}^*$. The fact that $\dot{m} = 0$ when convection and diffusion can be neglected at

the subgrid level in (5_1) further implies that $\overline{\Theta}_i^* = 0$, which in turn implies that $\overline{\mathrm{M}}_i^* = \overline{\Omega}_i^* = -\gamma^*\overline{\rho}(\psi_i^* - \psi_i^0)/\tau^*$. From the relation $\gamma^*\overline{\dot{\omega}}_i^* + \overline{\mathrm{M}}_i^* = 0$ it then follows that $\overline{\dot{\omega}}_i^* = \overline{\rho}(\psi_i^* - \psi_i^0)/\tau^*$, which may be further rearranged, using the aforementioned definition $\overline{\psi}_i = \gamma^*\psi_i^* + (1-\gamma^*)\psi_i^0$, to the more appropriate form,

$$\overline{\rho}(\psi_i^* - \overline{\psi}_i)/\tau^*/(1-\gamma^*) = \overline{w}_i^*, \qquad (11)$$

which can be recognized as the standard LES-PaSR model, [12]. Note also that the EDC model, [13, 21], bears some resemblance of the algebraic model (11). Equation (11) can be arrived at and understood also from simple mass balance considerations as done in the conventional PaSR and EDC models but is here (i) put on a more solid mathematical foundation and (ii) extended to non-equilibrium situations prevailing in some combustion applications.

The framework developed so far can be used to provide a more rigorous foundation for the LES-PaSR combustion model, [12], and to propose an extension of this model, referred to as the Extended PaSR (EPaSR) LES model. In the LES-PaSR model, [12], the continuity, momentum and energy equations, (1_1), (1_3) and (1_4), respectively, are solved together with the species equati-on (6), in which the filtered reaction rates are modeled by $\overline{w}_i = \gamma^*\overline{w}_i^* = \gamma^* w_i(\boldsymbol{\Psi}^*)$, in which ψ_i^* results from solving (11) in which γ^* is provided by γ_{eq}^*, yet to be specified. The PaSR-LES model has been proven reliable and accurate, [12, 38], but a better model is needed for more complex flows. In the proposed LES-EPaSR model the continuity, momentum and energy equations, (1_1), (1_3) and (1_4), respectively, are solved simultaneously with the species equation (6) in which $\overline{w}_i = \gamma^* w_i(\boldsymbol{\Psi}^*)$, where ψ_i^* results from solving the transport equations (5_1) with source terms $\overline{M}_i^*$, provided by (10_1) and γ^* provided by solving (9). To avoid calculating the fine-structure density, ρ^*, equations (5_1) and (9) will here be simplified by replacing ρ^* by $\overline{\rho}$ so that in the LES-EPaSR model the fine structure composition and enthalpy (or temperature) is given by,

$$\begin{cases} \partial_t(\overline{\rho}\gamma^*\psi_i^*) + \nabla\cdot(\overline{\rho}\gamma^*\psi_i^*\tilde{\mathbf{v}}) = \nabla\cdot(\gamma^*(\overline{\mathbf{k}}_i - \mathbf{b}_i)) + \gamma^*\overline{\omega}_i^* + \\ \qquad\qquad \dot{m}\psi_i^* - \gamma^*\overline{\rho}(\psi_i^* - \overline{\psi}_i)/\tau^*/(1-\gamma^*), \\ \partial_t(\overline{\rho}\gamma^*) + \nabla\cdot(\overline{\rho}\gamma^*\tilde{\mathbf{v}}) = -\overline{\rho}(\gamma^* - \gamma_{eq}^*)/\tau^*, \end{cases} \qquad (12)$$

for $1 \le i \le N+1$, in which $\overline{\psi}_i = \gamma^*\psi_i^* + (1-\gamma^*)\psi_i^0$ has been used to simplify the rhs of (12_1) and in which $\dot{m} = -\overline{\rho}(\gamma^* - \gamma_{eq}^*)/\tau^*$. To close (12) the value of γ_{eq}^* is required which will be discussed next.

2.4 Modeling the subgrid time scale and the equilibrium reacting volume fraction

To finally close the EPaSR and PaSR models, the subgrid time, τ^*, and reacting volume fraction, γ^*, needs to be provided. In what follows we propose sub-models for both these quantities based on the physical description provided in Section 2, and the references cited.

To estimate the subgrid time, τ^*, we first observe that the fine scale structures in a volume, ΔV^*, are generally anisotropic (sheets, ribbons and tubes) and influenced by the subgrid velocity stretch, ν'/Δ, the characteristic time of which is Δ/ν'. The smallest quasi-equilibrium scale of the fine structures, ℓ_D, is controlled by molecular viscosity and the characteristic time of the stretch Δ/ν', such that $\ell_D = (\nu\Delta/\nu')^{1/2}$. Its similarity with the Taylor length scale, $\ell_T = (\nu\ell_I/\nu')^{1/2}$, defined from the molecular viscosity and the integral time scale ℓ_I/ν', suggests that ℓ_D is the dissipative length scale of the smallest resolved scales. We further assume that area-volume ratio, $\Delta S^*/\Delta V^*$, is solely determined by ℓ_D so that $\Delta S^*/\Delta V^* \approx 1/\ell_D$. For small deviations from the equilibrium state, a simple relaxation equation can be formulated for the variation of ΔV^* so that,

$$d(\Delta V^*)/dt = -v_K(\Delta S^*/\Delta V^*)_{eq}(\Delta V^* - \Delta V_{eq}^*), \qquad (13)$$

in which we take into account that the change of the volume ΔV^* is due to the propagation of the surface ΔS^* with relative velocity on the order of the Kolmogorov velocity, v_K, [27]. From (13) it also becomes evident that the subgrid time scale may be expressed as,

$$\tau^* = (v_K(\Delta S^*/\Delta V^*)_{eq})^{-1} = \ell_D/v_K. \qquad (14)$$

Note also that (13) and (14) degenerates into (9) when divided by ΔV. It should however also be noted that if it assumed that area-volume density, $\Delta S^*/\Delta V^*$, is instead determined by the

Kolmogorov scale, ℓ_K, we obtain $\tau^* = \tau_K$, which contradicts the physical description of the fine structures discussed above. Using the definition of the Kolmogorov length- and time scales, $\ell_K = (\nu^3/\varepsilon)^{1/4}$ and $\tau_K = \ell_K / v_K$, respectively, this finally results in that $\tau^* = \sqrt{\tau_K \tau_\Delta}$ in which $\tau_\Delta = \Delta / \nu'$ is the time of the subgrid velocity stretch. This represents the geometrical mean of the (short) Kolmogorov time and the (long) time scale associated with the subgrid velocity stretch.

To model the equilibrium reacting fine-structure fraction, γ^*_{eq}, we use dimensional considerations and analysis of two limiting cases (fast and slow chemistry in comparison with mixing). More precisely, following from the dimensional considerations we write,

$$\gamma^*_{eq} = f(\tau_c/\tau_m, \tau_\Delta/\tau_K, \Delta/\ell_K). \qquad (15)$$

Since we consider the equilibrium state ($\dot{m} = 0$), the parameters that characterize unsteady and convective effects are not present in (15). Let us for simplicity denote the characteristic time and length scales ratios by $x = \tau_c/\tau^*$, $y = \tau_\Delta/\tau_K$ and $z = \Delta/\ell_K$, respectively, and by neglecting intermittency we have that $y = z^{2/3}$. Thus we consider further that γ^*_{eq} depends solely of x and y,

$$\gamma^*_{eq} = f(x, y). \qquad (16)$$

There are two limiting cases for the parameter y, namely y>>1 and y≈1. The first case is indeed LES since from above it follows that $\Delta >> \ell_K$, whereas the second case is indeed DNS since all scales are resolved, i.e. $\tau_\Delta \approx \tau_K$ and $\Delta \approx \ell_K$, and thus $\gamma^*_{eq} = f(x, y) = 1$ irrespectively of x. For the first case we consider two limiting situations: (i) x<<1 (or $\tau_c << \tau^*$), which corresponds to fast chemistry, in which combustion is limited by mixing, and (ii) x>>1 (or $\tau_c >> \tau^*$), which corresponds to slow chemistry, in which combustion is limited by the chemical reaction rate. In the first situation (x<<1 or $\tau_c << \tau^*$), when combustion is limited by mixing, the product $\gamma^*_{eq}\overline{\dot{\omega}}_i^*$ has to be of the order $1/\tau^*$, and if we take into account that $\overline{\dot{\omega}}_i^* \propto 1/\tau_c$,

$$\gamma^*_{eq} = f(x, y) \approx x, \; x << 1 \; and \; y >> 1. \qquad (17)$$

In the second situation (x>>1 or $\tau_c >> \tau^*$), when combustion is limited by the reaction rate, the product $\gamma^*_{eq}\overline{\dot{\omega}}_i^*$ has to be of the order $1/\tau_c$. Thus, if we take into account that $\overline{\dot{\omega}}_i^* \propto 1/\tau_c$,

$$\gamma^*_{eq} = f(x, y) \approx 1, \; x >> 1, \; y >> 1. \qquad (18)$$

In order to provide a reliable model for γ^*_{eq}, respecting the underlying cases and situations discussed above we propose to model γ^*_{eq} in the following manner,

$$\gamma^*_{eq} = f(x, y) = (1 - F(y)) + [x/(1+x)]F(y) = (1 - F(\tau_\Delta/\tau_K)) + |\tau_c/(\tau_c + \tau^*)]F(\tau_\Delta/\tau_K), \qquad (19)$$

where $F(y)$ is a monotonous function satisfying $F(1) = 0$ and $F(\infty) = 1$. In this paper solely the case $y >> 1$, ($\tau_\Delta >> \tau_K$) is considered resulting in that (19) reduces to,

$$\gamma^*_{eq} = f(x, y) = x/(1+x) = \tau_c/(\tau_c + \tau^*). \qquad (20)$$

This model for the reacting volume fraction is identical to the phenomenologically derived mod-el successfully used in previous LES, in which the chemical time scale is estimated as $\tau_c \approx \delta_u / s_u \approx \nu / s_u^2$ and the subgrid time scale is estimated as $\tau^* = \sqrt{\tau_\Delta \tau_K}$. Introducing $\tau_\Delta = \Delta/\nu'$ and $\tau_K = (\nu/\varepsilon)^{1/2}$, in which $\varepsilon = (\nu')^3/\Delta$, (20) becomes $\gamma^*_{eq} = (\nu^{3/4}\nu'^{5/4})/(s_u^2\Delta^{3/4} + \nu^{3/4}\nu'^{5/4})$.

3. Global hydrocarbon combustion chemistry

Accurate predictions of temperatures and species concentrations require the use of carefully selected reduced schemes, and here reduced three-step mechanisms for C_nH_m-air combustion are used. The mechanism for C_3H_8 are detailed in Table 1, for which the Arrhenius coefficients have been optimized to match the laminar flame speeds and temperatures of the Gri-Mech 3.0, in lean premixed flames, [40]. The third reaction step, modeling NO formation, is the sum of two rates, one for thermal NO (only dependent on temperature) and one for prompt NO (depending on the hydrocarbon fuel and H_2O). Most NO_X reacts to NO_2 after combustion, however, close to the flame, NO is dominant, and

Table 1. *Rate parameters for the reduced three-step C_3H_8-air mechanisms.*

No	*Reaction*	*A [m,kg,mol,s]*	n_{C3H8}	n_{O2}	n_{CO}	T_a[K]
1	$C_3H_8+3.5O_2 \leftrightarrow 3CO+4H_2O$	$2.00\cdot10^9$	1.0	0.5		10072
2	$CO+0.5O_2 \leftrightarrow CO_2$	$4.00\cdot10^8$		0.5	1.0	6047
3	$O_2+N_2 \leftrightarrow 2NO$	$1.50\cdot10^{16}$	-0.3			38440

Table 2. *Schmidt numbers.*

Specie	Sc_i
CH_4	0.68
C_3H_8	0.72
O_2	0.76
CO	0.76
CO_2	0.98
H_2O	0.60
N_2	0.75

therefore, it is sufficient to limit the mechanism to NO. Associated with the reaction mechanism is the treatment of molecular diffusion, that is here simplified and based on species Schmidt numbers so that $\bar{\mathbf{j}}_i \approx (\mu / Sc_i)\nabla\tilde{Y}_i$, where the values of the individual species Schmidt numbers are listed in Table 2. For a critical evaluation and discussion of this approach to model the molecular diffusion we refer to Giacomazzi *et al*, [41].

4. Numerical method

For this study we use the C++ library OpenFoam, [42], as the computational platform, which has previously been used for applications of varying complexity. The code employs an unstructured collocated Finite Volume (FV) method, [43], in which the discretization is based on Gauss theorem together with a semi-implicit time-integration scheme. Given the vector of unknowns, $\overline{\mathbf{u}} = [\bar{\rho}, \bar{\rho}\tilde{Y}_i, \bar{\rho}\tilde{\mathbf{v}}, \bar{\rho}\tilde{E}]^T$, the semi-discretized equations are,

$$\partial_t(\overline{\mathbf{u}}_P) + \frac{1}{\delta V_P}\Sigma_f[\mathbf{F}_f^C(\overline{\mathbf{u}}) - \mathbf{F}_f^D(\overline{\mathbf{u}}) + \mathbf{F}_f^B(\mathbf{u},\overline{\mathbf{u}})] = s_P(\mathbf{u},\overline{\mathbf{u}}), \tag{21}$$

where

$\mathbf{F}_f^C(\overline{\mathbf{u}}) = [\bar{\rho}\tilde{\mathbf{v}}, \bar{\rho}\tilde{\mathbf{v}} \otimes \mathbf{v}, \bar{\rho}\tilde{\mathbf{v}}E, \bar{\rho}\tilde{\mathbf{v}}Y_i]^T \cdot d\mathbf{A}_f$,

$\mathbf{F}_f^D(\overline{\mathbf{u}}) = [0, \bar{p}\mathbf{I} - \bar{\mathbf{S}}, \bar{\rho}\tilde{\mathbf{v}}\tilde{E} + \bar{p}\tilde{\mathbf{v}} - \bar{\mathbf{S}}\tilde{\mathbf{v}} - \bar{\mathbf{h}}, -\bar{\mathbf{j}}_i]^T \cdot d\mathbf{A}_f$,

$\mathbf{F}_f^B(\mathbf{u},\overline{\mathbf{u}}) = [0, \mathbf{B}, \mathbf{b}, \mathbf{b}_i]^T \cdot d\mathbf{A}_f$ and

$s_P(\mathbf{u},\overline{\mathbf{u}}) = [0, \mathbf{0}, \bar{\rho}\tilde{\sigma}, \overline{\dot{w}_i}]^T$ are the convective, diffusive, subgrid fluxes and source terms, respectively. For the convective fluxes, $\mathbf{F}_f^C(\overline{\mathbf{u}})$, a monotonicity preserving reconstruction of the form $\mathbf{F}_f^C(\overline{\mathbf{u}}) = \mathbf{F}_f^{C,H}(\overline{\mathbf{u}}) - (1-\Psi(\overline{\mathbf{u}}))[\mathbf{F}_f^{C,H}(\overline{\mathbf{u}}) - \mathbf{F}_f^{C,L}(\overline{\mathbf{u}})]$ is used, [43], in which $\mathbf{F}_f^{C,H}(\overline{\mathbf{u}})$ denotes a 2nd order linear reconstruction, $\mathbf{F}_f^{C,L}(\overline{\mathbf{u}})$ a 1st order upwind biased reconstruction and $\Psi = \Psi(\overline{\mathbf{u}})$ a non-linear flux limiter. The non-linear flux limiter is used to switch between the two underlying reconstruction algorithms, and here the MC limiter, [44], is used for the momentum, energy and species equations whereas only the higher order scheme is used for the continuity equation. To minimize the non-orthogonality errors in the viscous and subgrid fluxes, $\mathbf{F}_f^D(\overline{\mathbf{u}})$ and $\mathbf{F}_f^B(\mathbf{u},\overline{\mathbf{u}})$, respectively, these are split into orthogonal and non-orthogonal parts, [43]. Central difference approximation and gradient face interpolation are used for the orthogonal and non-orthogonal parts respectively. A 2nd order semi-implicit Crank-Nicholson time-integration scheme is used together with a PISO-like algorithm, in the spirit of Rhie & Chow, for the cell-centered data storage structure, [45]. Stability is imposed using compact stencils and by enforcing conservation of kinetic energy. The equations are solved sequentially, with iteration over the non-linear source terms to obtain rapid convergence, with a fixed CFL number of about 0.4.

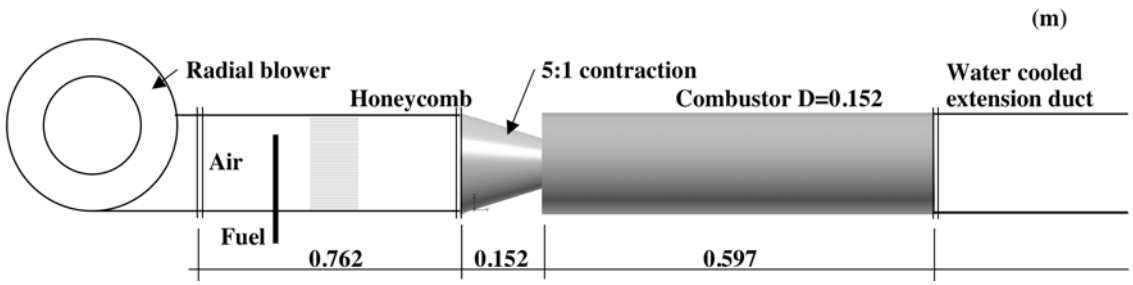

Figure 1. *Schematic of laboratory dump combustor of Gould, [53-54].*

5. Results from LES of a premixed dump combustor

The proposed LES combustion model is further examined using data from a lean premixed axisymmetric dump combustor experimentally studied by Gould *et al*, [53-54], and computationally by Afshari *et al*, [55], and Fedina & Fureby, [38]. The laboratory combustor, figure 1, consists of a radial fan blower followed by a multipoint fuel injector and a flow straightening and condition-ing section, after which a 5:1 contraction, with a length of 0.152 m, an inlet diameter of 0.170 m and an exit diameter of 0.076 m, provides the transition into the 0.597 m long combustor with a diameter of 0.152 m, and the following exhaust section of similar diameter. The combustor itself is made of quartz to facilitate simultaneous Laser Doppler Velocimetry (LDV) and thermocouple measurements of the axial and radial velocity components and the temperature. The experiments are performed for a lean (fuel equivivalence ratio $\varphi = 0.5$) propane (C_3H_8) air mixture, having an adiabatic flame temperature of approximately T_{ad}=1500 K. In the experiments the mean centerline velocity and temperature at the inlet of the contraction was fixed at v_0=5.25 m/s and T_0=298 K, resulting in a contraction exit velocity and temperature of v_C=21.5 m/s and T_C=298 K, respectively.

The computational domain (cf. figure 1) in-cludes the contraction at which Dirichlet inflow boundary conditions (v_0=5.25 m/s, p_0=1 atm, T_0=298 K and $Y_{i,0}$ according to the equivalence ratio) are provided and the combustor at the end of which wave transmissive boundary conditions, [46], are employed. The combustor walls are modeled as isothermal no-slip walls at which zero Neumann conditions for the species and pressure. The computational domain is discretized using a grid of 1.54 Mcells, refined towards the dump plane, walls and in the shear-layers. In the study of Fedina & Fureby, [38], grid refinement was investigated, and it was found that this intermediate grid resulted in a good compromise of accuracy and computational cost, and therefore it was selected for this investigation. The work of Fedina & Fureby, [38], also provides the predictions from the LES-TFM, EDC, PaSR and FPV models, against which the LES-EPaSR model predictions will be compared in addition to the experimental data, [54]. Based on v_C and the radial step height (D/4) the global Re-number is Re≈55800 whereas the turbulent Re number is estimated to be Re_t≈558. The Damköhler and Karlowitz numbers are estimated as Da≈167 and Ka≈0.15, respectively, placing the flame in the corrugated flamelet regime.

Figure 2 shows a perspective view of the axisymmetric dump combustor, cut-open to illustrate the flow in terms of instantaneous axial velocity, $\widetilde{v}_x$, and iso-surfaces of the second invariant of the velocity gradient, λ_2, colored by the temperature $\widetilde{T}$. The contraction accelerates the reactant flow so that the nozzle exit velocity is almost uniform, at v_C≈21.3 m/s, which corresponds well to the measured nozzle exit velocity of 21.5 m/s. As a result of the premixed reactants entering the combustor at the dump-plane, an annular recirculation region develop beneath the dump-plane, constrained by the combustor wall and the annular shear layer developing from the roll-up of the contraction wall-vorticity. The annular shear

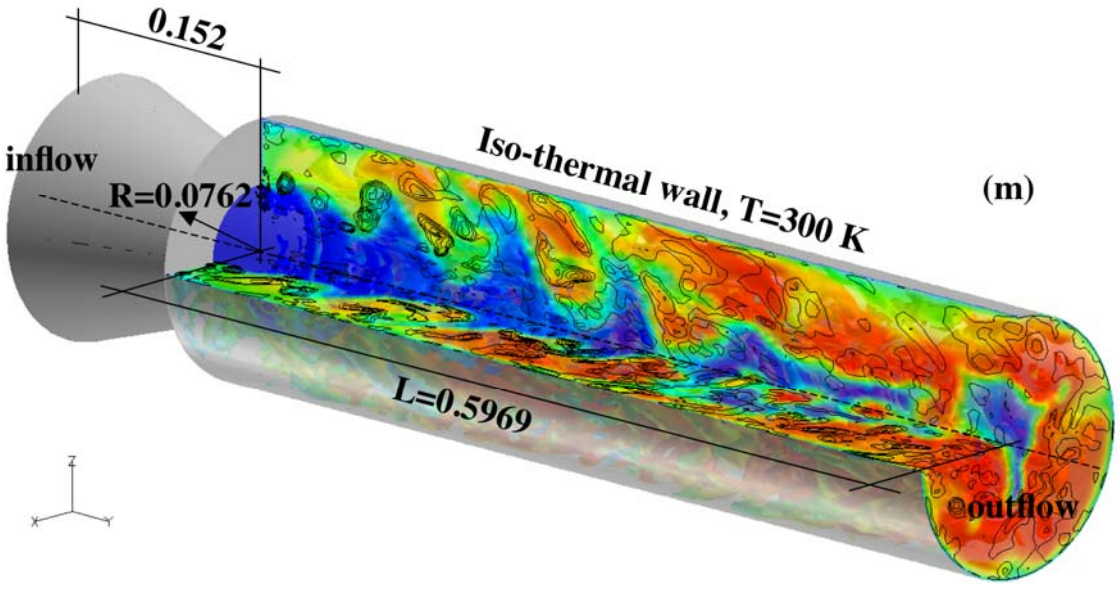

Figure 2. *Perspective view of the axisymmetric dump-combustor from the LES-EPaSR model, cut-open to illustrate the reacting flow in terms the instantaneous temperature and vorticity.*

layer is accountable for the mixing between reactants and products, with the mixing being assisted by the high strain rates in the shear layer that delays ignition and allow the annular vortex rings to develop from initial Kelvin–Helmholtz (KH) instabilities. Heat-release occurs some distance downstream of the dump-plane within the large-scale vortex structures that form early in the shear layer as they entrain reactants and products. The resulting volumetric expansion within these structures contributes to the growth of the annular shear layer and the downstream acceleration. The flame anchors beneath the dump-plane due mainly to the recirculation of hot products. The vorticity is governed by annular vortex rings originating from KH instabilities of the annular shear layer and longitudinal vortices that form in the braid regions between the annular vortex rings. The reactant core flow penetrate deep into the combustor and compared to non-reacting LES (not shown) the reacting core flow velocity do not decay as rapidly as the core flow velocity as a consequence of the low axial pressure gradient in the reacting case as compared to the non-reacting situation. The combustion dynamics is a combination of acoustics, dominated by the longitudinal mode frequency of 66 Hz and KH instabilities, having a roll-up frequency of 165 Hz that is close to 180 Hz, cf. [56]. A frequency analysis shows that the power spectral density of the pressure has a strong broadband peak around 160 Hz, multiple peaks between 45 and 115 Hz as well as higher-order harmonics.

Figure 3 compares time-averaged axial velocity, $\langle \widetilde{v}_x \rangle$, and rms-fluctuation, v_x^{rms}, profiles at five locations downstream of the dump plane for the proposed LES-EPaSR model, the reference LES-PaSR, EDC, TFM and FPV models and the experimental data, [54]. For LES-TFM the sensitivity study [38] suggests best performance of this model when the flame thickening parameter is assigned a value of F=3. All LES models show that the core flow is virtually unchanged from that of the cold flow case (not shown) from the dump plane to x/R≈3 due to the delayed volumetric expansion caused, in turn, by the high strain-rate of the annular shear-layer. Between x/r=3.0 and 5.0 volumetric expansion due to heat release start to influence the flow, resulting in higher $\langle \widetilde{v}_x \rangle$ outside of the core flow and higher values of $\langle \widetilde{v}_x \rangle$ in the annular shear layer developing on the outer edges of the core flow region. Between x/r=5.0 and 12.0, the volumetric expansion due to heat release accelerate the flow so that $\langle \widetilde{v}_x \rangle$ exceed the corresponding cold flow cross-

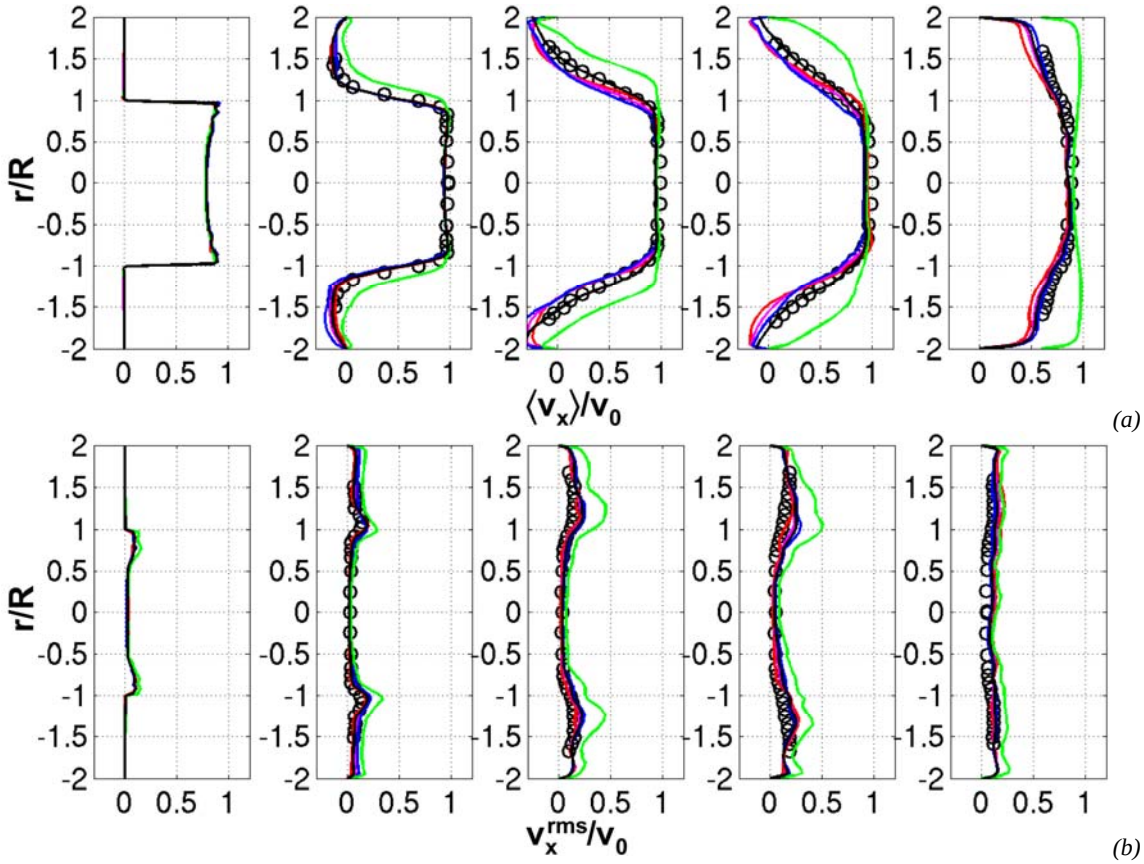

Figure 3. *Normalized (by the contraction exit velocity) mean axial velocity profiles (a) and axial rms-fluctuation profiles (b) at x/r=0.0, 1.0, 3.0, 5.0 and 12.0. Legend: experimental data, [54], (○), LES-PaSR (—), LES-EDC (—), LES-TFM (—), LES-EPaSR (—) and LES-FPV (—).*

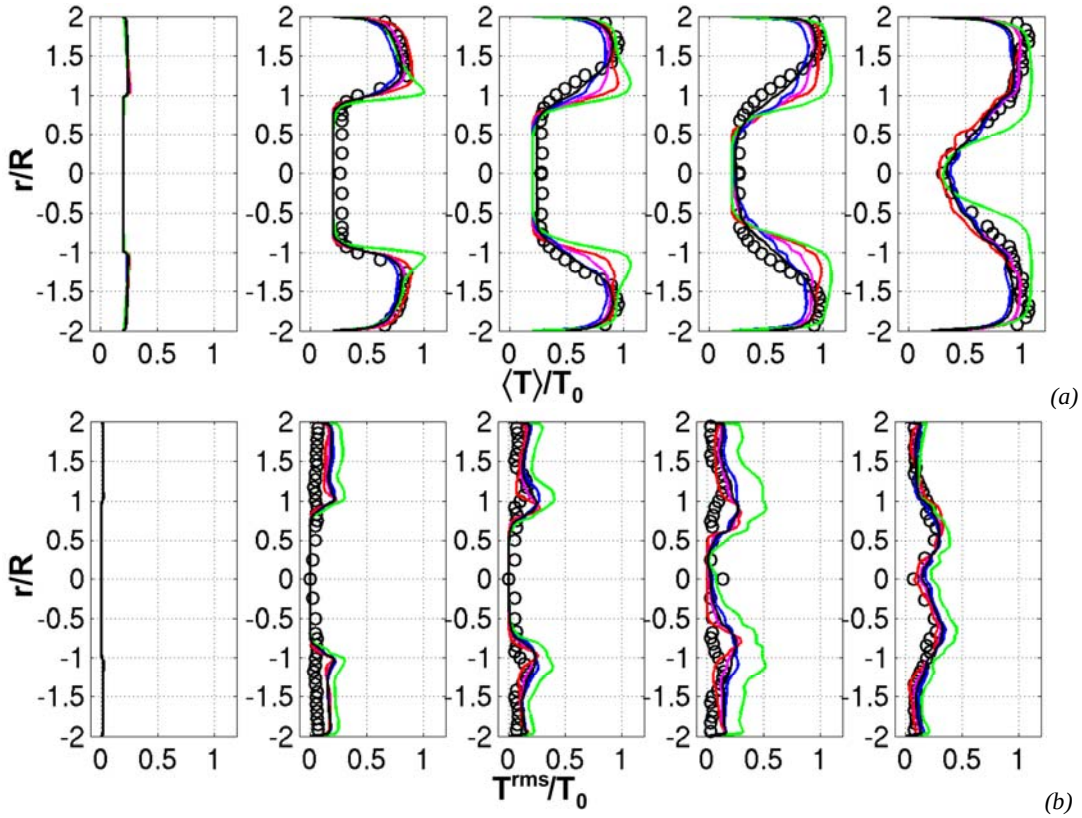

Figure 4. *Normalized (by the adiabatic flame temperature) mean temperature profiles (a) and temperature rms-fluctuation profiles (b) at x/r=0.0, 1.0, 3.0, 5.0 and 12.0. Legend: experimental data, [54], (○), LES-PaSR (—), LES-EDC (—), LES-TFM (—), LES-EPaSR (—) and LES-FPV (—).*

section-al mean velocity by almost 70%. Consequently, the rms-fluctuations also increase, particularly in the annular shear-layer. Furthermore, the annular recirculation region is found to be thinner and shorter in the reacting case compared to the non-reacting case, [54]. As found in [38], the LES-PaSR, EDC and TFM models all show good agreement with the experimental data for both $\langle \widetilde{v}_x \rangle$ and v_x^{rms}, whereas the LES-FPV model shows less satisfactory agreement as it overpredicts both $\langle \widetilde{v}_x \rangle$ and v_x^{rms} outside of the core flow region. Compared to this, the results of the proposed LES-EPaSR model shows even better agreement, in particular for $\langle \widetilde{v}_x \rangle$, for which the agreement with the experimental data, [54], is exceptionally good along the whole combustor. For v_x^{rms} the proposed LES-EPaSR model show similar agreement with the experimental data as the LES-PaSR and EDC models, which is to be considered acceptable. The improvements observed by the LES- EPaSR model is believed to be caused primarily by the influence of the large-scale convective processes incorporated into γ^* by solving the transport equation (12_1).

Figure 4 compares time-averaged temperature, $\langle \widetilde{T} \rangle$, and rms-fluctuations, T^{rms}, profiles at five locations downstream of the dump plane for the proposed LES-EPaSR model, the reference LES-PaSR, EDC, TFM and FPV models and the experimental data, [54]. The core flow remains cold whereas high $\widetilde{T}$ values dominate the recirculation region and the region between the (cold) core flow and the combustor wall. This agrees well with the experimental data, [54], and the $\langle \tilde{T} \rangle$ profiles indicate that the radial gradient of $\langle \widetilde{T} \rangle$ is positive in most of the shear layer. The tempe-rature fluctuations are initially small but increase between x/r=5.0 and 12.0. The high values of T^{rms} coincide with the maximum gradients in $\langle \widetilde{T} \rangle$ and agree well with experimental data, [54]. High $\widetilde{T}$ fluctuations occur in regions of high v_x^{rms} as found in figure 4b. The comparatively high values of T^{rms} near the centerline at x/r=5.0 and 12.0 results from a bimodal $\widetilde{T}$ probability distribution, characteristic of premixed combustion. As found in [38], the LES-PaSR, EDC and TFM models all show good

agreement with the experimental data for both $\langle \widetilde{T} \rangle$ and T^{rms}, whereas the LES-FPV model shows less satisfactory agreement as it predicts a wider high temperature region outside of the core flow region. Compared to this, the results of the proposed LES-EPaSR model shows even better agreement, in particular for $\langle \widetilde{T} \rangle$, for which the agreement with the experimental data, [54], is very good along the whole combustor. For T^{rms} the proposed LES-EPaSR model show similar agreement with the experimental data as the LES-PaSR and EDC models, which is to be considered fully acceptable. In particular we observe that the LES-EPaSR model improves predictions between x/r=3.0 and 5.0 by reducing the average radial turbulent flame propagation speed. Based on the formulation of the LES-EPaSR model (12_1) these differences seems to be caused by incorporating the effects of large-scale convective flow processes into the evolution of γ^*. This, in turn, affects the turbulent reaction rates and subsequently the heat-release, which in turn influences the volumetric expansion and the viscosity, which thereafter influences the large-scale momentum transport and the velocity as discussed above.

6. The ONERA/JAXA Scramjet Combustion Experiment

Figure 5a shows a photograph of the experimental supersonic combustion facility, consisting of JAXA supersonic combustor, [58-59], mounted in the ONERA/LAERTE vitiation air heater, [60], whereas in figure 5b a schematic of the combustor is shown. The combustor consists of a 0.36 m long constant area duct with a cross section of 0.05×0.10 m^2 followed by a 0.60 m long diverging area duct, with upper and lower expansion angles of 1.72°, respectively. For optical access, large quartz windows cover the sides of the combustor. In addition, pressure transducers are arranged along the centerline of the upper wall along the combustor. For the purpose of this investigation we have chosen to work with the ONH10 two-stage injection strut, [58], developed by ONERA and outlined in figure 5b. To facilitate ignition and enhance flame stabilization, this injector strut makes use of a first row of 4×ϕ2.0 mm Ma 2.5 injectors, installed on the top and bottom walls of the strut, 27 mm from its base, making 45º angle with the centerline, and a second row of 3×ϕ4.3 mm Ma 2.5 injectors installed on the strut base, 0.433 m downstream of the combustor entrance. All injector rows have a spacing of 25 mm, with the second stage injectors located between the rows of the first stage injectors to improve the fuel-air mixing in the recirculation region. Gaseous H_2, at a temperature of 124 K and a velocity of 2149 m/s, is feed into the $O_2/N_2/H_2O$ mixture with a mass fraction distribution of 0.23:0.70:0.07, at a density of 0.1335 kg/m^3, a temperature of 830 K, a velocity of 1449 m/s and a pressure of 34.2 kPa. The H_2 mass flow distribution between the first and the second stage injectors is 40% and 60%, respectively.

The computational configuration spans the entire combustor, cf. figure 5, which must be gridded so that the large-scale coherent flow structures, and as much as possible of the flame, are resolved whilst maintaining a manageable number of grid cells. Here, we use an unstructured grid, with finer cells near the walls, in the jet- and injector strut shear layers and around the estimated mean reaction zone, and larger cells inbetween these regions, thereby reducing the number of cells. The baseline grid contains ~8.5 Mcells but a coarser grid with ~2.5 Mcells, and a finer grid with ~17.0 Mcells, has been constructed to test the grid independence of the first and second order statistical moments of **v**, p, T and Y_i. Dirichlet boundary conditions are utilized for all variables at the inlet and H_2 injectors. At the outlet, all variables are extrapolated from the interior. At the walls, the no-slip wall model is used together with zero Neumann conditions for all other variables. All runs are initialized with the incoming vitiated
air and were left to develop freely for 10 flow-through times after which a fully developed flow was reached. The runs were continued for an additional 4 to 10 flow through-times (see Table 3)

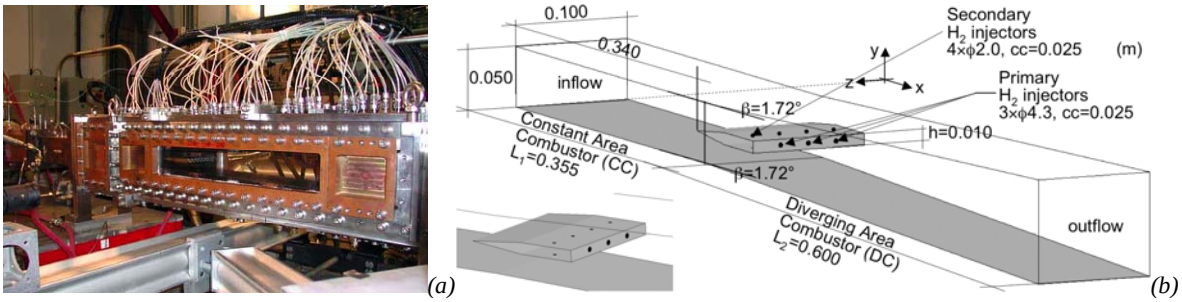

Figure 5. *Photograph (a) and schematic (b) of the JAXA supersonic combustor, [58], connected to the ONERA/LAERTE vitiation air heater, [60].*

Table 3. *Summary of the performed ONH10 simulations.*

Case	*Subgrid model*	*Chemistry*	*Reaction rate model*	*Grid*	*Sampling time*
1	*MM*	*0-step*	*—*	*8.5 Mcells*	*4*
2	*MM*	*7-step*	*PaSR*	*2.5 Mcells*	*5*
3	*MM*	*7-step*	*PaSR*	*8.5 Mcells*	*10*
4	*MM*	*7-step*	*TFM, F=5*	*8.5 Mcells*	*10*
5	*MM*	*7-step*	*EVM*	*8.5 Mcells*	*10*
6	*MM*	*7-step*	*EDC*	*8.5 Mcells*	*10*
7	*MM*	*7-step*	*PaSR*	*17.0 Mcells*	*4*

Table 4. *Rate parameters for the H_2-air mechanisms.*

No	*Reaction*	*A [m, kg, mol, s, K]*	*N*	*T_a[K]*
1	$H_2+O_2 \leftrightarrow OH+OH$	$2.66 \cdot 10^{10}$	*0*	*24044*
2	$H+O_2 \leftrightarrow OH+O$	$6.21 \cdot 10^{10}$	*0*	*8456*
3	$OH+H_2 \leftrightarrow H_2O+H$	$3.01 \cdot 10^{6} \cdot T^{1.60}$	*1.60*	*1660*
4	$O+H_2 \leftrightarrow OH+H$	$1.60 \cdot 10^{3} \cdot T^{2.67}$	*2.67*	*3163*
5	$OH+OH \leftrightarrow H_2O+O$	$5.21 \cdot 10^{6} \cdot T^{1.14}$	*1.14*	*50*
6	$H+OH+M \leftrightarrow H_2OM$	$1.30 \cdot 10^{21} \cdot T^{-2.00}$	*-2.00*	*0*
7	$H+H+M \leftrightarrow H_2+M$	$9.78 \cdot 10^{16} \cdot T^{-0.60}$	*-0.60*	*0*

Table 5. *Schmidt numbers.*

Specie	*Sc_i*
H_2	*0.29*
O_2	*0.76*
H_2O	*0.60*
OH	*0.51*
N_2	*0.75*
O	*0.20*
H	*0.10*

during which the first and second order statistical moments are sampled. The model EVM (extended Vulis model) mentioned in the Table 3 was developed in [61] and presents the revised Vulis model (VM) [62].

6.1 Combustion Chemistry

Based on the results of the previous studies, [63], comparing the influence of different reaction rate mechanisms, this investigation uses the 7-step mechanism of Davidenko *et al*, [64], with rate parameters according to Table 4. From [61] it is clear that the 7-step scheme predicts self-ignition and flame stabilization more accurately than the 1- and 2-step mechanisms used also in [63]. Associated with the reaction mechanism is the treatment of molecular diffusion and most chemistry models use polynomial fits for the diffusion coefficients, D_i. This approach is accurate but considered too expensive for this investigation and is here replaced by a simpler model based on that the Schmidt numbers, $Sc_i=\mu/D_i$, are virtually constant. Accordingly, we evaluate the molecular diffusivities as $D_i=\mu/Sc_i$, with Sc_k, given in Table 5. The thermal diffusivity is modeled similar-ly, with $D_t=\mu/Pr$, where $Pr\approx0.70$ is the Prandtl number. The flame speed, s_u^0, is obtained from 1D laminar flame calculations, based on the 7-step mechanism, resulting in a flame speed of ~1.4 m/s and a flame thickness of ~100 μm.

6.2 Results and Discussion

A first assessment of the LES predictions is provided by comparing spontaneous flame images, obtained by a normal video camera, [58], with corresponding images of the computed spanwise averaged temperature. An experimental flame image is shown in figure 6a whereas in figure 6b results from the LES-PaSR model are presented. From the experimental results of figure 6a we note that intensive and quite stable flame emission appears immediately downstream of the strut, with the flame gradually growing in thickness in the wake of the strut until it suddenly widens to a thickness of about 3h at around $x_{te}\approx9h$. This blunt flame front oscillates back and forth, with an amplitude of about 2h to 4h, and subsequently separate into an upper and lower branch at around $x_{te}\approx14h$. All four LES computations generally show good agreement with the experimental flame images, but with the LES-PaSR showing the overall best agreement, in particular considering the dynamics of the blunt front oscillating around $x_{te}\approx8.5h$. Based on the work of George *et al*., [65], the oscillating blunt flame may be a result of thermal blockage, or supercritical heat release, and as previously noted [63], cannot be modeled by simpler reaction mechanisms.

Figure 6c present a perspective view of the combustor flow from the LES-PaSR Case 3 in terms of iso-surfaces of the second invariant of the velocity gradient, λ_2, colored by the temperature, T, contours of the vertical gradient of the refraction index, $(\nabla n)_y$, at the centerplane, emulating a schlieren image, and contours of the axial velocity, v_x, on a horizontal plane in the middle of the combustor. The numerical schlieren image show oblique shocks at the leading edge of the strut, reflecting first in the combustor wall, then in the strut, and again in the combustor wall before impinging on the flame. Together with the weakly bent expansion fans, coming-off the trailing edges of the injection strut, this causes a distinctive shock-wave pattern to develop

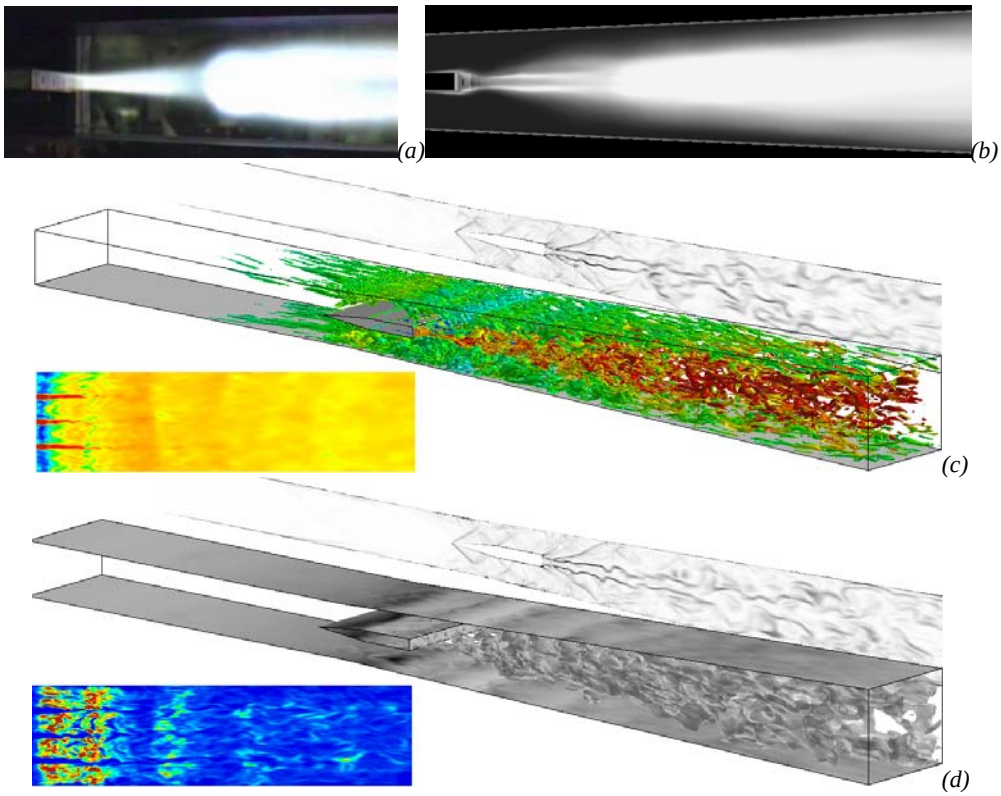

Figure 6. *Qualitative comparison. (a) Experimental spontaneous flame images, and (b) spanwise averaged temperature distribution from Case 3. (c) Iso-surface of the second invariant of the velocity gradient tensor, λ_2, colored by temperature, T, contours of the vertical gradient of the refraction index, $(\nabla n)_y$, at the centerplane, and contours of the axial velocity, v_x, on a horizontal plane through the injector strut for Cases 3. (d) Wall pressure distribution together with an iso-surface of the temperature at T=1400 K, $(\nabla n)_y$ at the centerplane, and contours of the logarithm of modeled heat release term $\overline{\Omega}$ on a horizontal plane through the injector strut for Cases 3.*

further downstream in the diverging area combustor. At the walls, the boundary layer thickens and the fluctuations increase as a consequence of the shock-boundary layer interactions. The boundary layers of the strut separate at the strut base to develop unstable shear-layers that break-up and develop Kelvin Helmholtz (KH) vortices on the boundary of the complex-shaped recirculation region that stabilizes the flame. The flow can be separated into the *induction zone*, in which turbulence controls mixing and combustion, in which the flame oscillates around the shear layers; the *transitional zone* which is dominated by large-scale coherent structures, convective mixing and exothermicity, in which the flame escapes the shear layers to develop three-dimensional (3D) ondulating structures, and the *turbulent combustion zone*, governed by large-scale coherent structures and mixing, in which the flame finally develops a strong 3D ondulating pattern. Intense longitudinal vortices develop between the spanwise KH vortices to rapidly merge with the toroidal-shaped vortex structures from the second-stage fuel-injector jets, making the flow and the mixing process very complicated. Comparing similar animations from all five LES computations show virtually the same dynamics and overall behavior.

In figure 6d the pressure, p, on the combustor walls, an iso-surface of T, and contours of the heat-release, $\overline{\Omega} = \Sigma_{i=1}^{N}(\overline{w_i} h_{f,i}^{\theta} - \nabla\cdot(\overline{\rho}\widetilde{Y}_i D_i \nabla \widetilde{Y}_i h_{f,i}^{\theta}))$, on a horizontal plane through the injector strut, from Case 3, are shown. The wedge shock and its reflections on the combustor walls and on the injection strut are clearly seen together with the bent expansion fan coming off the base of the injection strut, and the bow shocks forming around the secondary injectors. In the diverging combustor, the reflections of the pressure waves on both the combustor walls and on the flame (represented by T) can be noticed. The heat release distributions $\overline{\Omega}$ from the different LES models generally appear similar, but differ in many details. All $\overline{\Omega}$ distributions peak between the secondary fuel-jets, with lower values further downstream where primary burning occurs in the upper and lower branches of the flame (cf. figure 6b). The LES-PaSR model results in the smallest and most irregularly shaped reacting structures, whereas e.g. the LES-EDC and

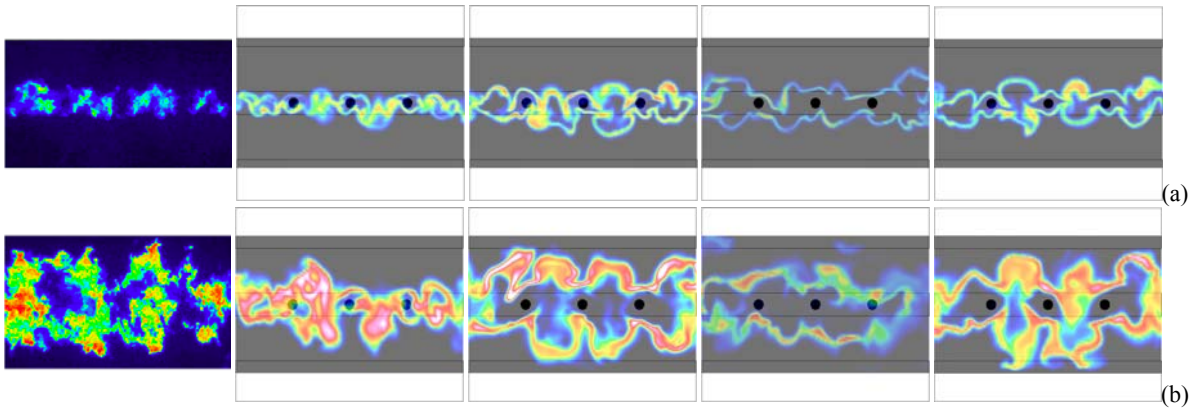

Figure 7. *Comparison of OH PLIF images from [58] with predicted short-time averaged Y_{H2O} mass fraction distributions from Cases 6, 7 and 8, respectively, at (a) x_{te}=4h and (b) x_{te}=10h. Note that the scale is the same for all computational Cases 3, 4, 5 and 6 and comparable to that of the experiments shown at the left. The results are (from left to right) from experimental data, [58], LES-PaSR, LES-EDC, LES-EVM and LES-TFM, respectively.*

the LES-TFM models both result in larger and more coherent burning structures. These reacting structures appears concentrated to specific regions between adjacent coherent vortical structures.

In figure 7 we compare measured and predicted OH-PLIF distributions after ignition at x_{te}= 4h and 10h, downstream of the base of the strut. The computed OH distribution is averaged over 50 time steps to match the intensifier gate width of 0.5 μs , essentially representing instantaneous comparisons. The following discussion is based on a number of measured and predicted images, and representative images are shown in figure 7. At x_{te}=4h the experimental data show high levels of OH between the second stage fuel jets, suggesting that ignition and combustion occur irregularly and early, using fuel primarily from the first stage injectors. This behavior is well captured by the LES-PaSR model, particularly featuring the pocket formation and burning, and reason-ably by the LES-EDC and LES-TFM models whereas the LES-EVM model predicts lower levels of OH in thin structures along the strut shear layers, suggesting too early ignition and poor fuel-air mixing. At x_{te}=10h the experimental data show high levels of OH in large volumes around the second stage fuel jets and low OH levels in the core of each jet, indicating that these are rather coherent. From these images, revealing the unsteady and strongly 3D reacting flow, it is difficult to grade the models, but it seems as if the LES-PaSR and LES-EDC models give the best agreement closely followed by the LES-TFM, although somewhat exaggerating the amount of OH, which seems somewhat better predicted by the LES-EVM. The OH structures are closely related to the vorticity dynamics, being influenced primarily by the baroclinic torque and the compressibility while vortex stretching is of less importance at high Ma numbers.

In figure 8 we compare time-averaged measured and predicted OH-PLIF distributions after ignition at x_{te}=4h and 10h, downstream of the strut

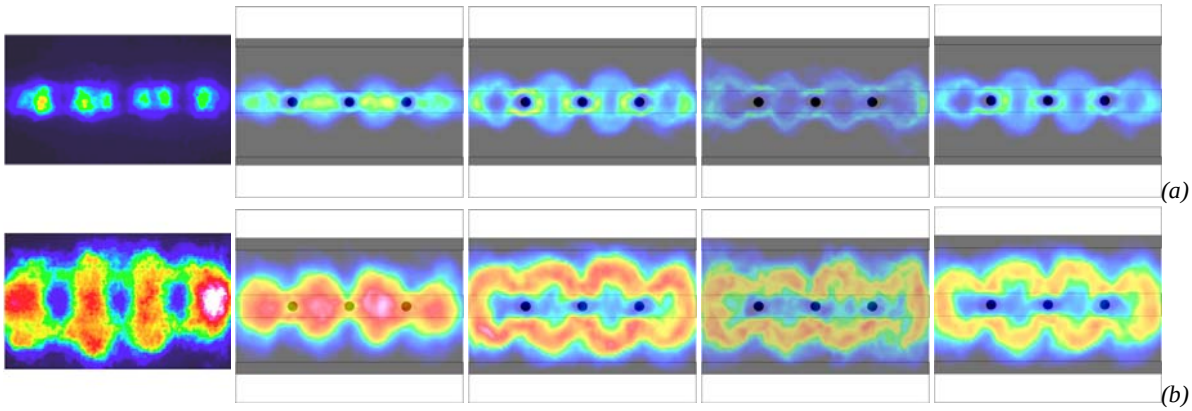

Figure 8. *Comparison of mean OH PLIF images from [58] with predicted long-time averaged $\langle Y_{H2O} \rangle$ mass fraction distributions from Cases 7, 8 and 9, respectively, at (a) x_{te}=4h and (b) x_{te}=10h. Note that the scale is the same for all computational Cases 3, 4, 5 and 6 and comparable to that of the experiments shown at the left. The results are (from left to right) from experimental data, [58], LES-PaSR, LES-EDC, LES-EVM and LES-TFM, respectively.*

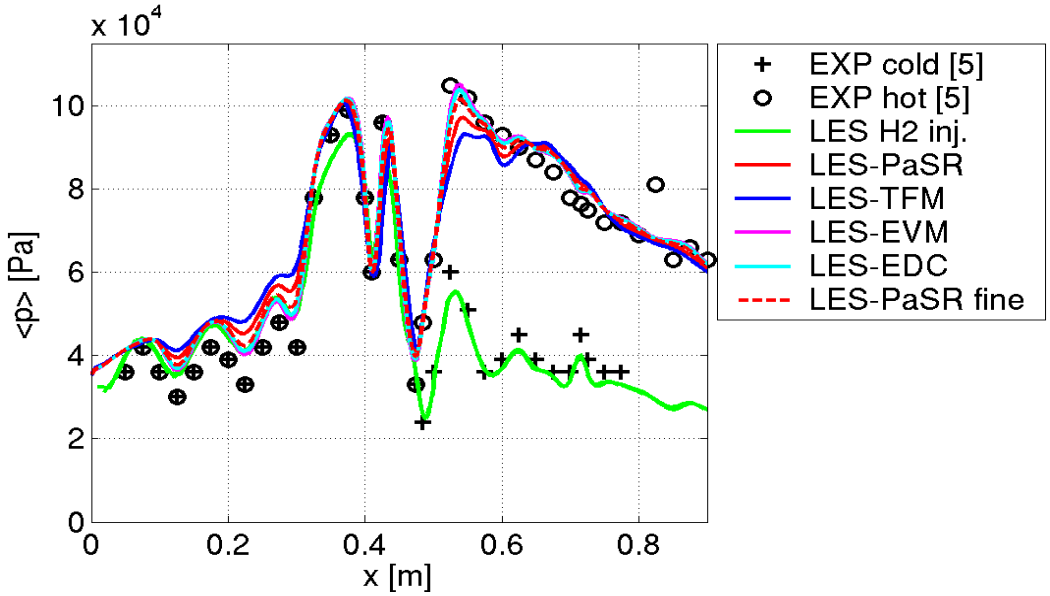

Figure 9. *Time-averaged wall pressure distributions along the lower combustor wall for inert H_2 injection (Case 1) and combustion (Cases 3, 4, 5, 6, 7 and 8).*

base. The computed OH distribution is averaged over 10 flow-through times to match the experimental averaging procedure, [58], using 30 to 50 instantaneous images, with images of poor combustion due to blow-off removed. At x_{te}=4h the best agreement with the experimental OH distributions is provided by the LES-PaSR model, which shows OH primarily in the regions between the secondary fuel jets, as seen in the experimental image, as a consequence of the first stage fuel burning in the wake of the strut. The LES-EDC and LES-TFM predicts OH formation by combustion of the first stage fuel before it has entered the wake, and also around the second stage fuel jets. The LES-EVM shows similar results as the LES-EDC, but with lower values of OH being formed, and primarily above and below the secondary fuel jets. At x_{te}=10h the best agreement between experimental data and predictions is again facilitated by the LES-PaSR model, with peak OH distribution between the secondary fuel jets. For all other LES models, the OH distribution shows higher values around the core region, and low values between the secondary fuel jets. The results of figures 7 and 8 suggest that LES-EDC, EVM and TFM predict self-ignition to occur too early compared to the experimental data, and thus also combustion to occur directly on the fuel-air interface of the first-stage fuel jets, whereas the LES-PaSR appears to predict the self-ignition to occur somewhat later.

Quantitative comparisons between measured and predicted wall pressures are presented in figure 9. Upstream of the strut all LES results overpredict the wall pressure, which may be the consequence of a too large viscous drag. Along the strut the wall pressure first increases and then decreases due to the blockage, and just at the end of the strut, the wall pressure increases rapidly due to the H_2 injection from the second stage fuel injectors. Further downstream, the pressure decreases, almost to the level of the freestream, around which it settles in the case of inert H_2 injection, whereas with combustion the wall pressure increases due to the volumetric expansion caus-ed by the combustion of injected H_2 to slowly relax with increasing distance from the strut trailing edge. The differences between the LES model predictions are small, with the LES-EDC and LES-EVM giving the best overall agreement with the measured wall pressure. As illustrated by the LES-PaSR model the agreement with the experimental data improves slightly with increasing grid resolution, and we take this as an indicator of the baseline grid being acceptable.

7. Summary and concluding remarks

This paper proposes a novel LES finite rate chemistry combustion model for turbulent flows. We start developing this model from a simple cartoon of turbulent flow (subsequently also involving combustion) that has evolved ever since Kolmogorov proposed his 1941 theory, [22]. Batchelor & Townsend, [18], made a strong case for non-uniform spatial distribution of the turbulent fine-structures based on experimental evidence in high Re number flows and thus also of molecular mixing and dissipation. Kuo & Corrsin, [24], showed that such fine-structure regions consist of vortex sheets, ribbons and tubes folded in certain regions of the flow. Chomiak, [16-17], refined these theories and

extended them into the field of combustion, proposing that at high Re numbers turbulent fine structure is not uniformly distributed but concentrated into small isolated regions, whose entire volume is a small fraction of the whole volume. DNS, e.g. [19], have provided support to this view, revealing that high intensity vortices amalgamate in filaments embedded into sheets of low intensity vorticity. For combustion, a similar organization of the flow has been observed from DNS, e.g. [20] and the results in this paper, supporting the earlier ideas of Chomiak, [16-17]. Such DNS suggests that the fine-structure vortices at the flame are essentially parallel to the flame whereas those behind the flame are mostly perpendicular to the flame. Regions of heat release and volumetric expansion are found to be regularly distributed among the fine-structure vortices in a background of low heat release and volumetric expansion. Magnussen, [13], used a similar cartoon of turbulent combustion to develop the Eddy Dissipation Concept (EDC) – the first heterogeneous multi-scale turbulent combustion model ever used.

The basic idea of the proposed model is to use the mathematical treatment of multi-phase flows for the description of fine-scale structures dissolved in the background turbulence, characterized by low intensity mixing. The model results in closing the filtered reaction rates (typically described by Arrhenius rate expressions), $\overline{\dot{w}_i(\rho,T,Y_k)}$, using the same rate expressions but evaluated at the fine-structure conditions and taking the fine structure volume fraction into account so that $\overline{\dot{w}_i(\rho,T,Y_k)} = \gamma^* \dot{w}_i(\bar{\rho},T^*,Y_k^*)$. In the proposed LES-EPaSR model, the fine structure conditions $\{Y_i^*,T^*\}$ are computed by solving a set of transport equations, thus being more general than the LES-PaSR model in which the fine structure conditions were obtained from local algebraic equations. For both the LES-PaSR and EPaRR models, the reacting fine structure volume fraction, γ^*, and the subgrid time scale, τ^*, needs to be provided by submodels. Based on the multi-phase analogy, a separate transport equation can be formulated for the reacting volume fraction such that $\partial_t(\bar{\rho}\gamma^*) + \nabla\cdot(\bar{\rho}\gamma^*\tilde{\mathbf{v}}) = -\bar{\rho}(\gamma^* - \gamma_{eq}^*)/\tau^*$, in which γ_{eq}^* and τ^*, needs to be modeled. A model for the subgrid time scale is here also proposed, based essentially on geometrical considerations, resulting in that $\tau^* = \sqrt{\tau_K \tau_\Delta}$, in which τ_K is the Kolmogorov time scale and τ_Δ is the time scale of the resolved shear. This particular time scale was recently found by Yeung *et al*, [57], to be the time scale that best characterized the Lagrangian statistics of dissipation, and therefore appears as a reasonable choice for representing the subgrid processes of interest to mixing and combustion at high Re-numbers. A model for the equilibrium reacting volume fraction, γ_{eq}^*, is proposed based on dimensional arguments and analysis of two cases (fast and slow chemistry in comparison with mixing) that takes the form $\gamma_{eq}^* = \tau_c/(\tau_c + \tau^*)$, in which τ_c is a chemical time scale. When subgrid convection is negligible the transport equation for γ^* degenerates into the analytical expression $\gamma^* = \tau_C/(\tau_C + \tau^*)$ that is employed in the LES-PaSR model, [12].

The proposed model, hereafter referred to as the LES-EPaSR model, was then successfully evaluated against other well-known LES combustion models such as the LES-PaSR, EDC, TFM and FPV models for a high Re number turbulent flame in a dump combustor. Experimental data of velocity and temperature, including the rms-fluctuations, were used to provide the reference against which all LES models could be bechmarked. The best overall agreement was obtained by the LES-EPaSR model closely followed by the PaSR model. In both cases the LES-FPV model resulted in the least accurate agreement with the reference data, whereas the LES-EDC and TFM models provided intermediate agreement with the reference data.

Acknowledgements

Dr T. Sunami is acknowledged for providing the experimental data and we also acknowledge Dr. Ph. Magre for valuable support and for valuable discussions. Financial support for this work was provided by the Office National d'Etudes et de Recherches Aerospatiales (VS) and by the Swedish Armed Forces (CF).

References

1. T. Poinsot and D. Veynante, Theoretical and Numerical Combustion, R. T. Edwards, ed., Philadelphia, 2001.
2. P. Sagaut, Large Eddy Simulation for Incompressible Flows, Springer Verlag, Heidelberg, 2001.
3. F.F. Grinstein, L. Margolin and B. Rider (Eds.), Implicit Large Eddy Simulation: Computing Turbulent Fluid Dynamics, Cambridge University Press, New York, 2007.
4. J. Janicka and A. Sadiki, Large Eddy Simulation of Turbulent Combustion Systems, Proc. Comb. Inst. 30 (2005) pp. 537-565.
5. H. Pitsch, Large Eddy Simulation of Turbulent Combustion, Annu. Rev Fluid Mech., 38 (2006) pp. 453-483.

6. C. Fureby, LES Modeling of Combustion for Propulsion Applications, Phil. Trans. R. Soc. A, 367 (2008) pp. 2957-2969.
7. P. Wang and X.S. Bai, Large Eddy Simulation of Turbulent Premixed Flames using Level-set G-equation, Proc. Comb. Inst. 30 (2005) pp. 583-591.
8. E.R. Hawkes and R.S. Cant, A Flame Surface Density Approach to Large Eddy Simulation of Premixed Turbulent Combustion, Proc. Comb.. Inst. 28 (2000) pp. 51-59.
9. R. Knikker and D. Veynante, Experimental Study of the Filtered Progress Variable Approach for LES of Premixed Combustion, in Advances in LES of Complex Flows, (Eds.) R. Friedrich and W. Rodi, Kluwer, Dordrecht, 2000 pp. 353-366.
10. P Givi, Filtered Density Function for Subgrid Scale Modeling of Turbulent Combustion, AIAA.J., 44 (2006) pp. 16-23.
11. O. Colin, F. Ducros, D. Veynante and T. Poinsot, A Thickened Flame Model for Large Eddy Simulations of Turbulent Premixed Combustion, Phys. Fluids 12 (2000) pp. 1843-1863.
12. M. Berglund, E. Fedina, J. Tegnér, C. Fureby and V. Sabelnikov, Finite Rate Chemistry LES of Self Ignition in a Supersonic Combustion Ramjet, AIAA.J. 48 (2010) pp. 540-550.
13. B.F. Magnussen, On the Structure of Turbulence and a Generalised Eddy Dissipation Concept for Chemical Reactions in Turbulent Flow, 19th AIAA Sc. meeting, St. Louis, 1981, USA
14. R.W. Bilger, Conditional Moment Closure for Turbulent Reacting Flow, Phys. Fluids A 5 (1993), pp. 436-444.
15. V. Sankaran and S. Menon, Subgrid Combustion Modeling of 3D Premixed Flames in the Thin-Reaction-Zone Regime, Proc. Comb Inst. 30 (2005), p 575-583.
16. J. Chomiak, A Possible Propagation Mechanism of Turbulent Flames at High Reynolds Numbers, Comb. Flame, 15 (1970) pp. 319-321.
17. J. Chomiak, Basic Considerations in the Turbulent Flame Propagation in Premixed Gases, Progress Energy Comb. Sci., 5 (1979) pp. 207-221.
18. G.K. Batchelor and A.A. Townsend, The Nature of Turbulent Motion at Large Wave-numbers, Proc. Roy. Soc. London A, 199 (1949) pp. 238-255.
19. P.R. Woodward, D.H. Porter, I. Sytine, S.E. Anderson, A.A. Mirin, B.C. Curtis, R.H. Cohen, W.P. Dannevik, A.M. Dimits, D.E. Eliason, K.-H. Winkler and S.W. Hodson, Very High Resolution Simulations of Compressible Turbulent Flows, Computational Fluid Dynamics, Proceedings of the 4th UNAM Supercomputing Conference Mexico City, June 2000, Ramos E., Cisneros G., Fernandez-Flores A., & Santillan-Gonzalez A., eds., World Scientific, p. 3..
20. M. Tanahashi, M. Fujimura and T. Miyauchi, Coherent Fine Scale Eddies in Turbulent Premixed Flames, Proc. Comb.. Inst. 28 (2000), pp. 579-587.
21. I.S. Ertesvåg and B.F. Magnussen, The Eddy Dissipation Turbulence Energy Cascade Model, Comb. Sci. Tech. 159 (2000), pp. 213-236.
22. A.N. Kolmogorov, Local Structure of Turbulence in an Incompressible Fluid for Very Large Reynolds Numbers, Comptes rendus (Doklady) de l'Academie des Sciences de l'U.R.S.S., 31 (1941) pp. 301-305. Reprinted in Friedlander S.K. & Topper L., eds., 1961, "Turbulence: Classic Papers on Statistical Theory", NewYork: Interscience Publishers
23. H. Tennekes and J.L. Lumley, A First Course of Turbulence, MIT Press, Cambridge, MA, USA, 1972.
24. Y.S. Kuo and S. Corrsin, Experiments on Internal Intermittency and Fine Structures Distribution Functions in Fully Turbulent Fluid, J. Fluid Mech., 50 (1971) pp. 285-319.
25. A.N. Kolmogorov, A Refinement of Previous Hypotheses Concerning the Local Structure of Turbulence in a Viscous Incompressible Fluid at High Reynolds Number, J. Fluid Mech., 13 (1962), pp. 82-85.
26. A.M. Obukhov, Some Specific Features of Atmospheric Turbulence, J. Fluid Mech. 13 (1962) pp. 77-81.
27. L.D. Landau and E.M. Lifshitz, Fluid Mechanics, (1959) Footnote on p. 126, Pergamon, London
28. [28] A.S. Monin and A.M Yaglom, Statistical Fluid Mechanics: Mechanics of Turbulence, 1971, Vol. 2, MIT Press, Cambridge, MA, USA.
29. U. Frisch. Turbulence: The Legacy of A.N. Kolmogorov, Cambridge and NewYork: Cambridge University Press, 1995.
30. A. Tsinober, An Informal Conceptual Introduction to Turbulence, Springer, 2009.
31. K.R. Sreenivasan and R.A. Antonia, The Phenomenology of Small-scale Turbulence, Ann. Rev. Fluid Mech., 29 (1997) pp. 435-472.
32. K.R. Sreenivasan and C. Meneveau, The Fractal Facets of Turbulence, J. Fluid Mech. 173 (1986) pp. 356-386.
33. R. Bensow and C. Fureby, On the Justification and Extension of Mixed Models in LES, J. Turb. 8(54) (2007) pp 1-12.
34. C. Fureby, On LES and DES of Wall Bounded Flows, Ercoftac Bulletin No 72, 2007, Marsh Issue.
35. F. Tichy, Laser-Based Measurements in Non-premixed Jet Flames, Ph.D. Thesis, Dept. of

Appl. Mech., Thermodynamics and Fluid Dynamics, Norwegian University of Science and Technology, Trondheim, Norway (1997).
36. B.F. Magnussen, The Eddy Dissipation Concept, ECCOMAS Thematic Conference on Computational Combustion, Lisbon, Portugal, 21-24 June (2005).
37. D.A. Drew, Mathematical Modeling of Two-Phase Flow, Ann. Rev. Fluid Mech., 15 (1983), pp. 261-291.
38. E. Fedina and C. Fureby, A Comparative Study of Flamelet and Finite Rate Chemistry LES for an Axisymmetric Dump Combustor, Submitted to J. Turb. (2010).
39. M. Boger, D. Veynante, H. Boughanem and A. Trouvé, Direct Numerical Simulation Analysis of Flame Surface Density Concept for Large Eddy Simulation of Turbulent Premixed Combustion, Proc. Comb. Inst. 27 (1998), pp. 917-925.
40. G.P. Smith, D.M. Golden, M. Frenklach, N.W. Moriarty, B. Eiteneer, M. Goldenberg, C.T. Bowman, R.K. Hanson, S. Song W.C. Gardiner, V.V. Lissianski and Z. Qin, http://www.me.ber-keley.edu/gri_mech/
41. E. Giacomazzi, V. Battaglia and C. Bruno C, The Coupling of Turbulence and Chemistry in a Premixed Bluff-body Flame as Studied by LES, Comb. Flame, 138 (2004), pp 320-335.
42. H.G. Weller, G. Tabor, H. Jasak and C. Fureby, A Tensorial Approach to CFD using Object Oriented Techniques, Comp. in Physics, 12 (1997), pp. 620-631.
43. D. Drikakis, C. Fureby, F.F. Grinstein & M. Liefendahl, ILES with Limiting Algorithms, In Implicit Large Eddy Simulation: Computing Turbulent Fluid Dynamics, Eds. Grinstein F.F., Margolin L. & Rider B., Cambridge University Press, 2007, pp 94-129.
44. B. van Leer, Towards the Ultimate Conservative Difference Scheme III. Upstream-Center-ed Finite-Difference Schemes for Ideal Compressible Flow, J. Comp. Phys., 23 (1977), pp 263-275.
45. C.M Rhie and W.L. Chow, Numerical Study of the Turbulent Flow Past an Airfoil with Trailing Edge Separation, AIAA J., 21 (1983), pp. 1525-1532.
46. T.J. Poinsot and S.K. Lele, Boundary Conditions for Direct Simulation of Compressible Viscous Reacting Flows, J. Comp. Phys., 101 (1992), p 104-129.
47. N. Jarrin, S. Benhamadouche, D. Laurence and R. Prosser, A Synthetic-Eddy-Method for Generating Inflow Conditions for Large Eddy Simulations, Int. J. Heat and Fluid Flow, 27 (2006), pp. 585-593.
48. I. Han and K.Y. Huh, Roles of Displacement Speed on Evolution of Flame Surface Density for Different Turbulent Intensities and Lewis Numbers in Turbulent Premixed Combustion, Comb. Flame, 152 (2008), pp 194.
49. J.H. Chen, T. Eckekki and W. Kollmann, The Mechanism of Two-Dimensional Pocket Formation in Lean Premixed Methane-Air Flames with Implications to Turbulent Combustion, Comb. Flame, 116 (1998), pp. 15-48.
50. J. Hult, S. Gashi, N. Chakraborty, M. Klein, K.W. Jenkins, S. Cant and C.F. Kaminski, Measurement of Flame Surface Density for Turbulent Premixed Flames using PLIF and DNS, Proc. Inst. Comb, 30 (2007), pp. 1319-1326.
51. Z.S. Li, B. Li, Z.W. Sun, X.-S. Bai and M. Aldén, Turbulence and Combustion Interaction: High Resolution Local Flame Front Structure Visualization using Simultaneous Single-Shot PLIF Imaging of CH, OH, and CH_2O in a Piloted Premixed Jet Flame, Comb. Flame, 157 (2010), pp. 1087-1096.
52. D. Veynante, G. Lodato, P. Domingo, L Vervisch and E. Hawkes, Estimation of Three-Dimensional Flame Surface Densities from Planar Images in Turbulent Premixed Combustion, Exp. Fluids, 49 (2010), pp. 267-278.
53. R.D. Gould, W.H. Stevenson and H.D Thompson, Investigation of Turbulent Transport in an Axisymmetric Sudden Expansion, AlAA.J., 28 (1990), pp. 276-283.
54. R.D. Gould, W.H. Stevenson and H.D. Thomson, Simultaneous Velocity and Temperature Measurements in a Premixed Dump Combustor, J. Prop. Power, 10 (1994), pp. 639-645.
55. A. Afshari, F.A. Jaberi, T. I.-P. Shih, LES/FMDF of Turbulent Combustion in Complex Flow Systems, AIAA 2007-1414 (2007).
56. A. Michalke, On Spatially Growing Distributions in an Inviscid Shear Layer, J. Fluid Mech., 23 (1965), pp. 521-544.
57. P.K. Yeung, S.B. Pope and B.L. Sawford, Reynolds Number Dependence of Lagrangian Statistics in Large Numerical Simulations of Isotropic Turbulence, J. Turb., 7 (2006), pp. 1-12.
58. Sunami T., Magre P., Bresson A., Grisch F., Orain M., & Kodera M.; 2005, "Experimental Study of Strut Injectors in a Supersonic Combustor using OH-PLIF", AIAA 2005-3304,
59. Sunami T., Murakami A., Kudo K., Kodera M. & Nishioka M.; 2002, "Mixing and Combustion Control Strategies for Efficient Scramjet Operation in Wide Range of Flight Mach Numbers, AIAA 2002-5116,
60. Collin G., Dessornes O. & Magre P.; 1997, "Installations d'essais pour les recherches

fondamentales en propulsion, PEP/FDP AGARD on Aerospace technology in the Service of the Alliance, Palaiseau, France.
61. George E., Sabel'nikov V., & Magre P.; 2007, "Large Eddy Simulations and Experimental Study of Self-Ignition of Supersonic Hydrogen and Methane-Hydrogen Jets in a Vitiated Confined Supersonic Air Stream", Computational Combbustion 2007, ECCOMAS Thematic Conference, Eds.; Roekaerts D., Coelho P., Boersma B.J. & Claramunt K., July, Delft. The Netherlands.
62. Vulis L.; 1961, "Thermal Regime of Combustion", Mac Graw-Hill, Chap. 3.
63. M. Berglund, E. Fedina, C. Fureby, V. Sabel'nikov and J. Tegnér. Finite Rate Chemistry Large-Eddy Simulation of Self-Ignition in Supersonic Combustion Ramjet, AIAA Journal Volume 48, Number 3, pp 540-550, 2010.
64. Davidenko D.M., Gökalp I., Dufour E. & Magre P.; 2006, "Systematic Numerical Study of the Supersonic Combustion in an Experimental Combustion Chamber", AIAA Paper 06-7915.
65. George E., Sabelnikov V. & Magre P.; 2007, "Self-Ignition of Ethylen-Hydrogen Mixtures in Unsteady Thermal Choking Conditions: Numerical Unsteady RANS Investigations", West-East High Speed Flow Field Conf., 19-22 Nov., Moscow, Russia.

7.2. TIME MEASUREMENT OF INDUCTION REACTION $H_2 + O_2$ IN THE DETONATION WAVE FORMATION IN A STOICHIOMETRIC MIXTURE AT THE PRESSURE WITHIN THE RANGE OF 1.1-2.3 ATM

P.V. Kozlov, S.A. Losev, Yu.V. Romanenko, O. P. Shatalov
Institute of Mechanics, Lomonosov Moscow State University, Moscow, Michurinsky pr. 1, kalevala@mail.ru

Abstract. The combustion of detonating gas in the high-pressure chamber was investigated on the double diaphragm shock tube. The regime of the optimum combustion of the mixture is obtained. The dependence of the H_2+O_2 reaction induction time on the initial pressure of mixture is determined. The rate constant and the activation energy for the reaction $3O_2 \rightarrow 2O_3$ was measured experimentally.

Introduction

Using a detonation mode of the high-pressure chamber (HPC) on shock tubes can increase the temperature and pressure test gas in the low-pressure chamber (LPC). For a better understanding of detonation and optimization of HPC using an oxyhydrogen gas, carried out research of modes for a particular installation. Detonation processes in the pipe under the ignition explosive mixture described in the classical experimental work and Urtiew, Oppenheim [1]. These studies were conducted in a tube of square section at a pressure of explosive mixture P≤1 atm using a microsecond electric discharge for ignition mixture. Their findings make it impossible to confidently work with HPC arbitrary designs in a wide range of pressures. Recently the number of researchers [2-4] they note that at low temperatures the ignition of oxyhydrogen gas, and mixtures of light hydrocarbon fuels with air they are not described by theory.

Now the researchers, compared with 60th years of the twentieth century, new opportunities - a multi-channel digital oscilloscope with a dynamic range of research input 14 bits, allowing recording the signal with sampling rate 2.5 MHz directly into computer memory for a second or more. This greatly facilitates studies on the mode of combustion and detonation.

Experimental setup

Fig. 1 shows a schematic double diaphragm shock tube. Tube consists of three sections made of stainless steel tubes with an inner diameter of 50 mm. For ignition explosive mixture in the center of a blank flange, the closing section of the HPC on the side opposite the diaphragm, is a spark gap (automotive spark plug FORCAM-1), through which one can make nanosecond discharge of high voltage ceramic capacitors KVI-3. Nanosecond discharge times provided so that the capacitors and spark gap is a low-inductance circuit. Discharge in the circuit occurs when self-breakdown spark gap during the pulse charge (300,400 microseconds) ceramic capacitors.

Along the high-pressure chamber located two pairs of piezoelectric pressure sensors P1-P4 (the distance between the sensors in a pair of 100 mm). At the end of the intermediate pressure chamber (IPC) was also located a pair of piezoelectric sensors P5-P6. Diaphragm between the HPC and LPC not installed. These chambers are filled with stoichiometric mixture of hydrogen and oxygen at pressures of 0.4 2.3 atm. This tube filled alternately with small portions of oxygen and hydrogen.

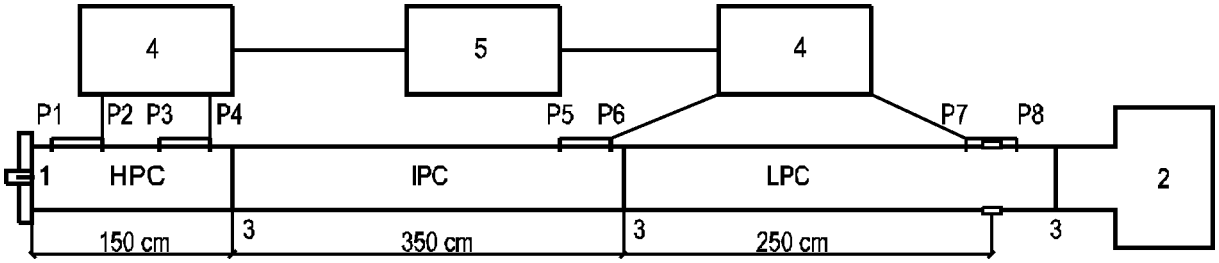

Fig. 1. *Schematic of double diaphragm shock tube. 1 – spark plug; 2 – dump tank; 3 – cooper or Mylar diaphragm; 4 - digital oscilloscope 14 bit 2.5 MHz; 5 – notebook.*

Filling and mixing continued for at least 2 hours. After ignition and combustion of gas in the tube diaphragm is rupture and occurs outflow of gas in dump tank.

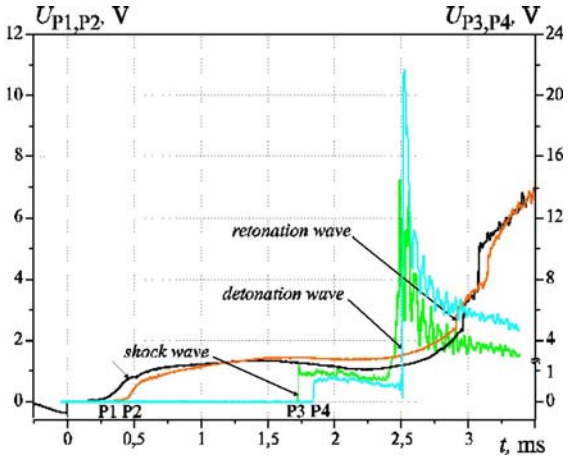

Fig. 2. *Oscillograms of the first four pressure sensors P1 P4 for the initial pressure of oxyhydrogen mixture 1.44 atm.*

Figure 2 shows an example of waveforms of signals of pressure sensors P1-P4 for the initial pressure of the oxyhydrogen mixture 1.44 atm. Start scan coincides with the beginning of charging the high voltage storage capacitor low-inductance discharge circuit. The first input signal oscilloscope except the first pressure sensor signal from the electric probe, which is located in a high-voltage discharge circuit. This signal shows the process of charging the capacitor and the time of electrical breakdown of the discharge gap spark plugs. From the oscillograms it is clear that in the first two sensors P1, P2, the compressional wave of cold gas due to combustion of the mixture and the increase in the volume of the combustion products of burning, does not have an abrupt front. On sensors P3 and P4, we see already formed the front of supersonic wave. Processing such waveforms allows us to construct *x-t* diagram of wave propagation in HPC and efficiency.

Results

Figure 3 shows the trajectory of the shock wave compression of cold gas caused by burning the mixture, the trajectories of the detonation and detonation waves and place of the initial explosion of the mixture. To determine the trajectories used signals from the pressure sensors P1-P6. Squares on the graph indicate the time of arrival of waves at the corresponding sensor. Coordinate L=0 corresponds to the location of the spark plugs. AB denotes the motion trajectory of the gas molecules were in the chamber cross section A, at the time of passage through it of a shock wave compression cold gas to the chamber cross section B in which the thermal explosion and formed detonation wave propagating in the same direction as the shock wave compression of cold gas.

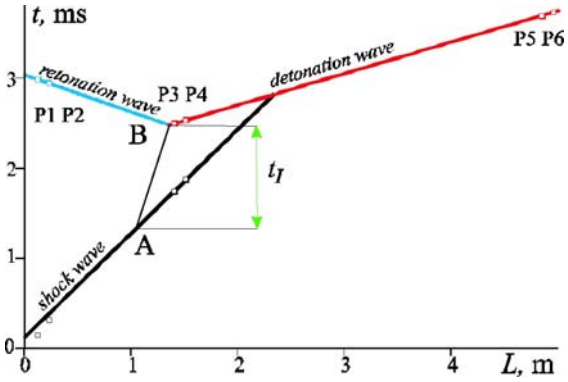

Fig. 3. *x-t diagram of the processes occurring in the high-pressure chamber after ignition the mixture.*

According to our measurements in the section of the chamber A Mach number of shock wave has a value of 1.56-1.6. We believe that the time t_I, indicated in Fig. 3 - this time the induction of the reaction caused by a mixture of shock wave of achievement in section A of this Mach number. Apparently, the time of thermal explosion and detonation time of formation in comparison with the induction time can be neglected. It well known that the thermal explosion is much smaller than the induction time. In [5] first showed that in terms of spatial heterogeneity in temperature or concentration of active centers, the detonation formed very quickly.

Note that such a simple form *x-t* diagram has, if the Mach number of shock wave of cold gas exceeds the value of 1.56-1.6. At lower Mach numbers, the picture has changed qualitatively. Either detonation is born at the shock wave reflection from the diaphragm, or a weak combustion, at the collision point reflected from the diaphragm of the first shock wave of cold gas and emanating from the combustion of a second or subsequent shock waves. Thus, we can state that the compressional shock wave of cold gas emanating from the combustion region when the number of M>1.56-1.6, excites in a stoichiometric mixture of oxygen and hydrogen, the ignition process. Note that the temperature behind the shock wave is low T_2=410 K. This means that the mixture behind the shock wave is outside the ignition peninsula in accordance with the classical work of Lewis and Elbe [6]. We assume, that the Mach number of shock waves larger than the value 1.56-1.6 in the shock front occurs translational nonequilibrium, which leads to the existence of the front, where there is high "longitudinal"

temperature T_{lng} exceeding the equilibrium temperature T_2 behind that may lead to the formation of this hot field centers to initiate the reaction. Earlier in [7], we experimentally demonstrated the existence of this effect in argon (with the number of M=6 have $<T_{lng}>=1.7 \cdot T_2$). Theoretically, this effect described for multicomponent mixtures [8, 9]. In these studies, show that for different mixes the "longitudinal" translational temperature in the shock wave front can exceed the equilibrium temperature behind the shock wave front several times.

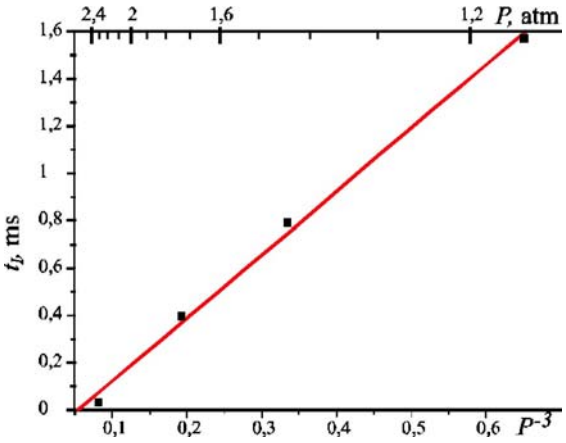

***Fig. 4. T**he dependence of the induction time of the reaction H_2+O_2 on the initial pressure of the mixture.*

Fig. 4 shows the obtained in our experiments the dependence of ignition delay t_I, the cube of the initial mixture pressure in the pressure range of 1.1-2.3 atm. We see this dependence is almost linear. This could mean that the induction time of thermal explosion of a mixture determined by trimolecular reactions. We can assume that in the shock wave formed initiating centers in accordance with the reaction

$$O_2 + O_2 + O_2 \rightarrow O_3 + O_3 \quad (1).$$

That is, the formed ozone molecules play the role of centers of initiation of the reaction H_2+O_2. Further possible following a chain mechanism involving trimolecular reactions, which supports the slow (during the induction time), burning the mixture until the heat of the explosion.

$$O_3 + H_2 + H_2 \rightarrow 2H_2O + O \quad (2)$$

$$O + O_2 + O_2 \rightarrow O_3 + O_2 \quad (3)$$

As for reaction (3) it is known and constant in her cold mixture of newly refined experimentally [10]. Reaction (2) also should not be slow, because, according to our estimates, the single act of energy E≈9.95 eV. We note, as an oxygen atom, resulting in reaction (2), very energetic (E_{max}≈6 eV), it can initiate the dissociation of oxygen

$$O + O_2 \rightarrow O + O + O \quad (4).$$

In this case, taking into account the reactions (2 4) we have a mechanism branched-chain reaction in a mixture of H_2+O_2 during the induction period.

The studies for high-speed modes in the low-pressure chamber, we used in HPC mixture H_2:O_2:He=2:1:3, and supplied prehamber [11]. In the tape between the sections of HPC, efficiency and gain were used knives and cooper diaphragm thickness of 0.08 mm. At filling out the HPC P=4.2 atm, the efficiency of helium P=20 kPa and a mixture of LPC 80%N_2+20%O_2 until P_1=33 Pa was obtained by the shock wave in the gain equal to 8 km/sec. At the same time provides a mode of occurrence of a detonation wave in HPC under the reflection of the shock wave compression of cold gas from the diaphragm located at the end of the HPC. A detonation wave propagates in the direction of the spark plugs.

In connection with the obtained results, it is necessary to note the following. The problem of the divergence of the experimental and theoretical delay times of the ignition of combustible mixtures at low temperatures, which are conducted on the shock tubes, for the purpose of the simulation of the processes, proceeding in the internal combustion engines [3, 4], is connected not with deficiencies in the existing theories. These divergences connected with the fact that for studies it adapts heating working mixtures in the reflected shock wave. Our experiments showed that the region of the reflected shock wave does not simulate the process of the adiabatic compression by the piston of working gas in the cylinder of engine, since piston with the compression moves with subsonic speed. In the reflected shock wave of the compressed gas is preliminarily "developed" by the shock wave front, which creates in it the centers of the initiation of chemical reaction. Possibly, the same process occurs also in the front behind of the reflected shock wave. This leads to the considerable decrease of the ignition delay of combustible mixture in the reflected shock wave in comparison with the theory. Without taking into account nonequilibrium in the front incident and reflected shock waves the formal fitting of the rate constants of chemical reaction in the authors [3, 4], that is conducted for the purpose of the agreement of the results of calculation and experiment on the measurement of the ignition delays of mixtures at low temperatures, does not have physical sense.

The following experiment carried out for checking our assumptions. Is executed a study of the presence of ozone behind the shock wave front in

pure oxygen at temperatures and pressures of those corresponding to the calculated parameters in the shock wave front of compression in the detonating gas, described above. Initial oxygen pressure changed from 0.53-1 atm, temperature behind the shock wave front was selected to the approximately equal average "longitudinal" temperature in the front with the Mach number ~1.56-1.6 [7], which corresponds to the Mach number of the incident shock wave of ~2.7 (T_2=685 K). For obtaining, such parameters shock tube worked in the double diaphragm regime. In this case the pressure of mixture H_2:O_2:He=2:1:3 in HPC composed 3.6-4.2 atm, and intermediate chamber was filled by helium at a pressure 0.8 atm. HPC was filled by oxygen of high purity ([O_2] =99.999%).

For measuring ozone concentration was used the traditional procedure of the measurement of the radiation absorption of mercury line at the wavelength 253.7 nm [12]. Optical diagram (Fig. 5) ensured spatial resolution not worse than 4.5 mm. the light radiant flux of mercury-vapor lamp I_0 passing through measuring volume it did not exceed 10^9 photons per second. An example of the measured radiation absorption I/I_0 by ozone formed behind the shock wave front to that extending with a velocity of 940 m/s (M=2.86) in oxygen at an initial pressure 0.67 atm, is presented in Fig. 6. In the same figure are shown signals from the pressure sensors P7 and P8.

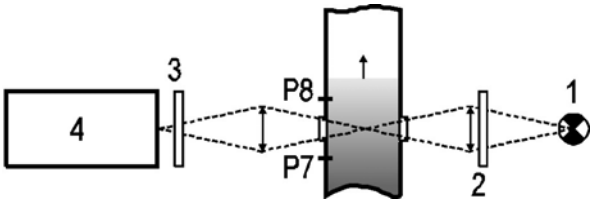

Fig. 5. *Optical diagram of the measurement absorption of mercury-vapor lamp. 1 - lamp mercury DRGS-12; 2 - the filter UFS-1; 3 - the interference filter of λ_0=254 nm, $\Delta\lambda$=10 nm; 4 – PMT (Hamamatsu R6838).*

Schlieren signal now of the time of t=0 corresponds to the passage of shock wave front through the light beam in the measuring section. After the passage of shock wave front is observed an increase in the radiation absorption of mercury-vapor lamp during 75 μs, and then the decrease of absorption connected, apparently, with the start of the reactions of those leading system O_2:O_3:O to the chemical equilibrium.

In accordance with the standard methods of measurements, this absorption assigned to the molecules of ozone. Measured thus concentration of ozone in the maximum of absorption (Fig. 6) composed $9.6\cdot10^{14}$ mol/cm^3, that into $6\cdot10^8$ times exceed the equilibrium concentration of ozone at this temperature [12]. Analogous absorption curves measured for other initial pressures of oxygen and shock wave velocities.

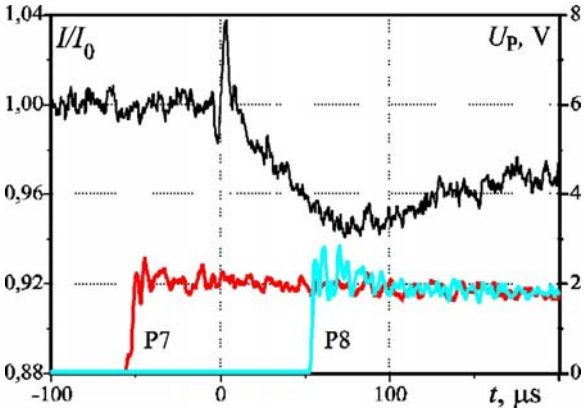

Fig. 6. *Absorption of mercury line 253.7 nm behind the shock wave front in pure oxygen.*

Если предположить, что за фронтом ударной волны начинают происходить реакции со скоростью k_1 и со скоростью k_2 то для начального участка кривой поглощения справедливо следующее соотношение

If one assumes that behind the shock wave front begin to occur the reactions $O_2+O_2+O_2 \rightarrow O_3+O_3$ with the speed k_1 and $O_3+O_3 \rightarrow O_2+O_2+O_2$ with a speed of k_2 that for the initial section of absorption curve the correctly following relationship

$$\frac{d[O_3]}{dt} = k_1[O_2]^3 - k_2[O_3]^2 .$$

As a result processing of experimental data were obtained the value of $k_1=1.56\cdot10^{-42}$ cm^6/s with T=686 K $k_1=9.1\cdot10^{-41}$ cm^6/s with T=760 K. The energy of the activation E_A of reaction (1) calculated for these conditions was 2 eV.

To on the basis obtained reaction rate of the formation of ozone at a temperature of 686 K of estimation they show that in the shock wave front with the Mach number 1.56-1.6 can be produced to ~10^7 of the molecules of ozone in one cubic centimeter of oxyhydrogen gas. This in our opinion is a sufficient value for the initiation of mechanism (2-4) of flow of induction period of reaction H_2+O_2 described above.

Conclusion

The studies of the regimes of operation of the high-pressure chamber of the double diaphragm shock tube carried out. Determined the optimum regime, with which the wave of detonation conceived in the shock wave reflected from the diaphragm, which ensures obtaining the maximum para-

meters of the investigated gas.

In the range the pressures of 1.1 - 2.3 atm is established the cubic dependence of the time of the induction of reaction on the pressure, with the forming of detonation in the oxyhydrogen gas in the shock tube by the diameter of 50 mm with its ignition by nanosecond electrical spark. The mechanism of the induction period of the reaction of oxyhydrogen mixture proposed the different from traditional. The leading role in this case the effects of progressive nonequilibrium in the shock wave front and trimolecular reactions with the participation of ozone play.

Is measured the nonequilibrium concentration of ozone, which is formed behind the shock wave front in oxygen in the range of the initial pressures of 0.53-1 atm with the Mach numbers of 2.7-2.9. Is determined reaction rate $O_2+O_2+O_2 \rightarrow O_3+O_3$ at temperatures of 686 K and 760 K, the energy of the activation of this reaction is obtained.

Reference

1. Urtiew P., Oppenheim A.K. // Experimental Observations of the Transition to Detonation in an Explosive Gas/Proc. Roy. Soc. Lond. 1966. Ser. A. V. 295. P. 13.
2. Павлов В.А. // Некоторые особенности измерения и интерпретации времени индукции воспламенения водородо–кислородных смесей за фронтом ударной волны/ 2009. Том 8, www.chemphys.edu.ru/pdf/2009-03-12-002.pdf.
3. G. A. Pang, D. F. Davidson, R. K. Hanson, //Experimental study and modeling of shock tube ignition delay times for hydrogen-oxygen-argon mixtures at low temperatures/ Proc. Combust. Inst. Volume 32, Issue 1, 2009, Pages 181-188.
4. K. A. Heufer H. Olivier// Determination of ignition delay times of different hydrocarbons in a new high pressure shock tube/ Shock Waves 20 (2010) 307 316.
5. Зельдович Я.Б., Либрович В.Б., Махвиладзе Г.М., Сивашинский Г.И. О возбуждении детонации в неравномерно нагретом газе // Прикладная механика и теоретическая физика.-1970.- №2.- 76-84.
6. Льюис Б., Эльбе Г. Горение, пламя и взрывы в газах. - М.: Мир, 1968.
7. Козлов П.В., Лосев С.А., Романенко Ю.В./ Поступательная неравновесность во фронте ударной волны в аргоне// Вестник Московского Университета. Серия 3. Физика. Астрономия. 1998, №5, стр.46-51.
8. Топчиян М.Е.//К энергетическим соотношениям в ударных и детонационных волнах/ Физико-химическая кинетика в газовой динамике 2005. Том 3, www.chemphys.edu.ru/media/files/2005-11-21-001.pdf.
9. Великодный В.Ю., Качармин С. В. /Структура ударных волн в трехкомпонентных газовых смесях //Физико-химическая кинетика в газовой динамике 2010. Том 10, www.chemphys.edu.ru/media/files/2010-01-21-001____.pdf
10. Azyazov V.N., Mikheyev P.A., Postell D.J., Heaven M.C.// $O_2(a^1\Delta)$ quenching in the $O/O_2/O_3$ system. / Chem. Phys. Lett. - 2009. - V.482. - P.56-61.
11. П.В. Козлов, Ю.В. Романенко // Экспериментальное исследование излучения ударно-нагретого воздуха на двухдиафрагменной ударной трубе/ 3-я Всероссийская Школа-семинар «Аэрофизика и физическая механика классических и квантовых систем»: Сборник научных трудов. – М. ИПМех РАН. 2010. С. 77-80.
12. В.В. Лунин, Попович М.П., Ткаченко С.Н.//Физическая химия озона/ Изд-во. МГУ, 1998.

7.3. ELECTRICAL DISCHARGE EFFECT ON A MULTISTAGE IGNITION AND COMBUSTION IN A CHEMICAL COMPRESSION REACTOR

Bityurin V.A., Bocharov A.N. and Filimonova E.A.
Joint institute for high temperatures of Russian academy of sciences,
125412 Moscow, st. Izhorskaya, 13, bl.2
E-mail: helfil@mail.ru

Introduction

Primordially, the interest to low temperature oxidation (T~550-700 K) of fuel-air hydrocarbon mixtures was associated with the study of combustion in a spark ignition engine (an engine knock) and diesel engine with homogeneous charge (for example, nature gas with air) [1]. The visible appearance of this oxidation is the fluorescence of formaldehyde (CH_2O) and formal radical (CHO) with the wave-length of blue spectral region. Since in some experiments on assisted combustion by discharge it is observed the blue color light emission before inflammation in closed volume [2], the low temperature ignition (600-720 K), the fast propagation flame (200 m/s and more), the almost instantaneous observed ignition of the whole volume [3], then, for these phenomena the multistage ignition in closed discharge systems may be responsible.

One of the directions, relating to the environmental preservation is NO reduction in internal combustion engine exhaust gas. For that reason it is suggested to use the lean fuel-air mixture. However, there are difficulties in ignition and combustion stabilization of lean mixture. Utilization of electrical discharge instead of spark is the state-of-the-art direction both a fundamental investigation [4] and in the field of creation of a new motor car.

Because the multistage inflammation is a characteristic feature of internal engine combustion at low in-flow temperature (temperature of heated fuel-air mixture before cylinder) the goal of given work was to develop the kinetic model including a low temperature ignition stage in hydrocarbon-air combustion mixture, to determine the effect of radical admixture – a result of discharge operation - on multistage ignition and to show the appearance of low temperature ignition in engine.

Description of model

The simulation of combustion process was carried out using the kinetic code for the constant volume condition with taking into account a heat emission. The cooling of walls was not taken into consideration, and nowadays insufficiently studied peroxide decompositions on the walls was accepted in some reactions just approximately. Multistage inflammation includes the cool flame stage (T ~ 550-750 K), blue flame (T ~ 800-1000 K) and hot flame (T>1000 K) stages. The appearance of low temperature oxidation of hydrocarbon-air mixtures is accompanied by stepped release of fuel mixture chemical enthalpy throughout the organic peroxide decomposition. In experiments the multistage ignition is identified throughout the stepped growth of pressure and light emission. In calculations the identification of those flames is the change of pressure or temperature, and concentrations of the key components.

The combustion process in an internal combustion engine was considered in the approach of a well-stirred chemical reactor. It is assumed that a working body is the uniform mixture of ideal gases in a whole volume at any operation stage [5]. The chemical compression reactor model consists of three main parts: a model of geometric and kinematics characteristics of cylinder-piston system; a valve operation model and a model of physical chemical processes in the working volume of cylinder. A total mass, species masses and internal energy conversation equations are solved. A heat exchange at the walls of cylinder and lid of piston are taken into account.

To consider the discharge effect on ignition in fuel-air mixture the initial concentrations of radicals were determined in an approximation of specified electric field. The concentration of primary active particles is estimated via the coefficients of corresponding processes of dissociation and excitation of species by electron impact and input energy per one molecule. All the kinetic and transport coefficients as functions of the reduced electric field E/n (where E is the electric field and n is the gas density) are obtained by averaging of corresponding cross sections with the electron energy distribution function. The latter is calculated using the BOLSIG+ kinetic code. The rate constants of processes by direct electron impact for propane-air mixture were taken from the work [6]. Initial concentrations of radicals were the inlet parameters for chemical kinetic code.

The basic set of species and reactions of present chemical kinetic code has been used earlier for the description of formation and removal of toxic impurities in the automobile exhaust gases, for the

simulation of physical and chemical processes in the chemical compression reactor [5], in the study of ignition of fuel-air counter-flow jets by electrical discharge and other tasks. To decide the low temperature inflammation problem that chemical kinetic scheme was added new reactions and components taken from several sources [7].

Influence of radicals on multistage inflammation

The results of verification of chemical kinetics scheme at the temperature higher than 1000 K for CH_4-C_2H_6-C_3H_8-O_2-Ar mixtures and the chemical kinetics of low temperature ignition for propane and acetaldehyde have been published in [7]. The first results of preliminary calculations [7] showed that radicals (O, H, CH_3 - the dissociation products by direct electron impact) reduce the induction time of cool flame ignition, conserving the duration of blue and hot stages the unchanged.

Taking into account the operation conditions for gas internal combustion engines: high pressures and propane-butane-air composition, a low temperature ignition for propane-air mixture at pressure of 5.5 Bar was considered. In Fig.1 the evolution of temperature and OH concentration resulted from a combustion modeling for $6.5\%C_3H_8+19.6\%O_2+73.9\%N_2$ mixture are shown for T_0=650 K. The first OH peak corresponds to appearance of cool flame (time is 1.16 s) with temperature increase at 130º, a weak OH peak at time of 1.202 s corresponds to the blue flame stage and the hot flame arises at time of 1.207s.

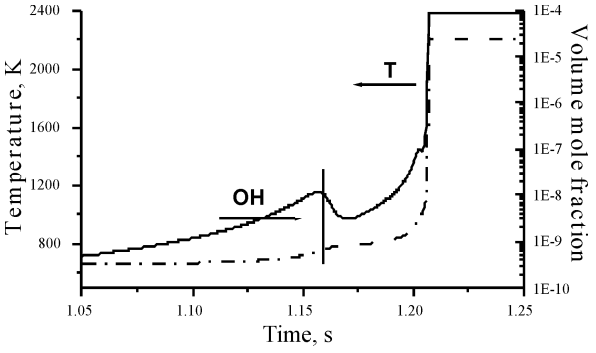

Fig.1. *Temperature and OH concentration in dependence on time in $6.5\%C_3H_8+19.6\%O_2+ 73.9\%N_2$ mixture. P_0=5.5 Bar, T_0=650 K.*

If the mixture is activated by discharge, the induction time noticeably reduced. In Fig. 2 the comparison of temperature dependence on time for two cases demonstrates the shift of induction time more than one order of magnitude: from 1.2 s to 0.09 s. The primary radical concentrations were calculated using the rate constants of dissociation and excitation for propane-air mixture [6] at the fixed reduced electric field of 200 Td, and in suggestion that the input energy into the system was equal to 0.01 eV/molecule. As a result the active particle concentrations generated by discharge were following: $[O]_0$=1500 ppm, $[H]_0$=500 ppm, $[n\text{-}C_3H_7]_0=[iso\text{-}C_3H_7]_0=[C_2H_5]_0=[CH_3]_0$=250 ppm. The transient spark discharge which is suitable for activation of methane-air mixture due to a good branched system of channels and tenability of energy input in to the channels has been simulated in [8]. Experimental study of radio-frequency discharge at higher pressures has been presented in [4].

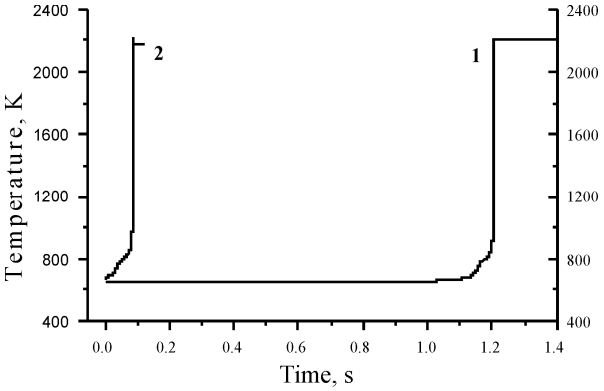

Fig.2. *Temperature in dependence on time: "1" is self-ignition, "2" is a mixture activated by discharge. Conditions are in Fig.1*

Overall result on an ignition time reduction at low temperatures in propane-air mixture activated by discharge in comparison with a self-ignition is presented in Fig.3. The experimental data [9] are also indicated. Some difference between experimental data and calculations at T=700-720 K may be related with a negative temperature coefficient of reaction process which did not observed in the modeling. In Fig. 3 it is clearly seen the strong influence of primary radicals on ignition time. The shift of time is by a factor of 20, and initial temperature is shifted up to 570 K instead of 650 K without activation.

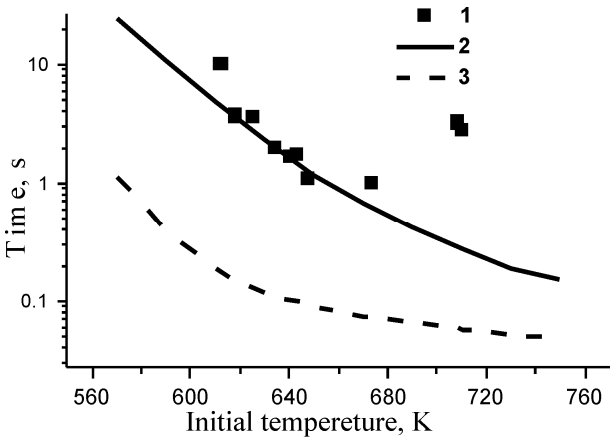

Fig.3. *Induction time verses temperature. "1" is experiment [9]; "2" is self-ignition, "3" is mixture activated by discharge. Conditions are in Fig.1*

The analysis of leading reactions of cool flame stage in C_3H_8:O_2 and C_3H_8:air mixture showed that the preferred mechanism of organic peroxide formation under conditions of alkyl radical (iso-C_3H_7, n-C_3H_7) production by discharge becomes the way via formation of propylperoxy radicals iso-$C_3H_7O_2$ and n-$C_3H_7O_2$.

Then the sequence of propylperoxide (C_3H_7OOH) formation may be written as follows:

$$C_3H_8+e \rightarrow \text{iso-}C_3H_7+H+e$$

$$O_2+\text{iso-}C_3H_7 \rightarrow \text{iso-}C_3H_7O_2$$

$$C_3H_8+\text{iso-}C_3H_7O_2 \rightarrow C_3H_7OOH+\text{n-}C_3H_7$$

$$C_3H_7OOH \rightarrow OH+\text{iso-}C_3H_7O$$

The C_3H_7OOH decomposition with OH production gives the main input in the cool flame inflammation when the enthalpy partially releases, and, as a consequence, the temperature and pressure increase. In contrast, the self-ignition of CH_4 and C_3H_8 containing mixtures the formation of hydro peroxides for the most part comes from the intermediate product – acetaldehyde [7].

Combustion modeling in chemical compression reactor

The importance of taking into account of low temperature ignition in the chemical kinetics scheme for description of processes in a chemical compression reactor is illustrated in Fig.4 for access air factor of α=0.43-0.459. Following initial parameters for chemical compression reactor were accepted: piston diameter is 11 cm, compression ratio (geometric) is 15, rotation speed is 1500 rpm, wall temperatures for engine-lid, piston-head and side-wall are 600 K, heat transfer coefficient is 200 W/m^2/K, in-flow pressure P_0=1.28 Bar, exhaust gas pressure P_{ex}=1.1 Bar. In experiment a mixture has been `preliminary heated up to obligatory temperature to initiate the combustion process. Only involving of low temperature ignition mechanism for propane in the kinetics scheme was permitted describing the experiments [10].

With a point of view of environmental preservation the influence of low in-flow temperatures at α=2 on combustion process in chemical compression reactor was simulated for the gas mixture containing air and 90%C_3H_8+ 10%C_4H_{10} fuel. In Fig.5 the maximum temperature of combustion and appropriate to it the NO concentration in dependence on T_0 is shown. For considered conditions the minimum in-flow temperature is equal to 380 K when an instable combustion is feasible. The lower in-flow flow temperature, the lower maximum temperature, and as a consequence, lower NO concentration.

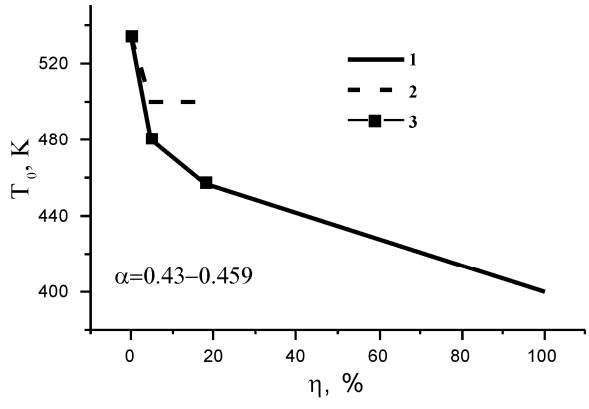

Fig.4. *Change of obligatory in-flow temperature for mixture ignition in dependence on total C3H8 and C4H10 fraction in the fuel (CH4): η = ([C3H8]+[C4H10])/([C3H8]+[C4H10]+[CH4]). "1" is C3H8 low temperature ignition is included, "2" is C3H8 low temperature ignition is not included,"3" is experiment [10].*

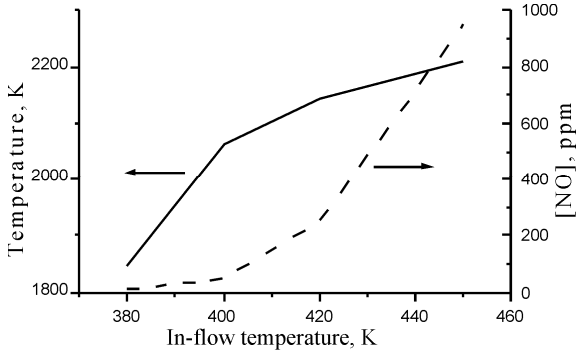

Fig.5. *Maximum temperature and NO production in air + (90%C_3H_8+10%C_4H_{10}) mixture at α=2.*

The evolution of pressure and temperature at T_0=380 K clearly demonstrates the appearance of low temperature ignition in the chemical compression reactor: a stepped increase of temperature and two peaks of pressure (see Fig.6). First peak is related with energy release at cool flame stage, after that due to descent of piston the pressure begins to decrease but because of initiated combustion the pressure increases again. However, the maximum is lower than that under stable combustion at higher in-flow temperature (50 Bar instead of 80 Bar).

The possibility in principle to initiate the combustion in internal (spark) combustion engine by electrical discharge similar to [4,8] at low in-flow temperature in lean gas mixture, is demonstrated in Fig.7.

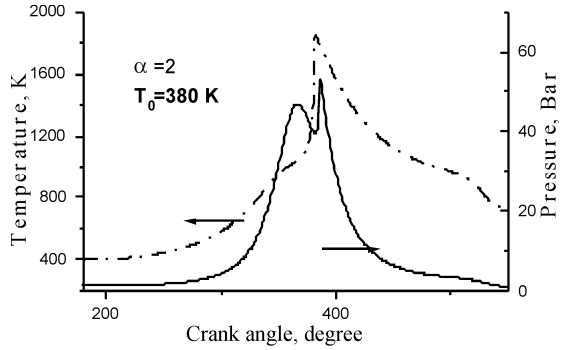

Fig.6. *Temperature and pressure evolution in air + (90%C3H8+10%C4H10) mixture at α=2 and obligatory in-flow temperature of T0 =380 K.*

To simulate the combustion process the compression ratio was reduced from 15 to 8 and rotation speed was increased to 3000 rpm, which is usual for spark ignition engine. Other parameters in the modeling have not been changed. An primary component concentrations resulted from discharge operation at T=800 K were estimated as considered above, and it was following: [O] = 2000 ppm, [H] = 150 ppm, $[CH_3]=[C_2H_5]=[C_3H_7]$=80 ppm. The treatment by discharge in top dead center was continued durine 5 degrees (about 280 μs). Without discharge there is no combustion, the maximum temperuture is 800 K, with dischage T =2000 K and P=45 Bar.

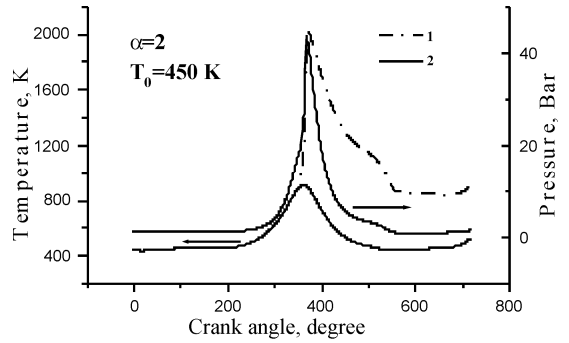

Fig.7. *Temperature and pressure evolution in gas internal (spark) combustion engine in air + (90%C3H8+10%C4H10) mixture at α=2 and T0=450K for two conditions: "1" is with activated by discharge, "2" is without it.*

To simulate the combustion process the compression ratio was reduced from 15 to 8 and rotation speed was increased to 3000 rpm, which is usual for spark ignition engine. Other parameters in the modeling have not been changed. An primary component concentrations resulted from discharge

Conclusions

The results of multistage inflammation simulation in propane-air mixture showed that the discharge operation promotes a quick hydro peroxide formation and, then, a partial release of chemical enthalpy throughout of organic peroxide decomposition. That process results in stepped gas heat at 50-200º.

Use of the chemical kinetics code involving low temperature ignition stage in the chemical compression reactor model is able to forecast the temperature and pressure evolution in a reasonable accuracy in dependence on in-flow temperature. The possibility in principle to initiate combustion in lean mixture in gas internal (spark) combustion engine by electrical discharge at low in-flow temperatures was shown.

This work has been executed in framework of Program of Fundamental Investigations of OEMMPU RAS "Fundamental problems of combustion and detonation in power engineering"

References

1. Sokolik A.S. *Spontaneous Combustion, Flame and Detonation in Gases*. M.: Academy of Sciences of USSR. **1960**. 427p., in Russian.
2. Pancheshnyi S, Lacoste D.A. et al / *Proc. of 17th Int. Sym. on Plasma Chemistry*, **2005**, Toronto, Canada.
3. Kazantzev S.Yu., Kononov *I.G.,* et al // *Fizika plasmi,* **2009**. V.35. p.281, in Russian.
4. Auzas F. , Tardiveau P. et. al.// *J. Phys. D: Appl. Phys*. **2010**. V.43. 495204.
5. Bityurin V.A., Bocharov A.N. and Filimonova E.A. *// In: Combustion and atmospheric pollution*, Edited by G.D. Roy, S.M. Frolov, A.M. Starik - Moscow: Torus Press Ltd., **2003**. p.188.
6. Bychkov V.L., Kochetov I.V. et. al. // *IEEE Trans. on Plasma Science.***2009**.V.37**.** p.2280.
7. Bityurin V.A., Бочаров А.Н, Filimonova E.A. / *17th Int. Conf. on MHD Conversion and 8th Inter. Workshop on Magnetoplasma aerodynamics,* **2009**, Moscow, Russia.
8. Naidis G. V. // *J. Phys. D: Appl. Phys*. **2007**. V.40**.** p**.** 4525.
9. Kane G.P.*, Proc. Roy. Soc.* **1938**.
10. Tolchinskii L.S., *private communication*.

7.4. FLOW STRUCTURE ANALYSIS BY CROSS-CORRELATION IMAGE PROCESSING

S.B. Leonov, A.A. Firsov, M.A. Shurupov
alexander.a.firsov@gmail.com

The paper describes method of velocity profile measurements by processing of images obtained by schlieren optical system with using of line-scan camera. Image obtained by line-scan camera presents set of instantaneous states of flow disturbances: exposure time of one line is 6 μs at the f = 100 kHz scan rate. The velocity of each small disturbance in the flow is equal to velocity of flow. The method is based on determination of the shift of disturbance dx for two nearest lines of line-scan camera image. Typical line-scan camera image is presented in Fig. 1. Knowing the shift dx, we can find the velocity as $V=f\times dx$. The image is divided to several parts by time and length to find out the local velocity for each part at fixed time. Utilizing the cross-correlation image processing of line-scan camera image, the time-depended lengthwise flow velocity profile averaged by flow width can be calculated. This approach is similar to the particle image velocimetry [1], but instead of introduced particles the natural disturbances are used as markers for velocimetry. In comparison with correlation method, described in paper [2], presented method allows us to obtain the velocity profile instead of velocity in one point.

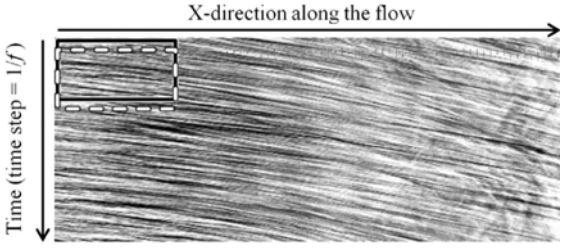

Figure 1. *Typical image obtained by line-scan camera for subsonic flow.*

Two-dimensional cross-correlation function (2D CCF) was used at image parts processing for determine dx:

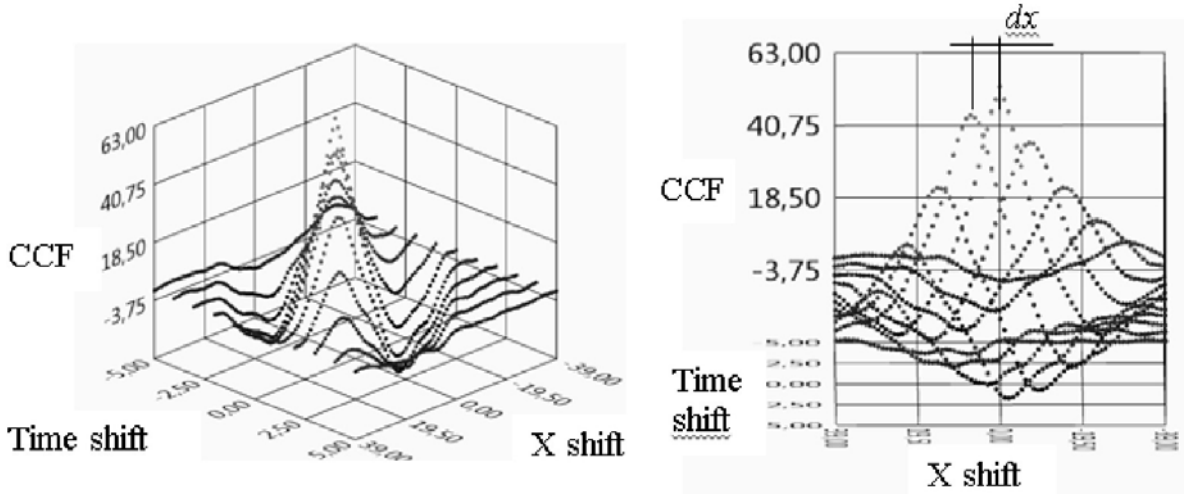

Figure 2. *Typical* two-dimensional *cross-correlation function.*

$$B_{12}(a,t) = \iint_{-\infty}^{+\infty} U_1(x,t)U_2(x+a,t+\tau)dxdt$$

Each 2D CCF calculation executed for two small parts of full image. These parts are equal by dimensions, but shifted by one line relative to each other in time (Fig. 1).

Typical 2D CCF is presented in Fig. 1. Coordinate of each maximum at fixed time shift is multiple to *dx*, so that make possible find the *dx* by using 2D CCF.

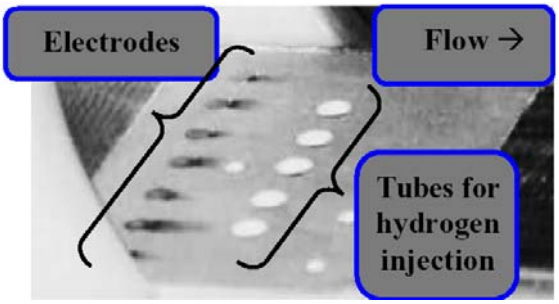

Figure 3. *Photo of down wall the channel.*

Described method was applied for two experimental configurations. First experiment was provided with airfoil in the subsonic flow. Airfoil was installed into the subsonic flow with velocity V=100 m/s. Injection of weak CO_2 jet was used for creation of flow disturbances above the airfoil plane. Field of view of line-scan camera was located in 5 mm above and parallel of the airfoil. Velocity obtained by described method near the leading edge is in a good agreement with initial flow velocity, and along the chord of the wing profile the measured velocity decrease from 100m/s to 60 m/s and this fact corresponds to the used experimental configuration.

Second velocity measurement with using of cross-correlation image processing was provided in experiment on the plasma associated hydrogen burning in supersonic flow. Flow parameters were following: Mach number M ~ 2, velocity V ~ 490 m/s, T_o = 300 K. Plasma was produced by direct current electric discharge between 7 cooper electrodes located on the down wall of supersonic channel. Photo of discharge without hydrogen is presented in Fig. 4. Downstream of the electrodes 5 tubes for hydrogen injection was located as it shown in Fig. 3. Field of view of line scan camera was located in a plan parallel and 2 mm over down wall. Because the discharge produce a lot of density disturbances there is not necessary to introduce some foreign elements like a particles in PIV or CO_2 jet like in previous experiment.

Figure 4*. Photo of discharge without H2.*

Measurements in the discharge and combustion area are accompanied by difficulties such as high temperature and voltage. Because of these problems utilization of other methods is difficult or impossible so the numerical simulation was used to obtain velocity field in reaction area.

Calculation of three-dimensional undisturbed flow in configuration close to experimental was performed by using FlowVision™ software. Numerical modeling of flow was based on solution of 3D time-dependent Navier-Stocks equations with the utilization of the wide used two-equation SST-model of turbulence. Model of perfect gas was used at modeling of supersonic flow. No-slip and adiabatic conditions were specified on upper, lower, and on lateral walls of the duct. Direct current electric discharge was simulated by introducing volumetric heat source whose dimensions were 21 mm length × ∅ 3,4 mm and power was about 1 kW. This approach was tested previously in paper [3]. Combustion was simulated by one gross reaction in the combined Arrhenius-Magnussen model. Symmetry conditions were used on both side walls of the channel to decrease the calculation domain which contained about 9×10^6 mesh points, i.e. calculation was produced for thin 11 mm layer which contained only one discharge filament and one tube for hydrogen injection.

The results, obtained by cross-correlation image processing and by CFD simulation are presented in Fig. 5. Zero point on X axis corresponds to center of hydrogen injection tube. Results obtained corresponds to each other, but numerical values have some variance because of some difference in experimental configurations, very simple model of combustion and absence of additional disturbances in numerical simulation introduced by electrical discharge. Main result of provided investigation is velocity values in two areas: 1) velocity in discharge area is 200-250 m/s; 2) velocity in combustion area is significantly lower than initial flow velocity (490 m/s) and it is in the range from 100 to 150 m/s, i.e. flow in combustion area is subsonic.

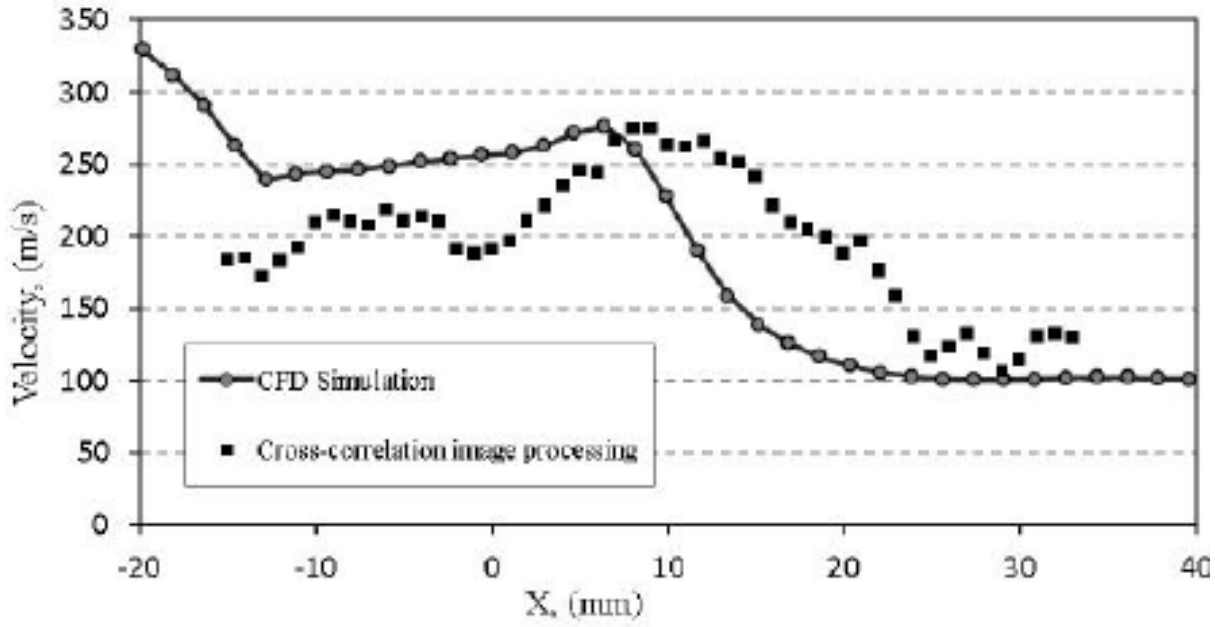

Figure 5. *Velocity profile for plasma assisted combustion zone in supersonic flo*

References

1. *M. Raffel, C. Willert, S. Wereley, J. Kompenhans* -Particle image velocimetry. A practical guide. Berlin : Springer. 2007. P. 448

2. *S.B. Leonov, A.A. Firsov, D.A. Yarantsev* - Determining the Supersonic Flow Velocity Using the Correlation Function of Signals from Refraction Sensors // Tech. Phys. Lett., 2009, Vol. 35, No. 6, PP. 548–551.

S.B. Leonov, A.A. Firsov, D.A. Yarantsev, F Falempin, M.A. Goldfeld - Plasma Effect on Shocks Configuration in Compression Ramp // 17th AIAA International Space Planes and Hypersonic Systems and Technologies Conference, 11 - 14 April 2011, San Francisco, California, AIAA 2011-2362.

8.1. SIMULATION OF HEAT TRANSFER TO THE SPASE VEHICLE EXPERT USING INDUCTIVELY HEATED PLASMATRON.

A.F. Kolesnikov, A.N. Gordeev, S.A. Vasilevskii.
IPMeh RAS, 119526, Moscow, prospect Vernadskogo 101/1
koles@ipmnet.ru

Simulation of the heat transfer from hypersonic air flow (V = 5 km/s) to a stagnation point of the vehicle EXPERT has been performed. For the altitude of 52.6 km in subsonic dissociated air flow the heat flux and surface temperature of the sample of sintered SiC is duplicated. Experimental prediction of heat flux and surface temperature of SiC sampleis realized at real values of the enthalpy, stagnation pressure and velocity gradient in stagnation point. The free stream conditions and surface recombination coefficients with regard to catalytic recombination of atomic oxygen and nitrogen are determined through comparison of the experimental data with CFD computations including the heat transfer rates. Numerical data are obtained by multiparameter computations of inductively heated plasma in the discharge channel, subsonic flow around a model and multicomponent dissociated boundary layer.

8.2. STRUCTURES OF THE SINGLE ELECTRODE RF GAS DISCHARGE IN SWIRLING AIR FLOW

V.G.Makaryan[1], N.E. Molevich[1;2], D.P.Porfiriev[1;2], I.P. Zavershinsky[1]

[1]Samara State Aerospace University, 34 Moskovskoe sh., 443086 Samara, Russia, zav@smr.ru
[2]Samara Branch of P.N. Lebedev Physical Institute of RAS, 221 Novo-Sadovaya Str., 443011 Samara, Russia

Abstract: Transitions between corona and torch forms of the single electrode radio frequency air discharge induced by the swirling flow in a duct are investigated. It is shown that observed transitions are connected with the gas-dynamic structure of the flow and thermal phenomena.

Introduction

A swirling gas flow structure in presence of plasma heat sources has recently been studied in connection with problems of control of aerodynamical characteristics by the gas discharge plasma, plasma insulation in plasmatrones, plasma induced combustion etc.

The practical aerodynamical problem of the swirling flows control proposes the plasma influence on the flow standoff the streamlined body. Therefore the most promising types of discharges for solution of the problem are the electrode less or single electrode capacity radio frequency (RF) and the microwave discharges. As a result, the RF, HF, microwave and direct current (DC) discharges interaction with swirling air flows is under intensive investigation last time. However, due to the complexity of the plasma created by such discharges and the plasma-flow interaction, their application is still largely based on empirical knowledge.

It is well known that the single electrode capacity radio RF discharge in the large air gap at atmospheric pressure in non-uniform fields can be in forms of the corona discharge or the torch discharge [1,2]. The transition between the corona and the torch discharge is not abrupt, but gradual [2,3] and can be induced by changing of parameter E/N [4], or by cooling and heating of a gas [1]. Accordingly to [5,6], this transition can be induced by the swirling flow creation as well.

In [5], the electrodeless torch microwave discharge in a cylindrical duct with the atmospheric pressure swirling flow is investigated. The structure of discharge changes strongly with growing of the swirl rate parameter S. The similar result is received in [6], where the structure of the single electrode capacity pulsed RF discharge in atmospheric pressure swirling flows is investigated. It is revealed that it is possible to separate and combine all obtained experimental results in three separate parts: a regime of stable and compact LP at small mass swirl flow ratios $Z = Q_t/(Q_t+Q_{ax})$, a RF torch discharge regime at supercritical mass swirl flow ratios $Z > Z_C$ and a transient regime of LP and RF streamers ($Z \sim Z_C$).

The objective of this work is to present results of analytical and numerical modeling of the swirling flow in presence of RF discharges explaning qualitatively the experimental results of [6].

Experimental background

In [6], the experimental investigations of plasma-flow interaction were conducted under conditions given below.

The cylindrical quartz duct with the open end has a radius $R = 2 \div 3$ cm and a length $L = 40 \div 100$ cm. The averaged RF power is equal to $N = 0.2 \div 1.5$ kW, field frequency $f = 0.3 \div 0.45$ MHz, pulse duration $\tau = 1$ ms, modulation frequency $F = 200 \div 500$ Hz. An electrode is made from tungsten with a diameter 2 mm and a length $l \sim 20$ cm and is injected from the open end of the duct in order to except a distortion of the axial symmetry of the flow. The averaged electric field strength is equal to 300 $V \cdot cm^{-1}$ at the electrical power $N = 700$ W. This value is sufficiently less than the value of the field of the streamer propagation, which in a dry air is equal to $E_S \approx 4.65$ $kV \cdot cm^{-1}$ [7]. The electron concentration in the discharge is equal to $n_e \sim 10^{12}$ cm^{-3}. The swirl mass flow rate Q_t and the axial mass flow rate Q_x are varied in swirl generator by the gas supplies. Axial and tangential mass flow rates differ from 0 to 12 g sec^{-1}, the initial flow temperature is equal to $T \sim 300$ K.

At small values of parameter Z, the discharge has the streamer corona form. This result corresponds to experimental results of [8,9], where structures of HF and glow discharges are investigated. The characteristic thermal diameter of corona filaments is approximately equal to 3 mm, characteristic channel length is equal to 3÷10 cm. The gas temperature in the channel at 1 cm from the tip is equal to $T \sim 500 – 600$ K.

At large values of parameter Z, the discharge have a form of the axisymmetric torch situated upstream from the electrode.

In the intermediate range of Z values, the discharge is combined from the torch phase in the paraxial region and the corona phase in the outer region.

The observed transition between these two forms has a threshold with respect to the RF power and the tangential mass flow rate.

It is important to mark that in all observed range of electric field strength and pressure a value of parameter E/P is approximately constant [6].

Basic equations and numerical scheme

Basic model of equations consists of Reynolds-averaged Navier-Stokes equations

$$\frac{\partial \rho}{\partial t} + \frac{\partial (\rho v_i)}{\partial x_i} = 0,$$

$$\frac{\partial (\rho v_i)}{\partial t} + \frac{\partial (\rho v_i v_j)}{\partial x_i} = -\frac{\partial P}{\partial x_i} + \frac{\partial}{\partial x_i}\left[\mu_{eff}\left(\frac{\partial v_j}{\partial x_i} + \frac{\partial v_i}{\partial x_j} - \frac{2}{3}\delta_{ij}\frac{\partial v_k}{\partial x_k}\right)\right],$$

$$P = \rho T$$

and the energy equation

$$\frac{\partial (\rho E + P)}{\partial t} + \frac{\partial [v_i (\rho E + P)]}{\partial x_i} = \frac{\partial}{\partial x_j}\left[\left(\kappa + \frac{c_P \mu_t}{Pr_t}\right)\frac{\partial T}{\partial x_j}\right] + \frac{\partial}{\partial x_j}\left[v_i \mu_{eff}\left(\frac{\partial v_j}{\partial x_i} + \frac{\partial v_i}{\partial x_j} - \frac{2}{3}\delta_{ij}\frac{\partial v_k}{\partial x_k}\right)\right] + N.$$

In outlet, the far-field boundary conditions are formulated. On other walls were used a boundary conditions

$$v_r(R,z,t) = v_\varphi(R,z,t) = v_z(R,z,t) = 0,$$
$$T(R,z,t) = T_0, \rho(R,z,t) = \rho_0.$$

The initial conditions have forms

$$v_r(r,z,0) = v_\varphi(r,z,0) = v_z(r,z,0) = 0,$$
$$T(r,z,0) = T_0, \rho(r,z,0) = \rho_0.$$

Here, ρ, E, P, T are the gas density, energy, pressure and temperature, N is the heat source power, c_P is the specific heat capacity, μ_t, μ_{eff} are turbulent and effective viscosity coefficients, κ is the thermal conductivity coefficient, Pr_t is the turbulent Prandtl number, v_i are gas velocity components.

Numerical simulation of the swirling flow structure with the heat source simulating the real Joule heating in discharge in the cylindrical quartz duct with the open end is conducted. Module FLUENT 6.3 in regime of full 3D non-stationary swirling flow is used.

Structures of the experimental duct and the swirl generator connected with duct are modeling using module GAMBIT 2.3.16. The inlet tangential mass flow rate Q_t and axial mass flow rate Q_x can be adjusted in FLUENT by program way. The grid consist approximately $1.2 \cdot 10^6$ cells.

The procedure of discretization of spatial operators of differential equations is carried out up to second order of accuracy. The third order scheme MUSCL has been used for calculation of convective terms.

Main results

A phase diagram on (Q_t, Q_{ax}) - plane for the swirling air flow regimes is numerically drawn. It was shown that regimes with the recirculation zone were realized at large mass swirl flow ratios Z corresponding to the zone above the dashed line in Figure 1, while the regimes without the recirculation zone occurred at small values of Z. This result is coincided with known data [10].

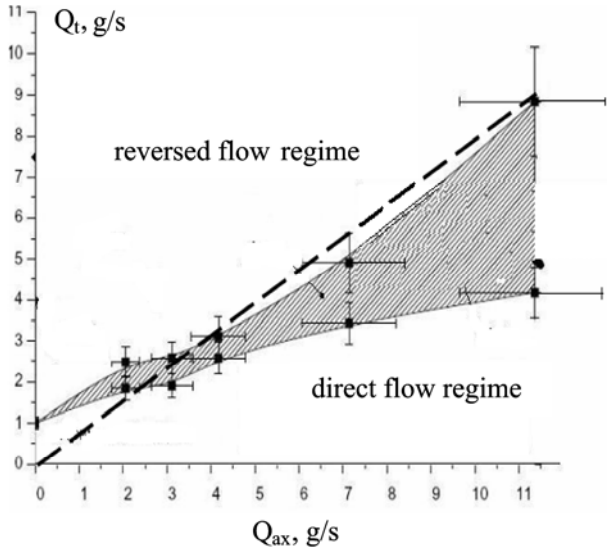

Figure 1. *Numerically received swirling flow regimes at different mass flow rates. Crosshatched region divided the regimes of torch discharge (upper area) and corona discharge (lower area) according to data [6]*

It is well seen that the numerically received (Q_t, Q_{ax}) – plane partition for flow structure is practically similar to experimentally received partition of RF discharge structure, Figure 1. Thus, we obtain the good qualitative agreement between

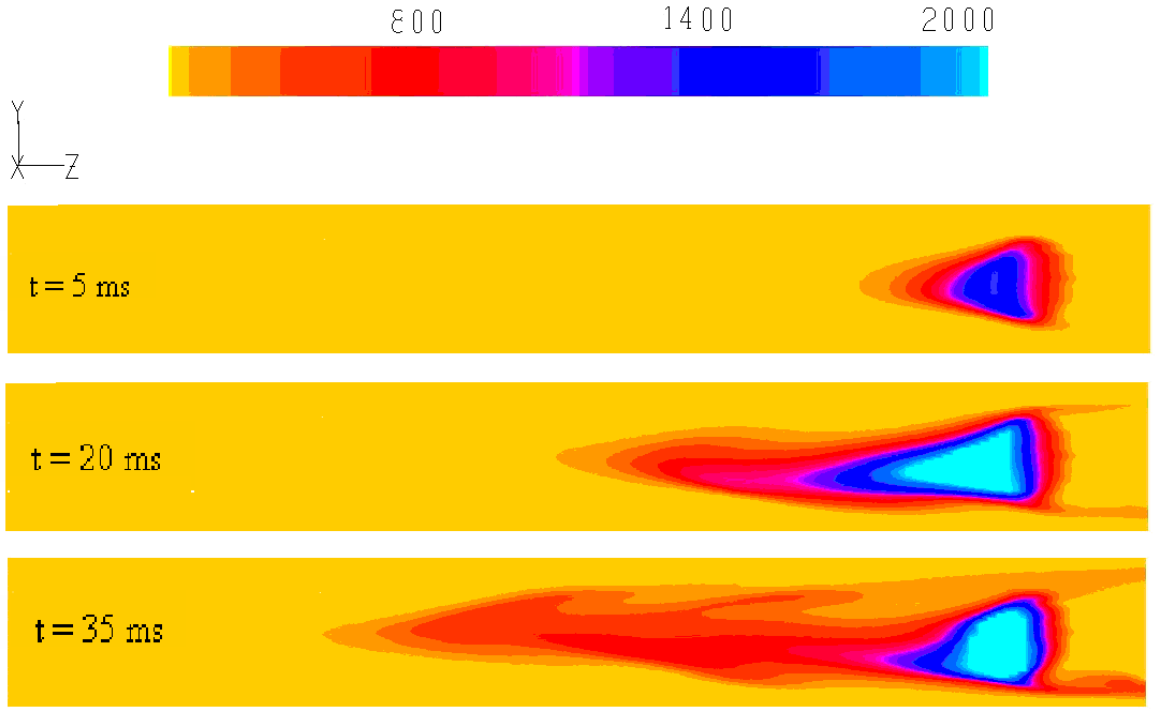

Figure 2. *Stages of the warm zone formation*

experimental results [6] and results of the numerical simulation of the swirling flow structure.

The initial stage of the thermal wave formation in the presence of the uniform heat source N = 700 W has been numerically simulated. A heat source is localized in the spherical region with the diameter D ~ 3 cm. The center of this region is situated 40 cm far from the swirl generator, which qualitatively corresponds to the experimental power distribution without the flow.

We obtained that the wave of gas heating arises under condition $Z > Z_C$. Its front propagates upstream with the velocity which is similar to the average flow velocity in the recirculation zone. At the final stage of wave evolution, the stationary paraxial warm zone is formed, Figure 2. This result corresponds qualitatively to experimental data [6] and theoretical calculations [11,12], where the stationary structure of thermal and velocity fields in the swirl flow with the transversal DC discharge is investigated.

In hot regions, the integral parameters of the discharge such as the linear conductivity of streamers $\sigma \sim \exp(1.92 \cdot 10^{-2} T)$ and the strength of the field of the streamer propagation E_S (Figure 3) are sufficiently increases and decreases, respectively [7]. Owing to the gas-dynamical and electrical parameters changing in the paraxial zone, the geometrical scales of plasma channel increases dramatically, Figure 3. Thus, a convectional heating of paraxial region in the zone of the reversed flow leads to the corona-torch discharge transitions.

Conclusions

As stated above, the observed structure transitions of the single-electrode RF discharge in the long gaps in the upstream zone are induced by gas-dynamics and thermal reasons.

Using 3D numerical simulation, we show that the mass swirl flow ratio *Z* is one of the main bifurcation parameters, which defines a single electrode RF discharge structure in the swirling air flow. We obtain a qualitative agreement between experimental results [6] and results of numerical simulation.

Acknowledgements

This work is partially supported by the analytical program "Development of scientific potential of the High School (2009 – 2011)" (project 2.1.1/309) and the federal target program "Scientific and pedagogic cadres of innovational Russia" on 2009-2013 years (project № P2315).

References

1. Trunecek V. Unipolar high – freguency discharge // Folia Fac. Sci. Nat. University. 1971. V. 12.-P.3-13.
2. Nova M., Sicha M., Kapichka V., Jastrabik L., Soukup L, Hubigka Z., Klima M, Sluvichek P., Brablec A. Generation of Supersonic

Plasma Flow by Means of Unipolar RF Discharges // J. de Physique IV. 1997. P. C4-331-C4-339.
3. El Gammal M., Proc. VIII. ICPIG. Vienna. 1967. P.237.
4. Alexandrov K.V., Grachev L.P., Esakov I.I., Fedorov V.V., Khodataev K.V. Domains of Existence of Various Types of Microwave Discharge in Quasi-Optical Electromagnetic Beams // Tech. Physics. 2006. V.51 №.11. P. 1448-1456.
5. Jeong H. Kim, Yong C. Hong, Hyoung S. Kim and Han S. Uhm Simple Microwave Plasma Source at Atmospheric Pressure // Journal of the Korean Physical Society, V.42. 2003. P. S876-S879.
6. Moralev I.A. Interaction of gas-discharge plasma with swirl flows. PhD Thesis. Moskow. 2010. JIHT of RAS 160 p.
7. Bazelyan E.M., Razhansky I.M. Spark discharge in air. Novosibirsk. Nauka. 1987. 165 p. (in Russian).
8. Grachev L.P., Esakov I.I., Khodataev K.V. Microwave streamer discharge in a supersonic air flow // Tech. Physics. 1999. V.33. № 11. P. 1271-1275.
9. Velikhov E.P., Golubev V.S., Pashkin S.V. Glow discharge in gas flow // Physics-Uspekhi. 1982. V.137. № 1. P. 117-150.
10. Gupta A.K.; Lilley D.G.; Syred N. Swirl flows. Abacus Press. 1984. 588 p.
11. Zavershinskii I.P., Klimov A.I., Makaryan V.G., Molevich N.E., Moralev I.A., Porfir'ev D.P. Features of the Transverse Discharge Glow Depending on the Gas Flow Rate in a Vortex Chamber // Tech. Physics Lett. 2009. V.35. №.12. P. 1152-1155.
12. Zavershinskii I.P., Klimov A.I., Makaryan V.G., Molevich N.E., Moralev I.A., Porfir'ev D.P. Numerical simulation of swirl flow in presence of transversal DC discharge // High temperature. 2010. V.48. №1. (Appl.). P. 142-147.
13. Raizer Yu.P. Physics of gas discharge. Nauka. 1992. 536 p. (in Russian).
14. Lutsenko Yu.Yu. Physics of high-frequency capacity type discharges. Tomsk. 108 p. (in Russian).
15. Bazelyan E.M., Raizer Yu.P. Spark discharge. CRC Press. 1997. 320 p.

8.3. OSCILLATION FREQUENCIES OF UNSTEADY VORTEX RINGS

Fedor V. Shugaev, Oksana A. Solenaya
Faculty of Physics, M.V. Lomonosov Moscow State University, 119991, Moscow, GSP-1, Vorobyovy Hills, Moscow, Russia,
shugaev@phys.msu.ru, +7-495-939-2816 (office), +7-495-932-8820 (fax)

The flow around a vortex ring with elliptical cross-section is analysed on the basis of the full Navier-Stokes equations. The parabolic system is reduced to the integral equations of the Volterra type[1,2]. The mathematical procedure consists in evaluating integrals by the use of Korobov method. The properties of the flow (density, temperature) have been calculated. It is shown that the solution is an oscillatory one. The spectrum of the oscillation and its temporary evolution are discussed.

Nonlinear solution of the navier-stokes equations

The full system of the Navier-Stokes equations can be written in Euler variables in dimensionless form as:

$$\begin{cases} \dfrac{d\Omega_i}{dt} = \nu\Delta\Omega_i + \Omega_m \dfrac{\partial v_i}{\partial x^m} + f_{1i} \\ \dfrac{dw}{dt} = s \\ \dfrac{ds}{dt} = \dfrac{4}{3}\nu\Delta s + \dfrac{1+h}{\gamma}\Delta w - \dfrac{1}{\gamma}\Delta h + f_2 \\ \dfrac{dh}{dt} = \dfrac{\gamma}{\mathrm{Pr}}\eta\Delta h - (\gamma-1)s + f_3 \\ \dfrac{d}{dt} = \dfrac{\partial}{\partial t} + v_j(\vec{x},t)\dfrac{\partial}{\partial x^j} \end{cases}$$

$$f_{ij} = f_{ij}\left(\vec{x},t,\psi_j,\partial\psi_j/\partial x^m\right),$$

$$f_l = f_l\left(\vec{x},t,\psi_j,\partial\psi_j/\partial x^m\right),\ i=1,2,3,\ l=1,2,3,$$

$$m=1,2,3$$

$$w=-\ln\rho,\ \vec{\Omega}=rot\vec{v},\ s=div\vec{v},\ h=T-1,$$

$$\nu=\mu/\rho,\ \eta=\lambda/\rho$$

$$\psi_1=w,\ \psi_2=s,\ \psi_3=h \qquad (1)$$

Here $\rho, T, \vec{v}, \mu, \lambda, \gamma$ are density, temperature, velocity, viscosity, thermal conductivity, adiabatic exponent, respectively. The first three of the Eqs.(1) are weakly connected with the next three ones. Initial conditions are: $\Omega(\vec{x},0)=F(\vec{x})$ inside the ring, $\Omega(\vec{x},0)=0$ out of the ring, $w(\vec{x},0)=s(\vec{x},0)=h(\vec{x},0)=0.$ The shape of the ring is shown in Fig.1.

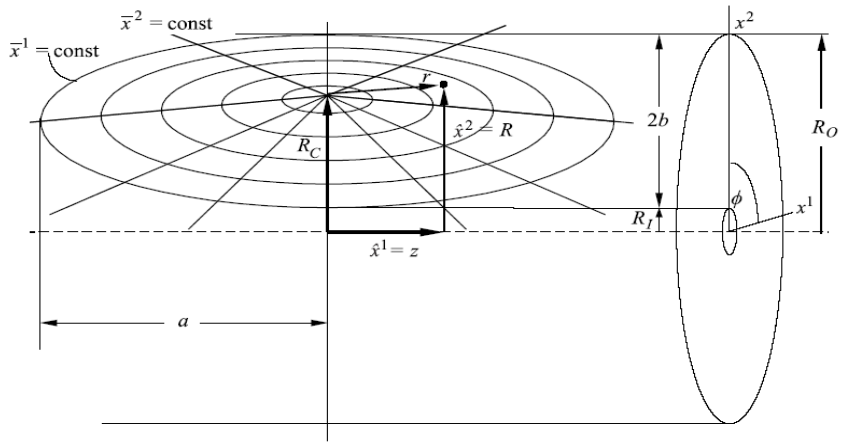

Fig.1. *Diagram illustrating the construction of the toroidal coordinate system [3].*

Toroidal coordinates are used for the distribution of vorticity inside the vortex ring. The connection between the Cartesian coordinates x^i and the toroidal ones u^i is given below

$$\begin{cases} x^1 = \left(u^1 B(\sin u^2 - g) + R_C\right)\cos u^3 \\ x^2 = \left(u^1 B(\sin u^2 - g) + R_C\right)\cos u^3 \\ x^3 = u^1 A\cos u^2, \quad A = \sqrt{2}, \quad B = 1, g = -0.5, R_C = 1 \\ 0 \le u^1 \le 1, \quad 0 \le u^2, \quad u^3 \le 2\pi \end{cases}$$

The velocity is given by the expression

$$v_i(\vec{x},t) = -\frac{1}{4\pi}\int_{R^n} \frac{s(\vec{x}'+\vec{x},t)x_i' + \varepsilon_{ijk}\Omega_j(\vec{x}'+\vec{x},t)x_k'}{|\vec{x}'|^3} d\vec{x}'$$

The frequency which corresponds to the linear solution is shown in Fig.2.

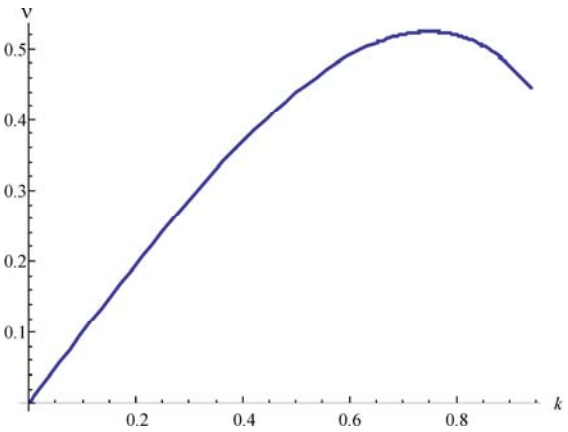

Fig.2. *Frequency against wave number (linear solution) [4].*

The Navier-Stokes system is a parabolic one. We reduced the system of the differential equations to the system of the integral equations of the Volterra type. The latter was solved by means of iterations. The solution to the linearized system was taken as the first iteration. When we seek for the second iteration we find the values of the coefficients at the derivatives of the highest order by using the first iteration.

The first iteration for $\Omega_\varphi(\vec{x},t)$ gives

$$\Omega_\varphi(\vec{x},t) = \frac{1}{\left(2\sqrt{\pi t}\right)^3}\int_{R^n}\Omega_\varphi(\vec{\xi},0)e^{-\frac{|\vec{x}-\vec{\xi}|^2}{4t}}d\vec{\xi}$$

We construct the fundamental solution to the parabolic system with the aid of the parametric method. We take into account in the system (1) only the first derivatives over time and the second derivatives over coordinates. Then we suppose that the coefficients at the derivatives depend on time. The coordinates *x* are considered as parameters *y*. Let us fulfils the Fourier transform. On substitution

$$\psi' = \tilde{\psi}\exp\left(-k_j\int_0^t v(\vec{y},\tau)d\tau\right),$$

where the wavy line designates the Fourier transform, we have

$$\frac{\Omega_i'^{(n+1)}}{dt} = -k^2 v^{(n)}(\vec{y},t)\Omega_i'^{(n+1)}$$

$$\frac{dw'^{(n+1)}}{dt} = s'^{(n+1)}$$

$$\frac{ds'^{(n+1)}}{dt} = -\frac{4}{3}k^2 v^{(n)}(\vec{y},t)s'^{(n+1)} - \frac{1+h^{(n)}}{\gamma}k^2 w'^{(n)}(\vec{y},t)s'^{(n+1)} + \frac{k^2}{\gamma}\vec{h}^{(n+1)}$$

$$\frac{dh'^{(n+1)}}{dt} = -\frac{\gamma}{\mathrm{Pr}}k^2\eta^{(n)}(\vec{y},t)h'^{(n+1)} - (\gamma-1)(1+h^{(n)}(\vec{y},t)s'^{(n+1)} \qquad (2)$$

System (2) can be reduced to the following system of integral equations

$$s'(k,\bar{y},t) = \alpha_2\exp(-c_3 f(\bar{y},t)) + c_1\exp(-c_3 f(\bar{y},t))\int_9^t \exp(-c_3 f(\bar{y},t))G_1 dq - c_1(-c_3 f(\bar{y},t))\int_0^1 dq\int_0^q d\sigma(c_3 f(\bar{y},q))G_2 s'(k,\bar{y},\sigma)$$

$$w'(k,\bar{y},t) = \alpha_1 + \int_0^t s'(k,\bar{y},t)d\sigma$$

$$h'(k,\bar{y},t) = \exp(-c_2 f(\bar{y},t))\times\left\{\alpha_3(\gamma-1)\int_0^t a(\bar{y},\sigma)\exp(-c_2 f(\bar{y},t)s'(k,\bar{y},t))\right\}d\sigma$$

$$G_1 = \alpha_3\exp(-c_2 f(\bar{y},q)) - \alpha_1 a(\bar{y},q)$$

$$G_2 = a(\bar{y},q) + (\gamma-1)a(\bar{y},\sigma)\exp\{f(\bar{y},\sigma) - f(\bar{y},q)\}$$

$$f(\vec{y},t) = \int_0^t\left(1+h^{(n)}(\vec{y},\tau)\right)^{3/4}\exp\{w^{(n)}(\vec{y},\tau)\}d\tau$$

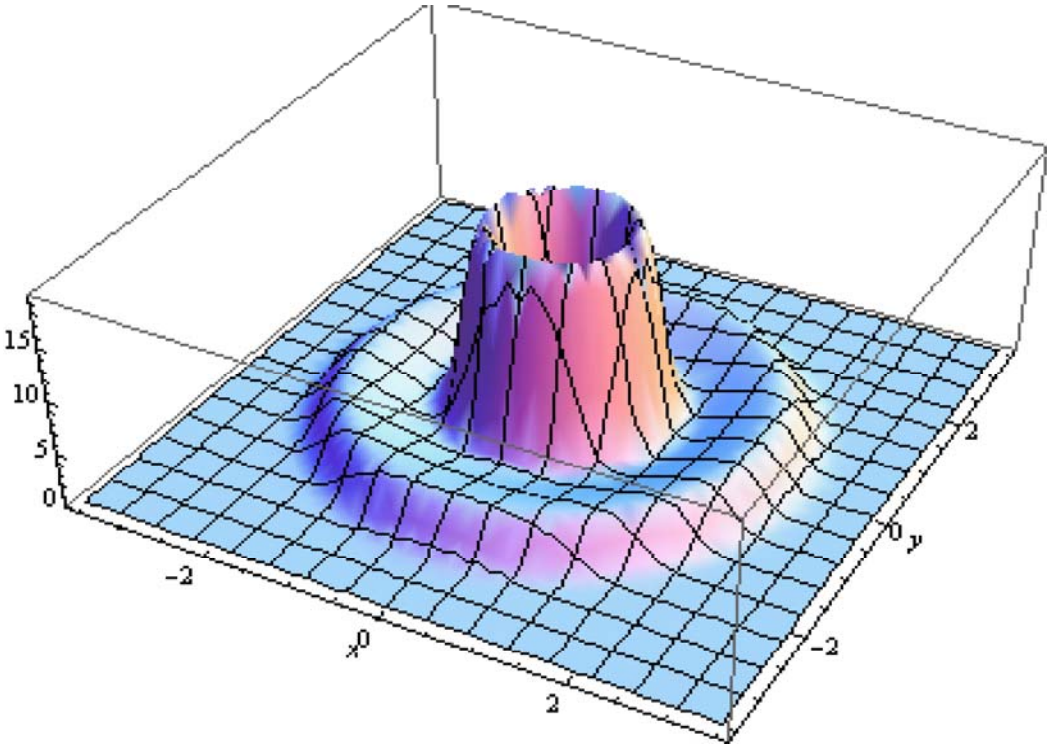

Fig. 3. *Vorticity on the plane z=0 (t=0.01)*

$$a(\vec{y},t)=1+h^{(n)}(\vec{y},t)$$

The quantities $\alpha_1,\alpha_2,\alpha_3$ are arbitrary constants. The parametrix $Y_{ij}\left(\vec{x}-\vec{\xi},t;\vec{\xi},\tau\right)$ can be found from the fundamental solution $M'_{ij}\left(\vec{k},\vec{y},t\right)$ to the system (2). If

$$\widetilde{M}_{lj}=M'_{lj}\exp\left(ik_j\int_0^t v_j d\tau\right)$$

Then

$$Y_{lj}\left(\vec{x}-\vec{\xi},t,\xi,\tau\right)=$$
$$\frac{1}{(2\pi(t-\tau))^{3/2}}\int_{R^n}\widetilde{M}_{lj}\left(\vec{k},\vec{\xi},t-\tau\right)\exp\left\{i\vec{k}\left(\vec{x}-\vec{\xi}\right)\right\}d\vec{k}$$

Thus the parametrix is determined. The fundamental solution to the system of the Navier-Stokes equations can be obtained with the aid of iterative procedure for solving integral equations of the Volterra type [1,2].

Results and discussion

The proposed technique was used for calculation of the unsteady flow in the vicinity of the ring. Fig. 3 shows the distribution of the vorticity on the plane *z*=0 at early instant (*t*=0.01). Figs. 4-5 demonstrate the distribution of temperature and density against the axis *z*. As seen, these parameters vary in oscillatory way. This property is intrinsic for unsteady solutions to the Navier—Stokes equations. Indeed, the linear solution is an oscillatory one. The subsequent iterations have the same property because the coefficients at the highest derivatives are oscillatory. The higher is the order of the iteration the more complex is its frequency spectrum. High-frequency oscillations decay faster than low-frequency ones. Thus low-frequency oscillations prevail for decaying flows.

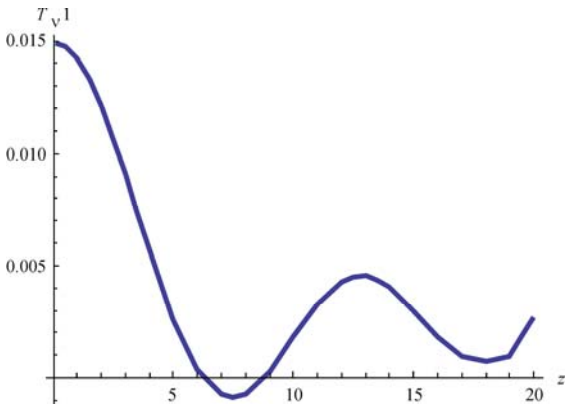

Fig. 4. *Temperature against axis z (t=1).*

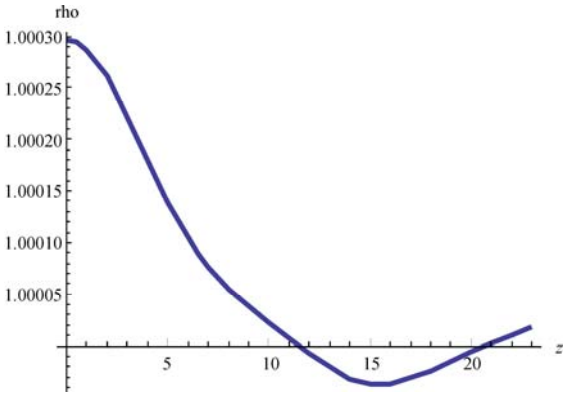

Fig. 5. *Density against axis z (t=1)*

Conclusion

- The evolution of vortex ring has been investigated numerically by the parametrix method. New results are presented. It is found that the temperature has its maximum at the axis near the point z=0 at early instants of time. The distribution of density is presented, too. The parametrix method will make possible to determine natural frequencies of the ring in future. Up to now those values have been calculated on the assumption that the air is a non-viscous incompressible fluid [5]. The present results will enable to model turbulence as an unsteady flow with interacting vortical structures. Natural frequencies of those structures must determine the acoustic spectrum of turbulence.
- It is necessary to note that the oscillation frequency depends on wave number only in the linear case. It depends on coordinates and time for nonlinear solution.

References

1. Friedman, A., [Partial Differential Equations of Parabolic Type], Prentice Hall, New York, (1964).
2. Eidelman, S. D., [Parabolic Systems], Nauka, Moscow, (1964).
3. Morton ,T. S., “The velocity field within a vortex ring with a large elliptical cross-section,” J. Fluid Mech., vol. 503, pp. 247-271 (2004).
4. Shugaev, F. V., Terentiev, E. N., Shtemenko, L. S., Dokukina, O. I., Petrova, T. A., "Characterization of a laser beam propagating though the turbulent atmosphere," in Optics in Atmospheric Propagation and Adaptive Systems XII, edited by Anton Kohnle, Karin Stein, John D. Gonglewski, Proc. SPIE 7476, 74760C (2009).
5. Kopiev, V. F., Chernyshev, S. A., ‘’ Oscillations of the vortex ring’’, Uspekhi fizicheskikh nauk, vol. 170, N 7, pp. 713-742 (in Russian).

8.4. STUDY OF A LONGITUDINAL PLASMOID CREATED BY CAPACITY COUPLED HF DISCHARGE IN SWIRL AIRFLOW

Klimov A., Bitiurin V., Tolkunov B., Moralev I,
Joint Institute of High Temperature RAS
Izhorskaya 13, bld..2, Moscow, 125412, Russia
E-mail: ivmoralev@gmail.com
klimov@ihed.ras.ru

Abstract. This work is devoted to study of plasma-vortex interaction. The following main new experimental results are obtained in this work:

1. Detail optical spectra of a longitudinal plasmoid (LP) created by capacity coupled HF discharge (CHFD) in swirl flow with a high space resolution. Processing of these spectra gives us important information about non- equilibrium plasma parameters of a LP in swirl flow.
2. Swirl flow around a LP is studied at wide range of gas dynamic parameters and plasma parameters.
3. The detail shadow pictures of a LP created by CHFD in swirl airflow at different flow velocities are obtained and analyzed. It is revealed that there are both a laminar LP and a turbulent one in swirl flow at the definite flow parameters and HF discharge parameters.
4. The pressure distributions in a free vortex are measured at HF plasma on and HF plasma off. It is revealed that there is pressure increase about of 20-30 % in swirl flow at plasma on. This result proves that there is vortex attenuation by HF plasma.

Nomenclature

LP = longitudinal vortex plasmoid
HF = high frequency
HFD = high frequency discharge
CHFD = capacity coupled HFD
F_{HF} = HF frequency
F_M = modulation frequency of CHFD
T_i = pulse duration
I_{HF} = HF electric discharge current
V_{HF} = HF electric discharge voltage
N_{HF} = pulse power input in plasma
M = Mach number
V_f = airflow velocity
V_x = axial component of the velocity
V_t = tangential component of the velocity
P_0 = stagnation pressure
P_{st} = static pressure
T_g = gas temperature
T_R = rotation temperature
T_V = vibration temperature
St = Strouchal's number

1. Introduction

Swirl flow control and vortex control near a vehicle by a non-equilibrium plasma formation is one of the important key task in Plasma Aerodynamics today. The experimental results obtained during this study may be used in aviation and plasma-assisted combustion [1-3]. A study of this problem is interesting both for plasma physics development and gas dynamics development, namely for

- Creation of a longitudinal plasma formation with extremely high parameters (N_e,T_e and others)
- Effective wing's lift control by plasma, fig.1.
- Effective flow separation control,
- Jet noise control,
- And others.

Physical properties of a LP created by CHFD in high-speed swirl flow are studied in this work in detail. This work is continuation of the previous ones [4].

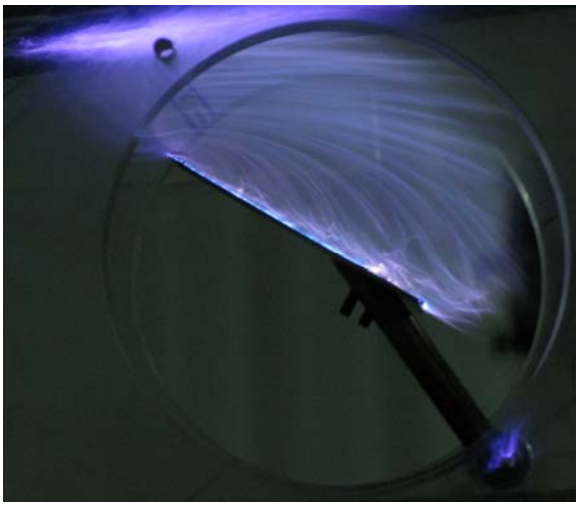

Figure 1. *Lift control near a delta wing model by CHFD* [5,8]

Remind that a stable longitudinal plasmoid (up to 2m) was created by sub-critical CHFD in high-speed swirl airflow (M~0.8; P_{st}~1 Bar) in our experiment at the first time ten years ago [6]. High voltage HF plasma generator (Tesla's coil HF plasma generator) is used to create this LP in high-speed swirl airflow. Note that it is possible to use this LP for flow control of a real plane.

Main tasks studied in this work are the followings:

1. Plasma-chemical kinetics and relaxation processes in a non-equilibrium LP created by a CFHD in high-speed swirl gas flow and their action on the LP's structure and its dynamics.
2. Study of stable LP's creation regime in high-speed vortical airflow by CHFD.
3. LP's physical properties and its parameters in swirl flow at different gas flow parameters and electric HF discharge parameters.
4. Amplification and destruction (decay) of vortex by LP created by CHFD.
5. Control of LP's location in space and time by additional external electrical field (or additional external ionizer)

2. Main experimental results

2.1. Experimental Set up

The experimental setup SWT- 1 and the experimental setup SWT-2 used in our experiments were described in the work[4, 5] in detail. Experimental set up SWT-1 is designed, manufactured and tuned to study of a longitudinal plasmoid created by CHFD in swirl airflow *at high atmospheric pressure* P_{st}*~ 1 Bar* and the maximal tangential velocity V_t~40m/s, fig. 2. The experimental set up SWT-2 is designed, manufactured and tuned to study of a LP created by CHFD in high-speed swirl flow *at low static pressure* P_{st}*= 40-300 Torr* and the maximal tangential velocity V_t~140m/s, fig.3. Note that the modified set up SWT-1M is used to create a free vortex and a LP in open atmosphere, fig. 4. A free vortex and a LP are created in the set up SWT-2M at low static pressure also.

HF plasma generator used in this work has the following parameters: HF frequency- F_{HF} = 13.6 MHz, HF power N_{HF}< 2 kW, operation regimes:- continuous one and pulse repetitive one. DC discharge is used in some experiments (U_{DC}<8kV, I_{DC}<2 Amp) also. The typical

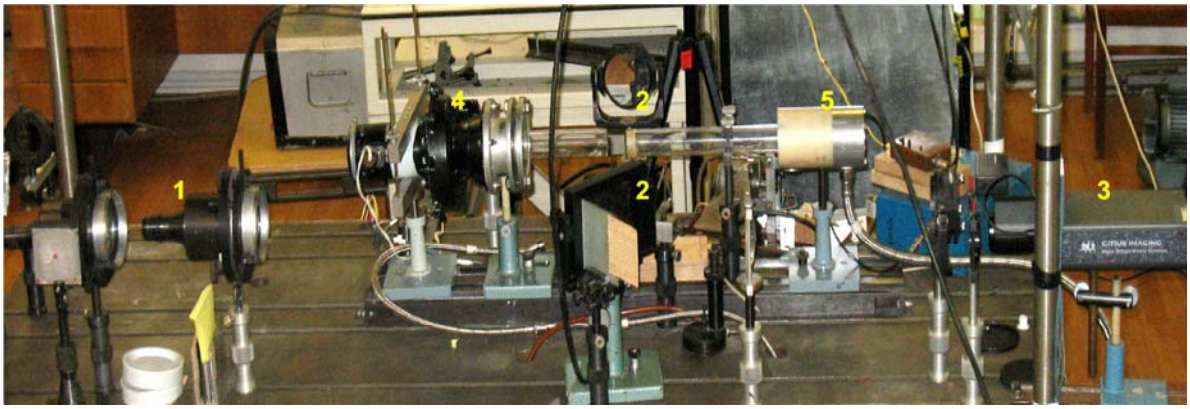

Figure.2. *Experimental set up SWT-1 with advanced optic interferometer (1, 2, 3). 4- ejector, 5- vortex generator*

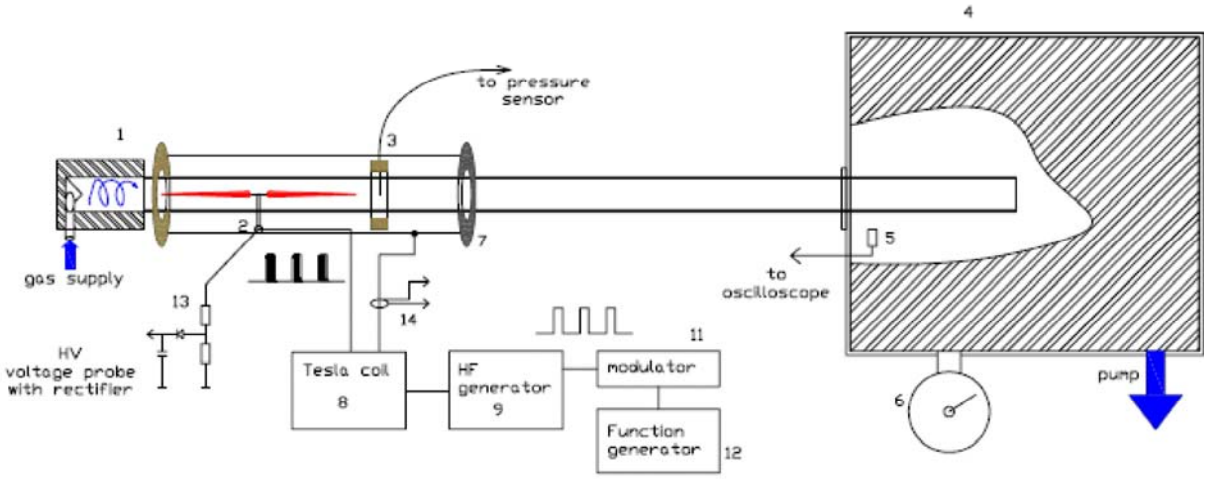

Figure.3. *Experimental set up SWT-2. 1-vortex generator, 2- HF electrode, 3-port with pressure sensor,4-vacuum chamber, 5-pressure sensor, 6- vacuum pump, 7-ground electrode*

parameters of a pulsed repetitive HF generator used in this work are the following: maximal output pulsed voltage ~ 60kV, pulsed HF power ~ 1÷10 kW, HF frequency- F_{HF1}=13.6 MHz; F_{HF2}= 0.45MHz, pulse frequency F_P=10÷10^4 Hz, pulse duration- T_p=10μs÷ 100ms.

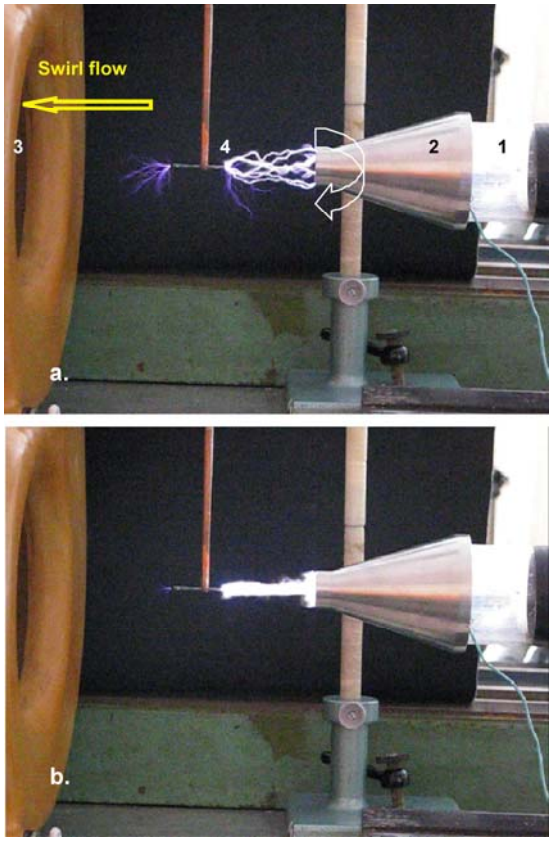

Figure 4. *A free LP created CHFD in free swirl airflow. FM ~ 0.8 kHz- a., FM ~ 2 kHz- b.; Vt~Vx~30m/s, Pst~1 Bar.1-swirl generator, 2-nozzle, 3-ejector, 4- HF electrode. Lateral view*

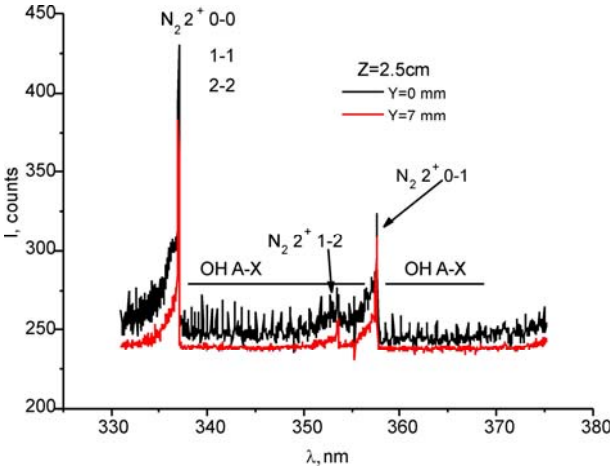

Figure 5. *The typical optical spectra of a longitudinal plasmoid created by CHFD in swirl flow. Distance X=2.5 cm from HF electrode for two different chords Y= 0mm and Y=7mm. V_f~30m/s. N_{HF}=240W*

Plasma and airflow parameters are measured by different diagnostic instrumentation including shadow optical device with excimer KrF laser (λ~248nm), optical interferometer with high-speed camera Citius (λ~638nm), electric and current probes, optical spectrometer (λ~200-800nm), MW interferometer G4-108 (λ~1cm) and others.

2.2. LP Created by Continuous CHFD in Swirl Flow

Two important tasks are studied in this work namely:- plasma-chemical kinetics and relaxation processes in a non-equilibrium LP created by a CFHD in high-speed swirl gas flow (1) and their action on the LP's structure and its dynamics (2).

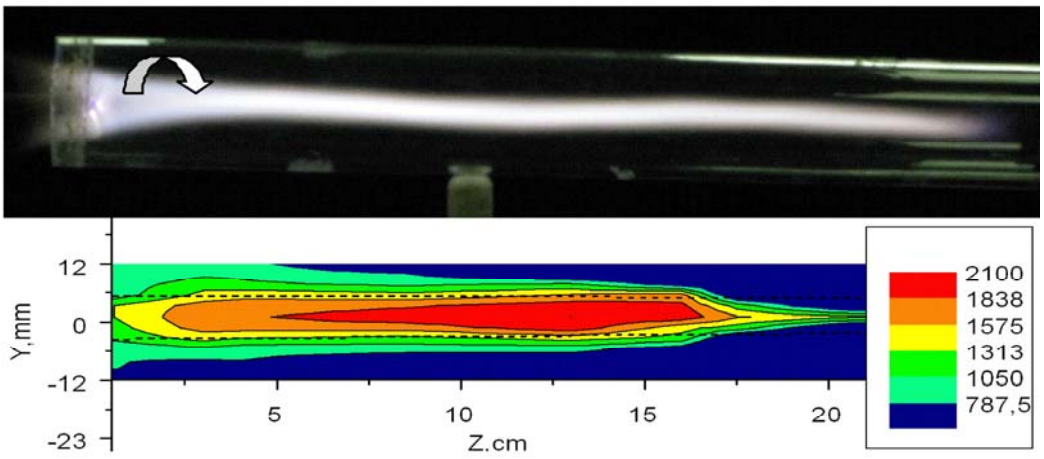

Figure 6. *The typical space gas temperature distribution in HF plasmoid created in swirl flow. Vt=30m/s, HF power NHF=240W Pulse duration t=1ms, modulation frequency FM=500Hz, Pst =1 Bar. Top picture- a longitudinal HF plasmoid in swirl airflow. Dashed lines on down picture show plasmoid's luminescence zone*

Plasma parameters inside a LP are studied by optical spectroscopy and optical interferometer. The detail optical spectra *with high space resolution* are recorded in different cross sections of a LP in swirl flow at the first time, fig.5, 6. Non-equilibrium processes in vortex plasmoid are studied. The typical optical spectrum obtained in a LP is shown in fig. 5. One can see that there is the OH molecular band, the N_2 2^+ molecular band in this optical spectrum. These spectra are processed, fig.6. It is revealed that there is a hot plasma kernel (T_R~1500- 2000K and Tv~ 3000-4000K) inside a LP. There is a "warm" plasma halo (T_R~600K and T_v~4000K) around LP's kernel. So, there are large temperature gradients in a non- equilibrium LP in this region. So, it is possible to suppose that there is relaxation mechanism associated with V-T relaxation of exited nitrogen molecules in this LP. Note that a LP is not created in a noble gas (for example, argon).

2.3. UV Spectra Obtained in a LP in free high-speed swirl flow

Remind that P. Kapitsa measured intensive UV radiation and soft X-radiation (10^2-10^3 eV) generated by a longitudinal MW plasmoid in swirl flow in his work many years ago [7]. This phenomenon is named as "UV- catastrophe" inside LP. UV spectra (λ=250-300nm) of a LP created by CHFD in swirl flow are recorded and analyzed in this work. The typical UV spectra obtained in a LP in free swirl flow by optical spectrometer Avaspec 2048 are shown in the fig.7. It is revealed that the intensity *I* of the optical lines and the optical bands in the wave range 250-300 nm are increased in a LP considerably. The value *I* is increased up to factor 10-20 during the transition between a filamentary (corona) HF discharge and a longitudinal HF plasmoid namely, fig.8. This value *I* is depended on duty cycle also. So, this phenomenon is depended on plasma formation overheating (average HF power input in plasma). UV radiation is increased in a non-equilibrium LP namely.

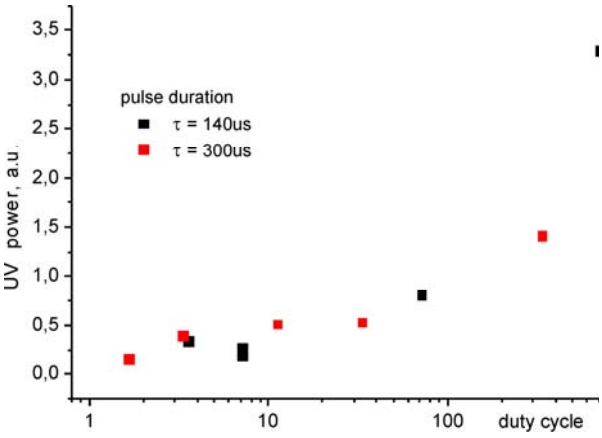

Figure 8. *UV intensity dependence on duty cycle in a longitudinal HF plasmoid in a free swirl flow. Pst~1 Bar, Vt~Vax~30 m/s*

2.4. LP's Parameters Measured by an Optic Interferometer

LP creation and its structure in swirl flow *at pulsed repetitive HF power pumping* are studied by high-speed camera and optical interferometer simultaneously in this work, fig.9-13. It is revealed, that a pulsed repetitive CHFD creates a hot cavern near vortex axis and a LP inside it. LP consists of a longitudinal plasma filament and a plasma corona in its top. The secondary HF filaments propagate in this hot cavern created by preliminary plasma filaments. LP's head propagation velocity is closed to the typical axial velocity of counter flow (reverse flow) V_p ~V_s~10-30 m/s in swirl flow, fig.9. Velocity V_p of LP top's propagation is measured in

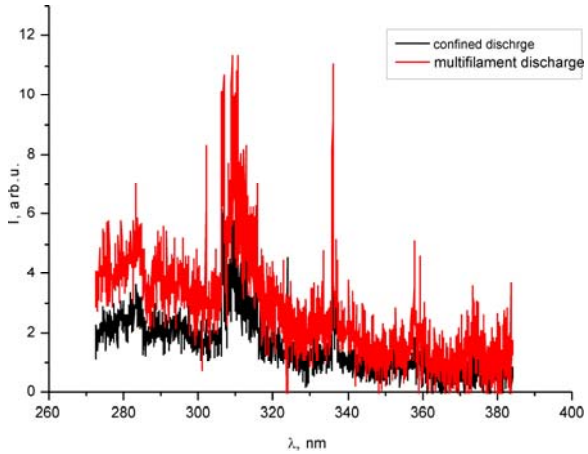

Figure 7. *UV optical spectra obtained in a longitudinal HF plasmoid in free swirl flow. Pst~1 Bar, Vt~Vax~30 m/s*

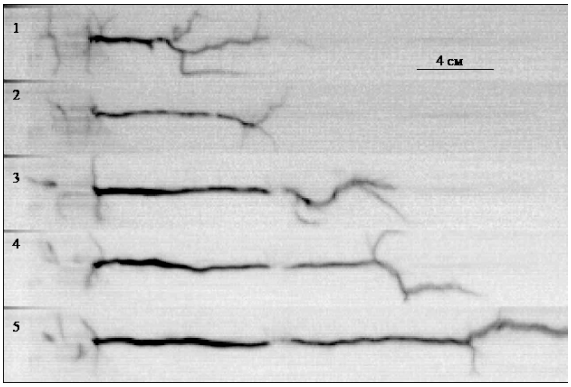

Figure 9. *The high-speed frames of LP's propagation in a swirl flow. Modulation frequency Fm=250Hz, Ti=0.5ms. Vt~20 m/s, Vax~ - 8 m/s, U~20kV, texp=300μs.*

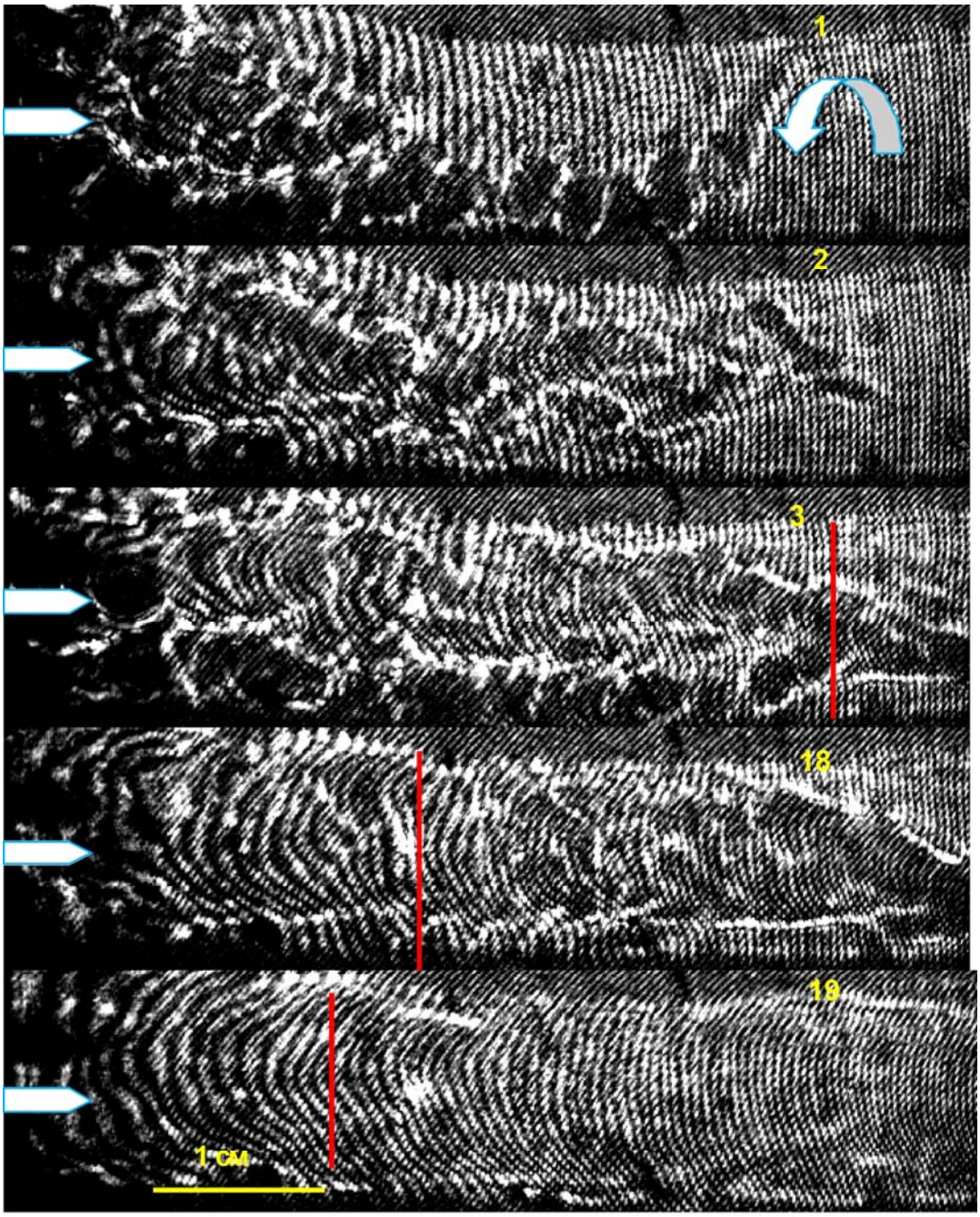

Figure10. *The high-speed interferometer frames of LP creation. Odd frame numbers correspond to pulsed HF power on, even frame numbers correspond to pulsed HF power off. FM=150Hz, Ti=2.5ms, FHF=350 kHz, Np~700W, Vt~ 30 m/s, exposure time texp=40μs*

swirl flow by high speed camera at *low static pressure (40÷100Torr)* also. The typical value V_p is about 30÷40 m/c and does not depend on swirl flow velocity in this regime.

The typical high-speed frames of LP's structure and its evolution in time obtained by optic interferometer are shown in the fig.10. Gas temperature distributions inside a LP are shown in the fig.11-13. One can see that there is fast gas heating up to T_g~ 2000-3000K in a plasma filament during HF power pulse. A homogeneous hot cavern (T_g~ 600K) is created between HF power pulses. Note that the typical diameter of a hot cavern is larger than the typical diameter of a luminous plasmoid by 2-4 times, fig. 13.

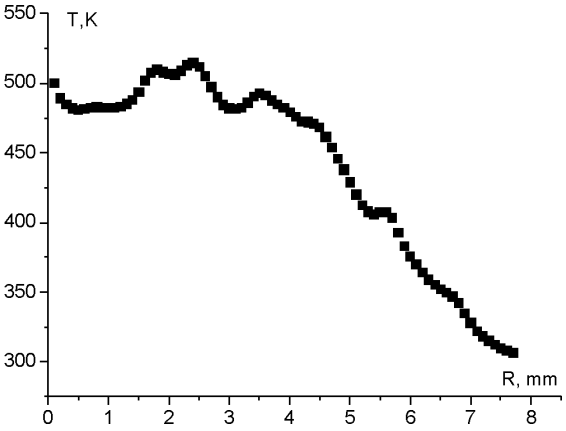

Figure11. *Gas temperature profile $T_g(R)$ inside the LP at pause (relaxation) time period (Fig.10 #18). LP's cross section is marked by a red line.*

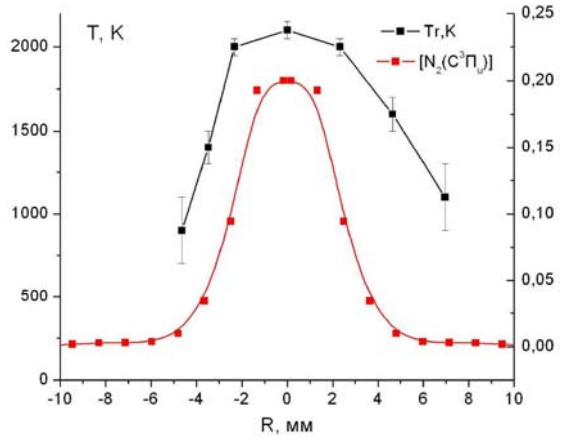

Figure 13. *The typical gas temperature distribution inside the LP and its luminescence intensity (relative units). P_{st}~1 Bar, V_f~20m/s, N_{HF}=240W*

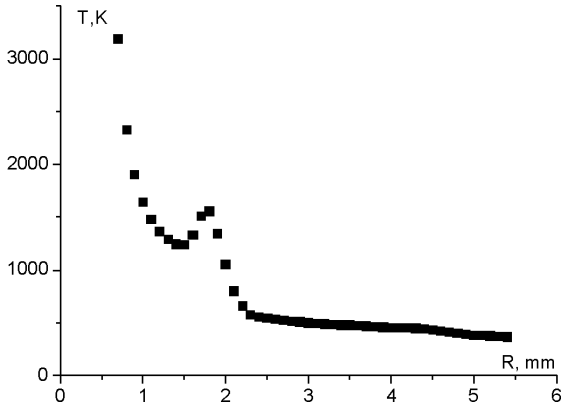

Figure 12. *Gas temperature profile $T_g(R)$ inside the LP at pause (relaxation) time period (Fig.10 #4). LP's cross section is marked by a red line.*

2.5. LP Created by Pulsed Repetitive CHFD

A free LP in free swirl flow created by CHFD is studied in this work. It is revealed that there is a compact homogeneous constricted longitudinal plasmoid in swirl flow at high modulation frequency $F_M > F_M$*~ 1kHz, T_i=0,5ms* namely, fig.4.

Swirl flow control by CHFD is studied in this work also. It is revealed that a free vortex is destructed by
a CHFD plasma effectively at $F_M > F_M$*~3 kHz* (or *St≥2-3*) namely. The detail shadow pictures of free vortex destruction by a longitudinal plasmoid created by CHFD at different flow velocity are obtained and analyzed, fig.14.

Study of a free LP created by a pulsed repetitive CHFD in free swirl airflow behind wedge (model W) is carried out in this work. The experimental set up WT-M used in the present

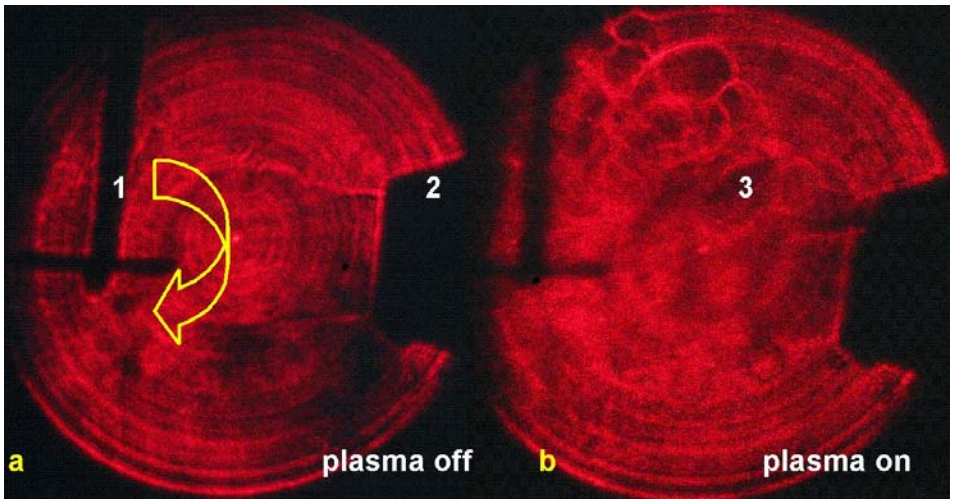

Figure 14. *Shadow pictures of swirl flow near nozzle at CHFD plasma on (b) and plasma off (a). V_f~V_z~30m/s, P_{st}~1 Bar, F_M~3,25 kHz, sin-type modulation, 1-HF electrode, 2-nozzle, 3-turbulent disturbances*

experiments is shown in the figure 15 and consists of dielectric wind tunnel (1), dielectric wedge (2), pressure sensors (2,3), electrodes (3) and HF generator (4) . Incoming airflow is created by fan.

The aerodynamic wedge model W is manufactured from PMMA and has the following dimensions and parameters:

- thickness 3mm
- height 25 mm
- length 40mm
- knife angle 30^o

The cross section of the aerodynamic duct used in this experiment is about of 40x40 mm.

The *experimental conditions* are the followings:

- Mach number M< 0.2
- Attack angle /AoA= 90^o
- Static pressure P_{st} ~1 Bar
-

The HF plasma generator has the following parameters:

- Pulsed HF power N_{HF}=200W
- HF frequency FHF =0,5 MHz
- Modulation frequency FM<2kHz
- Pulse duration Ti=200-500 μs

CHFD location is controlled by a vortex created behind the wedge model automatically (low static pressure, see below).

Swirl flow around this model is studied by the optical shadow method (λ=248 nm) and the high-speed camera Citius (F=2000 frames/s). A longitudinal HF plasmoid is recorded by a standard photo camera (exposure time is about 1/200÷1/1000s) also. The typical frames of the LP in swirl flow behind wedge are shown in fig.16. The typical shadow pictures are shown in the fig. 17,18. One can see that

1. LP is created by CHFD in vortex's kernel namely (in the region with low gas pressure and gas density). The stable LP is created at HF power pulse frequency F_M≥1 kHz and incoming airflow $V_f \leq$ 30 m/s namely, fig.17, 18.

2. A laminar LP is created in a vortex behind the wedge model at low velocity of incoming airflow about of $V_f \leq$ 30 m/s (Re< $V_f D/\nu \sim 10^5$). A turbulent LP is created at high velocity of incoming airflow V_f> 30 m/s (Re>10^5), fig. 16-18.

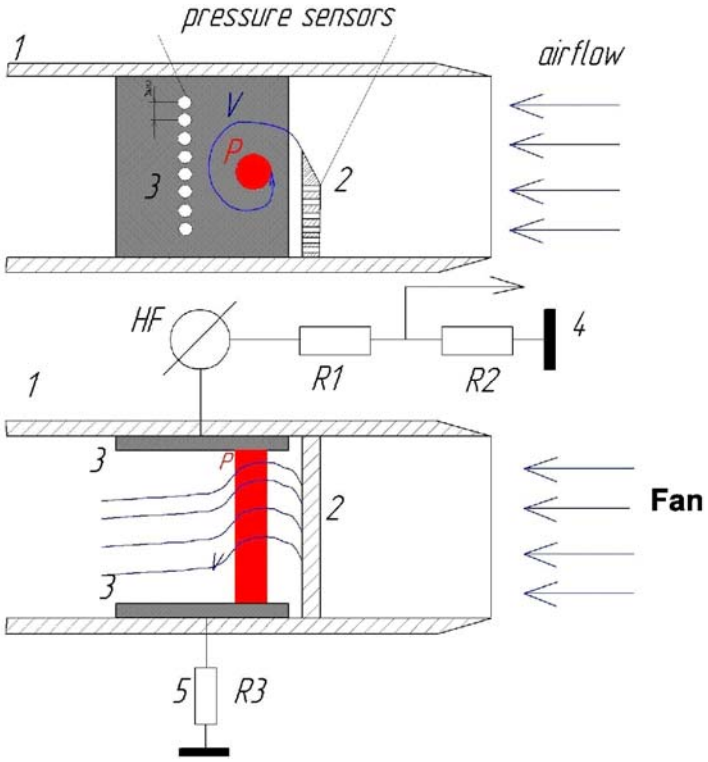

Figure 15. *The experimental set up WT-M for study of a LP created by HF discharge in swirl flow. 1- duct (PMMA) , 2- wedge (PMMA, model K), 3- electrode (aluminum), 4- grounded electrode, 5- shunt*

3. Plasmoid's structure depends on electrode's location near the model W. It is revealed that a stable LP is created by CHFD inside a vortex at electrode location near vortex axis namely. HF plasmod is arranged near a vortex boundary (near an external contact surface between a vortex and incoming airflow) at the electrode's location near a top part of the wedge. One can see that there is a contact surface instability in this regime.

4. It is obtained that there is a pulse-repetitive regime of a LP re-creation in swirl flow. Plasma is occupied the vortex core and then evacuated from it by incoming flow. The typical frequency of LP's re-creation cycle is about F_P= 30÷100 Hz. Note that the typical period of these pulsations is closed to the typical time of a particle rotation inside a vortex created behind the wedge namely.
5. It is revealed that there are pulsations of HF voltage signal and HF current signal connected with LP's re-creation process. The typical frequency of these pulsations $F_{I,V}$ are closed to the value F_P: - $F_{I,V} \sim F_P$

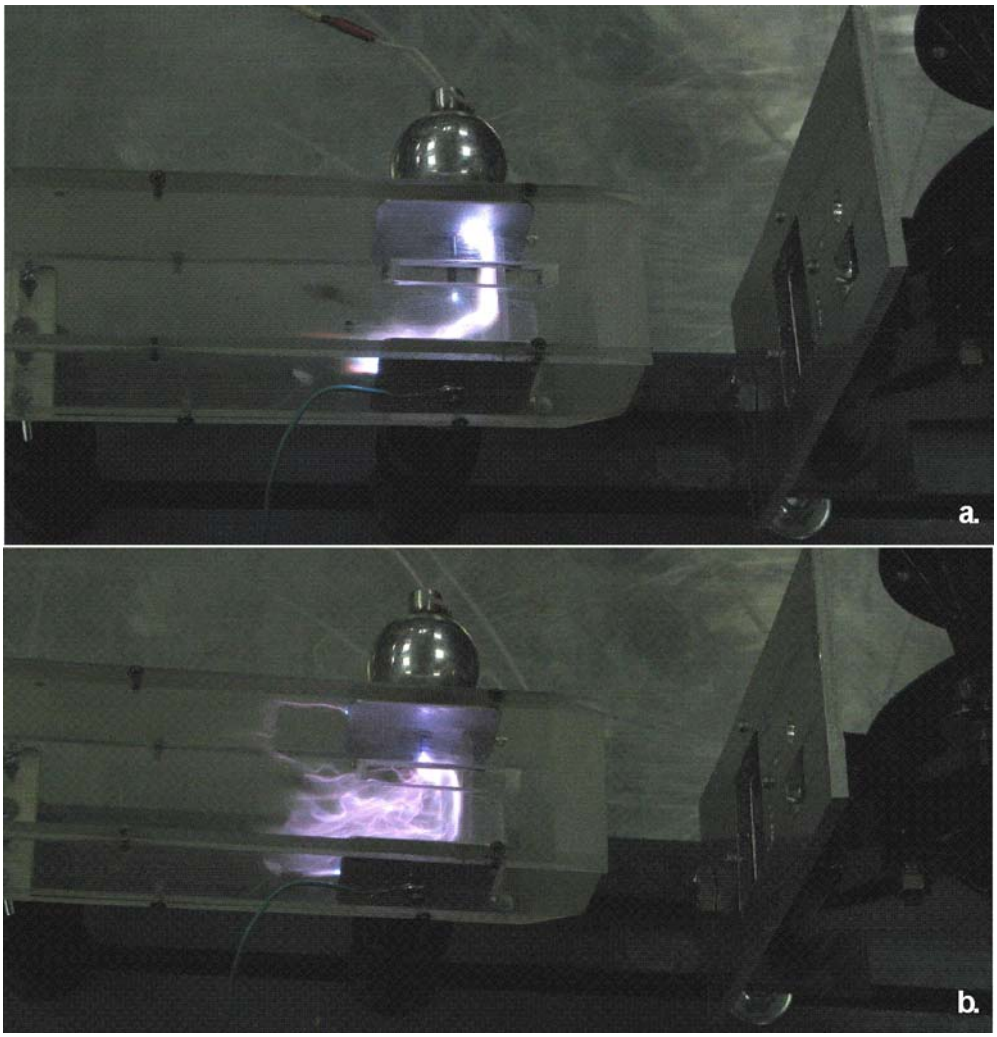

Figure 16a,b. *The typical pictures of the LPs created by pulse repetitive CHFD behind wedge model K. a.- stable plasmoid regime at V_{af}=10m/s, c.- unstable plasmoid regime at V_{af}=30m/s. F_M=1000Hz, T_i=500μs, mean HF power- 200W*

2.6. Pressure Distributions on Wedge's Surface at HF Plasma on and Plasma off

It is important to obtain reliable information about pressure distribution inside vortex at LP creation. This information helps us to clear question about vortex control by CHFD. However correct measurement of pressure distribution by Pitot's tube in 2-D swirl flow is difficult technical task (see [1-7]). So, we measure of pressure distribution on wedge surface and pressure distribution on duct wall with the well-known boundary conditions. The eight pressure ports are arranged on the wedge's surface and the eight ports are arranged on the duct's wall, fig. 15. The distance between them is about 3mm on the wedge surface and 3.5mm on the duct's surface.

The typical pressure distributions measured at HF plasma on, HF plasma off and different airflow velocity of incoming airflow are obtained in this experiment. The typical pressure distribution is shown in the fig. 19. One can see that there is pressure increase on wall surface about 20-30 %. This result proves that there is vortex attenuation by HF plasma.

Some additional experiments were carried out to prove the vortex attenuation by a longitudinal HF plasmoid. Small helium jet is injected near wedge wall by a thin dielectric tube, fig.18. This jet is deflected to wedge surface by swirl flow at plasma off, fig. 18b, d. Helium jet does not deflect to wedge surface by swirl flow at HF plasma on, fig. 18a, c. So, swirl flow is very weak to deflect of helium jet in the last regime. So, there is real vortex attenuation near the wedge at HF plasma on. Note that this conclusion is correlated with the one obtained by pressure distribution analysis.

Remind that static pressure increase inside vortex kernel has been measured in our previous

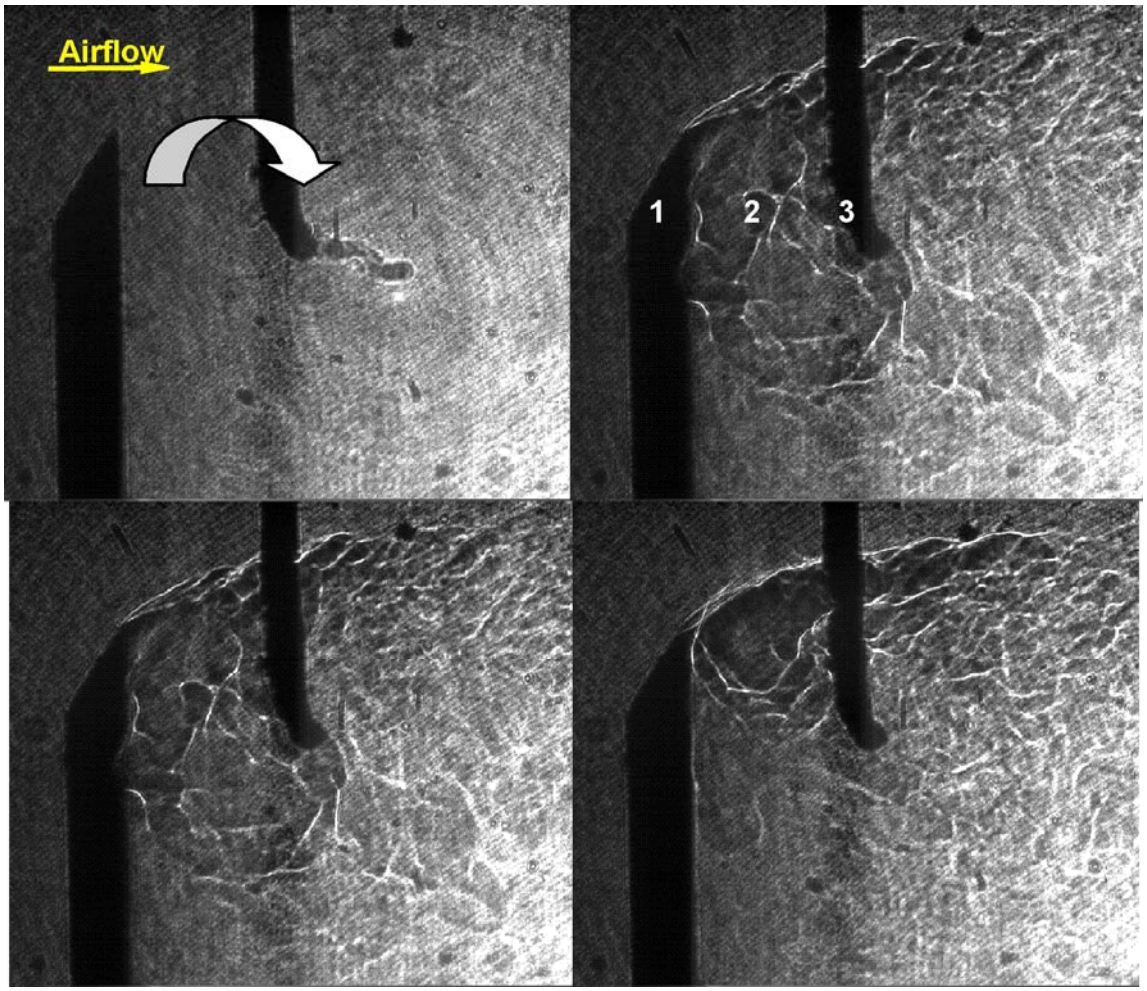

Figure 17. *The typical shadow pictures of the turbulent plasma formations created by continuous CHFD in swirl flow behind wedge model K. a.- V_{af}=10m/s, b.- V_{af}=30m/s, mean HF power- 200W. 1- wedge, 2- LP, 3- HF electrode*

works also [7,8]. The typical static pressure distributions in swirl flow in duct measured along its axis and duct wall are shown in the fig. 21, 22.

One can conclude that there is agreement between the experimental results obtained in swirl flow in a duct and the new ones obtained in free vortex. So, a longitudinal plasmoid created by CHFD can attenuate of vortex strength both in a duct and free vortex.

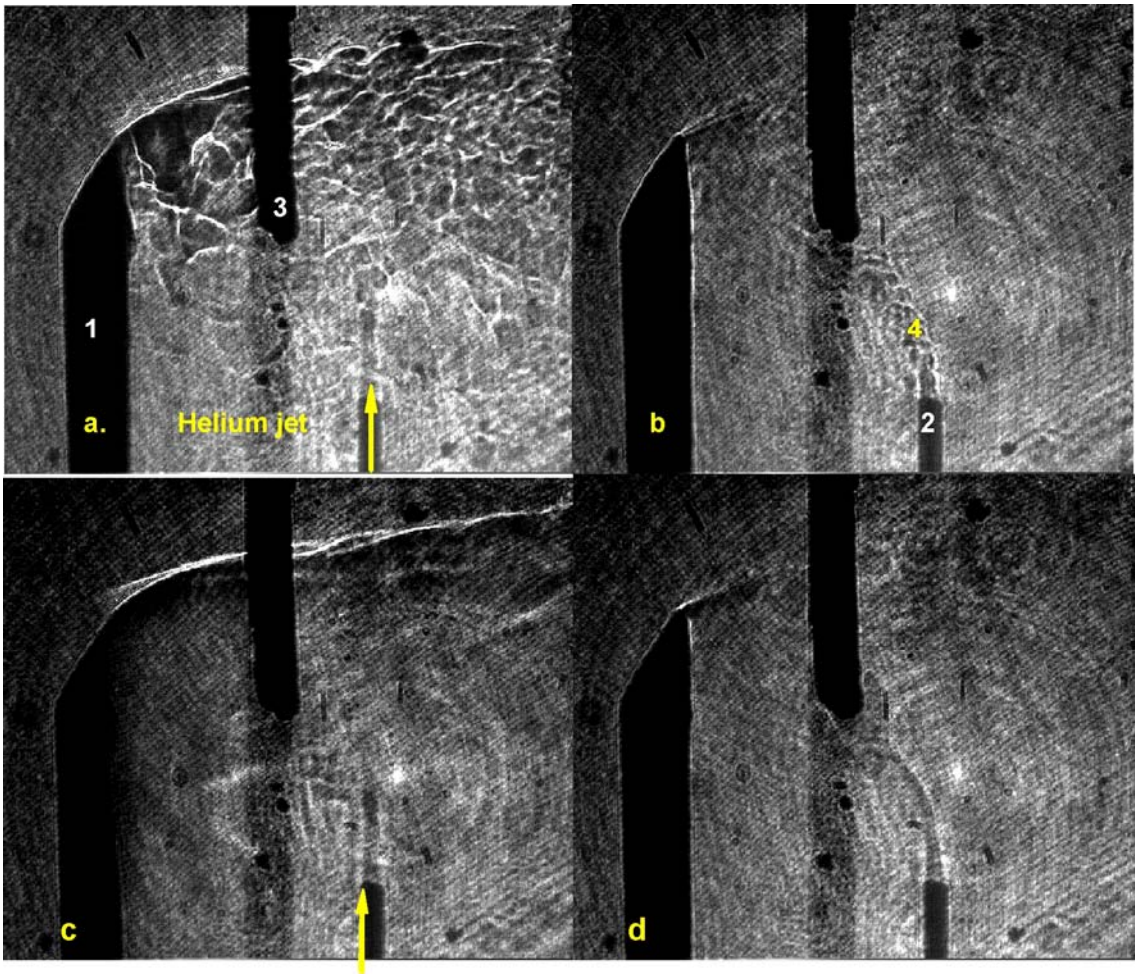

Figure 18. *The typical shadow pictures of the differnt plasma formations created by CHFD in swirl flow behind wedge model K at small helium injection. c,d.- V_{af}=10m/s, a,b.- V_{af}=30m/s, mean HF power- 200W. 1-wedge, 2- helium ejector, 3-HF electrode, 4-helium jet*

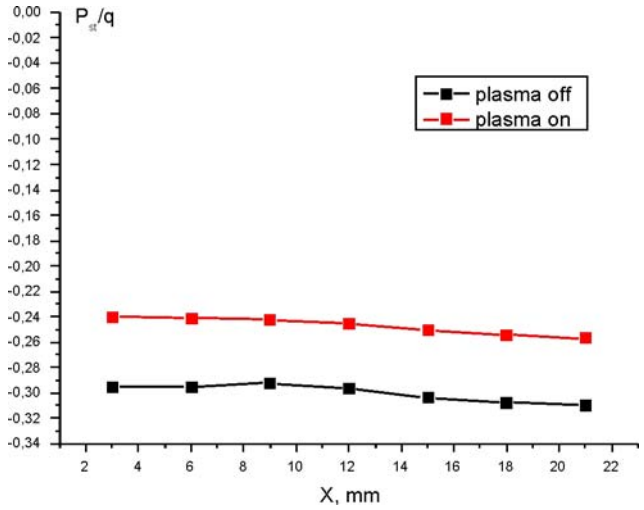

Figure 19. The typical pressure distributions on the wedge's surface at the velocity of incoming airflow V_f=30m/s

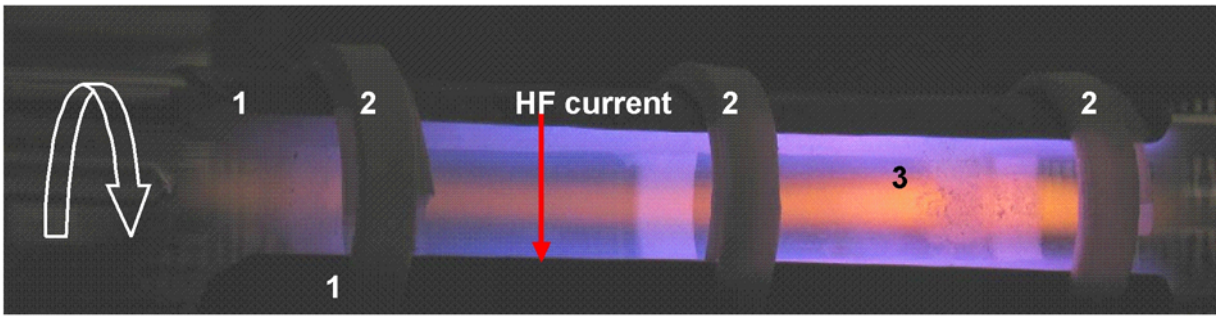

Figure20. *LP created by transversal capacity HF discharge. Lateral view -down.* V_t*~140 m/s* N_{HF}*=1.7kW,* P_{st}*= 40Torr, 1- electrode, 2- pressure sensor port, 3- LP*

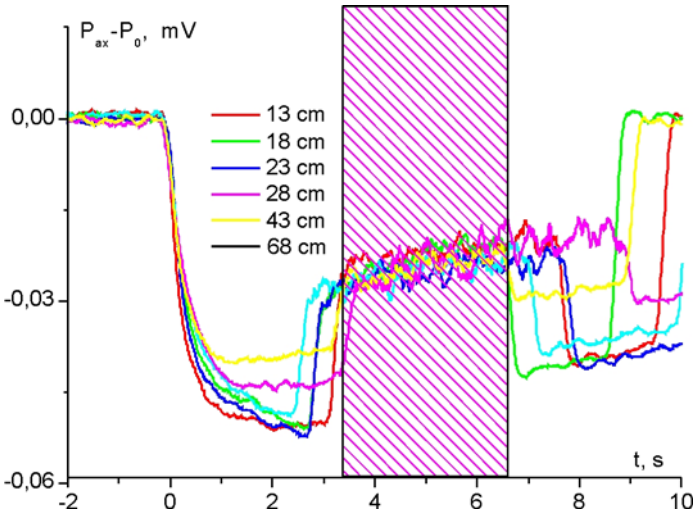

Fig.21. *Pressure sensor signals in the different duct's ports. Transversal CHFD in vortex airflow.* V_t*~140 m/s* N_{HF}*=1.7kW,* P_{st}*= 40Torr. HF plasma location is shown by magenta window*

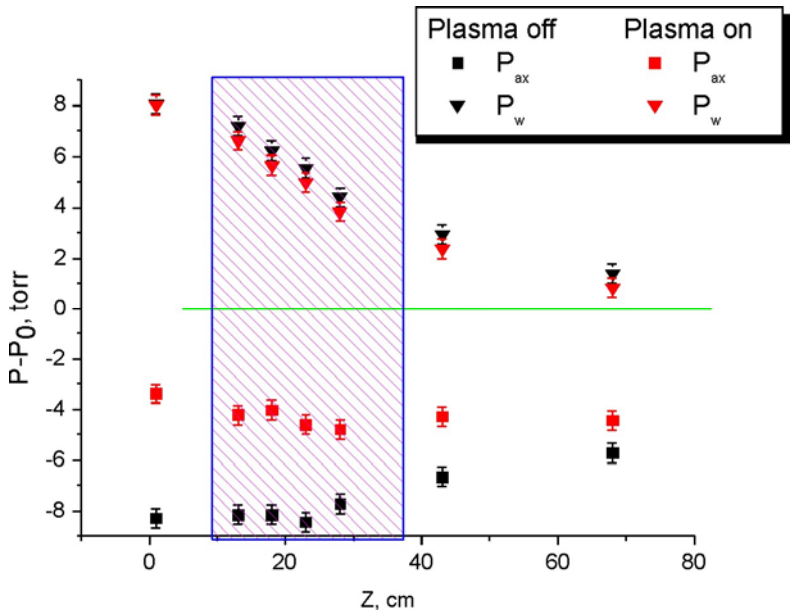

Fig.22. *Static pressure distribution in vortex airflow. Transversal HF discharge,* V_t*~140 m/s* N_{HF}*=1.7kW,* P_{st}*= 40Torr, electrode position is marked by a blue window, plasma region- magenta shading*

2.7. Control of a LP Location in Space by Additional External Electromagnetic Field

This task is very important for vortex control near airplane at large attack angle, flow separation control, drag control, lift force control by CHFD.

Experimental set up for study of free vortex control by plasma is shown in the fig. 23. It consists of a swirl generator (1), a needle HF electrode (2), additional DC electrodes (3, 4), ejector (5), pressure probes (6). External transversal electric field around HF plasmoid is created by plate DC electrodes (3, 4). Note that a special electrical disconnecting (separation) of HF power supply, DC power supply and grounded circuit is needed in this experiment.

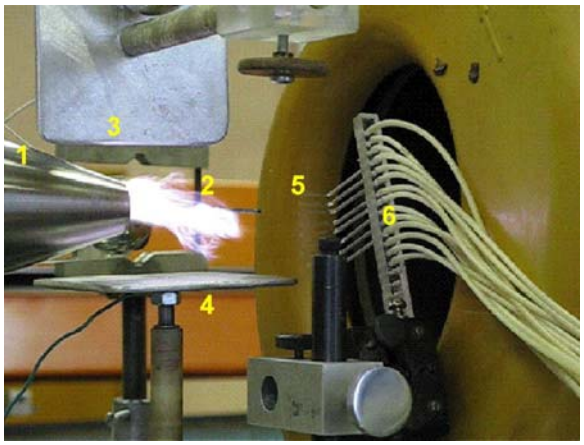

Figure 23. *Experimental set up for free vortex control by HF plasmoid and additional external DC field. 1-nozzle, 2- HF electrode, 3-4 – DC electrodes, 5- ejector, 6- pressure probe grid. Vertical arrangement of DC electrode (3)*

The typical picture of the vortex LP deflection by external electric field is shown in the figures 24. It is revealed that LP's deflection depends on electric field strength dramatically. It is revealed that the LP moves towards a top negative charged electrode in swirl airflow. It moves in opposite direction in swirl airflow at positive charged top electrode. These results are clear and understandable. Remind that LP has considerable positive potential (up to 2-3kV) measured in our previous experiments [7,8].

The new *unusual experimental result* is obtained by high voltage electric probe arranged behind HF electrode in down swirl flow. This probe measures a very high DC electric potential of the LP in region located behind DC electrodes. This LP has electric potential up to 2-3 times higher than the initial DC voltage applied to the electrodes (3, 4). For example, this plasmoid has DC potential about 30kV at initial DC voltage 10 kV applied to the electrodes (3, 4). The physics of this high plasmoid's potential is not clear today. Possibility of high electric potential generation in high-speed plasma flow by transversal DC electric field is discussed in our work [2].

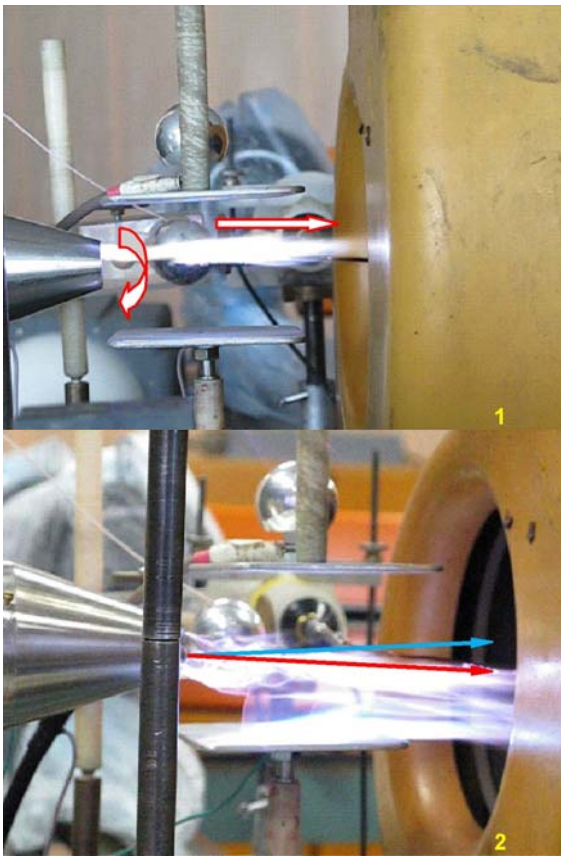

Figure 24. *Free vortex control by HF plasmoid and additional external DC field. 1-DC electric field is zero, 2- DC voltage U_{DC}=+10kV (top electrode is positive charged), HF voltage U_{HF}=2.8kV, V_t~V_x~30m/s*

2.8. Study of a Longitudinal Plasmoid in Free High-Speed Swirl Flow

Study of a longitudinal plasmoid (LP) created by capacity coupled HF discharge (CHFD) in *free high-speed swirl airflow* is carried out. The experimental set up WT-1L used in these experiments is shown in the figures 25, 26. Swirl generator (1) is connected with vacuum chamber by conical nozzle (2).

The conical nozzle has the following dimensions and parameters:

- Contraction angle 60^O
- Outer diameter 20 mm

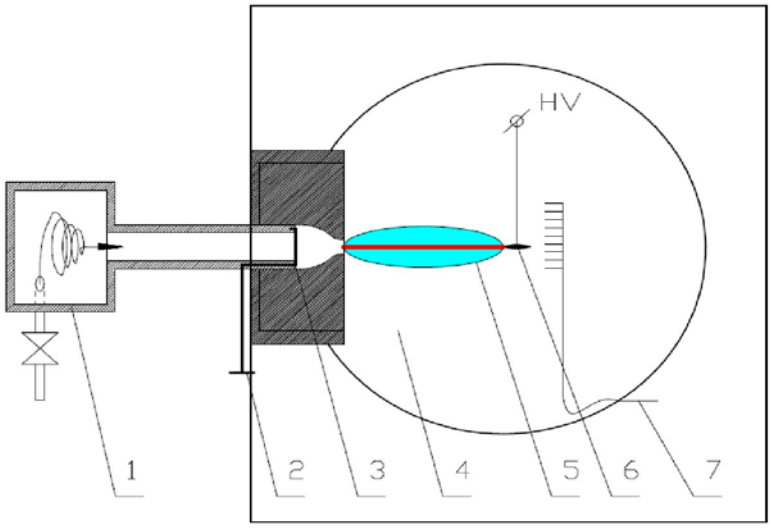

***Figure 25**. Scheme of the blow-down experimental set up WT-1L. 1-swirl generator; 2-conical nozzle, 3 - grounded forming duct; 4-grounded electrode, 5- CHFD; 6- needle HF electrode; 7- pressure sensors (grid); 8- vacuum chamber*

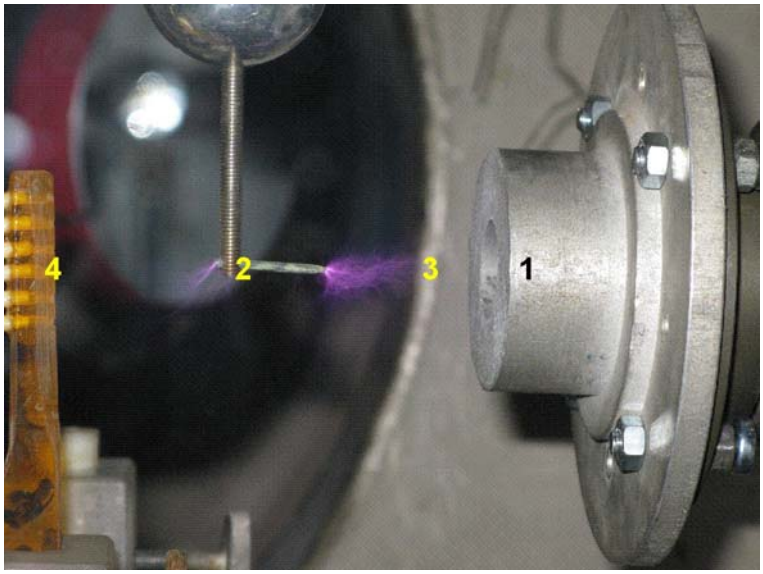

***Figure 26.** Blow-down experimental set up WT-1L. 1-swirl generator, 2- HF electrode, 3 – optic window, 4- pressure sensors (grid)*

The experimental conditions are the followings:

- Mach number of axial flow $M_x< 0.3$
- Mach number of tangential flow $M_t< 0.3$
- Testing gas Airflow
- Flow static pressure P_{st} ~100 Torr

The HF plasma generator has the following parameters:

- Pulsed HF power N_{HF}=200W
- HF frequency F_{HF} =1.2 MHz; 13.6 MHz
- Operation regime continuous, and pulse repetitive
- Modulation frequency F_M<20kHz
- Pulse duration T_i=50÷500μs

The typical pictures of free LPs created by CHFD in *swirl high-speed airflow* are shown in fig.27. One can see that there is multi-plasma filament corona in swirl high-speed airflow at the small swirl parameter $S=Q_\tau/Q_{ax}$~0.4 (where Q_τ- mass flow rate in tangential nozzle of swirl generator, Q_{ax}- mass flow rate in axial nozzle of swirl generator), fig.27a. There is a compact homogeneous constricted longitudinal plasmoid in swirl flow at the large swirl parameter S is about S~1.

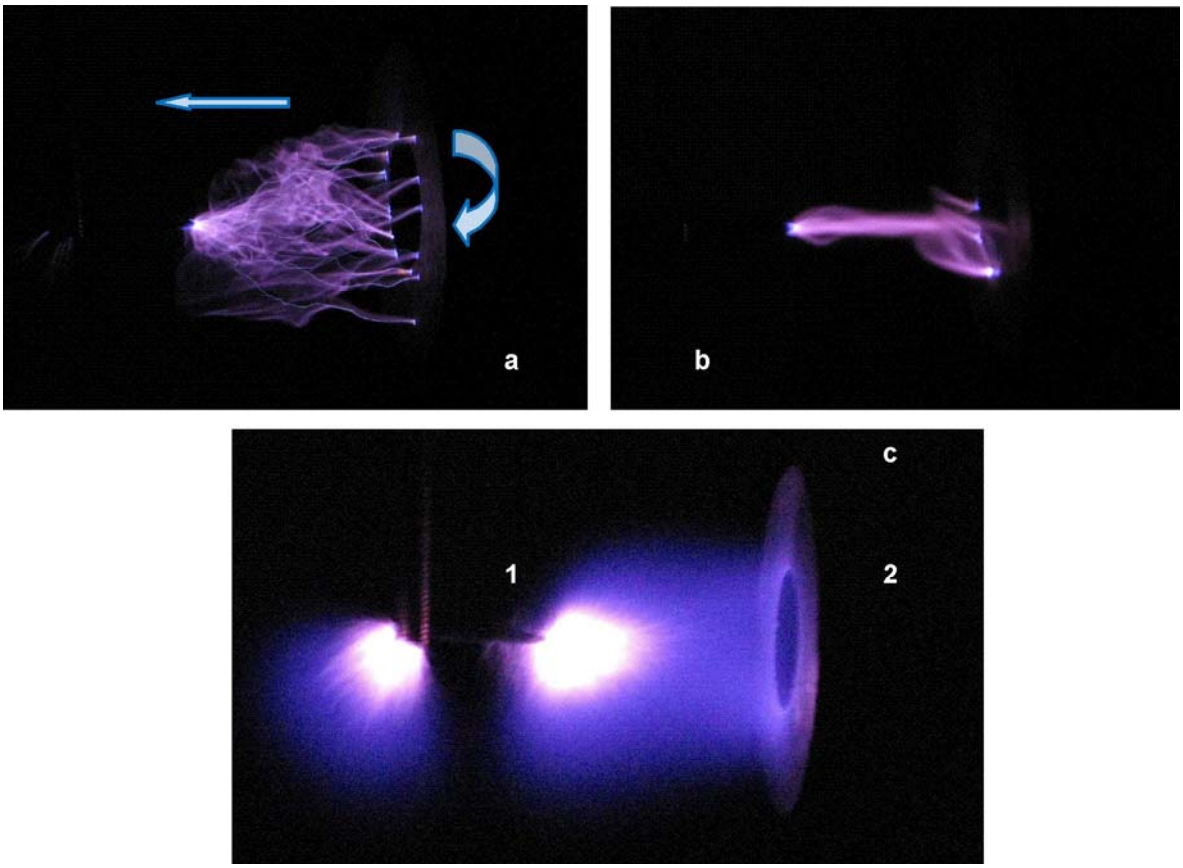

Figure 27. *Typical pictures of different plasma formations created by CHFD in high-speed swirl flow.*
WT-1L. a.- multi-plasma filament corona at small swirl parameter S=Qτ/Qax~0.4, Pst~100Torr, Vax~140m/s; b.-constricted longitudinal HF plasmoid at large swirl parameter S=Qτ/Qax~1, Pst~100Torr, Vax~140m/s.
c.- longitudinal charged HF plasmoid with blue halo at Pst~300Torr, Vax~90m/s
1-HF electrode, 2-conical nozzle

It is revealed at the first time that it is possible to create of a positive charged plasmoid in *high-speed swirl airflow* at high HF power input in plasma N_{HF}>800W and high velocity about V_{ax}~V_{τ}>70m/s. Bright white spherical plasmoid ~10mm diameter is created near needle HF electrode in this regime. External blue plasma halo 30mm diameter is created around this plasmoid. Electric potential of this plasma halo measured by electric high voltage probe Tektronix. The typical value of this electric potential is about φ~+1-3 kV, fig.28. This value is depended on value N_{HF}, pulse repetition frequency F_i and airflow velocity V_{ax}~V_{τ}. The maximal value φ~+3kV is measured at maximal value N_{HF}~ 800W, maximal pulse repetition frequency F_i ~10 kHz and maximal airflow velocity V_{ax}~V~ 140 m/s. It is not clear why measured plasmoid's potential is positive? This question will be cleared in future experiment.

Note that it possible to create *DC power supply* by this plasma-vortex convertor. Main question is efficiency of this plasma-vortex convertor in this regime. This question is studied now in detail.

The typical shadow pictures of swirl flow near nozzle obtained in the experimental setup WT-1L at HF plasma on are presented above and shown in the figure 29. One can see that swirl flow is transformed at plasma on. Large vortexes are created near swirl jet boundary (contact surface between swirl flow and ambient gas disturbed by HF discharge). Diverge angle of swirl flow is increased considerably at HF plasma from 0^0 on up to 60^0. Note that initial swirl jet is collimated in this shadow pictures (diverge angle is about zero). One can see considerable swirl flow turbulization by HF discharge in these pictures also.

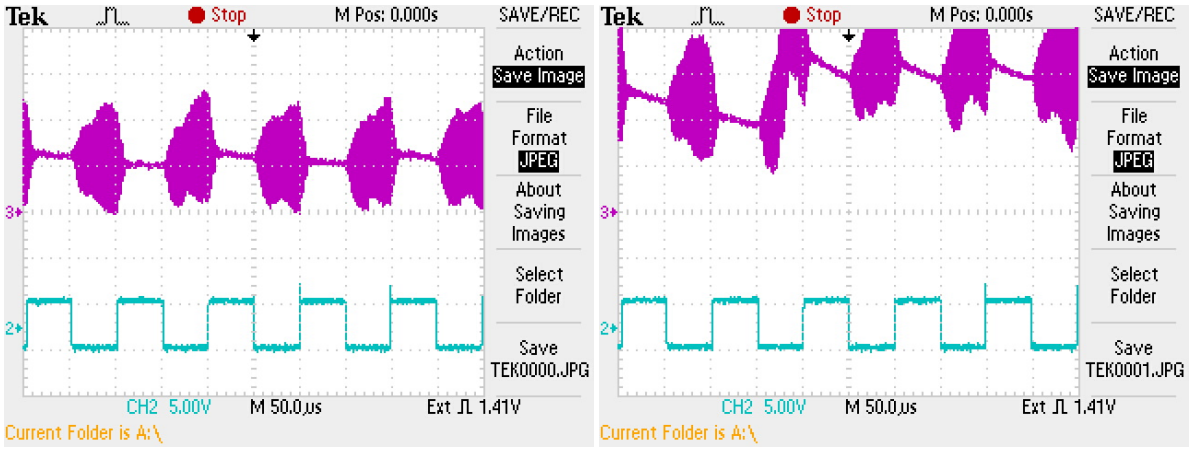

Figure 28. *Typical HF plasmoid's electric potential at different experimental conditions. WT-1L. Left.- longitudinal charged HF plasmoid with blue halo at Pst~300Torr, Vax~90m/s Right.- longitudinal charged HF plasmoid with blue halo at Pst~300Torr, Vax~140m/s*

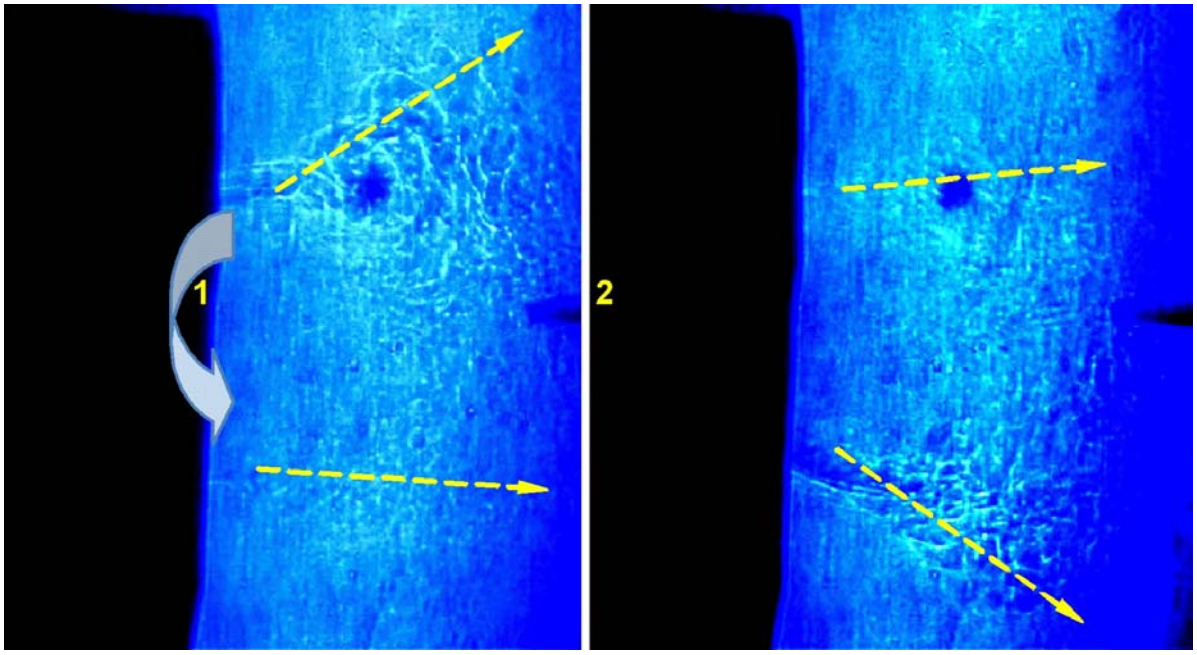

Figure 29. *Swirl flow near conical nozzle (1) at plasma on (top edge) and HF plasma on (down edge). Set up WT-1L. Asymmetric HF discharge, V_{af}~140m/s, P_{st}~0.5 Bar, N_{HF}~200, 1- nozzle, 2- HF needle electrode*

2.9. Pressure distribution in swirl flow at HF plasma on and plasma off

The experimental results on time dynamics of static pressure and stagnation pressure in high speed swirl flow (near its axis) at charge HF plasmoid on (see the fig. 27.) are shown in the fig.8. One can see that there is considerable static pressure increase up to 20-30% and small stagnation pressure decrease up to 1-3% in the vortex (near its axis) at HF plasma on. Note that the pressure value is estimated as a difference between pressure by measured Pitot' tube and pressure measured in test section. It is necessary to remind that a homogeneous *charge HF plasmoid (non-constricted)* is created in this experiment. So, electric double layer created on the boundary of this plasmoid can play important role in pressure redistribution inside incoming swirl flow. This question should be study in future experiment.

So, it is revealed that *high-speed swirl flow parameters* can be changed by HF plasma considerably. The obtained results may be used for

flow control, lift control, advanced mixing, plasma aerodynamics and plasma assisted combustion.

Numerical results on a LP's structure and its evolution are obtained and compared with numerical results. Simple plasma-chemical kinetics is used in this numerical study. It is shown that there is a good agreement between experimental results and theoretical ones

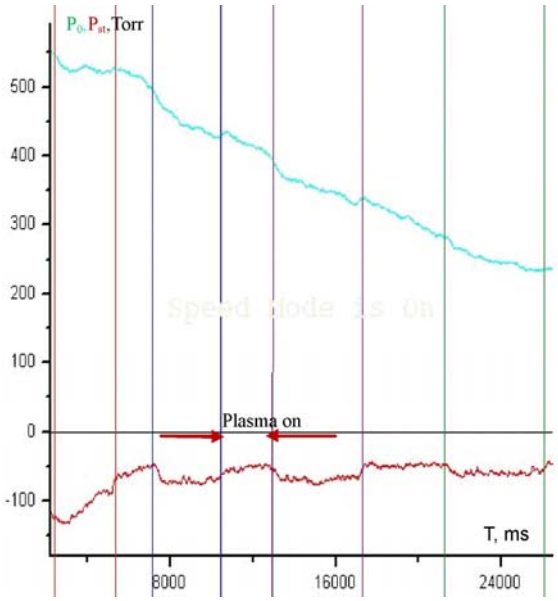

Figure 8. *Temporal dynamics of stagnation pressure P_o(top) and static pressure P_{st} (down) measured near swirl flow axis in the setup WT-L2 at HF plasma on (between the same color lines) and plasma off (between the different color lines)*

Conclusion

Experimental and theoretical study of a non-equilibrium plasma- vortex interaction has been fulfilled. A number of important results have been obtained in this work namely:

1. *A non- equilibrium LP is created by CHFD* (T_V~3000K> T_R~1500K) in swirl flow. This compact homogeneous constricted LP is created both by continuous HF power pumping and pulse repetitive HF power pumping in swirl flow. Note that a stable LP is created by pulse repetitive HF power pumping in swirl flow at high modulation frequency $F_M > F_M$*~ *1kHz* (T_i*=0,5ms)* only.
2. It is revealed that there is *vortex attenuation and its decay* by CHFD plasma on both in a duct and open air. Static pressure near vortex axis is increased up to 20-50% at CHFD plasma on. It is obtained that pressure gradient is about zoro near vortex axis at plasma on. So, there is stationary immovable gas inside central vortex region at plasma on. It is demonstrated that a free vortex in open atmosphere is destructed *by pulsed repetitive CHFD* effectively at $F_M > F_M$*~*3 kHz* (or *St≥2-3*) namely.
3. The pressure distributions inside vortex created behind a wedge model are measured at HF plasma on and HF plasma off and different velocity of incoming airflow. It is obtained that there is pressure increase on wall surface about of 20-30%. This result proves that there is vortex decay (attenuation) at HF plasma on. The additional experiment with small helium jet injection proves this conclusion about vortex attenuation by a longitudinal HF plasmoid also.
4. It is demonstrated that it is possible to change of a LP position in swirl flow by additional external DC electric field.
5. There is energy exchange between internal energy levels of exited nitrogen molecules and translation energy of these molecules in a longitudinal plasmoid (V-T relaxation process). This result based on analysis of obtained optical spectra of LP's luminescence at different swirl flow parameters, different HF power and different *initial pressure* P_{st}*=40÷760Torr*. A non-equilibrium plasma formation is created by CHFD in swirl flow near duct wall (plasma halo, T_V ~ 3200 ± 400 K, T_{rot}~ 600K) namely. Hot equilibrium plasma is concentrated near vortex axis (T_V ~ 3200 ± 400 K, T_{rot}~ 1600- 3000K). So, creation of a longitudinal vortex plasmoid may be associated with V-T relaxation process (or E-T relaxation process) of exited molecules (where V- vibration energy, E- electronic energy, T- thermal energy of excited molecules). Really it is impossible to obtain this phenomenon in noble gas swirl flow (for example, argon).

Acknowledgements

This work is supported in part by the Air Force Office of Scientific Research and Russian Academy of Science. We thank Dr. David Van Wie for his interest to this Work and discussions.

References

1. D Van Wie, Garscadden A.,Gunguly B., at.el., Plasma in High-Speed Aerodynamics, J. Phys. D: Appl. Phys., 38 (2005),R33-57
2. Bityurin V., Bocharov A., Klimov A., Leonov S., Analysis of Non-Thermal Plasma Aerodynamics Effects, In: 44rd AIAA Aerospace Sciences and Exhibit, Jan 9-12 2006, Reno, NV. AIAA Paper 2006-1209
3. Klimov A., Bityurin V., Study of Plasma-Assisted Combustion of Hydrocarbon Fuel in High-Speed Airflow, Combustion Laws, Ed. Acad. Polezhaev Yu., Moscow, RAS, 2006, P.93-10

4. Klimov A., Moralev I., et.al., Longitudinal Vortex Plasmoid Created by Capacity HF Discharge, AIAA Paper, Proc. 46th AIAA Conf. Reno NV, 7-11 Jan 2008, P.11
5. Klimov A., Moralev I., et.al., Study of a Longitudinal Plasmoid Created by Capacity Coupled HF Discharge in Vortex Flow, AIAA Paper 2009-1046, Proc. 47th AIAA Conf., Orlando FV, 5-8 Jan 2009, P.11
6. Klimov A., Calorimetric Measurements in plasma vortex, Proc. 14th Conf. on Cold Nuclear Transmutation and Ball Lightning, Dagomys, Sept. 19-26, 2006, P.246-253
7. Kapitsa P., HF Plasmoid in Gas at High-Pressure, JETPh, 1969, V.57, No 57, P.1801
8. Klimov A., Strategy of Plasma Aerodynamic Researches Today, Proc. EUCASS, 2009, P.16

8.5. ABOUT SOME FEATURES OF RADIO-WAVES PROPAGATION THROUGH EXTENDED NONUNIFORM PLASMA

V.I.Nikolayeva[1], A.S.Pashchina[2], M.K.Sidorenko[2]
[1]Joint Stock Company "GSKB "Almaz-Antei", 80-A, Leningradsky prospect, Moscow, Russia, 125178
[2]Joint Institute for High Temperatures RAS, Moscow, 125412, Russia

Abstract. Experimental results of radio-waves propagation through extended nonuniform plasma formed by erosive type discharge are presented. Depending on relations of plasma parameters (plasma frequency, electron collisions frequency) and electromagnetic wave frequency the modes of radio-waves absorption, reflection and dispersion can be realized. High plasmoid conductivity, comparatively low signal dissipation and noise temperature was revealed in experiments that allow considering plasmoid use as the receiving-transmitting antenna.

Plasmoid kern is surrounded by "coat", which radius essentially exceeds the kern size and can reach several tens of centimeters. High electron density in "coat" area (about 10^{11}…10^{13} cm^{-3}) can cause radio-waves reflexion, dispersion, absorption or combination of these processes that depend on plasma and radio-wave frequencies relation. 14…20 dB attenuation of MW signals (operation frequencies 4…25 GHz) was observed in experiments that allows considering plasmoid use as effective radio-waves absorber.

Introduction

Studying of artificial and natural plasma formations is stimulated by a wide spectrum of applied problems related to dispersing, reflecting, absorbing, transmitting, receiving and channeling of radio-waves [1-4]. For radio communication applications plasma formations can be used as receiving-transmitting antennas that in some cases offers advantages in comparison with traditional ones, in particular:

- invisibility on radars as consequence of limited antenna's lifetime;
- possibility of dynamic tuning of frequency, directional diagram, transmission capacity, amplification etc., that permits to substitute several antennas;
- radioelectronic warfare stability;
- lower noise level and higher data transfer speed on satellite frequencies;
- absence of influence on flying vehicles aerodynamic parameters in the case of onboard antenna's use, etc.

It was John Hettinger, who in 1919 proposed to use ionized gas column for the purposes of signaling [5]. Ultra-violet radiation, DC, HF discharges and their combination were offered for the conducting area formation.

Two main directions on plasma antennas creation (reflectors and transmitters) based on extended plasma formations are assumed now, especially:

- plasma reflector in atmosphere, formed by focused MW discharge [4] or by laser-induced discharge array [7] with additional MW excitation [6];
- receiving-transmitting plasma antenna formed by laser-induced spark [8-11], erosive type discharge in a pulse mode [3, 12] etc.

It is necessary to note significant progress in semiconductor plasma antennas creation (PSiAN - Plasma Silicon Antenna), commercial use of which promises technological breakthrough in radio and telecommunication [13, 14]. Semiconductor antennas use permits to essentially expand radiocommunication bandwidth (up to 100 GHz), that creates wide application perspectives.

Clearly each method of plasma antennas creation has own application field, that depends on various factors (frequency range, exploitation conditions, environment condition, such as pressure, gas flow velocity, temperature, presence of shielding plasma etc.).

Erosive type discharge in a pulse mode can be considered as one of methods of the extended plasma objects (EPO) formation, which length can vary from 30…60 cm at atmospheric pressure up to 1…3 m at lower pressure values [15]. At certain erosive type discharge parameters plasmoid can exist in high-speed gas flows without destruction and get through a plasma layers. These features allow considering plasmoid use as the receiving-transmitting antenna on hypersonic flying vehicles in the condition of plasma shielding.

Main parameters determining interaction of electromagnetic waves with plasma

Depending on relations of EPO parameters (plasma frequency ω_p, electron collisions frequency ν) and electromagnetic wave frequency ω the modes of radio-waves absorption, reflection and dispersion can be realized. In general case EPO's state can be characterized by complex relative dielectric permittivity that in hydrodynamic cold plasma assumption can be given by

$$\varepsilon = \varepsilon' - j\varepsilon'' = n^2 = 1 - \frac{\omega_p^2}{\omega^2+\nu^2} - j\frac{\nu}{\omega}\frac{\omega_p^2}{\omega^2+\nu^2} \qquad (1)$$

where $n = \sqrt{\varepsilon}$ – index of refraction, $\omega_p = \sqrt{\frac{N_e e^2}{m \varepsilon_0}}$ – plasma (Langmuir) frequency, $\omega=2\pi f$ – angular signal frequency, m, e, ε_0 – mass, electron charge, permittivity of free space, correspondingly.

Another parameter, characterized EPO state, is penetration depth of radio-wave into plasma, or in another words, the distance, on which radio-wave attenuates for 4,3 dB:

$$\delta = \frac{1}{2k_0 Im\sqrt{\varepsilon}} \qquad (2)$$

where $k_0=2\pi/\lambda=\omega/c$ – wave number.

It is possible to select three physical conditions of EPO depending on relationship between ω_p, ω and ν:

1. Radio-waves absorption, when $\nu<<\omega$. This mode can be realized, for example, at high altitudes (more than 10 km), where collision electron frequency $\nu<10^8$ s^{-1}. In the sense of frequencies relation (i.e. $\omega_p>>\omega$) plasma is dense. Penetration depth $\delta=c/\omega_p$ in this mode is little even for HF band. Obviously, this mode can be applied only for radio-waves absorption.

2. Conducting mode («metal rod»), when $Im\varepsilon_p>>Re\varepsilon_p$, from that follows $\delta \approx \frac{c}{2\omega_p}\sqrt{\frac{\nu}{\omega}}$. In this mode $c/\omega_p<\lambda/2\pi$, $\nu/\omega>1$, that means dense plasma (with electron density $N_e>10^{13}$ см$^{-3}$ and collision frequency $\nu>10^{12}$ c^{-1}). Such mode can be realized by plasma generators based on erosive type discharge.

3. Dielectric mode («dielectric rod»), when $\omega_p<<\omega$, from that follows $\delta \approx \frac{c}{2\omega_p}\sqrt{\frac{\omega}{\nu}}$. This mode can be realized by numerous methods in wide pressure range (up to 150 km altitudes, where density of air particles $N\approx10^{12}$ cm^{-3}).

Thus, selecting radio-waves frequency, and also, considering admissible energy expenses which determines such parameters as plasma ω_p and collision ν frequencies, it is possible to determine EPO state.

If to use conducting mode of EPO state the plasma antenna can be realized by HF currents excitation in plasmoid kern. This is a variant of pole plasma antenna.

In dielectric mode EPO can be used as travelling-wave antenna. Surface wave excitation can be made by metallic waveguide section. Thus plasmoid will be deceleration waveguide. Feature of dielectric wave-guide antennas is the narrow directional diagram that can be important for some applications.

Results of experimental researches on possibility of EPO use for radio-waves receiving, transmitting, absorption and dispersion

Researches of possibility of EPO application as receiving-transmitting antenna

Spent in 1989…91 in Scientific Research Institute of Radio Device Instruments experimental researches have shown the basic possibility of erosive type plasmoid use as the receiving-transmitting antenna [3] (fig.1). In experiments EPO was formed by small-sized erosive type discharger, that could form under atmospheric pressure conducting area with sizes 0,1…0,4 m in length and 0,5…1 cm in diameter for a time interval of *t=1…30 ms*. For investigations of signal receiving and transmitting the MW generator 1 on operation wavelength λ~15 cm have been used. MW generators have been connected to plasma antenna 3 via matching device 2. Erosive type plasmoid generator was mounted in nose cone model of flying vehicle 13.

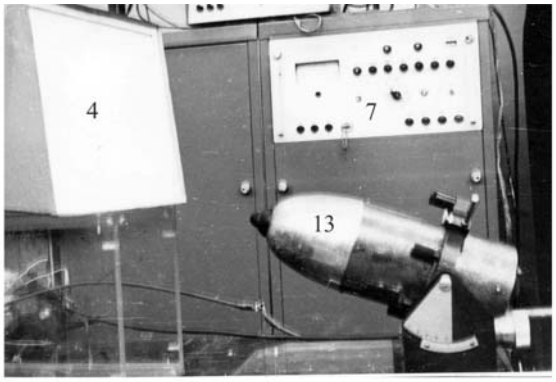

a)

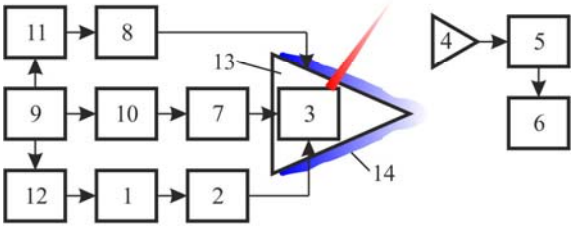

b)

1 - microwave transmitter
2 - matching device
3 - erosive type discharger
4 - horn receiving antenna
5 - detector
6 - oscilloscope
7 - erosive discharger power supply
8 - shielding plasma power supply
9...12 - pulse generators
13 - model of the flight vehicle nose cone
14 - shielding plasma layer

Fig.1. *General view (a) and principal scheme (b) of plasma antenna research stand.*

Horn antenna of П6-23А type 4 was used for signal receiving (and in some cases – transmitting). It was installed on appropriate distance from EPO's generator ($L>>\lambda$). Probe signal registered by oscilloscope 6 via detector 5. The last one was connected to horn antenna outlet. Low-frequency modulation of MW signal was used in experiments (П-type pulse duty about 0,1…10 ms). Plasma shield 14 created by DC discharge 8 was formed during experiments, that permitted plasma streamlining simulation on gas flow velocities 30…50 m/s.

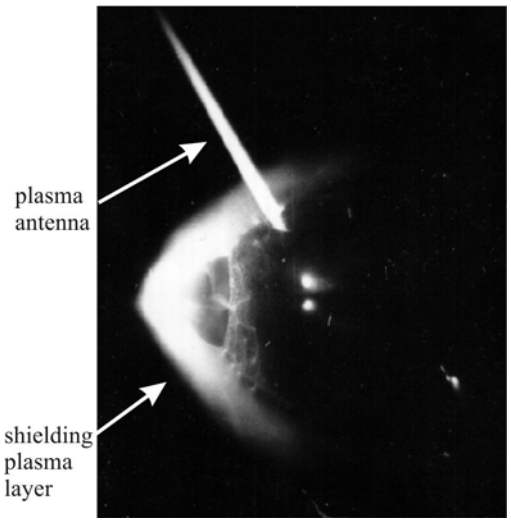

Fig.2. *Integral photo of plasma antenna in conditions of shielding plasma and incident gas flow.*

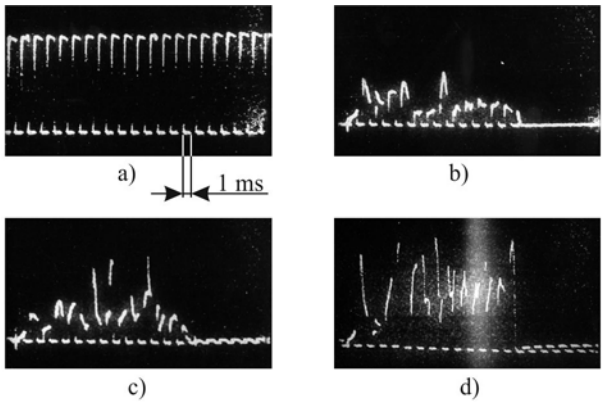

a) signal transmitting by metal rod
b) signal receiving by plasma antenna without shielding plasma
c) signal transmitting by plasma antenna in condition of plasma shielding layer
d) signal transmitting by plasma antenna without shielding plasma

Puc.3. *Typical oscillogramms of MW signal pulse envelope.*

Integral photo of plasma antenna in requirements of shielding plasma created near the model's surface is shown on fig.2. It is visible, that EPO get through plasma layer that makes possible signal transmitting and receiving.

Unlike cooper rod (fig.3a) transmitting (fig.3b and 3d) and receiving (fig.3c) by plasma antenna signal amplitude occurs to be not constant in time. Modulation of pulse envelope takes place because of plasmoid length changes in time that causes antenna detuning. Nevertheless received or transmitted by plasma antenna signal amplitude occurs comparable with the case of cooper rod.

Thus conductivity of plasma formation occurs close to conductivity of a copper rod of the same sizes. Dissipation of microwave signals (~2 GHz) for the transmitting mode was less than 30 %, and noise temperature for the receiving mode was less than 1000 K. Total losses in EPO and surface plasma layer have not exceeded 50 %.

Some features of radio-waves propagation through EPO area

Plasmoid has the complex coaxial structure (a plasma wave guide to some extend). It contains a high enthalpy kern, a thin coaxial shell and the "coat", which radius essentially exceeds the kern size and can reach several tens of centimeters. The electron concentration in a kern reaches $10^{15}…10^{16}$ cm^{-3} and decreases to 10^{11} cm^{-3} in the "coat" area [15]. In general EPO parameters are determined by erosive type discharger parameters and design features. Thus the plasmoid complex radial structure can cause simultaneous reflection, dispersion and absorption of radio-waves.

Plasmoid exposure by microwave signals on frequency of 25 GHz has revealed an essential role of "coat" in radio-waves dispersion.

Erosive type discharger, consisting of dielectric capillary 1 (polymethylmetacrylat), cathode 2, anode 3 (fig.4) used in experiments. Researches were spent at the increased values of the discharge energy, which value during discharge pulse time 12,5 ms was about 1,25 kJ. Transmitted signal voltage attenuation more than for 5 times (or for 14 dB) is observed in experiments (fig.5). Thus duration and behavior of attenuation correlates with plasmoid lifetime stages. In specified conditions plasmoid lifetime exceeds discharge duration.

Considering relation between EPO square in optical band (i.e. product of transversal EPO size 5 mm to maximal height of horn antenna) and horn antenna square, signal voltage attenuation must be $U_2/U_1=0,765$. It follows from relation $U_2/U_1=(1-S_{EPO}/S_{ant})^2$, where $U_1(U_2)$ – is signal voltage, registered with EPO presence (absence), correspondingly; $S_{EPO}(S_{ant})$ – EPO (horn antenna) cross-section, correspondingly. Mounted along discharger axis conducting rod causes diminishing of MW signal voltage for 23,88% that gives $U_2/U_1=0,7612$. It coincides with above-stated estimations. That's why plasmoid cross-section is

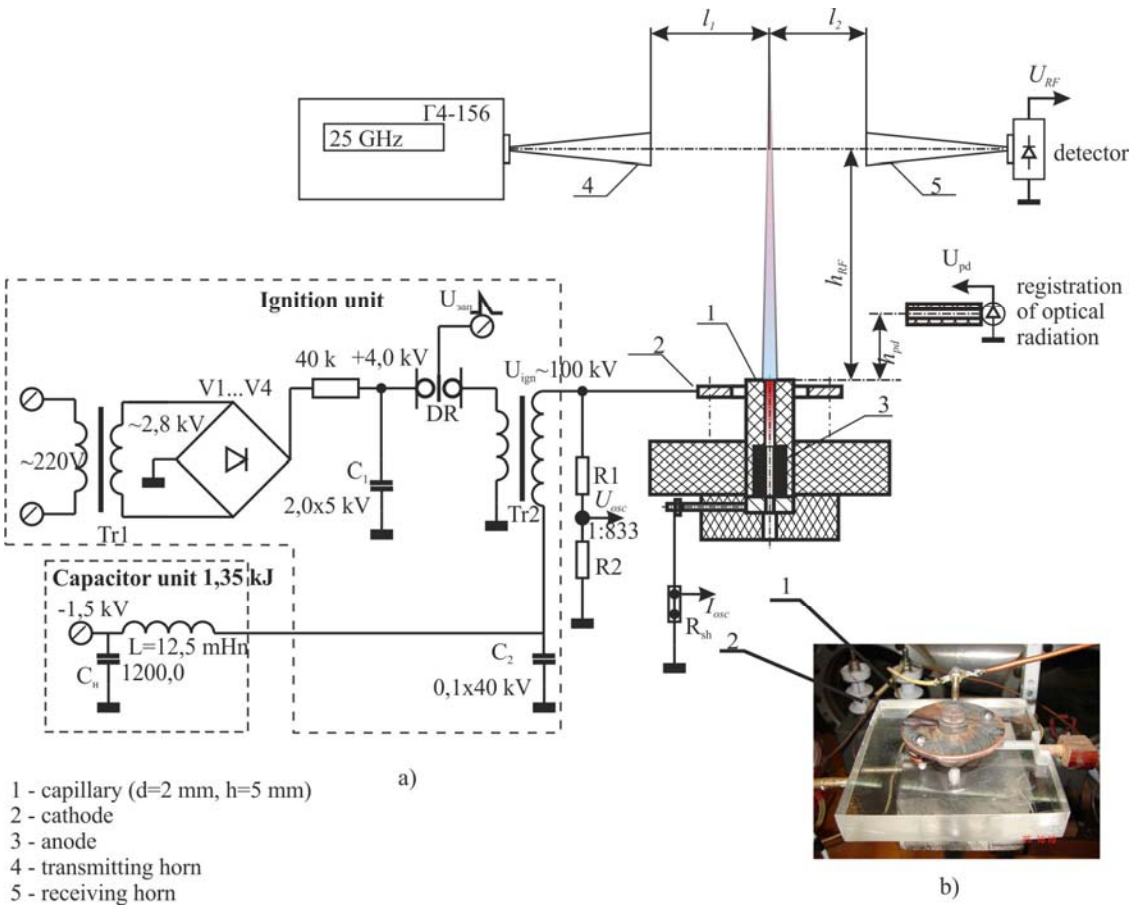

Fig.4. *Principal stand schematics (a) and general view of erosive type discharger model (b).*

insufficient for observed attenuation level that may be caused by "coat" area, which cross-section exceeds square of receiving horn antenna. Taking into account transmitted signal frequency, electron density in "coat" area is about $8 \cdot 10^{12}$ cm^{-3}.

It is typical that signal attenuation takes place after discharge termination during whole EPO lifetime (fig.5). Some correlation between receiving antenna (ch1) and EPO optical radiation (ch2) oscillogramms is observed. In particular, MW signal attenuation level almost does not change after discharge termination during EPO autonomous lifetime stage (linear site on optical signal oscillogramm, ch2). Attenuation level decrease (ch1) is observed during EPO dissipation stage (exponential site on optical signal oscillogramm, ch2). Thus, as in the case of optical radiation signal (ch2), the corresponding site on receiving horn antenna oscillogramm (ch1) takes the form of dumping exponent.

Investigations of plasmoid radiation in optical and near IR bands shows that visible EPO boundaries corresponds to optical band 400…700 nm.

Most close correspondence between integral photos (digital camera Sony DSC-N1, CCD resolution – 400…1100 nm) and visually observed EPO boundaries is reached when neutral light filter NS-13 is used (fig.6a). Specified light filter provides attenuation of light radiation up for 100 times in near IR band (700…1400 nm). "Coat" area radiation corresponds preferably to near infrared

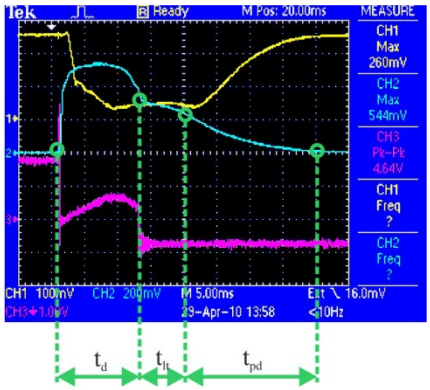

Fig.5. *Signal oscillogramms on receiving antenna (Ch1), of EPO optical radiation (Ch2) and discharge voltage (Ch3).*

a) b)

a) light filter NS-13 (intensity attenuation up to 100 in 700...1400 nm band)
b) light filter NS-2 (intensity attenuation up to 2 in 700...1400 nm band)

Fig.6. *Integral EPO photos in optical (a) and near IR (b) bands.*

band (at least 700…1100 nm). It is registered, in particular, when light filter NS-2 is used. Specified light filter attenuates light radiation in near IR band for 2 times (fig.6b).

EPO radial structure influence on signal transmitting

The formation of “coat" leading to radio signals dispersion, is observed also at enough low values of the erosive discharge energy. In particular, significant attenuation of transmitting signal (~4 GHZ) observed during plasmoid investigations as a pole transmitting antenna. Erosive type discharger model used in experiments (fig.7). Pulse discharge energy was about 40 J. Model’s design provided MW pulse transmitting (Π-like pulse duration 1…12 ms) to EPO by mean of directional coupler. Principal stand schematic is analogical to that presented on fig.1b.

Model’s design features provides MW transmitting without EPO or metal rod (because of radiation rereflection from construction elements). Given circumstance has allowed showing visually transmitted signal attenuation during plasmoid lifetime. In general, signal amplitude changes nonmonotonically during EPO lifetime (fig.8).

But unlike the case on figs.3b-3d, where periodical amplitude modulation of signal, caused by EPO length “tuning” for transmitting signal frequency is viewed, similar character of signal amplitude change in an explicit form is not observed for this case. It is remarkable, that signal abruptly attenuates more than for 20 dB after discharge ignition (fig.8). Next, after small surge the power of transmitting signal remains

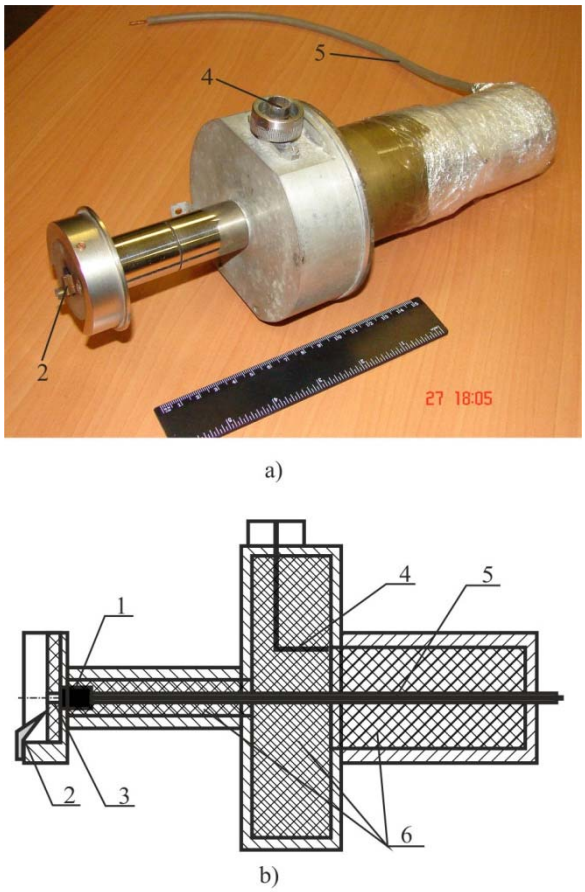

1 - cathode
2 - anode
3 - discharge capillary (d=1 mm, h=3...4 mm)
4 - directional coupler
5 - RF cable
6 - insulator

Fig.7*. General view (a) and design scheme (b) of plasma antenna model.*

approximately constant (on ~10 dB level) during enough long time interval and gradually diminishes to zero values in a moment of discharge break. Signal level restoration occurs exponentially and correlates with plasmoid dissipation stage. For given design and discharge parameters plasmoid lifetime practically coincides with discharge duration.[1]

Most probable reason of signal attenuation is “coat” dispersion (or absorption), electron density in which area can arise during discharge stage (as follows from MW signal oscillogramm). Taking into account transmitted signal frequency, electron density in “coat” area is about $2 \cdot 10^{11}$ cm^{-3}.

[1] Unlike a case presented on fig. 5 where the site of plasmoid autonomous lifetime after the discharge termination is expressed obviously.

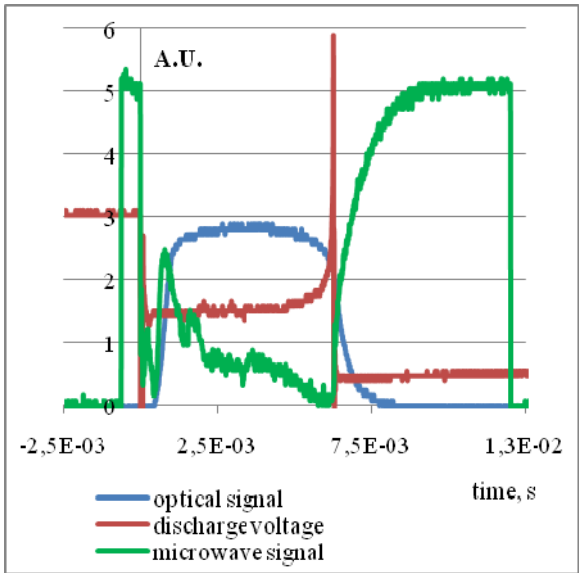

Fig.8. *Microwave signal on receiving antenna, EPO's optical radiation and discharge voltage oscillogramms.*

Conclusion

Spent experimental researches shows that formed by erosive type discharge plasmoids can be used for radio-waves transmitting, receiving, absorption, dispersion. Dimensions of "coat" area, where absorption and dispersion takes place, essentially exceeds visible plasmoid boundaries, and electron density in "coat" area can reach $10^{11}…10^{13}$ cm^{-3}. Specified feature permits EPO application for radio-waves effective absorption (or dispersion) up to millimeter band. Further experimental researches are necessary for concrete mechanisms revealing of electromagnetic waves interaction with plasmoid and its areas.

Acceptance of special measures for "coat" influence elimination is necessary in the cases of plasmoid using in a pole antenna mode. It is quite probable, that in a mode of dielectric rod the "coat" can act as a wave guide, and change of its parameters will allow changing of directional diagram. Besides, for EPO practical application as receiving-transmitting antenna it is necessary to research the possibility of EPO stable existence in super- and hypersonic gas flow. Systematic researches on the specified questions did not spend.

References

1. *I.R.Gecker.* Interaction of the strong electromagnetic fields with plasma . M. Atomizdat, 1978 (in Russian).
2. *V.I.Kolpakov, L.V.Norinsky, V.S.Rogov.* Effect of a dynamic channeling of electromagnetic radiation by extended plasma formations // JTP Letters, v.17, N 10, 1991 (in Russian).
3. *V.A.Grishin, V.I.Nikolayeva, A.S.Pashchina.* Plasma antenna/ Third International Aerospace Congress «IAC-2000». Theses. Moscow, 23-27 august 2000. M.: SIP RIA, 2000.
4. *A.V.Gurevich.* Ionized layer in a gas (atmosphere)// UFN, 1980, v.132, N.4, c.685-690 (in Russian).
5. *J.Hettinger.* Aerial Conductor for Wireless Signaling and Other Purposes. US Patent number 1,309,031, July 8, 1919.
6. Extended electrical discharged guided by laser. Scientific report. Theme "Tenon II MRP-B". M.: SRIRDI. 1992, 111 p. (in Russian).
7. *D.C.Jenn.* Plasma Antennas: Survey of Techniques and the Current State of the Art. *Technical Report*. Naval Postgraduate School, Monterey, CA 93943-5000 (2003-09-29).
8. *D.Tidman.* "Establishing Highly Conductive Path in Gas by Thermal Guidance of Discharge," US Patent number 3,775,638, November 27, 1973.
9. *L.M.Vallese, A.Shostak.* "Laser Beam Antenna," US Patent number 3,404,403, October 1, 1968
10. *J.R.Vaill.* "Laser Beam Techniques," US Patent number 3,719,829, March 6, 1973.
11. *T.Anderson.* "Plasma Antenna With Currents Generated by Opposed Photon Beams," US Patent number 6,169,520, January 2, 2001.
12. *V.A.Grishin, V.I.Nikolayeva, A.S.Pashchina.* Plasma receiving-transmitting antenna. Russia Patent №2255394, 02.06.2003 (in Russian).
13. *David Hambling.* Wireless at the speed of plasma. New Scientist (2010-12-13).
14. *R.E.Harper.* Solid state plasma amtenna. US Patent number 7,109,124 B2, September 19, 2006.
15. *R.F.Avramenko, B.I.Bahtin, V.I.Nikolayeva etc.* Investigations of the plasma formations initiated by the erosive type discharge // JTP, 1990, v.60, N 12, p.73 (in Russian).

8.6. THERMAL CALCULATION OF MAGNETOPLASMA ENGINE BASED ON FUSION POWER

Romadanov I.V., Ryzhkov S.V.
IPMech RAS, Russia

In this paper we consider a compact toroid [1] as a fusion reactor [2], namely field-reversed configuration where the plasma magnetized by a purely poloidal field. This magnetic configuration has attractive features, notably a linear geometry and high-β (beta is the ratio of plasma pressure to external magnetic field pressure). Fusion system based on a compact configuration where the plasma confined inside closed magnetic field lines and separated from a conducting wall by the area of the open magnetic flux allows to achieve high specific impulse and thrust.

The power losses due to charged particle transport, neutrons, and radiation are taken into account. The global plasma power balance is given by:

$$P_{fus} + P_{inj} = P_{brem} + P_{tran} + P_{syn},$$

where P_{fus} is the fusion power, P_{inj} is the injection power, P_{tran} is the charged particle transport power, P_{brem} is the bremsstrahlung power, and P_{syn} is the synchrotron radiation power.

Main plasma parameters and fusion energy gain factor are obtained. The comparison of D-T reactor with D-^{3}He source is made. Prospects of D-^{3}He fueled fusion jet are presented.

References

1. R.Kh. Kurtmullaev, A.I. Malyutin, V.N. Semenov, “Compact torus,” Itogi nauki i tekhniki. Fizika plazmy (Plasma physics in Russian) **7**, 80 (1985).
2. V.I. Khvesyuk, S.V. Ryzhkov, J.F. Santarius, G.A. Emmert, L.C. Steinhauer, “D-^{3}He Field Reversed Configuration Fusion Power,” Fusion Technology **39**, 410 (2001).

9.1. EXPERIMENTAL ACTIVITIES ON THE MHD INTERACTION IN A HYPERSONIC ARGON AND NITROGEN FLOWS

Andrea Cristofolini, Gabriele Neretti, Carlo Angelo Borghi
Department of Electrical Engineering, University of Bologna, Viale Risorgimento 2, 40135, Bologna, Italy
andrea.cristofolini@unibo.it
gabriele.neretti@unibo.it
ca.borghi@unibo.it

Abstract. This paper reports the experimental activities on MHD flow control carried out in Italy in the framework of few research projects. Experiments has been carried out in argon and nitrogen hypersonic flows. In the experiments reported, sharp and blunt bodies has been investigated at Mach 6 and Mach 15. Some detail of the experiments performed in CIRA Ghibli hypersonic facility are given. In Ghibli, the MHD interaction around a blunt body in a nitrogen flow has been investigated. The criteria utilized to define the proper test conditions and to design and realize the model are here described. Moreover, an MFD code has been used in order to calculate the expected interaction effect, under the assumption of low Re_m. The same procedure has been utilized for the design of an MHD test to be performed in the CIRA Scirocco facility.

I Introduction

In the last years, the growing interest in among the aerospace and scientific community toward the applications of MHD applications in aerospace field produced several theoretical and experimental studies [1-10]. A number of research has been carried out to develop physical models and numerical codes for the analyses of the MHD interaction in hypersonic flows. The inherent complexity of the physical phenomena involved in the applications of interest make the validation of the models a crucial prerequisite. However, due to the difficulties of reproducing the MHD interaction around a hypersonic vehicle in laboratory test facilities, experimental activities are few and often yield results that cannot be utilized to validate the numerical codes. The necessity to overcome these difficulties has given an important drive toward experimental research. Various research programs have been aimed to the measurements of the MHD interaction in a noble gas [11-14]. A noble gas offers a number of advantages for experimental activities, mostly related to the need to have a degree of ionization sufficient to sustain the MHD interaction. A noble gas has no excitable rotational and vibrational degrees of freedom. As a result, the ionization process in a noble gas is more efficient than in a molecular gas. Moreover, recombination processes in noble gases are usually slower than in other molecular gases of interest (i.e. air or nitrogen), so that one may expect to produce a ionized gas, to let it expand along a nozzle to a hypersonic regime and still maintain a sufficient ionization for MHD experiments. In addition, noble gases have also some appealing aspects for the modeling point of view. Kinetics in a noble gas is far less complex than in a molecular one, and a model has to deal with a relatively small number of species (electrons, positive ions and metastable) and of processes (molecular dissociation and recombination are absent). Thus, a noble gas appears to be a viable option for MHD experiments aimed to validate numerical models, and can be implemented in relatively small and flexible experimental facilities. A notable drawback in utilizing a noble gas in MHD experiments is related to the fact that the working fluid is ionized before it reaches the test section. This constitutes a fundamental difference with respect to real applications, e. g. a vehicle re-entry in a planetary atmosphere, where the ionization is generated by the shock. In the experiments with an ionized free stream flow, MHD interaction occurs well before the shock. This phenomenon spoils the concept of "free stream". In addition, Hall currents can, and usually will, develop closing paths within the incoming electrically conductive flow and in the surrounding fringes, eventually reaching the facility walls. The effects of Hall currents are usually difficult to be taken into account, and add some uncertainty to the results obtained in the experiments.

On the other hand, experiments utilizing a molecular gas as working fluid, being much closer to the intended application, can add a deeper insight on the physical phenomena playing a relevant role [15,16]. In relatively cold MHD experiments, an adequate degree of ionization has been reached exploiting some sort of ionization process. Alkaline metals seeding and electron beams are techniques which have been proposed in this field. Recently, some research groups proposed non-equilibrium plasmas generated by nano-pulse discharges to sustain ionization for MHD purposes [17,18]. However, if a facility capable of delivering a sufficient amount of specific enthalpy to the flow is available, ionization can be obtained almost entirely by the shock.

In the present paper, the design of an experimental campaign on MHD interaction around blunt bodies in hypersonic air flows will be reported. The hypersonic flow is realized in the Gibli arc-heated wind tunnel of CIRA (Capua-Italy) at Mach 11. The magnetic field in the shock layer is between 0.5 and 0.6 T. The aim of the experiments at first to investigate the effects of the

MHD interaction on an un-seeded air-flow. A further aim is to produce a data-base to be used for the validation of numerical codes which are utilized to analyze the magneto-fluid dynamics in hypersonic flows.

II. Test Body Design

The blunt body described in this paper has been designed and manufactured in the framework of the CAST research Project, sponsored by the Italian Space Agency (ASI) and has been denominated TC4. The TC4 test body has been designed for experiments in argon and in air.

The magnetic field needed for the MHD interaction around the blunt test body is produced by a single permanent magnet. The height, the minor and the major radius of the truncated cone are 96 mm, 45 mm and 60 mm respectively. The distribution of the magnetic flux density produced by the magnet has been calculated utilizing a FEM code and is shown in Fig. 1. In Fig. 2, a plot of the magnetic flux density magnitude before the small base of the truncated cone is reported. The two curves represent the B field along the radius at different distances from the small base.

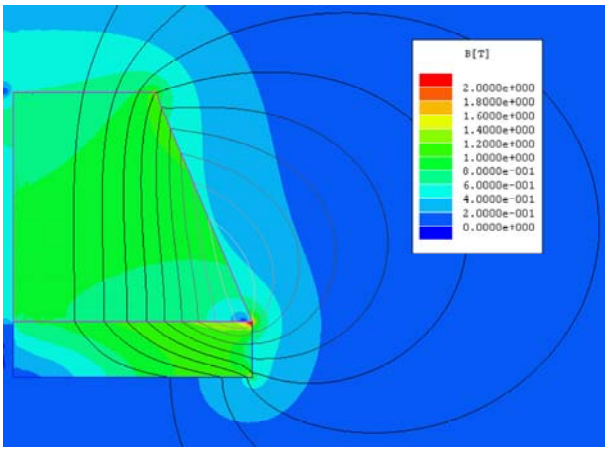

Fig. 1. *Magnetic flux density around the blunt model*

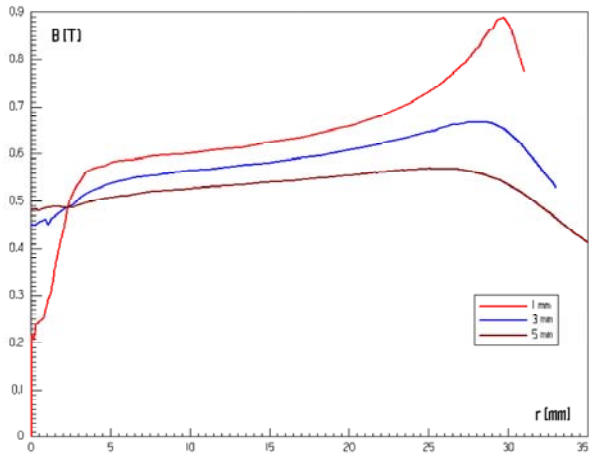

Fig. 2. *Magnetic flux density magnitude at various distances from the small base of the model*

The magnet has to be protected from the incoming flow and electrically insulated. In Fig. 3, a nylon 6/6 shell is shown. The nylon shell has been utilized to cover the magnet in an experimental campaign carried out in an ionized argon flow. The model has been equipped with a Kulite® XCS-062-5PSIA pressure sensors, located in the expansion region, in correspondence of the big base of the model. A pic of the assembled test body is shown in fig. 3. The electrostatic probes can be seen on the flat head of the test body. A set of electrostatic probes has been placed on the small base of the test body. A first probe is on the axis of the model (position "1" in Fig. 3), while other two probes are placed in along the radius of the small base (positions "2" and "3"). It should be noted that, to evaluate the effect of non uniformity in the flow, there are two "3" probes, in a diametrically opposed position.

Fig. 3. *Assembled blunt test body*

III. Experimental Activities in Argon

The blunt body described in the previous paragraph has been utilized in an experimental campaign carried out in the Alta High-Enthalpy Arc-heated Tunnel (HEAT) facility in Pisa. The test gas used in this experiment is argon. HEAT is a pulsed hypersonic wind tunnel operative since 1996 [19, 20].

It can produce Mach 6 flows in a low to medium Reynolds number range (104-106). In the wind tunnel settling chamber the gas is heated by means of an arc discharge powered by a 260 kW DC power supply and delivering arc currents up to 630 A during running times of 20-300 ms. In the settling chamber a total specific enthalpy up to 6 MJ/kg with stagnation pressures up to 9 bar can be obtained. The gas heater can be operated with air, nitrogen, argon, CO2 in a pulsed, quasi-steady mode. At the exit of the settling chamber a nozzle is mounted. The effective test section at the exit of the nozzle has a diameter of 55 mm. The arc heater scheme is shown in Fig. 4. The wind tunnel (gas heater and nozzle) is installed on a vacuum test section of 600 mm diameter. In the test section there are optical accesses from all sides. This section is connected to a vacuum chamber of a volume of 4.1 m3. The chamber is evacuated by four rotary pumps to reach an ultimate pressure of 10 Pa before each run. The flow characteristics are obtained by means of pitot probes provided with fast miniaturized piezo-resistive pressure transducers and stagnation temperature probes provided with fast coaxial thermocouples or thin-film gauges. In the settling chamber the pressure is measured by fast pressure transducers. Accuracies of about 3% are obtained in all pressure measurements. The total enthalpy is evaluated from the arc discharge power and compared with the values obtained from the stagnation temperature measured in the test section. The total enthalpy error is ±5-10%.

The ionized argon produced in the discharge section is accelerated in the contoured instrumented nozzle (Fig. 5) designed and manufactured for the CAST program TC 2, presented in [21], to produce a Mach 9 flow in air with ptot = 3 bar and htot = 4.5 MJ/kg. The nozzle was therefore characterized using low pressure argon, expecting a higher Mach number, lower test time and possibly a worse flow quality w.r.t. air due to the contour being not optimal for this application. The radial profile of the Mach number in the jet produced by the nozzle is shown in Fig. 6

Properties such as electron temperature and electron density are required for the evaluation of the electric transport properties of the plasma (i.e. electron mobility and electrical conductivity), which are essential data for the numerical rebuilding of the experiment and for the interpretation of the experimental results. Thus, a crucial point is the evaluation of the plasma parameter in the free stream flux at the nozzle exit. In order to do this, optical diagnostics and microwave measurements have been utilized. In order to perform the aerothermodynamic characterization of the produced flow, the following set of instruments was used:

- two absolute Kulite XCS-062 sensors in the tunnel settling chamber (one with a 250 psi FSO and one 100 psi),
- a supersonic pitot probe equipped with a Kulite XCS-062-5A miniaturized pressure sensor for high frequency Mach number retrieval
- a hemispheric stagnation point temperature probe equipped with a MEDTHERM coaxial thermocouple for the stagnation enthalpy and total enthalpy retrieval through the Sutton&Graves relations [22]. A complete mapping of the nozzle flow was performed both for different pressure

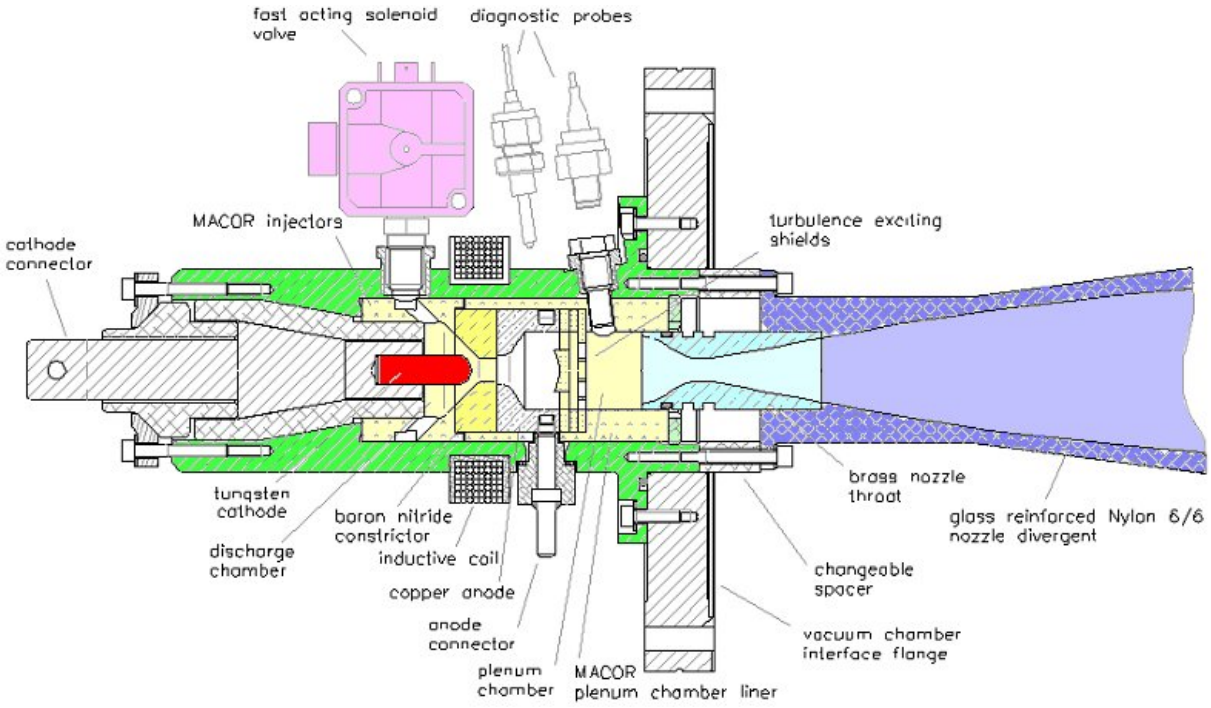

Fig. 4. *Arc heater scheme.*

conditions.

Fig. 5. *Mach 15 nozzle*

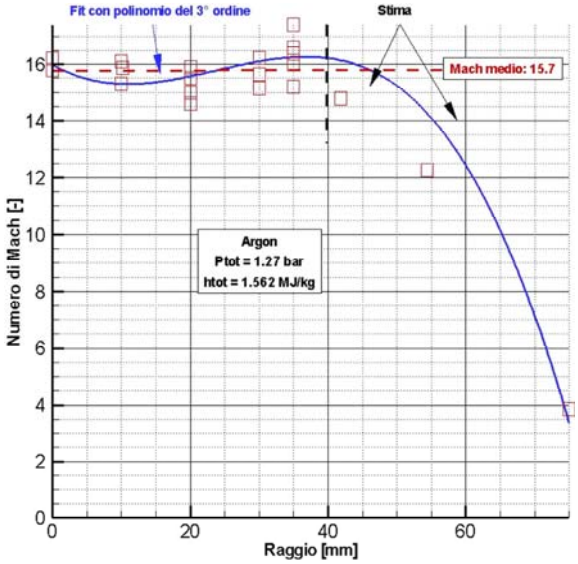

Fig. 6. *Radial profile of the flow Mach number: mean profile and experimental data.*

The core flow dimensions, actual axial symmetry degree of the flow, fluctuations both for what concerns Mach and temperature, repeatability of the test conditions has been evaluated. The results of the activity can be summarized as follows:

- core flow Mach number: 15.7 ± 0.4
- core flow diameter > 70 mm
- maximum test time @ centreline > 80 ms
- maximum test time @ core edge ~ 40 ms
- significant non symmetry in the Y = 0 plane (presumably due to the nozzle manufacture).

In Tables 1 and 2 the flow properties and the pressure measurements are reported for the blunt body. In this case, a slight increase of pressure can be observed for the MHD model, giving a 13 % variation with respect to the non magnetic test body.

The effects of the MHD interaction around the blunt test body in Mach 15 argon flow are shown in Fig. 7 and Fig. 8. As observed in other similar experiments, the shock appears to be considerably brighter when a magnetic field is applied.

The Hall field appearance has been observed on the blunt test body. In Fig. 9, the voltage arising due to the MHD interaction on the flat base of the model exposed to the plasma flow is shown. In this case the reference probe is the one located on the axis, and the quantities V12, V13 are the voltage between the reference probe and the others as numbered in Fig. 3. In this case, again, the voltage increases in the downstream probes (i.e. from the stagnation point to the edge of the model base). A 250 V/m average Hall electric field can be evaluated. However, the Hall electric field values are observed far from the stagnation point (between electrodes 2 and 3) and assumes a value of about 400 V/m

Table 1. *Flow properties for the blunt body at mach 15.*

	P_tot [mbar]	H_tot [MJ/kg]	Mach [-]	p_inf [Pa]	T_inf [K]
Non magnetic Model	826	1.6	15.3	1.487	38.96
Magnetic Model	820	1.6	15.3	1.477	38.96

Table 2. *Pressure measurements for the large cone at mach 15.*

	P tip [Pa]	P back [Pa]	Cp_tip [-]	Cp_back [-]	Std P_tot [Pa]	Std p_tip [Pa]
Non magnetic	23.3	28.2	0.075	0.092	3634.6	6.77
Magnetic	26.8	28.7	0.088	0.094	3572	51.2

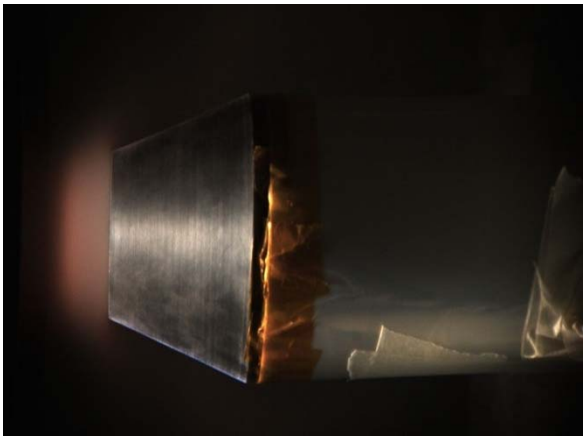

Fig. 7. *Mach 15 argon flow around the non magnetic conical test body*

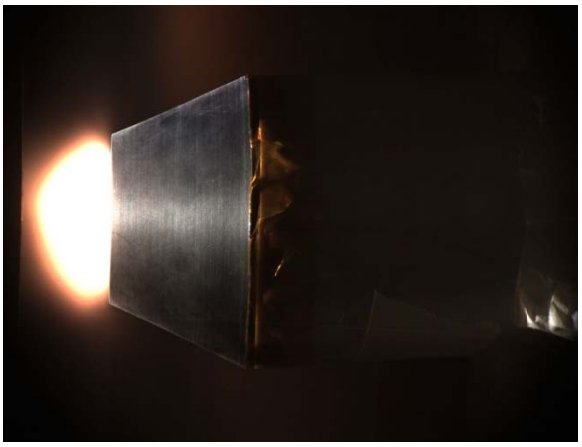

Fig. 8. *Mach 15 argon flow around the magnetic conical test body.*

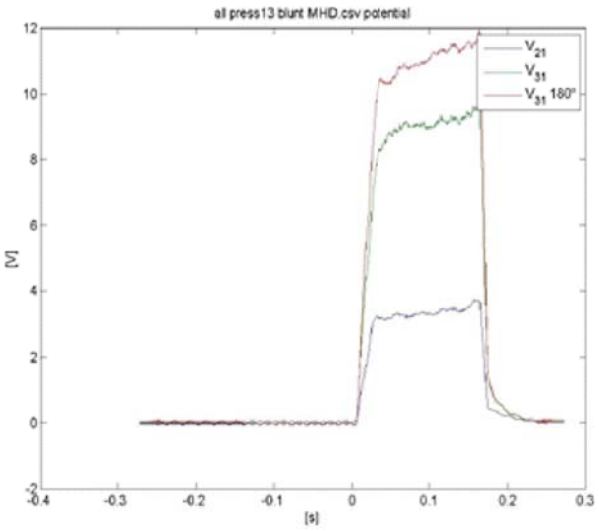

Fig. 9. *Hall voltages along the flat blunt surface exposed to the flow at Mach 15*

IV. Microwave Diagnostics.

The electron number density and the collision frequency of the plasma in the free stream at the exit region of the nozzle have been determined by the microwave absorption technique. In order to do this, the measurements have been carried out before the test body placing.

The microwave diagnostic set up consisted of a microwave generator, two horn antennas and a crystal detector. A Gigatronics 1018-009 microwave generator, able to produce a non-modulated microwave signal from 50 MHz up to 18.5 GHz with a power exit of 10 dBm, has been used. Two 15 dB horn antennas designed for an optimal working frequency between 12 and 18 GHz have been placed inside the vacuum vessel, at opposite sides of the plasma flow, at about 50 mm from the nozzle exit. A scheme of the experimental set up is shown in Fig. 10.

In this configuration the microwave beam crossed about 80mm with the Mach 15 one**.** An HP 8472A crystal detector with a bandwidth of 10 MHz - 18.5G Hz, was connected to the receiving horn. In order to enhance the signal to noise ratio, at each condition considered seven different signals have been detected and the transmission factor was determined from their average.

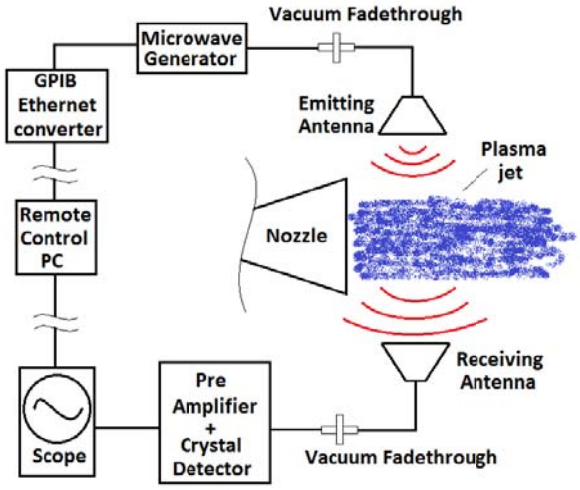

Fig. 10. *Schematic of the microwave diagnostic set up*

The transmission factor of an electromagnetic wave through the plasma is a function of the frequency of the microwave, the plasma dimension, the electron number density n_e and the collision frequency between electrons and heavy particles ν_{eH}. The transmission factor T_f is given by:

$$T_f = \frac{P_1}{P_2} = \exp\left(-2\chi\frac{\omega}{c}\Delta x\right) \qquad (1)$$

where P_1 and P_2 are the signals' power detected with and without the plasma flow respectively, χ is the attenuation constant, Δx is the length of the plasma crossed by the microwave beam, ω is the radian frequency of the microwave and c is the speed of light. The attenuation constant is given in [23] as

$$\chi = \left\{ -\frac{1}{2}\left(1 - \frac{\omega_p^2}{\omega^2 + \nu_{eH}^2}\right) + \frac{1}{2}\left[\left(1 - \frac{\omega_p^2}{\omega^2 - \nu_{eH}^2}\right)^2 + \left(\frac{\omega_p^2}{\omega^2 + \nu_{eH}^2}\cdot\frac{\nu_{eH}}{\omega}\right)^2\right]^{-1/2}\right\}^{1/2} \qquad (2)$$

where ω_p is the plasma frequency.

The cut-off frequency $f_{cut\text{-}off}$ is the microwave frequency below which the transmission factor is zero and above which it is different from zero. The cut-off frequency corresponds to the plasma frequency. The

electron number density is determined by the cut-off frequency as:

$$n_e = 4\pi^2 \frac{\varepsilon_0 m_e}{e^2} f_{cut-off}^2 = 1.241 \cdot 10^{-2} f_{cut-off}^2 \quad m^{-3} \quad (3)$$

When n_e is known, T_e can be used to determine the electron-heavy particle collision frequency through (1) and (2).

In the experiment described here, to obtain the cut-off frequency and the electron density, tests at several values of the microwave frequency were done and the behavior of T_f was determined.

The plasma jet produced by the Gibli facility has been investigated utilizing a microwave beam at different frequencies. The sequence of the utilized frequencies is shown in Table 3. In Fig. 11, is shown the recorded signals when the plasma is not flowing between the horn antennas. The signal can be compared with the signals recorded during an experiment, shown in Fig. 12 .

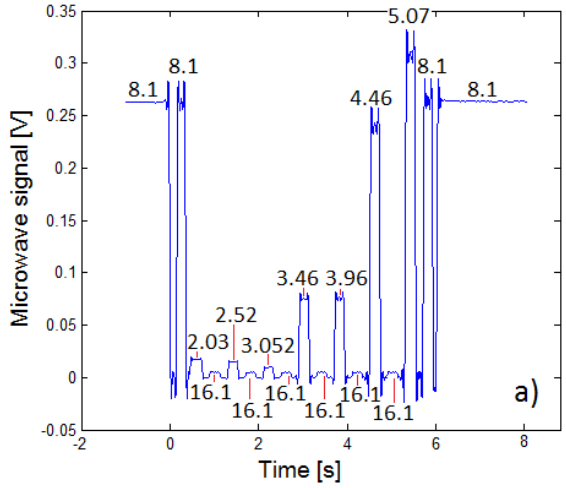

Fig. 11. *Signal from crystal detector when no plasma is flowing*

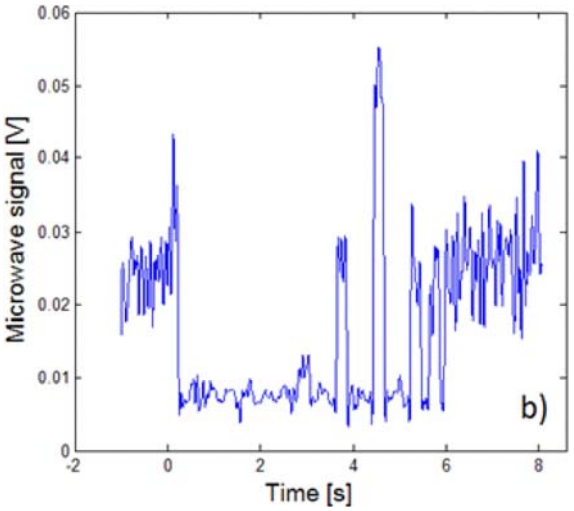

Fig. 12. *Signal from crystal detector when the plasma is flowing*

Table 3: *Frequency sequence utilized in the experiments in the Gibli facility*

	f [GHz]
f1	8.1
f2	2.03
f3	16.1
f4	2.52
f5	16.1
f6	3.052
f7	16.1
f8	3.46
f9	16.1
f10	3.96
f11	16.1
f12	4.46
f13	16.1
f14	5.07
f15	8.1

The value of the electron density calculated from the microwave measurements ranges between 10^{17} and 3 10^{17} m^{-3}, depending on the test conditions.

V. MHD Computations

Numerical calculations have been performed to evaluate the expected effects of MHD interaction on the TC4 test body and for studying the MHD interaction around a blunt body in a Mach 11 air flow. The latter calculation has been performed as a preliminary investigation in the frame of the research project "Advanced Flow Control in a Hypersonic Plasma Flow" (MHD AFC), funded by ESA. A 0.2 m radius cylinder coaxial with the free flow constitutes the blunt body. An electromagnet, accommodated in the blunt body, provides the magnetic flux density needed for the MHD interaction. The externally imposed magnetic field has been calculated by means of a FEM code and is shown in Fig. 13..

As ionization degree does not appear to vary significantly, a simplified approach has been adopted to evaluate mobility and conductivity. Electrical conductivity has been assumed to be constant within the calculation domain, while mobility is assumed to vary as a function of the inverse of the plasma density. Electron collision rate has been evaluated under the assumption of instantaneous electrons relaxation from[24]. A 100 T^{-1} free stream mobility has been taken. A 20 S m^{-1} value has been assumed for the electrical conductivity in the shock layer, while in 4 S m^{-1} is taken for the free stream flow. The working gas is treated as an ideal gas.

The MHD regime has been evaluated by means of a low Re_m 2D model[25]. A cell-centered finite volume formulation has been adopted for the spatial discretization of the fluid dynamics. Fluxes are evaluated by means of an Osher approximate Riemann solver. Time integration is performed utilizing an explicit scheme, based on a fourth-order Runge-Kutta method. Electrodynamics has been solved by means of

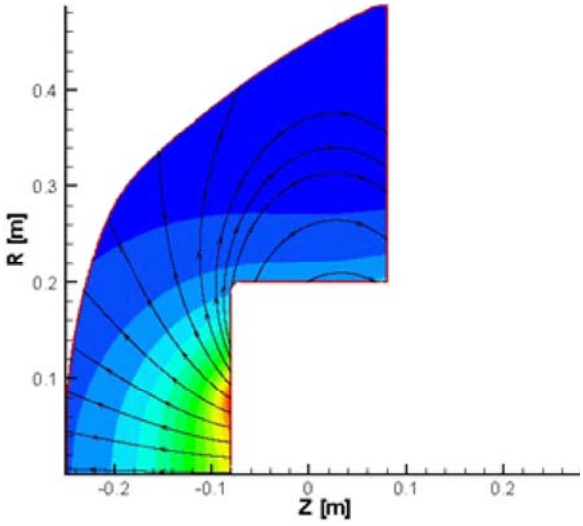

Fig. 13. *Induction field distribution around the bunt body (maximum field = 0,8 T)*

a finite element approach. The coupling between the fluid and the electrodynamics is accomplished quite straightforwardly. As the time dependent behavior of the model is governed by the fluid dynamics, at the generic nth time step, the fluid dynamic solver evaluates the source terms in the continuity equation for momentum and energy utilizing the values of E and J calculated at the previous time step. The steady state electrodynamic model then utilizes the value of **u** at the n^{th} step to compute **E** and **J**. These quantities will be utilized as input for the (n+1)th time step of the fluid dynamic solver.

In Figs. 14 and 15, the Mach number distribution around the blunt body without and with MHD interaction are reported. Calculation results show an increase of the standoff distance of about 1 cm.

The temperature in the calculation domain is shown in Fig. 16, along with the momentum streamlines. A recirculation pattern can be recognized near the stagnation point. The recirculation is responsible of a significant modification of the whole flow in the shock layer region.

An explanation to this phenomenon can be given observing the electrodynamics in the shock layer: in Fig. 17, the distribution of the electric potential on the calculation domain is shown. The potential distribution produce an electric field, namely a Hall field, roughly opposed to the direction of the flow. The azimuthal component of the current density (Fig. 18), as observed earlier, is largely dominated by the Hall field, rather than by the local value of the **u×B** term. Moreover, the azimuthal current density is higher where the Hall parameter is lower, that is just behind the shock (region 1 in Fig. 18, β_e is small because **B** is small) and near the flat head of the blunt body (region 2 in Fig. 18, β_e is small because of the compression near the body wall, which reduces the electrons mean free path and the mobility). As a result, in region 2 the maximum values of the body force **J×B** can be expected, as the maximum values of **J** and **B** (see field lines reported in Fig. 18) are found there.

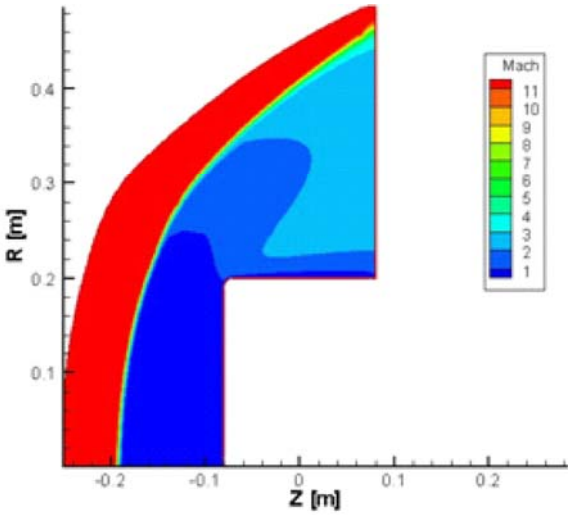

Fig. 14. *Mach number distribution without MHD interaction*

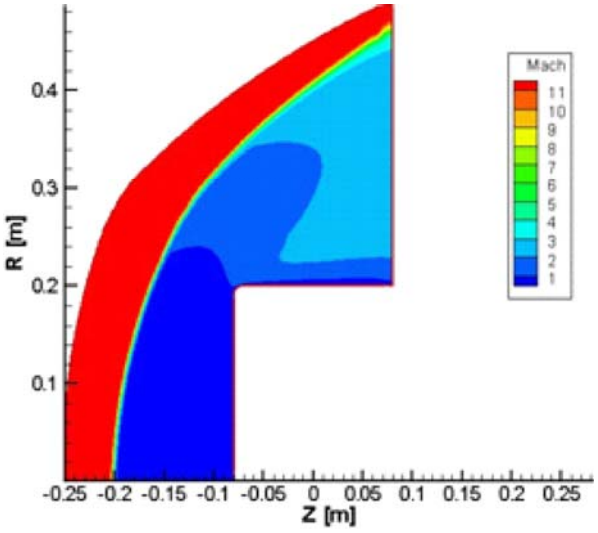

Fig. 15*. Mach number distribution with MHD interaction*

On the other hand, the kinetic energy of the gas is relatively low in region 2, due to a low flow velocity. Thus, the flow pattern in this region effectively reacts to the action of the MHD body force, forming the recirculation seen in Fig. 16.

A plot of the variation of the pressures calculated on the head of test body is reported in Fig. 19. A The computed pressure slightly rises near the stagnation point, and then decreases. A 10% decrease in pressure can be expected on the outer region of the test body head.

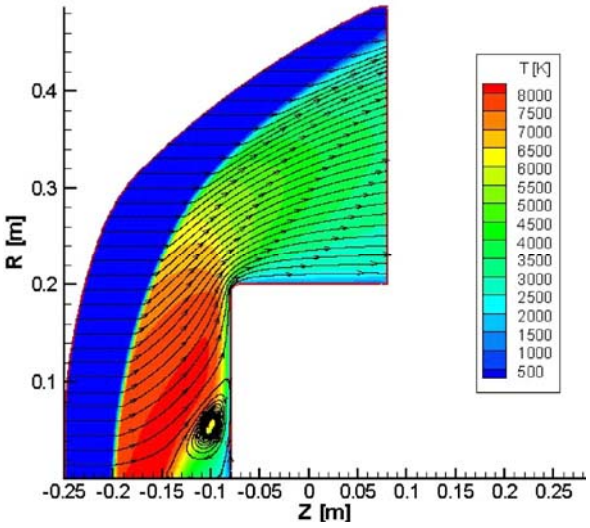

Fig. 16. *Temperature distribution and streamlines with MHD interaction*

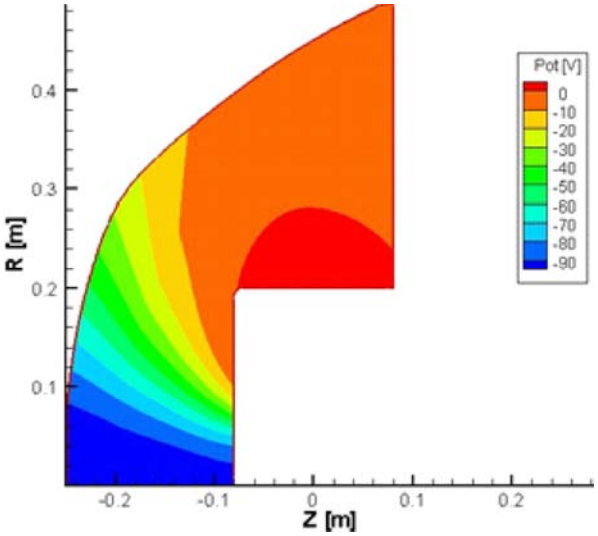

Fig. 17*. Electric potential distribution*

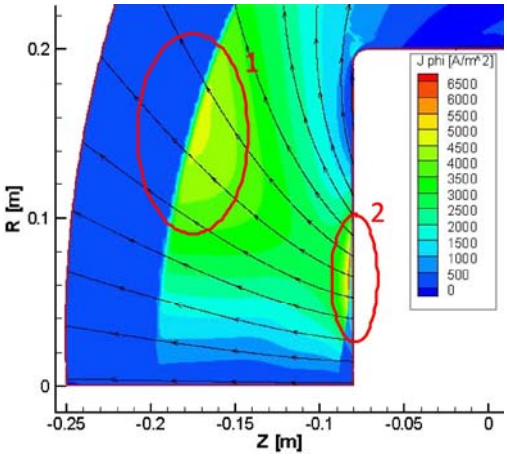

Fig. 18. *Azimuthal current density and B field lines*

In Fig. 20, the variation of the temperature gradient normal to the wall of the test body head is reported. A distinct decrease of the temperature gradient can be observed in the region interested by the recirculation discussed earlier. Outside this region, a slight increase of the gradient can be noted.

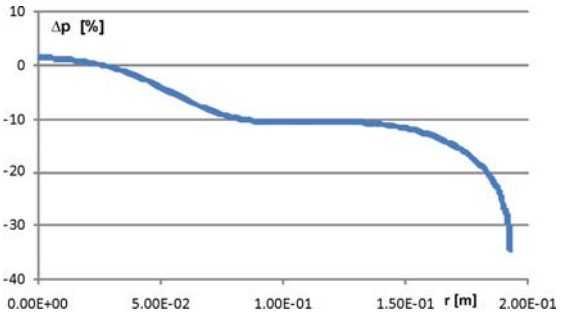

Fig. 19. *Pressure variation on the test body head.*

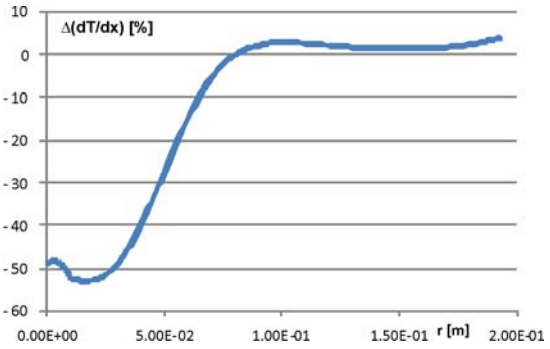

Fig. 30. *Temperature gradient variation on the test body head.*

VI. Conclusion

The MHD interaction in a hypersonic flow was experimentally investigated around a blunt body at the exit of an hypersonic nozzle delivering an argon flow at Mach 15. The electrical-connection scheme allowed short-circuiting of the Faraday current inside the plasma, enhancing the effect of the MHD interaction. Pressure, imaging, and electrical observations were done. A pressure variation has been registered due to the MHD interaction, and the appearance of the Hall field has been observed.

Microwave diagnostic has been utilized to characterize the plasma properties in a nitrogen operated wind tunnel. In an nitrogen flow at Mach 15 the value of the electron density derived from the microwave measurements ranges between 10^{17} and $3\ 10^{17}\ m^{-3}$.

Acknowledgments

The work described in this paper was carried out thank to the support of the Italian Space Agency (ASI), within the "Advanced Aerothermodynamic Configurations for Space Transport" (CAST) and of the European Space Agency (ESA) under the AFC-MHD research project.

References

1. Ziemer, R.W., "Experimental Investigation in Magneto Aerodynamics", *American Rocket Society Journal*, Vol. 29, No. 9, 1959, pag. 642.
2. V.A. Bityurin, et al., "Assessment of Hypersonic MHD Concepts", *28th Plasmadynamics and Lasers Conference*, Paper AIAA-97-2393, 1997.
3. J.T. Lineberry, et al., "Prospects for MHD Flow Control for Hypersonics", *31st Plasmadynamics and Lasers Conference*, Paper AIAA-2000-3057, 2000.
4. S.O. Macheret, et al., "MHD Power Extraction from Cold Hypersonic AirFlow with External Ionization", *30th Plasmadynamics and Lasers Conference*, Paper AIAA-99-4800, 1999.
5. D.J. Moorhouse and C.F. Suchomel, "Exergy Methods Applied to Hypersonic Vehicle Challenge", *32sd Plasmadynamics and Lasers Conference*, Paper AIAA-2001-3063, 2001.
6. J. S. Shang, S. T. Surzhikov, R. Kimmel, D. Gaitonde, J. Menart, and J. Hayes, "Mechanisms of plasma actuators for hypersonic flow control", *Progress in Aerospace Sciences*, Vol. 41, 2005, pp. 642, 668.
7. J.S. Shang, et al., "Magneto-Aerodynamic Interactions in Weakly Ionized Hypersonic Flow", *40th Aerospace Sciences Meeting & Exibit*, paper AIAA 2002-0349, Reno, NV, 2002.
8. J.S. Shang, "Recent Research in Magneto-Aerodynamics", *Progress in Aerospace Sciences*, Vol. 37, pp. 1-20, 2001.
9. E.P. Gurianov and P.T. Harsha, "AJAX: New Directions in Hypersonic Technology", *27th Plasmadynamics and Lasers Conference*, Paper AIAA-96-4609, 1996.
10. J.T. Lineberry, V.A. Bityurin et al., "Cylinder with current in Hypersonic flow", *3nd Workshop on Magneto-Plasma-Aerodynamics in Aerospace Applications*, Moscow, April 2001.
11. L. Biagioni, F. Paganucci, A. Passaro, G. Fantoni, A. Cristofolini, and M.R. Carraro, *Experimental Investigation on the Magneto-Hydrodynamic Interaction in the Shock Layer on a Hypersonic Body*, 43rd Aerospace Sciences Meeting and Exhibit Conference - Paper AIAA-2005-1181, Reno (Nevada), January 2005.
12. A. Cristofolini, C.A. Borghi, M. R. Carraro, G. Neretti, A. Passaro, G. Fantoni, and L. Biagioni, *Hypersonic MHD Interaction on a Conical Test Body with a Hall Electrical Configuration*, IEEE Transactions on Plasma Sciences, Vol. 36, n.2, pp. 530-541, 2008.
13. Matsuda, A., Wakatsuki, K., Takizawa, Y., Kawamura, M., Otsu, H., Konigorski, D., Sato, S., and Abe, T., *Shock Layer Enhancement by Electro-Magnetic Effect for Spherically Blunt Body*, 37th Plasmadynamics and Lasers Conference, AIAA Paper 2006-3573, San Francisco, June 2006.
14. A. Gülhan, B. Esser, U. Koch, et al., *Experimental Verification of Heat-Flux Mitigation by Electromagnetic Fields in Partially-Ionized-Argon Flows*, Journal of Spacecraft and Rockets Vol. 46, No. 2, March–April 2009.
15. V. Bityurin, A. Bocharov, J. T. Lineberry, *Studies on MHD Interaction in Hypervelocity Ionized Air Flow Over Aero-Surfaces*, 34th AIAA Plasmadynamic and Laser Conference, 23–26 June 2003, Orlando, Florida, paper AIAA 2003-4303.
16. V. Bityurin, A. Bocharov, D. Baranov, and J. Lineberry, *Experimental and Theoretical Study of MHD Interaction in Hypersonic Ionized Air Over a Wedge*, 4st AIAA Aerospace Science meeting and Exhibit 6- 9 Janaury 2004, Reno, Nevada, paper AIAA 2004-1195
17. Murray, R. C., Zaidi, S. H., Carraro, M. R., Vasilyak, L. M., Macheret, S. O., Shneider, M. N., and Miles, R. B., "Magnetohydrodynamic Power Generation Using Externally Ionized, Cold, Supersonic Air as Working Fluid," *AIAA Journal*, Vol. 44, No. 1, 2006, pp. 119–127. doi:10.2514/1.
18. Adamovich, I. V., Lempert W. R., Nishihara M., Rich J. W., and Utkin Y. G., "Repetitively Pulsed Nonequilibrium Plasmas for Magnetohydrodynamic Flow Control and Plasma-Assisted Combustion", *Journal of Propulsion and Power*, Vol. 24, No. 6, November–December 2008 DOI: 10.2514/1.24613
19. Scortecci, F., Paganucci, F., D'Agostino, L., Andrenucci, M., "A New Hypersonic High Enthalpy Wind Tunnel", *AIAA Paper 97-3017*, July 1997.
20. Scortecci, F., Paganucci, F., D'Agostino, "Experimental Investigation of Shock-Wave/Boundary-Layer Interactions Over an Artificially Heated Model in Hypersonic Flow", AIAA Paper 98-1571, April 1998.
21. Baccarella, D. , Passaro, A., Caredda, P., et al. "Characterization of a New Mach 9 Nozzle for the HEAT Hypersonic Wind Tunnel" *6th European Symposium on Aerothermodynamics for Space Vehicle*, Versailles, 2008.
22. Sutton, K. and Graves, R. A., "A general stagnation-point convective heating equation for arbitrary gas mixtures", NASA, Washington DC, NASA TR R-376, Nov. 1971.
23. M.A. Heald and C.B Wharton, "*Plasma diagnostic with microwaves*", John Wiley & Sons, 1965.
24. Baum, C. E., *"The calculation of Conduction Electron Parameters,"* Tech. rep., AFWL, 1965.
25. C.A. Borghi, M. Carraro and A. Cristofolini, "Analysis of MHD Interaction in the Boundary Layer of a Hypersonic Vehicle", *Journal of Spacecraft and Rockets*, 0022-4650, Vol.42 No.1, 2005, pp. 45-50

9.2. HEAT FLUX MITIGATION BY THE MAGNETIC FIELD IN MHD RE-ENTRY FLOW

V.A. Bityurin, A.N. Bocharov
Joint Institute of High Temperatures of Russian Academy of Sciences,125412, Moscow, Russia
e-mail: bocharov@ihed.ras.ru

Abstract. More than 50 years MHD flow control is the subject of intensive studies. As far as aerospace application is concerned, its potential could be utilized through, for instance, mitigation of heat loads on the spacecraft surface while re-entry path[1-7]. The feasibility of heat flux mitigation was shown in many studies to associate with increase of bow shock stand-off distance, and, consequently, decrease of the mean temperature gradient across the shock layer. This can be characterized as direct MHD effect due to electromagnetic forces acting in ionized gas behind a strong shock. Another feasibility of heat flux mitigation proposed recently also utilizes action of electromagnetic force, but the primary goal of the idea is to decelerate the vehicle before it comes into thermally dangerous atmosphere [1-3,7,8].
In the current paper some aspects of electromagnetic heat flux mitigation are considered on the example of Stardust re-entry capsule flight path. The influence of the dipole-like magnetic field is investigated for free-stream conditions corresponding to altitudes from 81 km to 55 km of entry path. MHD flow is numerically studied with 11 species air chemistry model. Effects of the induced magnetic field are taken into account.

Problem setup

The capsule geometry is shown in Fig.1. Radius of spherical part of the capsule is Rs=0.23 m, angle between heat shield and X-axis is 60O, angle between heat shield cone and rear-side cone is 90°, radius of spherical segment between two cones is 0.02 m, the height of rear-side wall is 0.38 m, middle cross section diameter was taken as D=0.84 м, angle-of-attack is 0°. The free-stream flow conditions and some characteristic values are given in Table 1. Data is taken from papers [9,10].
H is altitude; ρ is density; U is velocity; T is translational temperature; P is gas-kinetic pressure; Ma is Mach number; Re_D is Reynolds number based on the capsule diameter; $Kn_{Rs} = \lambda/R_s$ is Knudsen number based on the radius of spherical part of the capsule; λ is the free path length in the free-stream flow; $P^* = \rho U^2$; $Q^* = \rho U^3/2$;
$Rem_D = \mu_0 \sigma_* DU$ is magnetic Reynolds number; $Sm_{B=0.1} = \sigma_* B_*^2 D/(\rho U)$ is MHD interaction factor estimated for B^*=0.1Tl; B^* is characteristic magnetic induction value at critical point of the capsule.

We shall consider the case of so called short-circuit MHD generator, that is $E_z = -\partial\varphi/\partial z = 0$, where φ is electric potential, E_z is the mean z-component of electric field. Here and further z is the same as azimuthal angle θ, and y is the same as radial coordinate r. Assuming also that all flow variables do not depend upon z-coordinate (near electrode processes are neglected), we shall consider the two-dimensional flow, that is $= -\partial/\partial z \approx 0$ for any flow variables. The Faraday

Table 1. Free-stream flow conditions and important flow parameters.

H, km	51	55	60	65	71	81
ρ, kg/m^3·10^{-4}	7.21	4.29	2.34	1.06	0.557	0.127
U, m/s	7936	9719	11137	12004	12063	12385
T, K	253.6	248.5	238.5	229	221.6	217.6
P, Pa	52.13	30.4	15.9	6.92	3.545	0.794
Ma	24.9	30.8	36.1	39.7	40.3	41.8
Re_D·10^{-4}	27.7	20.5	13	6.5	3.6	0.8
Kn_{Rs}·10^2	0.1	0.17	0.32	0.7	1.3	5.8
P^*, kPa	45.4	40.5	29	15.3	8.1	1.95
Q^*,MWt/m^2	180	197	162	92	49	12
Rem_D	2.18	7.1	14	16.3	15.3	12.4
$Sm_{B=0.1}$	0.39	1.38	3.81	8.46	15	50.9

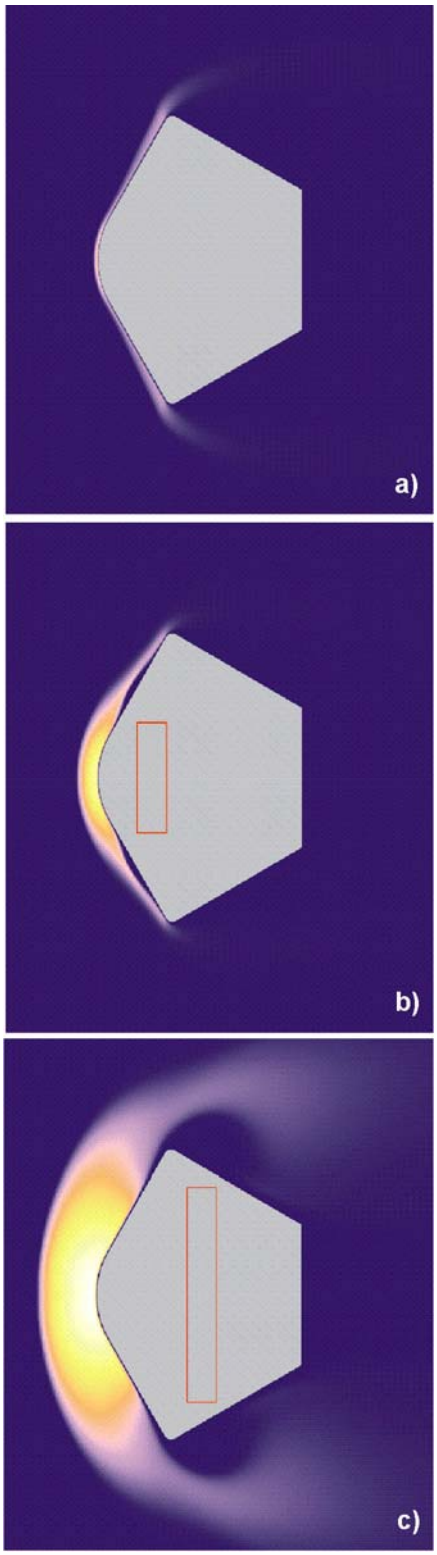

Fig.1. *Electron number density n_e/n_0 around the Stardust return capsule at altitude H = 65km.*
a) B = 0; b) B* = 0.2Tl, magnetic system MS1 (R_m=0.14m); c) B* = 0.2Tl, magnetic system MS2 (R_m=0.28m).*

electric current, j_z, and induced electric field, $E_z^*=[\mathbf{UB}]_z$ are only functions of (x,y). In two-dimensional problem, one can introduce the electric potential $\varphi(x,y)$, electric field $\mathbf{E}(x,y)=-\nabla\varphi$, and electric current density $\mathbf{j}(x,y,z)=(j_x,j_y,j_z)$.

Governing Equations

Under assumptions made above, the following set of two-dimensional equations is considered.

$$\frac{\partial\rho}{\partial t}+\nabla(\rho\mathbf{U})=0 \tag{1}$$

$$\frac{\partial\rho\mathbf{U}}{\partial t}+\nabla(\rho\mathbf{U}\cdot\mathbf{U})+\nabla\tau=-\partial P/\partial\mathbf{r}+\mathbf{j}\times\mathbf{B} \tag{2}$$

$$\frac{\partial\rho e^0}{\partial t}+\nabla(\rho e^0+P)\mathbf{U})+\nabla\mathbf{q}+\nabla(\mathbf{U}\tau)=\mathbf{jE} \tag{3}$$

$$\frac{\partial\rho_i}{\partial t}+\nabla(\rho_i\cdot\mathbf{U})+\nabla\Gamma_i=\omega_i \tag{4}$$

$$\nabla\mathbf{j}=0,$$
$$\mathbf{j}+\frac{\beta}{B}(\mathbf{j}\times\mathbf{B})=\sigma\left(\mathbf{E}+(\mathbf{U}\times\mathbf{B})+\nabla P_e/en_e\right),$$
$$\mathbf{E}=-\frac{\partial\varphi}{\partial\mathbf{r}} \tag{5}$$

$$\frac{\partial}{\partial\mathbf{r}}=\mathbf{e}_x\frac{\partial}{\partial x}+e_y\frac{\partial}{\partial y},\ \nabla=\frac{\partial}{\partial x}+\frac{1}{y^\xi}\frac{\partial}{\partial y}y^\xi,$$
$$\rho=\sum\rho_i \tag{6}$$

Here, $\mathbf{j}$ is the electric current density, $\mathbf{E}$ is the electric field strength, φ is the electric potential, σ is scalar electric conductivity, $\mathbf{B}$ is magnetic flux density, β is Hall parameter, ρ_i are the partial densities, ρ is the total fluid density. $\mathbf{U}=(U_xU_y)$ is the mass-averaged flow velocity, P is gas-kinetic pressure, e^0 is the total specific energy, $\mathbf{e}_x$, $\mathbf{e}_y$ are unit base vectors. ξ=0 for cartesian coordinate system and ξ=1 for cylindrical one, which is the case. The equations of state for the fluid are specified as follows.

$$e^0=e+\frac{U^2}{2},\ e=h-\frac{P}{\rho},\ h=\sum Y_ih_i,$$
$$h_i(T_i)=h_{i,f}+\int_{T_{ref}}^{T_i}C_{pi}(T)\,dT$$
$$P=\sum P_i,\ P_i=\rho_iR_iT_i,\ R_i=\frac{R^0}{W_i} \tag{7}$$

Here, e is specific internal energy, h is specific internal enthalpy, h_i is partial specific internal enthalpy, $Y_i = \rho_i/\rho$ is the mass fraction of i-th component, h_{if} is formation enthalpy of i-th component, $C_{pi}(T)$ is i-th heat-capacity at constant pressure. These are approximated by functions of temperatures.

Mass diffusion flux $\mathbf{\Gamma}_i$, total heat flux $\mathbf{q}$ are specified as:

$$\Gamma_i = -\rho D_i \frac{\partial Y_i}{\partial \mathbf{r}}\ ,\ \mathbf{q} = -\lambda \frac{\partial T}{\partial \mathbf{r}} + \sum_{i \neq e} h_i \Gamma_i \qquad (8)$$

Here, D_i is diffusion coefficient of i-th component, λ is the mixture heat conductivity coefficient. Viscous stress tensor is:

$$\tau_{ij} = \frac{2}{3}\eta \delta_{ij} \nabla \mathbf{U} - \eta \frac{\partial u_i}{\partial x_j} \qquad (9)$$

where δ_{ij} is Kronecker symbol. Coefficients D_i, λ and μ were determined in accordance with [11,12]. Conductivity was determined as follows.

$$\sigma = e n_e \mu_e\ ,\ \mu_e = \frac{\sigma}{e n_e} = e\frac{\tau_e}{m_e} \equiv \frac{\beta_e}{B}\ ,\ \tau_e = \nu_e^{-1}\ ,$$
$$\nu_e = \sum \nu_{ej}\ ,\ \nu_{ej} = n_j u_e Q_{ej} \qquad (10)$$

Here, e is electron charge, μ_e is electron mobility, ν_e is mean electron collision frequency, n_j is the number density of particles of j-th kind, u_e is mean thermal electron velocity, Q_{ej} is collision cross-section for collisions of electrons with particles of j-th kind.

Chemistry model

The production rate of i-th chemical component due to chemical reactions is given as:

$$\omega_i = W_i \sum_{r=1}^{N_r} \left[\nu''_{i,r} - \nu'_{i,r}\right] \cdot \left(k_{fr} \prod_{l=1}^{N} c_l^{\nu'_{l,r}} - k_{br} \prod_{l=1}^{N} c_l^{\nu''_{l,r}} \right),$$
$$c_i = \frac{\rho_i}{W_i} \qquad (11)$$

$$k_{fr,br} = a \cdot T_*^{\,b} \cdot \exp\left(-E_a / T_*\right) \qquad (12)$$

Here, c_i is molar concentration of i-th component, W_i is its molecular mass. $\nu'_{l,r}$ и $\nu''_{l,r}$ are stoichiometric coefficients of reagents and products in r-th reaction. k_{fr} и k_{br} are forward and backward reaction rate constants, respectively; a, b, E_a are reaction parameters, N_r is total number of reactions, N is total number of components. For thermal kinetics, E_a is activation energy and $T^*=T$. Thermal kinetics scheme consists of 98 reactions.

Magnetic field calculation

As in papers[7,8] magnetic field is calculated from Biot-Savart formula.

$$\mathbf{B}(\mathbf{r}_0) = \frac{\mu_0}{4\pi} \iiint \frac{\mathbf{j} \times (\mathbf{r} - \mathbf{r}_0)}{|\mathbf{r} - \mathbf{r}_0|^3} dV \qquad (13)$$

($\mu_0 = 4\pi 10^{-7}$ H/m is magnetic permeability of vacuum, $\mathbf{r}_0$ is position-vector of observation point, $\mathbf{r}$ is position-vector of elementary current $\mathbf{j}dV$, and $dV = dxdydz = rdrd\varphi d\theta$ is elementary volume, $\mathbf{B}$ is magnetic flux density (or magnetic induction). Integral (15) can be divided by two parts: over the coil conductors and over the plasma volume. The first one is calculated in advance assuming that current density is constant and $\mathbf{j} = (0,0,j_\theta)$ within conductors. Integration over the plasma volume is carried out in the same manner to yield so called induced magnetic field. Every computational cell (elementary volume) is considered as the coil in which azimuthal current $j_\theta\, d\Omega$ flows. Here $d\Omega$ is the cell area. Procedure (13) is rather expensive. Keeping in mind that only steady-state solutions are of interest one can do it once per several time-steps.

Initial and boundary conditions

To solve the set of partial differential Eqs.(1) through (5) the following initial and boundary conditions are specified for flow variables. Initial solution is those obtained at $B^* = 0$. On the inlet (left) boundary free-stream flow conditions are set given in Table 1. On the outlet boundary outflow conditions are set for all variables. At the capsule wall the following conditions are specified: T_w=1800 K, ρ_{jw} are those corresponding to free-stream (super-catalytic conditions), $\mathbf{U}_w$=0. Symmetry conditions are set at the symmetry axis, y=0. The boundary conditions for electric potential are as follows. The capsule surface is assumed to be non-conductive, $\mathbf{nj}$=0 ($\mathbf{n}$ is unit normal vector). At symmetry axis and outer boundary the normal-to-boundary electric field strength is set to zero. Typically, calculations were carried out such that characteristic magnetic field increased from smaller to larger value with the rate 1Tl/ms and hold then constant.

Results and discussion

Surface heat flux mitigation

We consider two kinds of magnetic coil schematically shown in Fig.1b and Fig.1c. The first (MS1) has inner radius (Fig.1b) R_m=0.14m, and the second (MS2) has the radius R_m=0.28m (Fig.1c). Fig. 2 presents the distributions of temperature and electron concentration along stagnation line for the

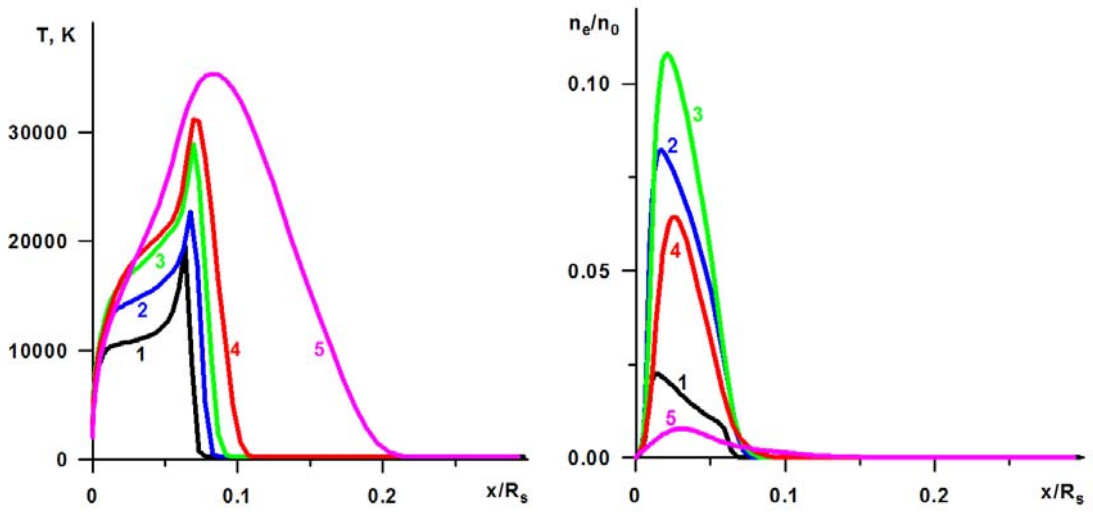

Fig.2. *Distribution of temperature (top) and electron concentration n_e/n_0 (bottom) along stagnation line. 1 – H=55km, 2 – H=60 km, 3 – H=65 km, 4 – H=71 km, 5 – H=81 km.*

case B^*=0. One can conclude from this data that the influence of Hall effect could be rather small. This is due to high ionization degree which could provide the dominative contribution of Column collisions to the mean electron collision frequency.

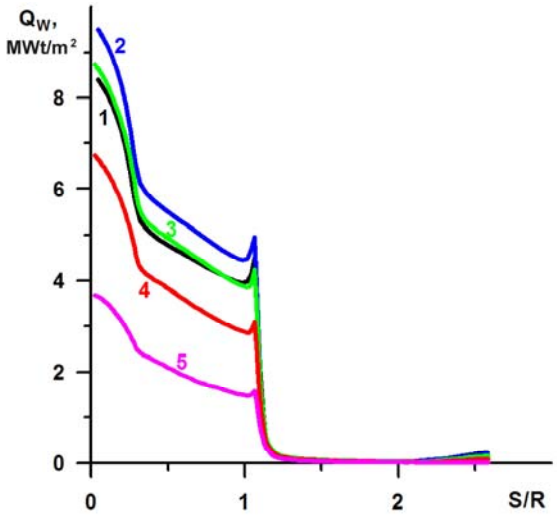

Fig.3. *Surface heat flux density at B*=0: 1 – H=55 km, 2 – H=60 km, 3 – H=65 km, 4 – H=71 km, 5 – H=81 km. R=D/2.*

Initial distributions of the surface heat flux density are shown in Fig.3. It is seen that maximal heat fluxes are achieved at altitude H~60км. The distributions of heat fluxes for different values of characteristic magnetic field are shown in Fig. 4 through Fig. 8. In general, efficiency of "electromagnetic cooling" is higher at higher altitudes. For magnetic system MS1, decrease in heat flux density at the critical point is $(q_0 - q_B)/q_0$ = 28% for H=55km and $(q_0 - q_B)/q_0$ = 58% for H=81km. For MS2, the same data is 34% for H=55km and 62% H=81km. Here, q_0 is heat flux at critical point for B^*=0, and q_B is heat flux for $B^*\neq 0$. We have the opinion from some private communication that decrease of heat flux in 20% could result in using another heat protection material. These distributions show that the value of heat flux at critical point is not sufficient criterion to characterize the heat transfer over the whole surface. In this relation two notes should be made.

It is seen from figures that strongly non-uniform distribution of surface heat flux takes place for all flow regimes. Considerable reduction of heat flux density in the region downstream of magnetic system MS1 is due to recirculation flow induced by the MHD deceleration. At the same time the heat flux rises on the rib between conical parts of the capsule. This undesirable property can be eliminated with using larger magnetic coil MS2. For MS2, uniform heat flux reduction occurs over the whole surface of heat shield. At the same time, heat flux increases on the rear-side of the capsule. Although rear-side fluxes are less than those at critical point, it is difficult to say now are they acceptable or not. Also note that the reason for increasing of heat flux downstream of magnetic coil is primarily due to increase in the mean temperature in the part of shock layer determining the heat fluxes into wall. The temperature increase is, in turn, due to deceleration of gas. In all the cases considered Joule heating plays a secondary role.

One more feature of the considered MHD flow could be called saturation effect. It is seen from the figures that decrease in heat flux occurs only at small magnetic fields. Further increase in magnetic induction doesn't result in further decrease of the surface heat flux. The reason for the saturation effect can be understand from Fig. 9 through Fig.13. In these figures, distributions of

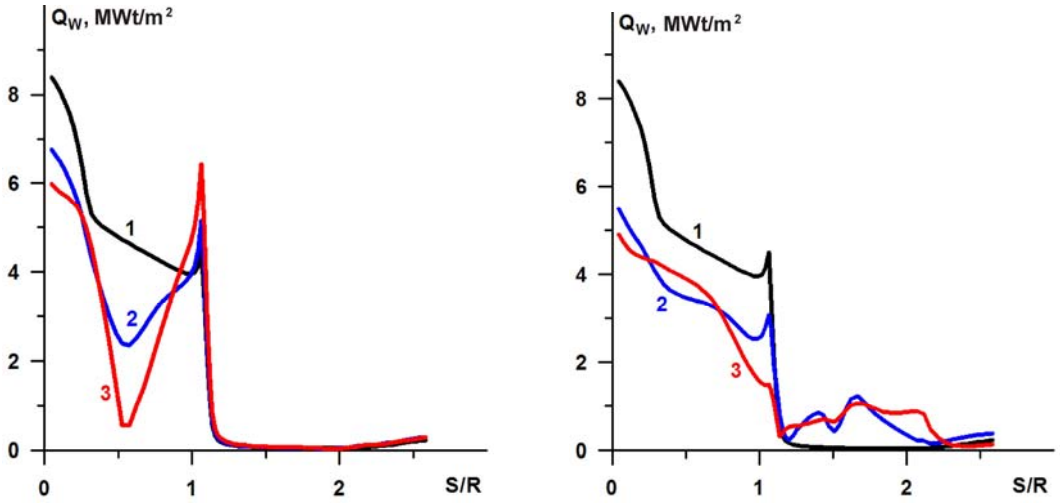

Fig.4. *Surface heat flux at altitude H=55 km for magnetic system MS1 (top) and magnetic system MS2 (bottom). 1 – B*=0, 2 – B*=0.2Tl, 3 – B*=0.4Tl.*

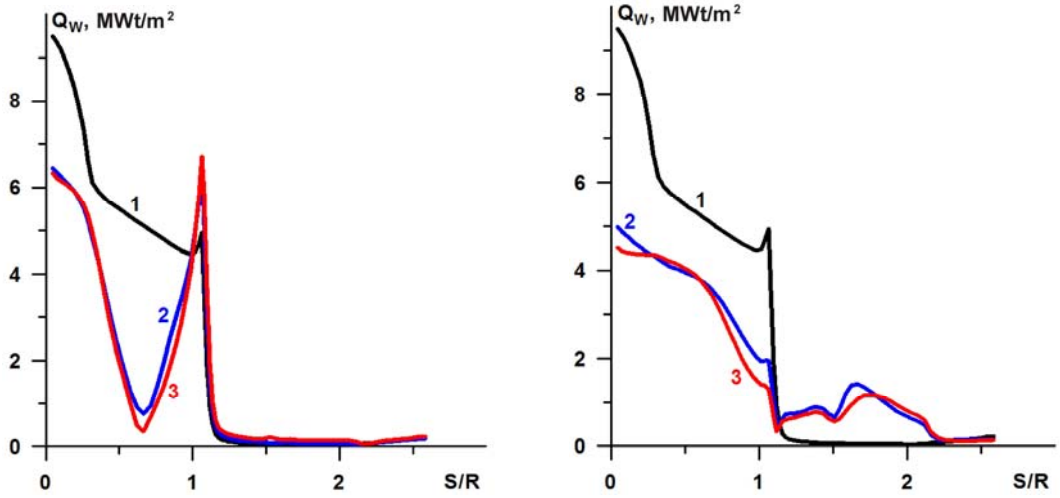

Fig.5. *Surface heat flux at altitude H=60 km for magnetic system MS1 (top) and magnetic system MS2 (bottom). 1 – B*=0, 2 – B*=0.2Tl, 3 – B*=0.4Tl.*

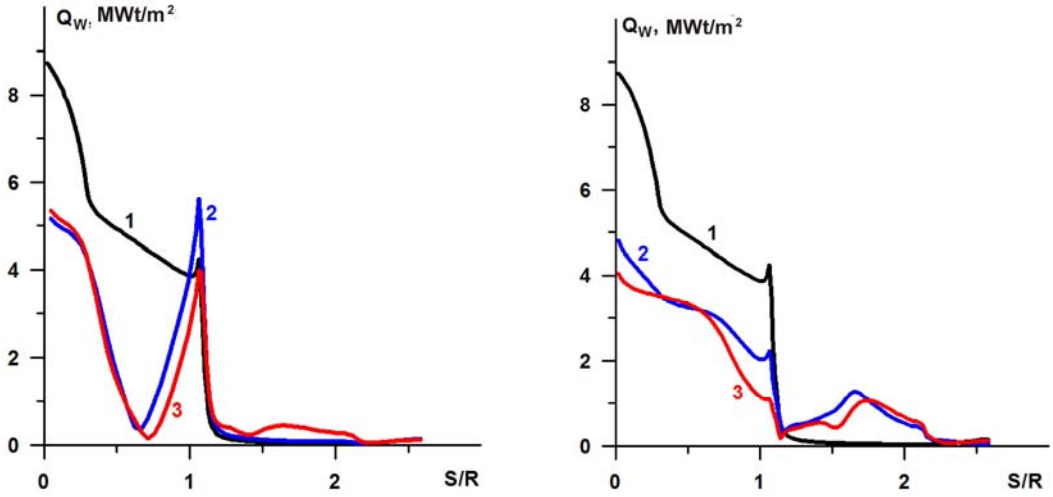

Fig.6. *Surface heat flux at altitude H=65 km for magnetic system MS1 (top) and magnetic system MS2 (bottom). 1 – B*=0, 2 – B*=0.2Tl, 3 – B*=0.4Tl for MS1; 1 – B*=0, 2 – B*=0.1Tl, 3 – B*=0.2Tl for MS2.*

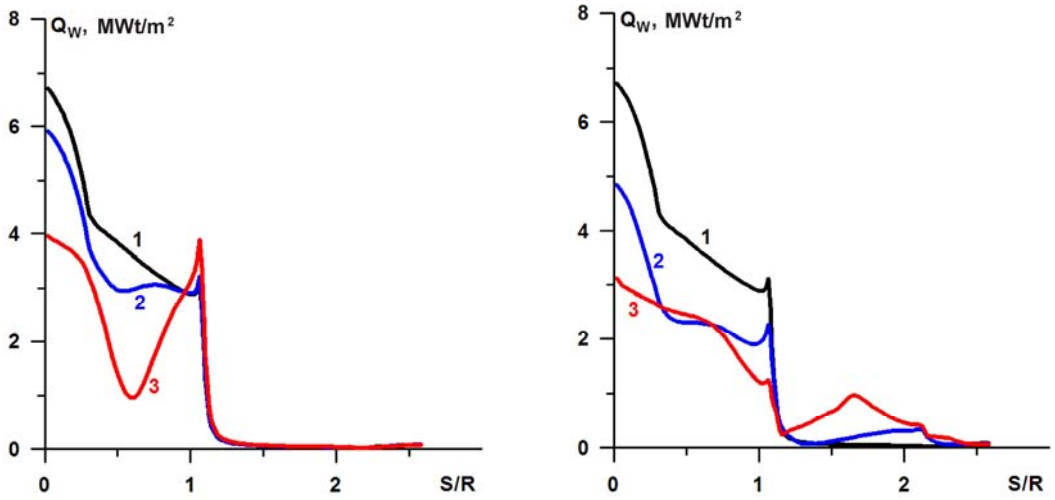

Fig.7. *Surface heat flux at altitude H=71 km for magnetic system MS1 (top) and magnetic system MS2 (bottom). 1 – B*=0, 2 – B*=0.05Tl, 3 – B*=0.1Tl.*

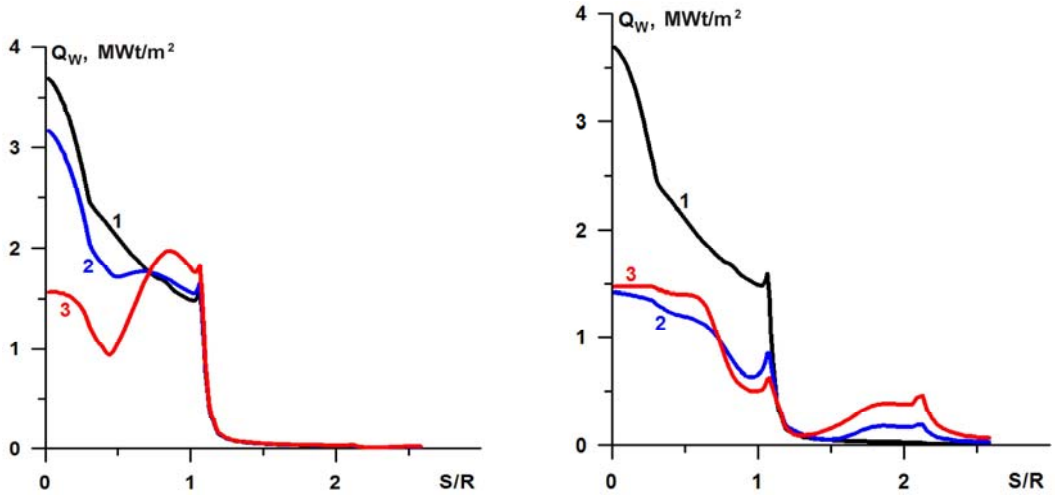

Fig.8. *Surface heat flux at altitude H=81 km for magnetic system MS1 (top) and magnetic system MS2 (bottom). 1 – B*=0, 2 – B*=0.05Tl, 3 – B*=0.1Tl.*

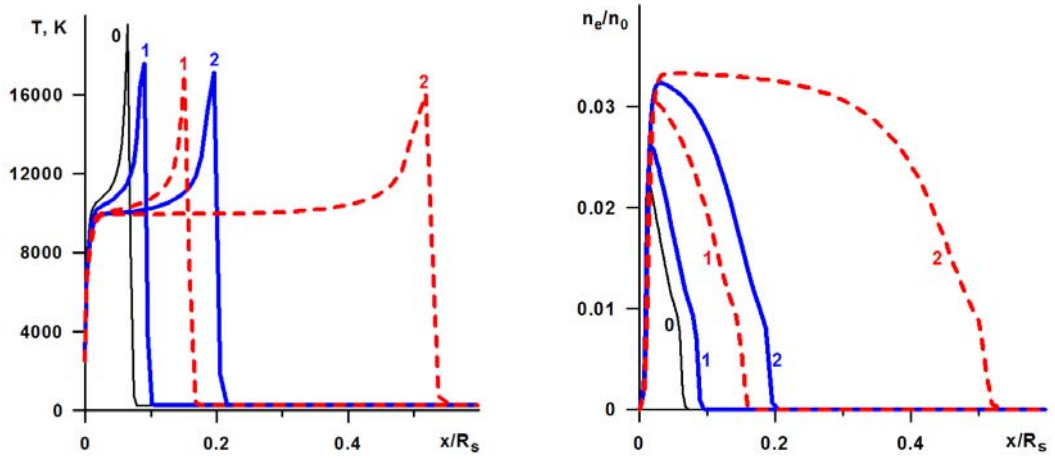

Fig.9. *Distribution of temperature (top) and electron concentration n_e/n_0 (bottom) at altitude H=55 km for magnetic system MS1 (solid lines) and magnetic system MS2 (dashed lines). 0 – B*=0, 1 – B*=0.2Tl, 2 – B*=0.4Tl.*

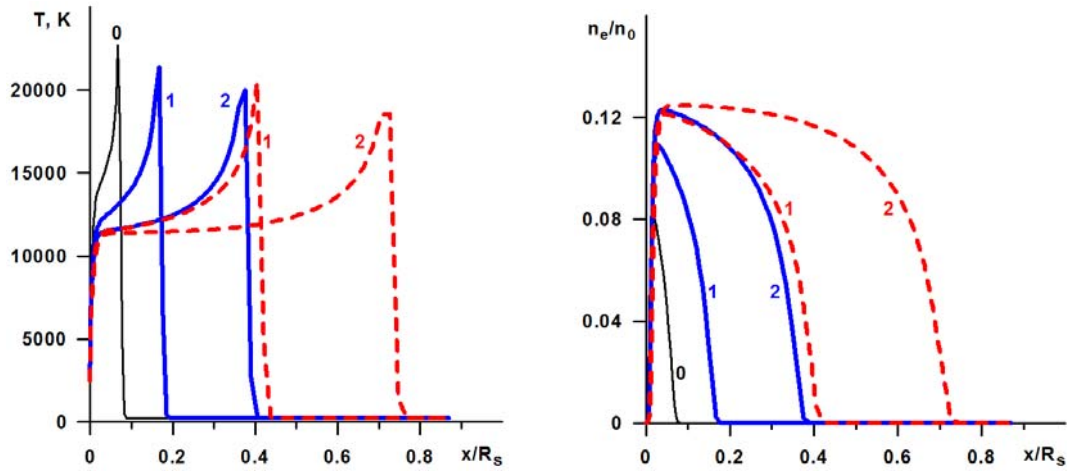

Fig.10. *Distribution of temperature (top) and electron concentration n_e/n_0 (bottom) at altitude H=60 km for magnetic system MS1 (solid lines) and magnetic system MS2 (dashed lines). 0 – B*=0, 1 – B*=0.2Tl, 2 – B*=0.4Tl.*

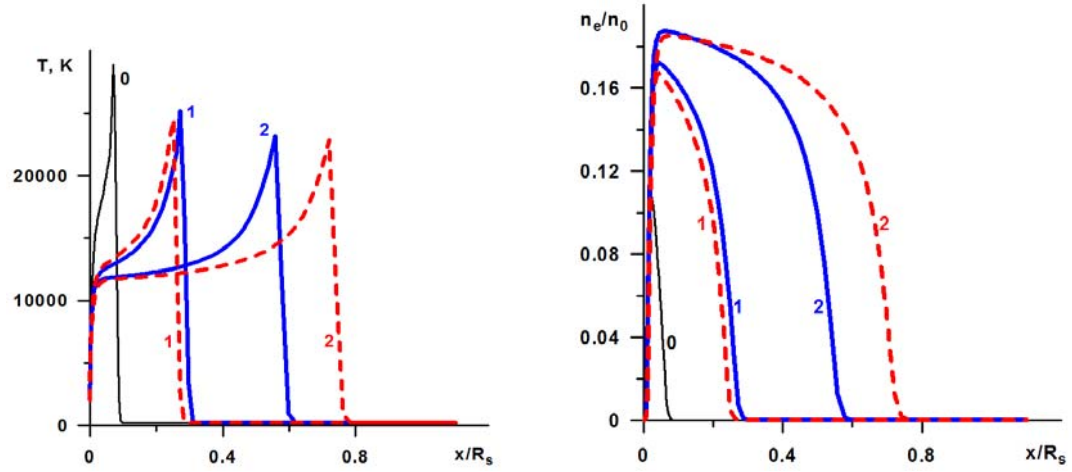

Fig.11. *Distribution of temperature (top) and electron concentration n_e/n_0 (bottom) at altitude H=65 km for magnetic system MS1 (solid lines) and magnetic system MS2 (dashed lines). 0 – B*=0, 1 – B*=0.2Tl, 2 – B*=0.4Tl for MS1; . 0 – B*=0, 1 – B*=0.1Tl, 2 – B*=0.2Tl for MS2.*

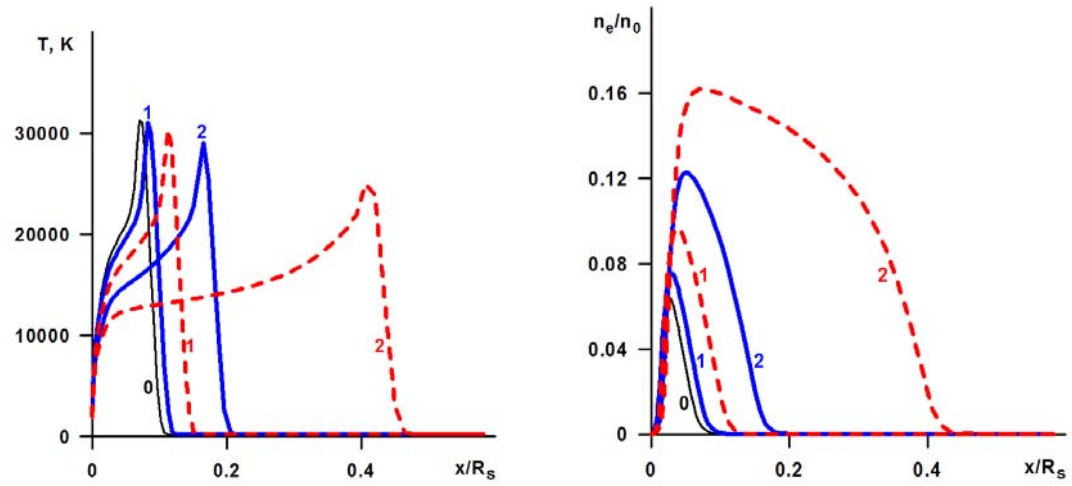

Fig.12. *Distribution of temperature (top) and electron concentration n_e/n_0 (bottom) at altitude H=71 km for magnetic system MS1 (solid lines) and magnetic system MS2 (dashed lines). 0 – B*=0, 1 – B*=0.05Tl, 2 – B*=0.1Tl.*

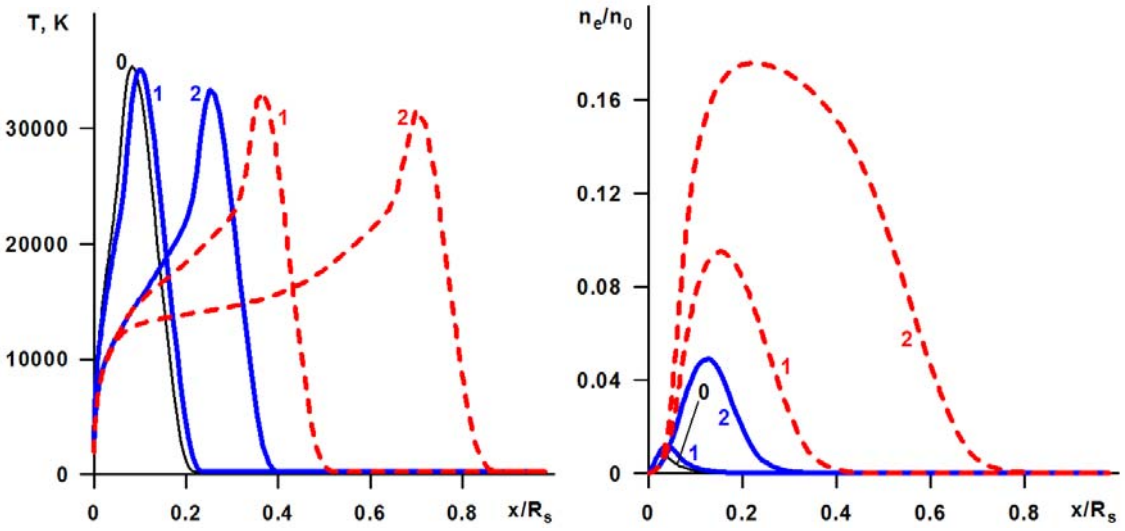

Fig.13. *Distribution of temperature (top) and electron concentration n_e/n_0 (bottom) at altitude H=81 km for magnetic system MS1 (solid lines) and magnetic system MS2 (dashed lines). 0 – B*=0, 1 – B*=0.05Tl, 2 – B*=0.1Tl.*

temperature and electron concentration along stagnation line are shown. The distributions demonstrate well known fact of increase of the shock layer thickness due to MHD interaction. However, significant increase in stand-off distance poorly correlates with the moderate decrease in the heat flux magnitude. We conclude from this that action of the magnetic field is effective only in the regions of large gradients of temperature and concentration that is near the wall. When the thickness of the shock layer increases due to MHD, the state of gas in most part of the shock layer tends to equilibrium one. This stabilizes temperature in the plasma bulk and, consequently, the temperature drop between plasma bulk and the wall. Stabilization of the mean temperature gradient results in the stabilization of the heat flux.

Integral characteristics of MHD interaction

Total heat flux to the whole capsule surface and total drag are presented in Fig.14. Total drag consists of pressure drag, electromagnetic force and viscous drag (which is typically small). Behaviour of the total heat flux is similar to that observed for heat flux densities. As magnetic field grows the total heat decreases, but saturation effect also presents. Efficiency of "electromagnetic cooling" also increases at higher altitudes: same decrease in total heat is achieved at higher altitudes and at smaller magnetic field. Efficiency of two magnetic systems, MS1 and MS2, is nearly same. It seems

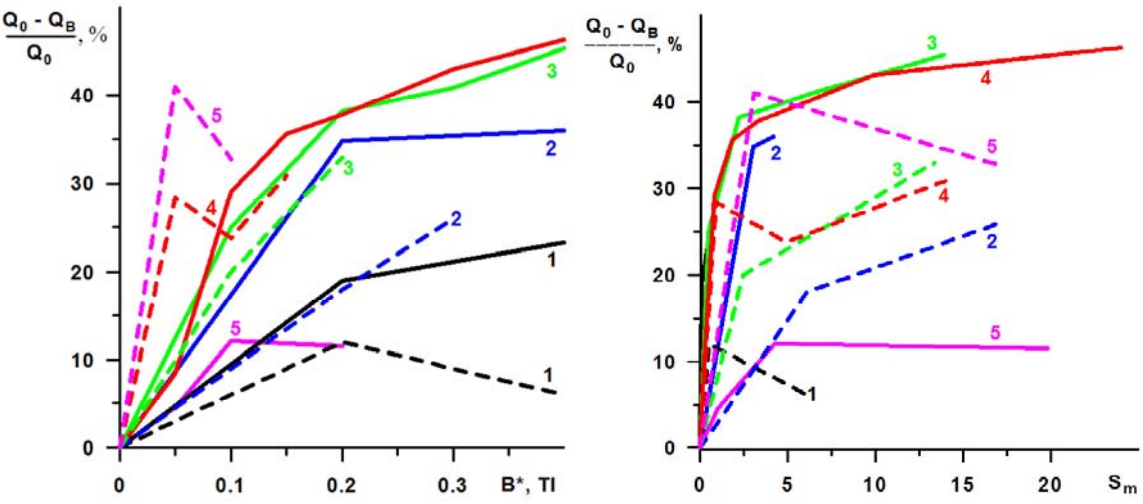

Fig.14. *Total heat against characteristic magnetic field B* (top) and against MHD interaction factor S_m (bottom) for magnetic system MS1 (solid lines) and magnetic system MS2 (dashed lines).*
1 – H=55km, 2 – H=60 km, 3 – H=65 km, 4 – H=71 km, 5 – H=81 km.

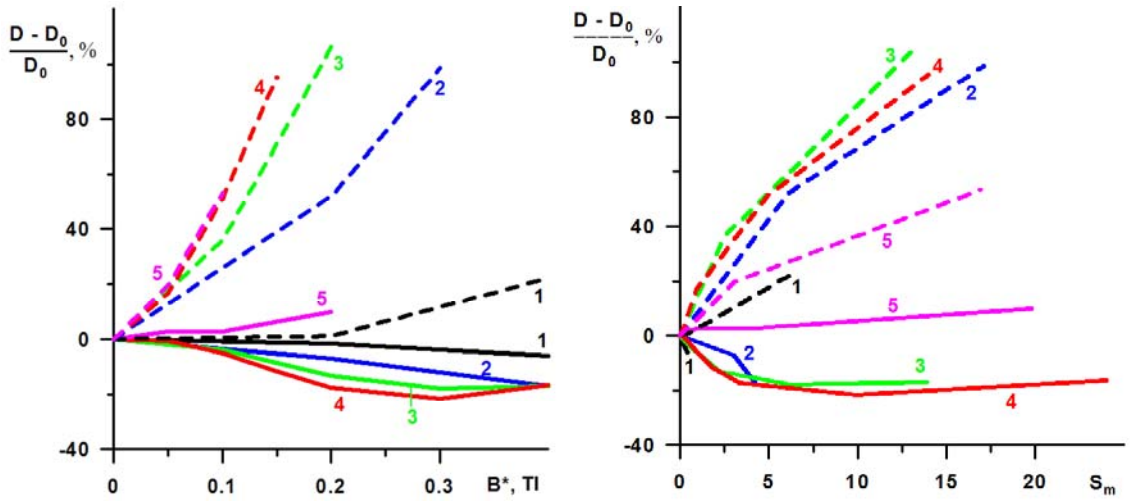

Fig.15. *Total drag against characteristic magnetic field B* (top) and against MHD interaction factor S_m (bottom) for magnetic system MS1 (solid lines) and magnetic system MS2 (dashed lines).*
1 – H=55km, 2 – H=60 km, 3 – H=65 km, 4 – H=71 km, 5 – H=81 km.

interesting to consider total heats in terms of characteristic MHD interaction factor, S_m defined in Table 1. Fig.14b shows that relative decrease in total heat depends poorly on the altitude and magnetic system scale for $S_m \le 2$. At higher values of MHD interaction factor saturation effect is well exposed.

Total drag is presented in Fig.15. Positive values of the drag change mean that total drag increases with growing magnetic field, while negative values mean decrease of total drag. Results for smaller magnetic system MS1 look somewhat unexpectedly. MHD interaction slightly diminishes total drag. That is, grow of electromagnetic drag doesn't compensate the decrease of pressure drag. The latter is certainly due to origination of secondary flow within a shock layer in front of the capsule's heat shield. The total drag behavior is more evident for larger magnetic coil, MS2. The drag increases in almost two times as magnetic field grows. Unlike total heat saturation effect is not present for total drag.

Induced magnetic field effects

The results discussed above were first obtained with low magnetic Reynolds number model which doesn't take into account magnetic field induced by plasma currents. At the same time estimations of magnetic Reynolds number given in Table 1 point out that effect of induced magnetic field should be taken into account. In the paper it is made with the model described above. Unlike paper [X], here magnetic field from Faraday current j_θ (or j_z) is only considered.

Example of calculation of MHD flow with taking into account induced magnetic field is presented in Fig.16 through Fig.18 for the flow conditions corresponding to the altitude H=65km, characteristic magnetic field B*=0.1 Tl, and magnetic system MS2. It is seen from Fig.16 that induced magnetic field looks as those generated by two coils of complicated shape with opposite currents. In the plot yellow-red color means positively directed current density j_θ, blue color means negatively directed j_θ, and green color corresponds to zero current. Effect of induced magnetic field can be seen in Fig.17 in which distributions of temperature and electron concentration along stagnation are shown for two models, original low magnetic Reynolds number model and high magnetic Reynolds number one. Induced magnetic field "works" against the applied one and, as a whole, diminishes the intensity of MHD interaction. This leads to decrease of shock layer thickness and some re-distribution of the current in the plasma bulk. However, small influence of induced magnetic field on the heat flux is observed for the conditions under consideration.

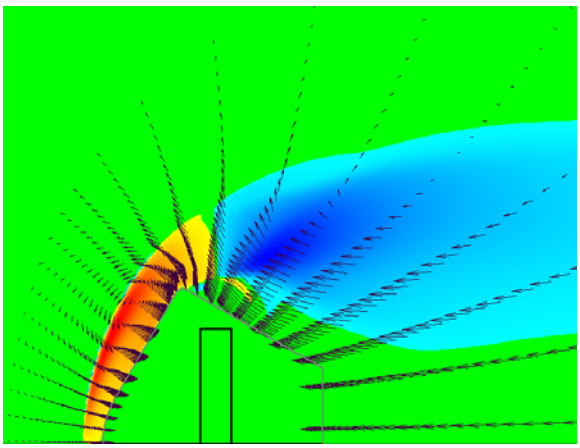

Fig.16. *Faraday current density (filled) and induced magnetic field (vectors) at altitude H=65 km, B*=0.1Tl.*

The reason for this is same as those for saturation effect. Magnetic field essentially effects on the size of the conducting zone while the heat flux is mainly regulated by the near-wall zone. As discussed earlier, the temperature drop in this zone is rather stable and poorly depends on the magnetic field. Even "positive" effect of induced magnetic field is observed on the rear-side surface. The heat flux on the rear-side surface typically grows with grow of magnetic field for the magnetic system MS2. Plasma currents diminish total magnetic field. Therefore, less heat fluxes on the rear-side surface correspond to less magnetic field amplitude.

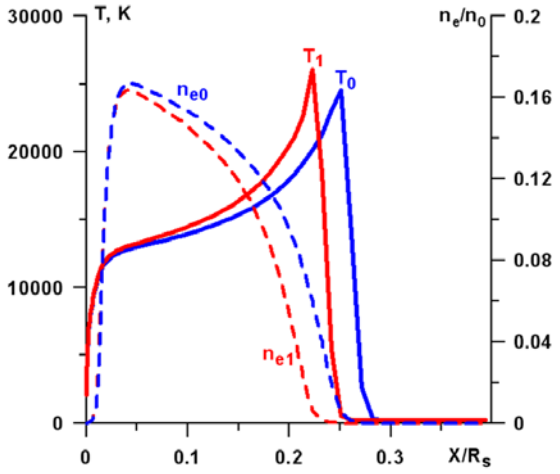

Fig.17. *Distribution of temperature (T_0 and T_1) and electron concentration n_e/n_0 (n_{e0} and n_{e1}) along stagnation line at altitude H=65 km, B*=0.1Tl, magnetic system MS2. T_0 and n_{e0} – low magnetic Reynolds number model, T_1 and n_{e1} – high magnetic Reynolds number model.*

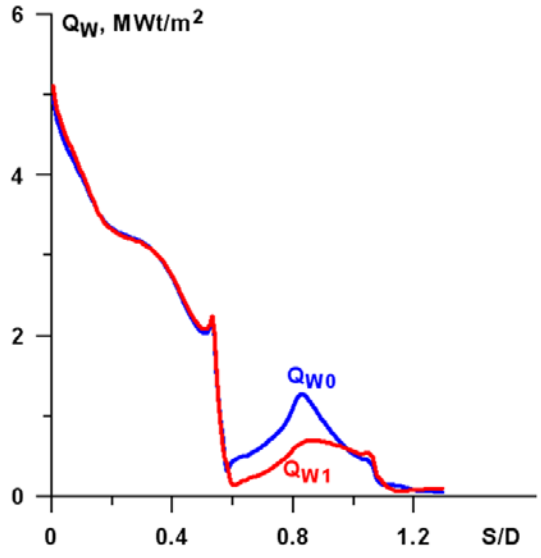

Fig.18. *Surface heat flux density at altitude H=65 km, B*=0.1Tl, magnetic system MS2. Q_{w0} – low magnetic Reynolds number model, Q_{w1} – high magnetic Reynolds number model.*

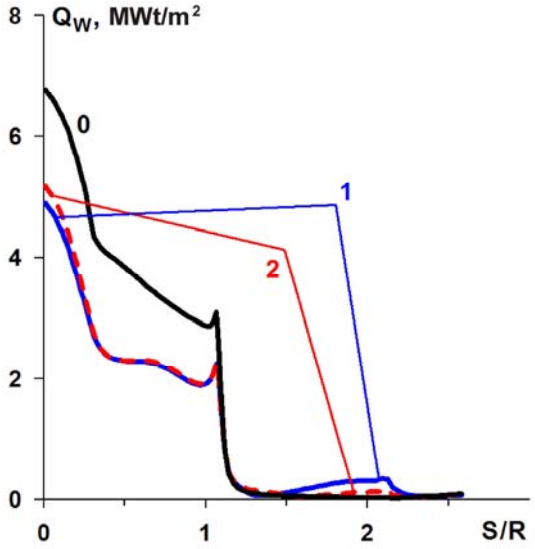

Fig.19. *Surface heat flux density at altitude H=71 km, magnetic system MS2. 0 – B*=0; 1 – B*=0.05Tl, low magnetic Reynolds number model; 2 – B*=0.05Tl, high magnetic Reynolds number model.*

One can expect that larger influence of induced magnetic field on the surface heat flux is achieved at smaller applied magnetic field magnitudes when the changes in the flow structure occur in the near-wall region. Example of such larger influence is presented in Fig.19 for flow conditions at H=71km, B*=0.05Tl, and MS2 magnetic system. As in the previous example, effect of induced magnetic field is equivalent to the MHD interaction at lower magnetic field (compared to applied one). As consequence, less decrease in heat flux is observed on the surface of heat shield along with the less increase in heat flux on the rear-side surface.

Summary

MHD flow has been considered in the paper for the flow conditions of the Stardust re-entry capsule flight pass. The primary goal of the paper was a study of heat flux mitigation due to magnetic field created by the coils.

It was shown that heat flux densities may be reduced due to MHD interaction by factor from 1.5 to 3. Such reduction may be achieved at rather low magnetic field magnitudes of order of 0.1Tl. At the same time, it was found that efficiency of the technique of electromagnetic cooling may be physically limited. Magnetic field effects on the heat flux if the near-wall region flow is influenced by the MHD interaction. At higher magnetic fields, the shock layer thickness considerably increases whereas near-wall temperature gradient remains rather stable. For almost same reason induced magnetic field effect poorly on the surface heat flux.

Total heat flux and total drag are also affected by magnetic field. While significant reduction of total heat was found, the lateral effect of electromagnetic cooling may be an appearance of heat flux over the rear-side surface. It was found that total drag may both increase and decrease. For the magnetic system of the size smaller than the capsule diameter, MHD interaction diminished total drag on 20%.

References

1. A.N. Bocharov, V.A. Bityurin, J. Lineberry. Study of MHD Interaction in Hypersonic Flows // The 15th International Conference on MHD Energy Conversion and the 6th International Workshop on MagnetoPlasma Aerodynamics, IVTAN, Moscow, 24-27 May, 2005, p.399.
2. V.A. Bityurin, A.N. Bocharov. MHD Flow Control in Hypersonic Flight // The 15th International Conference on MHD Energy Conversion and the 6th International Workshop on MagnetoPlasma Aerodynamics, IVTAN, Moscow, 24-27 May, 2005, p.429.
3. V.A. Bityurin, A.N. Bocharov, D.S. Baranov, S.S. Bychkov, A.V. Podmazov, Power Extraction Experiment with a Surface MHD Generator in Hypersonic Airflow, AIAA-2007-3882, 38th AIAA Plasmadynamics and Lasers Conference In conjunction with the 16th International Conference on MHD Energy Conversion , Miami, Florida, June 25-28, 2007.
4. Fujino, T. and Ishikawa, M.: Numerical Simulation of Control of Plasma Flow with Magnetic Field for Thermal Protection in Earth Reentry Flight, IEEE Transactions on Plasma Science, 34 (2006), pp.409-420.
5. Fujino, T., Yoshino, T., and Ishikawa, M.: Numerical Analysis of Reentry Trajectory Coupled with MHD Flow Control, Journal of Spacecraft and Rockets, 45 (2008), pp.911-920.
6. Fujino, T., and Ishikawa, M.: Numerical Simulation of MHD Flow Control in Mars Entry Flights, Proceedings of the 17th International Conference on MHD Energy Conversion, 14 – 17 September, 2009, Shonan Village Center, Kanagawa, Japan, p.3-1.
7. Bityurin V.A. and Bocharov A.N., Hypersonic MHD: Features and Problems, Proceedings of the 17th International Conference on MHD Energy Conversion, 14 – 17 September, 2009, Shonan Village Center, Kanagawa, Japan, p.IK1-1.
8. Bocharov A.N., An Investigation of MHD Deceleration in the Earth Atmosphere (Induced Magnetic Field Effects), High Temperature, 2010, Vol. 48, No. 4, pp. 461–465.
9. R. Goose and G. Candler. Diffusion Flux Modeling: Application to Direct Entry Problems, 43rd AIAA Aerospace Sciences Meeting and Exhibit, AIAA Paper 2005-0389, Reno, Nevada, Jan. 10-13, 2005, P.483.
10. I.D. Boyd, J. Zhong, D.A. Levin, P. Jenniskens. Flow and Radiation Analyses for Stardust Entry at High Altitude. AIAA Paper 2008-1215, 46th Aerospace Sciences Meeting and Exhibit, 7 – 10 January 2008, Reno, Nevada.
11. Zubkov A.I., Tirskiy G.A.,Levin V.A., Sakharov V.I. “Motion of bodies in Earth’s and Planet’s Atmospheres with Supersonic and Hypersonic Velocities under Conditions of Chemical Conversions, Heat Transfer and Radiation,” Rep. No.4507, Institute of Mechanics of Moscow State University, 1998 (in Russian).
12. Andriatis A.V., Zhluktov S.A., Sokolova I.A. “Transport Coefficients for Chemical Nonequilibrium Components of Air Mixtures," J. Mathematical Modeling, v.4, No.1, 1992, pp.44-64 (in Russian).

9.3. THE EXPERIMENAL STUDY OF THE ELECTRICAL DISCHARGE OVER THE FLAT PLATE IN A HYPERSONIC AIR FLOW AT THE MAGNETIC FIELD

V. P. Fomichev, M. A. Yadrenkin, V. E. Podzin, A. B. Shevchenko.
Khristianovich's Institute of Theoretical and Applied Mechanics SB RAS
630090, Novosibirsk, Russia,
fomichev@itam.nsc.ru, yadrenkin@itam.nsc.ru

The paper contains the experiment results of the electrical discharge occurs across the air flow over the flat plate with $M = 6$ in the magnetic field. It is shown that MHD-interaction over the plate can transform the attached oblique shock wave in the detached normal shock increasing the midsection of the interaction area of the body with the free stream.

The entry of the high speed vehicles into the upper atmosphere is accompanied by the high stagnation temperature. This makes possible to realize the MHD-effect in view of plasma flows with thermal ionization of air on the vehicle surface. The effect can be used to increasing the drag coefficient in particular [1, 2]. According to the numerical studies of the MHD-parachute phenomena, MHD-interaction initiates between the attached oblique shock and the body surface. In this case the oblique shock transforms in normal shock detached from the leading edge of the body [2]. The MHD interaction region greatly exceeds the middle transverse section of the body, which ensures effective braking at the low gas density in the upper atmosphere. Present work describes an experimental study of MHD-effects in the similar problem statement [2].

The transformation of the oblique shock wave into a normal detached shock has been studied experimentally at the MHD-test rig described in [3]. Figure 1 shows the test schematic.

Two electrodes are placed flush with the streamlined plane. The static magnetic field is normal to the plane and the incoming flow. MHD-interaction is provided by external electrical discharge with the thermal ionization of gas within 120 μs. Flow parameters: Mach number is $M = 5.8$, the static flow pressure is of 12 Tor, the static temperature is of 285 K, the flow rate is of about 2000 m/sec. The magnetic field of 2.5 T is generated by an electromagnet. The wave structure of the flow has been visualized by Schlieren-technique in 60 μs after the discharge initiation.

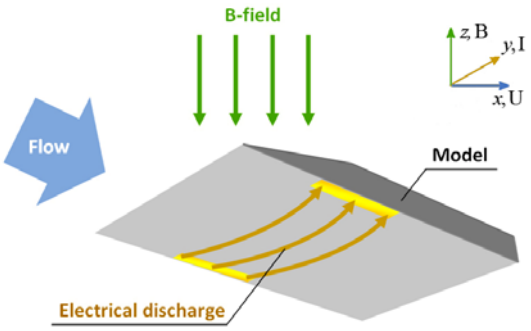

Figure 1. *Schematic of the experiment.*

Figure 2 shows photographs of the flow without magnetic field (a) and with magnetic field up to 1 T (b-f). One can see that the flow drifts the discharge outside of the model without magnetic field. The magnetic field returns the discharge in the area between the electrodes (Figure 2,b) at B = 0.21 T. As a result of increasing magnetic field up to B = 0.7 T, the discharge moves to the leading edge of the model (c, d). Further the magnetic field increasing put forward the conductive area ahead the model and transforms an oblique shock into the normal shock (e, f). When B > 1 T discharge region goes ahead the model on both sides of the plane, pushes away the shock wave of the model and significantly expands the area of the MHD interaction (f).

At the same time, comparison of the wave pattern in the numerical and experimental studies shows that this difference is not significant in case of comparable efficiency of the MHD-effect.

Figure 3 shows the pressure distribution over the plane in magnetic fields B > 1 T [1]. Comparison of wave patterns obtained in numerical studies and experiments shows a good agreement with one another.

The similar wave pattern of the hypersonic flow in the magnetic field with electrical discharge at the thermal ionization has been obtained numerically and experimentally. Comparison of results permits us to conclude that the experiment statement is suitable to study the MHD-braking of the reentry vehicles in the upper atmosphere.

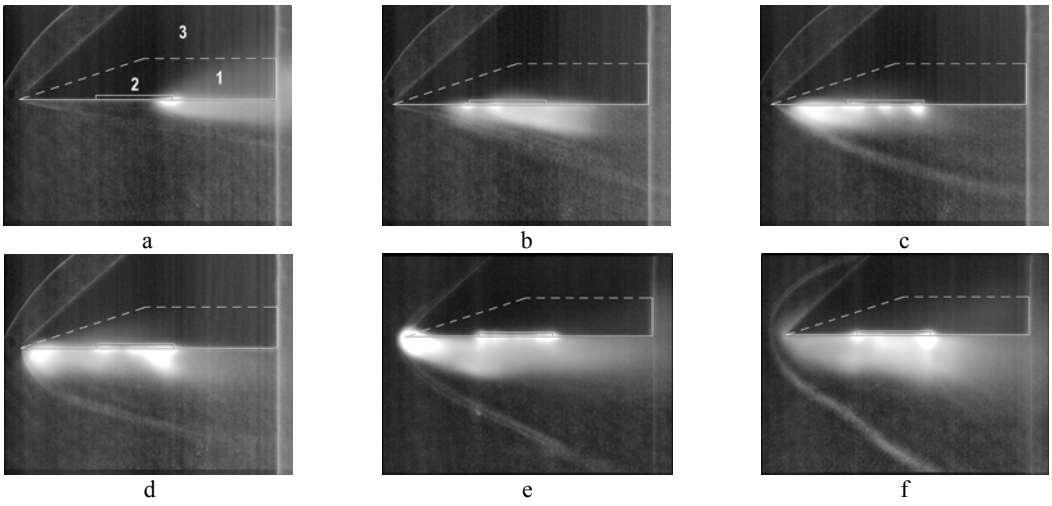

Figure 2. *Schlieren-photos of the flow over the plane at different magnetic field.*
a – without magnetic field, *b* – *B* = 0.21T, *c* – *B* = 0.29 T, *d* – *B* = 0.34 T,
e – *B* = 0.7 T, *f* – *B* = 1 T. 1 – model, 2 – electrodes, 3 - blinds.

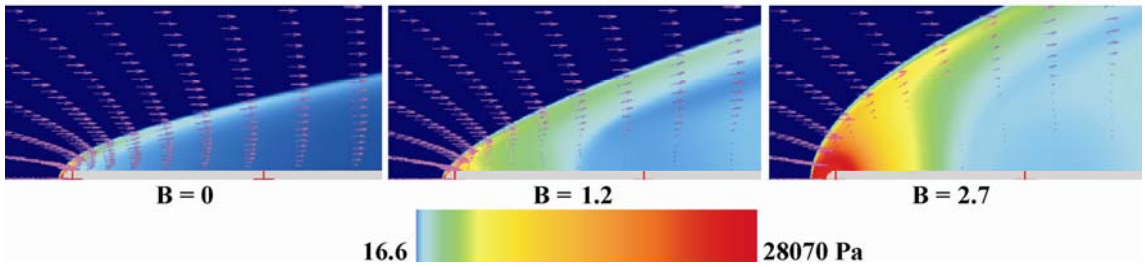

Figure 3. *Pressure and velocity as a function of magnetic induction.*

1. Bityurin V.A., Bocharov A.N. MHD Parachute in ReEntry Flight Induced Electric Field Effects in Hypersonic MHD Flow. In: 2nd International ARA Days, October 21-23, 2008, Arcachon, France.
2. V.A. Bityurin, A.N. Bocharov, D.S. Baranov, N.A. Popov. Non-equilibrium effects in hypersonic MHD flow // The 8th international workshop on magneto-plasma aerodynamics. Moscow. 31 March – 02 April 2009. P.281-290
3. Bityurin V.A. and Bocharov A.N. HYPERSONIC MHD: FEATURES AND PROBLEMS // Proceedings of the 17 th International Conference on MHD Energy Conversion. Shonan Village Center, Kanagawa, Japan. 14 –17 September 2009. Paper IK1-1.
4. Fomin V. M., Fomichev V. P, Golovnov I. A., Korotaeva T. A., Pozdnyakov G. A., Pravdin S. S., Shashkin A. P., Yakovlev V. I**.** Study of MHD-interaction in hypersonic streams // AIAA 2004-1193, 2004.

9.4. SUPERSONIC AIR FLOW AROUND BODY AT NEAR SURFACE GAS DISCHARGE

A.V.Erofeev, T.A.Lapushkina, S.A.Poniaev
Ioffe Physical Technical Institute of the Russian Academy of Sciences
26 Polytekhnicheskaya str., St.Petersburg, 194021, Russia
alex.erofeev@mail.ioffe.ru

Abstract. In the work the change of position of the bow shock wave arising at semicylindrical body streamline by supersonic flow at change of intensity of electrogasdynamic (EGD) action near-surface region of nose part of the body is studied. EGD action is made by organization of surface discharge near front part of the body that yields to control position of the bow shock due to energy deposition to the region between the shock wave and body. The main parameters of the gas discharge and the body streamline depending on heat parameter are given. The results of action in air are compared with analogous results at electrogasdynamic and magnetogasdynamic (MGD) actions on the body streamline by supersonic xenon flow.

I. Introduction

In the work a possibility to control the supersonic body streamline at the action on flow parameters in the near-surface region between the bow shock and body are investigated. As an action is used electrogasdynamic (EGD) action – the contribution of energy in the narrow near-surface region by organization of near-surface gas discharge, and magnetogasdynamic (MGD) action when the external magnetic field is applied. In the previous work[1] the possibilities of present actions on to streamlining of nose part of the body were designed experimentally using supersonic flow of ionized xenon. The experimental data showed the increase and decrease of a distance from the shock wave to body at the different degrees of EGD and MGD actions in the near-surface region were obtained. It is occurred due to the decrease or increase of a pressure in the discharge region between the shock wave and body as result from gas heating or action of Lorentz force.

In this work the streamlining of body by supersonic air flow with various ionization degrees are considered. The aerodynamic experiment makes it possible to investigate the action on the structure and parameters of streamline of the head parts of aircraft at the different altitudes and flow velocities. To carry out this work the experimental facility which was designed on the base of the shock tube and used in previous works [1,2] is used. The semicylindrical body is mounted on the axis of a supersonic nozzle connected with a low pressure chamber. The gas compressed in the shock tube enters to the nozzle and creates supersonic air flow in the region of body position. The experimental facility gives possibility to change the distance from body to the nozzle entry, that enables to organize the supersonic streamline of the body by air with various flow velocities. The brass electrodes installed in top and lower walls of the nozzle are used for preliminary ionization of incoming air flow, that enables to organize the surface discharge at the nose edge of body at the smaller discharge voltages.

The working regime of the shock tube was selected from following factors – sufficient time for formation of stationary flow in working region, particle concentration $N=10^{23}\div10^{24}$ m^{-3} in working region, at expanding in divergent nozzle gas temperature T_h must be higher than condensation temperature of air components and molecular impurities, temperature of heated gas after reflected shock wave in shock tube at end of shock tube must be lower than temperature at which a significant changes at molecular mixture of air occurs. Experiment was conducted at following parameters of shock-tube: Mach number in shock tube M_2 =6.2, initial pressure and temperature of gas p_1=30 Torr, T_1=300 K. Flow parameter near body in working region (X_0=20 cm) Mach number is M=4.3, T=395 K, $u=1.87\cdot10^3$ m/s, $N=5.34\cdot10^{23}$ m^{-3}, ρ=0.026 kg/m^3. Doubled kinetic energy of the flow per unit of the volume is $\rho u^2=9{,}06\cdot10^4$ J/m^3.

The main EGD action on the body streamline was made by creation of near-surface discharge near nose part of the body with the help of electrodes mounted in the body's wall (the Fig. 1).

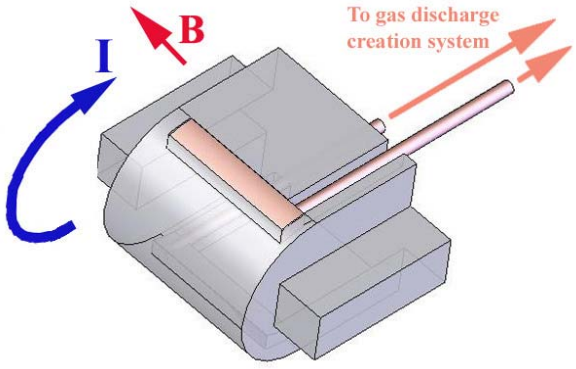

Figure 1. *Model of body with horizontal electrodes.*

As a voltage source a special LC-circuit were used that allow us to create a near-surface discharge of different intensities without special keys. The discharge switch-on at arriving of ionized flow to the body and flew near nose part of the body by semicircle trajectory. Discharge remains in the region near body after shock wave. This region has size about L=0.5cm×l=3.5cm×h=4.5cm. For organization of MGD action on the flow the additional magnetic field with the magnitude up to 1,5 T perpendicular to the flow created by Helmholtz coils were switched on during experiment. For flow visualization a special schlieren system on the base of semiconductor laser and digital camera were used.

Electrogasdynamics method (EGD) of action of flow structure is based on gas heating in electric field at gas discharges of high intensity. In this work energy input to the flow localized in narrow near-surface region between bow shock and nose part of the body, which lead to the increase of the pressure in this region and shift of the bow shock. The main task of this work is to investigate how bow shock shift changes at air supersonic body streamline at increase of heat parameter of EGD action $N = \frac{jE\Delta t}{\rho u^2}$ - a ratio between gas heating in the discharge and doubled kinetic energy of the flow. Change of heat parameter is due to change of near-surface discharge intensity near body's nose part. Also in the work a comparison of streamline parameters at the same EGD and MGD actions at streamline of the same model in air and xenon flows is made.

II. Experimental parameters of near-surface discharge

The typical oscillograms of a gas discharge current in the near-surface region and attainable at these conditions air plasma conductivity are shown on the Figure 2.

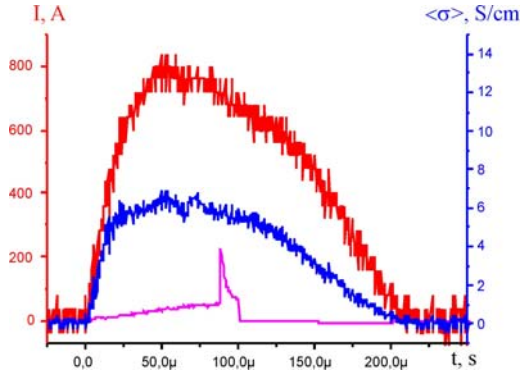

Figure 2. *Oscillograms of current (top curve) and integral conductivity (middle curve) of air plasma at near surface gas discharge. Bottom curve is diagnostic laser pulse.*

The duration of discharge is about 200 mks, that corresponds to the duration of the body streamline by air flow, the record of a schlieren-picture position of shock wave is made through 100 mks after the discharge beginning, that is enough for an establishment of the stationary streamlining [3]. The pulse of a laser luminescence of the schlieren-setup corresponds to low curve on the Figure 2.

The parameters of the surface gas discharge, which influences on the streamlining, were determined experimentally on current-voltage characteristic of the gas discharge current I in dependence from the voltage of gas discharge gap V_{pl}, shown on the Figure 3.

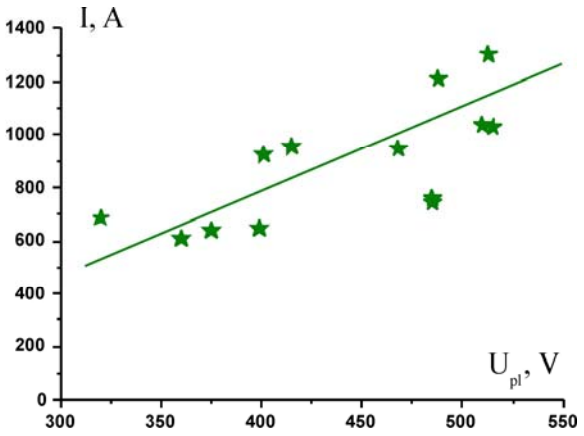

Figure 3. *Current-voltage curve of the near surface gas discharge in air.*

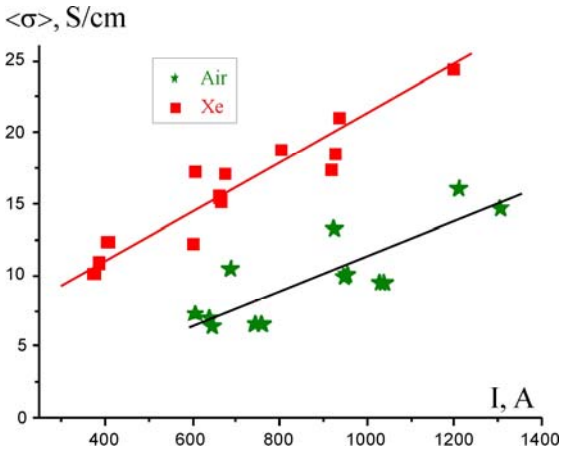

Figure 4. *Plasma conductivity in the near surface gas discharge in dependence on discharge current.*

Obtained the average effective air conductivity was determined according Ohm's law for plasma:

$$j=<\sigma>E, \qquad (1)$$

where the density of discharge current is

$$j = \frac{I}{S} = \frac{I}{hl}, \qquad (2)$$

and intensity of electrical field is

$$E = \frac{V_{pl}}{L}. \qquad (3)$$

The dependence of the average effective air conductivity obtained near surface of the model in the discharge is shown on the Figure 4. Here for comparison the xenon conductivity at the similar discharge is shown.

The average electron concentration in the discharge was determined as:

$$< n_e >= \frac{\langle j \rangle}{e v_d}, \qquad (4)$$

where the electron drift velocity in the discharge v_d for air was determined with help of reference data [4] on the base of $\frac{E}{p}$ values. The estimation of gas pressure in the streamlining zone p=45 Torr was made on the base calculated on ideal shock tube theory [5] of the relative values of the stagnation temperatures and density after reflected shock wave at the various values of Mach number of shock wave M_2, and according to the relative values of the flow parameters in a linearly divergence channel calculated on the base of the isentropic formula [6]. These dependences for air are presented in paper [7]. The change of electron concentration at the change of air conductivity in surface discharge is shown on the Figure 5. The average values of air conductivity in discharge at the surface EGD action are about <σ>=5-15 S/cm, then electron concentration changes as $<n_e>=2\text{-}4.5\cdot10^{15}$ cm^{-3}.

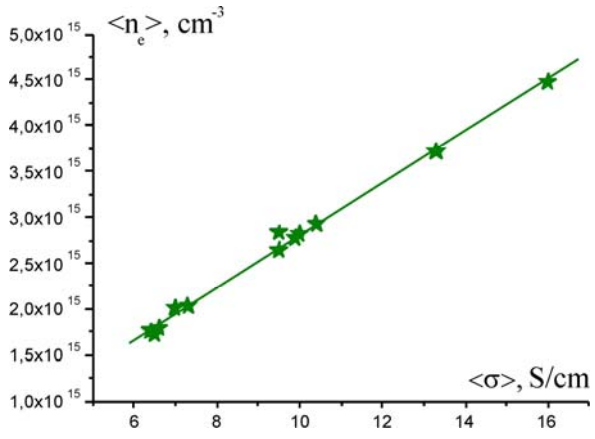

Figure 5. *Electron density of air in discharge in dependence on effective conductivity.*

The change, at the increase of surface discharge intensity, of heat (energetic) parameter ***N*** determine an energetic deposit in the near surface region of discharge and gas heat degree at the electrogasdynamic action on the streamlining structure are shown on the Figure 6.

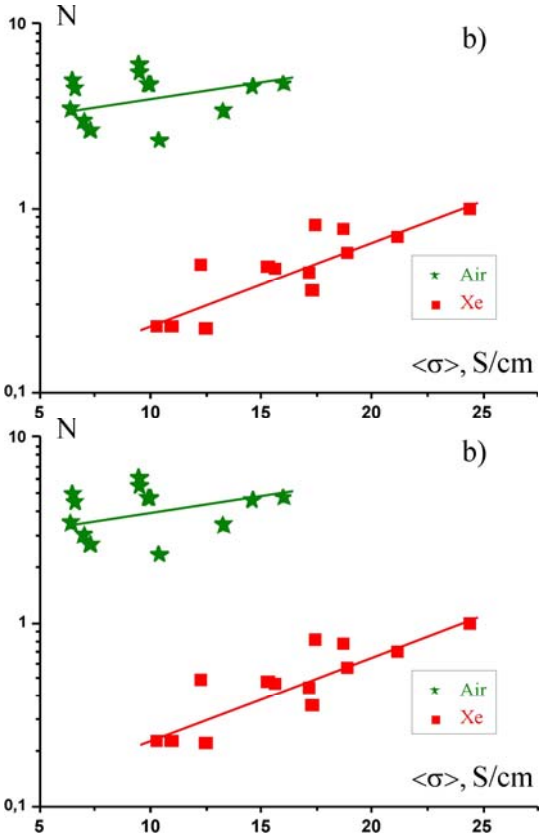

Figure 6. *Heating parameter in dependence on discharge current and conductivity.*

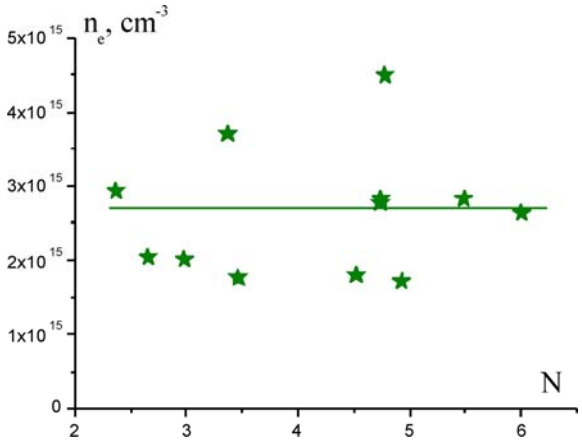

Figure 7. *Electron density in dependence on EGD parameter in near surface discharge.*

The Figure 6a shows how the parameter change depends on gas discharge current, and the Figure 6b show how it depends on plasma conductivity. Here for comparison the values of parameter ***N*** for surface discharge in xenon are given. One can see that at the same discharge intensities the values of heat parameter in air are in 5 times more than in xenon. It is explained that for creation of discharge

intensity compared with intensity in xenon, in air discharge it is need to increase the intensity of electrical field in discharge gap that leads to heat parameter increase. It is interesting that electron concentration in air discharge changes weakly with the energetic parameter growth that is seen from the Figure 7.

III. Change of body streamline at near-surface EGD and MGD actions

The examples of bow shock shift at air body streamline at EGD interaction in near-surface region are shown in the figure 8.

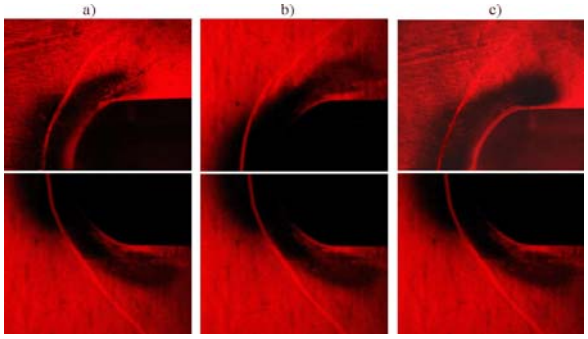

Figure 8. *Schlieren pictures of body streamline in air flow: top picture is obtained at near surface discharge without magnetic field; bottom picture is obtained without external action. a) j=3.5·10⁶ A/m², N=2.7, b) j=4.3·10⁶ A/m², N=4.9; c) j=5.9·10⁶ A/m², N=6.0*

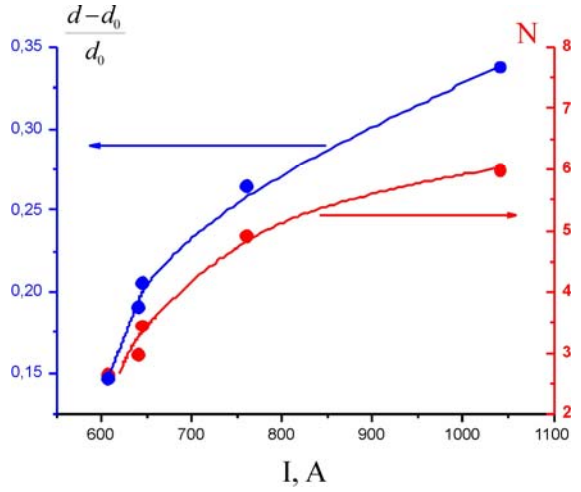

Figure 9. *Bow shock wave shift in dependence on discharge current and heating parameter.*

Here in the bottom part of the figures a picture of the flow without external action is shown, and upper part of the figures is the flow pictures at presence of the near-surface discharge with different thermal parameters of the action. It is clearly seen an increase of the distance between body's nose part and bow shock due to energy input to the near surface region that leads to pressure increase after shock wave.

The Figure 9 shows relative bow shock shift $\frac{d-d_0}{d_0}$ versus gas-discharge current and thermal parameter of EGD action. Here d_0 is a distance from the body's nose part to the shock wave without external actions. It is clearly seen that increase in discharge intensity and thermal parameter leads to increase of bow shock shift, shock wave moves from the body.

The obtained results of EGD action in air flow is reasonable to compare with results obtained at streamlining of same body by xenon flow [1]. A change of the bow shock wave position in this case was investigated not only at EGD interaction but an MGD interaction in the near-surface region. For this an additional external magnetic field was used. In this case a Lorentz force directed to (the Figure 10a) or from (the Figure 10b) the body (depending on the gas discharge current direction) influence on a gas flow.

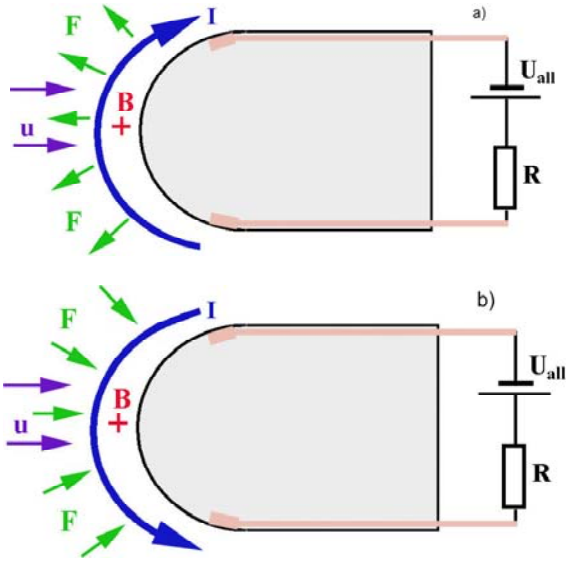

Figure 10. *Illustration of Lorentz force (vectors F) action at near-surface gas discharge.*

a) Current direction bottom-top, Lorentz force out presses gas;
b) Current direction top-bottom, Lorentz force presses gas.

As a result a Lorentz force drives gas to or from the body that leads to the increase or decrease a pressure in the region between bow shock and body and change in bow shock position. In dependence on Stewart parameter $St = \frac{jBL}{\rho u^2}$ (ratio between Lorentz force work on length of interaction and the doubled kinetic energy of the flow), which

determines an impact of Lorentz force action of body streamline and in dependence on discharge current direction in the region between bow shock and body a change of body streamline and possibility to move bow shock not only from the body but and to the body relative to initial position (a EGD action that there is at MGD action contradict to this) was investigated.

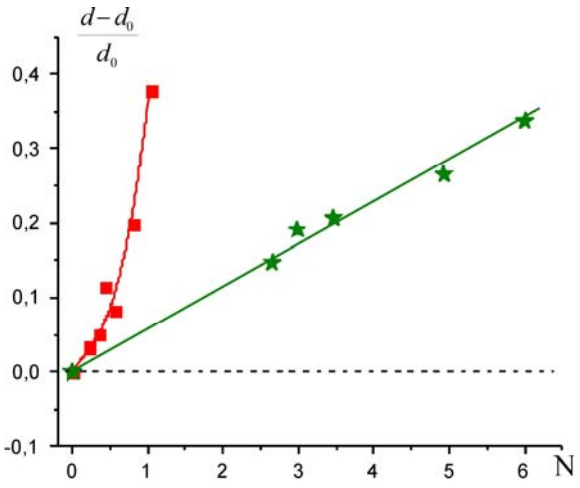

Figure 11. *Bow shock wave shift at EGD action: 1 - Xe, B=0 (squares); 2 - Air, B=0 (stares)*

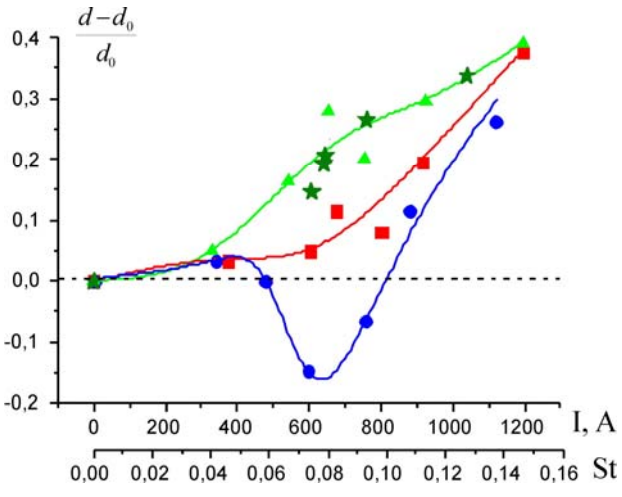

Figure 12. *Bow shock wave shift at EGD and MGD actions: 1 - Xe, B=0 (squeres); 2 - Xe, B=1.4T, Lorentz force direction out from body (circles); 3 - Xe, B=1.4T, Lorentz force direction up to body (triangles); 4: Air, B=0 (stars)*

The Figure 11 and 12 shows generalized data of relative bow shock shift versus of EGD and MGD parameters in the region between bow shock and body's nose part. The Figure 11 shows how bow shock change it position only at EGD interaction. An increase of the distance between bow shock and body's nose part at increases of the heat parameter of near-surface discharge at absence of magnetic field was observed both in xenon (squares) and in air (stars). As can be seen from figure a bow shock shift increase rapidly in xenon than in air at increase of energy input. Approximately the same bow shock shift in air is seen at value of parameter N 5 times higher then in xenon. This mean for flow control by EGD method in air a heat input must be 5 times higher than in xenon.

At MGD interaction in near-surface region in xenon flow (the Figure 12) there is an increase and decrease in bow shock shift. At increase of Stewart parameter at Lorentz force directed to the body (triangles) there is an additional shift of bow shock from the body. This shift becomes larger than shift at absence of magnetic field due to additional action of the Lorentz force. At Lorentz force action in opposite direction (circles) bow shock moves from the body, after this one moves to the body, again moves from the body when heat action of discharge become prevail over Lorentz force action. Relative shift of bow shock at streamlining in the air flow is shown in figure by olive stars. It is seen that this shift is nearly equal to the value obtained in xenon flow at EGD action with additional Lorentz force action. It can be described by more intense gas heating in air then in xenon at the same discharge intensity.

IV. Conclusions

Based on the results of this work it is possible to conclude that it is possible to control bow shock position of flight vehicle by energy deposition and MGD interaction in near-surface region near its nose part.

Electrogasdynamic method allows us to shift bow shock by organization of gas discharge on body's surface near it nose part after bow shock. This method is based on heating of the gas. A bow shock shift occurs due to strong gas heating in discharge in the region between bow shock wave and the model which leads to pressure increase after bow shock. By changing heating intensity (and electrogasdynamics parameter N) it is possible to change bow shock position. In the air a gas heating must be 5 times higher than in xenon.

At switching-on of external magnetic field orthogonal to the flow and near-surface gas discharge current it is possible to make magnetogasdynamic control of the bow shock-wave position by Lorentz force effect. At changing of gas discharge current direction to opposite one the Lorentz force direction is also changing. In this case Lorentz force will be force up or down gas near model, i.e. increase or decrease pressure in the region between bow shock wave and the model. By changing direction of Lorentz force and MHD interaction parameter *St* it is possible to change the bow shock-wave position as to move wave away

from body as to approach it to body. The same relative shift of shock wave in air and xenon occurs at the approximately same Stewart parameters.

The ranges of the energetic parameter and Stewart parameter values determined in the work, corresponding to the regions of the most effective EGD and MGD actions, allow to choose the gas discharge parameters and the magnetic field for the most effective control of the shock wave position both to the increase the distance from shock wave up to body and to the approach of the shock wave to body.

Acknowledgments

This work is supported by the Program #11 of the Presidium of RAS, grant RFBR #08-01-00330a and Federal program "Academic and teaching staff of innovative Russia in 2009-2013" (02.740.11.0201).

References

1. A. Erofeev, T. Lapushkina, S. Poniaev and S. Bobashev. "Supersonic Body Streamline at Different Configuration Gas Discharge", *AIAA-2010-1382, 48th AIAA Aerospace Sciences Meeting and Exhibit and 12th Weakly Ionized Gas Workshop, Orlando, Florida, Jan.4-7*, 2010.
2. T.A.Lapushkina, A.V.Erofeev, S.A.Ponyaev, S.V.Bobashev, "Supersonic flow of a nonequilibrium gas-discharge plasma around a body", *Technical Physics*, V.54, No 6, 2009, P. 840-848.
3. S. V. Bobashev, R. V. Vasil'eva, A. V. Erofeev, T. A. Lapushkina, S. A. Ponyaev, D. M. Van Wie. "Relaxation of the shock-wave configuration in a diffuser after termination of the action of magnetic and electric fields", *Technical Physics Letters*, V.32, N2, 2006, p. 106-109.
4. Raizer, Yu.P, *Gas discharge physics*, Springer, 2001, 449 p.
5. *Shock Tubes*, Ed. by Kh. A. Razmatullin and S. S. Semenov, Inostrannaya Literatura, Moscow, 1962 [in Russian].
6. L. G. Loitsyanskii, *Mechanics of Liquids and Gases,* Elsevier, Amsterdam, 1966.
7. R.V.Vasil`eva, A.V.Erofeev, B.G.Zhukov, T.A.Lapushkina, S.A.Ponyaev, S.V.Bobashev. "Generation of a gas-discharge air plasma in a supersonic magnetohydrodynamic channel", *Technical Physics,* V.54, N6, 2009, p. 829-839.

9.5. FORMATION OF THE SHOCK WAVE ON A WEDGE IN THE HYPERSONIC AIR FLOW AT THE LOCAL MHD-INTERACTION

V. P. Fomichev, M. A. Yadrenkin, V. E. Podzin, A. B. Shevchenko.
Khristianovich's Institute of Theoretical and Applied Mechanics SB RAS
630090, Novosibirsk, Russia

The paper contains experiment results of the flow over a wedge in the hypersonic air flow at the local magnetohydrodynamic (MHD) action with Mach number $M = 6$. It is shown that the flow reorganization realized during the one pass of the flow over the wedge surface. The time of the flow settling in the MHD-disturbed region less than 3 μs. Restructuring of the flow is induced by both thermal and force action on the flow at the local MHD-interaction supported by a pulsed electrical discharge.

At present, the experimental studies of a hypersonic flow under the conditions approaching the full-scale parameters are performed in hot-shot wind tunnels. The MHD-interaction in the hypersonic air flow is studied in ITAM SB RAS using the MHD-test rig [1] based on a shock wind tunnel. The time of quasi-stationary gas flow behind the nozzle is 1 – 2 ms. The MHD-interaction occurs within 100 μs. The model length is of 50 mm, the time of flow passage over the wedge is about 25 μs. MHD-interaction in the air flow around the wedge has been studied with $M = 6, 8$ in the simulation of free flight conditions at the altitude of 30 – 50 km [2 – 5]. The effect on the slope angle alteration of the pulsed test nature has not been studied. Hence there is a question if the studied flow is quasi-stationary when the time of the MHD-action on the flow is comparable with the time of flow passing over the model.

To solve the problem, the flow around the wedge by the air with the MHD-disturbed region about 10 μs has been studied experimentally similar to [5]. Ratio the MHD-action on the flow – time of the flow passing over the wedge is about 0.5. Figure 1 shows the Schlieren-pictures of the non-disturbed flow (Figure 1, *a*) and the flow with the MHD-disturbance (Figure 1, *b, c*); the pictures register the passage of the disturbed region above the wedge. Because the flow velocity is about 2000 m/s, it passes this part of the wedge about 15 – 18 μs.

Comparison of two consequent shots (*b*) and (*c*) with 3 μs between them shows that just after the disturbed region passing the wedge the shock wave angle in the apex region return to its initial state corresponding to the free-stream conditions, on this the time of the flow settling does not exceed 3 μs at test conditions. A similar effect has been observed with only the thermal action on the flow when the discharge occurs between the electrodes without magnetic field.

For instance, to analyze quantitatively the varying angle of shock wave inclination the authors of [4] use the Stewart number $\mathrm{S} = \dfrac{\sigma B^2 l}{\rho V}$. At the MHD-interaction, however, not only the force action dependent on the value $j \times B$ is important, but also the thermal action that is governed by the relation j^2 / σ. In present paper, we propose dimensionless parameters to describe the varying inclination angle of the oblique shock wave on the wedge at the local MHD-action. To define the dimensionless parameters we considered the hypersonic flow around a thin body, a plate, when the shock wave slope angle is relatively small. We considered the case of the MHD interaction on the hypersonic flow, when the conductivity of the flow is created by the external influence localized on the length l_x ahead the plate similar to [4, 5] without viscosity and thermal conductivity in the absence of volumetric heat sources except j^2 / σ. Leaving only the force and thermal effect on the flow of the electromagnetic field in the equations of motion and energy, $\dfrac{\partial P}{\partial x} = 0$, we obtain

$$\frac{d\alpha}{\alpha} = \left(1 + \frac{1}{3\mathrm{M}_\infty^2}\right)\left(\frac{1}{2}\frac{j^2 l_x}{\sigma \rho_\infty V_\infty C_{p\infty} T_\infty} - \frac{j \times B l_x}{\rho_\infty V_\infty^2}\right), \qquad (1)$$

where l_x is the size of the flow ionization region by the march coordinate. The sign before the vector product $j \times B$ determines the direction of the force action on the flow.

The criterion dependence (4) has been used to analyze the experimental data obtained at Mach numbers $M = 6$ at the conditions approaching to those described in [4, 5] at the flow ionization by the external electrical discharge.

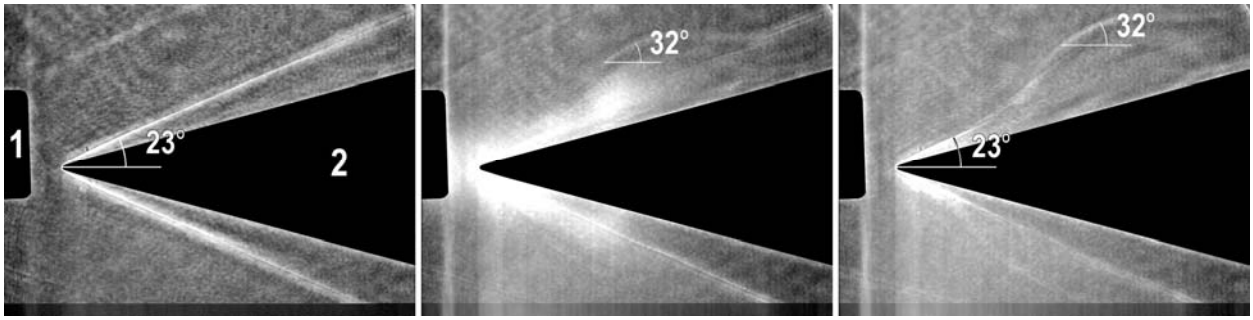

a *b* *c*

Figure 1. *Schlieren-photos of the non-disturbed flow (a) and MHD-disturbed flow (b, c)*
1 – electrodes, 2 – wedge.

1. Golovnov I.A., Pozdnyakov G.A. , Pravdin S.S. , Podzin V.E. , Pushkareva T.I. , Fomin V.M. , Fomichev V.P., Yakovlev V.I. An experimental complex to simulate and study the MHD-interaction in a hypersonic flow // Preprint No. 7-2003, ITAM SB RAS, Novosibirsk, 2003, P. 26.
2. Fomin V.M., Fomichev V.P., Golovnov I.A., Korotaeva T.A., Pozdnyakov G.A., Pravdin S.S., Shashkin A.P., Yakovlev V.I. Study of MHD-interaction in hypersonic streams//AIAA 2004-1193, 2004.
3. Fomin V.M., Maslov A.A., Korotaeva T.A., Shashkin A.P., Malmuth N.D. Simulation of the MHD-Effect Upon a Flow around a Wedge// 15th Int. Conf. on MHD energy conversion and 6th Int. Workshop on MPA, Moscow, May 24-27, 2005, Proc. V. 2, P. 583.
4. Fomin V.M., Fomichev V.P., Korotaeva T.A., Maslov A.A., Pavlov A.A., Pavlov Al.A., Pravdin S.S., Shashkin A.P., Yakovlev V.I., Malmuth N.D., Smereczniak P., Silkey J.S. Initiation of nonequilibrium conductivity of a hypersonic flow and MHD-interaction. // AIAA 2007-1376, 45th AIAA Aerospace Sciences Meeting and Exhibit: Reston, 2007, P. 11.
5. V.E. Podzin, V.P. Fomichev, A.B. Shevchenko, M.A. Yadrenkin, Investigation of the air flow around a wedge at $M = 6$ under the local MHD-influence// 9th Int. Workshop on MPA, Moscow, April 13-15, 2010.

10.1. NUMERICAL SIMULATION OF A FLOW WITHIN INDUCED MAGNETIC AND ELECTRIC FIELDS

A.E. Goncharov, T. A. Korotaeva, A. P. Shashkin
Institute Theoretical and Applied Mechanics SB RAS, Novosibirsk, Russia 630090

The paper presents description of a numerical method for solving 3-D Euler equations added with state equation, Om's law, and plasma kinetic equations that describe processes in a weakly ionized gas [1 - 4]. The problem is solved for low magnetic Reynolds numbers associated with a magnetic inductivity that is independent of the gas dynamics. The magnetic field is assumed constant in the computational domain, there is no need to use all the Maxwell equations; thus, only Ohm's law has been added to the governing equation system.

The system is solved with a finite-volume approach. The second-order difference scheme is employed.

It is well known that simultaneous numerical solution of the fluid and kinetic equations is difficult because of different timescale of processes. A procedure has been proposed to overcome the problem. The difference scheme is time-explicit for fluid and time - implicit for kinetics.

3-D E-field is defined by numerical solution of the equation written for Om's law. The equation is replaced by the unsteady one, and then the new equation is solved using Crank–Nicolson scheme and time asymptotic method.

The paper contains description of an algorithm and boundary conditions, as well as an example, how the method can be applied to the solution of a test problem. Electromagnet-field influence on the flow around a finite-width wedge after a pulse of discharge is considered under the test conditions. Experimental studies have been carried out at the MHD-test rig fabricated on the basic of a shock wind tunnel of ITAM [5-7]. Test schematic is given in Fig.1. It is the same as that used at the numerical simulation.

The flow around the test model, the symmetric wedge with the angle of 30 deg., has been investigated. Parameters of the air are: the flow Mach number is of M=6, static pressure is about 13mmHg, flow velocity is about 2000 km/s. Flow ionization is implemented by an electrical discharge. Current density is of 500 A/sm^2, voltage is of 140 V, B=0.21T. Intensity of the MHD interaction estimated by the Stewart number is of 0.13.

The work contains preliminary results that are in the good agreement with test data. Unsteady flow patterns of interaction between the area of the MHD-interaction and the oblique shock wave generated by the wedge with and without magnetic field are given in the work in comparison to the experimental results. Performed experimental and

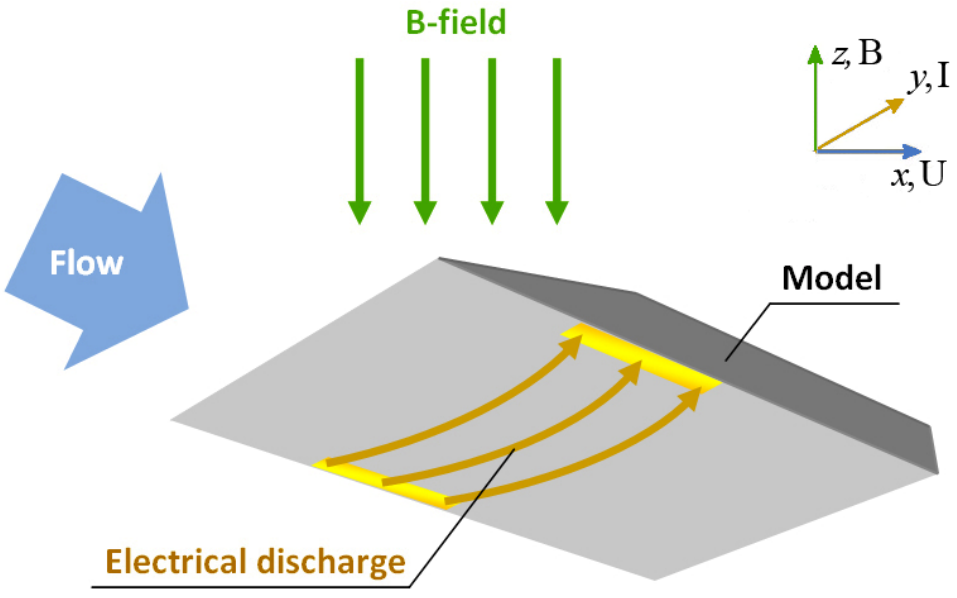

Fig.1 *Schematic of the problem*

numerical studies of the flow around the wedge have clearly showed significant changing of the wave structure within induced magnetic and electric fields.

References

1. SC Lin, JD Teare "Rate of Ionization Behind Shock Waves in Air, II, :Theoretical Interpretation", Physics of Fluid, 6, 1963, 355-375
2. I.V. Adamovich, J.W. Rich, A.P. Chernukho, S.A. Zhdanok "Analysis of the power budget and stability of high-pressure nonequilibrium air plasmas", 31st AIAA Plasmadynamics and Lasers Conf., 19-22 June 2000,Denver, CO, AIAA 2000-2418, 18p
3. R.C. Millican, D.R. White "Systematic of Vibration Relaxation", J. Chem. Phys., 1963, X, Vol. 39, No 12
4. S.O. Macheret, M.N. Shneider, R.B. Miles "Modeling of air plasma generation by electron beam and high –voltage pulses", AIAA paper 2000-2569.
5. Fomin V.M., Fomichev V.P., Korotaeva T.A., Maslov A.A., Pavlov A.A., Pavlov Al.A., Pravdin S.S., Shashkin A.P., Yakovlev V.I., Malmuth N.D., Smereczniak P., and Silkey J. S. "Initiation of nonequilibrium conductivity of a hypersonic flow and MHD-interaction", AIAA 2007-1376, 45th AIAA Aerospace Sciences Meeting and Exhibit, Reno, Nevada, 2007.
6. Golovnov I.A., Pozdnyakov G.A., Pravdin S.S., Podzin V.E., Pushkareva T.I., Fomin V.M., Fomichev V.P., Yakovlev V.I. "A Test rig for experimenatal simulation and study of the MHD- interaction in a hypersonic flow", Preprint № 7-2003. ITAM SB RAS. 2003 (in Russian).
7. Fomin V., Fomichev V., Golovnov I., Korotaeva T. Pozdnyakov G., and Malmuth N. "Study of MHD Iinteractions in Hypersonic Streams", AIAA-2004-1193.

10.2. GAS-DYNAMIC EQUIPMENTS AT THE IOFFE INSTITUTE OF RUSSIAN ACADEMY OF SCIENCES

S.V. Bobashev, A.V. Erofeev, I.V. Krasovskaya, V.A. Sakharov, Z.A. Stepanova, G.K. Tumakaev
Ioffe Physico-Technical Institute of RAS,1 94021, Saint Petersburg, Russia,
S.Bobashev@mail.ioffe.ru

The objective of the report is reviewing experimental capabilities of pulsed gasdynamic setups of the Laboratory of gasdynamics at the Ioffe Physoco-Technical Institute of Russian Academy of Sciences A part of this equipment in recent years has been intensively employed when implementing investigations into various physical phenomena, some of setups do not operate for various reasons.

Test benches engineered on the basis of shock tubes 30 – 40 years ago currently remain completely suitable for conducting contemporary investigations in the domain of gasdynamics and allied sciences. This amazing fact that after many years the setups remain contemporary is explained by that the principles of operation of shock tubes do not practically change. It is chipper to maintain a shock tube in proper working order than to engineer a new setup which will practically reproduce the setup already existing. Moreover, the expenses for constructing a new setup today turn out much greater than 30 – 40 years ago for many reasons. One of them is considerable appreciation of high-quality steels, other materials, and high-accuracy machining of metals. Therefore, it is no wonder that the arsenal of shock tubes in contemporary laboratories of the world (Stanford, CalTech, Aachen, and others) is enshrined.

As the practice of employment of shock tubes during the last 20 – 30 years shows, as modern physics and new technologies develop, new research problems arise for solving that shock tubes are the most appropriate tools. In the report the basic parameters of the research test benches of the Laboratory of gasdynamics at the Ioffe Institute and illustrative materials reflecting the results of some investigations at these setups are presented.

In the Laboratory there are six experimental complex based on shock tube: Big shock tube (BST), Shock tube with the rectangular cross section (RCST) Shock tube with the improved system of control of gas parameters (ISST), Shock tube with pulse magnet (STPM), Shock tube with disk channel (STDC) and Ludwieg tube (LT).

10.3. INVESTIGATION OF MINIATURE MAGNETO-PLASMA COMPRESSOR AS A BASIC PART FOR PERSPECTIVE PLASMA ACTUATORS FOR SUPERSONIC FLOWS

I.Ch. Mashek, Yu.I.Anisimov,
Physical Department of Saint-Petersburg State University, Saint-Petersburg, Russia,
V.A. Lashkov
Mathematical and Mechanical Department of Saint-Petersburg State University, Saint-Petersburg, Russia,
Yu.F. Kolesnichenko, V.G.Brovkin
Joint Institute of High Temperatures of Russian Academy of Science, Moscow, Russia,

Introduction

The principles of operating of Large – Scale and High-Current Magneto-Plasma Compressors were carefully described in [1-4]. These two-electrode quasi-coaxial discharge system may operate in Vacuum Regimes (working gas injected in MPC by the impulse gas valve) and in Residual Gas Regimes (MPC accelerate the surrounding gas).

The unique properties of plasma jets, generated by the MPC, operated in High-Pressure Residual Gas Regime (HPRGR), were demonstrated in [7-9]. Unfortunately, the specific energetic parameters of the large-scale MPC (outlet diameter 40 mm) are comparatively low (0,6-1,5 kJ/pulse) [7,9]. It stands to reason, the possible on-board variant of Plasma Actuator, using the MPC as the base unit, has to have essentially lower energy input with saving of acceptable level of thrust. It was the reason for creation and investigations of low dimensional, Miniature MPC (MMPC) [6]. This type of MPC with comparatively low input energy may be very important for problem of flow control, problems in high-altitude engines and MHD applications. Another way of possible construction of perspective plasma actuators was described in [4,6]. These types of actuators are based on "Spark-Jet" conception which uses the small cavity with micro nozzle and with internal electrode for gas heating by the electric spark. Unfortunately this kind of actuators has essential problems with operation under the low pressure (High Altitudes) and as it will be shown in the presented work, at the same condition, the specific impulse bit (ratio of impulse bit to inputted energy) of investigated variant of MMPC is essentially more than its "Spark Jet" analog has.

Construction of Mini-MPC and experimental setup

The construction of Miniature MPC (MMPC) was carefully described [10,11]. On the Fig.1 the general view of discharge electrodes system of MMPC is presented. Compressor has six bar anode (2 mm in diameter and 40 mm length). These anodes are placed along the circle of 12 mm diameter and are gathered round the cone cathode. The effective outlet diameter for this MMPC is about 12 mm. Usually MMPC has an additional electrode for auxiliary discharge. This low-power DC discharge (3kV, 10 mA) is placed near the critical section of MPC quasi-Laval nozzle, stabilizes operation regimes MMPC under the high pressures and may turning on before the main current pulse.

Fig.1. *The electrodes of investigated MMPC*

MMPC is placed in the pumped test chamber. It has the place holder for MMPC, high-voltage bushing for auxiliary discharge electrode, pressure sensor and tube for pumping. The windows of test camera permit to view and record all space phases of generating plasma jet. The low-inductance impulse current generator is used for organizing of discharge in MMPC. It has a standard

scheme and consists of capacity bank (800 μF, 2000 V), Hg-switchboard (100 kA, 5 kV) and sensors for measuring and recording of discharge current and voltage. Electrical parameters of the discharges in MPC are managed by the data acquisition system based on the CAMAC.

For recording the "integral in time" pictures of MMPC jets the color CCD camera with high spatial resolution (10 M pix) was used. This camera has the synchronization circuit and allows manage the impulse for MPC start relatively camera frame exposition. This camera was used too for pendulum position control for MMPC impulse bit measuring. The investigations of dynamics of plasma jet propagation were performed with using of gated CCD camera with minimal frame exposition 500 ns.

Results

On Fig.2 the general view of MMPC plasma jet under the residual gas pressure 35Torr is shown [11].

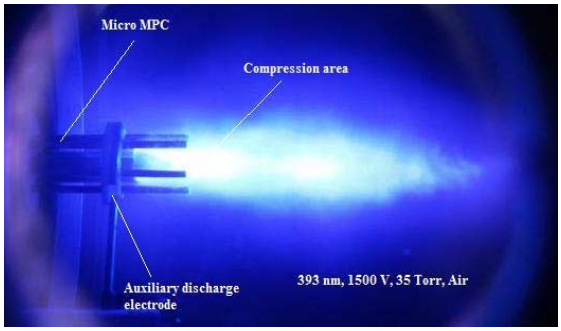

Fig. 2. *General view of plasma jet generated by Miniature MPC*

This photo was made through interference filter 393±10 nm with exposition time 1 ms. It includes the images of all spatial and temporal phases of jet life. On the presented photo clearly seen that plasma jet generated by investigated MMPC has a typical plasma focus (compression area corresponds to places of high brightness) and elongation more than 6-8 outlet diameters of used MMPC. The dynamics of MMPC jet propagation under the residual gas pressure 8 Torr is shown on Fig.3 (a,b). The photo on

Fig.3a was obtained at the 10 μs of the discharge process, the frame (b) - at the 15 μs. These pictures allow making the estimations of jet velocity under the assumption that velocity of stagnation area in gas approximately corresponds to jet velocity (it may be true for first steps of jet expansion). The distance between fronts of spots is about 10 mm, the jet velocity approximately 2000 m/s. The stagnation area moves in quiescent air under the normal temperature (300 K). The inclination of shock wave, clearly seen on Fig.3 gives the Mach number 5-5,5 which corresponds for getting velocity.

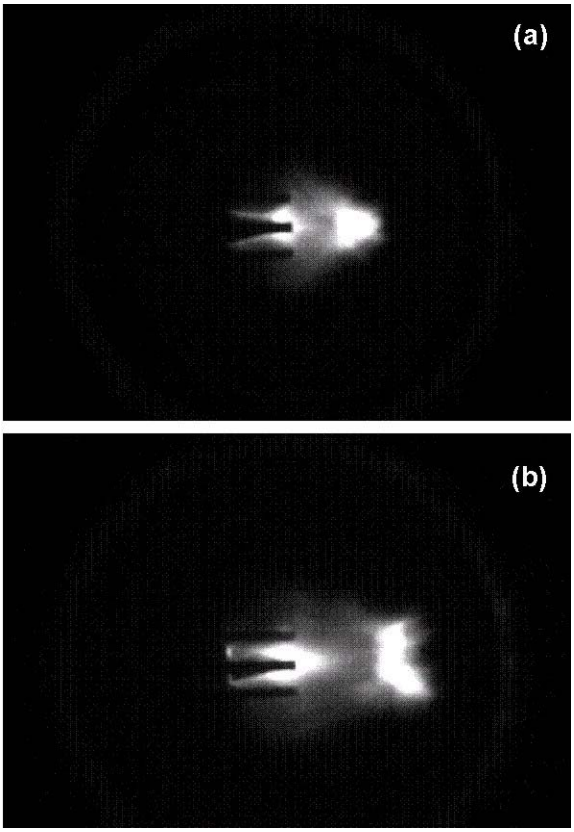

Fig.3. *Dynamics of MMPC jet propagation*

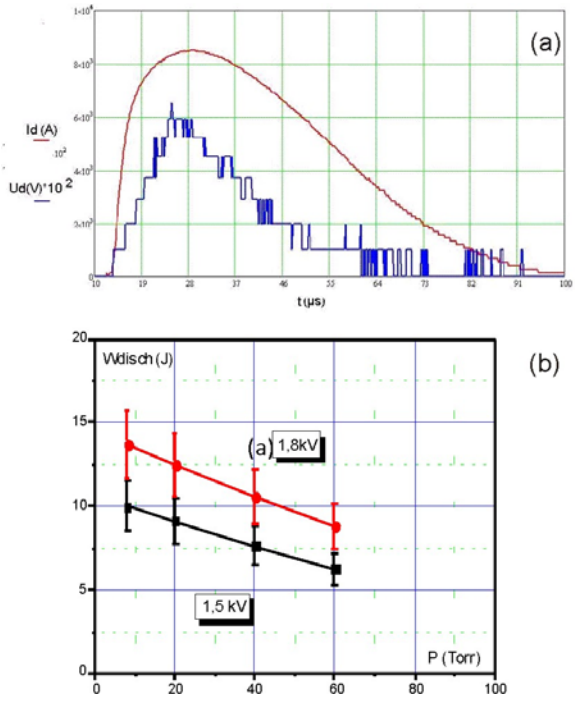

Fig.4. *Volt-Ampere and energetically parameters of MMPC discharges*

The typically Volt-Ampere characteristics for investigated type of MPC are presented on Fig.4a. The discharge was realized under the pressure 8 Torr and voltage of capacity bank 1,5 kV. The general energy input in discharge area (for this realization) may be estimated as 10 J. The levels of inputted energy in the discharges in MMPC under the different pressures are shown on Fig.4b (for capacity voltage 1500 and 1800 V).

It is clearly seen, that under the same battery voltage (approximately same discharge current) the inputted energy is decreased with pressure growth. It is very important to note, that under the pressure 60 and more Torr (altitudes about 17 km and lower) the inputted energy is less than 6-7 J.

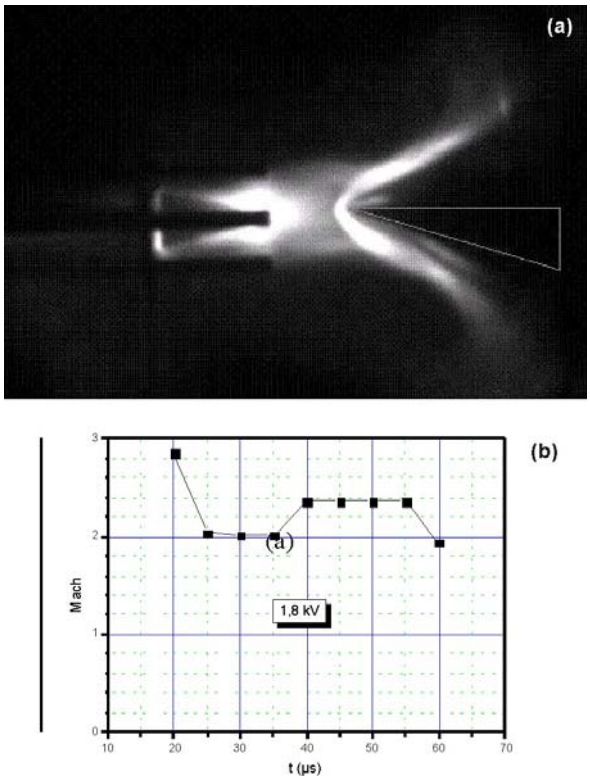

Fig. 5. *Monitoring of Mach angle in semi-wedge streamline (a) and Mach numbers, corresponding to different moments of jet propagation (b)*

The dynamics of plasma velocities in investigated plasma jets may be estimated by the monitoring of Mach angle variation under the semi-wedge flow observing. These measurements were performed and on Fig.5a the typical frame of this streamline is presented. On Fig.5.b the Mach numbers, corresponding to different moments of MMPC jet propagation are presented. This picture clearly shows that real lifetime of high-velocity plasma jet is longer than 50 μs and quasi-compression flow in investigated type of MMPC arises at the 10-th μs of discharge with finish at the 60-65 μs. The threshold current for compression flow formation may be estimated as 4-5 kA.

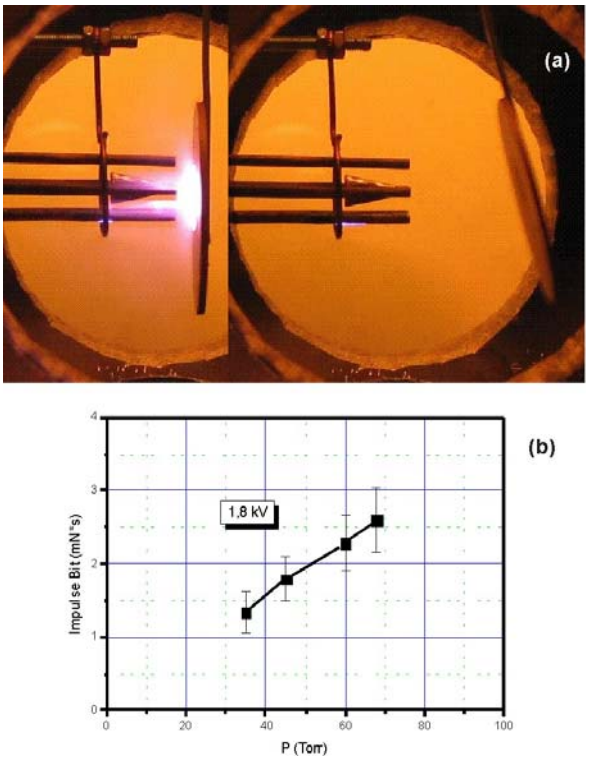

Fig. 6. *The view of testing MMPC in the vacuum chamber of experimental setup and the position of pendulum before jet action and after the action (a). The values of MMPC impulse bit under the different residual gas pressures (b).*

It is clear, that the main characteristic of possible actuators, used MMPC is the value of the thrust. The integrated in time thrust of such impulse propulsion is depended on the value of its impulse bit and possible repetition frequency. The possible frequencies of discharge repetition in MMPC will be discussed later and now we consider another main parameter of MMPC jet – its impulse bit. For impulse bit measuring the method of ballistic pendulum was applied (Fig.6). Pendulum consists of ceramic disk (diameter 41 mm, mass-7,2) and aluminum pendulum suspension (70 mm length). The general mass of pendulum is 8,5±0,1g, the integral moment of inertia $4{,}2\times10^{-5}$ m^2kg, the center of mass placed on the distance 67 mm from the axis of torsion suspension (the point of applying jet force was chooser near to this point). The processes of interaction of pendulum with plasma jet were recorded on CCD camera with frame repetition frequency 30 Hz. Such frame frequency was absolutely sufficient for valid registration of maximal inclination of pendulum. The analysis of these experimental data was performed under the consumption that the restoring coefficient of plasma jet velocity is approximately low. This assumption

has indirect confirmation from analysis of picture of jet interaction with pendulum (Fig.6a). On Fig.6b the values of MMPC impulse bit under the different residual gas pressure and capacity bank voltage 1,8 kV are presented. The growth of values of impulse bit with pressures under the constant discharge current (no discharge voltage, the inputted energy decreased with pressure!) gives very optimistic estimations for possible magnitudes of MMPC impulse bit for diapason 90-120 Torr (13-15 km altitudes).

Conclusion

The data obtained on the present step of our investigation show that spatial, temporal and energetic parameters of plasma jets, generated by MMPC under the surrounding gas pressure up to 70 Torr and the corresponding magnitudes of impulse bit are allow making the estimations of specific impulse bit for investigated simplest model of MMPC. This value for pressure 60 Torr is about 0,3 mN*s/J. So high magnitudes of specific impulse bit mean that real mass flow through our model MMPC may be estimated as 20-25 g/s (life time of quasi-compressed plasma jet is about 50-55 μs) and the volume of gas injected by MMPC jet more than 5 time upward of internal volume of MMPC. The last fact indicates that gas –dynamic processes in the area surrounding MMPC are very important and have to be carefully investigated in our future work.

As we noted above, the possible repetition frequency of MMPC discharges is the most important parameter too. On the present step of investigation this problem was not included, but the obtained data allow making several estimations. So, obviously that repetition frequency rate for investigated type MMPC is determined by minimal time for compression jet arising (fundamental limitation, it is about 5-10 μs for our type MMPC) and time for gas flushing of active area around MMPC. The last fact confirms the significance of investigations of gas-dynamics processes around MMPC too. If we make the reasonable assumption that characteristic dimensions of exactly unknown active area MMPC is about 5-cm and the velocity of gas flashing is about sound velocity, the possible level of discharge repetition rate may be estimate as 5-6 kHz. This level of frequency and obtained magnitudes of impulse bit give the possible specific thrust (N/J) about 1,5 N/J for pressure operation 60 Torr. It is large value, but it is a question, how this level of discharge frequency is connected with life time of electrodes of our discharge system? It is well known, that erosion processes on electrodes in arc discharge are very essential. Nevertheless our 3-year experience of MMPC maintaining shows that this problem is not so dramatic. On Fig.1 the results of erosion of MMPC Copper electrodes are presented. The whole number of discharges is about 1000. The reason of so comparatively low level of erosion processes is connected with very unusual kind of ion mass flow in MPC. This effect was carefully investigated in [1-4] and gives the optimistic opportunities for development of MMPC – based thrusters.

Acnowlegements

We are sincerely grateful to the European Office of Aerospace Research and Development (EOARD). This work was supported in part by ISTC grant 3058p.

References

1. Astashinsky B., Bakanovich G., Minko L. “Investigations of dynamic of plasma arising and forming processes of compression area in gas magneto-plasma compressor” Journal of Applied Spectroscopy, Vol. 33, 1980, p.629-633.
2. Morozov A. “The principles of coaxial quasi stationary plasma accelerators” Physics of Plasma, vol.16, 1990, p.131-146.
3. Ananin S., Astashinskii V., Bakanovich G. “Study of the formation of plasma streams in a quasistasionary high-current plasma accelerator” Sov.J.Plasma Physycs (Engl. Transl.)16 (2). February 1990. P. 102-108.
4. Ananin S., Astashinskii V. “Structure of plasma flow in quasisteady high-current accelerators with a penetrable cathode transformer” Plasma Physics Reports, V.23, N 1, 1998, P.37-40.
5. Cybyk. B., Wilkerson J., Simon D. “Enabling of High-Fidelity Modeling of High-Speed Flow Control Actuator Array” 14th AIAA/AHI Space Plans and Hypersonic Systems and Technologies Conference, Paper AIAA 2006-8034.

   [6]Cybyk B., Simon D., Land H., Chen J., Katz J. “Experimental Characterization of a Supersonic Flow Control Actuator” 44th AIAA Aerospace Meeting and Exhibit, January 2006, Reno, NV, paper AIAA 2006-0478.

   [7]Mashek I., Lashkov V., Anisimov Yu., Kolesnichenko Yu. “Quasi-Stationary Magneto-Plasma Compressor For Investigation of Plasma Jets in Aerodynamic” 44th AIAA Aerospace Meeting and Exhibit, January 2006, Reno, NV, paper AIAA 2006-1458.
6. Mashek I.Ch., Lashkov V.A., Anisimov Yu.I., Kolesnichenko Yu.F. “Hypersonic Plasma Jets Generated by Quasy-Stationary Magneto – Plasma Compressor and their Applications for Applied Plasma Dynamics” 5th Workshop Thermochemical and Plasma processes in Aerodynamics, Saint-Petersburg, 19-21 June, 2006, paper No 21

7. Mashek I.Ch., Lashkov V.A., Anisimov Yu.I., Kolesnichenko Yu.F. “Investigation of Plasma Jets Generated by Quasi-Stationary Magneto-Plasma Compressor under the High Static Pressure” 45th AIAA Aerospace Meeting and Exhibit, January 2007, Reno, NV, paper AIAA 2006-0221
8. Mashek I.Ch., Lashkov V.A., Anisimov Yu.I., Kolesnichenko Yu.F. “Investigations of Miniature magneto-Plasma Compressor” 7th Workshop on Magnetoplasma Aerodynamics, Moscow, April 2007
9. Mashek I.Ch., Lashkov V.A., Anisimov Yu.I., Kolesnichenko Yu.F. “Plasma actuator for supersonic flow based on Miniature Magneto-Plasma Compressor” 46th AIAA Aerospace Meeting and Exhibit, January 2006, Reno, NV, paper AIAA 2008-1408.

10.4. NUMERICAL SIMULATION OF SUPERSONIC IONIZED GAS FLOW ABOUT BODIES: THE WALL HEAT FLUX

S.V.Bobashev, Yu.P.Golovachev, A.S.Chernyshev, A. A.Schmidt
Ioffe Institute RAS, Saint Petersburg, 194021, Russia

Numerical investigations have been carried out of supersonic MHD flow of weakly ionized nitrogen plasma around model bodies at conditions of experiments on the Big Shock Tube (BST) of the Ioffe Institute of Russian Academy of Sciences. The purpose of the investigations was validation of a mathematical model and algorithm as well as analysis of predominant factors determining the MHD impact on the flow structure and thermal load on the model. The effect of the magnetic field induced by the coil installed in the model on the plasma flow was investigated and the efficiency of the MHD interaction was estimated. Comparison of the predictions with experimental data obtained on the BST was presented.

To enhance the efficiency of the MHD interaction in the vicinity of the model bodies, surface electric discharges were arranged on their surfaces. In the magnetic field induced by coils installed in the models the discharges rotate producing domains of high plasma electric conductivity near the surfaces.

Investigations showed that at conditions under study the predominant factors of MHD impact on weakly ionized plasma flow around the body determining the flow structure are both the ponderomotive force and the Joule heating. It is worth to be mentioned that in a wide range of incoming plasma flow parameters the flow around the body is turbulent one which also significantly influence on the flow structure.

The paper presents results of numerical simulation of laminar and turbulent weakly ionized plasma supersonic flows around cone-cylinder and cylinder bodies under MHD impact.

Algorithm of numerical simulation was based on a mathematical model which considers the plasma represented as a neutral electrically conductive fluid. Motion of such a fluid is described by equations of magnetic hydrodynamic.

The obtained results corresponded to coils and electric discharges parameters providing the characteristic values of the magnetic induction about 1.0 T, and characteristic time of magnetic field existence to be greater than flow reconstruction one. Electric discharge rotation frequency was about 30 kHz. Estimates showed that in this case the plasma electric conductivity near the cone surface was about $\sigma \approx 10^4$ S/m.

Characteristic structures of flows around the model bodies under MHD impact are shown in Fig.1.

It was demonstrated that effects of the turbulence manifest themselves mainly in dynamic and thermal loadings on the body. Under considered conditions MHD interaction results in noticeable decrease of the Mach number near the body, which is mainly due to temperature increase and flow deceleration because of the Joule heating and the ponderomotive force effect.

The study is carried out under financial support of the EOARD (ISTC projects) and Programs of the Presidium of RAS, P-12.

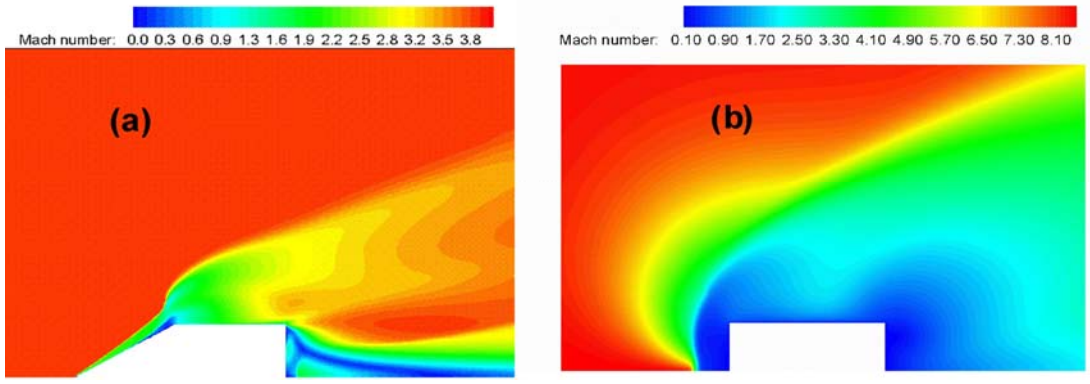

Fig. 1 *Mach number distributions around cone-cylinder and cylinder model bodies.*
(a) p_0=5 kPa; T_0=440 K; M_0=4.0; D=34 mm; L=40 mm; α=60°, (b) p_0=4.47 kPa; T_0=180 K; M_0=8.6; D=140 mm; L=100 mm.
MHD interaction parameters: B_0≈1 T, σ_0≈10^3S/m, I_0≈10^3A

10.5. EXPERIMENTS WITH CORONA DISCHARGE OVER LIQUIDS WITH ADDITIONS OF METALLIC MICRO PARTICLES

Bychkov V.L., Bychkov D.V., Volkov S.A., Chernikov V.A.
M.V. Lomonosov Moscow State University , Physical department.
bychvl@orc.ru

Abstract. New types of plasma macroscopic impact on surfaces of flammable and dielectric liquids are under investigation. Results of experimental works with corona discharges are represented, namely: gas discharge over tap water, alcohol and kerosene liquids with aluminum powder additions on their surfaces

Introduction

Recently has appeared an interest to discharges over a liquid surface. It is connected with application of such discharges at plasma assisted combustion, problems of water sterilization and ecology.

We consider an influence of the corona discharge on a liquid surface. Our experiments with corona discharges are a continuation of experiments [1-3]. The principle scheme of the experimental device is represented in Fig. 1.

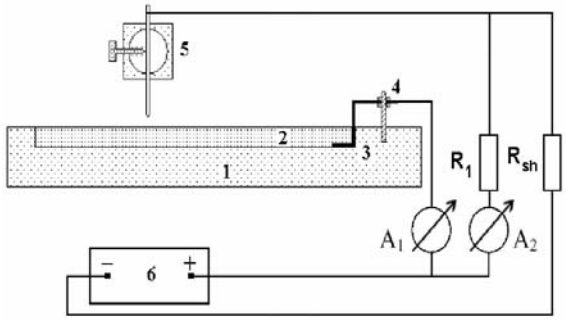

Fig. 1. *Principle scheme of the experimental set up. 1- Ditch, 2- Liquid (water, alcohol, kerosene), 3-Anode, 4- Post, 5- Cathode, 6-Power supply*

It consists of a ditch filled with a liquid (water, alcohol, kerosene), and electrical circuit. Upper electrode or a set of electrodes of diameter 0.9 mm (with radius of the tip-0.2 mm) or 2 mm (with radius of the tip-0.4 mm) was located at height 5-15 mm over a liquid surface. A distance between electrodes in upper multi-electrode formulation was 11 mm. Electrodes were under positive or negative potentials. Ditches were either metallic or dielectric. The metallic ditches were: cylindrical ∅ 130 mm, height 18 mm, rectangular 37×70×122 mm; the dielectric plastic ditch was: rectangular 45×95×130 mm.

A current in the discharge was measured by a milliamperemeter A_1, a voltage was measured by a chain consisting of resistance R_1 and a milliamperemeter A_2. We measured Ampere and Volt characteristics of the discharge and represent results in A-V^2 coordinates typical for corona discharges [4].

Experiments with kerosene

Experiments with application of dielectric dish showed that there was insignificant influence of the corona discharge on the surface of the liquid in case of the positive and negative potentials of the upper electrodes. The distance between the electrodes over the liquid surface was about 60 mm. At 10 kV was observed motion and shaking of the liquid near the electrode dipped in the liquid. At voltages between 10 and 30 kV current was in the range 05-3 mA.

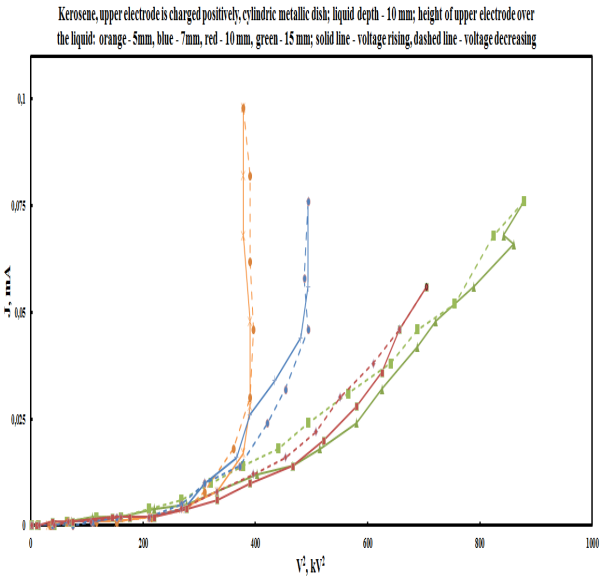

Fig. 2. *Ampere-Volt^2 characteristic of the corona discharge over kerosene at positive voltage of the upper electrode*

Results of experiments with the application of metallic dish are represented in Fig.3.2-3. Funnels appeared at voltages about 12-13 kV at both polarities of the upper electrodes. At voltages corresponding to the intermediate mode of the discharge with sharp rising of the current

appeared boiling of the liquid (see Fig.3.2-3). It continued even at transition of the discharge into the arc discharge with the glowing discharge current. Boiling was accompanied with appearance of the structures resembling bubbles. But unusual feature of these bubbles was that they did not burst. In Fig.3.4 we represent a photo of this phenomenon for negative corona over kerosene at using of the cylindrical metallic dish, at the upper electrode height over the liquid 8 mm, and the liquid depth 17 mm. This phenomenon requires additional investigations since we did not find its description in available literature.

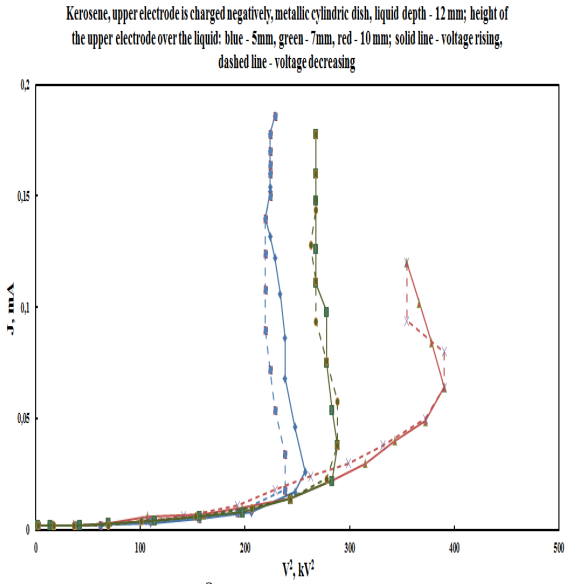

Fig.3. *Ampere-Volt^2 characteristic of the corona discharge over kerosene at negative voltage of the upper electrode*

Experiments with benzene.

Experiments have been carried out with a help of cylindrical metallic dish. We applied negative potentials of the upper electrodes. The distance between the electrodes over the liquid surface was about 7 mm. At 10 kV was observed motion and shaking of the liquid near the electrode dipped in the liquid. At voltages between 10 and 30 kV current was in the range 05-3 mA.

Results of experiments with the application of metallic dish are represented in Fig. 6. Funnels appeared at voltages about 12-13 kV of the upper electrodes. At voltages corresponding to the intermediate mode of the discharge at V>14 kV appeared boiling of the liquid. It continued even at transition of the discharge into the arc discharge with the glowing discharge current. Boiling was accompanied with appearance of the structures resembling bubbles. But bubbles were smaller than in case of kerosene. They didn't burst as in kerosene. In Fig. 5 we represent a photo of this phenomenon for the negative corona over benzene at using of the cylindrical metallic dish, at the upper electrode height over the liquid 7 mm, and the benzene depth 10 mm over water layer 30 mm thick.

Fig. 4. *A photo of the structure over kerosene surface at application of negative corona over kerosene at using of the cylindrical metallic dish, at the upper electrode height over the liquid 8 mm, and the liquid depth -17 mm.*

Fig. 5. *A photo of the structure benzene layer over water surface at application of negative corona at using of the cylindrical metallic dish, at the upper electrode height over benzene 7 mm, the depth of benzene 10 mm, and water depth -30 mm*

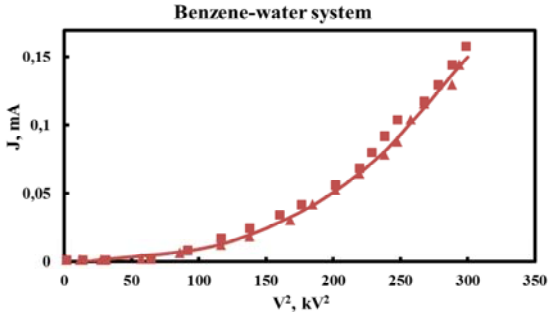

Fig. 6. *Ampere-Volt^2 characteristic of corona discharge over benzene at negative voltage of the upper electrode at using of the cylindrical metallic dish, at the upper electrode height over benzene 7mm, the depth of benzene 10 mm, and water depth -30 mm.*

Experiments with powder addition to liquids.

Having a goal of complex liquids investigation we have applied an aluminum powder in alcohol at negative upper electrode potential. Experiments were carried out with rectangular dielectric with sizes 12× 8 ×4 mm and metallic conical dishes (with the upper diameter109 mm and bottom diameter 91 mm ∅, at height 47 mm). We have used aluminum pigment powder of the mark PAP-1, GOST 5494.

Aluminum particles in the powder have the lamellar form and are covered thin oxide and a fatty film. Powder represents the product of silver-grey color which is not containing alien impurity visible with the naked eye. The bulk density of powder is about 0.15-0.30 g/cm^3, the maintenance of active aluminum - 85-93 %. The average thickness of petals is approximately 0.25-0.50 μm, and the average linear size is 20-30 μm.

We have added 1 and 2 ml of aluminum powder into a liquid. Because of hydrophobic property the powder was always on a surface of a liquid. It practically did not go down to a bottom of a dish with water, but at mixing it went down the bottom of a dish with kerosene. In all the liquids a film was created of aluminum powder. In water the powder was dissolved weakly- practically all the powder left on the surface, most part of it was removed from the water surface leaving a thin film. The aluminum powder was completely dissolved in alcohol and kerosene.

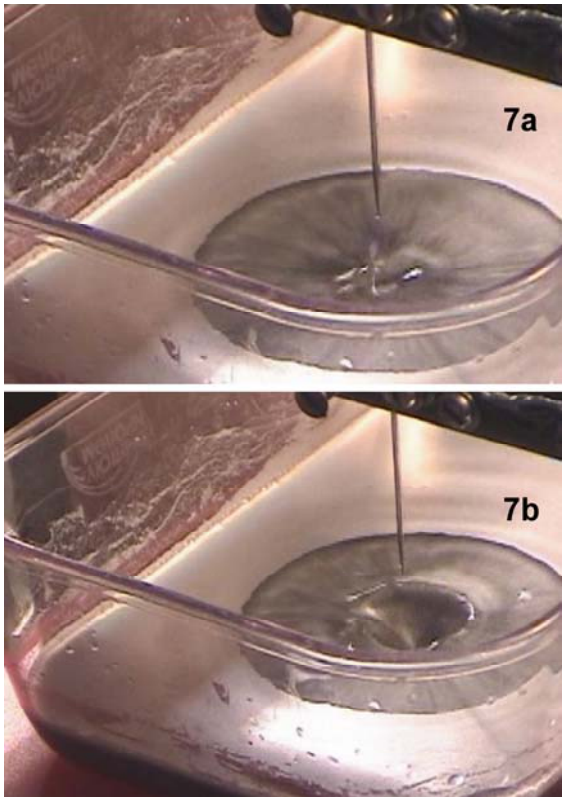

Fig.7. *Corona discharge over the alcohol surface. Negative polarity of the upper electrode. Alcohol depth is 12 mm. Height of the upper electrode over a surface of the liquid is 7 mm. 2 ml of Aluminum powder.*

In Fig.7 one can see a photo of the corona discharge over a surface of alcohol at negative polarity of the upper electrode, depth of alcohol is 12 mm, height of the upper electrode over a surface of the liquid is 7 mm, 2 ml of aluminum powder. To the left in Fig.7a one can see a funnel to the right in Fig. 7b one can see a column and traces of convective motion of the liquid.

In Fig.8 one can see a photo of the corona discharge over a surface of kerosene at negative polarity of the upper electrode, depth of kerosene is 12 mm, height of the upper electrode over a surface of the liquid is 7 mm, 2 ml of aluminum powder. One can see a funnel structure.

Fig. 8. *Corona discharge over kerosene surface. Negative polarity of the upper electrode. Kerosene depth is 12 mm. Height of the upper electrode over a surface of the liquid is 7 mm. 2 ml of Aluminum powder.*

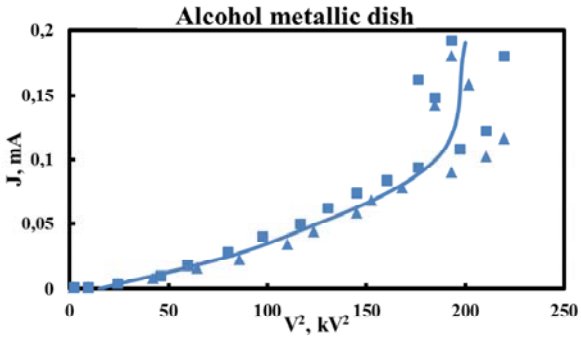

Fig.9. *Amper –Volt2 characteristic of corona discharge at negative polarity of the upper electrode. Alcohol, depth 12 mm, height of the upper electrode over a surface of the liquid is 7 mm, 1 ml of aluminum powder , a metallic dish.*

In Fig.9 one can see Amper –Volt^2 characteristic of the corona discharge at negative polarity of the upper electrode. Alcohol, depth 12 mm, height of the upper electrode over a surface of

the liquid is 7 mm, 1 ml of aluminum powder , metallic dish.

In Fig.10 one can see Amper –Volt^2 characteristic of the corona discharge at negative polarity of the upper electrode. Alcohol, depth 12 mm, height of the upper electrode over a surface of the liquid is 7 mm, 1 ml of aluminum powder , dielectric dish.

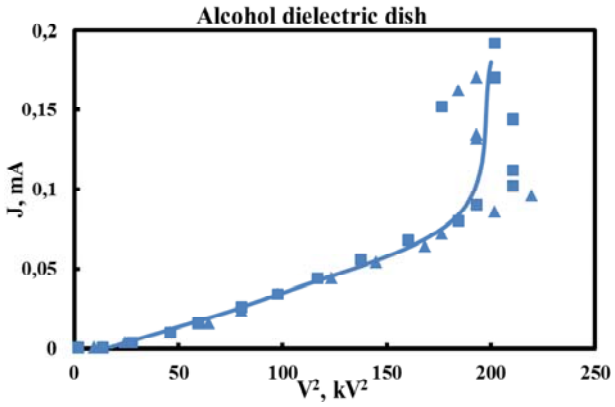

Fig. 10 *Amper –Volt 2 characteristic of corona discharge at negative polarity of the upper electrode. Alcohol, depth 12 mm, height of the upper electrode over a surface of the liquid is 7 mm, 1 ml of aluminum powder, dielectric dish.*

In Fig.11 one can see Amper –Volt^2 characteristic of the corona discharge at negative polarity of the upper electrode. Kerosene at 1 and 2 ml of aluminum powder in metallic dish.

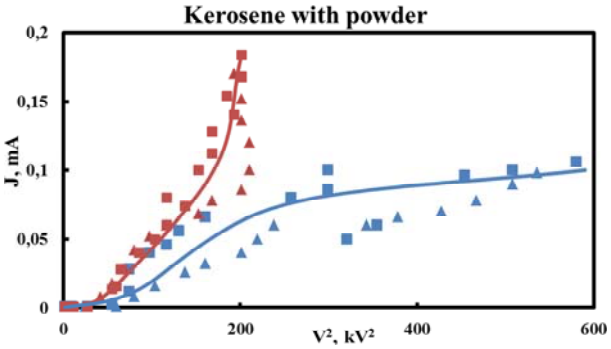

Fig. 11. *Amper –Volt 2 characteristic of the corona discharge at negative polarity of the upper electrode. Kerosene at 1 and 2 ml of aluminum powder in metallic dish.*

The analysis of measurement results shows, that addition of the aluminium powder in alcohol practically does not influence on Ampere-Volt^2 characteristics at negative polarity of the top electrode. Occurrence of funnels and columns is thus observed. Thus in the photo of Fig.7 it is clearly visible a convective liquid movement in the volume .

In the case of kerosene addition of the aluminium powder leads to change of Ampere-Volt^2 characteristics. Thus the increase in volume of a powder from 1 ml to 2 ml leads to sharp growth of the Ampere-Volt^2 characteristic that speaks about improvement of electric conductivity of such a dielectric liquid as kerosene. In kerosene in these conditions also appears bubbles which are formed at the bottom of metal dishes which has been used in these experiments.

Conclusions

Creation of corona discharges over kerosene, benzene over water, alcohol and kerosene admixture with aluminum powder has been realized.

Experiments with corona discharges helped to clarify modes of realization of discharges and their connection with appearance of funnels and columns on the surfaces of liquids.

Experiments with corona discharges over kerosene and benzene showed that at application of lower metallic electrodes (in the liquid) under the upper electrode in air (at minimal distance between them) allows to realize the corona discharge over these liquids. It was also found an unknown form of liquid kerosene and benzene behavior in a form of bubbled structure under the external electrical field impact.

Experiments with corona discharges over liquids with addition of powder have shown that powders can visualize processes in the liquids and on their surface. In particular they showed convective motion in a volume of alcohol. They indicated that bubbles in case of kerosene and benzene appear on the bottom of the dish. Addition of powders to highly dielectric liquid as kerosene has lead to change of its Ampere-Volt^2 characteristic that speaks about an improvement of electric conductivity of such liquids.

Acknowledgement

The work is performed with the financial support of EOARD (CRDF # RUP-1514-MO-06).

References

1. Aleksandrov A.F., Bychkov V.L., Ershov A.P., Kostiuk A.A., Chernikov V.A. AIAA-2008-1402.46-th AIAA Aerospace Sciences Meeting and Exhibit. 7-10 January 2008, Reno, Nevada.
2. Bychkov V., Chernikov V., Ershov A., Kostiuk A., Surkont O., Esakov I.I. Plasma jets over a surface of a liquid. AIAA-2009-

0693. 47th AIAA Aerospace Sciences Meeting. 5-8 January 2009. Orlando World Center Marriott. Orlando. Florida.
3. Bychkov V., Chernikov V., Ershov A., Esakov I.I., Kostiuk A.A. Corona discharge over a surface of a liquid. AIAA-2009-1554. 47th AIAA Aerospace Sciences Meeting. 5-8 January 2009. Orlando World Center Marriott. Orlando. Florida.
4. Raizer Yu.P. Gas discharge physics. Nauka. Moscow. 1992.

11.1. EXPERIMENTAL INVESTIGATION ON THE ENERGY TRANSFER IN A DBD PLASMA ACTUATOR FOR AIRFLOW CONTROL

Carlo A. Borghi, Andrea Cristofolini, and Gabriele Neretti
Department of Electrical Engineering of the University of Bologna, Bologna, 40136, Italy.

Abstract. In this work two dielectric barrier discharge fluid dynamic actuators have been experimentally investigated. A planar electrode pair separated by a dielectric constitutes each actuator. Two different geometries and dielectric materials have been utilized. Several a.c. supply voltages and frequencies have been utilized in order to deliver to the plasma the same amount of average power. The energy transfer mechanism has been investigated. This has been done in tests using same average power. The visualization of the vortex generated inside the plasma during the discharge ignition phase and in the steady regime has been obtained by using Schlieren diagnostics technique. Vortex propagation velocities for both the actuators in all supply conditions have been derived. The actuator influence region has been visualized and compared with the influence area obtained by Pitot velocity measurements performed at different distances from the upper electrode.

I. Introduction

The interest in active flow control i.e. the ability to directly manipulate a flow in order to create a desired change, has showed a quick growth in the last decade [1]. The application of a Dielectric Barrier Discharge fluid-dynamic (DBD) actuator in the aerodynamic flow control is in continuous development. Many experimental works have dealt on the application of Electro Hydro Dynamic (EHD) actuators applied in the aeronautical [2-10] and astronautical [11,12] fields, and in the turbine blades area [13,14]. The development of the discharge and the establishment of the EHD interaction have been investigated in several numerical works [15-19] too. In particular, the ability of the actuator to prevent or to induce separation and the possibility to reduce the drag and to enhance the lift of airfoils have been demonstrated.

The plasma jet generated by a DBD fluid-dynamic actuator is thus able to alter the velocity inside the boundary layer and can modify the interaction between fluid and body surface (a wing or a blade) without moving parts. Hence the EHD phenomenon allows a direct conversion from electric into kinetic energy with response times that can be considered negligible in comparison with the characteristic time of the fluid system. Furthermore a fully composed electric actuator with no moving parts could lead to reduced size, to reduce the input power and to enhance the flexibility of use.

In this work we present an experimental investigation aimed to achieve a better knowledge of the momentum transfer process involved in the EHD phenomenon. The visualization of the wall-jet generated by the actuator during the ignition phase and the steady regime using the Schlieren technique has carried out. This optical diagnostic is based on the variation in the refractive index of the medium in which the light beam propagates and presents in its complete non-intrusiveness its greatest value 20]. Schlieren imaging allows flow visualization without the exploitation of external seeding as occurring for Particle Image Velocimetry (PIV). In PIV diagnostic the use of right seeding and the exact concentration of the seeding can be a long and tedious work. Moreover seeding particles may get charged in the plasma and may depict the flow incorrectly and may affect the plasma dynamics and the gas flow. The Schlieren technique, applied to a DBD fluid dynamic actuator, is "self seeded" by the density gradients created by the hot wall-jet [21,22].

In a previous work [23] we pointed out that the velocity induced by a DBD actuator in the boundary layer, measured flush to the wall, is mainly related to the active power delivered by the power supply to the electrodes. A desired velocity can be reached with a defined amount of average power obtained with different supply voltage and frequency values. For dielectric materials of a small thickness, when very high voltages are applied, high efficiencies are reached. These results have been confirmed by measurements performed on actuators realized with different geometries, dielectric materials and a.c. supply conditions.

In the present study the transfer energy mechanism has been investigated. This has been done in tests which use the same average power. The morphology and the propagation velocity of the vortexes, generated in the ignition phase of the discharge, have been carried out by means of a Schlieren technique. Schlieren images of the boundary layer during the steady state operation are useful to visualize the region in which the actuator acts. This region has been then compared with the velocity profiles measured by Pitot scans.

The experimental data obtained are compared with the theoretical achievements available in the literature.

II. Experimental setup

All the performed experiments have been realized with Single Dielectric Barrier Discharge actuators immersed in still atmospheric pressure air. The actuator configuration is reported in Figure 1.

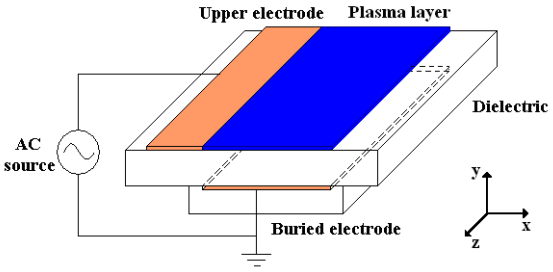

Figure 1. *DBD actuator geometry.*

The electrodes are made of copper strips with a thickness of 0.08mm. The upper electrode is 5mm wide. Two different materials have been used as dielectric: 2mm thick teflon sheet and 4 layers of 60µm thick kapton tape. When teflon is used, the buried electrode is 7mm wide, when kapton tape is adopted the buried electrode is 10mm wide. In both cases no gap is present. The spanwise length of the electrodes (z direction of Figure1) is 50mm.

The actuators have been fed by the power supply schematized in Figure 2. An HP-Agilent 33120A signal generator produces an AC signal delivered to an Elgar AC Amplifier able to provide voltages up to 260V with apparent powers up to 3kVA. A ferrite High Voltage Transformer increases then the voltage to the desired value.

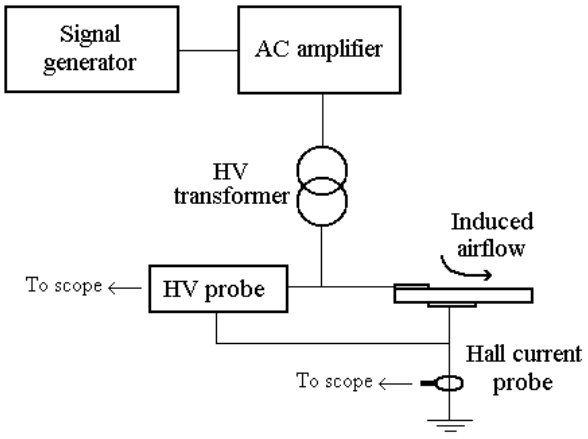

Figure 2. *Power supply electrical scheme.*

III. Diagnostics

Time resolved values of the electric voltage *v(t)* applied to the electrodes and of the electric discharge current *i(t)* have been measured. A Tektronix P6015A capacitive compensated high voltage probe, with a bandwidth up to 75MHz, is used to measure *v(t)*. A Tektronix TCP312 Hall current probe, with a bandwidth up to 100MHz, is utilized to measure *i(t)* (Figure 2). Therefore the value of the instantaneous power $p(t)=v(t)i(t)$ feeding the discharge is derived. The average power absorbed is obtained as the average of *p(t)* in a period of the AC supply waveform.

Schlieren images have been captured by a Z-type configuration setup (Figure 3).

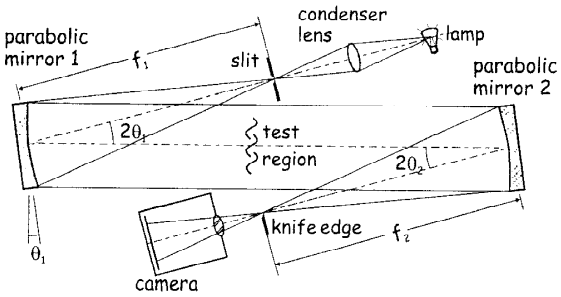

Figure 3. *Z-type configuration Schlieren setup (from reference [20]* ***Ошибка! Источник ссылки не найден.*** *pag. 42).*

The light source is a tungsten halogen low voltage lamp equipped with a rear reflector. The condenser is a Schneider-Kreuznach Xenon 40 mm double-Gauss lens with a focal ratio of *f/1.9*. The light beam is reflected by two off-axis parabolic mirrors of a diameter of 138 mm and a focal ratio of *f/3.5*. The knife edge has been positioned parallel to the actuator surface so that the Schlieren diagnostic can be sensitive to higher density gradients. The images are detected by a PCO CCD camera characterized by a super video graphics array (SVGA) resolution and a pixel size of 6µm x 6µm. The peak quantum efficiency is 55% at 380nm.

Velocity profiles have been determined by means of a glass Pitot tube moved by a step motor with linear resolution of 0.03mm. The Pitot tube has been connected to a DCAL401 Sursense ultra low pressure sensor with a sensitivity of 32mV/Pa.

IV. Discussion of the results

The electrical supply conditions that guarantee the same active power consumption of 140 W/m for both the kapton tape and teflon actuators are reported in Table I.

Table I. Electrical supply conditions.

Average Power [W/m]	Dielectric material	Voltage peak to peak [kV]	Frequency [kHz]
140	teflon	35	5
		27	8
	Kapton tape	14.5	5
		11.4	10
		10.4	15

In the kapton tape actuator the observed plasma covers the firsts 6 mm of the dielectric area over the bottom electrode. In the teflon actuator the plasma completely overlay the dielectric region of 7 mm over the bottom electrode.

Velocity profiles ad related standard deviations of the teflon actuator acquired with the Pitot probe at the end of the plasma region in the different supply conditions are reported in Figure 4. The "y" direction is perpendicular to the actuator surface as depicted in Figure 1. The measurements start at a distance equal to 0.5mm which matches to the Pitot tube axis when the probe is laid on the dielectric surface. This distance corresponds thus to the "zero heightt" of the Pitot tube.

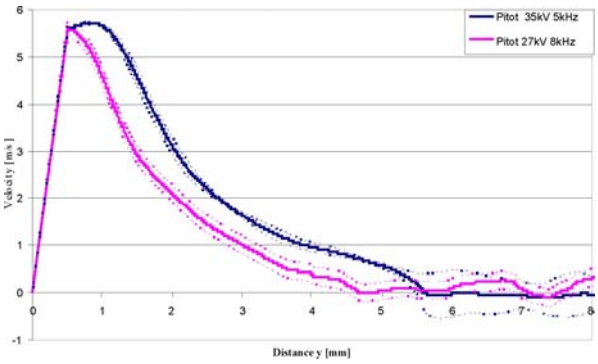

Figure4. *Pitot velocity profiles and standard deviations for teflon actuator at the end of the plasma region.*

Figure 4 shows as at "zero height" the velocities measured in the two supply conditions at the same average power are the same. However for the highest voltage condition the region in which the actuator expresses its action is wider.

A similar behavior can be noticed for the kapton actuator too. In Figure 5 the velocity profiles and the related standard deviations of the kapton tape actuator, acquired with the Pitot probe at the end of the plasma region in the different supply conditions are displayed.

For the two supply conditions at lower voltage, the speed at "zero height" is the same. The main difference is the thickness of the region in which the actuator shows its action that is larger for the condition at higher voltage. The supply condition at the highest voltage (14.5 kV) is characterized by the highest velocities and the larger perturbing area.

The velocity profiles obtained for kapton tape and teflon actuators demonstrate that the latter is more efficient. The reason could be explained by different discharge regimes between teflon and kapton. More inhomogeneous plasma is generated when kapton tape is used. It is well known that when visible streamers are produced the efficiency of the actuator decreases because a larger amount of active power is converted in heat and not in net thrust [23].

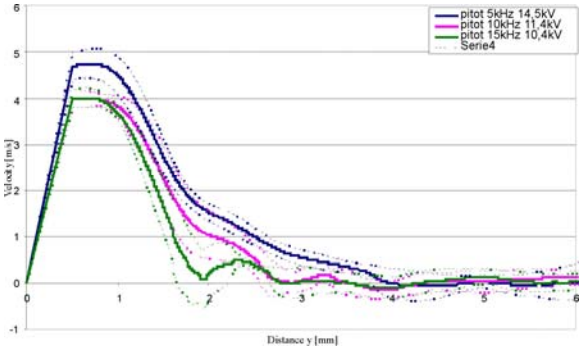

Figure5. *Pitot velocity profiles and standard deviations for kapton tape actuator at the end of the plasma region.*

A visualization of the vortexes generated by the actuator during the ignition phase and the wall jet reached in the steady regime, has been carried out by means of Schlieren imaging. The actuator has been positioned in the test area with the spanwise direction along the "z" axis and the surface parallel to the "*x*" direction (Figure 1). In order to detect the vortex propagation, the CCD camera has been triggered with increasing delay times. In this way, each image correspond as many discharge ignitions. The validity of this measurement methodology has been checked verifying the superposition of several images acquired at the same delay time. The exposure time of the camera has been set to 1ms.

In Figure 6 a comparison between Schlieren images related to the teflon actuator in the two supply conditions at different delay times is shown.

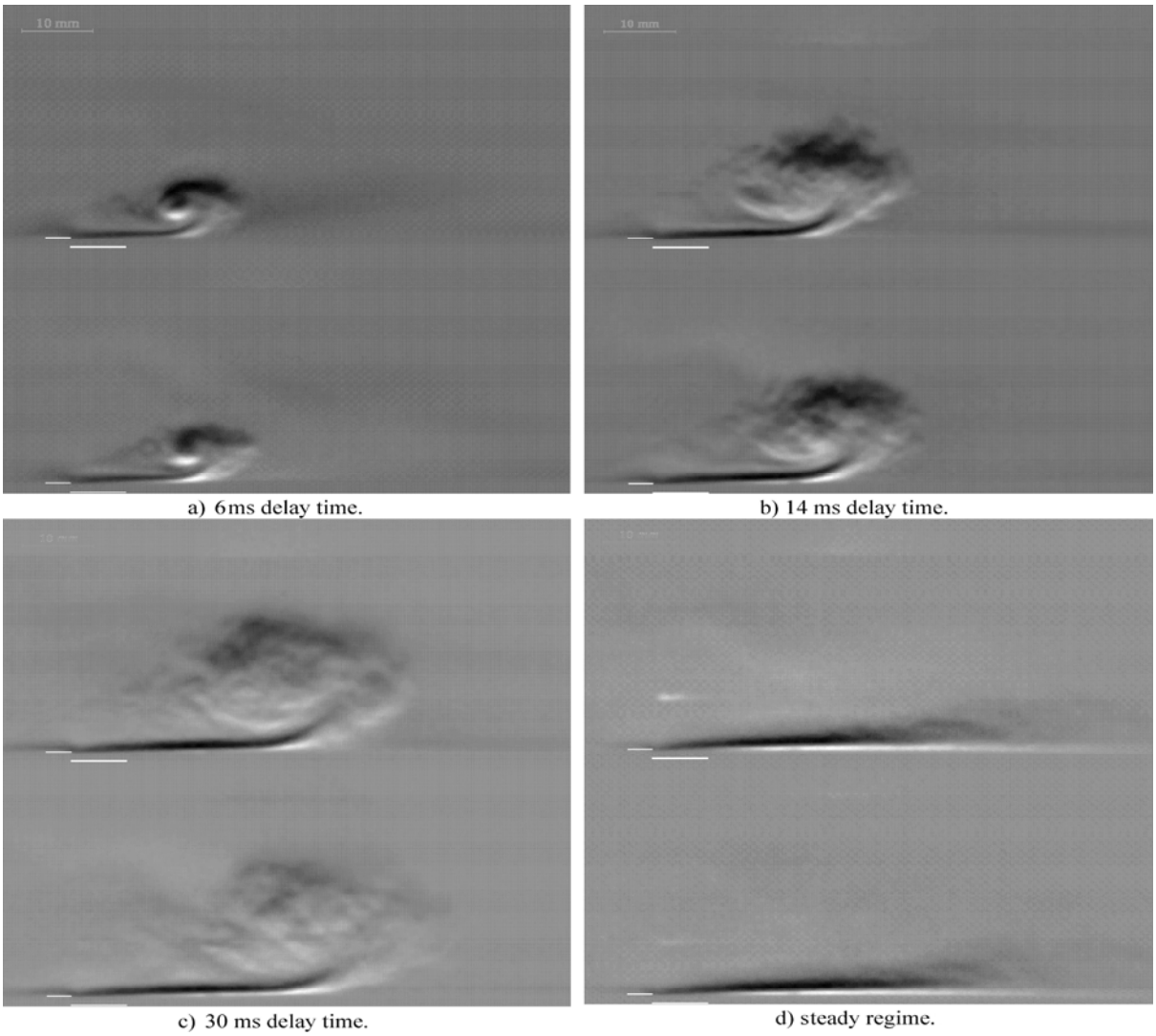

Figure 6. *Schlieren images of teflon actuator jet at different delay times.*

In the top of each picture there is the Schlieren image of the 27 kV and 8 kHz supply condition, in the bottom the 35 kV and 5 kHz one. The white lines represent the electrode position and the green line gives the scale proportion for a length of 10 mm. For a fixed delay time, vortexes generated in the two supply conditions are very similar. The vortex displacement velocity for both the supply conditions is around 1.5 m/s, as calculated comparing the images with 6ms and 14ms delay times. The vortex velocity extrapolated from the 30 ms and 14ms images is equal to 1m/s for the highest supply voltage and 0.8 m/s for the lowest one. The vortex generated with the actuator driven at higher voltage is thus little bit faster that the other one produced with lower voltage. This trend is the same shown by the Pitot velocity profiles carried out in the steady regime and reported in Figure 4. The two images with the actuator operating in the steady regime clearly show the hot wall jet that propagates away from the upper electrode till the end of the picture, thus for almost 70mm.

The same analysis has been carried out for the kapton tape actuator. The images captured for the two conditions at lower voltages (10.4 kV and 11.4 kV) have shown that the fluidynamic evolution of the vortexes is the same. This behaviour is in agreement with the velocity profiles obtained in the steady regime (Figure 5). In Figure 7 a comparison of the produced eddies at 12 ms and 30 ms delay times for 10.4 kV and 15 kHz (top) and 11.4 10 kHz (bottom) is displayed. The propagation velocity of the vortexes is around 0.65 m/s within the firsts 15 ms and then decreases at 0.55 m/s.

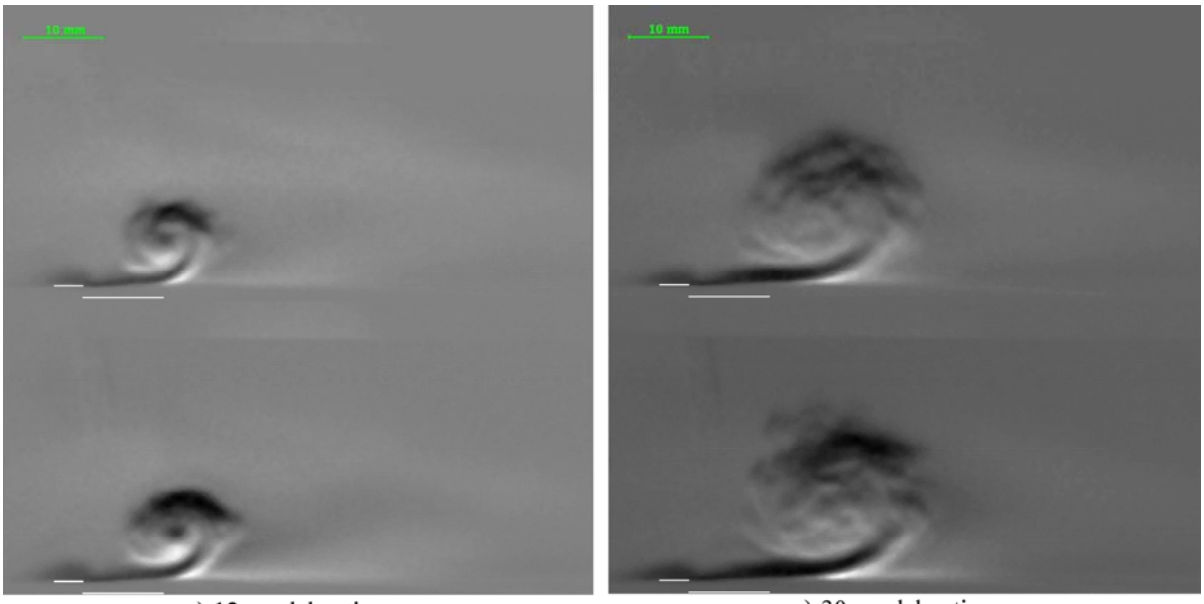

a) 12 ms delay time. c) 30 ms delay time.

Figure 7. *Schlieren images of kapton tape actuator jet for the two low voltage supply conditions at different delay times.*

In Figure 8 the vortex evolution for the kapton tape actuator driven at 11.4 kV and 10 kHz (top) and 14.5 kV and 5 kHz (bottom) at 6 ms, 14 ms, 30ms and steady regime is reported.

For the higher voltage supply condition, the propagation velocity of the vortex is around 1.6 m/s within the firsts 15 ms and then decreases at 0.6 m/s. This higher propagation velocity is reflected in the pitot velocity profiles displayed in Figure 5 too. The steady regime images state that the influence region of the actuator propagates for about 55mm away from the end of the upper electrode.

Comparisons between the area in which the actuator manifests its influence, obtained by the images captured with the steady state operation and Pitot scans have been realized for the teflon sheet actuator. The choice fell on this material because its velocity is more constant in time [23] and the Schlieren images present a more uniform background. The comparisons have been performed comparing the velocity profile along a line perpendicular to the surface actuator ("*y*" direction in Figure 1), at a certain distance from the upper electrode, and the pixel intensities of the Schlieren image along the same line. Three different lines at distances of 7, 20 and 30 mm from the exposed electrode have been selected (Figure 9).

The pixel intensities trend along the line at 7 mm is reported in Figure 10. Distance "0" corresponds to the actuator surface. The plot clearly shows how the influence region is about 4 mm for the 27 kV – 8 kHz supply condition and 5 mm for the 35 kV 5 kHz one. The Pitot velocity profile displayed in Figure 4 denotes a perturbing region of 4.8 mm for the low voltage condition and 5.8 mm for the higher one. Absolute values are different but proportions are maintained.

Figure 11 and Figure 12 report pitot velocity profiles with associated standard deviations and pixel intensities for the teflon actuator along the 20 mm and 30 mm lines respectively. Pitot scans confirm how the supply condition at higher voltage assures larger influence region. This behaviour is supported by the Schlieren measurements.

V. Conclusions

The fluid dynamic effects of two different DBD actuators supplied with the same average power have been evaluated using fluid dynamic and optical diagnostics.

Pitot velocity profiles have been measured at different distances away from the upper electrode, with the actuator operated in steady regime. For low supply voltages the speed at 'zero height' is roughly the same for all the conditions. However the region in which the actuator manifests its influence is higher for higher voltages. When larger voltages are applied also the velocity at 'zero height' is higher. Velocity profiles demonstrate a better efficiency of the teflon sheet actuator.

A Schlieren diagnostic, able to detect the morphology of the vortexes generated by the

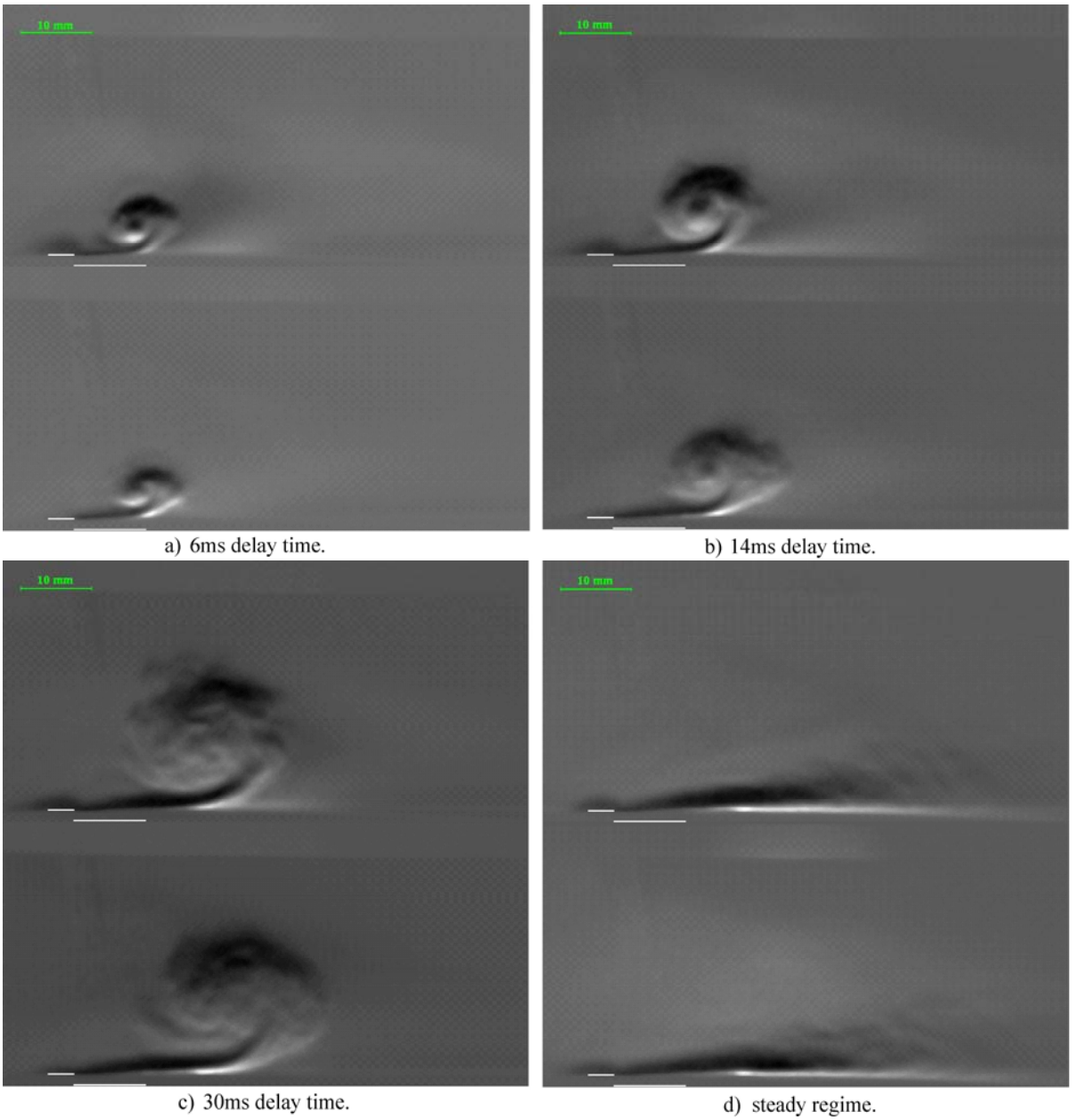

Figure 8. *Schlieren images of kapton tape actuator jet for the two high voltage supply conditions at different delay times.*

ignition phase of the discharge has been used. The acquisition of images in succession allows to the determination of the vortex propagation velocity. The vortex behavior found analogies in the Pitot scans. The images of the wall-jet generated by the actuator in the steady regime have been used to detect the region in which the actuator acts. An evaluation of the width of the influence area performed by Pitot tube scans and assessed by pixel intensities has been carried out along three different lines. Fluid dynamic and optical diagnostics show similar results. In the next work we will present further studies centered on the comparison between Pitot velocity profiles and pixel intensities.

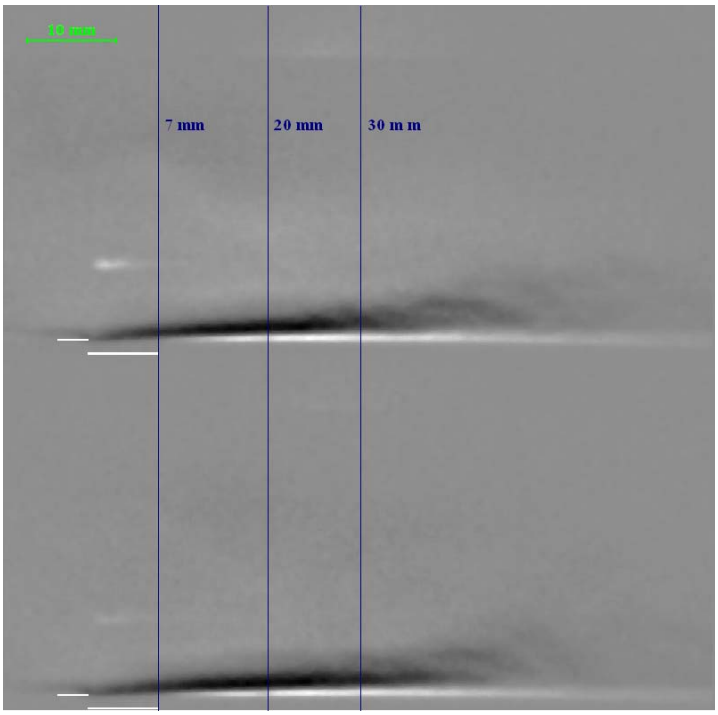

Figure 9. *Schlieren images of the teflon actuator in steady regime at 35kV 5kHz (top) and 27kV 8kHz (bottom). Outlined in blue are the three lines used for the comparisons.*

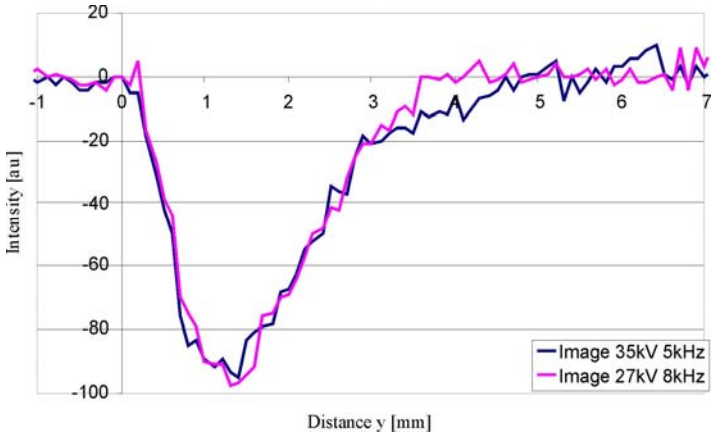

Figure 10. *Pixel intensities along the line at 7 mm for teflon actuator at the two supply conditions.*

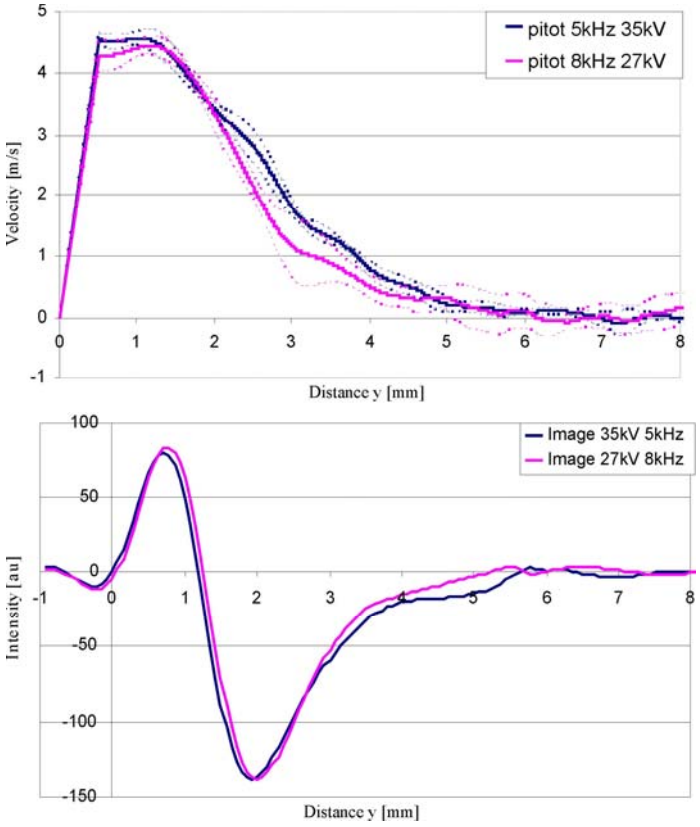

Figure 11. *Teflon sheet actuator. Pitot velocity profile (top) and pixel intensities (bottom) along the line at 20mm.*

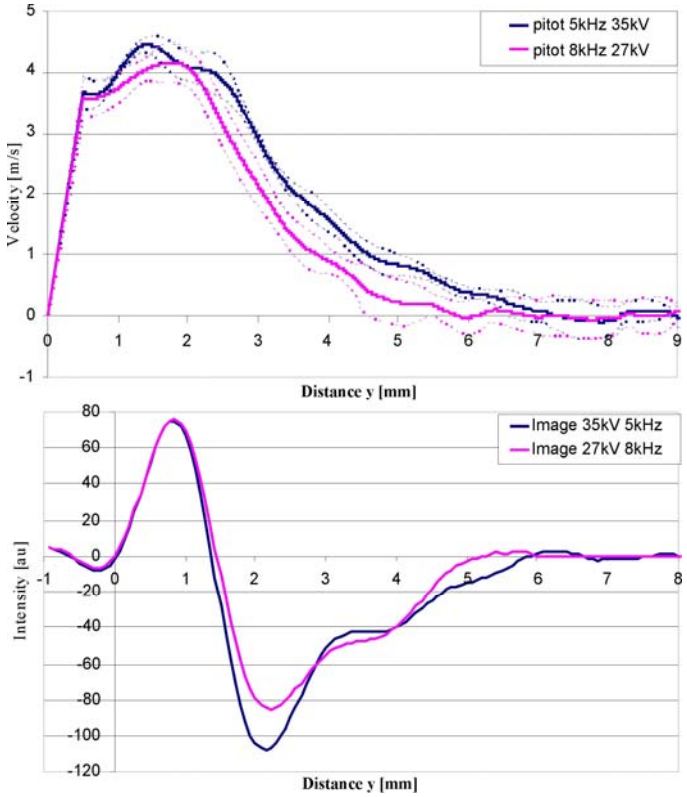

Figure 12. *Teflon sheet actuator. Pitot velocity profile (top) and pixel intensities (bottom) along the line at 30mm.*

References

1. Gad-El-Hak M 2000. "Flow Control". Cambridge University Press, 2000.
2. Cristofolini, A., Neretti, G., and Borghi, C.A., "EHD Plasma Actuators Utilizing a Dielectric Barrier Discharge", 39th AIAA Plasmadynamics and Lasers Conference, Seattle, WA USA, June 2008, Paper AIAA 2008-4286.
3. Borghi, C.A., Carraro, M.R., Cristofolini, A., and Neretti, G., "Experimental Investigation on the EHD Interaction Induced by a Dielectric Barrier Discharge," Journal of Applied Physics, Vol. 103, pp. 063304-1 - 063304-11, ISSN: 0021-8979, 2008.
4. Cristofolini, A., Borghi, C.A., Carraro, M.R., and Neretti, G., "A Study of The Electrical Supply System of a Barrier Discharge for EHD Flow Acceleration,", 38th AIAA Plasmadynamics And Lasers Conference, Miami, FL USA, June 2007, Paper AIAA 2007-4136.
5. Borghi, C.A. Carraro, M.R., Cristofolini, A., and Neretti, G., "A Surface Barrier Discharge System for EHD Flow Acceleration," Proc. of the 7th Workshop on Magneto-Plasma-Aerodynamics in Aerospace Applications, Moscow, April 2007.
6. J. Pons, E. Moreau, and G. Touchard. "Electrical and aerodynamic characteristics of atmospheric pressure barrier discharges in ambient air". Proc. ISNTPT, pages 370-410, 2004.
7. T. Corke, D. Cavalieri, and E. Matlis. "Boundary layer instability on a sharp cone at mach 3.5 with controlled input". AIAA-2002-0350, 2001.
8. D. Opaits, G. Neretti, S. Zaidi, M. Shneider, R. Miles, A. Likhanskii, and S. Macheret, "DBD Plasma Actuator Driven by a Combination of Low Freqeuncy Bias Voltage and Nanosecond Pulses", 46th AIAA Aerospace Sciences Meeting and Exhibit, Reno Nevada, Jan 7-10, 2008, AIAA-2008-1372.
9. M.P. Patel, Z.H. Solwe, T.C. Corke, and C. He. Autonomous sensing and control of wing stall using a smart plasma slat. 44th AIAA Aerospace Sciences Meeting and Exhibit, AIAA 2006-1207, 2006.
10. M.L. Post and T.C. Corke. Flow control with single dielectric barrier plasma actuators. 35th AIAA Fluid Dynamics Conference and Exhibit, AIAA 2005-4630, 2005.
11. B. Arad, Y. Gazit, and A. Ludmirsky. "A sliding discharge device for producing cylindrical shock waves". J. of Appl. Physics, 20: 360-367, 1987.
12. S.B. Leonov and D.A. Yarantsev. "Mechanisms of flow control by nearsurface electrical discharge generation". AIAA-2005-0780, 2005.
13. J. Huang. "Documentation and control of flow separation on a linear cascade of Pak-B blades using plasma actuators". PhD thesis, University of Notre Dame, 2005.
14. D.K. Van Ness II, T.C. Corke, and S.C. Morris. "Turbine tip clearance flow control using plasmas actuators". AIAA meeting, AIAA-2006-0021, 2006.
15. C.S. Kalra, M.N. Shneider, and R.B. Miles. "Numerical study of shockwave induced boundary layer separation control using plasma actuators". 46th AIAA Aerospace Science Meeting and Exhibit, AIAA-2008- 1095, 2008.
16. J.P. Boeuf and L.C. Pithford. "Electrohydrodynamic force and aerodynamic flow acceleration in surface dielectric barrier discharge". Journal of Applied Physics, 97-103307, 2005.
17. T.C. Corke, B. Mertz, and M.P. Patel. Plasma flow control optimized airfoil. 44th AIAA Aerospace Sciences Meeting and Exhibit, AIAA 2006-1208, 2006.
18. D.V Gaitonde, M.R. Visbal, and S. Roy. A coupled approach for plasma-based ow control simulations of wing sections. 44th AIAA Aerospace Sciences Meeting and Exhibit, AIAA 2006-1205, 2006.
19. A. Likhanskii, m. Shneider, D. Opaits, R.B. Miles and S. Macheret, "Numerical modeling of DBD plasma actuators and the induced air flow", 38th AIAA Plasmadynamic and Laser Conference, Miami, Florida, June 25-28 2007.AIAA-2007-4533.
20. G.S. Settles, "Schlieren and Shadograph Techniques", Springer 2001.
21. R. Sosa, E. Arnaud, G. Artana, "Schlieren Image Velocimetry applied to EHD flows", International Simposium on Electrohydrodonamics (ISEHD), Buenos Aires, Argentina, 2006.
22. D. Opaits, A. Likhanskii, G. Neretti, S. Zaidi, M. Shneider, R. Miles and S. Macheret, "Experimental Investigation on Dielectric Barrier Discharge Plasma Actuators Driven by Repetitive High-Voltage Nanosecond Pulses with DC or Low Frequency Sinusoidal bias", Journal of Applied Physics 104, 043304 (2008).
23. Borghi, C.A. Carraro, M.R., Cristofolini, A., Neretti, G., Gurioli A. and Pertile R., "Experimental results in DBD plasma actuators for airflow control", 41st Plasmadynamics and Lasers Conference, Chicago, Illinois, June 28-1, 2010. AIAA-2010-4763

11.2. DETERMINATION OF THE VELOCITY PROFILE IN A DBD PLASMA FLOW BY MEANS OF SCHLIEREN IMAGING.

Carlo A. Borghi, Andrea Cristofolini, Gabriele Neretti
Department of Electrical Engineering of the University of Bologna, Bologna, 40136, Italy.
Carlo Angelo Borghi <ca.borghi@unibo.it>

Abstract. In this work a dielectric barrier discharge fluid dynamic actuator has been experimentally investigated. A planar electrode pair separated by a dielectric constitutes the actuator. Four a.c. supply voltages at a fixed frequency have been utilized in order to generate different fluid dynamic regimes in still air. The visualization of the hot wall jet generated by the Electro Hydro Dynamic interaction has been achieved by using Schlieren diagnostics technique. Pitot velocity profiles have been obtained at several distances from the upper electrode. Along the same lines the integral of the pixel intensities of the Schlieren image has been calculated. The obtained function matches, with good agreement, with the Pitot velocity profile for all the distances in all the supply conditions.

I. Introduction

The interest in active flow control, i.e. the ability to directly manipulate a flow in order to create a desired change, has showed a quick growth in the last decade [1]. The application of a Dielectric Barrier Discharge (DBD) fluid-dynamic actuator in the aerodynamic flow control is in continuous development. Many experimental works have dealt on the application of Electro Hydro Dynamic (EHD) actuators applied in the aeronautical [2-11] and astronautically [12,13] fields, and in the turbine blades area [14,15]. The development of the discharge and the establishment of the EHD interaction have been investigated in several numerical works 16-20] too. In particular, the ability of the actuator to prevent or to induce separation and the possibility to reduce the drag and to enhance the lift of airfoils have been demonstrated.

The plasma jet generated by a DBD fluid-dynamic actuator is thus able to alter the velocity inside the boundary layer and can modify the interaction between fluid and body surface (a wing or a blade) without moving parts. Hence the EHD phenomenon allows to a direct conversion from electric into kinetic energy with response times that can be considered negligible in compare with the characteristic times of the fluid system. Furthermore a fully composed electric actuator with no moving parts could lead to reduced size, low input power and flexibility in the use.

In this work we present an experimental investigation finalized to the visualization of the actuator wall-jet during the steady regime by using the Schlieren technique. This optical diagnostics is based on the variation in the refractive index of the medium in which the light beam propagates and presents in its complete non-intrusiveness its greatest value [21]. Schlieren imaging allows flow visualization without the exploitation of an external seeding as occurs for Particle Image Velocimetry (PIV). In PIV diagnostics the use of the right kind and the exact concentration of the seeding can be a long and tedious work. Moreover the seeding particles may get charged in the plasma and may not only depict the flow incorrectly but may also affect the plasma dynamic and the gas flow. The Schlieren technique, applied to a DBD fluid dynamic actuator, is "self seeded" by the density gradients created by the hot wall jet [22,23].

In a previous work [24] we developed a Schlieren tool able to visualize with high accuracy the density gradients generated by a DBD plasma actuator. Images of the vortexes produced during the discharge ignition phase and the wall jet established during the steady regime have been captured. In particular we observed how the actuator influence region can be esteemed both by observing the images obtained in steady regime and by measurements performed with Pitot tube scans.

In this study we focus our attention to the values of image pixel intensities in the influence region. In particular we try to figure out if relations between trends of pixel intensities along directions perpendicular to the actuator surface and Pitot velocity profiles can be assessed. The presented Schlieren technique and the analysis of the pixel intensities of the actuator influence region bring both to qualitative and quantitative measurements leading to new possible scenarios on the use of this non-intrusive optical technique.

II. Experimental setup

All the performed experiments have been realized with Single Dielectric Barrier Discharge actuators immersed in still atmospheric pressure air. The actuator configuration is reported in Fig.1.

The electrodes are made of copper strips with a thickness of 0.08mm. The upper electrode is 5mm wide. A 2mm thick teflon sheet has been adopted as dielectric material. The buried electrode is 7mm wide. In both cases no gap is present. The spanwise

length of the electrodes (*z* direction of Fig.2) is 50mm.

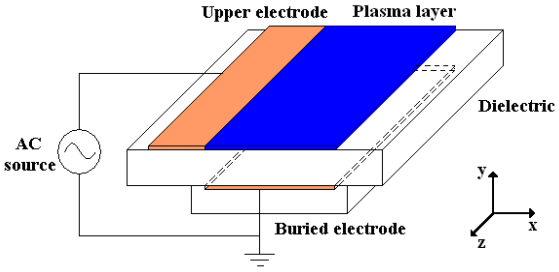

Fig.1. *DBD actuator geometry.*

The actuators have been fed by the power supply schematized in Fig.2. An HP-Agilent 33120A signal generator produces an AC signal delivered to an Elgar AC Amplifier able to provide voltages up to 260V with apparent powers up to 3kVA. A ferrite High Voltage Transformer increases then the voltage at the desired value.

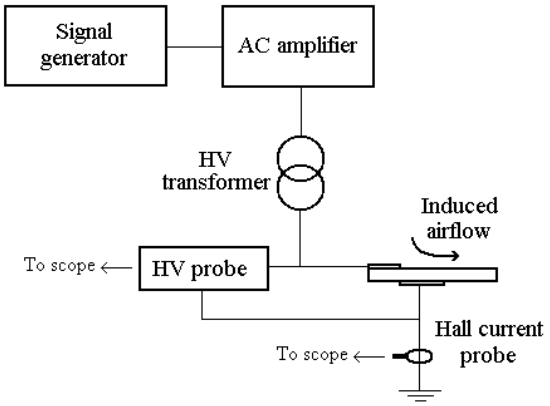

Fig.2. *Power supply electrical scheme.*

III. Diagnostics

Time resolved values of the electric voltage *v(t)* applied to the electrodes and of the electric discharge current *i(t)* have been measured. A Tektronix P6015A capacitive compensated high voltage probe, with a bandwidth up to 75MHz, is used to measure *v(t)*. A Tektronix TCP312 Hall current probe, with a bandwidth up to 100MHz, is utilized to measure *i(t)* (Fig.2). Therefore the value of the instantaneous power $p(t)=v(t)i(t)$ feeding the discharge is derived. The average power absorbed is obtained as the average of *p(t)* in a period of the AC supply waveform.

Schlieren images have been captured by a Z-type configuration setup (Fig.3)

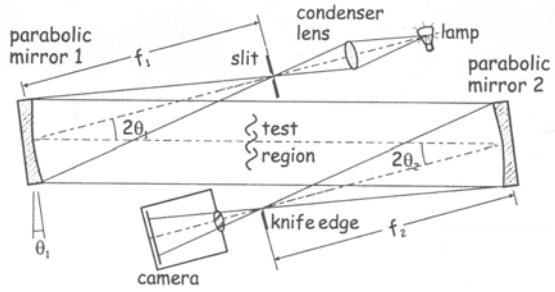

Fig.3. *Z-type configuration Schlieren setup (from reference [21] pag. 42).*

The light source is a tungsten halogen low voltage lamp equipped with a rear reflector. The condenser is a Schneider-Kreuznach Xenon 40 mm double-Gauss lens with a focal ratio of *f*/1.9. The light beam is reflected by two off-axis parabolic mirrors of a diameter of 138 mm and a focal ratio of *f*/3.5. The knife edge has been positioned parallel to the actuator surface so that the Schlieren diagnostic can be sensitive to higher density gradients. The images are detected by a PCO CCD camera characterized by a super video graphics array (SVGA) resolution and a pixel size of 6µm x 6µm. The peak quantum efficiency is 55% at 380 nm. The actuator has been positioned in test area with the spanwise direction along the light beam path.

Velocity profiles have been determined by means of a glass Pitot tube moved by a step motor with linear resolution of 0.03mm. The Pitot tube has been connected to a DCAL401 Sursense ultra low pressure sensor with a sensitivity of 32mV/Pa.

IV. Discussion of the results

The electrical supply conditions are reported in *Table I.* A single supply frequency of 5kHz and four different supply voltages have been chosen. In this way four different fluid dynamic regimes have been developed.

Table I. *Electrical supply conditions.*

Condition	Voltage peak to peak [kV]	Average power [W/m]
A	20	20
B	25	66
C	30	94
D	35	140

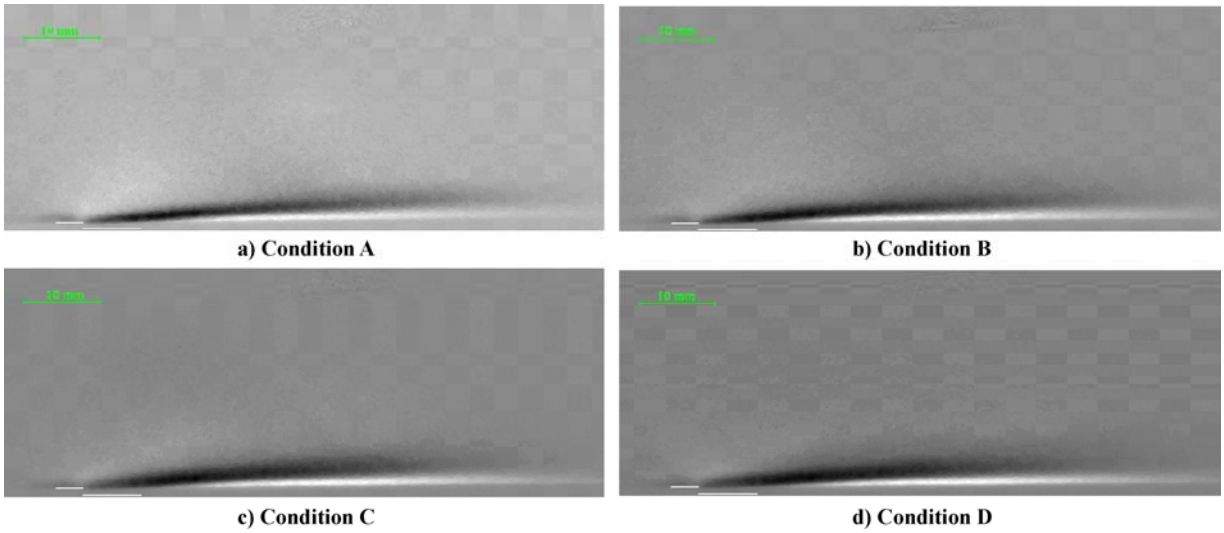

Fig.4. *Schlieren images of the wall jet produced by the actuator in the steady regime in the four conditions.*

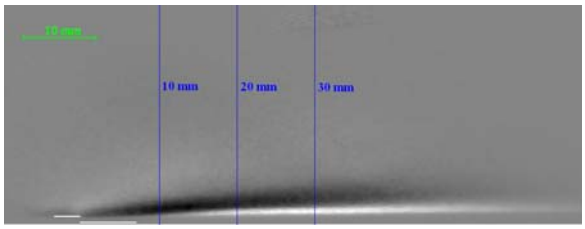

Fig. 5. *Schlieren image at condition D. Outlined in blue are the three lines used for the comparisons.*

In Fig.4 the Schlieren images obtained in the four supply conditions are shown. The white lines represent the electrode position and the green line gives the scale proportion for a length of 10mm. All the images showed below are obtained as the subtraction of the image with actuator turned on and the one with actuator turned off. A stable light source and the lack of external light radiation are essential conditions in order to achieve an uniform image background.

In each image a dark region over the upper electrode corresponding to a suction area is visible. For all the supply conditions the actuator manifests its influence at least up to the edge of the image, thus further than 60mm away from the upper electrode. A bright region is present between the actuator surface and the dark region of the wall jet. This area could represent the boundary layer developed by the wall jet itself.

Three Piton scans along lines perpendicular to the actuator surface (i.e. along the "y" direction in Fig.1) at several distances away from the upper electrode have been performed. The obtained velocity profiles have been compared with the pixel intensities of the Schlieren image along the same lines. Three lines at 10, 20 and 30mm have been chosen and represented in Fig.5 on the Schlieren image of the condition D.

A comparison between pixel intensities and Pitot velocity profile along the line at 30 mm for the supply condition D is shown in Fig.6. The distance "0" corresponds to the actuator surface. The Pitot measurements start at a distance equal to 0.5mm which matches to the tube axis when the probe is laid on the dielectric surface.

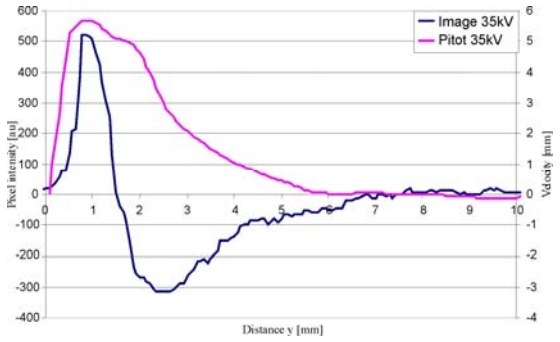

Fig.6. *Pixel intensities and Pitot velocity profile along the line at 30mm for the supply condition D.*

Both the optical and the fluid dynamic diagnostics clearly show that the region in which the actuator expresses its influence is about 7mm wide.

We consider now the following function *II(y)* which hereinafter we will call Intensity Integral:

In Fig.7 the trend of the function introduced in equation (1) and applied to the pixel intensities already displayed in Fig.6 is shown. The value y_0 has been set to 20 mm. In this way the integration starts in an area in which no fluid dynamic

perturbations are present. This function Intensity Integral clearly resembles a Pitot velocity profile.

$$II(y) = -\int_{y}^{0} I(y', y)dy' \qquad (1)$$

where *I(y',y)* is the intensity of the pixel identified by the coordinates *(y',y)*, *y* is a value that corresponds to a certain position above the actuator surface and "0" corresponds to the actuator surface itself.

Fig.7. *Function obtained integrating the pixel intensity measured at the condition D along the line at 30mm.*

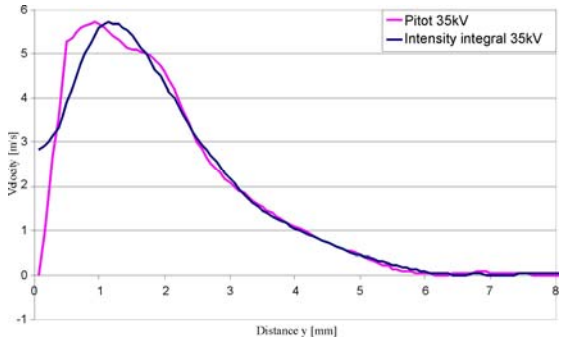

Fig.8. *Comparison between the Pitot velocity profile and the intensity integral obtained for the supply condition D along the line at 30mm.*

In Fig.8 the comparison between the Pitot velocity profile and the intensity integral obtained for the supply condition D along the line at 30mm is reported. The intensity integral values have all been divided by a normalization constant value so that the comparison can be facilitated. The agreement of the two trends is very good.

In order to verify the validity of this integrating method applied to the Schlieren images, the integral function (1) has been applied to the pixel intensities along the line at 30mm for the remaining supply conditions A, B and C. In Fig.9 the comparison between the Pitot velocity profiles and the image integrals along the line at 30mm and obtained for all the supply conditions is reported. The image integral values are all divided by the same constant value used for the comparison in Fig.8. Again a very good agreement between the profiles measured by Pitot scans and the ones obtained integrating the pixel intensities have been found.

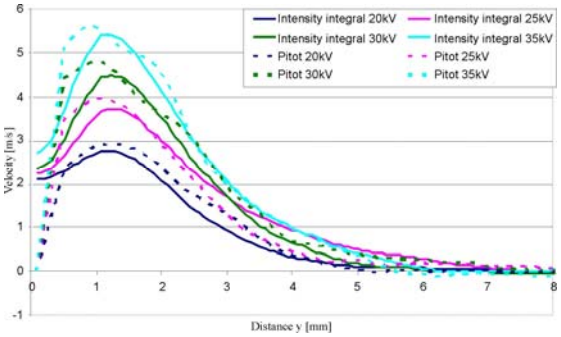

Fig.9. *Comparison between the Pitot velocity profiles and the intensity integrals along the line at 30mm obtained for all the supply conditions.*

The same integral procedure has been adopted for the pixel intensities along the other two lines for all the supply conditions. The comparisons between Pitot velocity profiles and the intensity integrals for the lines at 20 and 10mm are respectively shown in Fig.10 and Fig.11. The intensity integral values are all still divided by the same constant value used for the comparison in Fig.8.

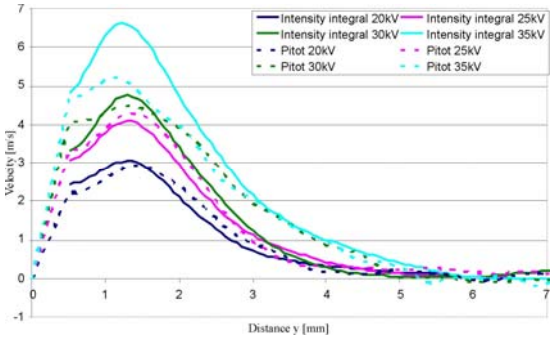

Fig.10. *Comparison between the Pitot velocity profiles and the intensity integrals along the line at 20mm obtained for all the supply conditions.*

For the line at 20mm (Fig.10) the agreement in the profiles is very good for the condition A and B. For the condition C the two profiles are similar only within the firsts 2mm. For the condition D (the one with the highest voltage) the profile obtained by the intensity integral shows higher velocity value especially close to the actuator surface.

For the line at 10mm (Fig.11) the profiles obtained by Pitot scans and by the intensity integrals present very similar trends in the region within the firsts 2mm, then the Pitot velocity profiles display higher values. The fairly agreement found for the line at 10mm can be explained as follow. In the region close to the plasma end, the

fluid dynamic measurements are less reliable because of the higher intrusiveness of the Pitot tube and because of the lower thickness of the wall jet.

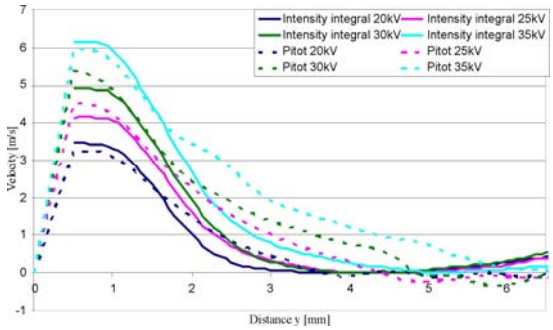

Fig.11. *Comparison between the Pitot velocity profiles and the intensity integrals along the line at 10mm obtained for all the supply conditions.*

Fig.9, Fig.10, and Fig.11 show how the integration performed by the equation (1) on the Schlieren pixel intensity along a certain line perpendicular to the actuator surface is a good estimator of the velocity profile of the wall jet induced by the DBD actuator. A possible explanation of this phenomenon is given below.

The deviation of a light beam within the Schlieren setup is due to density variations of the media. It can be demonstrated that the light pattern generated by the Schlieren apparatus is related to the first derivative of the index of refraction 21,25]. Thus the following relation holds:

$$I(x,y) \propto \int \left(\frac{\partial \rho(x,y,z)}{\partial x} + \frac{\partial \rho(x,y,z)}{\partial y} \right) dz, \quad (2)$$

where, as introduced before, *I(x,y)* is the intensity of the pixel identified by the coordinates *(x,y)* and *ρ(x,y,z)* is the density of the observed fluid at the physical point indentified by the three spatial coordinates *(x,y,z)*.

Considering that in this study the knife edge is positioned parallel to the *x* axis we can assume, in first approximation that the Schlieren setup is mainly sensitive to density gradients along the *y* coordinate. This assumption implies that, in equation (2), the derivative of the density with respect to the *x* coordinate can be neglected. Moreover the velocity field produced by the DBD actuator can be studied as an almost 2D-field, i.e. no density variations are present in the *z* direction. Equation (2) become

$$I(x,y) \propto \Delta z \frac{\partial \rho(x,y,z)}{\partial y}, \quad (3)$$

where *Δz* represents the width of the region in which the light beam is deflected.

Integrating now both the terms of equation (33) with respect to the variable *y* we obtain

$$\int I(x,y)\, dy \propto \Delta z \int \frac{\partial \rho(x,y,z)}{\partial y} dy. \quad (4)$$

The left hand side of equation (4) represents the integral operation *II(y)* through which we obtained the profiles from the Schlieren image (see equation (1)) compared than with the Pitot velocity profiles. Equation (4) states that these profiles represent quantity proportional to the density of the medium (air in this study).

We must consider now the heating mechanism of the DBD fluid dynamic actuator. Within the plasma region the air is ionized and heated up and in this area a variation in density-occur. Subsequently the air surrounding the plasma is heated up too. By means of collisions this hot air is pushed away and the EHD effect is generated. An infinitesimal air volume, characterized by a certain density, will move in a determinate direction and with a specific intensity depending on the velocity flow field generated by the DBD actuator. The integral of the Schlieren image pixel intensities depict a density distribution and can be directly related to the velocity distribution. With this assumption we assume that convective phenomena induced by buoyancy forces can be neglected when compared with the convection effects due to the velocity field generated by the EHD force.

V. Conclusions

The fluid dynamic effects of a DBD plasma actuator supplied with different a.c. regimes have been evaluated using fluid dynamic and optical diagnostics. Pitot velocity profiles at different positions away from the upper electrode and Schlieren images of the hot wall jet generated by the actuator have been obtained in steady regime operations.

The function calculated integrating the pixel intensities of the Schlieren image along a line perpendicular to the actuator surface has been compared with the corresponding Pitot velocity profile. For the three positions and the four supply conditions a good agreement has been found. A new scenario in the use of the Schlieren technique has been opened. Quantitative information about the velocity flow field can be reached with a diagnostic completely non-intrusive and applicable in large scale facilities.

Further work must be done in order to understand the physical relationship between the velocity profiles, the integral of the pixel intensities and the Schlieren setup.

References

1. Gad-El-Hak M 2000. "Flow Control". Cambridge University Press, 2000.
2. Cristofolini, A., Neretti, G., and Borghi, C.A., "EHD Plasma Actuators Utilizing a Dielectric Barrier Discharge", *39th AIAA Plasmadynamics and Lasers Conference*, Seattle, WA USA, June 2008, Paper AIAA 2008-4286.
3. Borghi, C.A., Carraro, M.R., Cristofolini, A., and Neretti, G., "Experimental Investigation on the EHD Interaction Induced by a Dielectric Barrier Discharge," *Journal of Applied Physics*, Vol. 103, pp. 063304-1 - 063304-11, ISSN: 0021-8979, 2008.
4. Cristofolini, A., Borghi, C.A., Carraro, M.R., and Neretti, G., "A Study of The Electrical Supply System of a Barrier Discharge for EHD Flow Acceleration,", *38th AIAA Plasmadynamics And Lasers Conference*, Miami, FL USA, June 2007, Paper AIAA 2007-4136.
5. Borghi, C.A. Carraro, M.R., Cristofolini, A., and Neretti, G., "A Surface Barrier Discharge System for EHD Flow Acceleration," *Proc. of the 7th Workshop on Magneto-Plasma-Aerodynamics in Aerospace Applications*, Moscow, April 2007.
6. J. Pons, E. Moreau, and G. Touchard. "Electrical and aerodynamic characteristics of atmospheric pressure barrier discharges in ambient air". *Proc. ISNTPT*, pages 370-410, 2004.
7. T. Corke, D. Cavalieri, and E. Matlis. "Boundary layer instability on a sharp cone at mach 3.5 with controlled input". AIAA-2002-0350, 2001.
8. D. Opaits, G. Neretti, S. Zaidi, M. Shneider, R. Miles, A. Likhanskii, and S. Macheret, "*DBD Plasma Actuator Driven by a Combination of Low Freqeuncy Bias Voltage and Nanosecond Pulses"*, 46th AIAA Aerospace Sciences Meeting and Exhibit, Reno Nevada, Jan 7-10, 2008, AIAA-2008-1372.
9. M.P. Patel, Z.H. Solwe, T.C. Corke, and C. He. *Autonomous sensing and control of wing stall using a smart plasma slat*. 44th AIAA Aerospace Sciences Meeting and Exhibit, AIAA 2006-1207, 2006.
10. M.L. Post and T.C. Corke. *Flow control with single dielectric barrier plasma actuators*. 35th AIAA Fluid Dynamics Conference and Exhibit, AIAA 2005-4630, 2005.
11. Borghi, C.A., Cristofolini, A., Neretti, G., Gurioli A. and Pertile R., "Experimental results in DBD plasma actuators for airflow control", 41st Plasmadynamics and Lasers Conference, Chicago, Illinois, June 28-1, 2010. AIAA-2010-4763.
12. B. Arad, Y. Gazit, and A. Ludmirsky. "A sliding discharge device for producing cylindrical shock waves". *J. of Appl. Physics*, 20: 360-367, 1987.
13. S.B. Leonov and D.A. Yarantsev. "Mechanisms of flow control by nearsurface electrical discharge generation". AIAA-2005-0780, 2005.
14. J. Huang. "Documentation and control of flow separation on a linear cascade of Pak-B blades using plasma actuators". PhD thesis, University of Notre Dame, 2005.
15. D.K. Van Ness II, T.C. Corke, and S.C. Morris. "Turbine tip clearance flow control using plasmas actuators". *AIAA meeting*, AIAA-2006-0021, 2006.
16. C.S. Kalra, M.N. Shneider, and R.B. Miles. "Numerical study of shockwave induced boundary layer separation control using plasma actuators". *46th AIAA Aerospace Science Meeting and Exhibit*, AIAA-2008- 1095, 2008.
17. J.P. Boeuf and L.C. Pithford. "Electrohydrodynamic force and aerodynamic flow acceleration in surface dielectric barrier discharge". Journal of Applied Physics, 97-103307, 2005.
18. T.C. Corke, B. Mertz, and M.P. Patel. *Plasma flow control optimized airfoil*. 44th AIAA Aerospace Sciences Meeting and Exhibit, AIAA 2006-1208, 2006.
19. D.V Gaitonde, M.R. Visbal, and S. Roy. *A coupled approach for plasma-based ow control simulations of wing sections*. 44th AIAA Aerospace Sciences Meeting and Exhibit, AIAA 2006-1205, 2006.
20. A. Likhanskii, m. Shneider, D. Opaits, R.B. Miles and S. Macheret, "*Numerical modeling of DBD plasma actuators and the induced air flow*", 38th AIAA Plasmadynamic and Laser Conference, Miami, Florida, June 25-28 2007.AIAA-2007-4533.
21. G.S. Settles, "*Schlieren and Shadograph Techniques*", Springer 2001.
22. R. Sosa, E. Arnaud, G. Artana, "*Schlieren Image Velocimetry applied to EHD flows*", International Simposium on Electrohydrodonamics (ISEHD), Buenos Aires, Argentina, 2006.
23. D. Opaits, A. Likhanskii, G. Neretti, S. Zaidi, M. Shneider, R. Miles and S. Macheret, "*Experimental Investigation on Dielectric Barrier Discharge Plasma Actuators Driven by Repetitive High-Voltage Nanosecond Pulses with DC or Low Frequency Sinusoidal bias"*, Journal of Applied Physics 104, 043304 (2008).
24. Borghi, C.A., Cristofolini, A., and Neretti, G., "*Experimental investigation on the energy transfer in a DBD plasma actuator for airflow control*", 10th International Magneto-Plasma Aerodynamics, 22-24 March, Moscow.
25. Goldstein, R.J., Kuehn, T.H., "*Fluid Mechanic Measurements*", Taylor and Francis, 1996.

11.3. PLASMA ACTUATOR BASED ON A SECTIONED DIELECTRIC BARRIER CORONA DISCHARGE

Yu.Akishev, M.Grushin, N.Trushkin, A.Petryakov
SRC RF TRINITI, Pushkovykh St-12, Troitsk, Moscow region, 142190, Russia
akishev@triniti.ru

Promising design of plasma actuator on the basis of so-called sectioned dielectric barrier corona discharge is offered. This scheme allows us to take the basic advantages from both ? sectioned corona discharge and dielectric barrier discharge. Such discharge combination gives an opportunity to diminish drastically a distance between neighbor needles without misgiving of spark formation. Besides, this design is available for unlimited scaling in a transverse direction and enables to generate a transverse uniform electric wind. Some fresh results obtained with new plasma actuator will be presented.

11.4. METHODS AND RESULTS OF PLASMA SPECTRAL RESEARCHES IN AR-AL-H2O STEADY-STATE DISCHARGE

Biturin V.A., Klimov A.I., Grigorenko A.V., Efimov A.V., Kutuzov D.S., Chinnov V.F.
Joint Institute of High Temperature RAS, 125412, Moscow, st. Izhorskaya, 13, presley1@mail.ru

1. Formulation of the problem.

The aim of this work is to create a system of optical and spectral studies of space-time state of the plasma in the quasi-steady state Al-H2O reactor, allowing real-time to determine the temperature distribution and concentration of major plasma components responsible for the efficiency of processes of formation of hydrogen and solid products in a reactor.

2. Reactor mode of operation.

We consider a stationary dc discharge, $I_D \approx$ 2 A, $U_D \approx$ 800 V, $L_D \approx$ 100 mm. Plasma form in the reactor(Fig.1) indicates that in the steady arc is observed bright conducting core of an electrical discharge with an effective diameter $d_0 \approx$ 1 cm, an electrical energy input $jE \approx$ 300-800 W/cm^3 and diffuse zone of flow of plasma reactions involving aluminum and water vapor with a diameter D of about 2.5 cm. In this area, apparently released the bulk of the heat in the exothermic reaction of combustion (15 MJ/kg Al) M_{Al}= 300W - taking into account the occupied volume $V = (\pi/4)(D^2-d_0^2) L_D$ is about 6 W/cm^{-3}.

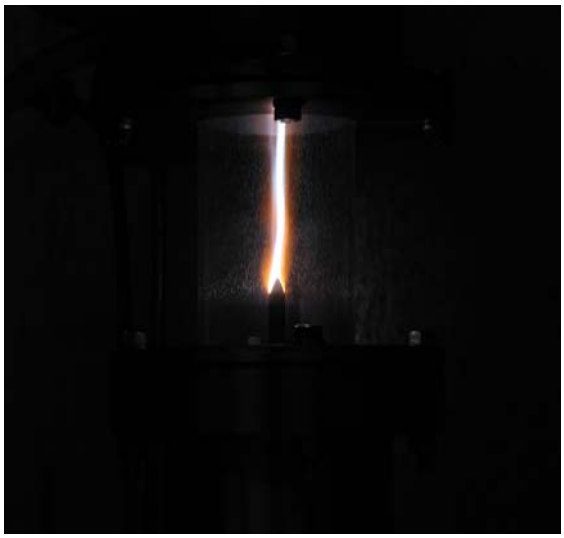

Fig 1. *Type of study discharge*

There are tens of plasma processes and chemical reactions in the test reactor and spectral studies aim should be to establish the spatial pattern of their occurrence. Scheme of optical and spectral

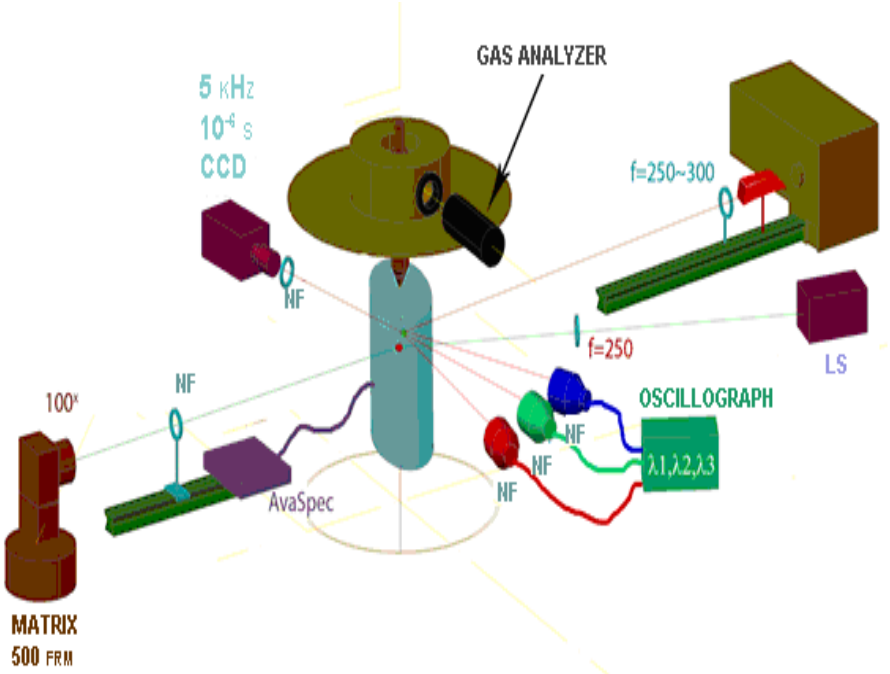

Fig 2. *Registration Scheme of the local characteristics of the plasma*

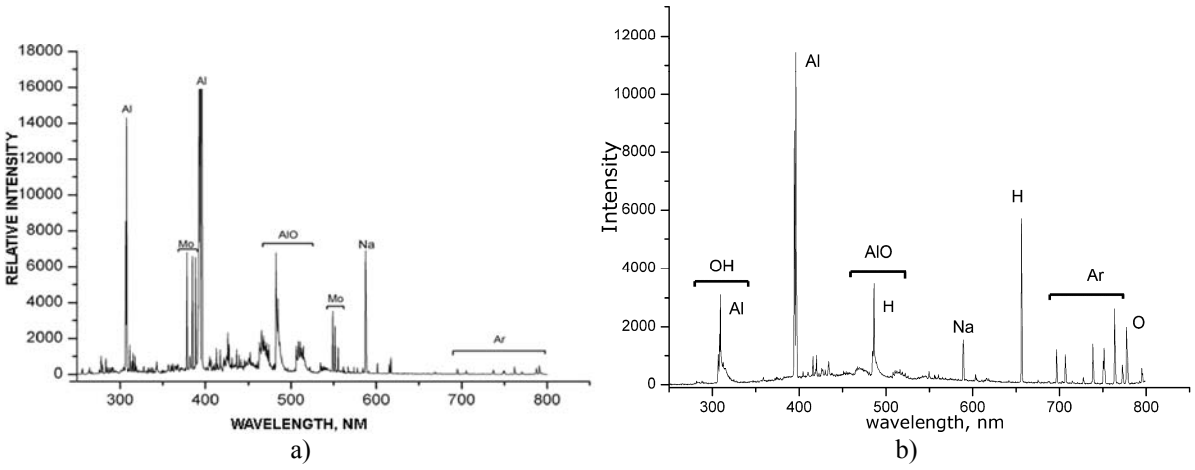

Fig 3. *Panoramic spectrum of the plasma*

measurements is shown in Fig. 2. Survey spectra were recorded with a spectrometer AvaSpec 2048. MS257 spectrometer with a matrix output allows the registration of the radiation spectrum in a selected range of wavelengths (Δλ : 50 nm, 300-400 nm - OH* and AlI; 650-750 - H_α and ArI) with a resolution of 0.05 nm:

a) along the height of the reactor (at the entrance slit projected vertical thumbnail software);
b) along the radius of the plasma formation at the selected height (using the Dove prism to rotate the image);

Simultaneously, the high-speed CCD-camera with a selected narrow band filters at the input registers plasma reactor glow in the removed filter spectral range - and we can get a picture of the spatial distribution of the major emitters of the investigated plasma (after Abel transformation of chord distributions).

3. Preliminary analysis of the plasma composition in the reactor.

Analysis of equilibrium composition of the plasma with the initial ratio of components [Ar]: [H2O]: [Al] = 90,8:9:0,2 shows that up to 10-11 kK temperature defining the ionized component is the ion Al^+: $n_e \approx [Al^+] \gg [H^+], [Ar^+]$. The maximum n_{Al^+} is achieved at $T_e \approx$ 6-7 kK. Upon reaching the temperature of 5-6 kK (for $p_\Sigma \approx 1$ atm) all the molecular components (H_2O, H_2, O_2, OH, AlO, Al_2O_3) are completely dissociate, while the optimum temperature output Al_2O_3 (solid) is the range of. 2,5 - 3.0 kK (T_{melt} = 3253 K).

At temperatures of 5-8 kK main expected plasma components are:

Ar (0,85): H (0,05): O (0,02): Al (0,01 - 0,001): Al^+ (0,001 - 0,01): Ar^+ (0-0,001): H^+ (0 -0.001).

4. Analysis of the plasma emission spectra

At Fig. 3a, 3b are examples of typical survey spectrum of plasma emission of atmospheric pressure recorded by the spectrometer AvaSpec, with a converging lens with focal length 10 mm and a light guide at the entrance.

This method of registration of the spectrum carries out the integration of the radiation from a large and heterogeneous volume of plasma:

$$i_\lambda(t) = \int\Delta\Omega \int v \int t\, \varepsilon\lambda\ (x, y, z, t)\, dv\, d\Omega\, dt \quad (1)$$

It is obvious that the recorded emission spectrum (Fig. 3) is a superposition of radiation from all areas of the plasma covered aperture solid angle of $\Delta\Omega$. Due to the integration along the rays of radiation within $\Delta\Omega$ only by analyzing the expected distribution of emitters in the plasma formation can set the priority area of the radiation of a plasma component.

Examples of the matrix spectra are shown in Fig. 4. Explanation of the review of the spectrum detected in a wide range of wavelengths indicates the presence of following emitting components:

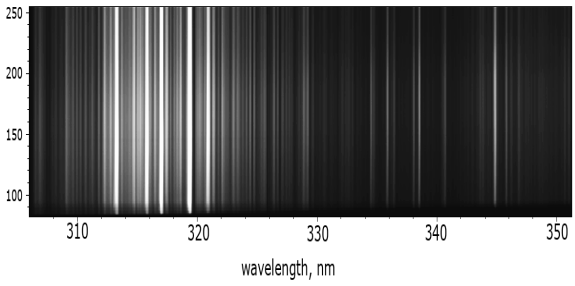

Fig 4. *Chord distribution of intensity in the UV-region*

Band (O-O), radical OH * (transition $A^2\sum^+ \rightarrow X^2\Pi i$) in the region 306-320 nm;

The resonance doublet of Al I 394,4; 396,1 nm [the line with a common upper level $g_k = 4$; $A_{396} = 0{,}98 \cdot 10^8$ s^{-1}; $g_i^{3/2} = 4$; $A_{394} = 0{,}45\ 10^8$ s^{-1}, $g_i^{1/2} = 2$)]:

Excited atoms ArI, with excitation energy from 13.1 to 14.8 eV;

Atomic hydrogen H_α lines (656,2 nm) and H_β (486,3 nm)

Oxide radiation AlO: (band $B^2\sum^+ \rightarrow X^2\sum^+$, transitions 2-0, 1-0, 0-0 and 0-1)

Weak continuous emission (continuum), with increasing the wavelength and intensity extending from 300 to 800 nm.

5. The results of optical and spectral measurements.

The main results of the determination of plasma parameters obtained from analysis of survey spectra of plasma radiation, given in Figure 3. Obtained using the matrix detailed spectra, if necessary brought to the analysis. But even in the absence of absolute calibration of the spectral intensity and its spatial distribution was possible to identify the main parameters of the plasma.

a). The electron temperature near the axis of the discharge.

Comparison of results of high-speed imaging in the integrated light at the selected spectral regions (λ = 390-410nm, 470-520 nm, 650-680nm) with the matrix spectra, reproduced in Fig. 4 indicates that the bright glow of the core level emission lines provided ArI, HI and MoI (molybdenum - electrode material). Therefore, the temperature near the axis of the discharge was estimated from analysis of distribution patterns distribution of excited ArI, HI and MoI on the excitation energies of the upper levels of the observed optical transitions. The so-called "Boltzmann exponent" (dependence ln $n_k/g_k(E_k)$, when the excitation energy $\Delta E_k \geq kT$), based on the predominance of collisional interaction processes of excited atoms with electrons in comparison with radiation [1] was used to identify those values along the lines of ArI and MoI.

Excited atoms Ar. Observed in the spectrum of ArI lines covering the energy range of excitation of the upper energy levels E_k = 13.1 - 14.8 eV. This provides a definition of the electron temperature of the form depending on the populations of the states with excitation energy with an error inversely proportional to ΔE: $\delta T_e \sim (T_e/\Delta E)$. Fig. 5 shows the result of determination: $T_e = 6500 \pm 500$ K.

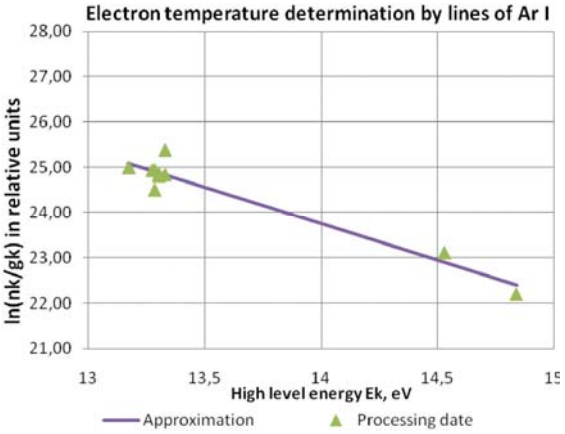

Figure 5. *Measurement of electron temperature along the lines of Ar I.*

Additional opportunity to evaluate the electron temperature provides an analysis of atomic excited states of molybdenum - in the case of molybdenum electrodes. In Fig.6 the temperature TE obtained from the slope of "Boltzmann exponent, is 7000 ± 500K.

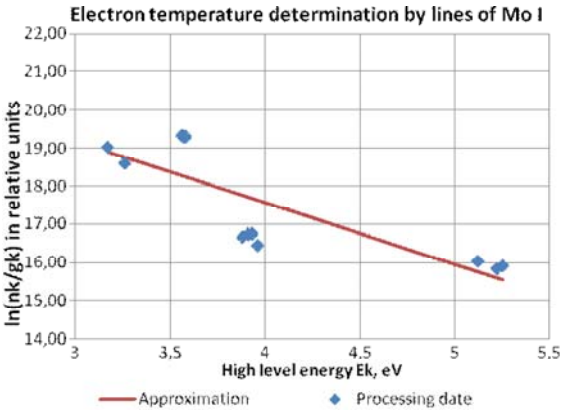

Fig 6. *Measurement of electron temperature along the lines of Mo I.*

b). Electron concentration.

Spectral resolution of the spectrometer AvaSpec was not enough for the analysis of half-width of the spectral lines of HI, - so we used the results of the matrix spectroscopy. Measured using a hollow cathode discharge apparatus function of MS 257 - the matrix has a Gaussian contour with a width of (0,1 ± 0,01) nm. Doppler broadening H_γ, H_β and H_α at T = 6500 K are respectively 0.025, 0.030 and 0.036 nm.

The resulting contours of the Balmer lines are a convolution of the dispersion (linear Stark

effect) and Gaussian ($\delta^2 = \delta^2_{ann} + \delta^2_{dop}$) circuits. As a result, the software selection width of the Stark component of the line H_β from the experimental width (0,2 ± 0,01) nm using the procedure of separation of Voigt units [2], we estimate the axial (max) value of the electron concentration: ($\delta_{½} = cn_c^{2/3}$ [2,3]: n_e (0) ≈ (2 ± 1) · 10^{14} cm-3.

n_e score using experimental values of j [A/cm^2] and E [V/cm]:

σ = j/E = $e^2 n_e/m\sum\nu_{em}$ ≈ 20 Mo/м gives the value of $n_e \approx 4 \cdot 10^{13}$ cm-3.

c) The temperature of heavy particles (atoms).

The observed molecular spectra of OH and aluminum oxide AlO allow us to determine the rotational and vibrational temperature of the plasma. For the transverse (chord) detection of radiation of the inhomogeneous object, you must carry out Abel transformation of chord distributions. Figure 7 shows the result of such transformation for the head of the band O-O transition $A^2\Sigma^+ \rightarrow X^2\ \Pi_i$ OH molecules. It can be seen that the maximum intensity of the band called up not on the axis of the discharge, and at some radius r*. Consequently, the value of the rotational temperature, which we obtain by comparing the simulated and experimental partial resolution of the electron-vibrational-rotational spectrum of OH * to be assigned to a zone with $r = r$*. Should emphasize the following basic fact in the analysis of molecular spectra. Temperature range of their existence (and observation) is their small, for example, for an equilibrium plasma at atmospheric pressure H_2O vapor concentration of OH in the ground state reaches a maximum at T = 3300 K and T = 6000 K decreases by 2 orders of magnitude (see Figure 1.3 Monograph [3]). Equilibrium concentration of the excited OH* able $A^2\Sigma^+$ reaches its maximum value at T* ≈ 4500 K. Hence, for recording the spectra with the integration of radiation in an inhomogeneous plasma volume (as occurs when using fiber-optic spectrometers), we determine the temperature of heavy particles in I^{OH} (max) - in our case (T_{axis}> T* = 4500 K) is the region near r*.

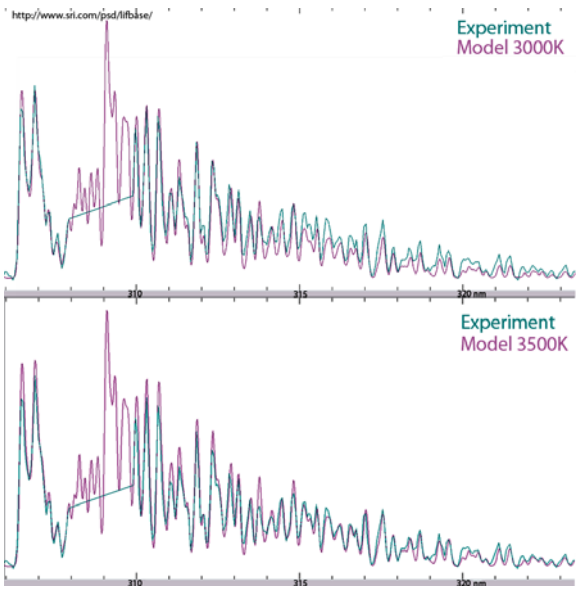

Fig.7. *Rovibronic analysis of the emission spectrum of the radical OH.*

<u>OH radical</u>. At the equilibrium of plasma with a maximum emission band of OH * (transition 0-0) corresponds to a temperature T_{OH}^{max} ~ 4,5 ÷ 5 кК - hence the band-OH *, we measure the plasma in the zone with T ≤ 4 кК (in our case - the shell of the plasma formation). We used the following programs: LIFBASE [4] and SPECAIR [5]. Experimental spectra were loaded into the program, scale, and compared with a model program calculated spectrum.

The result of this simulation is displayed in Figure 7. Defined value of the temperatures

$T_r = T_v$ = 3200±200 K.

<u>Oxide AlO radiation: band B $^2\Sigma^+ \rightarrow X^2\Sigma^+$, transitions 1-0, 0-0 and 0-1)</u>

In the absence of a standard treatment program of the molecule spectrum , we restricted ourselves to the estimate of the vibrational-rotational temperature by comparing the integrated intensities of the transitions 1-0, 0-0 and 0-1: $T_r = T_v$ = 3000-4000 K, - this value is consistent with T_r = 3200K (the spectrum of OH) and is most likely to diffuse region of the plasma formation.

<u>Weak continuous emission (continuum), with increasing the wavelength and intensity extending from 300 to 800 nm</u>. If we assume that the responsible for this radiation is the emission of corundum particles that are the product of oxidation of aluminum, the use of Planck's law to describe the frequency of progress along this continuum (with the assumption of weak changes in the frequency degree of blackness of particles) in the frequency range 16000-30000 cm-1 gives value of T = 3700 ±500 K.

d) <u>The resonance doublet of Al I 394,4, 396,1 nm.</u>

In the analysis of changes with increasing temperature the intensity of the resonance radiation of aluminum atoms in a TD-equilibrium must take into account the optical thickness $\tau_0 = k_0 R$, where k_0 - the absorption coefficient at line center [1,3,6]. The analysis shows that the absorption coefficient

at line center AlI 396.1 nm, proportional to the concentration of aluminum in the ground state n_{Al}, is given by

$$k_0 = 6 \cdot 10^{-11} \cdot n_{Al} \Big/ \sqrt{T(K)} \qquad (2)$$

Thus, since the concentration of aluminum atoms $n_{Al} \geq 10^{12}$ cm^{-3} resonance emission becomes optically thick, and the effective probability of optical transition becomes dependent on the probability of photon emission θ_{ki} [1]. In the temperature range of 5-10 kK and at a partial vapor pressure of aluminum over 10^{-4} concentration of plasma electrons is entirely determined by the ionization of aluminum: for example, $\alpha_{Al} = 10^{-1}$% $ne \approx [Al^+] \approx p_{Al} / kT \approx (1{,}4 - 0{,}7) \cdot 10^{15}$ cm^3.

e) Analysis of relative intensities of AlI, ArI and HI.

For the resonance doublet AlI need an estimate of the optical thickness τ_0. In this range of parameters, the width of the resonance lines due to the Doppler effect and is about 10^{10} s^{-1}. Optical thickness at a concentration of aluminum atoms $\sim 10^{14}$ cm^{-3} is $\tau_0 \sim 100$, and the effective probability of optical transition is reduced by hundreds of times [1]:

$$\theta_{ki}(\tau) = \sqrt{\pi}\left(4\tau\sqrt{\ln \tau}\right)^{-1}$$

- outside the considered volume will be released only a small fraction of the radiation, created in the paraxial region.

Lower levels of the optical transitions observed lines ArI and HI have the excitation energy over 10 eV, and the concentration of absorbing particles at these low levels at T = 6-7 kK - less than 10^{10} cm^{-3}. Therefore, the emission of these lines is optically thin, and the comparison of the relative intensities of hydrogen and argon can be a way to estimate the volume fraction of hydrogen atoms in the plasma reactor. Comparing the experimental values of the intensities of specific lines of hydrogen and argon and using the law of the Boltzmann relation of concentration of particles in the ground and excited states, we obtain:

$$\frac{n_H}{n_{Al}} = \left(\frac{I^H}{I^{Al}}\right)^{\exp} \frac{\lambda_H}{\lambda_{Al}} \frac{A^{Ar}}{A^H_{mn}} \frac{\left(\frac{g_k}{g_0}\right)^{Ar}}{\left(\frac{g_m}{g_0}\right)^{H}} \exp\left(\frac{E_m - E_k}{kT_e}\right) \qquad (3)$$

Substitution of numerical values for the lines ArI 750,3 and 763.5 nm lines and Hα, Hβ when T = 6500K gives an estimate (n_H/n_{Ar}) ~ 3 10^{-2}.

Trying to use a relation similar to (3) to estimate the partial pressure p (Al), shows that it is many orders of magnitude less than the original (0,2%): in the observation area is very significant reabsorption of resonance radiation of aluminum.

If the ionization of the plasma in the surveillance zone is not determined by the ionization of aluminum (which may be small, α_{Al} : 10^{-6}), and ionization of hydrogen (α_H : $3 \cdot 10^{-2}$), then by Saha formula can estimate the concentration of hydrogen ions:

$$\frac{n_e \cdot n_{H^+}}{n_H} : 3 \cdot 10^{21} T_3^{3/2} e^{-12.6/kT_e} : 4 \cdot 10^{10}$$

$$n_e : n_{H^+} : n_H,$$

$$n_H : \frac{p_H}{kT_e} : 3.5 \cdot 10^{16} \text{ cm}^{-3}$$

Hence,

$$n_e : n_{H^+} : 3.5 \cdot 10^{13} \text{ cm}^{-3} :$$

$$n_e(\sigma = j/E) : 4 \cdot 10^{13} \text{ cm}^{-3}$$

References

1. L.M. Biberman, V.S. Vorob'ev, I.T. Yakubov Kinetics of Nonequilibrium Low-Temperature Plasma. Moscow. Nauka, 1982.
2. I.I. Sobelman. Atomic Spectra Theory Introduction. Moscow. Fizmatgiz, 1963.
3. V.N. Ochkin. Spectroscopy of low-temperature plasma. Moscow. Fizmatlit, 2006.
4. http://www.sri.com/psd/lifbase/
5. http://www.specair-radiation.net/
6. Methods of Plasma Research. Ed. V.Lohte-Holtgreven, Wiley, 1971.

11.5. PLASMOID WITH STRONG MAGNETIC FIELD

Alexander N. Vlasov
The Ryazan State Radio Engineering University, 59/1 Gagarin St., Ryazan, 390005, Russia
anv@fulcra.ryazan.ru

Abstract. It is considered the plasmoid with the strong magnetic field concluded in a vacuum tube placed inside of a plasma clot with a superficial current of ultrarelativistic electrons, and magnetic pressure of the field is counterbalanced by pressure of external gas. It is shown, that such plasmoid can be generated during action of back front of powerful impulse of the primary current, creating in discharge volume a pulse magnetic field with peak value of magnetic pressure much greater, than pressure of external gas. Speed of downturn of the induced current is found and expected lifetime of the plasmoid is estimated. Threshold value of amplitude of a primary impulse current when there is possible a formation plasmoid with the geometrical sizes and time of a life same as at a natural ball lightning is found. Experimental results on forming plasmoid are resulted by a method of electric explosion of the wire spirals curtailed into toroidal form.

PACS: 52.55.Dy, 52.58.-c, 52.27.-h

1. Introduction

Research plasmoid with a strong magnetic field is of interest for experimental investigations in the field of the gas discharge with the big force of a current. Plasmoid is limited equilibrium magnetohydrodynamical (MHD) configuration of currents in plasma, and the greatest interest among them represents a ring with a current supported in balance pressure of external gas as such system can be stable [1]. Also in [1] it has been come out with the assumption that research of such configurations can be of interest in the theory of the phenomenon of ball lightning.

One of the major questions of research limited equilibrium MHD configurations is the question on a method of input of energy in their plasma. It is obvious that directly to enter energy into plasma such MHD configurations it is possible only an induction method, i.e. by means of induction discharges. Such discharges can be raised in discharge volume with quickly enough changing magnetic field, for example, inside of the coil through which coils pass a current of high frequency or strong impulses of a current [2]. The big interest in application considered by us is represented with pulse modes at which especially high intensity of a stream of the energy entered into plasma is reached. An example is θ-pinch, developing at fast increase of a strong magnetic field [3]. In this case in digit volume there is plasma coil with a current that cooperating with quickly increasing magnetic field of the coil, aspires to compress plasma to the center of the discharge chamber. At the same time the law of an electromagnetic induction allows to develop to the pulse induction discharge not only at fast increase of a strong magnetic field, but also at its fast recession. In the latter case also the plasma coil with a current as well as in θ-pinch, but with an opposite direction therefore this current, cooperating with a magnetic field of the coil, aspires to supersede plasma from the central area of digit volume can be generated. But process of replacement of plasma is resisted with forces of external pressure, therefore at the certain stage of development of this discharge the equilibrium condition therefore the configuration can be formed limited equilibrium MHD configuration in the form of the cylinder or a ring with a current [4] depending on used geometry of plasma can be established. Such discharge from the point of view of a direction of induced currents and directions of action of forces on a coil with a current is full, contrast in relation to the discharge «θ-pinch», therefore in [5] it has been named «rotating θ-pinch». This term has been used and in [6], however by more successful, apparently, is the term «inverse θ-pinch» (Iθ-pinch), which we shall use further.

Except for the mentioned appendices the discharge «Iθ-pinch» is of interest for an explanation of the phenomenon of electric explosion in a free atmosphere curtailed in tor wire spirals when long-living shone objects [7] were observed. In this case inside of spirals the proceeding current creates a strong magnetic field with the magnetic pressure essentially exceeding pressure of an atmosphere, and at disintegration of delays this magnetic field quickly falls down. Such field can quite raise the induction discharge, and according to model offered in [4] and developed in [6] the plasma ring with poloidal current inside of the vortex gas ring, similar to a ring with the screw current, considered earlier in [1] in this case can be formed.

However in [4] and [6] processes of energy pumping in plasma are considered only at a qualitative level, and requirements to parameters of a primary current impulse have been received, leaning only on a parity for equilibrium current of the MHD configuration. It causes quite justified

questions, answers on which can be given on the basis of essential completion of theoretical model spent further.

The present work is devoted to research of processes of energy pumping in plasma of the discharge of type Iθ-pinch, and features of dissipating of the reserved energy in formed MHD configuration, representing plasmoid with strong magnetic field. The primary purpose of work is specification of theoretical model of formation mentioned plasmoid for development of practical techniques on experimental modelling the natural phenomenon of ball lightning.

2. The equation for the induced current

The real experiments for example connected with electric explosion curtailed in tor wire spirals, deal with toroidal geometry of plasma, but at the small attitude of small and big radiuses of tor, accepted further, the analysis of electromagnetic processes is more convenient for spending with use of cylindrical geometry, entering then if necessary corresponding amendments. Therefore in the beginning we shall consider developments of the discharge of type Iθ-pinch with cylindrical geometry of plasma, Fig. 1.

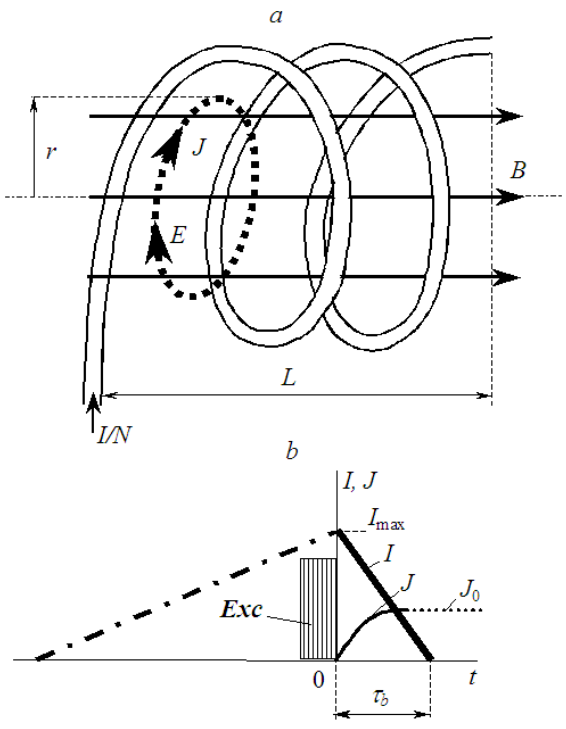

Figure 1. *The scheme of excitation of the induction discharge at fast recession of strong magnetic field (a), and idealized diagram of current impulses (b). Exc is impulse of energy for preliminary warming up of plasma*

Let the magnetic field is created by the long cylindrical coil, having N coils and length L through which coils the single impulse of a current I/N is passed, and in discharge volume inside of the coil the magnetic field with an induction B (fig. 1) is created. As a result in any contour with radius r the vortex electric field with intensity E is induced. Here I is an impulse of a primary current (amperes-coils), τ_b is duration of its back front, J is he induced current in a plasma coil, J_0 is the equilibrium current which has established upon termination of process of humping of energy in plasma.

Magnetic field we shall consider strong, and its change fast enough if conditions are satisfied

$$B_{\max}^2 >> 2\mu_0 p\,, \tag{1}$$

$$|\partial B/\partial t| \geq 2E_a/r\,. \tag{2}$$

Here $B_{\max}$ is the maximal induction of a magnetic field, and $\partial B/\partial t$ is speed of its change, p is pressure of external gas, E_a is intensity of an electric field in a contour with radius r, $2\pi r << L$, at which there is an electric breakdown of gas, $I_{\max}$ is the maximal value of a primary current, μ_0 is the magnetic constant.

Let the primary current of the coil represents a triangular impulse with abrupt back front (Fig. 1, *b*), and it is supposed, that before action of front of recession of a primary current preliminary warming up of plasma by an impulse of energy Exc, for example, by impulse of HF current [8] is made. All processes of input of energy in plasma we shall consider on an interval of time $0 \leq t \leq \tau_b$. In this case intensity of a vortex electric field E along a line $l = 2\pi r$ of a contour of formation of a plasma coil with a current can be found on the basis of integrated Maxwell equation

$$\oint\limits_{(2\pi r)} E\,dl = -\frac{d}{dt}\int\limits_{(\pi r^2)} B(r,t)\,dS\,, \tag{3}$$

in which

$$B(r,t) = \mu_0\left[I(t) + J(r,t)\right]/L\,, \tag{4}$$

where $J(r,t)$ is the induced current in a plasma coil (Fig. 1).

Let's take advantage of the Ohm law

$$J(r,t) = 2\pi r E/Z(r,t), \tag{5}$$

where $Z(r,t)$ is electric resistance of a plasma coil. Then having substituted (4) in view of (5) in (3) we

shall receive the equation for the induced current $J(r,t)$ in a plasma coil:

$$\oint_{2\pi r} \frac{LJ(r,t)Z(r,t)dl}{2\pi\mu_0 r} + \frac{\partial}{\partial t}\int_{\pi r^2} I(t)dS + \frac{\partial}{\partial t}\int_{\pi r^2} J(r,t)dS = -2\pi r I(t)\frac{\partial r}{\partial t} - \frac{\partial r}{\partial t}\frac{\partial}{\partial r}\int_{\pi r^2} J(r,t)dS. \quad (6)$$

3. Model of the vacuum tube

The common solution of the equation (6) is not obviously possible, we shall search therefore for the approached solutions for the fixed contour $(\partial r/\partial t = 0)$. In the beginning we shall consider two limiting cases:

1) $Z(r,t) = \infty$;
2) $Z(r,t) = 0$.

In the first case from the parity (5) follows, that $J(r,t) = 0$, $\partial J/\partial t = 0$. Then the equation (6) in view of (5) has the solution:

$$\begin{cases} J = 0, \\ E = -\dfrac{\mu_0 r}{2L}\dfrac{\partial I}{\partial t}. \end{cases} \quad (7)$$

In the second case from (5) follows, that $E = 0$, and (6) and the equation (6) in view of (5) has the solution:

$$\begin{cases} \dfrac{\partial}{\partial t}J(r,t) = -\dfrac{\partial}{\partial t}I(t), \\ E = 0. \end{cases} \quad (8)$$

Parities (7) are fair for the empty chamber, and parities (8) are fair for ideally conducting environment.

Let's find the approached solution of the equation (6) for intermediate values $0 < Z < \infty$. We shall admit, that on an interval of time $0 \le t \le \tau_b$ takes place

$$I(t) = I_{\max}(\tau_b - t)/\tau_b, \quad (9)$$
$$r = a = const, \quad (10)$$
$$Z(r,t) = Z_0 = const. \quad (11)$$

These assumptions are accepted within the limits of model which we shall conditionally name «model of the vacuum tube» which, as a matter of fact, is similar to model of MHD configuration in the form of a ring with a screw current [1]. Feature of offered model consists that the real plasma coil is replaced by with idealized system in the form of a thin-walled tube with a current, from within which as it will be shown further, plasma is completely evacuated. In this case pressure of external gas is counterbalanced by magnetic pressure of an internal magnetic field of the tube created by equilibrium current J_0. This current is easy for finding from balance of magnetic pressure inside of a tube and pressure of external gas:

$$J_0 = L\cdot\sqrt{2p/\mu_0}. \quad (12)$$

At $J = 0$ or $J = const$ intensity of an electric field on the basis of (7) and (9) is equal a contour of formation of a vacuum tube

$$E(a) = \frac{\mu_0 a}{2L}\cdot\frac{I_{\max}}{\tau_b} \quad (13)$$

It is obvious, that the current in a contour of a tube arises, if the condition (2), i.e., if $E(r) \ge E_a$ is satisfied. From (13) restriction on the minimal value of radius of a plasma coil with the induced current follows:

$$r \ge a = \frac{2L}{\mu_0}\cdot\frac{E_a\tau_b}{I_{\max}}. \quad (14)$$

In view of (9), (10) and (11) equation (6) has solution in a kind of

$$\frac{dJ(t)}{dt} + \frac{J(t)}{\tau_L} = \frac{I_{\max}}{\tau_b}, \quad (15)$$

Where

$$\tau_L = \frac{\pi\mu_0 a^2}{LZ_0}.$$

The solution of the equation (15) looks like

$$J(t) = I_{\max}\cdot\frac{\tau_L}{\tau_b}\left[1 - \exp\left(-\frac{t}{\tau_L}\right)\right]. \quad (16)$$

In a limiting case $\tau_L >> \tau_b$, i.e. when $Z_0 \to 0$, the parity (16) is led to a kind $J(t) = I_{\max}(t/\tau_b)$, that in view of (9) corresponds earlier to the received result (8) for ideally spending environment.

Practical interest represents a case when the condition is observed

$$\tau_L/\tau_b << 1, \quad (17)$$

as thus as it will be shown further, in plasma significant energy of the directed movement of electron can be entered. At performance of condition (17) parity (16) is led to parity

$$J(t) = \eta J_{\max}\left[1 - \exp\left(-\frac{t}{\eta\tau_b}\right)\right], \qquad (18)$$

where η is factor of transfer on currents:

$$\eta = \tau_L/\tau_b = J_0/I_{\max}\ . \qquad (19)$$

The curve of a current according to (18) is resulted on Fig. 1, *b*.

4. Generation of run away electrons

It is known [8] if the electric field that size is same or surpasses a Dreicer field a great bulk electrons, creating a current of plasma is enclosed to plasma, for short time (the order of time of collisions электронов with ions) become escaping. The Dreicer field $E_{\rm cr}$ is set by a parity [9]

$$\frac{m_e v_{\rm cr}^2}{2e} = \frac{e^2 n \ln\Lambda}{4\pi\varepsilon_0^2 E_{\rm cr}}\ . \qquad (20)$$

Here m_e is mass of electron, $v_{\rm cr}$ is critical speed, e is elementary charge, $\ln\Lambda$ is the Coulomb logarithm, ε_0 is electric constant, n is concentration of plasma [8],

$$n = p/(2kT), \qquad (21)$$

where k is Boltzman constant, and T is temperature.

Let's notice, that if after an impulse of initial warming up dense enough plasma was formed, for example $n_0 \approx 3\cdot10^{23}$ m^{-3}, $p = 10^5$ Pa, $\ln\Lambda = 20$, and the electron energy $m_e v_{\rm cr}^2/(2e) = 1$ eV, the critical field is equal $E_{\rm cr} \sim 10^8$ V/m. From this follows that during the initial moment of development of the considered induction discharge run away electrons cannot be. However in process of increase in the induced current $J(t)$ (18) situation varies. It is easy to see, that at increase in a current $J(t)$ the difference of magnetic pressure on border of a tube grows, and at $J(t) \approx J_0/2$ this difference reaches for size pressure of plasma.

In this case there is a fast evacuation of plasma from internal volume of a tube (calculation of time of evacuation will be given further). As a result in a zone of course of a current $J(t)$ concentration of plasma n promptly falls, and transition of electrons in a mode of continuous acceleration, becomes possible at the moderate values of an electric field E_{cr}. We shall estimate necessary concentration for this case, having made in (20) substitutions $m_e v_{\rm cr}^2/2 = kT$, $kT = p/(2n)$ and, believing $n = n_{\rm cr}$:

$$n_{\rm cr} = \sqrt{\frac{2\pi\varepsilon_0^2 E_{\rm cr} p}{e^3 \ln\Lambda}}\ .$$

Let's admit, for an example, that $E_{\rm cr} = 500$ V/m, then $n_{\rm cr} \approx 7\cdot10^{20}$ m^{-3}. As we see $n_{\rm cr} << n_0$.

Let's estimate time of evacuation of plasma from within tubes down to achievement of concentration $n_{\rm cr}$ for this purpose on the basis of the non-stationary one-dimensional MHD equation [10] we shall write down the equation of indissolubility for plasma in a cylindrical tube:

$$\frac{\partial\rho}{\partial t'} + \frac{1}{r}\frac{\partial}{\partial r}(r\rho v) = 0\,, \qquad (22)$$

where ρ is density of plasma inside of the tube, v is speed of evacuation of this plasma, t' is current time with the beginning of readout in the beginning of process of evacuation of plasma. For approximate estimations we shall lead to (22) replacements of variables: $\rho(r,t) = \bar{\rho}(t)$, $v(r,t) = v_A(t)$, where $\bar{\rho}(t)$ is average on all volume of a tube density of plasma, $v_A(t)$ is the average speed as which we shall use Alfven speed as the first approximation:

$$v_A(t) = B_{\max}/[\mu_0\bar{\rho}(t)]^{1/2}\ . \qquad (23)$$

Here $B_{\max}$ is the maximal induction of the magnetic field created by the coil. Then in view of (23) and proportionality of density $\bar{\rho}(t')$ and concentration of plasma $n(t')$, we shall receive the solution of the equation (22) at $t' \le \tau_a$ in the form of

$$n(t') = n_0(1 - t'/\tau_a)\,. \qquad (24)$$

Here boundary conditions $r(t') = a$ and entry conditions $\bar{\rho}(0) = \rho_0$ have been used, $\rho_0/n_0 = const$, n_0 is initial concentration of plasma, τ_a is time of "full evacuation":

$$\tau_a = 2a\sqrt{\mu_0\rho_0}/B_{\max}\ . \qquad (25)$$

From a parity (24) follows, that through time $t' = t_{\rm cr}$, where $t_{\rm cr}$ is critical time, concentration of plasma can decrease to value $n(t_{\rm cr}) = n_{\rm cr}$. As according to the estimations $n_{\rm cr} << n_0$, lead above on the basis of (24) it is had $t_{\rm cr} \cong \tau_a$.

For an illustration of the received results we shall accept $B_{\max} = 2.5\ {\rm T}$, $a = 1 \cdot 10^{-2}\ {\rm m}$, $\rho = 5 \cdot 10^{-3}\ {\rm kg/m^3}$, then by (25) we have $\tau_a \approx 5 \cdot 10^{-7}\ {\rm s}$. Thus during the moment of transition of electrons in a mode of continuous acceleration their energy presumably reaches size $p/(2en_{\rm cr}) \approx 450\ {\rm eV}$, that looks is quite realistic, considering low concentration of plasma and strong enough vortex electric field.

Let's estimate also typical time of back front at $E_a = 500\ {\rm V/m}$ and conditions of the previous problem. According to (13) in view of (4) it is had

$$\tau_b = aB_{\max}/(2E_a) \approx 5 \cdot 10^{-5}\ {\rm s}.$$

As follows from the resulted estimations $\tau_b >> \tau_a$, therefore in the further calculations by time τ_a we shall neglect.

For simplification of the analysis spent further we shall allocate conditionally on the period τ_b two intervals of time:

– $0 \le t < \eta\tau_b$ is the period of a set a tube of equilibrium current with evacuation of plasma a flesh before occurrence run away electrons;

– $\eta\tau_b \le t \le \tau_b$ is the time of acceleration of run away electrons.

A run away electron in a considered case with originally small energy $W_{\rm cr}$ gets in strong enough vortex electric field E and in a contour with radius $r = a$ it receives an impulse P_e and accordingly energy W_e for the period of time $(1-\eta)\tau_b$. Let's consider further a practical case interesting to us ultrarelativistic electron

$$\gamma = \left[1 - (v_e/c)^2\right]^{-1} >> 1, \qquad (27)$$

where γ is the relativistic factor, v_e is speed of electron in the end of the period of acceleration, c is speed of light. In this case energy of electron reaches size $W_e = \gamma m_e c^2 = cP_e$, where $P_e = eE(1-\eta)\tau_b$. On the basis of told in view of (13) and (19) it is had

$$\gamma = \alpha_s I_{\lim}/I_\gamma, \qquad (28)$$

where $I_{\lim}$ is «limiting current», is that part of peak value of a primary current which is necessary for produce ultrarelativistic electron, having the set relativistic factor γ:

$$I_{\lim} = I_{\max} - J_0, \qquad (29)$$

I_γ is a constant that has such dimension as a current,

$$I_\gamma = \frac{4\pi c m_e}{\mu_0 e} \approx 17 \cdot 10^3\ {\rm A}, \qquad (30)$$

and α_s is form-factor of system, it is the parameter entered for convenience of transition from cylindrical geometry of plasma to toroidal geometry,

$$\alpha_s = 2\pi a/L. \qquad (31)$$

5. Energy losses of the ultrarelativistic electron

Within the limits of the accepted model we shall believe, that in the field of distribution ultrarelativistic electrons on a surface of a vacuum tube there are only ions of hydrogen isotopes. It is based on quite reasonable assumption that penetration thermal electrons and heavy ions with the electronic rests are reliably blocked by local potential of collective of ultrarelativistic electrons.

Let along some axis x moves ultrarelativistic electron that distance up to a scattered ion makes r_e, and the electric field of electron is described by the known formula [11]

$$E_r = \frac{e}{4\pi\varepsilon_0 r_e^2} \cdot \frac{1 - v_e^2/c^2}{\left[1 - \left(v_e^2/c^2\right)\sin^2\vartheta\right]^{3/2}}. \qquad (32)$$

Here $\sin\vartheta = b/r_e$, where b is a sight parameter. Further according to the standard procedure [12] we shall consider only a cross-section component of an impulse of an ion, using the formula:

$$P_i = \int_{-\infty}^{\infty} eE_r \sin\vartheta dt. \qquad (33)$$

Substituting (32) in (33), doing replacement $dt = dr_e/v_e = -bd\vartheta/\left(V_e \sin^2\vartheta\right)$, making integration to standard procedure [13], and believing then $v_e \cong c$, we receive

$$P_i = e^2/(2\pi\varepsilon_0 bc\gamma). \qquad (34)$$

From (34) follows, that at individual collision a not relativistic ion with mass m_i gets the energy

$$W_i = P_i^2 / (2m_i). \quad (35)$$

It is obvious, that ultrarelativistic electron loses this energy and in this case in a cylindrical layer of ions with concentration n_0 in radius b, thickness db at length dx ultrarelativistic electron loses energy dW_e according to the formula

$$d\left(\frac{dW_e}{dx}\right) = W_i \cdot 2\pi n_0 b db, \quad (36)$$

where dW_e/dx is an energy loss of ultrarelativistic electron on unit of length of run.

Substitution in (36) formulas (35) both (34) and integration of the received expression within the limits of $b_{\max} \le b \le b_{\min}$ in view of (21) gives result

$$\frac{dW_e}{dx} = \frac{e^4}{8\pi\varepsilon_0^2 c^2 k} \cdot \frac{p \ln\Lambda}{T m_i \gamma^2}. \quad (37)$$

Here $\ln\Lambda$ is the logarithm:

$$\ln\Lambda = \ln(b_{\max}/b_{\min}). \quad (38)$$

Here $b_{\max}$ and $b_{\min}$ are the maximal and minimal values of sight parameter, accordingly.

6. Calculation of the coulomb logarithm

For a finding of numerical value of the Coulomb logarithm we shall traditionally accept the Debye radius of shielding in plasma as $b_{\max}$:

$$b_{\max} = r_D = \sqrt{\frac{\varepsilon_0 kT}{e^2 n_0}}. \quad (39)$$

Size $b_{\min}$ we shall find, using quantum consideration [13], according to which $b_{\min}/b_{\min}^{(cl)} = 1/\alpha$, where $\alpha = e^2/(4\pi\varepsilon_0 c\hbar)$ is – a constant of thin structure, and $b_{\min}^{(cl)}$ is the bottom limit of integral according to the classical point of view when at a head-on collision kinetic and electrostatic to energy of a particle are equal $\gamma m_e c^2 = e^2 \Big/ \left(4\pi\varepsilon_0 \gamma^2 b_{\min}^{(cl)}\right)$ (the effect of relativistic compression of an electric field of electron in γ^2 time here is considered at $\vartheta = 0$ (32)). On the basis of told it is had

$$b_{\min} = \frac{b_{\min}^{(cl)}}{\alpha} = \frac{\lambda\!\!\!^{-}}{\gamma^3}. \quad (40)$$

Here $\lambda\!\!\!^{-} = \hbar/(m_e c)$ is the Compton length of electron. Substituting (39) and (40) in (38) and considering (21) it is received

$$\ln\Lambda = \ln\left(\frac{k\sqrt{2\varepsilon_0}}{e\lambda\!\!\!^{-}} \cdot \frac{T\gamma^3}{\sqrt{p}}\right). \quad (41)$$

If, for example $T = 11600$ K, $p = 10^5$ Pa according to (41) at $\gamma = 5$ it is had $\ln\Lambda \approx 15$, and at $\gamma = 30$ it is had $\ln\Lambda \approx 21$. Such values of the Coulomb logarithm are typical for plasma.

7. Toroidal geometry of plasma

Let's pass now to toroidal geometry of plasma. It is obvious, that the tube can be curtailed into a ring, and this ring from the point of view of electromagnetic processes will be equivalent to the considered tube, if at the identical size a

$$L = 2\pi R, \quad (42)$$

where L is length of a tube, R is the big radius of a ring, a is small radius of a ring and a tube. In this case all positions and the formulas received first part of the work for MHD configuration with cylindrical geometry of plasma will be fair and for toroidal geometry, thus in view of (31) forms-factors of a ring will make

$$\alpha_s = a/R. \quad (43)$$

Two versions limited equilibrium MHD configurations with toroidal geometry of plasma are known: a ring with screw current in an atmosphere of motionless gas [1] and a ring with poloidal current inside of a gas vortex ring [4]. The general attribute of these rings is the toroidal magnetic field; therefore conditions of their balance practically coincide. However conditions of stability are various. In first of rings a tension force of a toroidal magnetic field it is counterbalanced by forces of pressure of poloidal magnetic field created by a toroidal component of a screw current, and in the second of rings these forces are counterbalanced by centrifugal forces of rotating layers of gas of a vortex ring. We shall notice, that the ring with a screw current demands exact maintenance of the set parity poloidal and toroidal components of the

screw current, that in the technical plan difficultly to execute. To receive cleanly poloidal current in a vortex ring technically is much easier; therefore in the further we shall concentrate attention to second of the mentioned rings, Fig. 2.

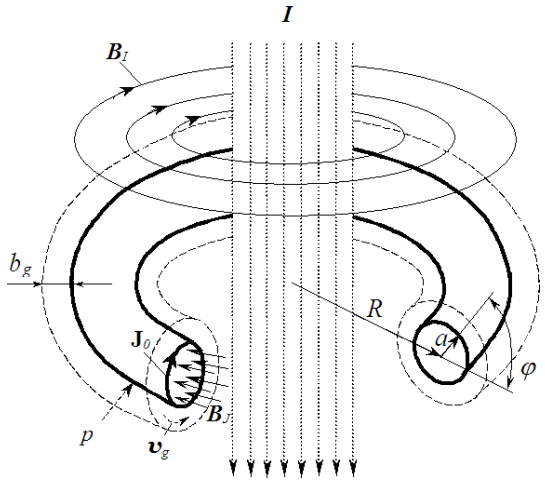

Figure 2. *The schematic image of the stable MHD configuration in the form of a ring with induced poloidal current* $\mathbf{J}_0$*, and electroconductive channel with primary current* ***I****.*

Vacuum ring shown on fig. 2 is inside of a vortex gas ring, in which is root-mean-square speed of movement of gas layers, p is pressure of adjoining gas layers, b_g is effective thickness of the gas ring, φ is an any corner.

8. Lifetime of the ring without additional charging from the outside

As it has been shown earlier [1], the ring with a current is capable to exist without additional charging from the outside; its lifetime t_σ is defined by time of easing of originally created current owing to collisions of electrons with ions, and according to the formula [1] takes place

$$t_\sigma \approx 10a^2(v_e/c)^3 .$$

As a numerical example in the [1] it was accepted $a \approx 1$ cm, $v_e/c \approx 10^{-2}$, and it has been calculated $t_\sigma \approx 10^{-5}$ s. This time is represented uninviting, however it is necessary to pay attention to following circumstance. The parity $v_e/c \approx 10^{-2}$ in [1] was accepted any way and if, for example, to accept $v_e/c \approx 0.98$ (that corresponds $\gamma \approx 5$), it is received $t_\sigma \approx 9$ s. Certainly, the formula given in [1] is inapplicable for ultrarelativistic electrons, but it formally illustrates the fact of an opportunity of sharp increase of lifetime of MHD configuration if electrons possess significant energy. This feature has been considered in [4], however thus reserved kinetic energy of electrons in calculation was not accepted, therefore the results received in [4] it is necessary to consider only as preliminary.

Let's lead a rough estimation of expected lifetime τ_E of a ring, believing, that it possesses the total energy including energy of a toroidal magnetic field W_M and kinetic energy of electrons $W_e K_e$, where W_e is kinetic energy of one ultrarelativistic electron, K_e is number of such electrons. Let total energy due to Coulomb collisions of electrons with ions dissipates with speed dW_e/dt. Then, considering, that in our case $dW_e/dt \approx c\, dW_e/dx$, it is possible to write down in rough approximation:

$$\tau_E = \frac{W_M + W_e K_e}{c(dW_e/dx)K_e} . \qquad (44)$$

Energy of a magnetic field in view of (12) and (42) makes

$$W_M = 2\pi^2 a^2 R \cdot \frac{\mu_0}{2}\left(\frac{J_0}{2\pi R}\right)^2 \equiv 2\pi^2 a^2 R p . \qquad (45)$$

Energy of one ultrarelativistic electron and their total at $v_e/c \approx 1$ make, accordingly,

$$W_e = \gamma m_e c^2 , \qquad (46)$$

$$K_e = 2\pi a J_0/(ec) . \qquad (47)$$

Substituting (45), (47), (37) and (46) in (44) we receive the formula for an estimation of lifetime of a ring in the form of

$$\tau_E = C_E D_E \cdot \frac{T m_i a \gamma^2}{\sqrt{p}\ln\Lambda} + C_E \cdot \frac{T m_i \gamma^3}{p \ln\Lambda} . \qquad (48)$$

Here C_E and D_E are constants:

$$C_E = \frac{8\pi k \varepsilon_0^2 m_e c^3}{e^4} \approx 1\cdot 10^{27}\ \mathrm{K^{-1}m^{-1}s^{-1}} ,$$

$$D_E = \frac{e\sqrt{\mu_0}}{2\sqrt{2 m_e c}} \approx 0.23\ \mathrm{kg^{-1/2}m^{-1/2}s} .$$

Let, for example, $T = 2\cdot 10^4$ K, $p = 10^5$ Pa, $\gamma = 5$, $m_i = 1.67\cdot 10^{-27}$ kg, $a = 0{,}01$ m, $\ln\Lambda = 15$, then $\tau_E \approx 3$ s.

The formula (48) can be simplified. We shall pay attention to following circumstance. If in the right part in the ratio (48) takes place

$$2C_E D_E \cdot \frac{Tm_i a\gamma^2}{\sqrt{p}\ln\Lambda} \le C_E \cdot \frac{Tm_i\gamma^3}{p\ln\Lambda},$$

that at

$$a \le \frac{\gamma}{2D_E\sqrt{p}} \tag{49}$$

the first component in the formula (48) can be neglected. Then for small rings the lifetime τ_E^{small} will be approximately equal

$$\tau_E^{\text{small}} = \tau_\gamma \cdot \gamma^3 . \tag{50}$$

Here τ_γ is the size depending on conditions of experiment:

$$\tau_\gamma = C_E \cdot \frac{Tm_i}{p\ln\Lambda} . \tag{51}$$

The formula (50) is convenient for approximate estimations of expected lifetime of MHD configurations at planning experiments in the open atmosphere. For example, at $T = 2\cdot 10^4$ K, $\ln\Lambda = 15$, $p = 10^5$ Pa, $m_i = 1.67\cdot 10^{-27}$ kg we have according to (51)

$$\tau_\gamma \approx 0.022 \text{ s} .$$

Thus, if $\gamma = 5$, the formula (50) can be used according to (49) for the sizes

$$a \le 0{,}03 \text{ m} .$$

This condition is usually carried out for experiments in the open atmosphere, as it will be shown further.

9. Conditions of MHD stability of the ring

Found lifetime of a ring is achievable only in dynamically stable formation. According to the theory [1] the question on stability of system in the form of a ring with current has three aspects:

- Existence of an equilibrium condition of a ring,
- Stability of a ring in relation to change of the form,
- Stability of a ring to change of the sizes in a condition of balance at the constant form.

In the beginning we shall define an equilibrium condition of a ring. For this purpose we shall allocate any small platform s for surfaces of a ring and we shall consider the forces acting on this platform, taking into account, that the induction of a magnetic field in the field of a platform B_J is function of a corner φ (fig. 2). Force of magnetic pressure $s\cdot B_J^2/(2\mu_0)$ is counteracted with force of external pressure $s\cdot p_g$ from motionless external gas, which is weakened by centrifugal force F_g of rotating layers of gas. The total force F_s acting on a small platform s in a direction of increase in small radius a is equal

$$F_s = s\cdot B_J^2/(2\mu_0) - (s\cdot p_g - F_g). \tag{52}$$

The formula (52) can be used for definition of the form of section of an equilibrium configuration. For thin rings $(a << R)$ according to conclusions of [1] this section represents a circle, and in this case formulas are fair

$$B_J = \mu_0 J_0/[2\pi(R + a\cos\varphi)] \approx \\ \approx \mu_0 J_0[1 - (a/R)\cos\varphi]/(2\pi R), \tag{53}$$

$$F_g \approx s\cdot b_g \rho_g v_g^2/a , \tag{54}$$

$$p_g s - F_g = ps . \tag{55}$$

Here ρ_g is average density of substance of a gas ring..

Balance of system will take place, if

$$F_s = 0 . \tag{56}$$

In this case, substituting (53) and (54) in (42) in view of (55) on the basis of (56) we define a condition of balance which exists under condition of

$$J_0 = 2\pi R\cdot\sqrt{2p/\mu_0} .$$

As we see, the received formula in view of (42) coincides with the formula (12).

Stability of a ring in relation to change of the form we shall consider on the basis of the criterion deduced in [1] for a case of superposition toroidal and poloidal fields for a ring with a screw current:

$$B_{10}^2 > B_{20}^2\left(\ln\frac{\lambda}{\pi a} - C\right).$$

Here B_{10} and B_{20} are inducted toroidal and poloidal fields, accordingly arising at superposition

of poloidal and toroidal currents on surface of ring, λ is length of a wave of indignation in a ring, C is a constant. For considered by us МГД configurations takes place $B_{10} > 0$ and $B_{20} = 0$ (is present only poloidal current, and toroidal current is absent), therefore the criterion in relation to change of the form of a considered ring with a current is carried out at any λ.

Let's consider now stability of balance of a ring at an invariance of its form. In this case conditions of stability according to the [1] are defined by formulas

$$\partial F_S / \partial R < 0 . \quad (57)$$

$$\partial F_S / \partial a < 0 . \quad (58)$$

To solve this problem within the framework of accepted models assume that the magnitude ρ_g, b_g and v_g unchanging. Then (57) and (58) with (52) (53) (54) (55) and (12) with (42) take the form:

$$\frac{\partial F_S}{\partial R} = \frac{s\mu_0 J_0^2}{4\pi^2}\left(-\frac{1}{R} + \frac{3a\cos\varphi}{R^2}\right) < 0 ,$$

$$\frac{\partial F_S}{\partial a} = -\frac{s\mu_0 J_0^2 \cos\varphi}{4\pi^2 R^3} - \frac{s\rho_g v_g^2 \Delta_a}{a^2} < 0 .$$

The first of these conditions are satisfied if $a < R/3$, or, using (43)

$$\alpha_S < 1/3 . \quad (59)$$

The second condition is satisfied if $v_g > v_c$, where v_c is the critical velocity:

$$v_c = \sqrt{\frac{2p\alpha_S a}{\rho_g b_g}} . \quad (60)$$

Note that the usual $F_g << sp_g$, and guideline for assessment under the assumed model can be assumed $p \approx p_g$. In addition, we note that formula (60) with (43) coincides with the formula for the critical speed, obtained earlier in [4], according to which the rate is about 40% of the speed of sound.

10. Stable mhd configuration and theory of the ball lightning phenomenon

For several reasons, the theory of ball lightning (BL) has not yet been established. "The main reason for the" recalcitrance "of the problem lies in the random nature of its occurrence and short duration of its life," as noted in [14], and further: "There is another reason why the knowledge of the properties of BL. This - the apparent simplicity of its formation in nature. In fact, the nature without any sophisticated instruments can do it from the usual linear lightning. Why not try to organize a powerful electric discharge in the environment (air, sand, water, etc.) and see what happens. The vast majority of experiments on laboratory reproduction of ball lightning is constructed on the basis of this simple scheme. Sometimes, in these experiments, in fact, obtained glowing formations similar to BL. However, the chance of occurrence and non-repeatable, these experiments do not differ much from the "experiments" that "makes" nature. " Indeed, numerous attempts to model the effects of BL, as described, for example, in [15], [16], [17] were not successful in the sense of obtaining the plasmoids with a lifetime of about 10 s, characteristic of the natural phenomenon of ball lightning [18]. Reasons for the failure may lie in ignoring the theory of equilibrium MHD configurations. Note that in this theoretical model of the formula (51)

$$\gamma = \sqrt[3]{\tau_E^{\text{small}} / \tau_\gamma} , \quad (61)$$

and, therefore, that the MHD configuration had a lifetime $\tau_E^{\text{small}} \approx 10$ s is only necessary to provide $\gamma = \sqrt[3]{10/0.022} \approx 7.7$. It is quite possible, as shown below.

It follows that, apparently, the most realistic way of addressing the BL is an experimental simulation of natural phenomena, based on the theory of MHD configurations.

11. Possibility modeling of ball lightning using a powerful spark discharges

If a channel spark discharge passed through the center of the gas vortex ring [4], the inside of the ring may, in principle, the formation of MHD equilibrium configuration shown in Fig. 2. Abstracting from the particular problems of formation of such a system will focus on the most important issue, we estimate the amplitude of the current spark necessary for the formation of equilibrium MHD configuration having dimensions and lifetime, similar to the natural ball lightning. In addition, we compare the theoretical results about the amplitude of the primary current with known information about the usual linear lightning in nature.

Let them be considered given the following parameters of the MHD equilibrium configuration: $\tau_E^{\text{small}} \approx 10$ s, $R = 0.04$ m. The geometric size R adopted here is not arbitrary, it is the same size as the fragment of window glass, natural ball lightning knocked out [19]

Solution of the problem will begin with the calculation of the relativistic factor on the basis of (61):

$$\gamma = \sqrt[3]{\tau_E^{\text{small}} / \tau_\gamma} \approx 7.7 .$$

Further, on the basis of formulas (28) (30) and taking into account (59), we calculate the limiting current assuming $\alpha_s = 0{,}33$:

$$I_{\text{lim}} = I_\gamma \gamma / \alpha_s \approx 4 \cdot 10^5 \text{ A} .$$

We find the equilibrium current (12) with (42):

$$J_0 = 2\pi R \cdot \sqrt{2 p_0 / \mu_0} \approx 1 \cdot 10^5 \text{ A} .$$

The required amplitude of the primary current on the basis of (29) is

$$I_{\max} = J_0 + I_{\text{lim}} \approx 5 \cdot 10^5 \text{ A} .$$

Consequently, it is the pulse amplitude of the primary current level of about 500 kA in the experiments should strive to model the phenomenon of ball lightning when using the spark discharge. Note that in natural conditions, this current pulse amplitude actually possible for a positive linear lightning discharge [30]. And here it should be emphasized that these are the linear lightning have a "right" direction of current, which is most favorable for the formation of ring with current (Fig. 2). In this case, the direction of the electron and gas flows in the ring are the same, and in such a situation, the transmitted pulse in head-on collisions of electrons to the ions contributes to long-term preservation of the gas vortex ring configuration, providing the stability of the MHD.

12. The threshold effect

Note the presence of a threshold effect for the primary current associated with the strong dependence of the expected lifetime of the MHD equilibrium configuration (51) of the relativistic factor γ , and consequently, the amplitude of the primary current. We specify a minimum value of the parameters: $\tau_E^{\min} = 3\,\text{s}$ is the minimum allowable lifetime, $R_{\min} = 0.02\,\text{m}$ is a minimum size. Then combining (28) (29) (30) (50) and (12) with (42) we obtain for the minimum amplitude of the primary current $I_{\max}^{\min}$:

$$I_{\max}^{\min} = 2\pi R_{\min} \sqrt{2p/\mu_0} + \\ + \sqrt[3]{\tau_E^{\min} / \tau_\gamma} I_\gamma / \alpha_s \approx 3 \cdot 10^5 \text{ A}. \qquad (62)$$

13. Obtaining plasmoid by electric explosion of wire spiral that coiled into a torus

The discharge «ΙΘ-пинч» can be realized experimentally, at least in principle, by the electrical explosion of spirals of wire, coiled into a torus, Fig. 3.

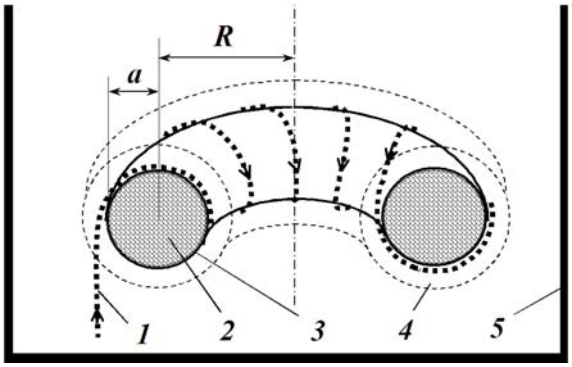

Figure 3. *Schematic illustration of exploding spirals of wire, coiled into a torus.*

The physical idea of experiments [21] lies in the fact that a helix 1 (Fig. 3) passes a current so strong that it created within the magnetic field of 2 with the induction $B_{\max}$, in which the magnetic pressure $B_{\max}^2 / (2\mu_0) >> p_A$, where p_A - is the atmospheric pressure. In the explosion of the helix had at it with the magnetic field induction $B_{\max}$ decreases rapidly, but some of it $\eta < 1$ may be captured plasma coil 3 so that $\eta^2 B_{\max}^2 / (2\mu_0) = p_A$.

It is assumed that form strong MHD configuration in the form of a ring with a current, maintains the balance of the outer gas, which then exists without any make-up from the outside. In implementing the ideas set out the physical, but above, provides for the formation of a vortex gas ring 4 (Fig. 3), which enhances the stability of the MHD configuration. Gas ring 4 is formed by the nozzle 5.

In the experiments, a technique which is described in [7] used the image of a toroidal structure two wire spirals to the left and right winding 30 turns of wire diameter, electrically connected in parallel. Large radius of the torus was, was a small radius of the torus. The best result was obtained with the voltage and line current of spirals, it is shown in Fig. 4 in the form of successive

frames video (see below for frame-fitting 5, its diameter is 12 cm).

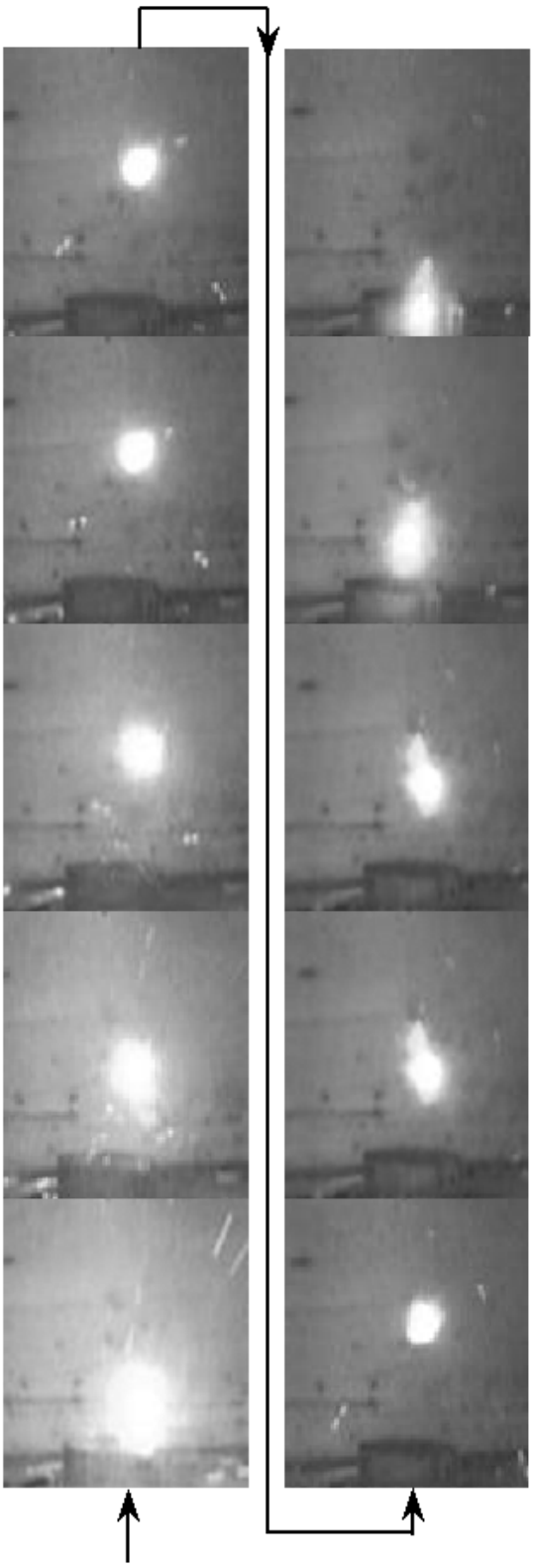

Figure 4. *Sequential frames (30 s-1) video of the process of electrical explosion of wire spirals coiled into a torus.*

It should be noted that due to various instabilities that accompany the electric explosion of conductors [22], the percentage of positive results of long-lived plasmoids getting very low. Nevertheless, high precision and careful execution of spirals configuring the installation, were obtained plasmoids with abnormally long lifetime, evidence in favor of the fact that the lifetime of MHD stable configurations in the form of a ring with a current, supported by the pressure of external gas, can significantly exceed a pessimistic estimate, given in [1].

We carry out numerical calculations of the lifetime obtained in experiments with the MHD configuration of these parameters of the experiment, given that the

experiment in which the primary current value was

$$I_{\max} = I \cdot N = 5 \cdot 10^3 \cdot 30 = 150 \cdot 10^3 \text{ A}.$$

Solution of the problem will begin with the calculation based on equilibrium current (12) with (42):

$$J_0 = 2\pi R \cdot \sqrt{2p_0/\mu_0} = 2\pi \cdot 0.0075 \cdot \sqrt{2 \cdot 10^5 / \left(4\pi \cdot 10^{-7}\right)} \approx 19 \cdot 10^3 \text{ A}$$

Urther, based on (29) we find the limiting current:

$$I_{\lim} = I_{\max} - J_0 = 150 \cdot 10^3 - 19 \cdot 10^3 = 131 \cdot 10^3 \text{ A}$$

We define the relativistic factor (28) (30):

$$\gamma = \alpha_s I_{\lim} / I_\gamma = 0.33 \cdot 131 \cdot 10^3 / \left(17 \cdot 10^3\right) \approx 2.54$$

The expected lifetime of the plasmoid is (50):

$$\tau_E^{\text{small}} = \tau_\gamma \cdot \gamma^3 = 0.022 \cdot (2.54)^3 \approx 0.36 \text{ c}.$$

The resulting theoretical estimate agrees well with the experimental results shown in Fig. 4: 10 fps video recording at 30 s^{-1} corresponds to the experimentally derived lifetime of the plasmoid $\tau_E^{\text{experim}} = 10 \cdot (1/30) = 0.3 \text{ s}$.

14. Conclusion

Thus, the rapid decline of the strong magnetic field in the discharge volume may occur inductive discharge, tentatively called "inverse theta-pinch", and according to the model proposed in this discharge, along with ohmic heating of the plasma can be realized the following processes:

- The formation of thin-walled tube with a current,
- The seizure of the tube a certain amount of falling external magnetic field,
- Evacuation of the plasma inside the tube,
- Acceleration on the surface formed by the vacuum tube of runaway electrons to ultrarelativistic energies.

As a result of these processes can form a plasmoid with a strong magnetic field. The results of experiments associated with obtaining the plasmoids in the electric explosion of wire spirals give the lifetime of the plasmoid, which agrees well with the calculated values of the considered theoretical models.

Under certain conditions, the estimated lifetime of the considered equilibrium limited MHD configuration is consistent with a lifetime of natural ball lightning, and the amplitude of the primary current required for the formation of this configuration corresponds to the amplitude of natural linear positively charged lightning. This allows the use of inductive discharge considered to simulate the natural phenomenon of ball lightning. If the experimental results confirm the main findings of these theoretical models, this model can be adopted as the basis for developing the theory of the phenomenon of ball lightning. Such a theory could easily explain the fact of a rare observation of natural phenomena BL, this is due to the presence of a threshold effect for the amplitude of the primary current (62). This effect eliminates the usual linear lightning discharge with negative polarity [20] from the list of possible sources of pulsed magnetic fields that can produce a ball lightning. At the same time are linear in nature, lightning, an overwhelming majority.

Revealed a threshold effect on the minimum amplitude of the primary current of 300 kA (62), was apparently the deciding factor that led to failures in experiments to model the phenomenon of BL [15], [16], [17]. The foregoing should be considered when planning experiments to model natural phenomenon of ball lightning.

References

1. Shafranov V.D. / / JETP 1957. T. 33. P. 710-722.
2. Raizer Yu.P. Physics of gas discharge [In Russian]. – Moscow: Nauka, 1987.
3. Kroll N. and Trayvelpiese A. Principles of Plasma Physics. – New York: McGraw Hill, 1973.
4. Vlasov A.N. / / JETP 1990. T. 97. P. 468-475.
5. Vlasov A.N. *Possible creation and stabilization of a rotation θ-pinch* [in Russian], Dept. of Electronics Rep. No. 10296, TsNII, 1986.
6. Vlasov A.N. / / Journal RGRTU. Vol. 21. Ryazan, 2007. P. 73-81.
7. Kolotilin B.I. and Kolesnikov S.A. / / Journal RGRTU. Vol. 21. Ryazan, 2007. P. 65-68.
8. Artsimovich L.A. Controlled thermonuclear reactions. – New York: Gordon and Breach, 1964.
9. Miyamoto K. Fundamentals of plasma physics and controlled fusion [in Russian] / Translated from English under the general editorship. V.D. Shafranov. – Moscow: Fizmatlit, 2007.
10. Tikhonov A.N., Samarskii A.A., Zaklyazminsky and etc. / / Reports of USSR Academy of Sciences. 1967. T. 173. No 4. P. 808-811.
11. Landau L.D. and Lifshitz E.M. Theoretical Physics [in Russian]: A Handbook. allowance. In 10 vols II. Field theory. 7th ed. – Moscow: Rev. Nauka, 1988.
12. Sinelnikov K.D. and Rutkiewicz B.N. Lectures on Plasma Physics [in Russian]. – Kharkov: Kharkov Univ KSU, 1964.
13. Sivukhin D.I. General physics course. T. V. Atomic and nuclear physics [in Russian]. – Moscow: Fizmatlit, 2006.
14. Nikitin A.I. / / Chemical Physics, 2006. T. 25, № 3. P. 18-37.
15. Boychenko A.M. / / Technical Physics, 1999. T. 69, no. 10. P. 131-134.
16. Furov L.V. / / Technical Physics, 2005. T. 75, no. 3. P. 96-99.
17. Egorov A.I. and Stepanov S.I. / / Technical Physics, 2008. T. 78, no. 6. P. 15-19.
18. Bychkov V.L. / / Chemical Physics, 2006. T. 25, № 3. P. 7-17.
19. Schelkunov G.P., Nikitin A.I., Bychkov V.L., Nikitina T.F., Velichko A.M. and Vasiliev A.L. Examination of a Window Pane Exposed by Ball Lightning // A 92 AIS-2008: Atmosphere, ionosphere, safety: Book of Abstracts; Supported by Russian Foundation of Basic Research / Editor I.V. Karpov. – Kaliningrad, 2008. 257.
20. Aleksandrov G.N. / / Technical Physics, 2006. T. 76, No. 12. P. 101-105.
21. Vlasov A.N., Kolesnikov S.A. and Manoshkin A.B. / / Abstracts of the XXII International Conference "The impact of intense energy fluxes on substance" / ed. V.E Fortov et al - Elbrus, 2007. P. 192-193.
22. Martyniuk M.M. Phase transitions under pulsed heating [in Russian]. Monograph. – Moscow: Moscow People's Friendship University, 1999.

12.1. PLASMA-ASSISTED REACTION OF HETEROGENEOUS AL-H_2O MIXTURE IN HIGH-SPEED SWIRL FLOW

Klimov A., Bityurin V., Chinnov V., Grigorenko A., Efimov A.V., Kutuzov D.S., Tolkunov B.N., Polyakov L.B.
Joint Institute of High Temperature RAS
Izhorskaya 13/19, Moscow, 127415, Russia
klimov@ihed.ras.ru

Abstract. There is considerable interest to a creation of new alternative power sources today[1-4]. The present work is devoted to consideration of a high-effective hydrogen generator design and its operation based on Al-H20 chemical reaction assisted by a non- equilibrium plasmoid. This work is the continuation of the previous one[5-7]. The rate of this reaction may be increased up to factor 10^3 by non-equilibrium plasma. Active excited particles, radicals and ions are created by a non-equilibrium electrical discharge in swirl flow in plasma-chemical reactor (PCR). It is well-known that these particles can accelerate a creation of the chains in a reaction zone. High gas temperature in a plasma zone accelerates this reaction rate also. The main goal of this work is a design, manufacture and testing of the demo- PCR with hydrogen mass flow about of 0.1- 1G/s. The following tasks are studied in these experiments:

1. Study of the optimal parameters of a swirl flow in the PCR (component mass flow rates, flow velocity distribution, gas temperature distribution and so on).
2. Study of a stable electric discharge regimes in swirl gas flow. Optimization of power supply electric parameters.
3. Measurement of plasma parameters in the PCR.
4. Chemical analysis of the final species in this PCR.

The parameters and characteristics of electric discharge, plasma and swirl flow are measured in this work. Minimal energy balance of hydrogen molecule creation will be measured in this PCR namely.

Nomenclature

PCR	= plasma-chemical reactor
HF	= high frequency
HFD	= high frequency discharge
F_{HF}	= HF frequency
F_M	= modulation frequency of HFD
T_i	= pulse duration
I	= electric discharge current
V	= electric discharge voltage
N	= power input in plasma
M	= Mach number
V_x	= axial component of the velocity
V_t	= tangential component of the velocity
P_{st}	= static pressure
T_g	= gas temperature
T_R	= rotation temperature
T_V	=vibration temperature
T*	=electron excitation temperature
T_b	=black body temperature

I. Introduction

Today there are many discussions about a low-coast aluminum fuel for electric power production [1-5]. This method is named aluminum- hydrogen power production and based on the following chemical reaction:

$2Al + 3H_2O = Al_2O_3 + 3H_2 + Q$, where Q~15MJ/kG Al- energy release.

However the characteristic rate of this heterogeneous reaction (aluminum powder + water steam) is rather small. So, it is important to study *a plasma-assisted oxidation* of Al powder in water steam in detail to accelerate this reaction. *This is a main task of this work.* The rate of this reaction may be increased up to factor 10^3 by non-equilibrium plasma. Active excited particles, radicals and ions are created by a non-equilibrium electrical discharge in swirl flow inside plasma-chemical reactor (PCR). It is well-known that these particles can accelerate a creation of the additional chains in a reaction zone. High gas temperature in a plasma zone accelerates this reaction rate also. Note that there are active dusty (cluster) charged particles in a reaction zone of this PCR. Non- ideal plasma is created in this reactor (parameter $G=Ze^2/(N_d)^{-1/3}kT_g>>1$). High amplitude local electric field is created near a surface of this charged dusty (cluster) particle. So, traditional chemical kinetics may be wrong (uncorrected) near surfaces of these particles. So, measurement of a local electric potential in this heterogeneous plasma is very important task.

The second important task of this work is to study of the properties and the parameters of a heterogeneous plasma created by pulsed repetitive HF discharge (or DC discharge) in swirl flow. Hot

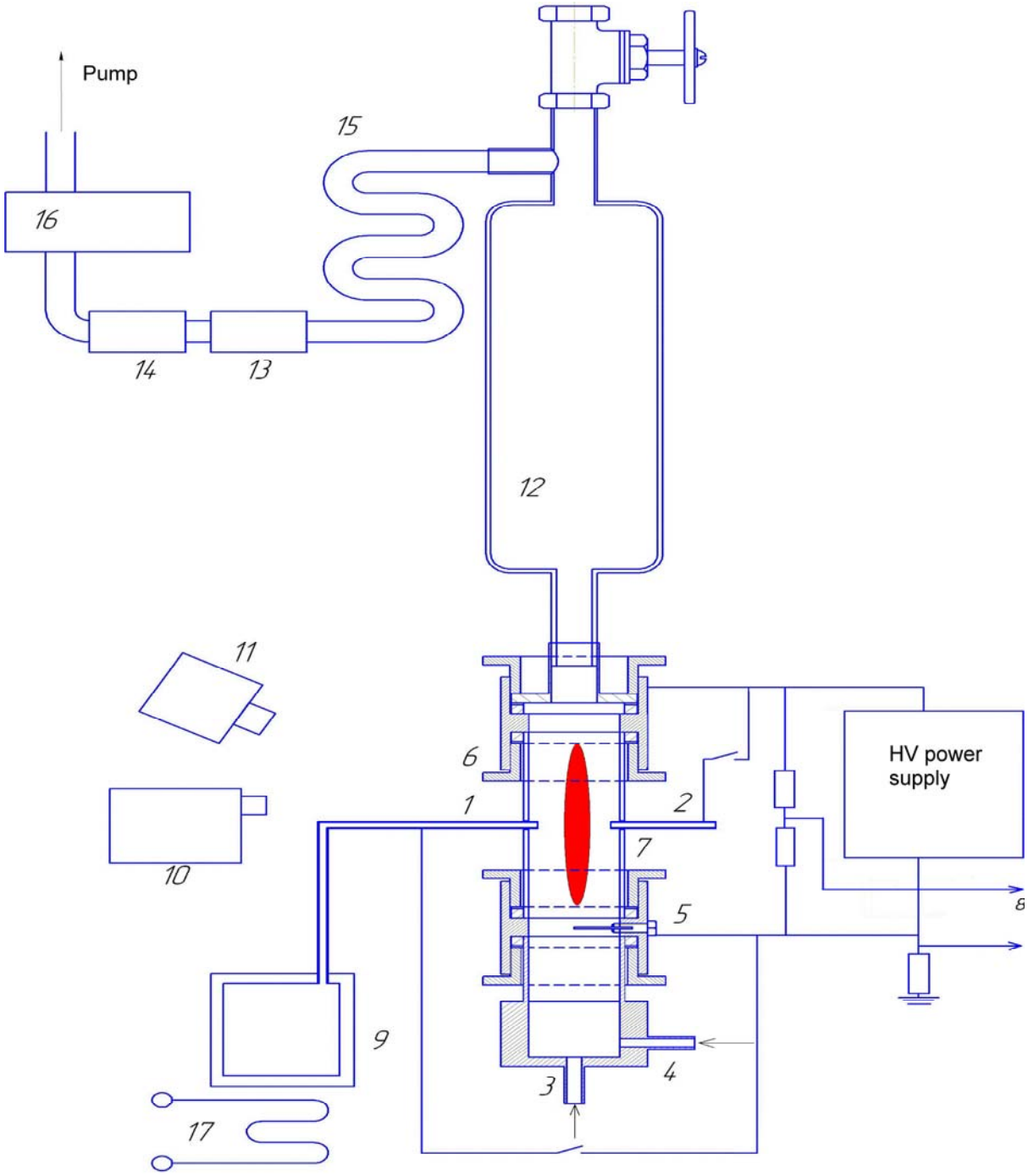

Figure 1. *Scheme of the PCR.*
1,2- tube electrodes - injectors for H2O+Al, 3,4- nozzles – injectors for argon flow, 5- tungsten electrode; 6- reactor chamber; 7- quartz tube; 8-oscilloscope; 9- H2O steam generator; 10- spectrometer AvaSpec 2048; 11-CCD camera Citius; 12- gas silence chamber; 13- gas filter; 14-chemical sensor; 15- water cooling tube; 16-pump; 17-electric heater

ionized hydrogen flow (T_g~ 3000K, N_e/N_a~10^{-4}-10^{-2}) obtained in this PCR will be used in MHD power generator in future. Design of this power generator and its operation are discussed in the work [3, 4].

II. II Experimental Setup

The scheme of the experimental setup is shown in the fig.1. The general view of this setup is shown in the fig.2. The PCR is made of quartz tube diameter 60-80 mm. Tube's thickness is about 3-5 mm. Swirl gas flow (or non-swirl one) is created by the tangential injector (4) and the axial injector (3) in this reactor. Aluminum powder is injected through tube electrode (2). This powder is pushed by argon jet in a mixer-container. Swirl argon flow is created in this reactor by swirl generator (3). It is possible to control of a vortex parameter $S= Q_\tau/Q_z$, (where Q_τ – tangential flow mass rate, Q_z- axial mass flow rate) in this experiment. Note, that this reactor design is optimal one for a separation of hydrogen and Al_2O_3 by inertial body force. Hydrogen is evacuated from reactor by thin quartz tube (chemical probe) arranged near axis. Both a vertical electric discharge and horizontal electric discharge are created in this set up. Hydrogen mass flow rate is measured by the gas analyzer AVP-01G. Water steam is generated by the electric heater (9, 17). Optical spectra of a plasma formation are recorded by the spectrometer Ava Spec 2048 (λ=200-800nm, resolution 0.08 nm). A heterogeneous plasmoid in gas flow is recorded by the high-speed camera Citius.

The following power supplies are used in this work:

- DC power supply (8kV, 2Amp),
- Tesla's coil HF generator (F_{HF}= 450 kHz, N_{HF}=1÷10 kW, pulse duration- T_i= 10 ÷10000μs, pulse repetitive frequency- F_M=10÷10^4 Hz,
- Pulsed repetitive plasma generator (pulse duration-T_i= 1000 ÷10000μs, pulse repetitive frequency- F_M<10^4 Hz, I_p~1-2 Amp, U_p<2 KV).

Note that it is possible to create combined discharge in this PCR (for example, DC+HF, PRD+HF), fig. 3, 4. So, it is possible to use independent ionizer and electron heating by this discharge. Both self-sustained discharge and non- self- sustained discharge can be created in this set up. It is possible to change pulse duration and duty cycle in this combined discharge also. So, it is possible to realize of plasma separator for metastable (long-lived) excited molecules during pause between power pulses.

Parameters of an electric discharge is measured by voltage probe Tektronix P-6082, current probe Tektronix and oscilloscope.

Figure 2. *General view of the experimental set up. 1- hot electrode 2- tube electrodes - injectors for H2O, 3- nozzle, 5-reactor chamber; 6- quartz tube; 7-water steam generator; 8- gas silence chamber; 9- water cooling tube; 10- electric probe, 11-injector Al*

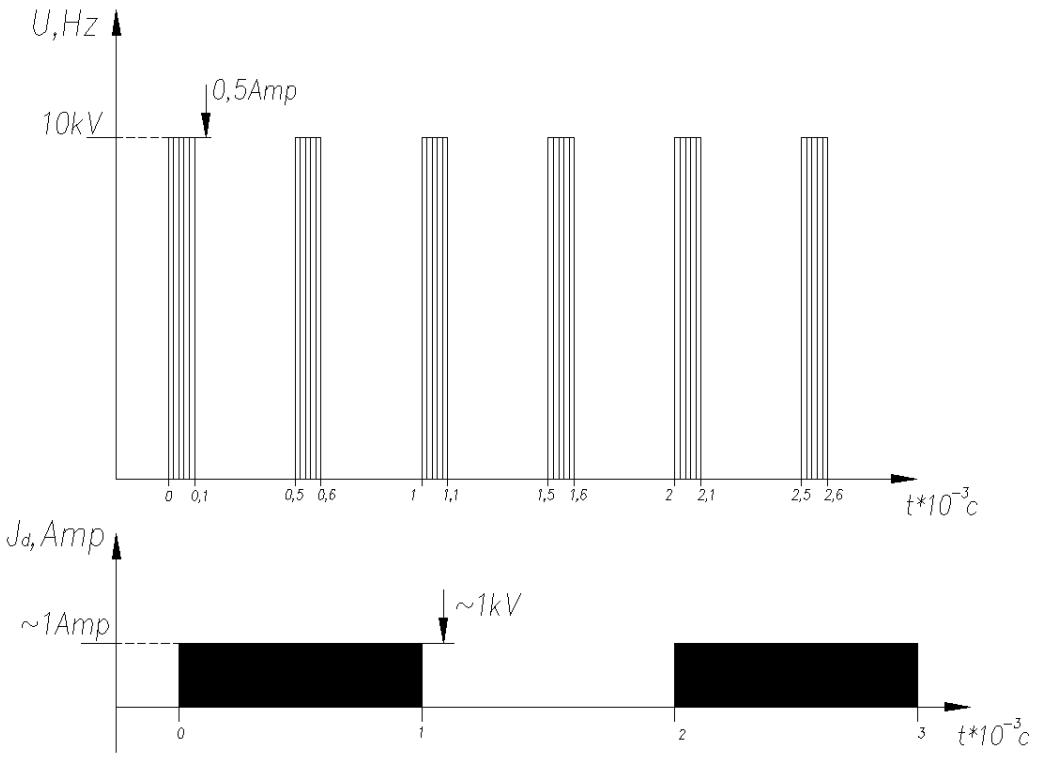

Figure 3. *Combined discharge (HF+PRD). N_{PRD} ~200÷400W, T_i ~0,5÷1ms, F_i=1kHz, `N_{HF} ~500W, F_{HF} ~2MHz, $F_{i,HF}$ ~100÷10^4Hz, $T_{i,HF}$≥10μs*

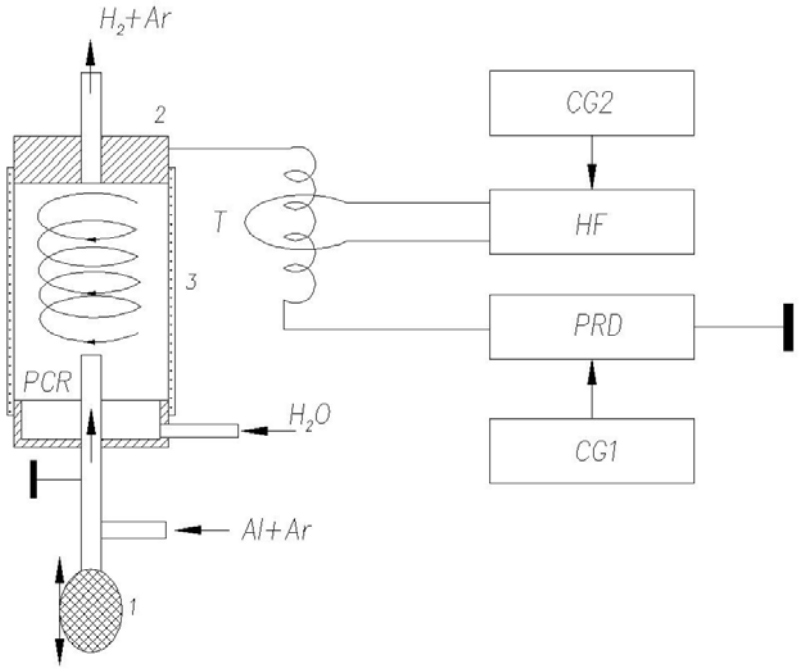

Figure 4. *Scheme of power supply for PCR. $CG_{1,2}$- command generator, HF- power supply of HF generator, PRD- power supply of PRD generator*

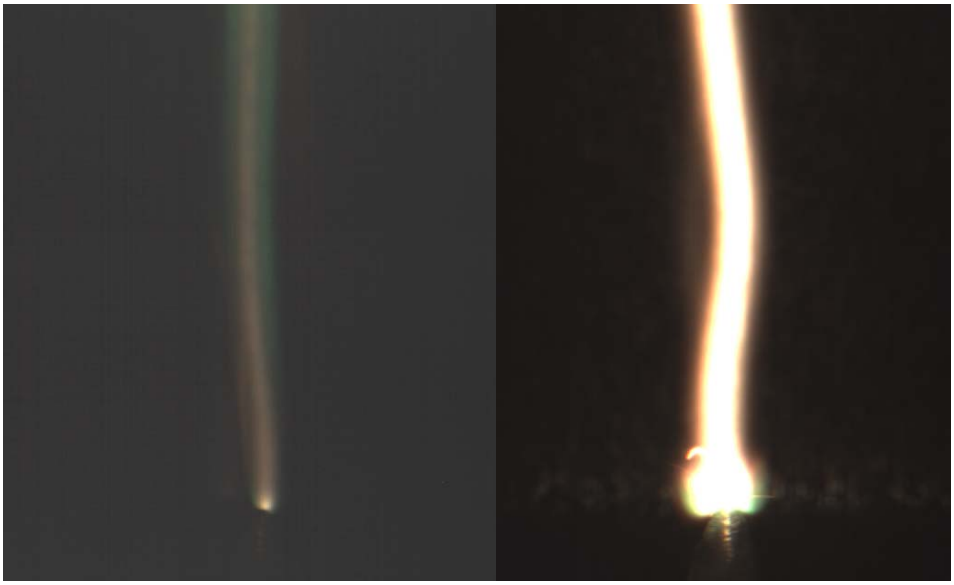

Figure 5. *The typical pictures of a combined discharge in PCR. HF discharge –right, combined discharge - left*

III. Main Experimental Results

The physical processes in heterogeneous plasma and its parameters are studied in this work. The composition and the concentrations of the final species in this PCR are measured.

The experimental conditions are the followings:

Mean voltage	200-800V,
Mean current	2Amp
Aluminum mass flow rate	<0,3G/s
Water mass flow rate	~0.3G/s
Argon mass flow rate	<1.5 G/s
Tangential gas flow velocity	<10m/s
Axial gas flow velocity	<10m/s

The typical picture of a plasmoid in argon swirl flow is shown in fig.6. One can see the different locations of hydroxyl-hydrogen (red-violet kernel near vortex axis) and AlO (blue halo around this axis) in this plasmoid.

The typical optical spectrum of heterogeneous plasma is shown in the fig.7. One can see that there are the atomic optical lines (Al, H, Ar, electrode's metal atoms), the molecular bands (OH, AlO, O), the continuous spectrum in this figure. Note that a continuous spectrum is connected with a hot dusty (cluster) particle radiation. The obtained spectra are processed. The measured rotation temperature in plasma is about of T_R~2000-3000K, the atom excitation temperature T*~3000K, the black body temperature T_b~3500K.

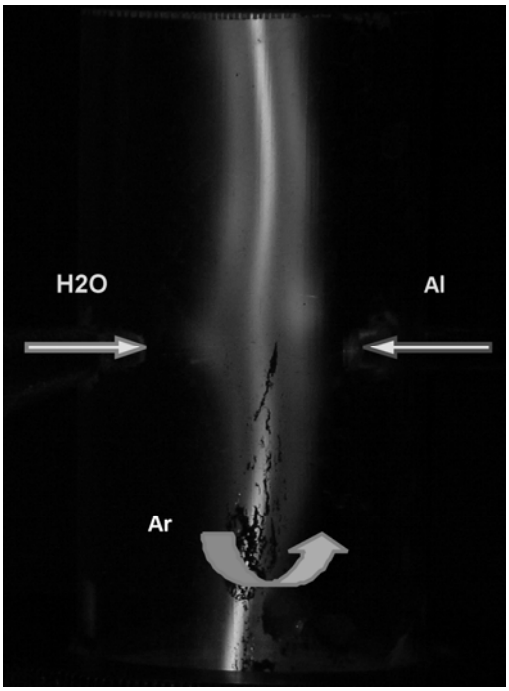

Figure 6. *The typical heterogeneous plasma formation created by vetical electrical DC discharge in swirl flow. DC current-1Amp, DC voltage -200V, V_t~10m/s, P_{st}~1 Bar, Q_{AL}~0.05G/s, Q_{H2O}~0.3G/s*

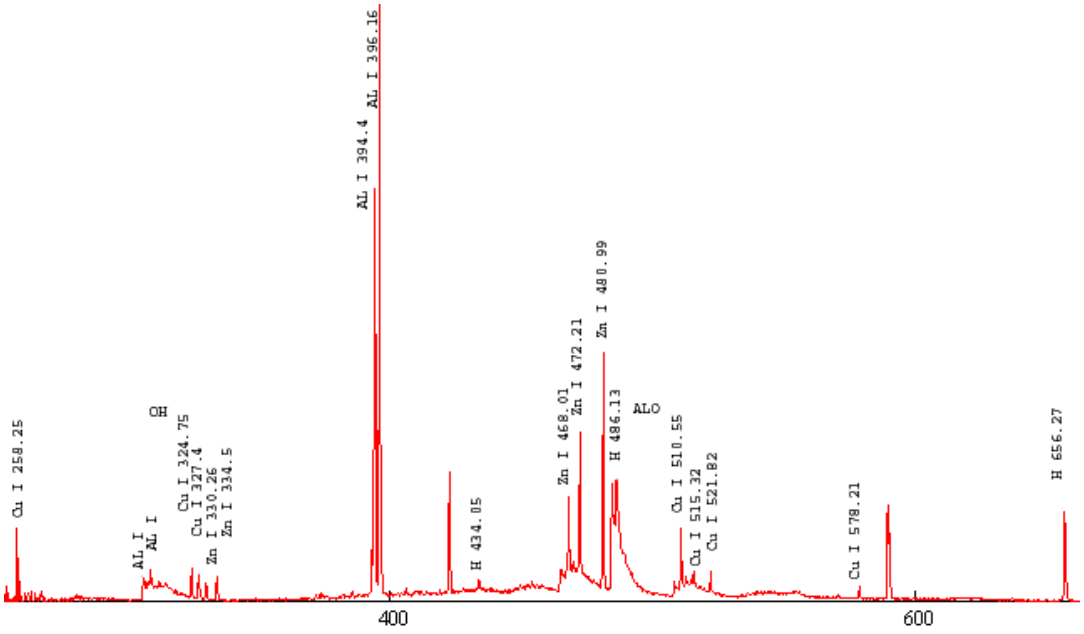

Figure 7. *The typical optical spectrum of heterogeneous H2O-Al plasma formation created in the PCR*

The value N_e is estimated by a measured plasma conductivity σ in our experiment. The value σ is estimated by voltage V_d and current I_d measured between the electrodes. The diameter D and the length L of plasma formation are measured from the obtained high-speed frames. The typical value σ is about 20 $Ohm^{-1}m^{-1}$. The typical electron concentration in plasma is about of $N_e=10^{14}$ cm^{-3}.

The analysis of the final species of output gas flow in PCR is fulfilled. It is obtained that the main dusty particles are the fine-dispersed Al_2O_3 particles and fine-dispersed Al particles (non-reacted powder). The typical average diameter of these dusty particles is about 1 μ and less. Note that the typical average diameter of initial aluminum particles is about of 100 μ.

Hydrogen is evacuated from this reactor by the chemical probe. This gas sample is analyzed by the chromatograph. The maximal H2 concentration measured in this experiment is about 20%. The measured hydrogen mass flow rate obtained in this demo- reactor is about of 0,1G/sec. Plasma parameters such as electron concentration, conductivity, power input are measured in this work.

It is revealed that there are positive charged dusty ions AlO and Al_2O_3 in cylindrical plasma formation, fig.6.

There is considerable sedimentation of these ions in the cathode electrode. So, one can conclude that there is localization of the negative charged ions OH^- near vortex axis in the PCR. The positive ions $Al_2O_3^+$ (AlO^+) are concentrated in plasma halo around plasma kernel. In a result a double electric layer is created in this plasma formation. High positive potential about several kV is measured near external boundary of this plasmoid. This double electric layer stabilizes this plasmoid considerably. Note that this radial gradient electric field can change the plasma-chemical kinetics considerably also. This question will be studied in detail in future experiments.

It is measured that power budget of hydrogen generation in this PCR is about q=2÷4 eV/ particle. Note that this value q is comparable with the one q (C_nH_m)~ 1 eV obtained by plasma catalysis of hydrocarbons [8].

Aluminum electrodes and liquid water are used as reagents in the PCR in some experiments also. Erosive aluminum clusters and erosive water clusters are created by pulse repetitive HF electric discharge in this reactor. The scheme of this PCR is shown in the figure 8. One can see that the design of this PCR is very simple (Al powder injector and water steam injector are absent).

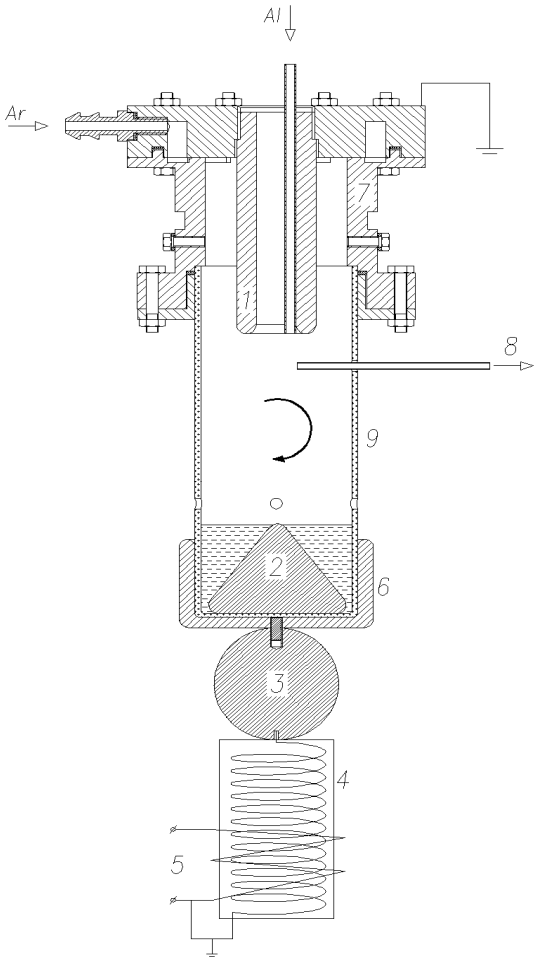

Figure 8. *Scheme of Al-water plasma-chemical reactor: 1- top grounded electrode (Al), 2- down conical electrode (Al)+liquid water , 3- ball "hot electrode, 4- Tesla's coil, 5- inductor, 6- down cylindrical electrode (container), 7- swirl generator, 8- chemical probe, 9- quartz wall*

Pulse repetitive HF generator is used in this work with the following parameters:

HF frequency	F_{HF}=450 kHz
Pulse repetitive frequency	F_M=100-1000Hz
Pulse duration	Ti=0.5 ms
Pulse power	<10kW
Mean power	<1 kW

The stable operation of this PCR in this regime is shown in the fig.9. One can see combustion of the final products (H2+Al+….) near output nozzle of this PCR in open air. Maximal hydrogen mass flow about 1G/s is obtained in this regime namely. This promising optimal regime obtained in this PCR will be studied in detail in our future experiments

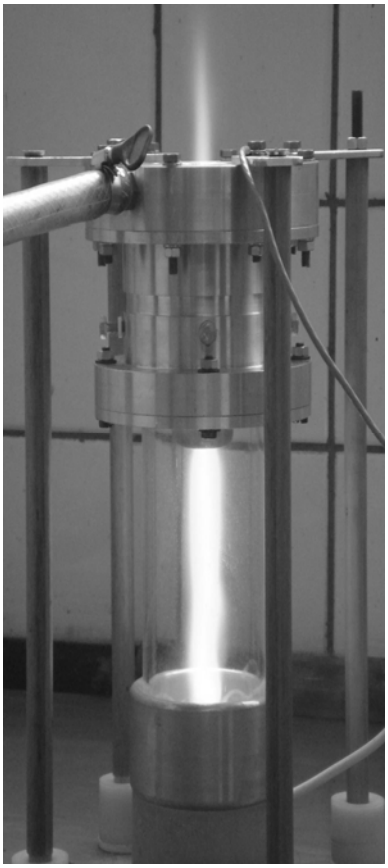

Figure 9. *Plasma chemical reactor with pulsed repetitive HF discharge and aluminum electrodes and liquid water*

IV. Conclusion

1. Stable cylindrical flame of heterogeneous plasma-assisted reaction of Al-H2O mixture is obtained in swirl argon flow in the PCR.
2. High completeness of Al oxidation in water steam at plasma assistance is realized in this experiment.
3. High electron concentration N_e~10^{14} cm^{-3} is obtained in Al plume in H2O-Ar flow at plasma assistance.
4. High temperature T_g~3000K is measured in Al-H2O plume in the PCR.
5. Al-H2O chemical reaction assisted by HF plasma is studied in this work. Aluminium electrodes and liquid water is used in the PCR. Maximal hydrogen mass flow rate about 0.1-1G/s is obtained in this regime namely.
6. Heterogeneous plasmoid with strong double electric layer in created in H2O-Ar swirl flow.

The typical value of charged plasmoid's electric potential is about several kV.

7. It is measured that power budget of hydrogen generation in this PCR is about q=2÷4 eV/ particle/

References

1. Sheyndlin A. E., Al-H_2 power stations, JIHT RAS, M., 2007, P.139
2. Sheindlin A.E., Zhuk A.Z., et.al., Using of Low-Coast Aluminium in Electric Energy production, J. Power Sources, 2006
3. A. Sheindlin, V. Bityurin, A Bocharov, P. Ivanov, A. Klimov, V Miroshnichenko ,V Zalkind, A Zhuk On Prospective of MHD Electrical Power Generator on Aluminum Oxidation Products, AIAA paper, AIAA-2009-3829.
4. A. Sheindlin, P.P. Ivanov, V.I. Miroshnichenko, MHD Electrical Power Generation on Products of Aluminum Oxidation by Steam, AIAA paper, AIAA-2010-4303.
5. Klimov A., Bityurin V., Grigorenko A., Kutlaliev V., Moralev I., Tolkunov B, Plasma Assisted Combustion of Heterogeneous Fuel in High-Speed Airflow, AIAA Paper AIAA-2009-1411-250, P.11
6. Klimov A., Moralev I., et.al., Non-Premixed Plasma-Assisted Combustion, AIAA Paper, Proc. 45th AIAA Conf. Reno NV, 7-11 Jan 2007, P.11
7. Combustion Laws, 2006, Moscow, RAS IVTAN, P.352
8. Potapkin B., Zhivotnov V., Rusanov V., Plasma Catalysis: - Phenomenon and Applications, Chemistry of Low- Temperature Plasma, Low-Temperature Encyclopaedia, 2005, P. 4-36

12.2. TWO APPROACHES TO THE CONDENSATION MODEL OF THE ALUMINUM OXIDE IN STEAM

V. A. Bityurin, E.A. Filimonova, A.S. Dobrovolskaya, Yu.V. Alekseev
Joint Institute for High Temperatures of Russian Academy of Sciences

Introduction

This work is inspired by the experimental research of plasma-assisted combustion of Al particles with steam [1]. The resulting products of the process are hydrogen and various Al oxides and suboxides. This highly exothermic reaction is accompanied by condensation of aluminum oxide Al_2O_3 (alumina) with additional heating release. Therefore, if one can find a way to condense more aluminum suboxides into liquid Al_2O_3 then temperature of final mixture and released amount of hydrogen will increase. Detailed mechanism of Al_2O_3 condensation is not known well for now, but this matter is of great interest for researchers not only for understanding of the products condensation mechanism but also for better investigation of initial combustion stage because of existence of oxide cap on Al particles.

Model for simulations

In this work the physical-chemical kinetics mechanism of aluminum oxidation by steam is analyzed with computer simulation in terms of zero-dimensional kinetics. Thirty chemical reactions in a gaseous phase were considered along with two different models of alumina condensation.

During the simulation we used some simplifications that should not influence main qualitative results but facilitate the calculations significantly. First of all we consider that condensation occurs on the macroparticles inputted from outside. This is much faster then formation of the nucleation centers with later condensation on them. Also, we assumed that the radii and temperatures of all particles are the same. It allows us to avoid time-consuming averaging over the particle ensemble. Also we do not consider mass and heat gradients and flow around Al and Al_2O_3 particle and energy radiation losses from them.

a. Chemical kinetics reactions

According to experiments with plasma assisted combustion of Al in steam temperature in discharge zone is above then boiling temperature of Al (2791 K). In this case simulation where Al oxidation occurs in gaseous phase is correct. Thirty chemical reactions occurring in a gaseous phase are considered along with the condensation of alumina (Al_2O_3). In this work the following expression for rate constants was used:

$$W_i = k_i \cdot T^n \cdot \exp(-\frac{E_a}{RT}), \qquad (1)$$

where k_i is preexponential factor, E_a - activation energy, T - temperature and R - gas constant.

Chemical kinetics mechanism for combustion are listed in Table 1, the rate constants for first 18 reactions are taken from [2], for the reactions from 19th to 28th are taken from [3], and for the two last reactions are calculated from fist principles simulation using GAMESS (US) package [4].

Preliminary calculation [5] of gas phase kinetics without condensation was performed and after reaching the stationary state there was found that result temperature and mixture composition are far away from what expected from experiment and don't agree with results of thermodynamic equilibrium calculations (see table 2 below).

b. Alumina condensation from supersaturated vapor of Al_2O_3

At first we considered simplified model based on the microkinetic approach [6]. In that case condensation depends on the excess of saturation pressure over partial pressure of gaseous Al_2O_3. For more detailed description of the model one can see [5]. It was found that condensation of alumina effects on chemical composition of mixture and energy balance. If we take into account condensation then the temperature of the gaseous mixture increases slightly. Nevertheless the differences between simulation and experimental results are significant. In experiments there was a huge amount of hydrogen, the temperature was about 3000 K and there wasn't gaseous alumina at all. But simulation shows us temperature about 2500 K (and it continue to decrease) and a lot of gaseous alumina after termination of condensation because of the saturation pressure of Al_2O_3 already became to exceed the partial one at 2500. One can take into account that there is no mention of gaseous Al_2O_3 in numerous experimental papers about aluminum oxidation with water and there is lack of theoretical information about its thermodynamic properties. So it is naturally to suppose that such model is irrelevant for the system under consideration.

This results and absence of gaseous alumina in various combustion experiments led us to the assumption that formation of liquid phase of alumina occurs directly from sub-oxides like Al_2O and AlO.

Table 1. *Chemical kinetics mechanism*

№	Reaction	k, $sm^3s^{-1}mole^{-1}$	K, s^{-1}	n, $(T)^n$	E/R	E, kal
1	Al + H2O = AlO + H2	9.60E+13			2868.60	5700.48
2	AlO + H2 = Al + H2O	2.61E+13			2868.60	5700.48
3	Al + H2O = AlOH + H	1.14E+12			442.80	879.93
4	AlOH + H = Al + H2O	1.00E+11			442.80	879.93
5	Al2O3(gas) = Al2O2 + O		3.00E+15		49144.40	97659.75
6	Al2O2 + O = Al2O3(gas)	5.68E+10		1	2944.50	5851.31
7	Al2O3(gas) = AlO + AlO2		3.00E+15		63915.40	127012.68
8	AlO + AlO2 = Al2O3(gas)	2.10E+09		1	-3296.00	-6549.81
9	Al2O2 = 2 AlO		1.00E+15		59335.70	117911.90
10	2 AlO = Al2O2	5.12E+09		1	-5062.00	-10059.21
11	Al2O2 = Al2O + O		1.00E+15		52466.00	104260.44
12	Al2O + O = Al2O2	2.83E+10		1	-7288.00	-14482.71
13	AlO2 = AlO + O		1.00E+15		44564.60	88558.77
14	AlO + O = AlO2	1.40E+11		1	1230.00	2444.26
15	AlOH = AlO + H		1.00E+15		57725.20	114711.52
16	AlO + H = AlOH	2.65E+10		1	-1930.00	-3835.30
17	AlOH = Al + OH		1.00E+15		66431.80	132013.27
18	Al + OH = AlOH	2.65E+10		1	-580.00	-1152.58
19	H+H +M = H2+M	6.40E+17		-1	0.00	0.00
20	H2+M = H+H +M	5.88E+18		-1.1	52462.30	104253.08
21	OH+ OH = H2O + O	6.00E+18		1.3		0.00
22	H2O + O = OH+OH	6.30E+09		1.3	8542.70	16976.05
23	H + H2O = H2 + OH	1.00E+09		1.5	9346.70	18573.76
24	H2 + OH = H + H2O	2.20E+08		1.5	1758.80	3495.09
25	O + OH = H + O2	2.80E+15		-0.8	-50.30	-99.96
26	H + O2 = O + OH	1.90E+14			8241.20	16376.91
27	O + H2 = OH + H	1.50E+13			4472.40	8887.55
28	OH + H = O + H2	6.90E+12			3517.60	6990.17
29	Al + H = AlH	5.00E+13			1076.89	2140.00
30	AlH = Al + H	1.00E+15			14291.47	28400.00

Table 2. Comparison with thermodynamic calculations

	Our simulation with short-lived Al_2O_3	Thermodynamical simulation
T	3208.4	3251.0
P	2.4	1.80
[H]	1.24E-01	1.93E-01
[H2]	5.76E-01	6.70E-01
[Al]	7.82E-03	6.55E-02
[AlO]	2.00E-03	2.59E-03
[H2O]	3.94E-02	7.07E-03
[AlOH]	2.94E-02	2.75E-02
[OH]	3.24E-03	8.78E-04

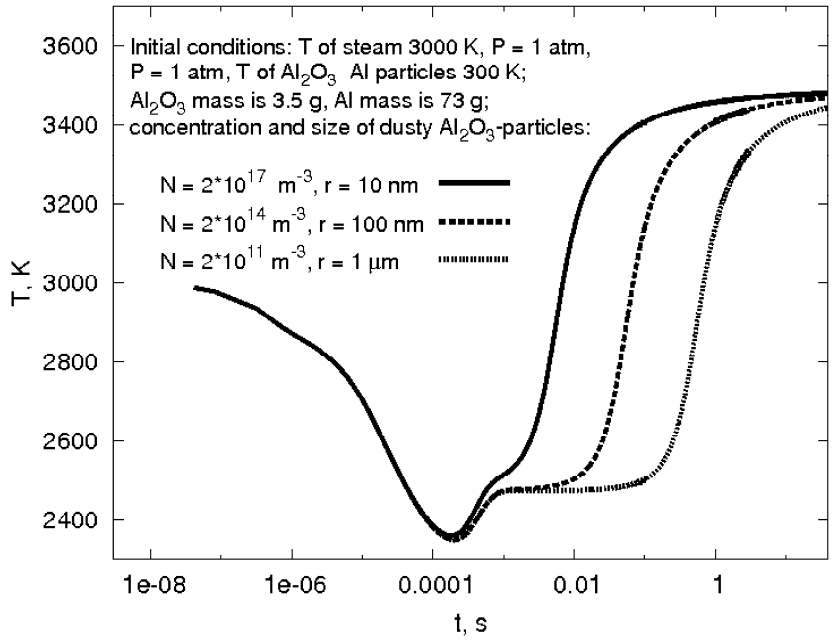

Figure 1. Gas temperature for different runs with "short-lived" Al_2O_3 model

c. Alumina condensation from different suboxides with "short-lived" Al_2O_3

Taking into account the thoughts from above we proposed the following model. Liquid alumina condensed from various suboxides: AlO, Al_2O, Al_2O_2. Gaseous Al_2O_3 is considered as an intermediate compound between gas and liquid phase, so we can use our chemical mechanism without any changes. After formation Al_2O_3 can condense on the dust particle (if molecule encounters particle) or dissociate to oxides. Lifetime of Al_2O_3 molecule is determined with its chemical dissociation. Heating of Al- and Al_2O_3 -particles and energy losses for Al-evaporation are also considered. Here are main equations for model with «short-lived» gaseous alumina. Equation (2) describes change of concentration of gas-phase alumina due to condensation. Next one (3) is heat balance; (4) is a change of average particle radius. And the last (5) is heating of aluminum and alumina particle.

Index "chem" refers to the chemistry part, "liq" – to the condensed phase, "gas" – gas phase, n is a concentration of gaseous alumina, q_{vap} – specific vaporization heat, W – chemical reaction rate, ΔH – chemical reaction heat, N_z – concentration of Al_2O_3 grains, C – heat capacity, T – gas mixture temperature, r – particle radius, u – thermal velocity of Al_2O_3 molecules, σ – cross-section of alumina macroparticle, ρ – liquid phase density, $T^{liq}(r)$ – temperature inside of particles, Q_{heat} – energy losses to the heating of particles in equation (5).

$$\frac{dn_{Al_2O_3}}{dt} = W_{chem}^{Al_2O_3} - n_{Al_2O_3} \cdot \sqrt{2} N_z \cdot u(T) \cdot \sigma \quad (2)$$

$$C_V^{gas} \frac{dT}{dt} = \sum_{all} W_{chem}^{j} \cdot \Delta H_{chem}^{j} + q_{vap} \cdot n_{Al_2O_3} \cdot \sqrt{2} N_z \cdot u(T) \cdot \sigma - Q_{heat} \quad (3)$$

$$\frac{dr}{dt} = \frac{V_{liq} \cdot n_{Al_2O_3} \cdot \sqrt{2} N_z \cdot u(T) \cdot \sigma}{4\pi r^2} \quad (4)$$

$$\rho^{liq}_{Al_2O_3,Al}\Gamma^{liq}_{Al_2O_3,Al}\frac{dT^{liq}_{Al_2O_3,Al}}{dt}=\frac{K}{r}\frac{\delta}{\delta r}\left(r\frac{\delta T^{liq}_{Al_2O_3,Al}}{\delta t}\right) \quad (5)$$

The condensation model is as simple as possible — if molecules of gaseous alumina collide with macro-particle of alumina during their lifespan so they condense. Otherwise they dissociate. But even such a primitive approach significantly changes temperature and composition of mixture during simulation.

Results and discussion

On the figure below there are changes in concentration of main gas fractures and temperature of the whole gas mixture. Initial conditions for this calculations was: water steam pressure is 1 atm, T of steam is 3000 K (because of heating in discharge zone), stoichiometric amount of solid Al (1 mkm particles), Al and Al_2O_3 particles temperature is 300 K, Al_2O_3 particles mass is 3.5 g per m^3. Alumina particles were adding at 1 mks after beginning of the calculation. The initial concentrations and size of Al_2O_3 particles was varied but full initial mass of condensed alumina was the same in different runs. The main qualitative result for this model is increasing of temperature and concentration of hydrogen and decreasing of aluminum sub-oxides concentration. The calculations show us temperature in stationary state above 3400 K in spite of spending some energy to the heating of cold macroparticles (Al and condensation centers). The production of hydrogen increases too and that is also much closer to the experimental results than with previous condensation model.

Another result is comparison between condensation on nano- and microparticles. Condensation is faster on smallest particles due to increasing of Al_2O_3 surface exposed to gas. Our calculations didn't take into account radiation losses from particle but some works (e.g. [7]) said that radiation heat losses are less for particles with radius 100 nm than 1 mkm. This subject requires further accurate consideration.

Also the resulting concentrations and temperature (on the final plateau – see Figure 1) was compared with thermodynamic simulation result [8] with the same initial conditions (Table 2). There is good agreement between these results though our model is not very detailed. Presumably the differences in temperature and pressure are induced by incompleteness of model which does not consider alumina vaporization and radiation losses at all.

Concluding remarks

The kinetic scheme was created, this allow us to find intermediate oxides during Al_2O_3-formation. It was established that using of infinite-rate kinetics is incorrect for this system.

It was found that model where condensation depends on supersaturation of gaseous Al_2O_3 is incorrect for the system under discussion. Based on collisional kinetics model of condensation was proposed. The results of simulation with this model are in good agreement with thermodynamic data.

The results show that condensation on alumina nanoparticles is less time-consuming and more useful for heating than on microparticles.

The further liquid phase formation mechanisms research is necessary for full understanding of this process.

It shows that these simple assumptions can be useful as basis for later research. The next steps are including diffusion processes around the macroparticles in our simulation and detail consideration of condensation mechanism (may be with engaging of molecular dynamics). And taking into account not only initial gas heating but other effects of discharge too.

List of references

1. Klimov A., Bityurin V., Grigorenko A. et al, Proceedings of The 9th International Workshop on Magneto-Plasma Aerodynamics, Moscow, 2010, p. 260
2. E. B. Washburn, J. N. Trivedi, L. Catoire and M. W. Beckstead, The simulation of the combustion of micrometer-sized aluminum particles with steam, Combust. Sci. and Tech., 180: 1502-1517, 2008.
3. Bityurin V, Bocharov A, Filimonova E. Effect of nitrogen oxide on ignition of non-premixed system, 44th AIA Aerospace Science Meeting and Exhibition, 2006, AIAA 2006-1218.
4. Schmidt, M. W., Baldridge, K. K., Boatz, J. A., Elbert, S. T., Gordon, M. S., Jensen, J. H., Koseki, S., Matsunaga, N., Nguyen, K. A., Su, S., Windus, T. L., Dupuis, M. and Montgomery, J. A. (1993), General atomic and molecular electronic structure system. Journal of Computational Chemistry, 14: 1347–1363
5. Dobrovolskaya A., Proceedings of The 9th International Workshop on Magneto-Plasma Aerodynamics, Moscow, 2010, p. 295
6. Ю. В. Алексеев, В. А. Битюрин, Журнал Физической Химии, 2000, т.74, №4 с 611-618**.**
7. V.A. Bityurin, A.V. Galaktionov, A.V. Kolpakov. Evolution of Radiation Losses in A1-H2 MHD Generator Tract. Proceedings of The 9th International Workshop on Magneto-Plasma Aerodynamics, Moscow, 2010, p. 276
8. А.Е. Шейндлин, В.А. Битюрин, А.З.Жук, В.И. Залкинд, П.П. Иванов, В.И. Мирошниченко, Алюмо-водородные МГД генераторы электроэнергии, ДАН, Энергетика, 2009, т.425, №4, с.1-3.

12.3. ANALYSIS OF THERMAL RADIATION IN COMBUSTION CHAMBER OF AL-H_2 MHD GENERATOR

Bityurin V.A., Galaktionov A.V., Ivanov P.P.
Joint Institute for High Temperatures RAS, 125412, Moscow, Russia
andrei.v.galaktionov@gmail.com

1. Introduction

There is a growing interest in novel concept for hydrogen production and energy conversion based on the aluminum combustion with water [1, 2]. This concept creates very favorable conditions for developing high-performance magnetohydro-dynamic (MHD) generators. In such generators working fluid is hydrogen, which is heated to a temperature ~ 3000-3500K.

High electric conductivity, low molecular weight, and high velocity of hydrogen plasma make it possible to remove some principal physical limitations that hindered the use of MHD generators instead of traditional thermal power stations. At the same time, the development of aluminum-hydrogen technology encounters some new problems that range from ensuring the safety of high-pressure hydrogen discharge in emergency situations to providing effective hydrogen purification from alumina dust and reducing radiative losses in the MHD tract.

The oxidation of aluminum with water goes with intensive thermal radiation mainly from melted alumina drops. In the combustion chamber, radiation from burning aluminum drops introduces additional appreciable contribution besides the alumina.

In the completely reacted mixture which mainly consists of hydrogen and alumina drops one can estimate radiation losses based on temperature of the mixture and the drops size distribution function. The alumina drops size dispersion may exceed three orders of magnitude and the drops size distribution function has complex structure. Moreover, large and small drops distributions may be strongly correlated in space. The structure is determined by initial aluminum powder size distribution and alumina nanodrops which are growing from burning aluminum vapor.

One can easily calculate optical properties of spherical alumina drops by classical Mie theory using refractive index and absorption coefficient of melted alumina. This is enough to calculate reacted mixture radiation losses on the walls by radiation transport equation or by its radiation diffusion approximation. Unfortunately, experimental data spread for absorption coefficient of melted alumina is too large. Thus, we have to consider the calculations as a crude estimation.

The calculations show that wall radiation losses have very complex non-monotonic character [3]. Multiple scattering dominates in the flow if mean aluminum powder size is about one micrometer. In the different parts of the flow path with various flow velocities, drops sizes and concentrations, the flow optical thickness may vary from several hundredths to several tens of unity. Thus, effective emissivity of the flow may vary from 3% to 35% [3, 4]. Unfortunately, in the majority of cases wall radiation losses are unacceptably large. So, we have to find new ways to remove alumina drops from the flow.

In the combustion chamber, the calculation of radiation losses is complicated by very complex way of aluminum drops burning [5, 6]. In this paper, we propose a simplified model of burning aluminum drops emission and estimate radiation losses in combustion chamber.

2. Features of aluminum drops burning

Aluminum powder has been added to solid rocket propellants for many years as an extra energy source because of the large amount of heat generated during the aluminum oxidation reaction. In both the propellant and explosive applications, one of the main oxidizers that react with the aluminum particles is the steam. Aluminum also has potential in underwater propulsion applications due to its high energy density and ability to react with water.

Thus, research on the combustion mechanism of aluminum burning has been an ongoing effort [5, 6]. In most papers, aluminum burning studies in the combustion products rocket propellants which mainly consisting of a gas mixture of CO_2 and H_2O. In the pure H_2O vapor burning process is faster and at least qualitatively the same. Usually thin alumina layer on its surface prevents aluminum powder ignition. Entire combustion process has five major stages:

- Particle heating with phase transformation;
- Melting of core and ignition due to melting/cracking;
- Heterogeneous reactions/healing of cracks;
- Melting of oxide layer to form a cap;

– Vaporization of Al with detached flame/particle burnout due to heterogeneous combustion.

The last stage is of great interest because most of the heat and thermal radiation are realized on this stage. A drop vaporizes and the aluminum vapor burns around the drop (see Figure 1). Cloud of alumina nanodrops with high temperature about ~4100 K condenses around the drop. Then the nanodrops diffuse and fall to the drop and grow as alumina cap on the drop. The temperature of the aluminum drop with alumina cap is limited by energy consuming process of aluminum vaporization. At air pressure, the temperature is about 2400 K [7, 8], which may be much lower than temperature of surrounding gas mixture. The temperature of alumina nanodrops and aluminum drop with alumina cap weakly depends on surrounding gas temperature and pressure.

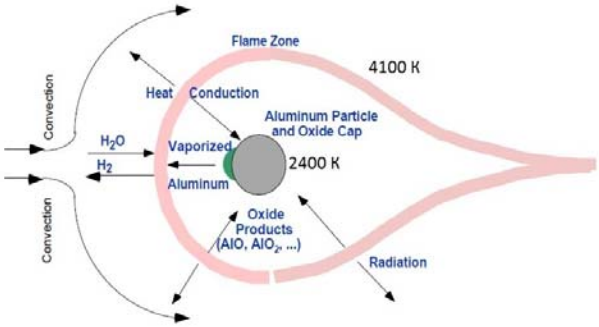

Figure 1. *Conceptual schematic of the combustion an aluminum drop*

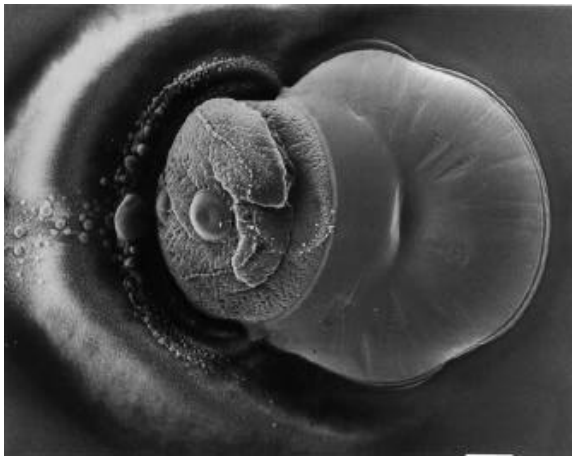

Figure 2. *SEM micrograph of a 70 μm aluminum particle quenched 2.5 to 3 msec after ignition [4]*

This complicated way of aluminum particles burning is a fixed experimental fact. A series of tests were performed interrupting the burning process with a glass slide, and then taking scanning electron microscope (SEM) photographs of the residual particles [4]. Figure 2 is an example.

3. Optical properties of molten aluminum and alumina

While aluminum and its melt have well known and predictable optical properties [9], alumina has anomalous optical properties. Its absorption coefficient abruptly increases at melting point by several orders of magnitude [10, 11] and strongly depends on impurities, gaseous environment and may be thermal history of a sample. That is why experimental data spread for absorption coefficient of melted alumina is too large.

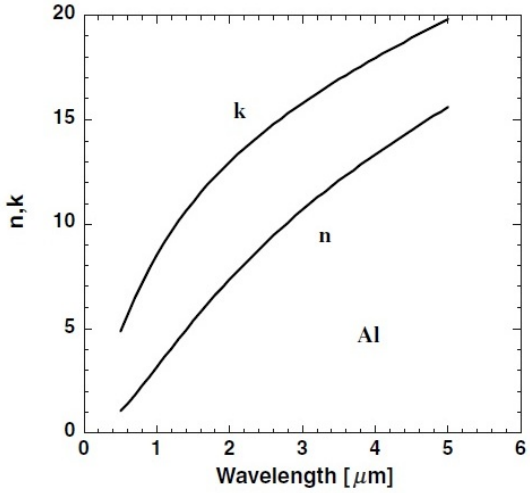

Figure 3. *Optical properties of melted aluminum at 2414 K [7]*

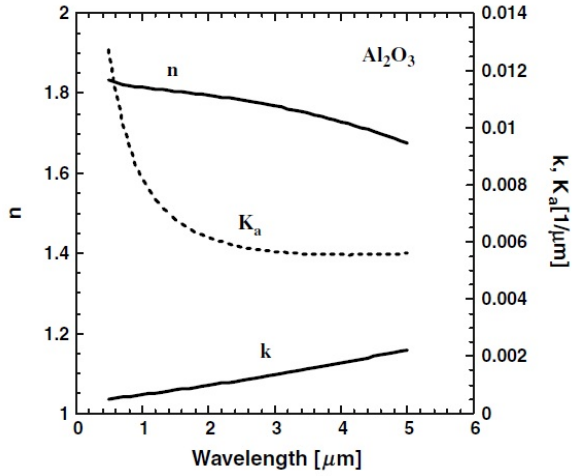

Figure 4. *Optical properties of melted alumina at 2414 K [7]*

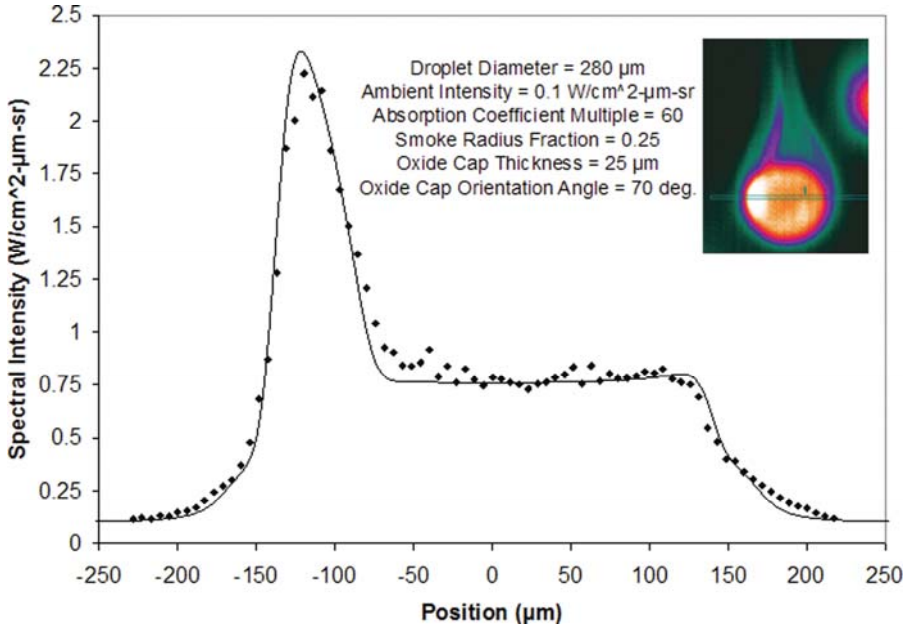

Figure 5. *Ray optics model [6] and infrared (λ = 3.4 µm) experimental data comparison with the oxide cap (left) oriented 90◦ to the flow (from below)*

While aluminum and its melt have well known and predictable optical properties [9], alumina has anomalous optical properties. Its absorption coefficient abruptly increases at melting point by several orders of magnitude [10, 11] and strongly depends on impurities, gaseous environment and may be thermal history of a sample. That is why experimental data spread for absorption coefficient of melted alumina is too large.

4. Optical properties of large (>50 mkm) drops

Recently optical properties of large (>50 µm) burning aluminum drops was carefully calculated [6]. This calculation was based on ray optics assumptions. This means that a drop size must be much greater than characteristic wavelength of thermal radiation (1 µm).

For large drops the calculations is in a good argument with infrared measurements.

Total emissivity (directionally and spectrally integrated) of large drops significantly increase while a drop burns and percentage of alumina enlarges. Experimental data shows that radiation emission of surrounding alumina nanocloud very unstable and usually may be neglected.

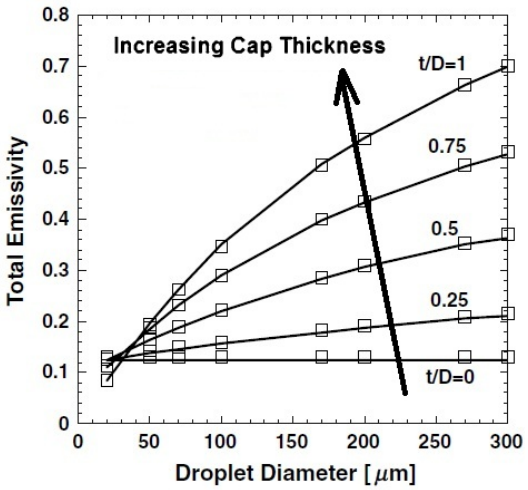

Figure 6. *Total emissivity of burning Al/Al_2O_3 drops at 2413 K (1 atm) for varying oxide-cap thickness, ignoring oxide nano smoke emission [7]*

5. Optical properties of small (<50 mkm) drops

For small drops ray optics assumptions fails. In this case one has to apply very complex electrodynamical calculations which take into account correlated emission of aluminum drop, alumina cap and surrounding alumina nanocloud. It must be based on detailed model of burning aluminum drop kinetics. Fortunately, in two limiting cases the calculations are simple.

Experimental data [6] shows that for small drops thermal emission of surrounding alumina nanocloud may be neglected. This hypothesis is to be tested in future research, but is accepted here. At the beginning and at the end of a drop burning it is spherical particle of aluminum and alumina. In this case we can use simple Mie theory [11] to rigorously calculate absorption Q_{abs} and scattering efficiencies Q_{tra} of the drop.

In intermediate case we simply assume

$$Q_{abs} = (1-x) * Q_{abs}{}^{Al} + xQ_{abs}{}^{Al_2O_3},$$
$$Q_{tra} = (1-x) * Q_{tra}{}^{Al} + xQ_{tra}{}^{Al_2O_3},$$

where x is the percentage of burned alumina.

Thus, optical properties of the flow in combustion camber may be calculated by usual expressions: absorption coefficient : $\alpha = NQ_{abs}\pi r^2$, transport scattering coefficient: $\beta_{tr} = NQ_{tra}\pi r^2$, and radiation diffusion coefficient: $D = 1/3(\alpha + \beta_{tr})$, where N is the drops concentration and r is the drops radius. Real flows contain some mixtures of drops with different diameters. In this case one can simply average optical properties over known drops diameters distribution because absorption and scattering of different drops are independent and additive.

Mie theory calculations show (see figures 7,8):

- the scattering Q_{tra} is greater than absorption Q_{abs} for alumina drops with a radii between 30 nanometers and 30 microns;
- the scattering is greater than absorption for aluminum drops from 200 nanometers;
- the scattering may exceed absorption by several orders of magnitude;
- absorption Q_{abs} of aluminum drops is greater than absorption of alumina for drops with a radii less than 10-20 micron.

The optical properties of the flow allow us to estimate effective flow emissivity and radiation loses in combustion chamber using radiation diffusion approximation [3].

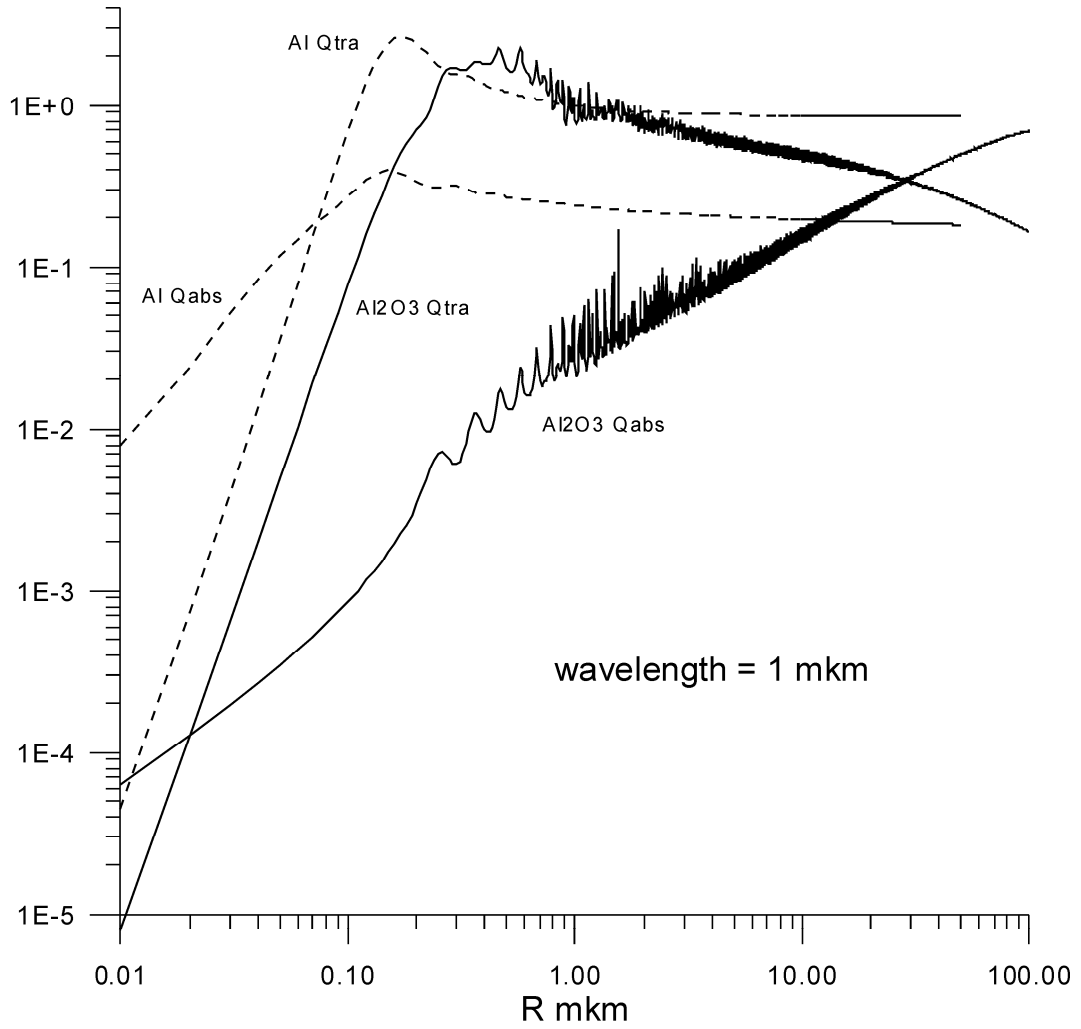

Figure 7. *Dimensionless absorption* Q_{abs} *and transport scattering* Q_{tr} *cross-section of aluminum and alumina drops for wavelength 1 micron (T~3000K).*

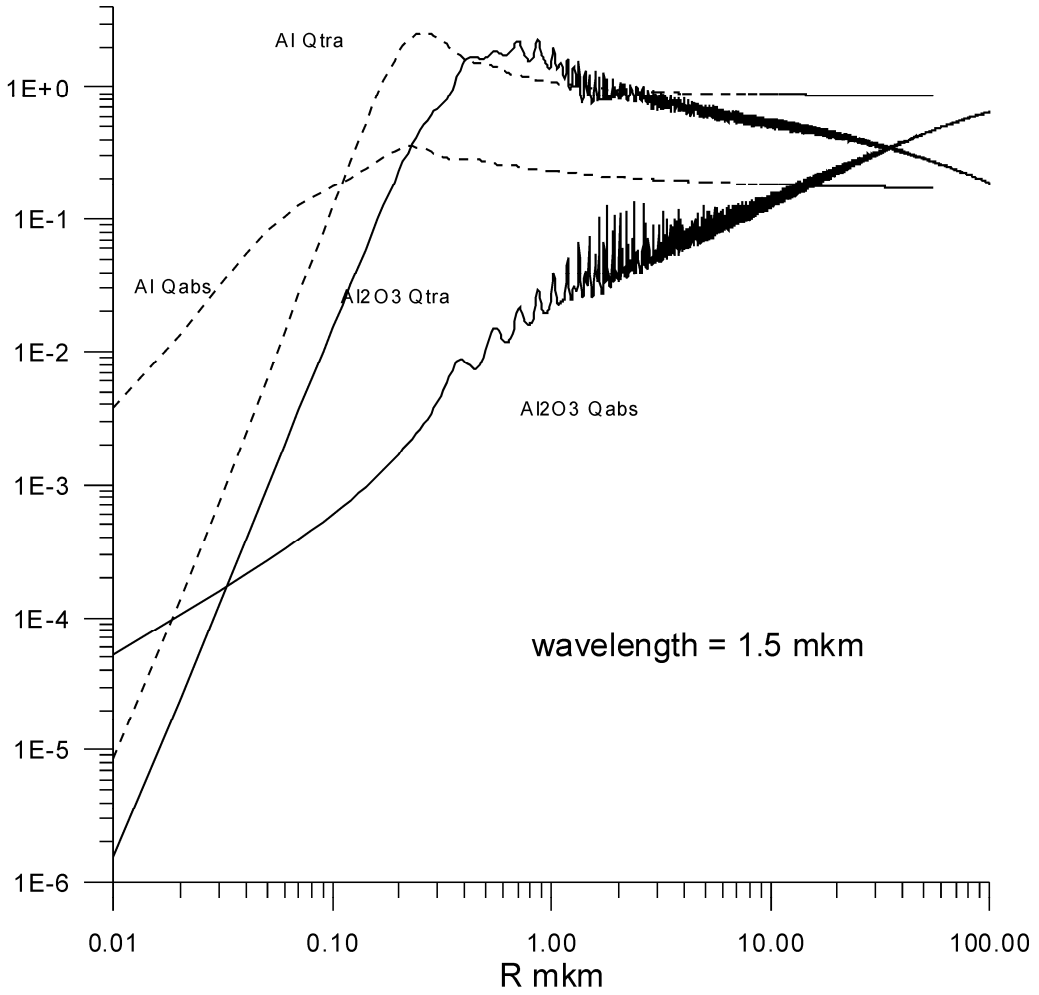

Figure 8. *Dimensionless absorption* Q_{abs} *and transport scattering* Q_{tr} *cross-section of aluminum and alumina drops for wavelength 1,5 micron (T~2000K).*

6. Flow optical properties and radiation losses in combustion chamber

Rigorously speaking, to correctly calculate mixture radiation losses on the combustion chamber walls one may have to develop complex three temperature model with hot alumina nanodrops and relatively cold aluminum drop with alumina cap in middle temperature gas mixture.

Here we assume that all burning drops have the same size and temperature 2400 K [6,7] and neglect radiation emission of gas and hot (~ 4000 K) alumina nanocloud. In this case we can use the following expression for effective flow emissivity [3]

$$\varepsilon_{eff} = \frac{2\varepsilon_w D\xi I_1(\xi r_0)/(2-\varepsilon_w)}{D\xi I_1(\xi r_0) + \varepsilon_w I_0(\xi r_0)/2(2-\varepsilon_w)},$$

where ε_w is the boundary emissivity, $\xi = \sqrt{\alpha/D}$, I_0, I_1 is the modified Bessel functions, r_0 is the combustion chamber radius.

As an example, we consider estimation of radiation losses in experimental combustion chamber with aluminum mass rate $R_{Al} = 100\ g/s$. The chamber has radius $r_0 = 0.1$ m and wall temperature 2000 K and wall emissivity $\varepsilon_w = 0.5$. Tables 1 and 2 show the flow optical properties and radiation heat flux to the walls at the beginning and at the end of aluminum drops burning.

Table 3 shows effect of wall emissivity. It is easily seen that reducing of wall emissivity may appreciably decrease radiation losses in combustion chamber especially for small (<10 mkm) drops.

Table 1. *Flow optical properties and radiative heat flux at the beginning of drops burning*

Drops diameter mkm	Drops concentration $1/cm^3$	Absorption coefficient 1/cm	Diffusion coefficient cm	Optical thickness in deep mode	Flow emissivity	Heat flux MW/m^2
0.1	1,00E+11	9,20E-01	2,79E-01	18,169	0,498	0,485
1	1,00E+8	2,13E-01	2,84E-01	8,647	0,387	0,377
10	1,00E+5	1,60E-02	3,93E+00	0,639	0,209	0,204
100	1,00E+2	1,43E-03	4,09E+01	0,059	0,027	0,027

Table 2. *Flow optical properties and radiative heat flux at the end of drops burning*

Drops diameter mkm	Drops concentration $1/cm^3$	Absorption coefficient 1/cm	Diffusion coefficient cm	Optical thickness in deep mode	Flow emissivity	Heat flux MW/m^2
0.1	1,00E+11	2,70E-03	8,02E+00	0,184	0,050	0,049
1	1,00E+8	1,07E-02	2,44E-01	2,094	0,120	0,116
10	1,00E+5	7,34E-03	5,88E+00	0,353	0,119	0,116
100	1,00E+2	3,89E-03	5,63E+01	0,083	0,070	0,068

Table 3. *Effect of combustion chamber wall emissivity*

	Drops diameter	0,10 mkm	1,00 mkm	10,00 mkm	100,00 mkm
Drops composition	Wall emissivity	Effective flow emissivity			
Al	0,05	0,050	0,049	0,044	0,018
$(Al+Al_2O_3)/2$	0,05	0,050	0,047	0,042	0,026
Al_2O_3	0,05	0,026	0,038	0,038	0,031
Al	0,30	0,299	0,255	0,164	0,026
$(Al+Al_2O_3)/2$	0,30	0,297	0,226	0,138	0,046
Al_2O_3	0,30	0,047	0,103	0,103	0,064
Al	0,70	0,696	0,498	0,238	0,028
$(Al+Al_2O_3)/2$	0,70	0,685	0,398	0,187	0,051
Al_2O_3	0,70	0,051	0,128	0,128	0,073
Al	1,00	0,992	0,632	0,265	0,028
$(Al+Al_2O_3)/2$	1,00	0,970	0,479	0,204	0,052
Al_2O_3	1,00	0,052	0,136	0,135	0,075

7. Conclusions

We analyze combustion mechanism of aluminum particles with water and the burning particles radiative properties. We proposed and motivated new simple model for optical properties of small (<20-30 mkm) burning aluminum drops. Aluminum thermal radiation dominates for small burning drops and on the contrary for large drops (>20-30 mkm) alumina radiation dominates. Thus, thermal radiation may be useful for heating small aluminum particles in combustion chamber before ignition. Aluminum drops is to be performed in future research though rigorous electrodynamical calculations of optical properties of burning

We perform analytical estimations of radiation losses to the walls of combustion chamber of Al-H_2 MHD generator. In combustion camber, multiple scattering of thermal radiation dominates in majority of cases and reduce radiation losses. Reducing of wall emissivity usually appreciably decrease radiation losses of a flow with small (<10 mkm) drops.

References

1. Alyumovodorodnaya energy. Ed. Sheindlin E.M.: High Temperatures RAS, 2007. - 278 pp.
2. F. Franzoni, M. Milani, L. Montorsi, V. Golovitchev, Combined hydrogen production and power generation from aluminum combustion with water: Analysis of the concept //International Journal of Hydrogen Energy Volume 35, Issue 4, February 2010, Pages 1548-1559
3. Bityurin V.A., Galaktionov A.V., Kolpakov A.V., Evaluation of radiation losses in Al-H2 MHD generator path // Proceedings the 9th Workshop on Magneto-Plasma Aerodynamics. Ed. V.A. Bityurin, Moscow, JIHT RAS, 2010, p.308, pp 276-280.
4. M.W. Beckstead, A Summary of Aluminum Combustion, Brigham Young University Provo, Utah, USA, RTO/VKI Special Course on "Internal Aerodynamics in Solid Rocket Propulsion", held in Rhode-Saint-Genèse, Belgium, 27-31 May 2002, and published in RTO-EN-023, 2004
5. E. B. Washburn, J. N. Trivedi, L. Catoire, and M. W. Beckstead, The simulation of the combustion of micrometer-sized aluminum particles with steam, Combust. Sci. and Tech., 180: 1502–1517, 2008
6. J. Harrison; M. Q. Brewster, Analysis of thermal radiation from burning aluminium in solid propellants, Combustion Theory and Modelling, 2009, Vol 13: No 3, 389 — 411
7. J. Harrison; M. Q. Brewster, Simple Model of Thermal Emission from Burning Aluminum in Solid Propellants, Journal of Thermophysics and Heat Transfer, Vol. 23, No. 3, 2009 pp 630-634
8. B. Huttner, Optical properties of polyvalent metals in the solid and liquid state: aluminium,J. Physics: Condensed Matter, 6 (1994), pp. 2459–2474.
9. Linhart J.K. and others, Optical properties of leucosapphire at high temperatures. TVT 1982 V. 20 № 5, p. 872 and № 6, p. 1085.
10. Sarou-Kanian V., Rifflet J.C., Millot F. IR radiative properties of solid and liquid alumina: Effects of temperature and gaseous environment. Int. J. Thermophys., 2005, v.26, No.4, p.1263-1275.
11. Bohren K. Haffman D. Absorption and scattering of light by small particles. Wiley, New York, 1983.

12.4. STUDY OF KEROSENE COMBUSTION STIMULATED BY DISCHARGES IN SUPERSONIC FLOW

[1]V.Yu. Velikodny, [1]A.A. Bykov, [2]V.V. Dyrenkov, [1]A.I. Krikunova, [3]V.V. Popov,
[2]B.N. Tolkunov
[1]Moscow Institute of Physics and Technology
[2]Joint Institute for High Temperatures RAS
[3]Institute for Applied Mechanics RAS

Research of the "activated porous fuel" spraying processes, its ignition and flame stabilization in the supersonic flow under discharges occurs to be of great fundamental and practical importance. The significant unsolved problem is to implement a wide-range air-breathing direct-flow jet engine. There is a specific task to provide combustion for the supersonic aero-kerosene flow in the direct-flow engine, with Mach number of the inlet flow being equal 3-6. The concept of "activated porous fuel" combined with flame stabilization through electric discharges is being developed [1, 2].

The experimental installation is shown in Fig 1. Several types of discharges, including the high voltage arc, both surface and volumetric diffusion discharges, are used to ignite and stabilize the flame. Fig.2a and Fig.2b illustrate the arc discharge stabilizing flames and combustion, the arc pulse voltage being equal 40 kV, average current 0.12 A, average power 167 W.

The pictures of the kerosene stream ignition under the surface discharge are presented in Fig.3 and Fig.4. The discharge parameters are following: the primary coil current is around 10 A, with its duration around 4 ms, the idle voltage in the second coil is 25 kV, inter-electrode breakdown current is 150 mA, its duration around 1 ms, inter-electrode span is 4 mm. Voltage storage provides 14 V with electric current of 10 A.

The bubbling jet ignition secures the combustion stability. Processes of shock wave interaction with bubble mixture are studied both theoretically and experimentally to produce the "activated porous fuel" so that to obtain radicals and bubble droplets. In particular, the effect has been studied for the shock wave to fracture the bubbles owing to translational non-equilibrium, the bubble fragmentation to be provided by the shear

Fig. 1. *Experimental installation*

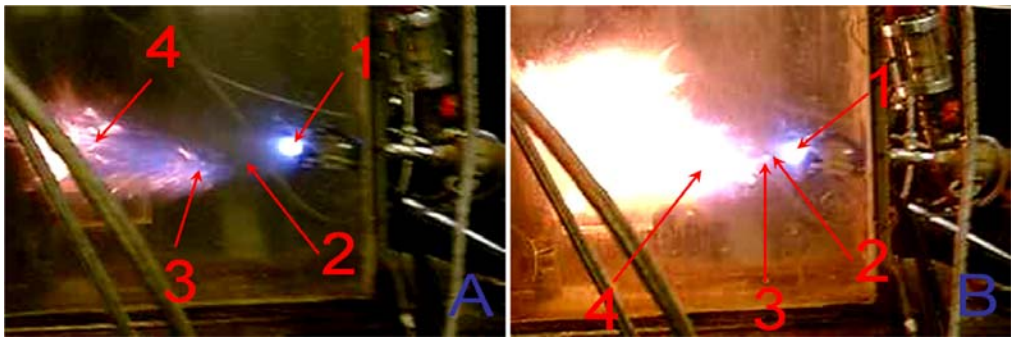

Fig.2 A. Fig.2 B.

Fig. 2A: *Kerosene ignition step ~ 0,05- 0,08 s.1- arc discharge, 2- ignition delay zone, 3- blue flame zone, 4- zone of fire origins [3].The ignition delay time is 3*10^4 s.*

Fig. 2B: *Kerosene combustion. 1- arc discharge, 2- ignition delay "dark" zone, 3- blue flame zone, 4- combustion zone. The ignition delay time is 8,4*10^5 s.*

Fig.3. *Non- bubbling jet ignition.*

Fig.4. *Bubbling jet ignition.*

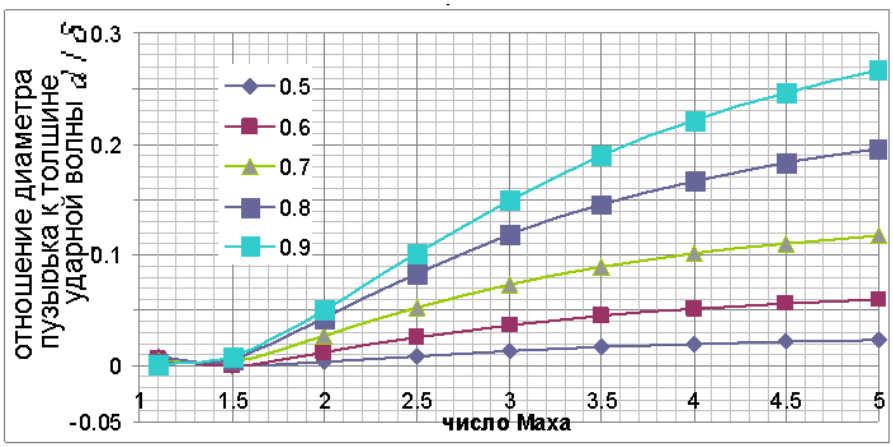

Fig.5. *Dependence of dimensionless bubble diameter d/δ on Mach number M (d- bubble diameter, δ - shock wave width)*

stress anisotropy at shock wave front.

References.

1. V.Yu. Velikodny et al. Micro-bubble technology for a wide-range air-breathing direct-flow jet engine.// "Contemporary Problems for Mechanics of Heterogeneous Media", IAM RAS, Proceedings, 2005, vol. 2, p. 167-180.
2. Eremeev A. V., Grishin V. G., Nikitenko L.K., Velikodnyi V. Yu., Vorotilin V. P., Timofeev I. B., Yunovsky Yu. G., D. Van Wie Enhanced Ignition and Mixing of Kerosene Fuil in High – speed Air Streams// AIAA (Paper) 2005-614. P. 1-15.
3. E.S. Shetinkov. Physics of Gas Combustion: M. 1965. 739 p.

12.5. ENERGETICS OF BALL LIGHTNING

A.I.Nikitin
Institute for Energy Problems of Chemical Physics, Russian Academy of Sciences
Moscow, Russia, anikitin@chph.ras.ru

Abstract. The main problem of ball lightning is an explanation of its extremely high energy content. This problem may be solved if one assumes that ball lightning is composed of positively charged system of moving charges and dielectric shell.

1. Introduction

Data on cases of ball lightning observations come to us from a far antiquity. At our ancestors, ancient Slavs, the ball lightning was called "rodia" and, apparently, was somehow "ideologically" connected with the higher pagan deity Rod [1]. The words "rdet" and "rdyanoy", which have retained in Russian, remind us about red colour of rodia – of ball lightning. Mikhailo Vasilyevich Lomonosov mentioned ball lightning existence in his "The word about air phenomena, resulting from the electric force". He was one of the first who has tried to find an explanation of this phenomenon: he considered that ball lightning is a result of burning of the fats which somehow have gathered in air (that is he was the author of the first hypothesis of ball lightning with chemical energy source) [2].

Interest to ball lightning has cleared up again in the middle of 19th century in France. In 1838 Francois Arago has published results of 30 observations of ball lightning and has tried to explain existence of ball lightning by condensation "of a lightning matter" [3]. In 20th century properties of ball lightning were discussed in the Walther Brand's book "Der Kugelblitz" [4] (1923), in reviews of McNally and Rayle [5, 6] (1966), in books of Stanley Singer [7] (1971), Igor Pavlovich Stakhanov [8] (1979 - 1996), Ilia Moiseyevich Imianitov [9] (1980) and James Barry [10] (1980). Basing on the analysis of dependence of probability of energy density of ball lightning measurements on density of its energy Barry has drawn a conclusion that in the nature there is only one type of ball lightning. In 1993 there was George Egely's [11] review, and in 1999 – Mark Stenhoff's book [12]. In 2006 Alexander Ivanovich Grigoriev's monography [13] has been published.

In 1988 in Japan the First International Symposium on Ball Lightning was held, and in 1989 the collection of the reports presented to this symposium had been published [14]. The symposium has served as the beginning of the organizing of the international interaction of the scientists, working in the field of ball lightning studying. For the past 22 years 11 symposia have been held, last has taken place in 2010 in the city Zelenogradsk of the Kaliningrad area in Russia. Activity of the International Committee on Ball Lightning for 20 years is described in the book [15].

The analysis of data, collected in the mentioned books, allows drawing a conclusion, that the typical properties of ball lightning are already revealed. It, as a rule, is a red sphere in diameter about 20 cm, existing about 10 seconds and moving in air in an intricate trajectory. Occurrence of this sphere is somehow connected with a thunder-storm. The sphere, as well as usual linear lightning, can strike a breather with a current or fuse a metal conductor. Along with the general properties it is possible to find especial, atypical features of ball lightning in the description of each observation.

If to give equal "weight" both typical, and to rarely observable properties of ball lightning, we receive extremely inconsistent "portrait" of this phenomenon. Repeatedly attempts to "cut" from this list of properties insignificant ones and to construct model of an "average" ball lightning was made, which have come to an end failure [8, 16]. One of the reasons of this failure is that it is impossible to define in advance, which properties of ball lightning are essential and which – are not essential. Therefore in the solving of ball lightning problem, apparently, the correct decision must be developing of the model considering all its properties – both frequent and rare ones.

2. Energy of ball lightning

One of the most important properties of ball lightning is its ability to accumulate energy in itself. Already the fact of luminescence of ball lightning says that the stock of its energy should be no less than 1-10 kJ. However in the history of ball lightning observations there were some amazing cases when the store of its energy was measured enough precisely, and this energy has appeared to be much more than 10 kJ. In view of the considerable importance of these cases we give below the detailed description of these events.

On November, 5th, 1936 London newspaper "The Daily Mail" has published the following letter of Mr. W. Morris from Dorstone, Hereford, to the editor of the newspaper: "Sir, – During a thunderstorm I saw a large, red hot ball come down from the sky. It struck our house, cut the telephone wires, burnt the window frame, and

then buried itself in a tub of water which was underneath. The water boiled for some minutes afterwards, but when it was cool enough for me to search I could find nothing in it". The Dorstone's case was investigated by Prof. B.J. Goodlet [17]. He has found out that the ball had the size of a big orange, water was hot for hands within approximately 20 minutes, and the tub contained about 4 gallons (18 liters) of water. To heat up 1 liter of water on one degree, energy 4.2 kJ is required, hence, energy $W_{ht} = 4.2 \cdot 18 \cdot 80 = 6$ MJ has been spent for heating of 18 liters of water from 20°C to 100°C. Apparently, from conversation with Mr. Morris Prof. Goodlet has learnt, that while boiling 1/10 part of water volume (1.8 liters) has been evaporated from the tub. For evaporation of 1 kg of water energy 2.26 MJ is required, hence, in addition to found 6 MJ energy $2.26 \cdot 1.8 = 4$ MJ could be contained in the ball lightning. As a result we find that in a volume of a sphere of diameter 10 cm (the size of an orange) energy up to 10 MJ could be contained. The volume of a ball of 5 cm radius is equal to $0.523 \cdot 10^{-3}$ m^3, from here energy density of ball lightning substance is $\rho_{wbl} = 10 \cdot 10^6 / 0.523 \cdot 10^{-3} = 1.9 \cdot 10^{10}$ J/m^3. This is in 10 times greater than the energy density of solid explosive trinitrotoluene. We notice also, that according to the message of Mr. Morris ball lightning energy was transferred to water not in the form of explosion, but slowly: water was boiling within several minutes. From daily experience we know, that if to remove a boiling teapot from fire boiling in it stops at once.

The obtained result could not be explained by the known means of energy storage, therefore it has been panned by the critics. It was considered, that Mr. Morris, not using the thermometer, could be mistaken in definition of temperature of water, that water did not boil, but fizzed up, as soda water fizzes up when you open a bottle, that water has not boiled away, but was simply spilt, etc. [8, 12]. However all these "specifications" could reduce an estimation of ball lightning energy release only in 2-3 times.

The second case of ball lightning energy measuring we find in [9]. The following message has come to Prof. I.M. Imjanitov, collecting data of ball lightning observations in the Soviet Union, from Mr. S.S. Makh, living in a city Perechin in the Western Ukraine: "In August, 1962 about 11-12 p.m. the ball lightning as big as a tennis ball fall into a trough with water for cattle. It was shining with the colours of the rainbow during approximately 10 seconds. Water from a trough had almost all boiled away, the cooked frogs laid at the bottom. The size of a trough was 0.3×2.5 m. Depth of water mass was 15 cm. In two other troughs also the cooked frogs have been found out" [9]. Water volume in the trough $V = 0.3 \times 2.5 \times 0.15 = 0.112$ m^3, its mass is 112 kg. This water was heated to boiling (from 10°C to 100°C), this demanded an expense of energy $W_{ht} = 4.2$ kJ/kg·K×112 kg×90 K = 42.3 MJ. About 100 kg of water was evaporated, for this energy $W_{ev} = 2.26$ MJ/kg×100 kg = 226 MJ was expended. Thus, the ball lightning has transferred to water energy 42 + 226 = 268 MJ. Radius of a tennis ball (to which the ball lightning was compared) is 3 cm, its volume is $1.15 \cdot 10^{-5}$ m^3. From here we find density of the energy, containing in ball lightning, $\rho_{wbl} = 2.3 \cdot 10^{12}$ J/m^3. We have received fantastic result: the energy density has appeared to be in 100 times more, than in the "English" ball lightning! And this is only the lowest estimation for the "Ukrainian" ball lightning. Mr. Makh wrote that in other troughs water had been heated up to the temperature, which had led to the death of frogs. We will accept it equal to 40°C. If these troughs were filled half, they contained about 100 liters of water. For water heating on 30 K (from 10°C to 40°C) energy W_{ht} = 4.2 kJ/kg·K×100 kg×30 K = 12.6 MJ was required. The "Ukrainian" case has shown that water, really, was heated up to a high temperature. For reliability of this result "the frogs laid down their lives". Besides, this case says that ball lightning is capable to heat up water, not contacting with it directly, but transferring the energy through a trough wall (most likely, made of wood).

The third case of ball lightning energy measurement using a "water calorimeter" was described by Hungarian researcher George Egely. Let him have the floor: "It happened in clear, bright, sunny weather in July, 1972. At noon most of the workers of our factory were having lunch but several of them stayed in the factory building. Suddenly they caught sight of a bright sphere of a football size rolling along the lightning conductor. It was accompanied with a hissing sound and was coloured transient between pink and yellow. It had come through the long glass window on the roof. Then it vanished in the water-pit at the outer corner of the building next to the lightning conductor with a tremendous crack. Afterwards the air felt rich in ozone. The water disappeared from the pit, leaving no trace behind. Though already totally dry the pit was still steaming after half an hour. The phenomenon was seen by about 30 people for approximately 8-10 seconds. The velocity of the bright sphere was about 3-5 m/s. The sound it emitted was similar to that of a supersonic plane, that is it was a hissing, whistling sound. The pit originally contained about 120 liter water since it had not been full, only on to its 2/3 part. My colleagues examined it thoroughly but no water was splashed on the walls, all the water evaporated. It is sure, it was steaming even a long time after the event. None of my colleagues felt either any heat radiated or perceived an impulse…One of my colleagues when the ball lightning fell into the water-pit …saw not only the steam but also that

some leaves of grass round the pit caught fire and burned down eventually" [11].

Let the initial temperature of water in the pit was 30°C. For heating of 120 liters of water to 100°C energy W_{ht} = 4.2 kJ/kg·K·120 kg·70 K = 32 MJ is necessary. To evaporate 120 liters of water, energy W_{ev} = 2.26 MJ/kg·120 kg = 271 MJ is required. All-in-all we obtain W_{bl} = 303 MJ. Diameter of ball lightning was 25 cm (the size of a football), its volume was $8.2 \cdot 10^{-3}$ m^3, whence the energy density of this ball lightning was $\rho_W = 303 \cdot 10^6$ J/$8.2 \cdot 10^{-3}$ m^3 = $3.7 \cdot 10^{10}$ J/m^3. As we see, the energy density of the "Hungarian" ball lightning is close to the energy density of the "English" ball lightning. It could not been excluded, that the witness of the "Ukrainian" ball lightning has underestimated its size a little, thus the density of its energy may be below than the one calculated by us ($2 \cdot 10^{12}$ J/m^3).

On August, 8th, 1989 in the newspaper "Pravda (Truth)" (Moscow) a short note "Visit of the fiery lady" was published. In this note it was told how once in Khabarovsk city (Russia) "the ball lightning had flown into a copper with 7000 liters of water. At once water had begun to boil. About ten minutes lightning had been bathing in water, and then it had gone out". For heating of $7 \cdot 10^3$ kg of water from 20°C to 100°C energy W_{ht} = 4.2 kJ/kg·K×$7 \cdot 10^3$ kg×80 K = $2.4 \cdot 10^9$ J is necessary. The size of ball lightning was not specified in the note. It is natural, that it was less than the size of the copper. If the copper form was close to spherical, its diameter was equal 2.4 m. Let diameter of ball lightning was 1 m. Then its volume was equal to 0.52 m^3, and energy density of its substance was $\rho_w = 4.5 \cdot 10^9$ J/m^3. We have again obtained the figure close to values of energy density in "English" and "Hungarian" ball lightning.

The ball lightning, having lost a considerable part of energy, can keep its form and survive. In 1981 in Journal of technical physics (USSR) there was an article about how on August, 12th, 1978 in the city of Khabarovsk (Russia) during a strong rain the big group of the spectators who have left a cinema, observed a ball lightning [18]. "Suddenly the sharp whistle reminding work of the jet engine and accompanied by a crash appeared. It became light, as in the day-time. Then over the cinema "Zarya" building ball lightning of bright orange colour with diameter about 1.5 m appeared. Sparks were flying out of it. Then the ball lightning began to descend and passed to the earth surface through branches of trees. For an instant it has flashed over a part of earth and again rose. Strong explosion was heard, and it became dark and silent. In all ball lightning existed about one minute. At the spare of up to 100 m wiring was put out of action. Despite a considerable quantity of water in soil and a torrential downpour, in a zone of diameter ~ 1.5 m and depth of 20-25 cm the soil has been charred and fused. The total volume of the zone, filled with slag, was ~ 0.4 m^3. Slag consisted not of a solid crust, but of many pieces of the wrong form with the average size of 5-6 cm, mutually alloyed with each other. Altogether it was found about 1000 such pieces. Near the place where ball lightning flash occurred, the vegetative cover did not renew". Carrying out experiments with the action on the ground of various kinds of energy – radiant heating, the high-voltage discharge, a strong current and high-frequency radiation, the authors of this article have found, that the results, closest to the described case, have turned out at a high-frequency heating of the soil. Assuming that mass of the heated soil was equal to 440 kg, and mass of water, containing in it, was equal to 175 kg, researchers estimated energy of ball lightning flash, spent for slag formation, as 10^9 J. However the authors supposed that if one considers the energy of flash to be dissipated in all directions, and not just downwards, to the earth, its value should be estimated as $7 \cdot 10^9$ J. The volume of ball with diameter 1.5 m is equal to 1.8 m^3, hence the energy density of the "Khabarovsk's" ball lightning should be not less than $4 \cdot 10^9$ J/m^3. In the same article the authors have informed, that "at the same thunder-storm in other area of the city the ball lightning was observed, which energy was estimated as $8.3 \cdot 10^9$ J (by water heating)". Apparently, it was the same ball lightning, the message about which has appeared in the newspaper "Pravda" in 1989, that is, within 11 years after the event. The energy estimated by us ($2.4 \cdot 10^9$ J) is 3.5 times less than was specified by the authors of the quoted article. The possible reason of a discrepancy between results is that we did not take into account the energy which was spent on evaporation of water.

The description of an other case when the ball lightning, having made mechanical work, remained unhurt, we find in a report of Egely at the First International Symposium on Ball Lightning in Japan in 1988 [14]. "A storm passed and the weather was already calm, cloudy at about 8 p. m. Suddenly, I spotted a floating, grayish spherical object floating above the brook. It had a diameter of about 2 meters. It was about 30-40 meters from us and moved towards our building with the speed of a running man. I told my husband to come and look at it, but in 2-3 seconds, by the time he reached the window, we heard a loud crash above our heads, and 35×15 meter roof of the building was lifted off and fell on the neighbour's oat field…A girl at the neighbouring farm…saw a reddish ball moving away from the ruined house right after the loud crash. It floated just above the oat field and moved horizontally. The average weight of the roof…is estimated about 20 kg/m^2, and it was lifted at least 1 meter". Mass of the roof was 20kg/m^2×(35×15)m^2 = $10.5 \cdot 10^3$ kg. Having lifted it on height 1 m, ball lightning had made work 100 kJ.

Some more cases when ball lightning made mechanical work, digging ditches and holes in soil, destroying houses and moving apart their walls, are described. All it forces to accept, that ball lightning is capable to hold a considerable energy, and this is one of the basic properties of ball lightning. Certainly, not all ball lightning have large store of energy: many of them finish a life with a weak clap, not causing any consequences, or die out without a trace. But it does not mean at all, that ball lightning with different energy should have the different nature. On the contrary, most likely that the structure of every ball lightning allows it to have a large store of energy, however not all of them realize this possibility.

Ball lightning is a source of visible radiation. Ball lightning of different colour – from red to blue were observed, up to white, and sometimes "black" ball lightning, not radiating visible light, were met [4, 7, 8-10, 12, 13]. More often ball lightning retains colour and intensity of luminescence up to destruction, but sometimes its colour can vary quickly enough. There are messages, that in the end of "life" colour of ball lightning becomes red. The witnesses, who saw ball lightning at a short distance (nearby 1 m), often speak about absence of sensation of heat which should proceed from the heated sphere [4, 7, 8, 12, 13].

The ball lightning can be the generator of electric currents – from a direct current to high frequency currents. These currents can cause fusion of conductors or appear to be a reason of decease of people and animals – up to a deadly outcome. At ball lightning occurrence electric bells start to ring, the electric bulbs, disconnected from a network, flash, ring metal subjects (wedding rings, gold bracelets and chains) instantly evaporate [4, 9, 11]. In [15] the case when the ball lightning has blown up near to the man, who has left water after bathing, is described. This blow has evaporated a gold chain, hanging on the man's neck. On a breast and a neck of the victim there were traces of a burn in the form of a dashed line. The mass of the chain was nearby 17 g, so energy, necessary for its evaporation, was not less than 36 kJ.

Character of ball lightning movement is one more feature, allowing to distinguish it from other phenomena, similar to it. The direction of its movement is changeable: it can move both upwards, and downwards, and horizontal. It can "fade" on a place and, on the contrary, to move with speed of the flying plane. As a rule, it avoids collisions with conducting bodies. Having flown up to them on a short distance, it often starts to move lengthways their surfaces. It is able to "proceed" through narrow cracks and small apertures. Passing through an aperture, it is extended in a thin cord, and then again restores the form. It can cut out in glass a disk in diameter of 5-8 cm [19, 20]. The most surprising, it is that ball lightning can pass through glass, not having damaged it.

The ball lightning has short enough life: it "is born" and "dies"". This is one of the main reasons because of which it remains poorly investigated. It seems reasonable to consider ball lightning as non-equilibrium open thermodynamic system. "Openness" means, that in the course of existence it exchanges with energy and entropy (orderliness level) with an environment. "Non-equilibrium" means, that ball lightning is a system with low entropy, aspiring to transfer in the condition of equilibrium with higher value of entropy. Speaking in other words, ball lightning is a highly ordered system of particles and charges, existing until this order is supported. Extremely large time, during which it is supported, – tens seconds and even minutes – is amazing. For disordered systems, for example, for hot plasma, merge of charges with opposite sign (recombination) occurs all for shares of second.

Ball lightning occurrence is connected with thunder-storms, but sometimes they were observed in fine weather. Many ball lightnings arise in clouds and "fall from the sky", however sometimes they arise at blow of linear lightning in the earth or in any subject. Sometimes (as a rule, during a thunder-storm) ball lightning, slowly leaving apertures of electric and radio-sockets, were observed. The stream of leaving substance as though was collected in any cover, gradually inflating it. The cover took the form of a sphere which eventually came off the socket.

The ball lightning form in most cases is an ideal sphere, but sometimes it takes the form of ellipsoid, pears, cylinder or thread. Ball lightning often gets into premises and usually moves along walls on some distance from them. It was informed on cases of occurrence of ball lightning in all-metal planes. They, as a rule, were moved on an axis of a fuselage from a nose to a tail [12].

Usually "not radiating heat" ball lightning, having got under clothes, leaves deep burns on a skin. Sometimes after visiting a premise by ball lightning there is in it a smell, characterized by witnesses as a smell of ozone or burning sulphur [4, 7, 8-10, 11-14]. The magnetic field of ball lightning is insignificant: on distance more than 50 cm it does not render action on steel subjects. However the case, when at school during examination in physics ball lightning, having flown up to a table with two horse shoe shaped magnets, has lifted them in air and has taken off with them on street through an open window leaf, is described [9].

3. Model of ball lightning

So, having in hands a "bouquet" of ball lightning properties, we will make attempt to "design" mentally an object which could have the specified

properties. Key and most mysterious property of ball lightning is its ability to accumulate in the limited volume the energy, which density can reach to 10^9 J/m^3. In advance we will agree, that we will search for the system, capable to keep the specified energy inside it, instead of to receive it from any external source.

If to assume, that ball lightning is a sphere of heated gas, which expansion is restrained by the force of atmospheric pressure P_a = 10^5 Pa, the limiting density of gas energy in such sphere will make $\rho_w = 3P_a/2 = 1.5 \cdot 10^5$ J/m^3. It is in 10^5 times less than energy density which can contain substance of the real ball lightning. If to ionize completely air in sphere, the density of the reserved energy will make nearby $\rho_{wi} = 4 \cdot 10^7$ J/m^3, it is in 10^3 times less than limiting energy density of ball lightning.

If one fill a sphere with a mix of chemically active gases at atmospheric pressure, the energy density will not exceed $\rho_{wcg} = 4 \cdot 10^6$ J/m^3, that is in 10^4 times less than energy density of ball lightning. Basically, the necessary value of energy density of ball lightning can be reached if to assume, that the sphere is filled by radioactive gas with a half-life period comparable to time of a life of ball lightning. But if energy of ball lightning had the radioactive nature, the majority of its witnesses would perish from radiation sickness. However cases of radiation injury of people at meeting with ball lightning occur extremely seldom (that, of course, does not remove a question of research of their reasons), and the overwhelming majority of observers does not have problems with health.

Let's try to find an alternative way of formation and holding in small area of space of energy with density, characteristic for ball lightning. Kinetic energy of particles can be very capacious tank of energy. However, the strong container is necessary for holding of such particles in the restricted area of space. The nature and techniques show us examples of the systems having an appreciable stock of energy and at the same time occupying the limited volume of space – the planets, rotating round a star, electrons, rotating round an atomic nucleus, rotational accumulators of kinetic energy

In the middle of 20th century the design of "the hydromagnetic capacitor", in which energy was stored in a disk of the plasma, rotating in an external magnetic field, has been proposed [21]. In this capacitor under the influence of orthogonal electric and magnetic fields there was a rotation electrons on a circle of small radius, and positive ions rotated on a circle of large radius. Energy in such capacitor was reserved, basically, in kinetic energy of ions and surpassed energy of usual solid-state capacitors of the comparable sizes in 10^4 times. The lack of such capacitors, which have not allowed them to sustain a competition with traditional, had appeared their "inertia" – impossibility to "remove" quickly the stored energy from them.

The configuration of "the hydromagnetic capacitor" has served the author of the present article as an occasion to consider as an element of ball lightning a system of the moving separated charges, which has been named by "the dynamic electric capacitor" [22]. New in this approach were attempt to refuse an external magnetic field and the assumption, that the reason, supporting circular movement of electrons, was the magnetic field, created by movement of positive ions (among which the lightest from them – protons was chosen).

In this capacitor electrons move in orbit of radius r in the radial electric field **E,** existing in space between separated charges of different sign, and in perpendicular to **E** magnetic field **H**, which is generated by movement of protons in circular orbit of radius R. Electrons make so-called drift movement: originally rested electron starts to move in direction of field **E** (in direction, opposite to direction of vector **E**), but in process of increasing of speed its trajectory is more and more bent by magnetic field **H**, it comes back to an orbit and stops the movement in direction of vector **E**. After that the cycle repeats. As a result the electron's trajectory reminds the rosette: it moves in orbit of radius r, making oscillations in radial direction. In a similar way electrons move in the magnetron – the generator of electromagnetic waves of a usual microwave stove. Calculations show, that for electrons were moving in a circle, instead of shorting an interval between proton's and electron's orbits, the magnetic field should be strong enough: condition $H \geq (\varepsilon_0 / \mu_0)^{1/2} E$ should be satisfied [23]. (Here ε_0 is an electric constant, $\varepsilon_0 = 8.854 \cdot 10^{-12}$ F/m, μ_0 is a magnetic constant, $\mu_0 = 1.2566 \cdot 10^{-6}$ V·s/A).

In the case, when protons' orbits lay in the plane of electrons' orbit, one can visually present a magnetic field lines in the place of electrons location in the form of ears' sheaf, which has been tied up in one place (in the electron's orbit plane). In such magnetic field electrons can easily leave an orbit plane in direction, perpendicular to it. That it did not occur, the direction of magnetic force lines should be opposite to considered: they should be inclined towards to axis of electron ring (the sheaf should be tied up in two places – above and below the orbit plane). Such configuration ("barrel-shaped" magnetic field) is used in cyclic accelerators of charged particles (in betatrons and cyclotrons) for holding of charges in an orbit plane. "Barrel-shaped" magnetic field may be created by protons if they will rotate round the electron ring in orbits, not laying in one plane.

As the first approach we will accept, that protons are kept in orbit by electric field **E,** which creates force, compensating the centrifugal force,

acting on protons. We will pay attention that the considered system of charges is unstable. In "the hydromagnetic capacitor" [21] expansion of system was restrained by pressure of magnetic field, which, in turn, aspired to stretch the coil with a current. We have no this support in our system.

As the first step it is natural to assume, that the considered system is electrically neutral. However the estimation of the strength of magnetic field, generated by movement of protons, shows, that in the case of equality of total charges of protons and electrons the intensity of this field appears to be considerably below demanded (defined by condition $H \geq (\varepsilon_0/\mu_0)^{1/2}E$). The magnetic field can be made stronger if the number of protons is increased, that is if the system has a superfluous positive electric charge. It, of course, will make heavier satisfaction of the requirement of stability supporting of the system because to the problem of compensation of centrifugal forces the problem of overcoming of Coulomb repulsion of the charges with the same sign will be added.

Thus, given to itself, this system will extend beyond all bounds. However expansion can be stopped, if proton orbits "will rest" against a wall of any strong container. Besides, such container is necessary for separating of area, where charges move (and they should move in vacuum), from atmospheric air. Let us discuss, what there can be this strong container, capable to sustain pressure of the considered system of moving charges. Let it represents something like a soap bubble – a spherical shell of water with internal radius R and thickness of a wall a.

If one will place inside the water shell a positive electric charge Q, then in electric field $E = Q/4\pi\varepsilon_0 R$ of this charge water molecules will aspire to be oriented so that negatively charged part of molecule has been turned to the cavity centre, and positive – to outside. Differently, there will be a water shell polarization: molecules will be built in chains of length a, therefore the internal surface of sphere, which is on distance R from the centre, will appear charged negatively, and the external surface, removed from the centre on distance $R + a$, will be positively charged.

The distance between water molecules in an ice crystal is about $3\cdot10^{-10}$ m, so on the area 1 m^2 10^{19} molecules can be placed. If to accept a charge of the end of water molecule equal to electron's charge $e = 1.6\cdot10^{-19}$ C, the charge of surface unit σ will be equal to 1.6 C/m^2. The chain of the polarized molecules of length a, on which ends charges $+e$ and $-e$ are located, represents an electric dipole with the moment $d = e\cdot a$. The value of the dipole moment of the whole spherical shell with internal radius R and thickness a is equal to $D = 4\pi R^2\sigma a$.

In non-uniform electric field E the force, directed towards increase of intensity of a field, acts on electric dipole D. This force is proportional to product of gradient of electric field grad E and the moment of dipole D [24]. For radial-symmetric electric field, created by charge Q, placed inside a water shell with internal radius R and wall thickness a, the force, pulling together the shell in direction to the centre of sphere, is equal to

$$F_{sh} = \sigma a \text{ grad } E\cdot 4\pi R^2 = -4\,\sigma a Q/\varepsilon_0(2R+a). \quad (1)$$

Here at definition of gradient E for radius size value $R + a/2$ is accepted. The forces, stretching a shell, are the centrifugal force of protons F_{cf} and also the force of Coulomb and magnetic repulsion of charges F_{em}. If the total mass of protons is M_p, their speed is v_p and radius of their orbit is R, then

$$F_{cf} = \frac{M_p v_p^2}{R} = \frac{2W_k}{R}. \quad (2)$$

Here W_k is a total kinetic energy of protons. The electromagnetic force, stretching sphere of radius R, which bears a charge Q, is

$$F_{em} = \frac{Q^2}{4\pi\varepsilon_0 R^2}. \quad (3)$$

Having added to these forces a force of atmospheric pressure $F_a = -4\pi R^2\cdot P_a$, we receive a condition of equality of forces at which the shell is in balance [15, 22, 25-27]:

$$F_{cf} + F_{em} - F_{sh} - F_a = \frac{2W_k}{R} + \frac{Q^2}{4\pi\varepsilon_0 R^2} - \frac{4\sigma a Q}{\varepsilon_0(2R+a)} - 4\pi R^2\cdot P_a = 0 \quad (4)$$

In Fig. 1 the dependencies of shell thickness a on the power core charge Q, constructed by formula (4), for inner radius R=3 cm and kinetic energy of protons W_k from 1 J to 10^7 J are shown. One can see that at values of energy $W_k > 16.96$ J curves of dependence a (Q) have a minimum. With growth of energy W_k values of the minimum charge of ball lightning and thickness of its shell increase.

So, for ball lightning with internal radius of the shell R = 3 cm and with shell wall thickness about 1 cm at charge $Q = 10^{-2}$ C the total kinetic energy of protons W_k is equal to 10^7 J. Having divided W_k on volume of a ball of radius $R+a$=4cm, we find energy density of ball lightning $\rho_w = 3.8\cdot10^{10}$ J/m^3. This figure is close to values of energy density for "English" ball lightning ($1.9\cdot10^{10}$ J/m^3), the "Hungarian" ball lightning ($3.7\cdot10^{10}$ J/m^3) and the "Khabarovsk" ball lightning ($4\cdot10^9$ J/m^3). The analysis of the equation (4) has shown that the considered system is steady in relation to changes of radius R [25].

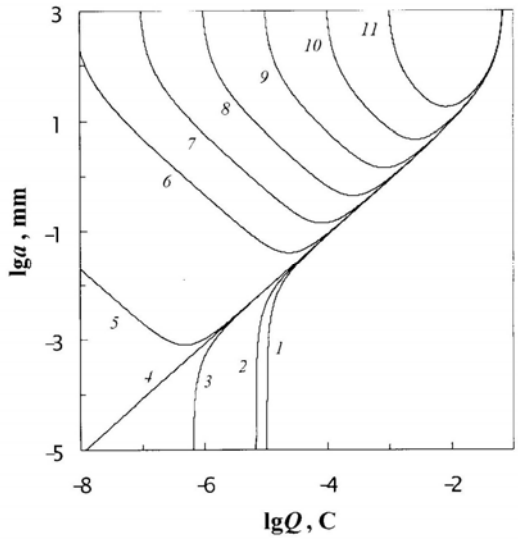

Fig. 1. *The dependence of shell thickness a for the ball lightning with inner shell's radius R = 3 cm on the charge Q of power core for values of kinetic energy of protons W_k equal 1 J (curve 1); 10 J (curve 2); 16,9 J (curve 3); 16,9646 J (curve 4); 17 J (curve 5); 10^2 J (curve 6); 10^3 J (curve 7); 10^4 J (curve 8); 10^5 J (curve 9); 10^6 J (curve 10) and 10^7 J (curve 11).*

As we see, the "designed" system, consisting of charges and a shell, is capable to keep in itself the energy which is equal to energy of real ball lightning. Besides in it along with kinetic energy of protons energy of the electric field, created by charge Q, and approximately equal to it energy of magnetic field contains. The electric capacity of a sphere of radius R is equal to $C = 4\pi\varepsilon_0 R$, and the potential of the sphere, possessing charge Q, is $U = Q/C$. Energy of electric field of the charged sphere is $W_e = CU^2/2 = Q^2/8\pi\varepsilon_0 R$. At $Q = 10^{-2}$ C and $R = 4\cdot10^{-2}$ m $W_e = 1.12\cdot10^7$ J. From here we find the total energy of ball lightning $W_t = W_k + 2W_e = 10^7$ J + $2.24\cdot10^7$ J = $3.24\cdot10^7$ J. Density of this energy is $\rho_{wt} = 1.2\cdot10^{11}$ J/m^3.

The same energy can be stored if to collect a considerable quantity of small ball lightning (for instance, of the size 1 mm) in the common cover. This cover will be compressed due to presence of non-compensated charge of ball lightnings inside it and will be stretched because of repulsing of charges of these lightnings. If the cover is enough transparent, it will be possible to see these small balls through its wall [13, 28].

Finishing the description of the electrodynamic model of ball lightning, we will pay attention to its some details. To remain inside a shell, the element of the power core at impact with it should be reflected into the sphere. As this element bears on itself a positive charge, the reflection process will proceed effectively if the shell will be also charged positively. The shell gets a charge due to constant inevitable losses of charge by the core. This charge, having passed through a shell wall, then flows down to atmosphere. Rate of charge flowing off from an external surface of shell depends on air conductivity λ_a. The characteristic time τ_l of charge flowing off, comparable with average lifetime of ball lightning, is defined by the formula $\tau_l = \varepsilon_0/\lambda_a$. At $\lambda_a = 3.5\cdot10^{-14}$ (Ohm·m)$^{-1}$ $\tau_l = 300$ s [26].

Time of ball lightning existence substantially depends on ability of its shell to constrain expansion of the power core. According to the considered model, at collision of the core's element with shell the mechanical impulse of the proton is directed on a tangent to a shell surface, and only small part of the impulse, caused by rather slow increase of radius of protons' orbit, is transferred to it. At chaotic movement of protons at the same value of their total energy the much larger impulse would be transferred to the shell, and it could collapse. Therefore it is not excluded, that destruction of ball lightning is caused by disturbance of the ordered movement of charges in its power core.

The new element in the considered model is presence of large non-compensated charge in ball lightning. The value of this charge can be so much, that the electric field intensity near to its surface may exceed the value of intensity for air breakdown $E_{bra} = 3\cdot10^7$ V/m. In nature and technique such over-breakdown intensities of electric field are sometimes observed near to pointed conductors, but this not always leads to development of spark or arc discharge. Instead of them corona discharge arises, possessing a "mechanism" of self-restriction of current. Apparently, such corona discharge is formed in immediate proximity from the surface of ball lightning [29, 30]. Halo of radius 1-2 m round ball lightning, which sometimes is observed in darkness, apparently, arises because of air luminescence in corona discharge [8, 31].

4. An explanation of ball lightning properties of on the basis of model

So, we could find a satisfactory explanation of how the substance of ball lightning reserves inside it a considerable quantity of energy. Now we will discuss how it is possible to explain other properties of ball lightning using the described model.

It is follows from the model, that ball lightning is an object heavier than air. For example, the mass of ball lightning with diameter 20 cm and with thickness of the shell wall of 1 cm (defined, basically, by mass of the shell) is equal to 1.3 kg. Therefore there is a lawful question: how this heavy ball lightning can rise upwards to clouds? The typical storm cloud in the bottom part bears negative charge Q_{cl} of value nearby 50 C, and in the top part of the cloud the positive charge of the same value is located. If the distance of the cloud bottom edge from the earth is H = 1 km, the intensity of

electric field near to earth surface under cloud (at account of contribution of a so-called "mirror" charge) is $E_{cl} = Q_{cl}/2\pi\varepsilon_0 H^2 = 9\cdot10^5$ V/m, and this field vector is directed from below upwards. As we have shown above, ball lightning possesses a positive electric charge. At radius 10 cm and thickness of shell wall 1 cm its maximum value is equal to $Q_m = 4\cdot10^{-2}$ C. In the field E_{cl} a force $F_{cl} = Q_m \cdot E_{cl} = 3.6\cdot10^4$ N acts on this charge. This force is capable to lift a cargo of weight $3.6\cdot10^3$ kg, that is not only a ball lightning itself, but also a subject which has "casually clung" to it. And such cases were. We will recollect, for example, a case when ball lightning has lifted in air two magnets [9]. There is also an event description when ball lightning has transferred on distance about 100 m an iron cage of weight 100 kg [32].

Away from a storm cloud the vector of its electric field is directed from top to down. Therefore the ball lightning, which has been thrown out sideways from a cloud, will fall on the earth. However in this case we can face with paradoxical behaviour of ball lightning: some of them, having come nearer to an earth surface, do not fall on it, but hang over it at some height. It seems strange for ball lightning, possessing a charge. After all at approach to the earth, which is a conductor, the positive charge of ball lightning will collect under itself in the earth negative charges, which will force it to fall to the earth. Experiments on measurement of attraction of the flat capacitor plates, between which corona discharge was lighted, have allowed find an explanation of such behaviour of ball lightning [30]. As it was already spoken, near to surface of ball lightning corona discharge arises. The positive charges, drifting to the earth from a zone of the discharge, weaken electric field near ball lightning, reducing thereby the force of its attraction to the earth.

Presence of an electric charge allows explain easily and other "strangenesses" of ball lightning movement. The near-ground space even at fine weather "is penetrated" by force lines of electric fields, and ball lightning simply chooses to itself a way along any force line. Considerable enough charge, which ball lightning can possess, explains display of electric properties by it: fusion of conductors and blows by electric current of people and animals. The ball lightning of radius 0.1 m has capacity $C = 10^{-11}$ F, at the value of its charge $Q = 10^{-2}$ C its potential relative to earth is $U=10^9$ V, and energy of electric field is $W_e=5\cdot10^6$J. If ball lightning is discharged through a conductor with resistance $R_c = 10^4$ Ohm, the characteristic time of discharge will be $\tau_{dh} = R_c \cdot C = 10^{-7}$ s, and a maximum of discharge current $I_m = Q/\tau_{dh} = 10^5$ A. Spreading about the ground, this current can create a potential difference between feet of live beings standing on the earth, which is dangerous to life. Because distance between feet and, hence, the induced potential difference for animals, standing on four feet, more than for people, currents, flowing in the ground, represent for them the greater danger.

Elements of ball lightning core (dynamic electric capacitors) represent small magnetic dipoles. It is possible to expect, that because of disordering of orientation of separate magnets ball lightning as a whole will not have an appreciable magnetic field. However in the presence of an external magnetic field there can be a magnetization of ball lightning, and it can draw to it, for example, a magnet or an iron cage.

Special interest represents the mechanism of ball lightning radiation in ranges of visible light and radio-waves. According to the electrodynamic model, in the centre of the dynamic electric capacitor electrons are located. These electrons move in a ring orbit under the influence of mutually orthogonal electric E and magnetic H_p fields. Speed of this movement is near to velocity of light. Usually frequency of radiation f_e, generated by a charge, moving in the closed orbit, is equal to number of turns of charge for 1 second. For mentioned above an example of ball lightning with internal radius of the shell $R = 3$ cm and thickness of its wall $a = 1$ cm, which is capable at charge $Q = 10^{-2}$ C possess an energy $W_k = 10^7$ J, at radius of an electron orbit $r = 2\cdot10^{-2}$ m frequency $f_e = 2.39\cdot10^9$ s^{-1}. This corresponds to wavelength 12.56 cm. However, the resulted definition of frequency of electron's radiation is true only when electron's speed is much less than velocity of light. Otherwise a synchrotron radiation is generated. One of its reasons is the Doppler effect: period of the wave, radiated by electron, moving towards to the observer, decreases. As a result the characteristic frequency of radiation shifts from a radio range to a visible range. More strict analysis shows, that spectrum of synchrotron radiation consists of a set of harmonics of orbital movement frequency f_e, and the maximum of radiated energy falls on harmonic, which value is proportional to a cube of the relation of electron's energy to $m_e c^2$ (m_e is mass of electron, $m_e = 9.109\cdot10^{-31}$ kg, and c is velocity of light) [33]. The power of synchrotron radiation is inversely proportional to product of squares of radius of an electron's orbit r and parameter $\alpha = 1 - v_e/c$. (Here v_e is an electron's speed) [33].

Calculations show, that at the assumption, that there is some mechanism of protons' kinetic energy transfer to electrons (something like "dynamo"), full energy of ball lightning can "be highlighted" by electrons during 10^{-3} - 10^{-2} s. It contradicts results of observations of ball lightning, according to which its luminescence can last in 10^3 - 10^4 times longer. However usually used formulae for power of synchrotron radiation are valid only for the description of radiation of single electron or a clot of electrons. In the case if electrons would be placed in an orbit absolutely in regular intervals

they would not radiate any light [34]. For example, the coil of a wire with a direct current, circulating on it, does not radiate electromagnetic energy. The reason of radiation power reducing is interference, when for a wave, radiated by one electron, always there is a wave with the opposite phase, radiated by another electron. Radiation can fall outside the limits of the system only at disruption of uniformity of electrons' distribution in an orbit. It means, on the one hand, the maintenance of a constancy of radiation intensity of ball lightning during its life and, on the other hand, the possibility of the sharp increase of radiation intensity, for example, at the moment of ball lightning destruction.

If the nature of ball lightning radiation is, really, a synchrotron radiation, in some cases it can proceed from it in the form of a narrow beam and to be partially polarized. It is possible to expect, that at reduction of electrons' speed at the end of a life colour of ball lightning will become red. Probably also the existence of ball lightning, which spectrum of radiation completely lays in infra-red area, is possible. Such ball lightning will look as black.

Search of the mechanism of ball lightning interaction with window panes still remains a difficult problem. It concerns as the considered model, so as all models, in which ball lightning is regarded as a material object (not a field). As to cases of cutting in windows of round apertures by ball lightning, that, according to modeling experiments, it occurs thanks to local heating and the subsequent fast cooling of glass [20]. Thus it is revealed, that glass heating can occur not on the side, where ball lightning is located, but on the opposite side [19].

It is more difficult to understand, how ball lightning can pass through glass, not having caused its destruction. At the decision of this problem two approaches are possible. The first is to consider, that ball lightning perishes on one side of glass, generating thus an impulse of high-frequency electromagnetic radiation. Under the influence of energy of this impulse on the glass opposite side the new ball lightning is formed. However, we yet do not know details of processes of formation and destruction of ball lightning. Besides, witnesses do not speak about any explosions and claps at ball lightning pass through glasses. On the contrary, it is said, that ball lightning passes through glass, as though not noticing it [13]. The second approach is the account of features of ball lightning and the specificity of glasses structure. On the one hand, glass, as a rule, represents the overcooled mix of two not mixing up phases, between which grains there can be cavities of the size to 100 nanometers. It is known, that some gases, for example, helium, are capable to pass through glass through these cavities. On the other hand, the analysis of the considered model of ball lightning leads to result, that existence of ball lightning with the minimum size of elements of its power core about 10-20 nanometers is possible [15, 28]. Such elements (possessing non-compensated charge) under the influence of electric field can quite "filter" through glass and be gathered again in a new cover on its opposite side [28].

5. Ball lightning formation in the nature

It was repeatedly informed on cases of origin of ball lightning in storm clouds. There are even photos of ball lightnings, which are taking off from the channel of a linear lightning [10, 12]. Therefore there are bases to consider, that as the generator of ball lightning the discharge of linear lightning or, generally speaking, a short impulse of strong current, most likely, serves. Energy of discharge of ordinary linear lightning makes about $5 \cdot 10^9$ J. This is quite enough for generating of ball lightning with extremely high stock of energy. The most probable places of formation of ball lightning, apparently, are areas near to bends of the channel of the linear lightning. In pictures of lightning discharges with scanning in time (when the film moves, and the objective is motionless) it is possible to notice, that sometimes these areas are shone longer, than other

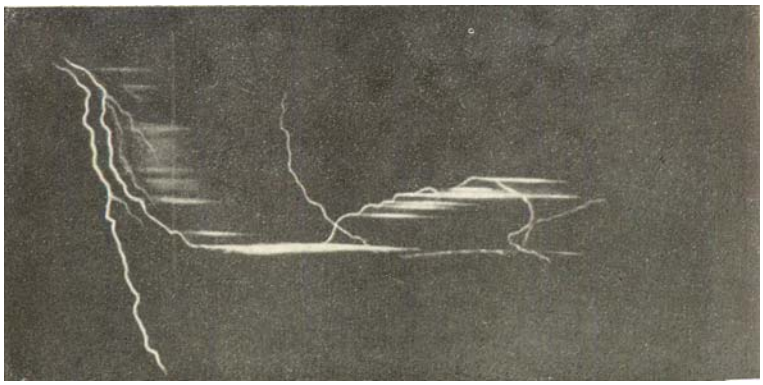

Fig. 2. *A photo of linear lightning discharge consisting on three consecutive impulses [35]. The picture is obtained using camera with moving film. The sequence of impulses is from left to right. A delay between the first and second impulse is 23 ms, between the second and the third – 240 ms. The typical duration of luminescence of the lightning channel is no more than 0.1 ms. It is possible to see that some parts of the channel continue to be shone from 70 to 270 ms.*

parts of lightning channel (see Fig. 2) [35].

Let's discuss, what processes can occur inside a loop of the channel of lightning [26, 36]. Let the form of this loop is close to a ring of radius R_{ch} = 0.1 m. Usually a current impulse of lightning discharge has a short front and a slowly falling down back part. For convenience of calculations we will accept, that the current linearly increases from zero to $I_{max} = 4 \cdot 10^5$ A during Δt_1 = 10 μs, and then it linearly decreases to zero in time Δt_2 = 50 μs. This current generates in the area inside a ring the magnetic field impulse, which maximum intensity in the centre of the ring loop is $H_{max} = I_{max}/2R_{ch} = 2 \cdot 10^6$ A/m.

The channel of the lightning discharge is a powerful source of ultra-violet radiation, therefore air near to the channel will be almost completely ionized. Besides, the lightning discharge generates radio-frequency radiation (recollect a crash in a radio receiver at lightning stroke). In a powerful field of this radio emission plasma from the central area of the loop (where intensity of radiation is maximum) will be pushed out to periphery (in area of minimum of radio-frequency field). As a result air density in the centre will decrease and there can appear a vacuum cavity.

In time Δt_1 of magnetic field intensity increasing inside the coil an eddy electric field E_{up}, which vector direction will be opposite to direction of current, passing throw the ring channel of lightning, will arise. The intensity of this field on distance R_{ch} from the centre of the ring during time Δt_1 will be equal to

$$E_{up} = \frac{R_{ch}\mu_0}{2} \cdot \frac{H_{\max}}{\Delta t_1}. \qquad (5)$$

At parameters chosen by us $E_{up} = 1.26 \cdot 10^4$ V/m. Here we see already familiar to us configuration of the mutually perpendicularly oriented vectors of electric and magnetic field. Under action of electric field E_{up} plasma charges will aspire to move lengthways its vector direction: positive charges – along the field vector, and negative – against the vector. However the magnetic field will bend their trajectories and will force them to move in a circle arch. Because of distinction of masses the radius r_h of this circle for protons will be in $2 \cdot 10^3$ times more than radius of a circle for electron. Protons, as well as electrons, moving in a circle, will be displaced towards the loop centre. Far from the centre of a vacuum cavity charges will move, making collisions with gas molecules. At each collision the charge will "forget" about direction of its speed. After collision the stopped charge will speed up again, will change the trajectory – and so until the next collision. Between impacts the charge will have time to pass small distance, inversely proportional to circle radius r_h. Thus, at each "jump" electrons will move ahead more and more to the centre, and protons will "be practically trampled down" on a place. Separation of charges in space becomes result of it. Electrons will gather in the cavity centre, and protons remain on its periphery.

During the period Δt_2 of magnetic field intensity reduction the vector of eddy electric field E_{dn} will replace a direction with the opposite, and the intensity of this field will be in 5 times less, than intensity E_{up}. Moving under action of field $E_{dn} = 2.5 \cdot 10^3$ V/m, protons will increase their energy. If the average speed of proton is $v_p = 5 \cdot 10^7$ km/s, in time $\Delta t_2 = 5 \cdot 10^{-5}$ s it will pass way $L = v_p \Delta t_2 = 2.5 \cdot 10^3$ m and can get in the field E_{dn} energy $w_p = e \cdot E_{dn} \cdot L = 10^{-12}$ J = 6.3 MeV.

In same time the considerable part of electrons, moving along force lines of magnetic field, will leave our system, therefore it will get a superfluous positive charge. As we see, during the considered processes the configuration of the dynamic electric capacitor, which is a base element of our model of ball lightning, can be formed. Process of ball lightning formation should come to the end with formation of shell from the drops of water, which are on periphery of vacuum cavity.

At attempt of ball lightning creation in laboratory it is desirable to reproduce sequence of processes, which lead to its formation in the nature. It is necessary somehow (by means of gas whirlwind or non-uniform high-frequency electromagnetic field) to make vacuum cavity in air, to make gas ionization (by an impulse of ultra-violet radiation), to act on ionized gas with impulse of magnetic field and somehow remove from system some part of electrons. Work in this direction is already conducted [26], but whether it will be possible to overcome inevitable difficulties on a way of its realization, it is impossible to foresee in advance.

6. Conclusion

Let us once again briefly consider the basic concepts of the article. The main sense of it is that within the frames of traditional physics it was possible to find a way to solve the most difficult problem of ball lightning – its ability to concentrate and store energy with extremely large density. For this purpose it was necessary to refuse concepts, which within almost two centuries were considered firm, but it has appeared, that they only constrained the development of ball lightning theory. The first, what it was necessary to refuse, it – from electrical neutrality of ball lightning. The hypothesis of presence inside it of non-compensated charge has made trivial an explanation of its stability, features of movement and display of electric effects. The second is a refusal of the requirement of equality of average density of ball lightning to air density. Refusal of it has allowed to "design" the rather power-intensive systems, which levitation is

provided not with Archimed force, but electrostatic forces. The third is a refusal of homogeneous system (for example, plasmoid, kept by own fields) and its replacement by heterogeneous system – "symbiosis" of plasma core and dielectric shell. The fourth is refusal of idea of chaotic plasma and replacement it with an ordered system of moving charges. More widely – that ball lightning represents the open thermodynamic non-equilibrium system, capable to self-organizing. The fifth (that directly follows from the fourth) is a conclusion about essential non-equilibrium character of electromagnetic radiation of ball lightning both at optical, and at microwave ranges.

Certainly, this change of paradigm will cause occurrence of new difficulties both theoretical and experimental character, but, in my opinion, they are quite surmountable. One thing can only ruin development of works: more and more amplifying scornful indifference of "true"" scientists to this problem, which, in particular, is shown in refusal of some physical journals in Russia to accept in press articles, in which there are words "ball lightning".

References

1. Rybakov B.A. Heathenism of the Old Slaves. Moscow: Nauka, 1994.
2. Lomonosov M.V. Selected Works on Chemistry and Physics. Moscow: AS USSR Publishers, 1961. P.220-256.
3. Arago F. // Annuare au Roi par le Bureau des Longitudes. Notices Scient. 1838. P.221.
4. Brand W. Der Kugelblitz. Hamburg: H. Grand, 1923.
5. McNally J.R. Preliminary Report on the Ball Lightning. Oak-Ridge National Lab. Report № ORNL3938, 1966.
6. Rayle W.D. Ball Lightning Characteristics. NASA Technical NOTE-D-3188, 1966.
7. Singer S. The Nature of Ball Lightning. New York: Plenum, 1971.
8. Stakhanov I.P. On Physical Nature of Ball Lightning. Moscow: Nauchny Mir, 1996.
9. Imianitov I., Tikhiy D. Beyond Boundary of Science Laws. Moscow: Atomizdat, 1980.
10. Barry J.D. Ball Lightning and Bead Lightning. New York: Plenum, 1980.
11. Egely G. Analysis of Hungarian Ball Lightning Observations. In: Progress in Ball Lightning Research. Ed. Keul A.G. Proc. VIZOTUM. Salzburg, Austria, 1993.
12. Stenhoff M. Ball Lightning. An Unsolved Problem in Atmospheric Physics. New York: Kluwer/Plenum, 1999.
13. Grigoriev A.I. Ball Lightning. Yaroslavl: YarGU Publishers, 2006.
14. Science of Ball Lightning (Fire Ball). Ed. Y.-H. Ohtsuki. Singapore: World Scentific, 1989.
15. Bychkov V.L., Nikitin A.I., Dijkhuis G.C. Ball Lightning Investigations. In: The Atmosphere and Ionosphere. Dynamics, Processes and Monitoring. Eds. V.L. Bychkov, G.V. Golubkov, A.I. Nikitin. Dordrecht: Springer, 2010. P.201-373.
16. Smirnov B.M. The Problem of Ball Lightning. Moscow: Nauka, 1988.
17. Goodlet B.L. // IEE Journ. London. 1937. V.81, P.1.
18. Dmitriev M.T., Bakhtin B.I., Martynov V.I. // Zhur. Tech. Fiz. 1981, V. 51, No. 12, P. 2567-2572.
19. Nikitin A.I., Bychkov V.L., Nikitina T.F., Velichko A.M., Shchelkunov G.P. // Elektrichestvo, 2011, No. 1, P. 45-50.
20. Nikitin A.I., Bychkov V.L., Nikitina T.F., Velichko A.M. // Khim. Fiz. 2006. V. 25. No. 4. P.106-109.
21. Anderson O., Baker W.R., Bratenahl A., Furth H.P., Kunkel W.B. // J. Appl. Phys. 1959. V.30. No. 2. P.188-196.
22. Nikitin A.I. // Elektrichestvo, 1998, No. 11, P. 14-23.
23. Landau L.D., Lifshits I.M. Field Theory. Moscow: GIFML, 1961.
24. Kalashnikov S.G. Electricity. Moscow: Nauka, 1985.
25. Nikitin A.I. // Elektrichestvo, 2004, No. 3, P. 29-36.
26. Nikitin A.I. // Khim. Fiz. 2006. V. 25. No. 3. P.38-62.
27. Nikitin A.I., Velichko A.M., Nikitina T.F. // Izvestia RAS. Energetics. 2008. No.2. P.115-132.
28. Nikitin A.I. // Proc. 11th Intern. Symp. on Ball Lightning (ISBL-10) and 4th Intern. Symp. on Unconventional Plasmas (ISUP-10). Eds. V.L. Bychkov, A.I. Nikitin. 2010. Kaliningrad, Russia. P.127-134.
29. Nikitin A.I., Leipunsky I.O., Nikitina T.F. // Prikladnaya Fizika. 2010. No. 2. P. 15-22.
30. Nikitin A.I., Nikitina T.F., Velichko A.M. // Elektrichestvo, 2010, No. 3, P. 16-22.
31. Ryabtsev A.N., Stakhanov I.P. // Zhur. Tech. Fiz. 1987, V. 57, No. 8, P. 1583-1587.
32. Nikolaev G.V. The Mysteries of the Electro-magnetism. Tomsk: Znamya Mira, 1999.
33. Ternov I.M., Mikhailin V.V., Ternov I.M., Khalilov V.R. Synchrotron Radiation and its Applications. Moscow: Moscow State University Publisers, 1980.
34. Artsimovich L.A., Lukianov S.Yu. Movement of Charged Particles in Electric and Magnetic Fields. Moscow: Nauka, 1978.
35. Meek J.M., Craggs J.D. Electrical Breakdown of Gases. Oxford: Clarendon, 1953.
36. Nikitin A.I. // Elektrichestvo, 2000, No. 3, P. 16-23.

P1. EFFECT OF AMBIENT AIR PRESSURE ON INITIATION OF MW DISCHARGE BY LASER RADIATION

S. Afanas'ev, V. Brovkin, Yu. Kolesnichenko and I. Mashek*
Joint Institute for High Temperatures RAS, Moscow
Yu. Kolesnichenko" <kolesnichenko@ihed.ras.ru>
*Saint-Petersburg State University, Saint-Petersburg

Abstract. The results of investigation of laser spark gas-dynamic processes influence on MWD structure at different MW-LS interaction stage and different air pressure are presented. The MW discharge formation dynamics was studied by Schlieren method. It was shown experimentally that maximum delay time of MWD initiation by laser spark depends upon E/p parameter. Numeric modeling of processes in decaying laser spark domain was carried out to quantify the regimes of laser plasma interaction with MW field.

A promising method for the distant initiation of MW discharge employs laser radiation. Such a phenomenon is of considerable interest, and can be used in numerous practical applications [1-3]. This work reports the results of an experimental investigation of threshold characteristics and gasdynamic processes in laser spark (LS), which influence on MW discharge formation. We also present data on ultimate delays in MW discharge origination in decaying LS domain, as well as the results of numeric modeling of LS plasma components relaxation and regimes of its interaction with MW field.

The layout of experimental installation is presented at Fig.1. Experiments were performed using a magnetron in the centimeter wavelength range (λ_{MW} = 2.3 cm) with output power about 600kW. Linearly polarized MW radiation was emitted via a horn into a vacuum chamber and focused by a metal mirror to a region with dimensions on the order of wavelength. An electric field amplitude in a focus attained 5 kV/cm. The duration of MW pulses τ_{MW} did not exceed 4μs. The beam of second harmonic radiation (λ = 532 nm)of a Nd:YAG laser (LF117, SOLAR TII, Minsk) with a pulse duration of τ_{las} = 10 ns was oriented along the electric field vector in the MW and

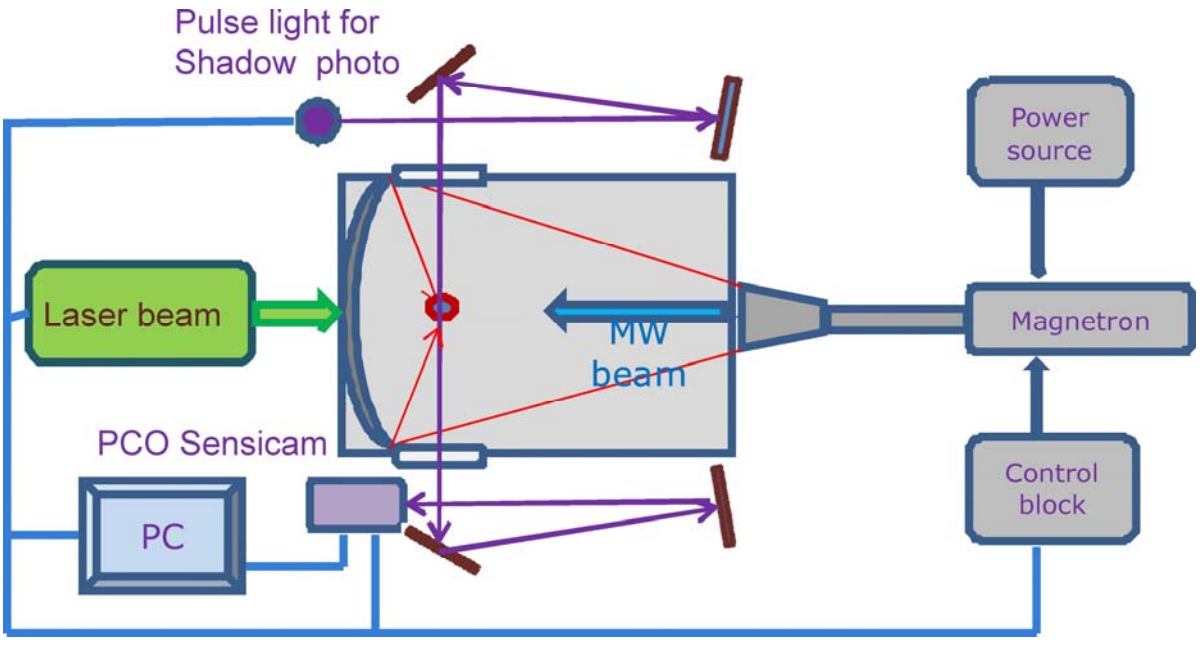

Fig.1. *MW installation scheme*

introduced into the chamber with the aid of a mirror via a quartz window. Laser spark was created in air in pressure range P from 150Torr to 750Torr by focusing of light beam by a lens with a focal distance of f = 45 mm into a region of the main lobe of the MW directivity pattern. The energy of laser pulse varied from 200mJ to 550mJ. The time T_{del} of the MW pulse delay with respect to the laser pulse varied within broad (from zero to several tens of milliseconds) limits. Repetition rate of synchronized MW and laser pulses was 1 Hz.

The dynamics of gasdynamic disturbances produced by the triggering LS and MW discharge was registered by means of impulse Schlieren system. Time resolution of the system attained 0.5μs and was determined by the exposure time of a high speed camera (Sensicam PCO AG, Germany). The necessary delay and exposure times and operating modes during experiment were settled with the aid of PC, at which the control program of PCO.Sensicam was displayed. The intensity and duration of MW radiation, light pulses of LS and MWD and launching impulses of camera, laser and light-emitting diode via appropriate facility were displayed on 4-beam oscilloscope Tektronix TDS 3014B.

By use of the mentioned means the threshold characteristics of MW discharge initiated by laser sparks of different intensity – 250mJ, 375mJ and 525mJ – were measured under different delays of MW pulse relative laser one. After switching on of the laser with fixed output energy gradual rise of the level of MW energy was implemented until the appearance of luminosity from the interaction domain. The breakdown fields were registered both at the stage of LS luminescence and later stages of its decay. Besides, the ultimate delays of MW discharge initiation under different values of E/P parameter were measured.

The results obtained in air of atmospheric pressure are presented in Fig.2. In whole, the tendency of MW breakdown threshold decrease and increase of initiation ability time of LS with increase of spark intensity. However, there is a time interval about 10mcs where breakdown thresholds are minimal and practically coincide under all applied laser pulse energies. Most considerably the rise of laser pulse energy affects on MW discharge initiation under delays from several tens of microseconds till millisecond and more.

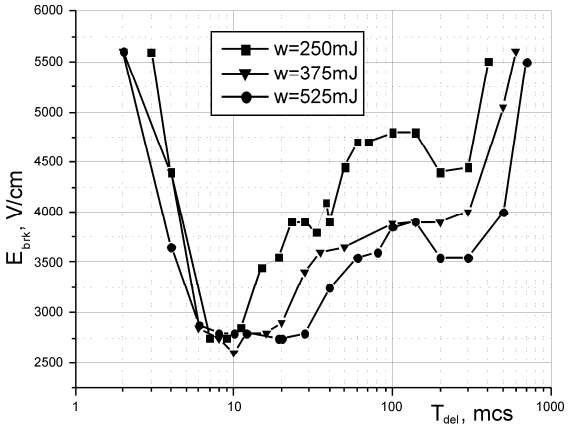

Fig.2. *Influence of laser pulse energy on MW breakdown levels dependence over delay time*

With ambient air pressure decrease the initiation ability of LS rises up to time intervals of tens and even hundreds of milliseconds. This parameter is governed mostly by E/P value. Under the fixed E/P value the ultimate delay varies insufficiently in rather broad range of air pressure (Fig.3).

Integral photo with small exposure time (1mcs) of MW discharge developing in gasdynamic disturbance produced by laser spark were obtained under different time delays. These photo show luminosity and localization of separate elements of MW discharge at time moments inside MW pulse (Fig.4). It can be also seen that in some cases MW discharge illuminates gasdynamic structure boundaries of decaying laser spark.

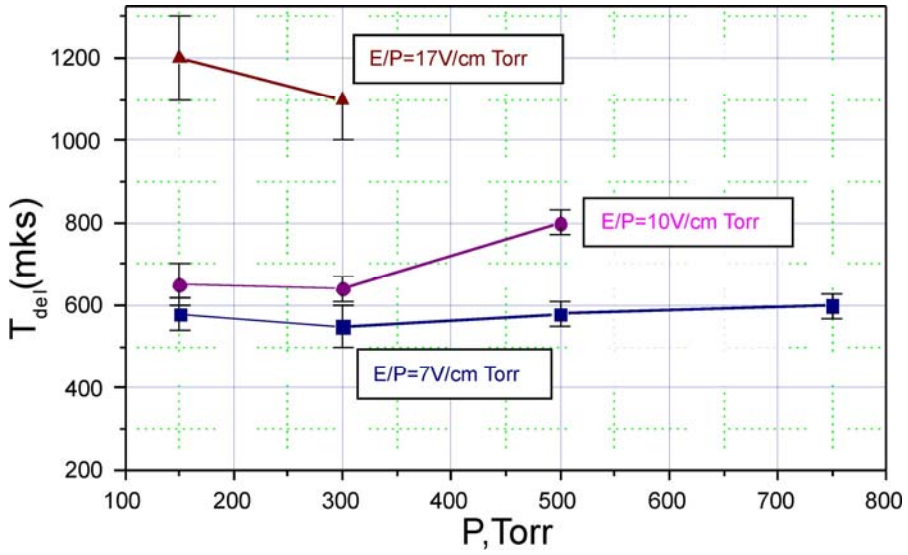

Fig.3. *Maximum delay of MWD initiation by laser spark*

More detailed investigation of MWD formation was carried out by means of Schlieren system. For this, afterspark gasgynamic phases with initiated of MW discharge were registered in wide range of air pressure and delays. Such experimental data gives opportunity to resolve the spatial domains of MW channels origination at different moments of MW wave interaction with remnant gasdynamic medium disturbances.

Since several microseconds after LS formation gasdynamic disturbances in the form of divergent shock wave appear (Fig.5-6). By tenth microsecond the ellipsoidal domain of heated rarefied gas (density "hole") slightly elongated in the direction of laser beam propagation and formed in the area of laser energy absorption is well seen against the

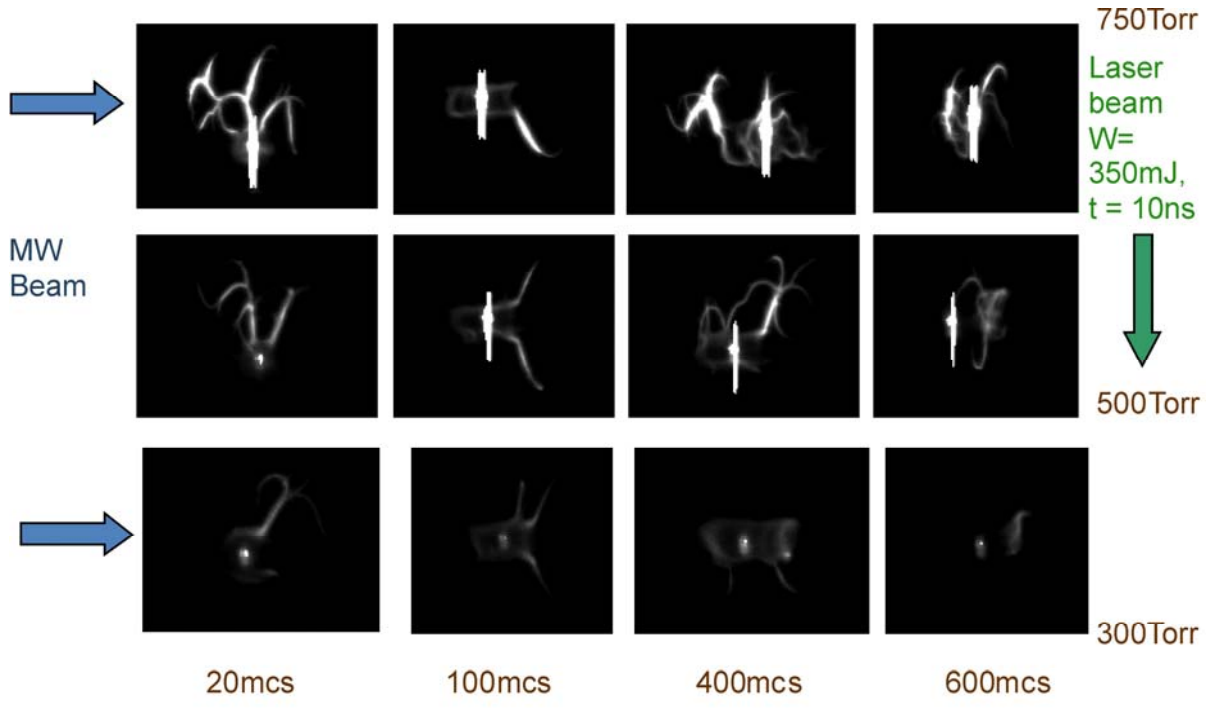

Fig.4. MWD + LS integral photo at 4 different delays

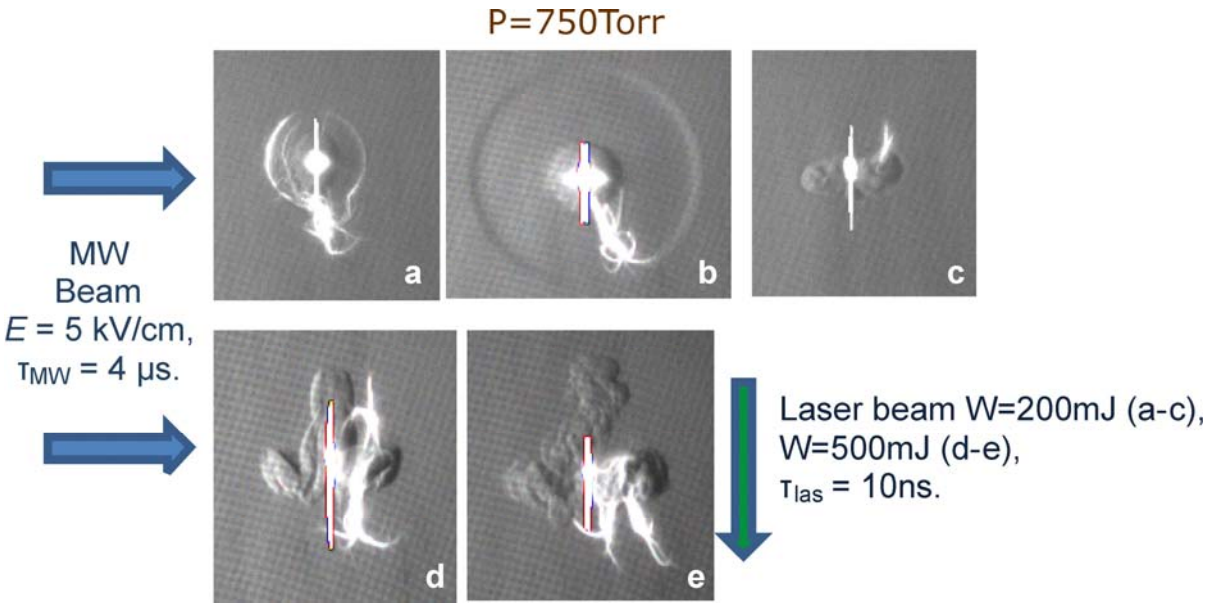

Fig5. *Schlieren photo of MW discharge initiated by LS, exposure time 0.5mcs (a-c) and 3,5mcs (d-e). MW – laser delay (mcs): a) 5, b) 20, c) 210, d) 505, e) 964.*

polarization plane in accordance with stimulated MW discharge electrodynamics [5]. Frequently MW channel (or one of MW channels) later develops along the front of shock wave. While MW channel intersecting shock wave front its break and displacement is registered. Under the reduced pressure MW channels initiation takes place exactly at the boundary of density "hole" near its poles (Fig.6) with subsequent development as in the case of high pressure discharge. In the range of large delays, after 100-300mcs, the character of gasdynamic disturbances changes – the toroidal type disturbance begins to form and at later stage (t≥400mcs) residual vortical footprint is well seen in air. Namely in these domains under the MW field imposing one can observe the appearance of diffusive volumetric luminescence with further development of MW channels oriented along the electric field vector of MW wave (Fig.6). Besides, part of MW channels trace also the geometry of disturbed vortical zone, i.e. their development follow along density boundaries (Fig.6). Such scenario is observed for a sufficiently long time so far gasdynamic disturbance exists in the focal volume of MW radiation. In

The idea of such investigation was, starting from the plasma condition, which is experimentally detected as local thermal equilibrium and taking as a guiding parameter experimentally measured gas temperature time dependence, calculate evolution of electron concentration/ conductivity in decaying domain.

Kinetic calculation of laser spark decay was performed in the following assumptions:

- During the decaying phase the spark medium temperature dynamics was taken according to measurements [6, 7].
- Electron temperature was supposed to be equal to gas temperature all over the decay phase.
- At start calculation time the medium composition was assumed to be in the local thermodynamic equilibrium under the temperature 16000 K and the pressure 1 atm (for 100Torr – ≈14000 K). This moment corresponds to time interval after laser spark origination of about 2-3 microseconds.
- Conditions in spark medium were supposed as isobaric ones and equal to ambient air pressure.

The choice of start time is explained by the fact that according to the mentioned above

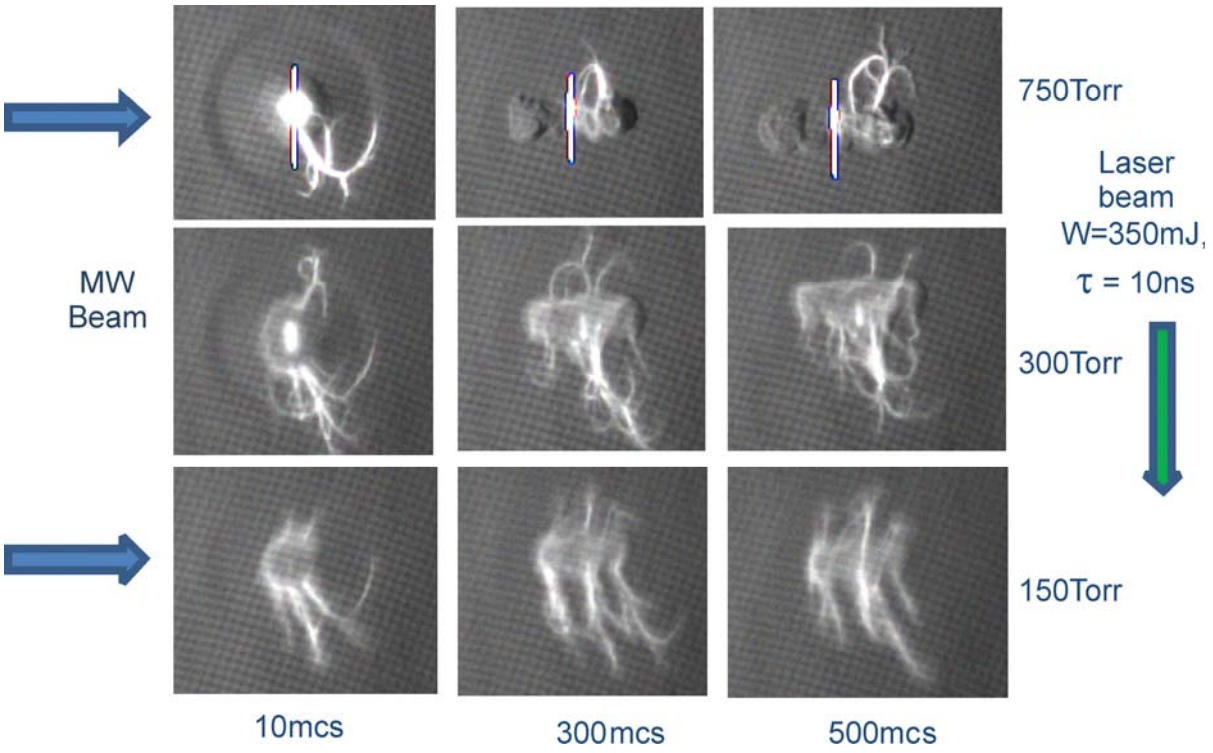

Fig.6. MWD + LS Schlieren photo

experimental results in about one microsecond after breakdown laser spark plasma is still close to thermal equilibrium.

Fig.7 presents the result of decaying stage parameters calculation for ambient air pressure 750Torr and 100Torr. The recombining character of decaying plasma results in deviation of charged particles concentration from their thermodynamic values to over-equilibrium ones. The difference becomes more and more significant while gas temperature goes down. At low gas temperatures (about 3000K and less) the dissociative recombination $e + NO^+ \rightarrow e + N + O$ leads to rapid de-ionization of plasma

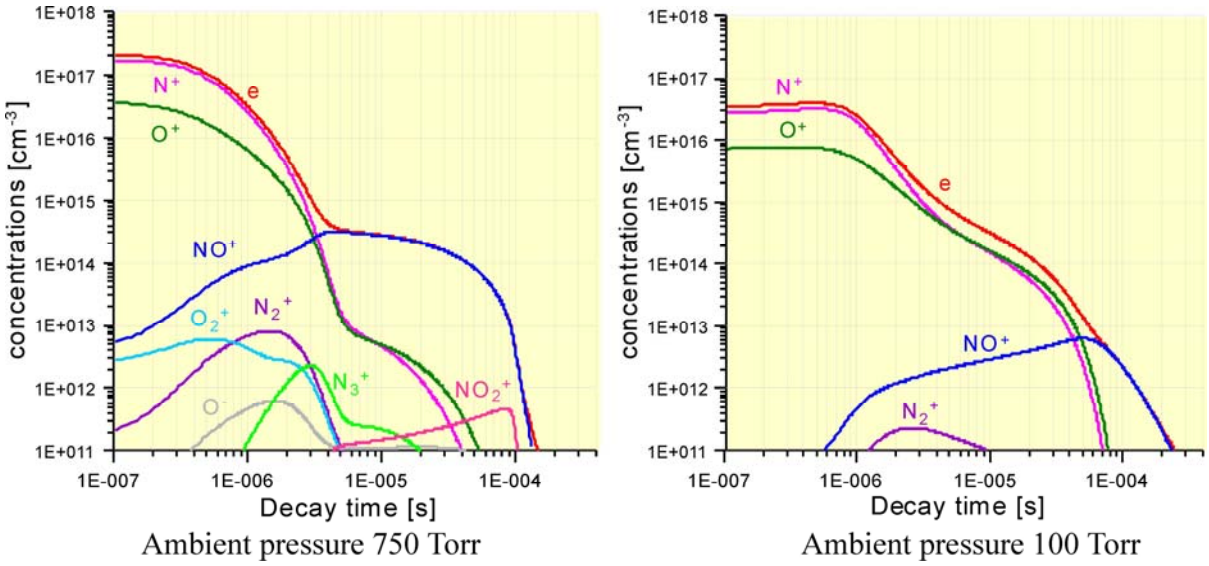

Fig.7. *Dynamics of charged particles during decay of laser spark*

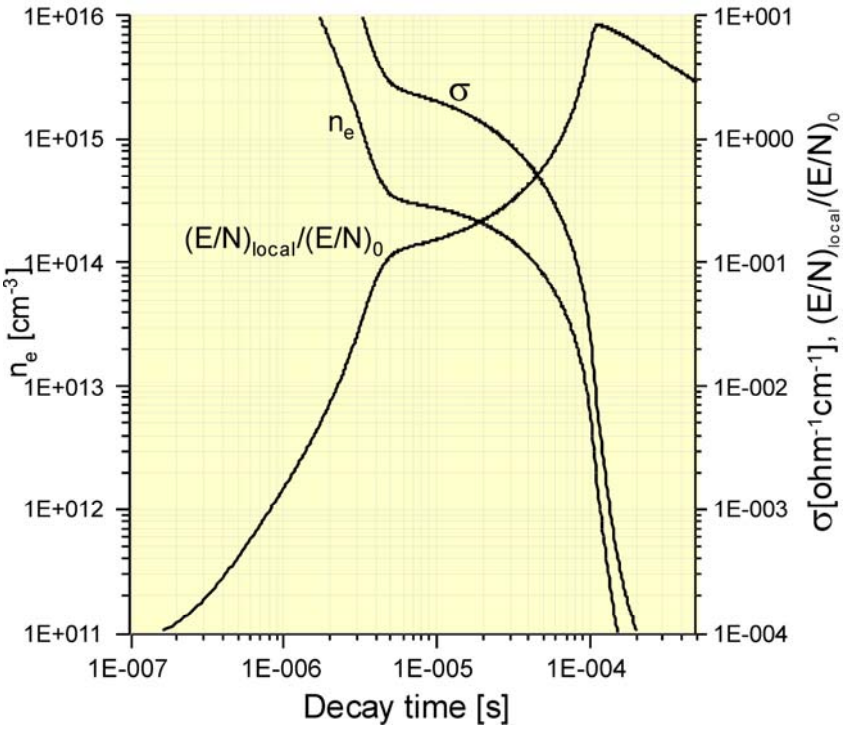

Fig.8. *Dynamics of electron concentration, electro-conductivity of plasma and relation of internal/external reduced fields (p=750Torr)*

domain. At the same time the incident electric field is able to penetrate inside this domain.

For estimation of the moment of MW field penetration in plasma we assumed the shape of the decaying spark domain to be a sphere, thus depolarization factor $n^{(d)}$ to be equal to 1/3. At this, the polarization parameter $4\pi\sigma n^{(d)}/\omega$ is also diminishing in time, starting from the values much greater unity, what implies that decaying spark domain resembles metallic sphere, then coming to the unity at time moment about 80μs for atmospheric pressure conditions. From this moment plasma becomes more and more transparent for an incident MW field. At time moment 80μs gas temperature in the decaying domain falls down to the value 3000K and electron concentration – to about $2\cdot10^{13}$cm^{-3}. Dynamics of electron concentration and electron conductivity σ of ionized volume is shown in Fig.8.

The behavior of the reduced electric field E/N inside decaying plasma domain is presented at Fig.8. The reduced field is normalized on the reduced electric field outside the plasma domain. Thus, the curve gives opportunity to estimate the possibility of MW breakdown onset inside the plasma region. If the breakdown field in the ambient undisturbed gas medium exceeds the imposed electric field E_0 greater than the value of curve maximum (in our approximate model this maximum is about 10), no breakdown can be obtained. Thus, for electric field strength less than ~3kV/cm the breakdown can not be realized. Nevertheless, the calculated value is sensitive to the behavior of electron concentration and gas density and demands more detailed knowledge of their evolution. In opposite case (for E_0 > 3kV/cm) there appears time interval when breakdown is possible. As for electric field intensification on a sphere poles, the process takes place from the very beginning (spark origination) up to about 80μs, the intensification value being about 3.

Three regimes of MW beam interaction with decaying laser plasma can be distinguished for atmospheric air pressure. The first is MW discharge initiation on highly conductive laser plasma and is limited by the first 80μs. The second regime is initiation of MW discharge via breakdown in rarefied and moderate-conductive spark domain when electric field begins to penetrate in it. And the last is spark plasma heating (or energy deposition) in sub-breakdown undisturbed field. This regime ranges in time up to several hundreds of microseconds. Qualitatively, these regimes are inherent to LS-MW interaction under all investigated pressures.

Thus, the performed experiments let us reveal factors affecting on MW discharge initiation by laser spark at all stages of its decay. The value of ultimate time of LS initiation ability depends upon E/P parameter and strongly increases with its growth. Another important parameter which affects in the same manner is laser pulse energy. Thereby, both under atmospheric and reduced air pressure the significant decrease of MW discharge breakdown thresholds, as well the magnitude of time interval of LS initiation ability is due to gasgynamic disturbances created by laser spark.

References

1. S. A. Afanas'ev, V. G. Brovkin and Yu. F. Kolesnichenko, Pis'ma Zh. Tekh. Fiz. **36** (14), 73-78 (2010) [Tech. Phys. Lett. **36** (7), pp. 672-674 (2010)].
2. Yu. Kolesnichenko, V. Brovkin, O. Azarova, V. Grudnitsky, V. Lashkov, I. Mashek, Proceedings of the 41st AIAA Aerospace Sciences Meeting & Exhibit (January 6–9, 2003, Reno, NV), AIAA Paper 2003-0361.
3. *MW Discharge: Fundamentals and Applications*, Ed. By Yu. A. Lebedev (Yanus_K, Moscow 2006).
4. Kolesnichenko Yu., Khmara D., Brovkin V., and Afanas'ev S. Proceedings of the 45th AIAA Aerospace Sciences Meeting & Exhibit (Reno, NV, 8-11 January 2007). AIAA Paper 2007–1228.
5. V. G. Brovkin and Yu. F. Kolesnichenko, Pis'ma Zh. Tekh. Fiz. **16** (3), 55-58 (1990) [Tech. Phys. Lett. **16**, (1990)].
6. N. Glumac, G. Elliott, and M. Boguszko, AIAA J. **43**, 1984 (2005).
7. N. Glumac, G. Elliott, Proceedings of the 44th AIAA Aerospace Meeting and Exhibit, (Reno, NV, 9-12 January, 2006). AIAA Paper 2006–399.

P2. INFLUENCE OF ELECTRICAL DISCHARGE IN EXTERNAL MAGNETIC FIELD ON SWIRLING FLOW PARAMETERS

Klementyeva I.B., Moralev I.A., Bityurin V.A., Klimov A.I.*
*Joint Institute for High Temperatures of RAS, 13/2 Izhorskaya, 125412, Moscow, Russia
Irina Klementyeva < ira.klementyeva@mail.ru>

Abstract. The objection of the work presented in current paper is to investigate dynamical impact of constricted electrical discharges in external magnetic field on gas flows. In this paper results of experimental study of electrical discharge interaction with swirling flow in external magnetic field are presented. Pressure drop value versus magnetic field induction magnitude and polarity is given for two cases: electrical discharge rotates co-current and counter-current with swirling flow. Tangential velocity rise rate caused by electrical discharge rotation is evaluated. Measured velocities are of the same order that calculated from balance equation for considered experimental conditions. It is shown that the main contribution into flow tangential velocity can be expected only near central electrode that is explained by electrical discharge spiral evolution in external magnetic field.

1. Introduction

Study of electrical discharges interaction with gas flows of different configurations in external electric and magnetic fields is an important part of plasma aerodynamics. Obtained results can be used for improvement of characteristics of high speed combustion chambers of air-breathing jet engines and power generating systems, for improvement of aircraft aerodynamical characteristics, for environmental conditions improvement.

Electrical discharges characteristics in co-current and counter-current axial gas flows in external magnetic field, interaction between electrical discharges and gas medium in external magnetic field, mechanisms of influence of that interaction on flow structure and mixing have been studied and are described in [1 – 8].

The main purpose of current work is to study dynamical impact of constricted electrical discharges in external magnetic field on gas flows experimentally. Motivation for investigations is to use the impact for vortex structures modification in tasks of flight control and for mixing intensification in tasks of plasma assisted mixing in practical applications. Study of the dynamical impact of constricted electrical discharges in external magnetic field on gas flows is also of fundamental interest.

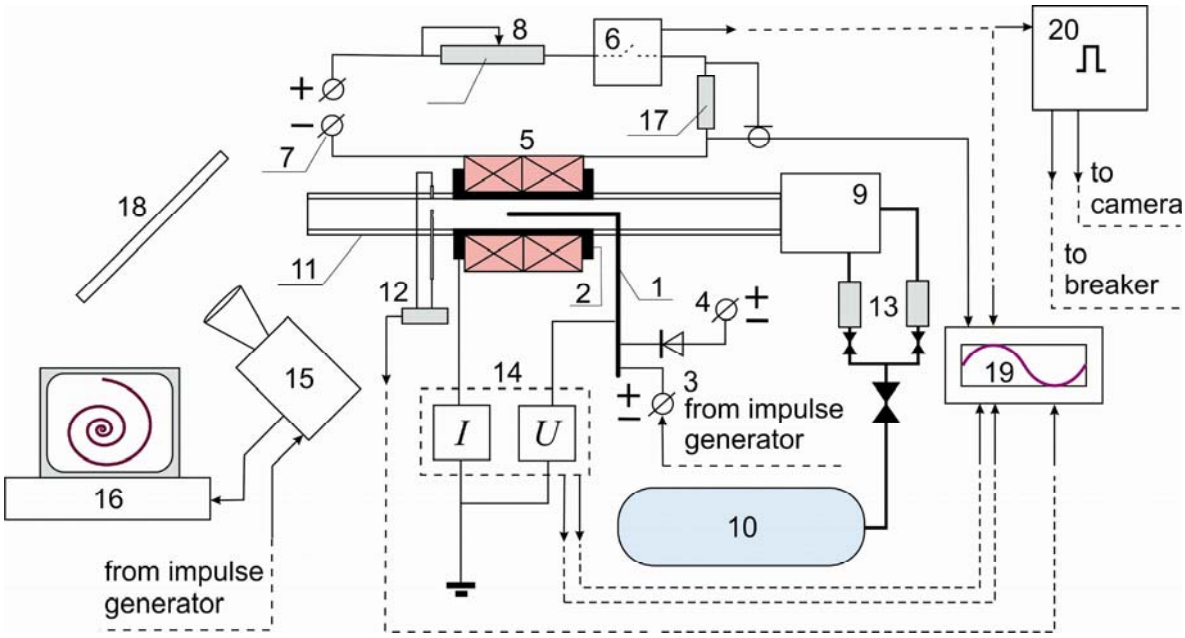

Fig.1. *Experimental setup scheme.*
1-central wire electrode, 2-annular electrode,3-breaker, 4-power source, 5-magnetic coil, 6-magnatic field switching on/off system, 7-accumulators, 8-rheostat, 9-swirler, 10-compressor, 11-quartz tube of aerodynamical duct, 12-pressure differential sensor, 13-flowmeters, 14-current and voltage measurement scheme, 15-high speed digital photo camera, 16-computer, 17-current shunt, 18-mirror, 19-oscillograph, 20-puls generator.

In this paper results of investigation of electrical discharge interaction with swirling flow in external magnetic field are presented. The main focus is made on following:

1. Discharge and swirling flow parameters under considered experimental conditions.

2. Dynamical mechanism of electrical discharge influence on swirling flow structure and its gas-dynamic characteristics in magnetic field.

3. Swirling flow control by discharge in magnetic field of different induction value and polarity.

4. Evaluation of tangential velocity rise rate that is caused by the discharge moving in magnetic field.

2. Experimental Investigation

2.1. Experimental Setup

Experimental setup scheme is presented in Fig. 1.

The base element of the experimental setup is test section that is an aerodynamical duct with coaxial system of electrodes and magnetic coil.

The aerodynamical duct of 80cm in length is used for swirling flow organization and consists of following elements: swirler *9* with axial inlet and four tangential gas inlets and quartz tube *11* of 34mm diameter. Gas comes into the test section through compressor *10*. The aerodynamical duct length ensures stabilized velocity profiles in the test section.

The electrical discharge is initiated between annular aluminum electrode *2* of 34mm diameter and 50mm width that is built in quartz tube and central wire tungsten electrode *1* of 1mm diameter that is mounted along aerodynamical duct axis.

Magnetic field in the system is created by magnetic coil *5* that is made of copper wire of 2.2mm in diameter and is situated coaxially with the aerodynamical duct. The magnetic coil is powered by accumulator battery *7*. Electric current of magnetic coil circuit is regulated with rheostat *8*.

The direct current electrical discharge is organized by stabilized power source *4* with open circuit voltage U=7kV and by ballast resistance that keeps up short circuit current up to I=2.8A.

It is possible to change polarity of magnetic field and polarity of the electrodes in experiments, but the annular electrode is always grounded.

Synchronization scheme gives required time sequence and time intervals between switching on/off of flow, the electrical discharge, magnetic field and triggering of recording equipment. Flow rates of longitudinal and tangential components of swirling flow are set up by flowmeters *13*. The electrical discharge is initiated in gap between the electrodes by breaker. When magnetic field is switched on, signal from pulse generator *20* triggers video camera *15* and oscillograph *19* that record processes before and after magnetic field switching on.

Electrical discharge and swirling flow parameters are measured by electric current and voltage probes and pressure differential probes correspondingly.

Discharge visualization is performed with high speed digital photo camera Citius Imaging C10 of following specification: maximum matrix resolution – 652×496, pixel size – 10mkm, maximum registration rate – 10000 frames per second, time of exposure – from 6mks, synchronization accuracy – 1mks.

Discharge circuit current I_{arc}, discharge voltage U_{arc}, current of magnetic coil electrical circuit, signal of magnetic field switching on are registered with four-channel digital recording ocsillographs Tektronix TDS 2014.

2.2. Task Setting

The initial air swirling flow, that is created as a result of combination of direct flow and tangentially injected flows, comes into the test section. The electrical discharge is initiated between the central wire and annular electrodes. In external magnetic field under electromotive body force it moves and impacts the swirling flow.

Experiments were carried out for different polarities of magnetic field at the same direction of initial swirling flow rotation so the discharge moved co-current or counter-current the swirling flow.

Typical parameters of the experiments are following: flow rate ~10^{-2}kg/s, discharge current I_{arc} ~1.3 – 1.8A, discharge voltage U_{arc} ~0.8 – 2.2kV, magnetic field induction B – 0.09, 0.27T, gas – air, P ~10^5Pa.

2.3. Results Discussion

Tangential velocity rise rate, that is caused by the discharge moving in magnetic field, are of the main interest in the study. It can be defined from the comparison of pressure drop values obtained for the same induction magnitudes but for opposite polarities of magnetic field for the same other experimental conditions. Differences between pressure drops with co-current discharge rotation and pressure drops with counter-current discharge rotation reflects a double input of the rotating discharge into tangential velocity of the swirling flow:

$$\Delta\left(\Delta P\right) = \Delta P_{+B} - \Delta P_{-B}$$

where ΔP_{+B} is measured at co-current discharge rotation with the swirling flow, ΔP_{-B} – at counter-current discharge rotation with the swirling flow.

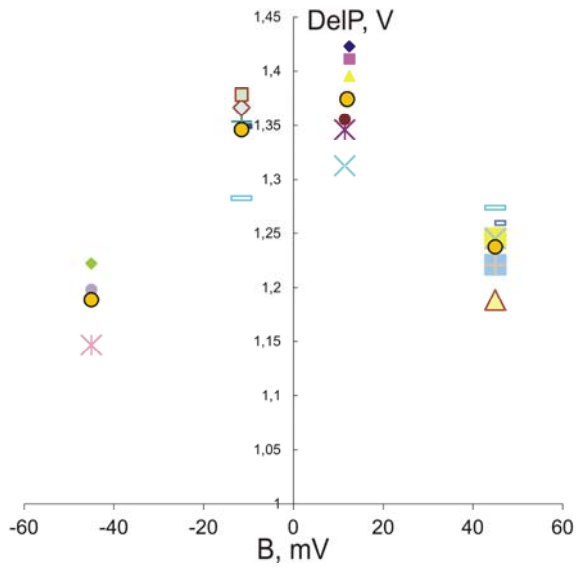

Fig.2. *Pressure drop versus magnetic field induction magnitude and polarity. X-axis: 1mV=0.006T, Y-axis: 1mV=0.357Pa.*

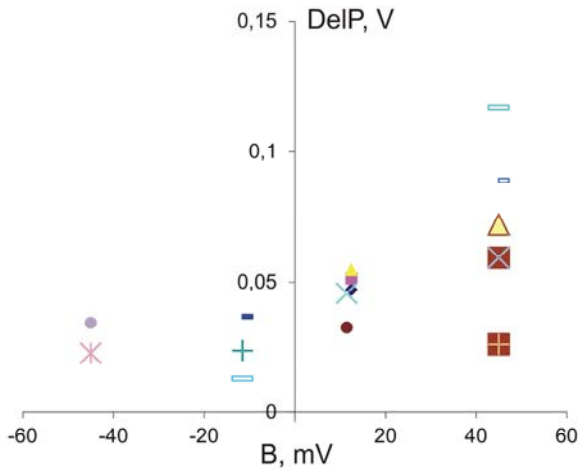

Fig.3 *Pressure drop, normalized by pressure drop in initial swirling flow, versus magnetic field induction magnitude and polarity. X-axis: 1mV=0.006T, Y-axis: 1mV=0.357Pa.*

In Fig.2 and Fig.3 pressure drop measured for four magnetic field induction values (-0.09T, +0.09T, -0.27T, +0.27T) is shown. Fig.3 represents pressure drop, normalized by pressure drop in initial swirling flow, versus magnetic field induction magnitude and polarity.

Pressure drop measurements were taken at a distance of 5.5×10^{-2}m downstream from the central electrode within radius of 2mm in the experiments.

For B=-0.09, +0.09T and B=-0.27, +0.27T $\Delta(\Delta P)$ ~10 and 17Pa correspondingly. Obtained values mean that the moving discharge "adds" 3, 5m/s to the swirling flow tangential velocity for two cases.

Input into the tangential velocity can be estimated with balance equation:

$$I_r(r)Bl=G(r)w(r)+\rho w^2(r)S(r)/2$$

where I_r is radial component of discharge current, B is magnetic field induction, l is discharge element length, G is gas flow rate, w is tangential velocity of the discharge, ρ – air density, S – inner surface area of the aerodynamical duct at the distance of 5.5×10^{-2}m downstream from the central electrode, C_f~1.

Estimated "added" velocity varies from 4.2 to 1.1m/s for B=-0.09, +0.09T and from 10 to 2.6m/s for B=-0.27, +0.27T at the distance of 5.5×10^{-2}m and in the range of 1mm from the central electrode.

Measured velocities are of the same order that calculated from the balance equation for considered experimental conditions.

Fig.4 shows distribution of the estimated added tangential velocity. It is seen that main contribution from the rotating discharge into the flow tangential velocity can be expected only near the central electrode that is explained by electrical discharge spiral evolution in external magnetic field.

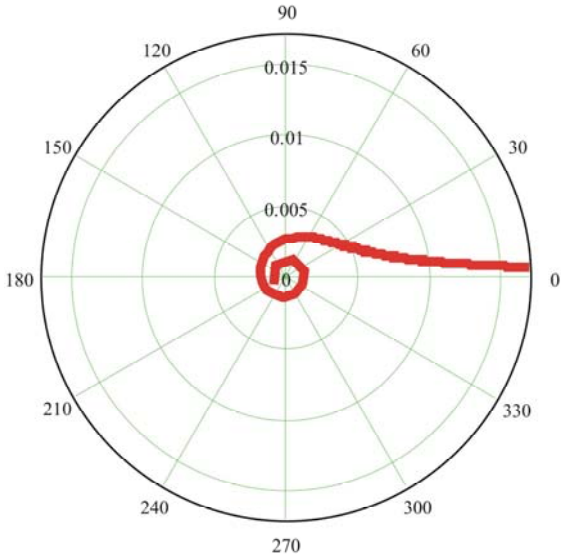

Fig.4. *Estimation of added tangential velocity distribution.*

3. Conclusions

The constricted electrical discharge in external magnetic field has the dynamical impact

on gas flow swirling. Measured in the experiments the added tangential velocities are 3 and 5m/s for B=-0.09, +0.09T and B=-0.27, +0.27T correspondingly at a distance of 5.5×10^{-2}m downstream from the central electrode within radius of 2mm. They are of the same order that calculated from the balance equation for considered experimental conditions. But the main contribution from the rotating discharge into the flow tangential velocity can be expected only near the central electrode that is explained by electrical discharge spiral evolution in external magnetic field.

The work is carried out through support of Russian Federation President Grant MK-3155.2011.8.

4. References

1. A. Bocharov, V. Bityurin, I. Klement'eva, and S. Leonov, Experimental and Theoretical Study of MHD Assisted Mixing and Ignition in Co-Flow Streams, In: 14th International Conference on MHD Power Generation and High Temperature Technologies, Maui, Hawaii, 2002, AIAA Paper 2002-2248.
2. I. Klement'eva, A. Bocharov, V. Bityurin, A. Klimov, Experimental and Numerical Study of MHD Assisted Mixing, In: 15th International Conference on MHD Energy Conversion and 6th International Workshop on Magnetoplasma Aerodynamics, Moscow, May 24-27, 2005, pp. 365-374.
3. I. Klement'eva, A. Bocharov, V. Bityurin, A.Klimov, MHD Assisted Mixing through the Experimental and Numerical Study, In: 27th ICPIG, Eindhoven, the Netherlands, July 18-22, 2005.
4. V.A. Bityurin, I.B. Klement'eva, A.I. Klimov, The Investigation of the Electrical Discharges Interaction with Gas Flows in External Magnetic Fields for Problems of Mixing and Combustion Intensification, In: 16th International Conference on Gas Discharges and their Applications, Xian, China, Sept. 11-15, 2006, pp. 425-428.
5. I. Klementyeva, V. Bityurin and A. Bocharov, Constricted Discharge Interaction With High Speed Gas Flows, In: 38th AIAA Plasmadynamics/16th MHD Energy Conversion Conference, Miami, FL, 2007, June 25-28, AIAA Paper 2007-4141.
6. Klement'eva I. and Bityurin V., Electrical Discharge – Gas Flows Media Interaction in External Magnetic Field, The 46th Aerospace Sciences Meeting and Exhibit, Reno, NV, 2008 AIAA Paper 2008-1393.
7. I. Klementyeva, V. Bityurin and A. Bocharov, Electrical Discharge Influence on Gas Flow Structure and Mixing, In: 47th AIAA Aerospace Sciences Meeting Including The New Horizons Forum and Aerospace Exposition Orlando, Florida, 5-8 January, 2009, AIAA 2009-1045.
8. I.B. Klementyeva, V.A. Bityurin, A.N. Bocharov, Electrical Discharge Interaction with Gas Medium in External Magnetic Field and its Influence on Flow Structure and Mixing, The 9th International Workshop on Magneto-Plasma Aerodynamics, Moscow, 13-15 April, 2010, pp. 298-303.

P3. SPATIAL SYMMETRY OF CONVERGING SHOCK WAVES IN HARD-SPHERE MODEL: CARNAHAN-STARLING EQUATION OF STATE

A.V. Konyukhov, A.P. Likhachev*, V.E. Fortov
Joint Institute for High Temperatures, Russian Academy of Sciences
Izhorskaya ul. 13 bld. 2 Moscow 125412, Russia
*apl@ihed.ras.ru

Introduction

The converging shock waves (CSW) being a powerful tool for generation of high pressures and temperatures are of great interest in the high energy density physics and some applications. The CSW stability needed to provide efficient matter compression was studied by many authors both theoretically and experimentally. It was found the CSW in ideal or weakly non-ideal gas are unstable with respect to small symmetry violation. The influence of thermodynamic properties of shock compressed matter on the CSW stability remains unclear. It is reasonable to expect that this influence becomes increasingly sufficient as the CSW approaches to the centre of convergence. Some factors of the medium imperfection may be considered using van der Waals (vdW) equation of state (see, for instance, [1-3]), but post-shock densities interesting for research go beyond the feasibility of this approximation. More accurate results can be obtained on the basis of Carnahan-Starling (CS) equation of state [4] being valid at much higher compression degree. As well known, thermodynamic non-ideality of the hard-sphere system is characterized by the compressibility factor $Z=pV/RT$, which depends on the packing fraction $\eta=N\pi D^3/(6V)$, where D is a diameter, N is a number of spheres in the volume V. In the case of the CS approximation

$$Z(\eta)=\frac{1+\eta+\eta^2-\eta^3}{(1-\eta)^3}$$

(remind that in the case of the *vdW* approximation $Z(\eta)=1/(1-4\eta)$).

In our study hydrodynamic simulations of the CSW behavior have been performed on the basis of compressible Euler equations on moving grid with the equation of state accounting for hard-sphere repulsion in Carnahan-Starling approximation. Internal degrees of freedom were assumed to be frozen, $c_V=const$. Taking into account that CS fails to reproduce actual hard-sphere physics at $\eta > 0.5$, such values of packing fraction were not used in calculations. The research is aimed to estimate influence of finite matter compressibility on the CSW stability on the basis of simple tractable model.

Numerical method and problem formulation

Accurate simulation of CSW behavior requires the layer concluded between the shock and the limiting characteristic that comes to the reflection point in *R-t* plane to be resolved on the computational grid. For this purpose method of integration of the Euler equations on contracting grid has been applied. Conservation of mass, momentum and energy for moving volume G can be written in the following form

$$\frac{d}{dt}\iiint_G \mathbf{U}d\omega+\iint_{\partial G}(\mathbf{F}_n+\mathbf{U}(\mathbf{v}_g\cdot\mathbf{n}))d\sigma=0$$

where the vector $\mathbf{U}=(\rho,\rho\mathbf{v},\rho(e+\frac{1}{2}\mathbf{v}^2))^T$ represents conservative variables, whereas $\mathbf{F}_n=(\rho v_n,\rho\mathbf{v}v_n+p\mathbf{n},\rho(e+p/\rho+\frac{1}{2}\mathbf{v}^2)v_n)^T$ are the fluxes of the conservative variables in the direction of the outward unit normal $\mathbf{n}$ of the surface element $d\sigma$ is velocity of the element. Semi discrete approximation can be written as follows

$$\frac{d}{dt}(GU)_i=-\sum_j(\mathbf{F}_n+\mathbf{U}(\mathbf{v}_g\cdot\mathbf{n}))_j,$$

$$\frac{d}{dt}G_i=\sum_j(\mathbf{v}_g\cdot\mathbf{n})_j,$$

where the index i denotes the values of grid functions, referred to the cell i, and summation is carried out over the cell faces, $\mathbf{n}_j$ is a normal, absolute value of which is equal to the area of the face j of the considered cell, the grid velocity vector $(\mathbf{v}_g)_j$ is evaluated at the face centers. The modified fluxes at the cell faces of a smooth structured grid were approximated on the basis of the Harten-Yee numerical flux and Glaister's method of linearization [5]. The calculations were carried out on rectangular grids. Grid motion was defined as follows

$$\mathbf{x} = \mathbf{x}_0 \exp\left(-\int_0^t c(\tau) d\tau \right)$$

where $c(t)$ controls the grid velocity $\mathbf{v}_g$ = -$\mathbf{x}$ c(t). The front of the symmetrical convergent shock wave is steady on the moving grid if

$$c(t) = \frac{V_0}{R(t)} \left(\frac{p_1(t) - p_0}{V_0 - V_1(t)} \right)^{1/2}$$

V_0, p_0 are the specific volume and pressure in pre-shock state, V_1, p_1 are the front parameters, R is the current radius. Since in the case under consideration the shape of the shock wave and post-shock front parameters are perturbed, the averaging over N control points is used. The points are located on the shock front in such a way that angle between the points is θ/N, where θ is the angular period of the perturbation.

$$c^{n+1} = (1 - \omega) c^n + \omega c^*,$$

$$c^* = \sum_{k=1}^{N} \sigma_k \frac{V_0}{|\mathbf{x}_k|} \left(\frac{p_{1k} - p_0}{V_0 - V_{1k}} \right)^{1/2}$$

Here, σ_k are the weights. The parameters $V_{1k}, p_{1k}, \mathbf{x}_k$ are evaluated at the control points at time level n. Two-dimensional problem formulation is considered. The CSW is generated by the break up of the discontinuity:

$$(\rho, v, p) = \begin{cases} (\rho_0, 0, p_0), & x \in \Omega \\ (\rho_1, 0, p_1), & otherwise \end{cases}$$

Here, ρ_0, p_0 characterize pre-shock state, $p_1 > p_0$ is a driving pressure, Ω is a perturbed circle in (x, y) plane with the center of symmetry at $\mathbf{x}$ = 0. We used particular forms of perturbations one of which is a small shift of the half-circles on distance δr as shown in the left panel of Figure 1 by solid line, and another can be expressed in polar coordinates (r, φ) in the form $r(\varphi) = r_0 + \delta r \, \mathrm{sgn}(\cos(n\varphi))$. For given types of a perturbation the problem solution depends on four dimensionless parameters: deviation of the shape from cylinder $\delta r / r_0$, dimensionless driving pressure p_1 / p_0, and dimensionless pre-shock density is η_0 provided that $6m/(\pi D^3)$ is the unit, where m is a mass of the sphere. In all calculations the ratio p_1 / p_0 is 160. Influence of η_0 and rotational symmetry of a perturbation was considered on the problem solution. Calculations were performed on rectangular grid with resolution 400 cells per initial radius. Validation included tests on invariance of the solution with respect to orientation of the initial data on the rectangular grid, tests on conservation of solution symmetry in the case of cylindrical shock wave, and comparison with Guderley's solution in the case of ideal gas. Figure 1 demonstrates independence of the solution on orientation of the cutting plane. The solutions correspond to rotation of the initial data to the angle $\pi/4$ before projection on rectangular grid. The lines of constant pressure are shown at grid contraction 10^{-2}. The computed front pressure histories for unperturbed cylindrical shocks are shown in Figure 3 by dot-dash line. All the solutions indicate nearly linear dependence in the log-log plot at $r/r_0 < 10^{-1}$. Linear fit in the range $10^{-3} < r/r_0 < 10^{-1}$ gives the Guderley's exponent value within error 2% for the ideal gas.

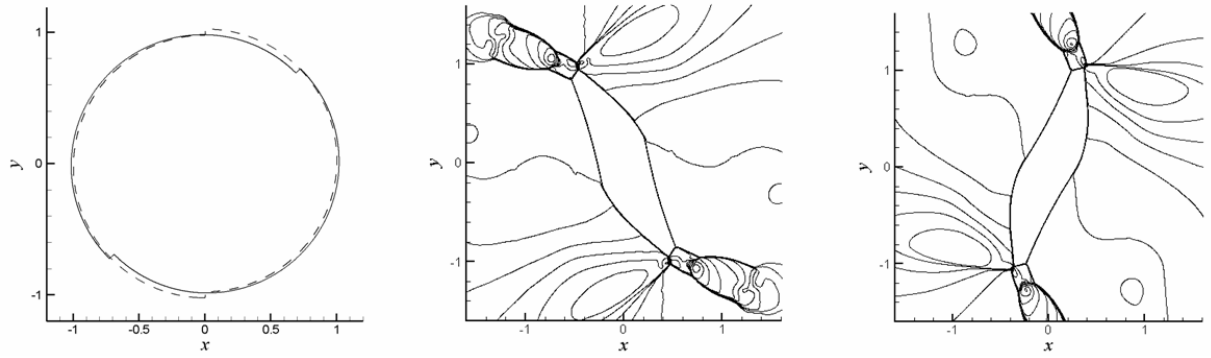

Figure 1. *Invariance of the solution under rotation of the initial data to the angle $\pi/4$ on the rectangular grid. Cylindrical form of the discontinuity is perturbed by small shift (10 grid intervals) of half-cylinders. Lines of constant pressure (the same in the both pictures) are presented at the moment when the size of the shock is 10^{-2} (unit in the middle and right panels is 10^{-2} r_0).*

Results

Consider the influence of the packing fraction on stability of the shape of the cylindrical converging shock wave in the case of the perturbations with angular period $\pi/2$. It is well known that in the case of ideal gas the perturbations with angular period $\pi/2$ increase in time. The instability leads to formation of the shock front shape which is close to polygonal one. In particular, the initial phase of the instability development of this mode was observed in the experiment [6]. Let us consider front pressure behavior during implosion. The amplitude of front pressure fluctuations can be estimated from difference of the front pressures at two front points such, that the angle between these points is equal a half of the perturbation period. If the polygonal shape of the shock is formed, the front pressure is piecewise constant function of the distance from the focus. Discontinuity indicates existence of triple points on the shock wave front. Results obtained with the use of vdW and CS equations of state are presented in Figure 2, where the front pressures are shown against radius for the cases $\eta_0 = 0.03$ and $\eta_0 = 0.1$ ($\delta r / r_0 = 0.025$). It follows from the figure that the discrepancy between these models increases with η_0. This discrepancy is manifested not only in change of the exponent in power law dependence of the average front pressure on the radius, but also in the different development of the instability. The shock wave surface is smooth in the case of vdW equation of state with $\eta_0 = 0.1$.

Calculations of the development of the shock wave perturbations with the period π revealed that the cylindrical converging shock waves are unstable everywhere in the region of applicability of CS equation of state. Front pressure history at a pair of front points is shown in Figure 4 for each calculation. Represented data correspond to the following three values of the pre-shock packing fraction ($\eta_0 = 0; 1/10; 1/3$). The post-shock packing fraction approaches the strong shock limit. The values 0.217 and 0.444 were detected for $\eta_0 = 1/10$ and $\eta_0 = 1/3$, when the front pressure growth was completed. The front pressure histories for the unperturbed cylindrical shock waves are shown by the dash-dot line. One can conclude from the figure that the front pressure follows the solution for the symmetric case in average until some critical value of pressure and radius is reached.

If the pre-shock packing fraction corresponds to the upper part of the domain of applicability of the CS equation of state, the shape of a cylindrical converging shock wave become stable against perturbations with the period $\pi/2$. Moreover, the stability is observed even in the case of strong initial asymmetry.

Figure 3 (left panel) shows the result for strong initial perturbation, when the initial discontinuity is square in shape. In this case the shock wave has polygonal shape at the moment of the discontinuity break up. It follows from the figure that the triple points disappear from the shock surface, and the growth rate of the average front pressure is higher than the growth rate of the front pressure perturbations. Polygonal shaped due to strong initial perturbation shock wave becomes cylindrical near the focus.

This critical point depends on the packing fraction in the pre-shock state and coincides in time with formation of the quadruple points on the shock wave surface. Quadruple points are the stationary points on the shock wave surface where four shocks meet each other; two of them represent segments of the converging shock wave while the other two correspond to the outgoing shocks. In the particular case of symmetry this kind of shock interaction can be considered as a pair of regular shock reflections. Condition when this configuration is formed from two triple points depends on criterion of transition from regular to Mach reflection. This type of shock interaction provides a mechanism of decreasing of the shock surface area without increasing of the average front pressure. Detailed pictures of the front shape shown at different scale are shown in Figure 4, where the phenomenon is illustrated. The upper sequence of the pictures corresponds to the ideal gas; the lower one represents the case $\eta_0 = 1/10$. The last panel in each sequence shows the shock front with the quadruple points formed.

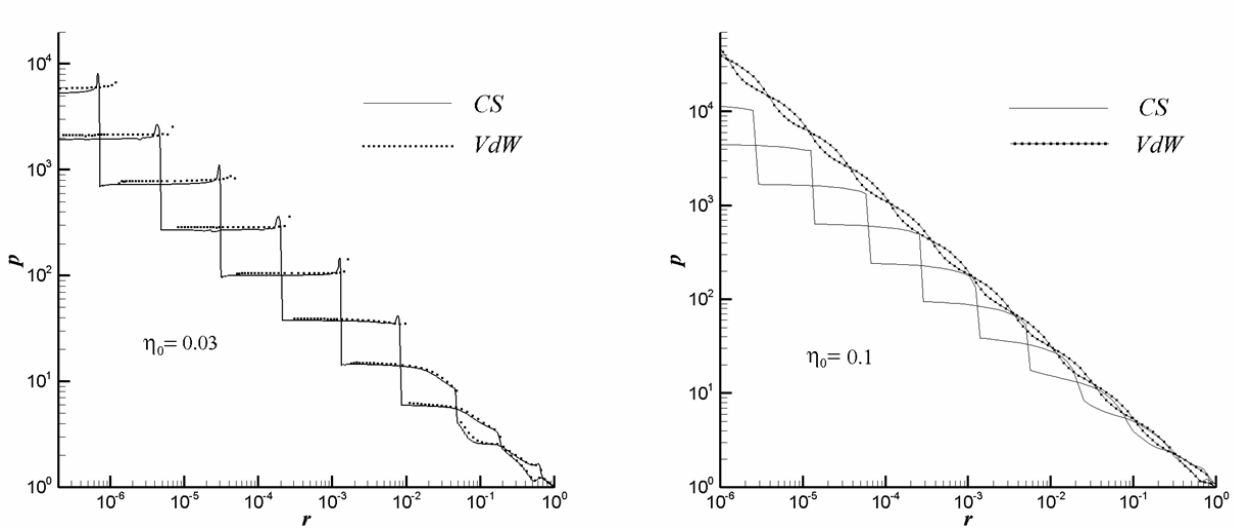

Figure 2. *Comparison of the front pressure history for van der Waals (VdW) and Carnahan-Starling (CS) equations of state*

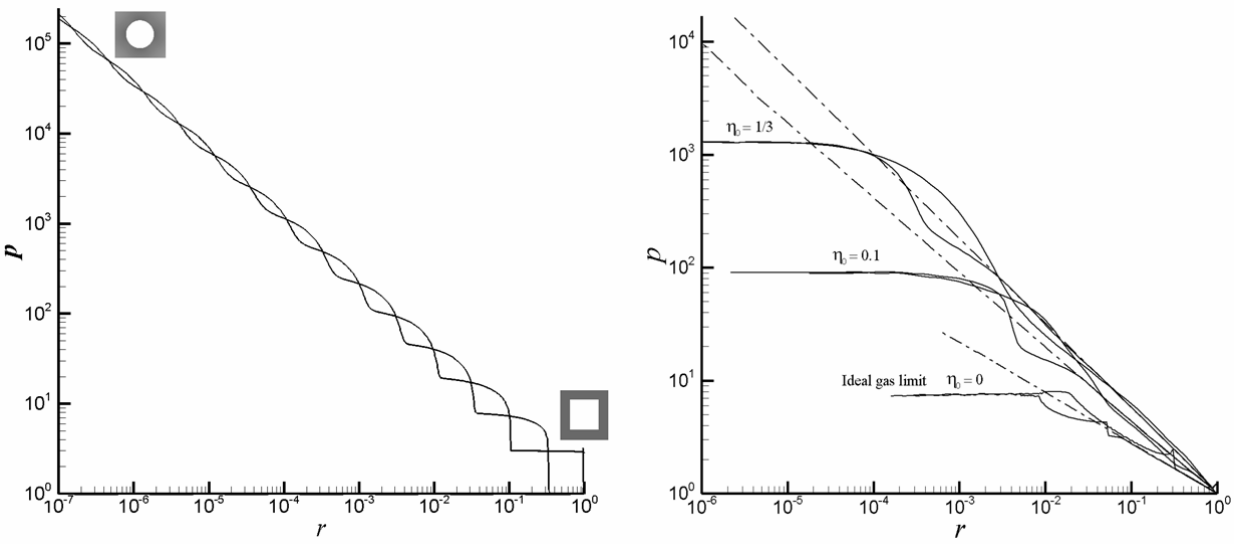

Figure 3. *Left: case of stability of the cylindrical shape of CSW under strong initial perturbations of symmetry with the smallest angular period* $\pi/2$ *(*$\eta_0 = 1/3$*); Right: Influence of the pre-shock packing fraction on the instability of CSW to small initial perturbations with period* π *.*

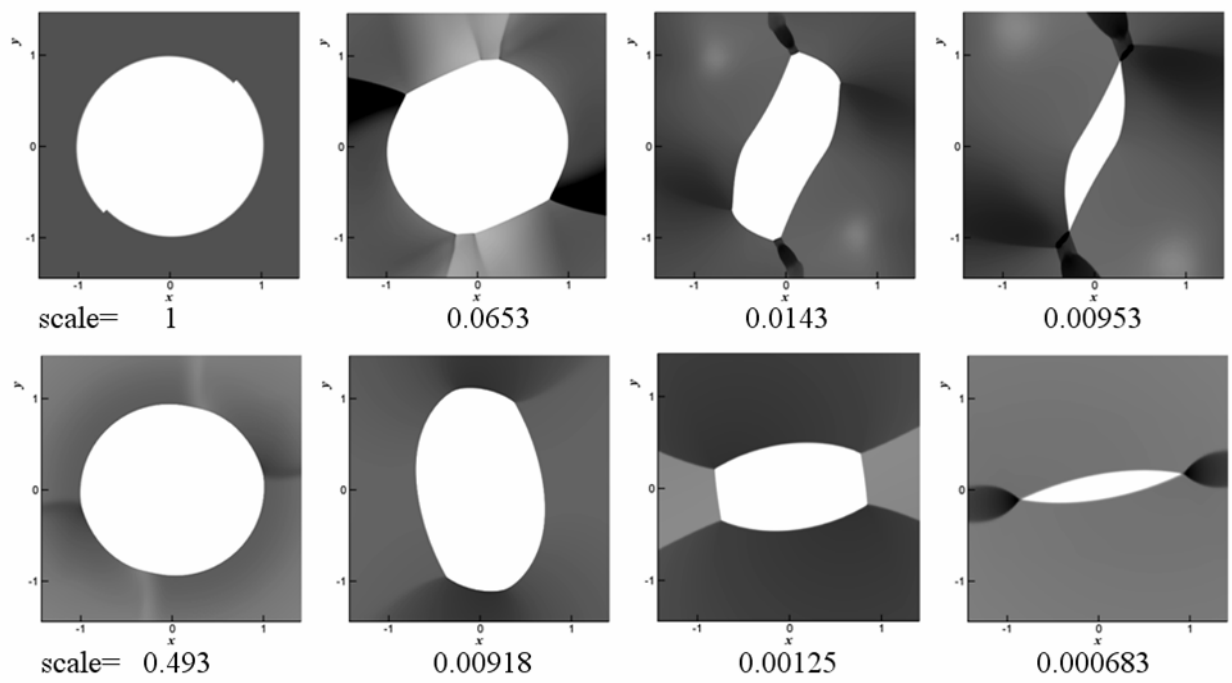

Figure 4. *The shape of the perturbed converging shock wave at different scales is shown. Upper: ideal gas; Lower: hard sphere fluid* $\eta_0 = 1/10$ *. The last figure in each sequence corresponds to appearance of quadruple points on the front; the front pressure does not grow after this moment.*

Conclusion

Numerical study of the cylindrical CSW stability has shown that at the description of thermodynamic non-ideality in the framework of the CS approximation the increasing of the packing fraction has the stabilizing effect on CSW.

References

1. Evance A. K. (1996) Instability of converging shock waves and sonoluminescence. Phys. Rev. E. Vol. 54:5004--5011.
2. Wu C.C., Roberts P.H. (1996) Structure and stability of a spherical shock wave in a van der Waals gas. Q. Jl Mech. Appl. Math. 1996. Vol. 49, No. 4:501--543.
3. Somogyi Z., Roberts P.H. (2007) Stability of an imploding spherical shock wave in a van der Waals gas II. Q. Jl Mech. Appl. Math. 2007. Vol. 60, No. 3:289--309.
4. Carnahan N.F., Starling K.E. (1969) Equations of state for non-attracting rigid spheres. J. Chem. Phys. Vol.51, No 2: 635-–636
5. Glaister P. (1988) An Approximate Linearized Riemann Solver for the Euler Equations for Real Gases. J. Comp. Phys. Vol.74: 382--408.
6. Watanabe M., Takayama K. (1991) Stability of converging cylindrical shock waves. Shock waves. (91) 1: 149--160.

P4. HYPERSONIC MHD FLOW OVER ROTATION BODY AT FINITE MAGNETIC REYNOLDS NUMBERS

E.V. Gubanov, A.P. Likhachev, S.A. Medin
Joint Institute for High Temperatures, Russian Academy of Sciences

A number of two-dimensional problems of stationary hypersonic MHD flow over rotation body with magnetic dipole are solved numerically. The flight altitude and velocity are selected in the interval of re-entry parameters where the magnetic Reynolds number Re_m calculated for the shock layer width in front of the body is of the order of unity. The main feature of the solutions obtained is taking into account the induced magnetic field.

Problem formulation and numerical technique

Stationary hypersonic MHD flow over rotation body with magnetic dipole are considered in three two-dimensional formulations. First two problems are concerned with the transverse flow past the cylinder of revolution at normal (problem 1) and parallel (problem 2) orientation of the dipole magnetic moment and incoming flow velocity vectors. The third problem relates to the case of the flow over the sphere with parallel orientation of these vectors. Every of the problems has been solved in two variants: in variant A pressure and density of the incoming flow correspond to the parameters of atmosphere at an altitude of 65 km, the velocity is 7 km/s; in variant B these values are 80 km and 11 km/s respectively. The flow over cylinder has been simulated in cylindrical frame of reference (axis z coincides with the cylinder axis), the flow over sphere has been modelled in spherical coordinates.

The body diameter in all solutions is equal to 4 m. The dipole magnetic field is generated by electrical current flowing in two infinite parallel wires (cylinder, problems 1 and 2) or ring coil (sphere, problem 3) disposed symmetrically inside a body. The distance between wires as well as the coil diameter are equal to 2 m. The electric current has been assigned to be equal to $2\cdot10^7$ A. The Biot-Savart law has been used to calculate the dipole magnetic field. The geometry of calculation region and the dipole magnetic field distributions are shown in Fig. 1.

The medium flowing over the body is described in the approximation of the perfect non-radiative gas. The values of the specific heat ratio γ and gas constant R were chosen to provide a minimum error in definition of the air plasma parameters behind the bow shock. In version A γ =1.13, R=458 J/(kg·K), the incoming flow parameters are the following: longitudinal and transverse components of velocity $u_1=7\cdot10^3$ m/s, $v_1=0$, pressure $p_1=10$ Pa, density $\rho_1=1.765\cdot10^{-4}$ kg/m^3 (for convenience of performance the velocity components are given in Cartesian coordinates). In version B γ =1.118, R=657 J/(kg·K), $u_1=11\cdot10^3$ m/s, $v_1=0$, $p_1=1$ Pa, $\rho_1=1.765\cdot10^{-5}$ kg/m^3.

The low-frequency approach is used to describe the electrodynamic phenomena. The Hall effect and the external (Earth) magnetic field are neglected. The total magnetic field B is determined

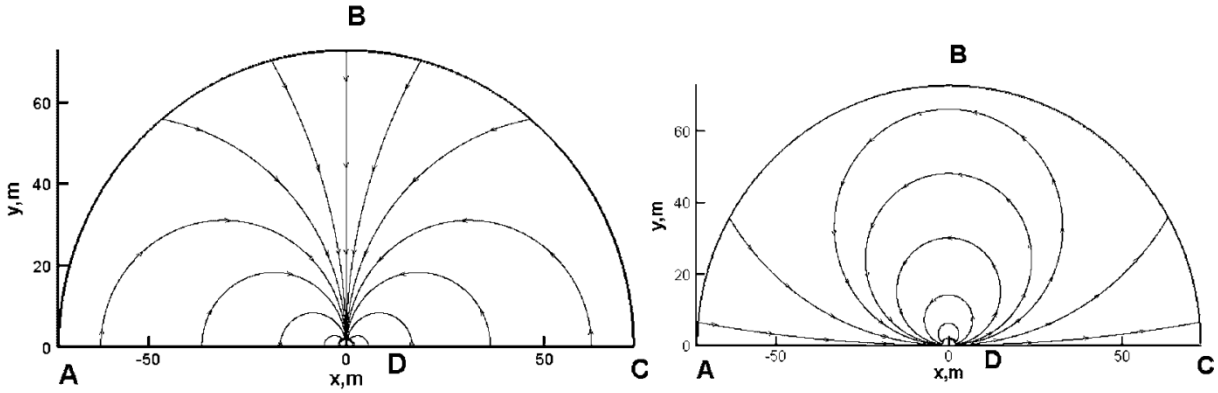

a) b)

Figure 1. *The geometry of calculation region and the dipole magnetic field distribution: a – problem 1, b - problem 2 and 3*

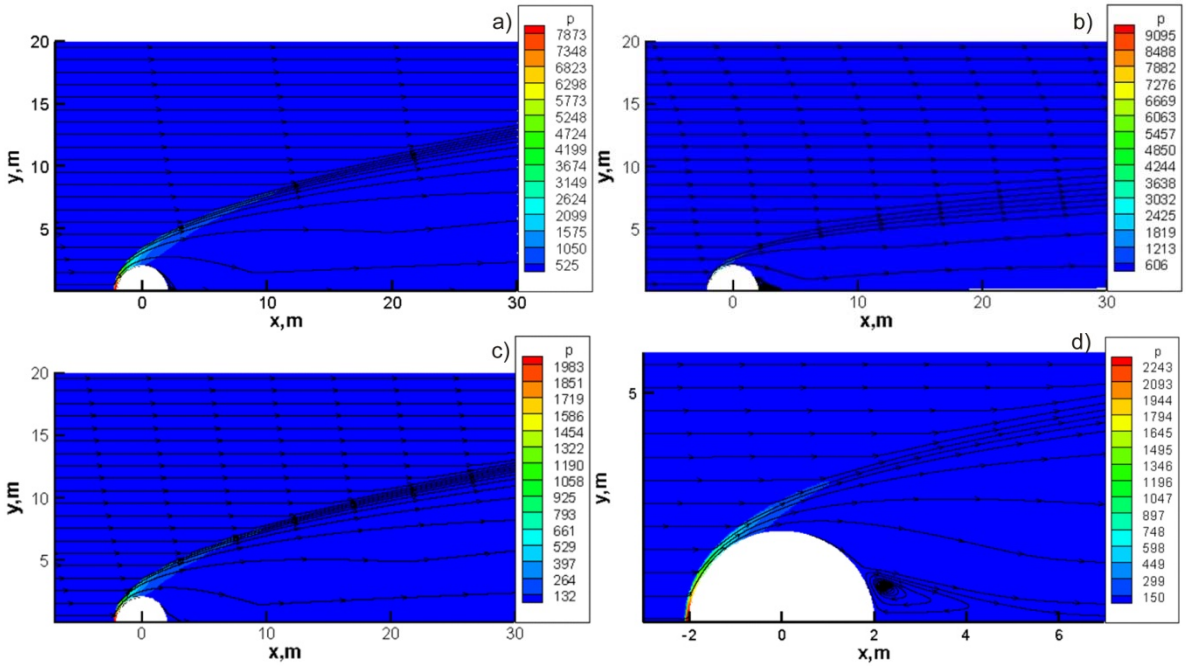

Figure 2. *The initial gasdynamic conditions: a – problems 1 and 2, variant A; b – problems 1 and 2, variant B; c – problem 3,variant A; d – problem 3, variant B*

as superposition of the dipole magnetic field B_d and the induced magnetic field B_i, i.e. $B=B_d+B_i$. The electrical conductivity of the shock-compressed plasma was described by the approximate expression

$$\sigma = 1/(\sigma_1^{-1} + \sigma_2^{-1}) \ ,$$

where

$$\sigma_1 = 8.09 \cdot 10^{16} T^{3/4} \exp(-14 \cdot 11600/T) p^{-1/2}$$
$$\sigma_2 = 7.07 \cdot 10^{-4} T^{3/2} \ .$$

The numerical solution of the problem was obtained using the stabilization method with splitting of the system of equations into electrodynamic and gasdynamic subsystems. The solution of the gasdynamic subsystem was based on the Harten's method of second order approximation. To solve the magnetic induction equation we used a specially designed and tested numerical scheme with a non-uniform approximation pattern of the convective term which depended on the local properties of the solution. The problems have been solved on multiprocessor computer systems using MPI parallel programming technology.

Initial and boundary conditions

The stationary gasdynamic solution in the absence of the MHD interaction with the incoming flow parameters mentioned above has been used as initial gasdynamic conditions. The boundary conditions were the following (see Fig. 1): AB – "supersonic" conditions, BC - "soft" conditions, AC – symmetry conditions. The "no-flow" condition has been assigned on the external body boundary. The solutions used as initial gasdynamic conditions are shown in Fig. 2.

The zero induced magnetic field $B_i=0$ has been assigned as initial electrodynamic conditions. The "soft" boundary conditions have been used on boundaries AB and BC, the symmetry conditions have been assigned on boundary AC. The body electric conductivity has been set to zero, so that the numerical cells inside body have been excluded from calculations. The zero electric field has been assigned on the body external boundary.

Results of calculations

Problem 1, variant A

Dimensionless parameters: Mach number M_1 = 27.7, magnetic Reynolds number Re_m = 0.5, magnetic pressure number R_H =15

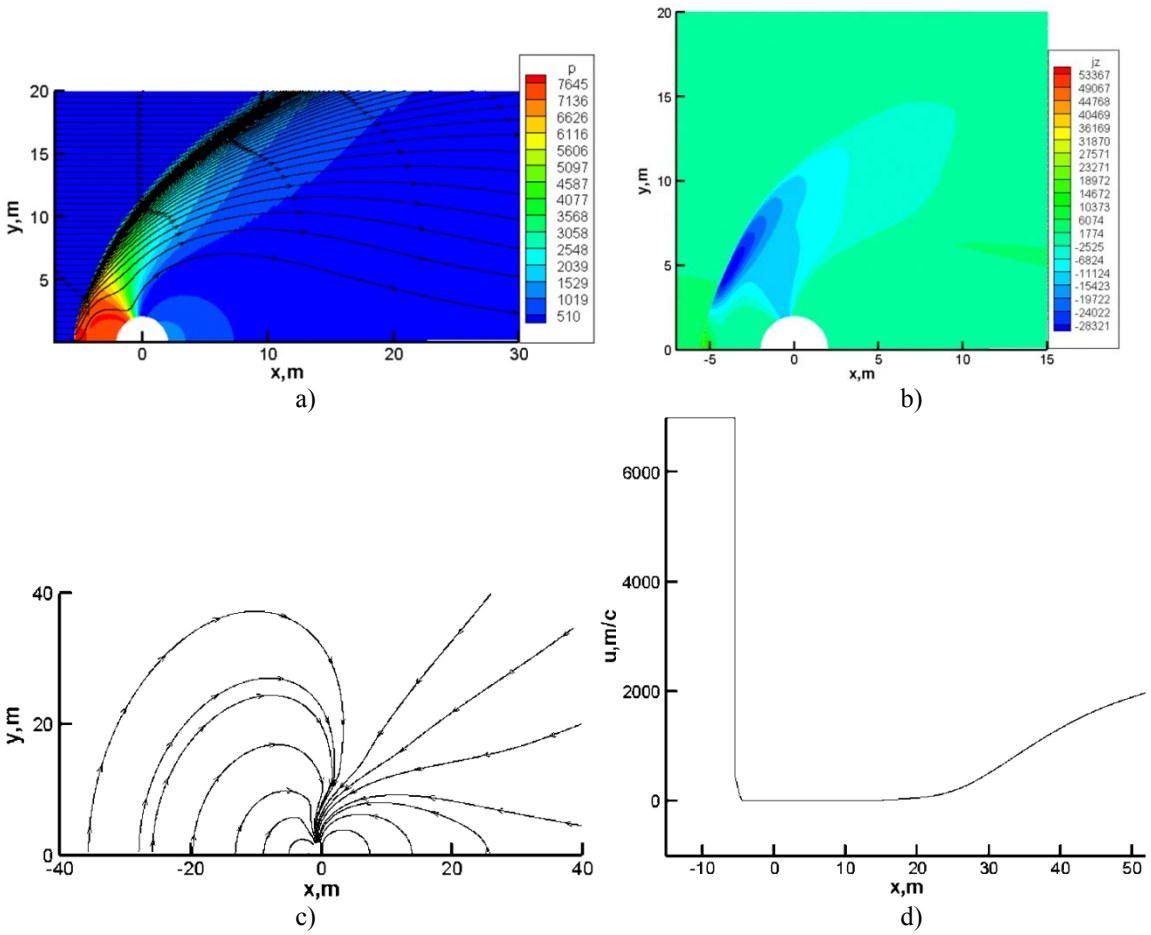

Figure 3. *The MHD flow over body (problem 1, variant A): a – pressure distribution in combination with gasdynamic streamlines; b – z-component of electric current density; c – magnetic field vector lines; d – distribution of r-component of velocity vector along symmetry axis*

Problem 2, variant A

Dimensionless parameters: Mach number M_1 = 27.7, magnetic Reynolds number Re_m = 0.5, magnetic pressure number R_H =15

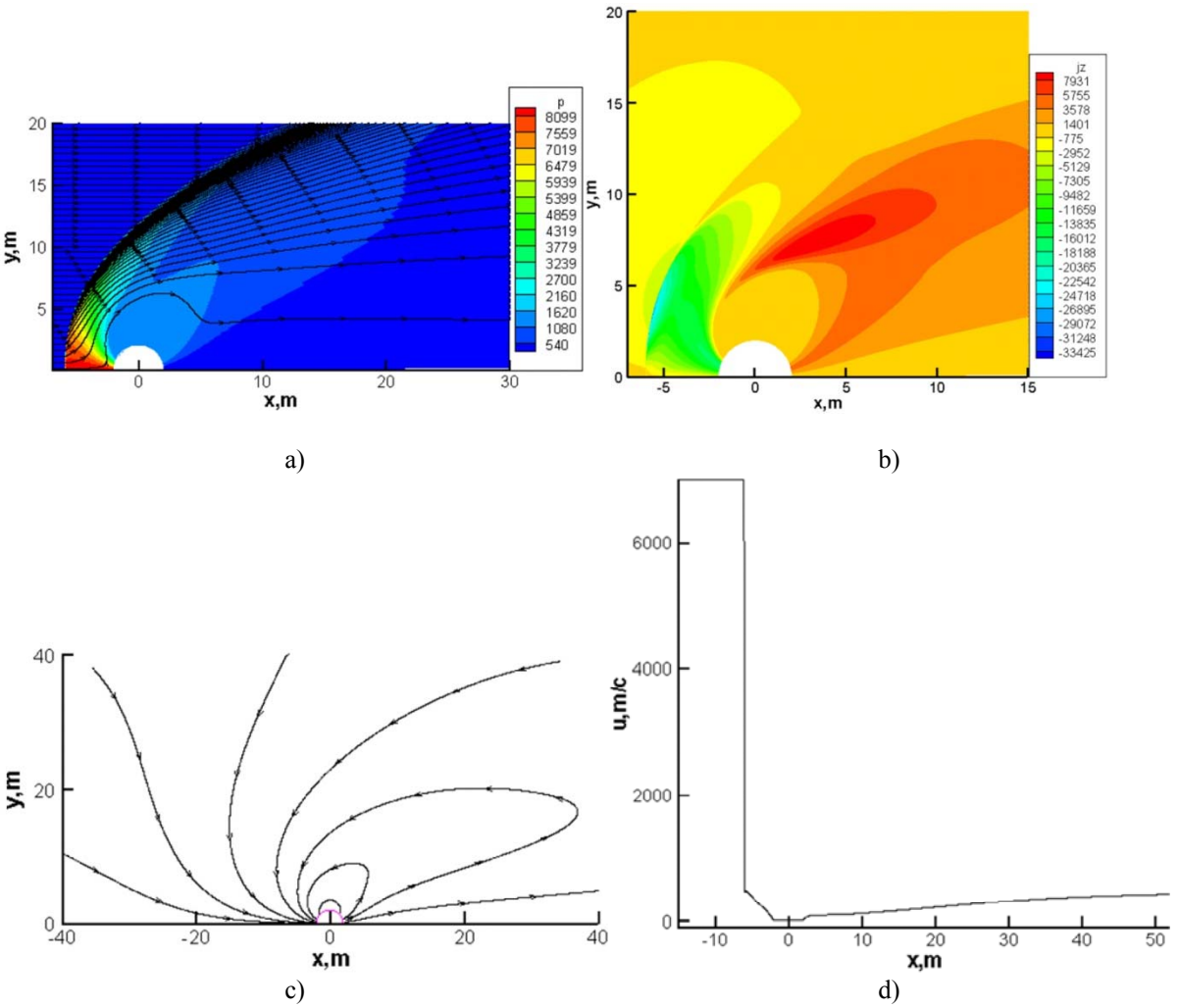

Figure 5. *The MHD flow over body (problem 2, variant A): a – pressure distribution in combination with gasdynamic streamlines; b – z-component of electric current density; c – magnetic field vector lines; d – distribution of r-component of velocity vector along symmetry axis*

Problem 2, variant B

Dimensionless parameters: Mach number M_1 = 43.6, magnetic Reynolds number Re_m = 3.2, magnetic pressure number R_H =70

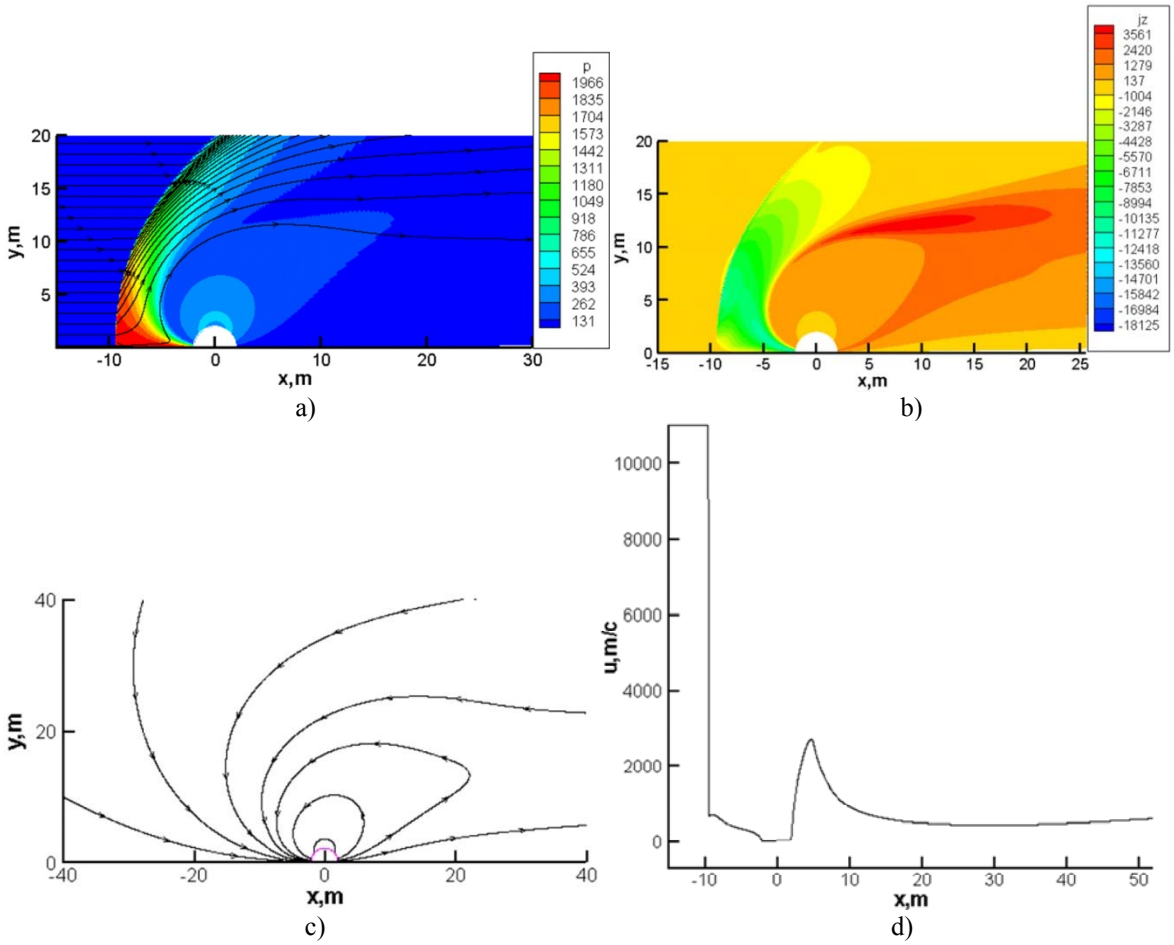

Figure 6. *The MHD flow over body (problem 2, variant B): a – pressure distribution in combination with gasdynamic streamlines; b – z-component of electric current density; c – magnetic field vector lines; d – distribution of r-component of velocity vector along symmetry axis*

Problem 3, variant A

Dimensionless parameters: Mach number M_1 = 27.7, magnetic Reynolds number Re_m = 0.25, magnetic pressure number R_H =15

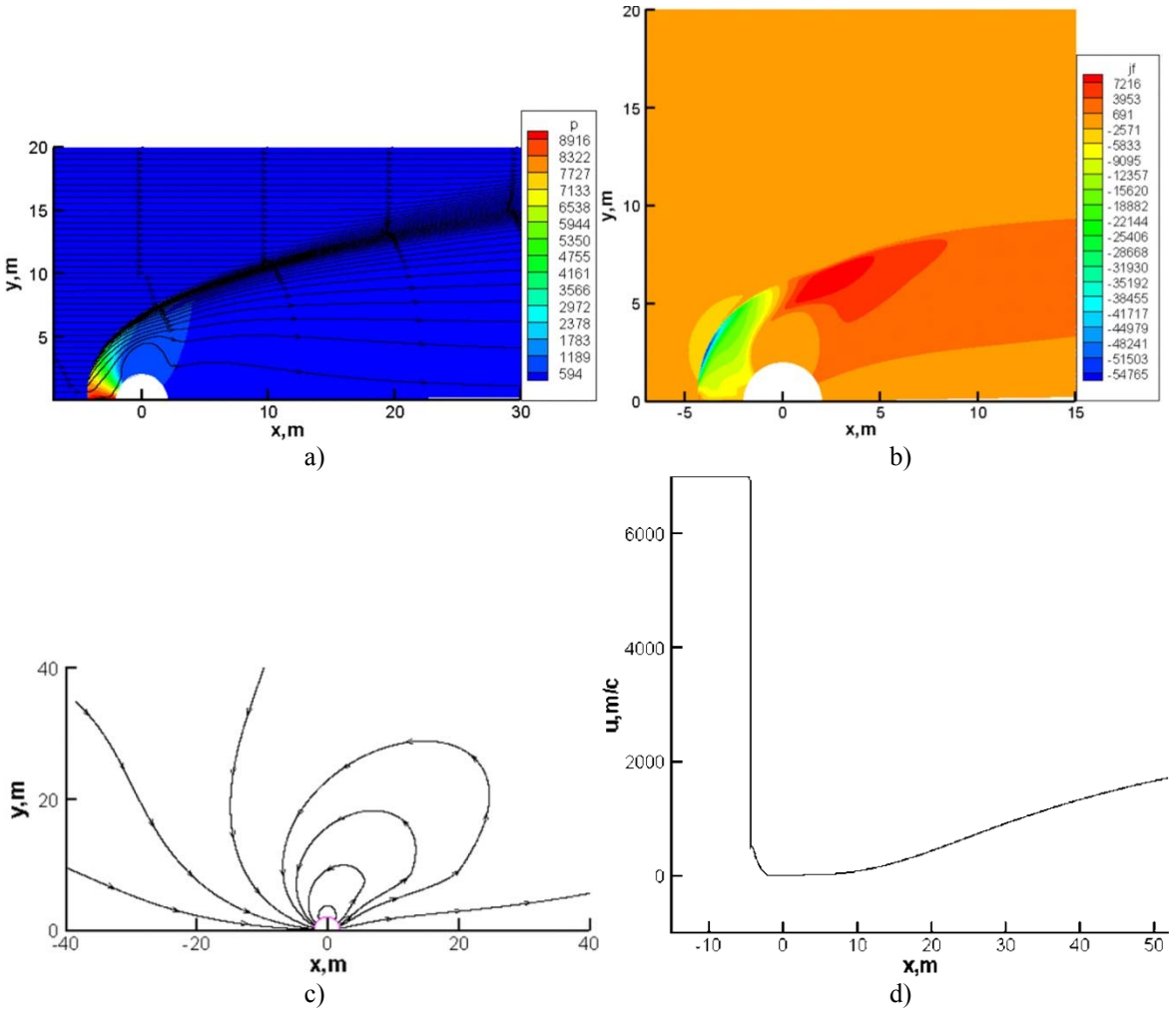

Figure 7. *The MHD flow over body (problem 3, variant A): a – pressure distribution in combination with gasdynamic streamlines; b – z-component of electric current density; c – magnetic field vector lines; d – distribution of r-component of velocity vector along symmetry axis*

Problem 3, variant B

Dimensionless parameters: Mach number M_1 = 43.6, magnetic Reynolds number Re_m = 1.5, magnetic pressure number R_H =70

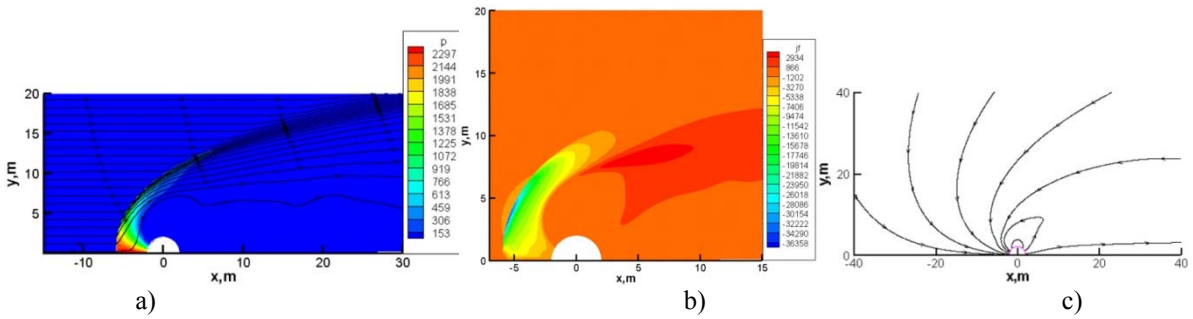

Figure 8. *The MHD flow over body (problem 3, variant B): a – pressure distribution in combination with gasdynamic streamlines; b – z-component of electric current density; c – magnetic field vector lines*

Features of solution obtained

The solutions obtained have a number of common features: due to the MHD interaction the bow shock turns off from the body; the flow is pushed out from the body surface (in variant A of the problem 2 pushing out tends to be global); effects of finite magnetic Reynolds number are observed – magnetic lines of force are drifted and stretched downstream with sufficient changing of magnetic field structure; two oppositely directed current vortices are generated in plasma flow over the body etc. The differences between solutions are caused by the orientation of the dipole magnetic moment vector relatively the velocity vector, values of the incoming flow parameters and the body shape.

The summary drag force and its gasdynamic and electrodynamic components (for running meter in the case of cylinder) have been calculated from data obtained and tabulated (see below).

It is seen from table that MHD interaction leads to growth of the drag force from 6 till 25 (problem 3, variant B) times.

P 5. OBSERVATION OF THE STRUCTURE OF CHARGED MACROSCOPIC PARTICLES ON THE METAL SURFACE (ANALOG DUSTY PLASMA)

D.S. Baranov* and O.D Baranova
* Joint Institute for High Temperatures of Russian Academy of Sciences, Moscow, Russia
baranovd@rambler.ru

Abstract. Experimentally observed spontaneous emission of macroscopic particles (~ 1 micron) from specially prepared samples, which contained about 20 mg of bismuth salts (nitrate or sulfate).
Preferential direction of emission was in the horizontal plane. On the polished gold surface located at 3 mm from the sample form a structure of deposited particles, the observed field rounded-free particles (the so-called void). The results are compared with those of standard experiments on dusty plasmas.

The experiment revealed that the sample prepared from bismuth salts capable of emitting jets of macroscopic particles. For sample preparation we used a saturated solution of bismuth nitrate (or sulfate), which is exposed to an electric field ~ 10^6 V / cm. After 15 minutes of exposure solution was

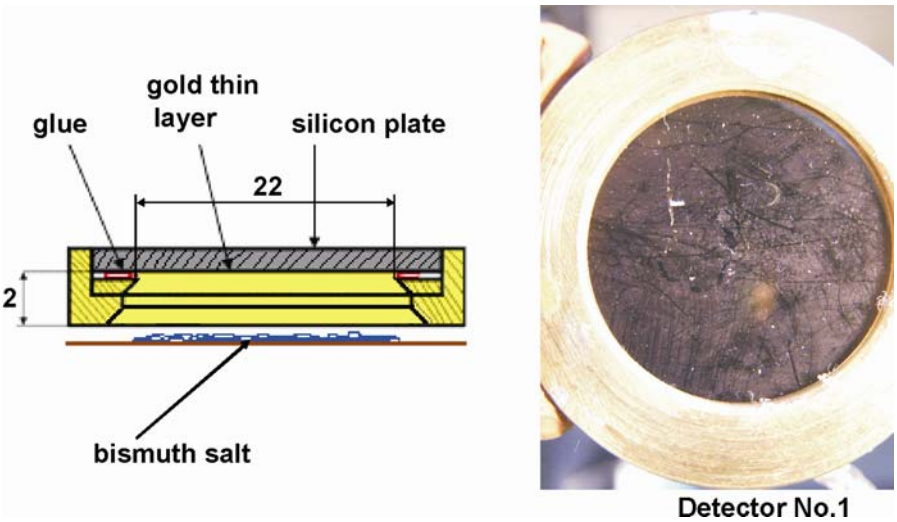

Fig. 1. *The silicon detector of alpha particles*

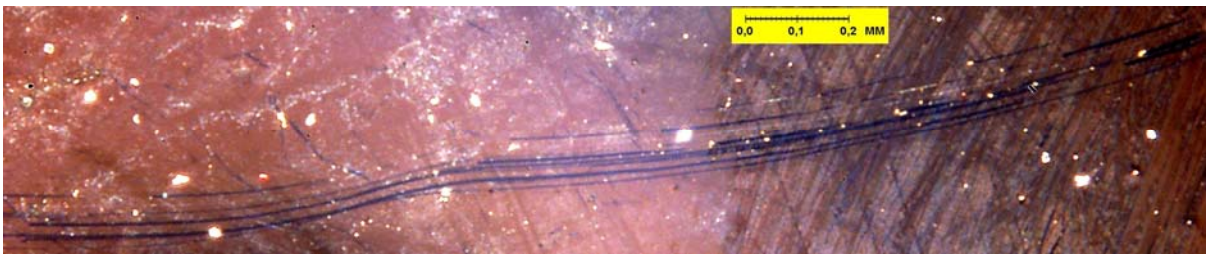

Fig. 2. *Cumulative emissions of the jet macro-particles on the surface of the detector number 1. He was missing the first two weeks after the experiment was found after 19 months.*

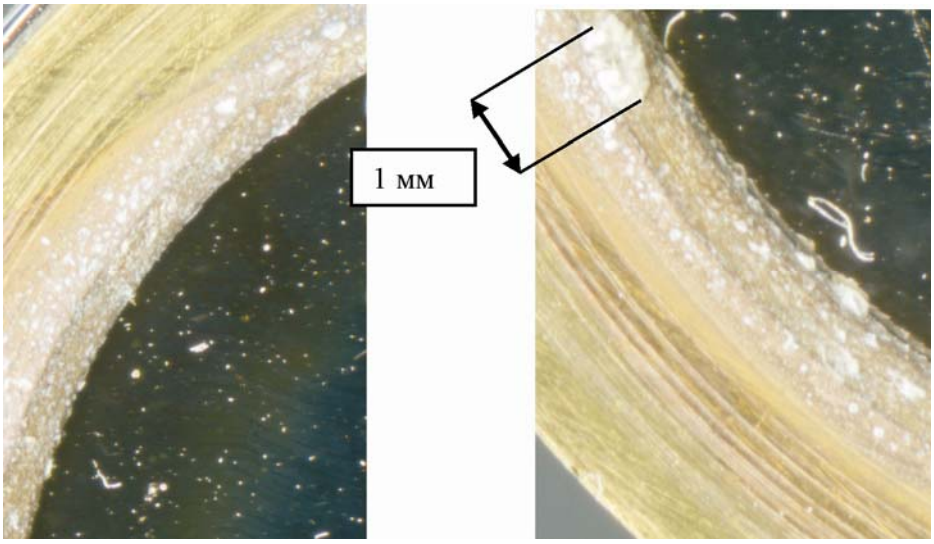

Fig.3. *Internal skirting and a fragment of a gold surface (dark area) of the detector number 2. Snapshot obtained by a scanner.*

dried on the substrate for 15 minutes and placed in a detection system to measure alpha and beta activity/1/. The sample covered the top surface of the silicon detector of alpha particles with a diameter of 22 mm. Gold surface separated from the sample at a distance of 3 mm. With space limited to the ends of brass washer with a diameter of 22 mm (Fig. 1).

We emphasize that lies under the gold surface of the sample with salt is not exposed to any special field and radiation.

From a sample simulated jets of macroscopic particles. The jets of macroscopic particles can appear from a particle that had previously settled on the detector. This can occur with considerable delay in time (Fig. 2).

The typical particle size of ~ 1 micron, but there were other dimensions from 10 nm to 100 microns.

The density of the bombing of cumulative jets surface and a side strongly divergent, then the angle of emission of cumulative jets from the sample, usually no more than 0.1 radians to the horizontal plane (Fig. 3).

In some cases the particles bounced off the gold surface (top) and back again to it (Fig. 4).

Scattered over the surface of the particles within a maximum relative to each other (Fig. 5).

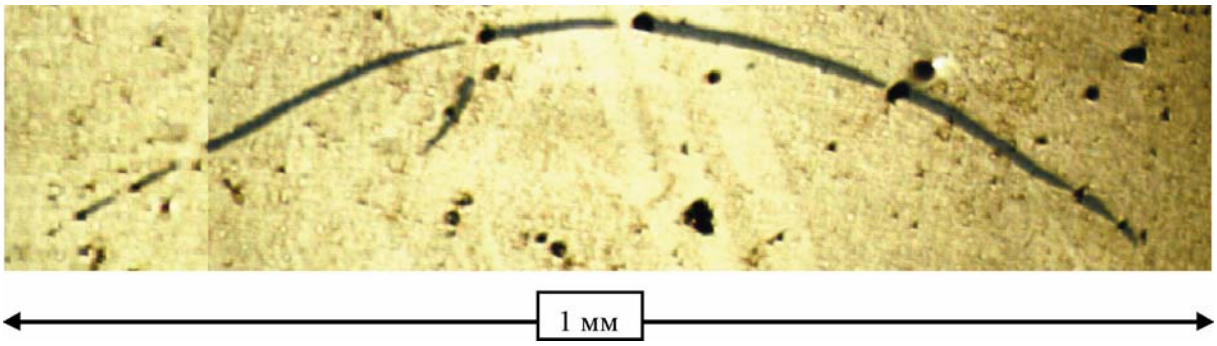

Fig. 4.*Charged particle spins and jumps on the golden ceiling*

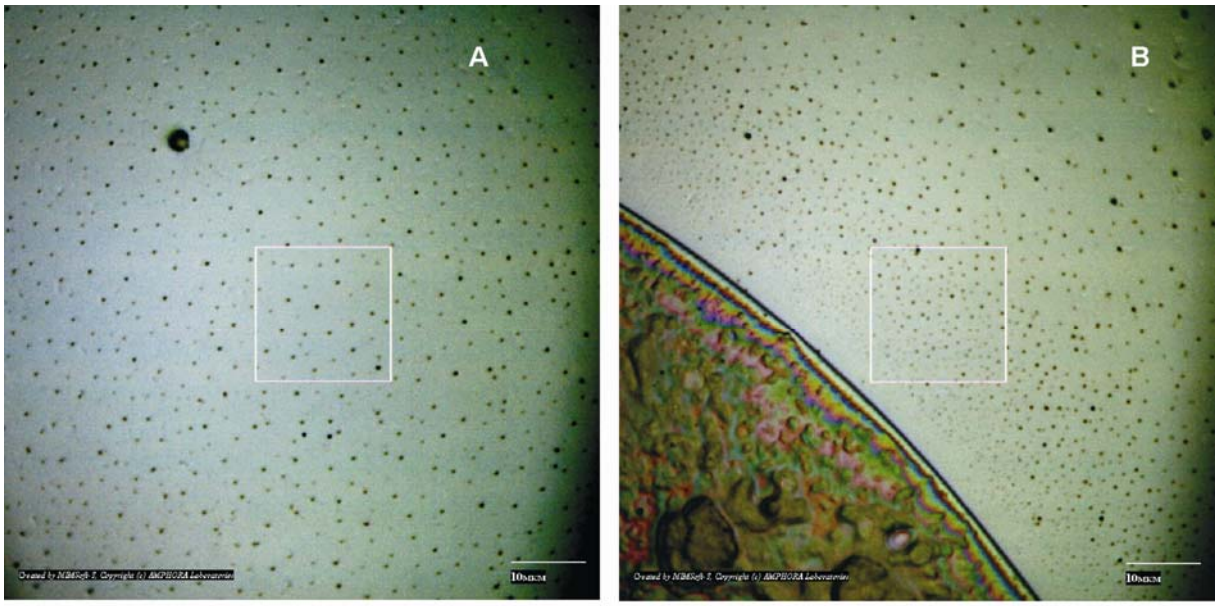

Fig. 5. *Charged particles are distributed along the golden ceiling*

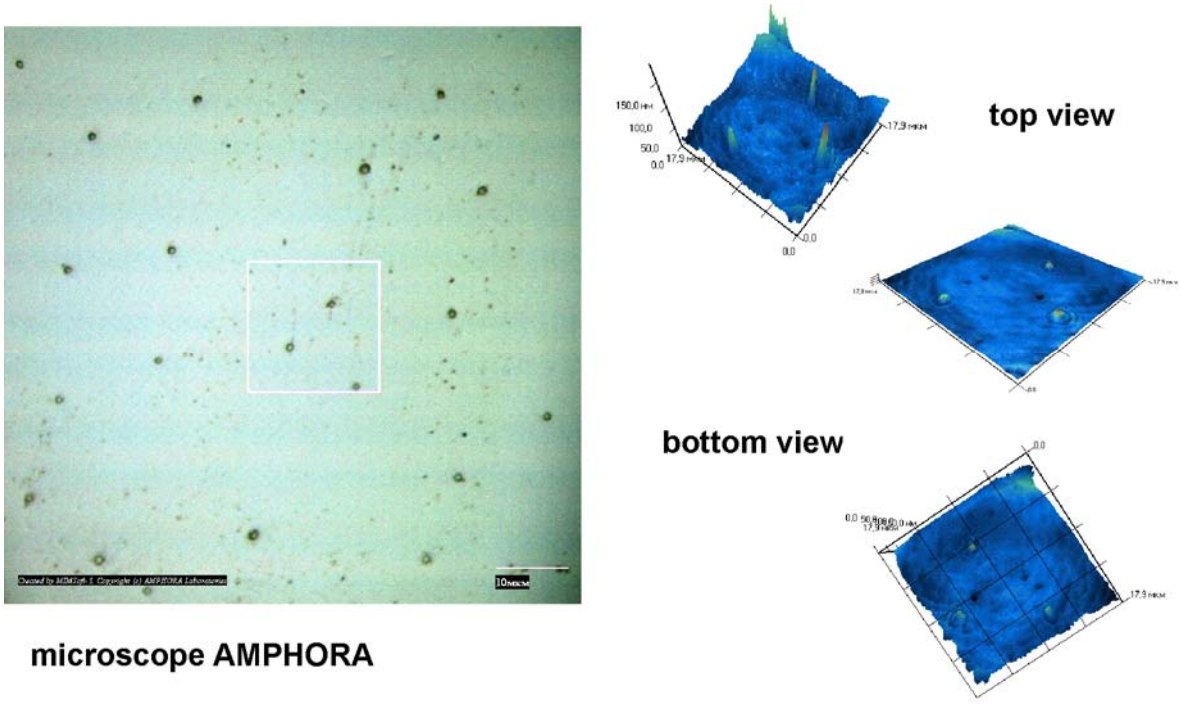

Fig. 6. *Balls and pits on the gold surface*

Based on this we can conclude that the particles are charged. Separate measurements showed that the charge is negative.

On bulk photos with higher resolution shows that the balls are hidden in wells at depths greater than its radius. There are also blank wells. The appearance of holes is obviously connected with the rotation of balls. (Fig. 6).

Observed alignment of the particles in sequential structure (Fig. 7), which can be attributed to the existence of macroscopic particles of a significant magnetic moment. Some particles are attracted to permanent magnet

It turned out that there are areas on the gold surface where the scattered particles do not penetrate. These areas are usually surrounded by an

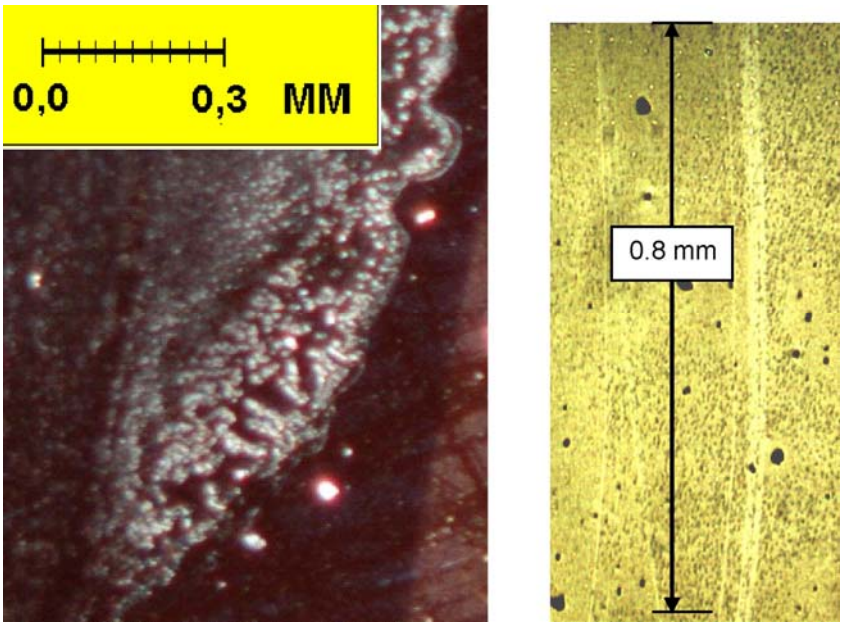

Fig. 7. *Sequential structure.*

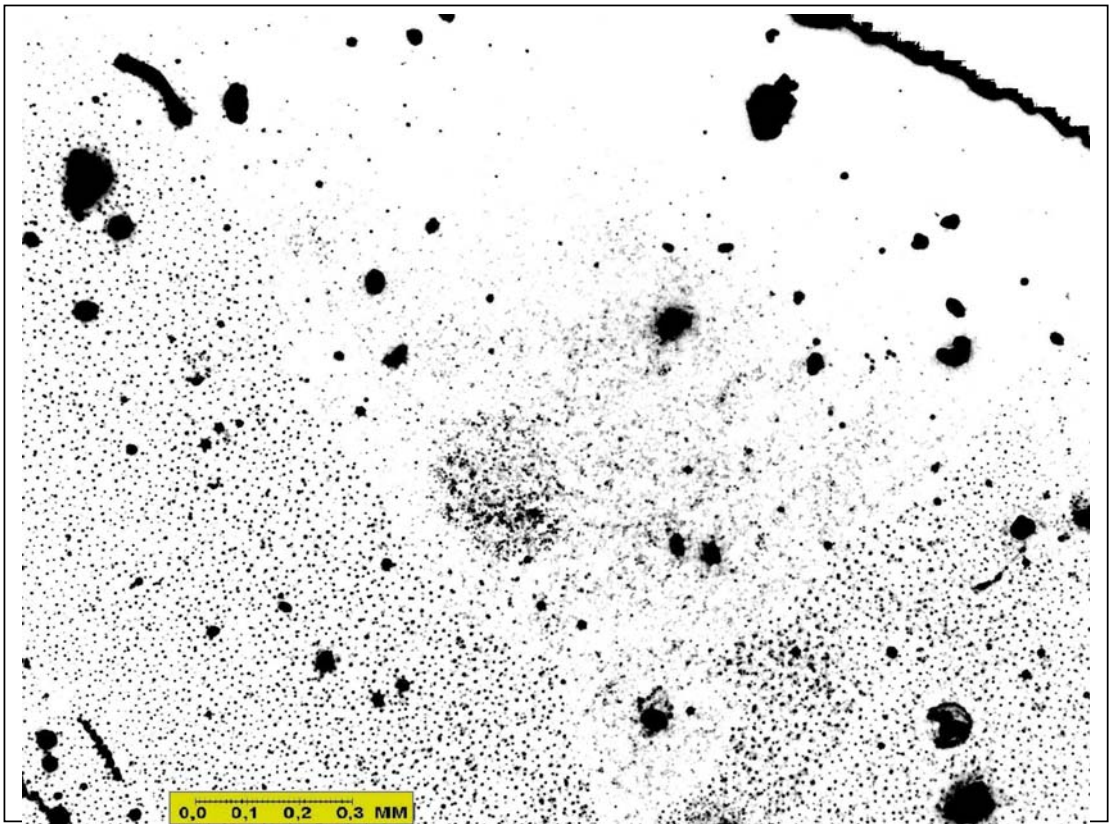

Fig. 8. *Void on the edge of a gold surface*

observable macroscopic particles or the formation of a crater (Fig. 5 b) But there is a region free of observable objects (the so-called void (Fig. 8, 9)).

Painting aligned macroscopic charged particles and free them from areas like the picture formed by dust particles in plasma (Fig. 10).

Terms and conditions of this experiment are radically different from experiments with dusty plasmas/2/. But we can assume that the particle charge and void can be explained everywhere within a unified theoretical approach /3-6/.

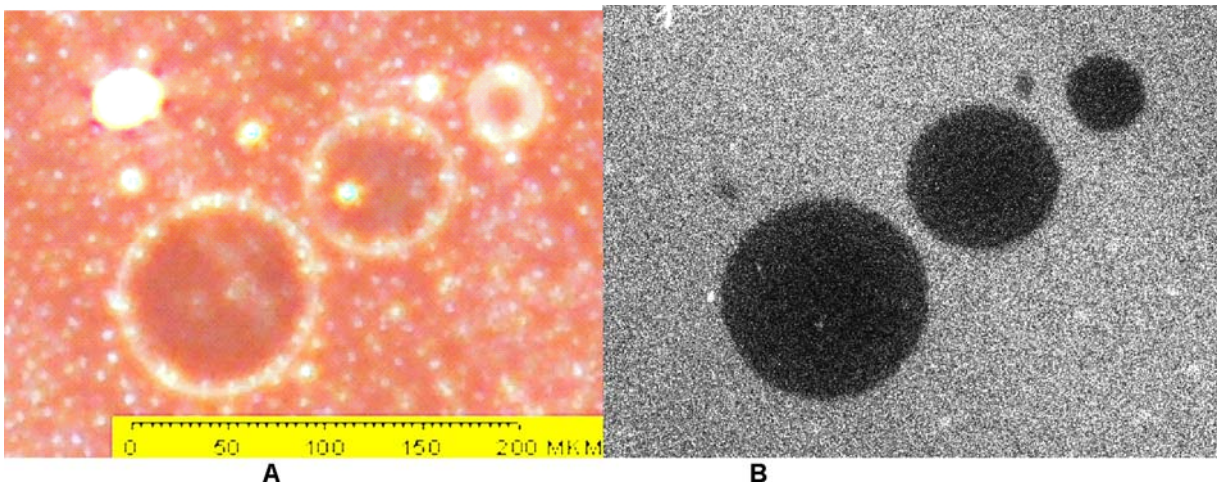

Fig. 9. *Voids on the golden ceiling. A- camera. B-electron microscope*

.

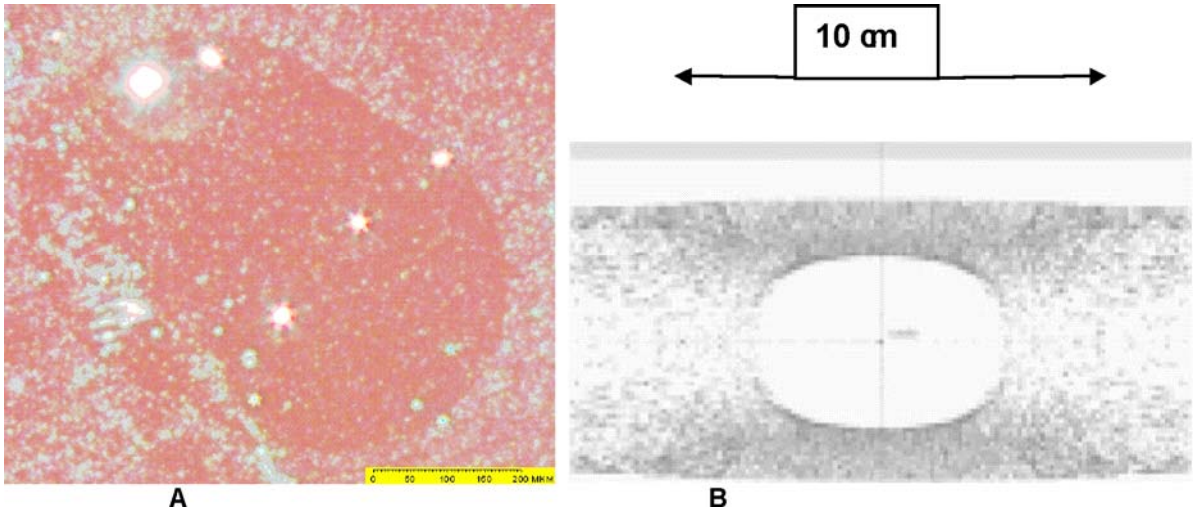

Fig. 10. *Voids. A- on the golden ceiling (camera). B- dusty plasmas /2/.*

References

1. D.S. Baranov. and O.D. Baranova AIP Conf. Proc. v. 1224. p. 241
2. V.E Fortov, A.G. Khrapak, S.A. Khrapak,V.I. Molotkov, O.F. Petrov UFN v.174 №5, p. 496 (2004)
3. A.O. Barut and J. Kraus, J. Math. Phys. 17(1976) 506.
4. J.P. Vigier. Phys. Lett. A 221, (1996), 138-140.
5. Dragic´, Z. Maric´, J.P. Vigier. Physics Letters A 265 _2000. 163–167
6. A.V. Mitin (private communication)

P7. ON THE THREE INTERPRETATIONS FOR THE THEORETICAL EXISTENCE OF THE SHOCK WAVE DISCONTINUITY IN THE EULERIAN SUBSTANCE

overview

©Valentine A. Belokogne, Moscow, Russia, 2010
(Oceanology Institute (RAS), RANS, Academia Cosmonautica)

The finite, and smooth initially, Poisson (1808) compression wave in homothermic gas tends to overturn like Tsunami. Scientific apostles of C XIX resolved this paradoxical "difficulty" phenomenological – by setting the plausible discontinuity:

Stokes (1848): *isothermic* shock (analogue of the sound)

$$\Delta Q < T\cdot\Delta S < 0$$

Riemann (1860): *isentropic* shock (the same analogue)

$$\Delta Q < \int_{-}^{+} T\, dS = 0$$

The prominent folio by Courant–Friedrichs (§51) contains bluff: the Riemann idea on «reversible and adiabatic» shock.

Clausius (1865): Entropy formalism of thermodynamics:

$$\Delta Q \le \int_{-}^{+} T\, dS$$

Rankine (1870), Hugoniot (1887): adiabatic shock (not only analogue)

$$\Delta Q = 0 < \int_{-}^{+} T\, dS$$

Dirac (1928), Author (1958):

$$(\Delta S)\delta(t)\, dt \equiv dS \ge (1/T)\, dQ$$

Now let mention some general: the arbitrary permanent (steady state) 1D nonlinear wave front implies that

$\Delta E \equiv \Delta Q+\Delta W = \Delta Q-(1/2)(p_{in}+p_{fin})\Delta V$, where $p=p_{xx}$ at the almost arbitrary *EOS*.

The ((tutorial interesting): for the ***EOS*** $E = (f/2)PV) \equiv PV/(\gamma -1)$, where **f** = number of freedom degree for molecules in the equipartition case, the **Rankine- Hugoniot *adiabat*** implies triple equality between compression, shock Mach Number, and molecular degrees of freedom:

$$\rho_+/\rho_- \equiv V_- / V_+ = (f+1)/(1+f/M^2) = f \quad \text{at } M = f.$$

Meanwhile, the non-phenomenological derivation of the shock discontinuity is possible in Eulerian hydrodynamics where any dissipation "mechanisms" are ignored – if imply the permissibleness of the wave overturning and triple (or more) valueness. These are averaging on velocity and density, i.e. the area of such multivalueness must be a region of transformation deterministic reversible Eulerian description to the realistic irreversible one. This approach is understandable in view of the macroscopic measurability, associated with the fundamental principles of the statistical thermodynamics.

The "entanglement" problematics is interesting here enough.

Thus, the theoretical "existence" of the shock wave discontinuity implies the threefold interpretation: phenomenological (traditional, semiempiric), "pure mathematical", and statistics-thermodynamic. The "pure mathematical" one corresponds to the formalization nuances of the shock wave presentation by the Heaviside Function, and by Dirac Function. Then

$$dS/dt \equiv (\Delta S)_{shock}\, \delta(t-t_{shock}),$$

besides the inevitable problem of "shock front point structure", i.e. $S(t = t_{shock}) = ?$ (Author: Sov. Phys. "Doklady" 1972, in rus., and our figures here).

References

1910 Baron Rayleigh: Proc. Royal Soc. A, vol. LXXXIV, pp 247-284.
1938 R. Tolman: "The Principles of Statistical Mechanics", Oxford, U.P.
1948 R. Courant, K. Friedrichs: Supersonic Flow and Shock Waves, "Interscience" 1948, Springer 1956, Москва ИЛ 1950.
1949 J. von Neumann: in "Problems of Cosmical Aerodynamics", Datton (US) 1951; (сокращ. русский перевод, Москва ИЛ 1953).
1951 H. M. Mott-Smith: Phys. Rev., v. 82, p 885-892.
1958 R. von Mises: "Mathematical Theory of Compressible Fluid Flow", Acad. Press NY; Москва ИЛ 1961.

Physics Institute of Ac. Sci. USSR). Also on MHD Conference, Riga, 1962.

1962 Valentine A. Belokogne: ТРУДЫ МФТИ, Москва, Оборонгиз. 1958, 1962.

1972 Valentine A. Belokogne: Доклады АН СССР т. 202, п 6.

2001 Valentine A. Belokogne: "The Radiative Substructure in the Intense Shocks", at the 3Workshop on Magneto-Plasma aerodynamics, Moscow, April 2001, PAPERS, ed. by IVTAN, Moscow (and refs in it).

2010 Valentine A. Belokogne: How shock wave happened, Shock wave interaction, International conf.; Moscow, September.

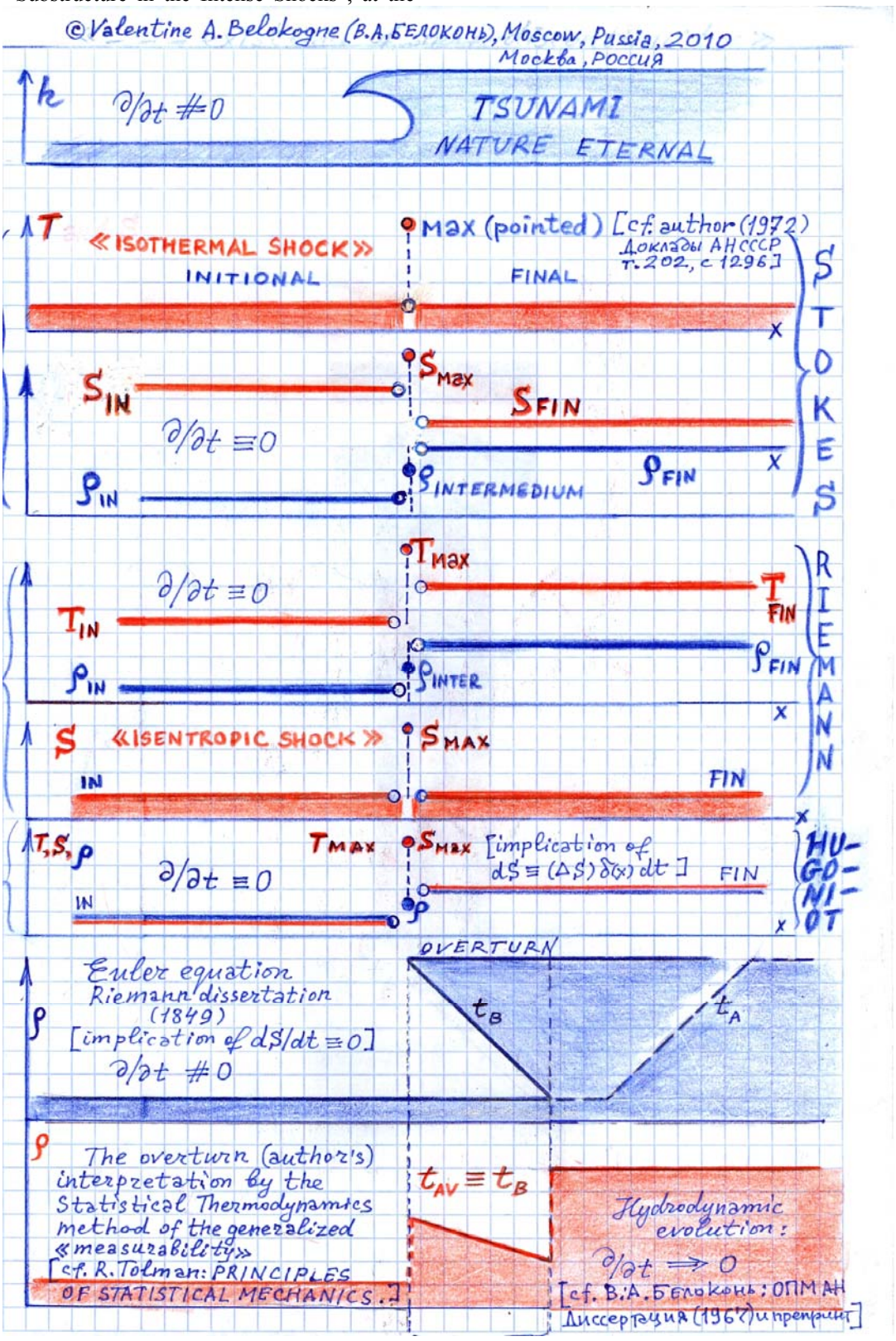

P8. THE GENERAL AND PECULIAR IN THE MICROFUSION FLYING MACHINE (MFFM) FEASIBILITY

overview

© *Valentine A. Belokogne*
Oceanology Institute (RAS), Academia Cosmonautica, Moscow, 2010

The laser driven microfusion planned by LLNL for year 2012 still doesn't imply immediate airspace application instead of high heat ($\approx 10^{11}$ J/g) and plasma blow-off ($\approx 10^{3\text{-}4}$ km/sec) potentials. The recent microfusion efforts promises microexplosions up to 100 MJ based on the reaction.

$$\mathbf{5\cdot 10^7\ {}^0K + D + T = {}^4He + n + 339\ J/ng + \approx 5\cdot 10^8\ {}^0K}$$

This gives ≈ 60-70 % energy in neutrons, and is dangerous from the Tritium (**T**) and neutrons (**n**).

The advanced fusion, by Helium-3 instead of T, has the "ecologic" main channel:

$$\mathbf{4\cdot 10^8\ {}^0K + D + {}^3He = {}^4He + p + 352\ J/ng + \approx 5\cdot 10^9\ {}^0K}$$

This plasma is more useful for MHD airspace design.

Then Helium-3 requires the comparatively big and sophisticated MFFM as soon as the minimum energy **Y** (J) of the microexplosion of fusion fuels implies the low entropy supercompression to max**ρ** (g/cc):

$$\mathbf{Y \approx 10^{14}/\rho^2(DT) \ldots \approx 10^{16}/\rho^2(D\ {}^3He)}.$$

$$\Rightarrow \quad \mathbf{Y \approx 10^{8\text{-}10} J}$$

means $\mathbf{\rho_{max}(DT) \approx 1000\text{-}100\ at\ {}^0K \approx 5\cdot 10^8}$

and $\mathbf{\rho_{max}(D\ {}^3He) \approx 10000\text{-}1000\ g/cc\ at\ {}^0K \approx 5\cdot 10^9}$ (the key problem of relation $\mathbf{G \cong Y/E_d}$, where $\mathbf{E_d}$ =fusion driver energy pulse, is ignored still).

As soon as the mass **M** of the total system depends on the typical dimension **L** by $\mathbf{M \sim L^a}$ and the ICF reactor size $\mathbf{r \sim L}$, then **Y**(at repetition rate **ν**) $\sim \mathbf{r^{1/b}}$ with $\mathbf{Y \sim 1/\rho^c}$

$$\Rightarrow \quad \mathbf{M \sim 1/\rho^{abc}}$$

For instance: $\mathbf{a = 3, b = 2/5, c = 2}$ then $\mathbf{M \sim 1/\rho^{2.4}}$.

Meanwhile, the mechanical power $\mathbf{P_m}$ of MFFM with velocity **U** at **K** = **L**ift/**D**rag, is

$$\mathbf{P_m = UM/(L/D) \equiv MU/K}$$
or $\mathbf{P_{tot} = P_m/\eta = MU/K\eta}$.

As soon as (important!) $\mathbf{K\eta = const \approx 3\text{-}5}$ for jet airplane and $\mathbf{P_{tot} \equiv Y\nu}$ then $\mathbf{U \sim \rho_{max}^{0.4}\ \nu}$.

The hypothetic application of the MFFM consists in effective "refueling" futuristic flying machines by the electricity.

Therefore the advance in fusion fuel supercompresion is necessary imperative for the ICF MFFM advent, probably since 2017-2025.

References

1. John H. Nuckolls: ICF papers, LLL 1960-1962; Reprint UCRL-JC-131075, (1999), Physics Today 1982 (УФН 1984).
2. Ray Kidder: ICF papers, LLL 1962-1964 (Declassified).
3. John H. Nuckolls, L.L. Wood, R. Hyde: ICF aerospace application, LLL 1972-1979.
4. D.Kuchemann: AERODYNAMIC DESIGN OF AIRCRAFT, Pergamon Press 1978.
5. Laser Program Annual Reports, LLL-LLNL, 1972-1994.
6. John Lindl: INERTIAL CONFINEMENT FUSION, Springer (and refs in it), N-Y, 1998.
7. V.A. Belokogne: УФН № 500 1977; Доклады АН СССР 1975; PROGRESS IN FUSION POWERED FLYING MACHINE DESIGN (and 120 refs in it), 15th International Conference on MHD Energy Conversion and 6th Workshop on Magnetoplasma Aerodynamics for Aerospace Applications, Moscow, Russia, May 24-27, 2005. Proceedings, v.3.
8. Charles Orth: VISTA, Final Report, LLNL 2003.
9. М.М. Баско: ФИЗИЧЕСКИЕ ОСНОВЫ ИНЕРЦИАЛЬНОГО ТЕРМОЯДЕРНОГО СИНТЕЗА (лекции МФТИ/МИФИ) Москва 2009.
10. Erik Storm: National Ignition Facility (NIF), and National Ignition Campaign (NIC) advances, LLNL, September 2010.
11. John Lindl et al: Physics of Plasmas, May 2011.
12. В.А. Белоконь: «Двигатель» № 4, ЦИАМ 2011.

P9. THE REALITY FOR THE LABORATORY (2017-2022) IMITATION OF THE STELLAR NUCLEOSYNTHESIS BY SUPERCOMPRESSION OF IRON, AND NICKEL

overview

©Valentine A. Belokogne

Oceanology Institute (RAS), Academia Cosmonautica, Moscow, 2010

The stellar-like synthesis of elements requires conditions [1976] $\mathbf{T \geq 100\ KeV,\ \rho \approx 100\ kg/cm^3}$ during the photodesintegratic [1983] scenario $\mathbf{^{56}Fe \rightarrow 13\,^4He + 4n}$ together with $\mathbf{^{54}Fe \rightarrow 13\,^4He + 2n}$ and $\mathbf{^{56}Ni \rightarrow 14\,^4He}$ → SPECTRUM OF NUCLEYS in the initial expansion (rarefaction) flow.

The Laboratory realization of these scenario is foresee in 2017-2022 by the beam drivers $\mathbf{E_d \approx 30 \div 100\ MJ}$ for big targets designed before for ignition "advanced" fuels DDT, DD, DT^3He etc.

Proposed by the author [papers since 1973] supercompression by the simultaneous collision of **N=20** identical layers, where substance compressed during multireverberation of shocks.

The surprising, and interesting here, **generalized Riemannian invariants** with the shock velocity **D** instead **a** sound velocity. It occurs valid for such compression by shock reverberation. This fact means the following:

RIEMANN (1859): $\mathbf{u \pm 2a/(\gamma\text{-}1) \rightarrow u \pm 2D/(\gamma\text{-}1)}$ **[V.A.B. (1973)]**

Therefore, supercompression amounts to

$\mathbf{\rho_{max}/\rho_{ininitial} \cong (N^f)/f!}$

at $\mathbf{1 \leq f \leq 6}$

for $\mathbf{f \equiv 2/(\gamma\text{-}1) = 2E/pV.}$

Such 20 plates simultaneous collision with the approach each pair at 1000 km/sec promises imitate the conditions for supernova processes [see M. Basko, cit. by author in 1985], and other interesting phenomena (gravitation waves, short wave lasing, and the variety of new things).

The multiimpact compression (see figures): The right side demonstrates piston (pusher) induced compression by shocks generated in the subsequent instantaneous accelerations to new constant velocity, and by correspond reflections against the opposite hard wall. This mode implies very high intensity (power) of the piston (pusher) energetics.

The left side (and below) demonstrates the same compression attained by the simultaneous mutual collisions of identical layers with the reverberation of the impact-generated shocks.

This mode of super compression does not required superhigh power generator.

Both schemes corresponds to the perfect gas of $\mathbf{c_p/c_v = 3,}$ or $\mathbf{f = 1.}$

References

1973 Belokogne V.A.: Sov. Phys. Doklady (1975;1983).

1976 Belokogne V.A., Ilyinsky Yu., Khokhlov Rem,: JETPh Letters, October 20 (1976).

1979 Belokogne V.A.: "Energy … Conference" (Italy), Plenum Press, 1983.

1983 Clayton D. "Principles of stellar Evolution and Nucleosynthesis", Chicago U. Press.

1985 Belokogne V.A.: Conference on Detonation, Tallinn, Estonia.

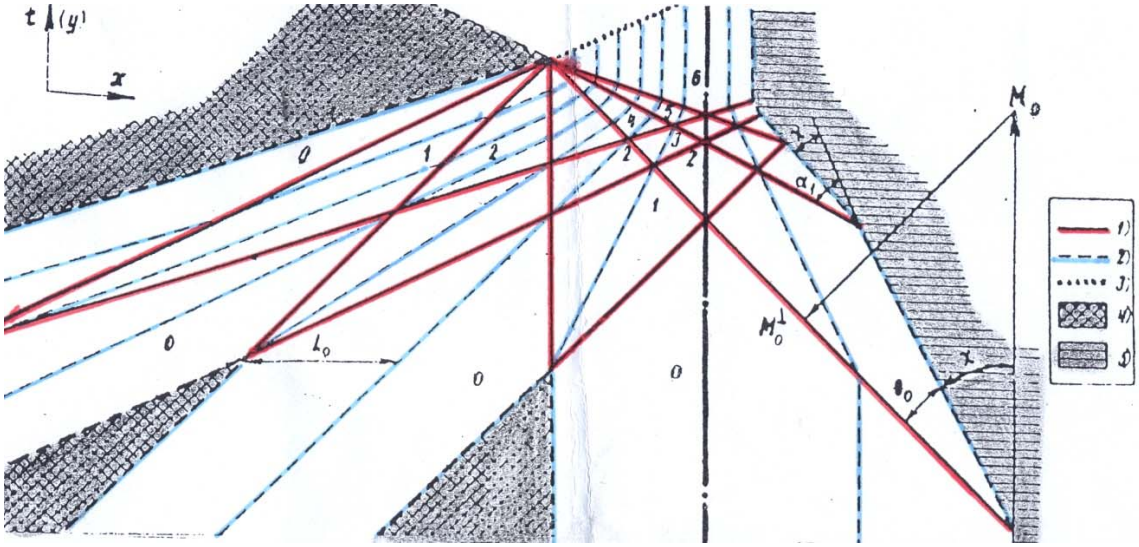

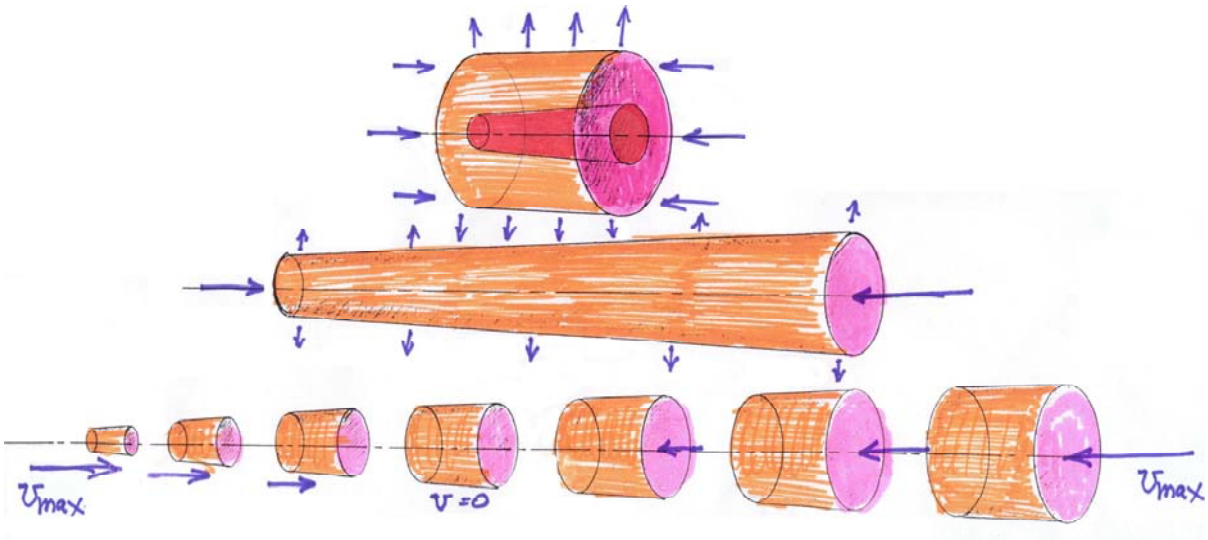

1) shocks
2) particle (of the compressed substance) trajectory
3) rarefaction front
4) void (vacuum)
5) pusher (piston let magnetic also)

P10. THE NON-PARADOXICAL "FORBIDDEN" ARISING OF THE SUBSHOCK ISOTHERMAL IN THE ONE-DIMENSIONAL ($c_p/c_v \equiv 3$) PLASMAS BY A THERMODYNAMIC INPUT OF THE "PHOTON STEAM"

overview

©Valentine A. Belokogne, Moscow, Russia, 2010
(Oceanology Institute (RAS), RANS, Academia Cosmonautica)

The isothermal irreversible compression shock was invented by Stokes (1848) as a trick to obtain so called "generalized solution" in the world of Leonard Euler formalism. And later (1910) Baron Rayleigh introduced in a theory of subshock for the integrally adiabatic shock structure governed by the pure heatconducted flow (Pr = 0). Around 1955, independently the author, and Belenky considered flow with **LTE** (Plank) radiation, where the pressure is determined as (Pr = 0 again) follows:

$$\mathbf{P = P_{matter} + P_{radiation} = n_m kT + 0.902 n_{photons} kT = (\gamma - 1)E_m/V + 18.3kT^4.}$$

$$\Rightarrow \mathbf{\Delta(S \cong kn \sim T^3)_{photons} = 0}$$

If $P_m << P_r$, then $P_{flow} \rightarrow P(T)$ only, i.e. isotherms are parallel to V-axis on (PV) diagram. This means the monotonous continual evolution of temperature along the "Rayleigh line"

$$\Delta P/\Delta V = (dP/dV)_{RL} \sim -M^2_{shock}.$$

Therefore, isothermal subshock must be liquidated by the strong radiation pressure.

Nevertheless, as this author established in papers of 1958, 1972, in the flow with $\gamma \equiv (c_p/c_v)_m = 3$ ($f \cong (2/(\gamma-1)=1$), where the radiationless shock structure contains no any subshock isothermal, even an arbitrary small admixture of Plank radiation initiates the formation of the subshock isothermal. So the radiation, instead of flattened, steepened the shock structure initially. Then, becoming strong enough, it liquidates the shock isothermal.

As far as application of the Second Law of Thermodynamics, for the shock isothermal (isophotonic here) we have:

$$\mathbf{T\Delta S - \Delta Q \equiv (T\Delta S - \Delta Q)_{matter} + + (T\Delta S - \Delta Q = 0)_{photons} = = (f/2)N_m kT(X - 1/X - 2\ln X) > 0, \text{ where } X = X_m \equiv (\rho_+/\rho_-)_m > 1.}$$

This result is interesting enough both for terrestrial, and stellar and other astrophysical problems.

This result is interesting enough both for terrestrial, and stellar and other astrophysical problems.

Meanwhile, the some engineering approximation looks like (cf. Brode 1968):

$$\mathbf{E(J/g) \approx 10T°K + 10^{-21}T^4\ °K/\rho(g/cm^3).}$$

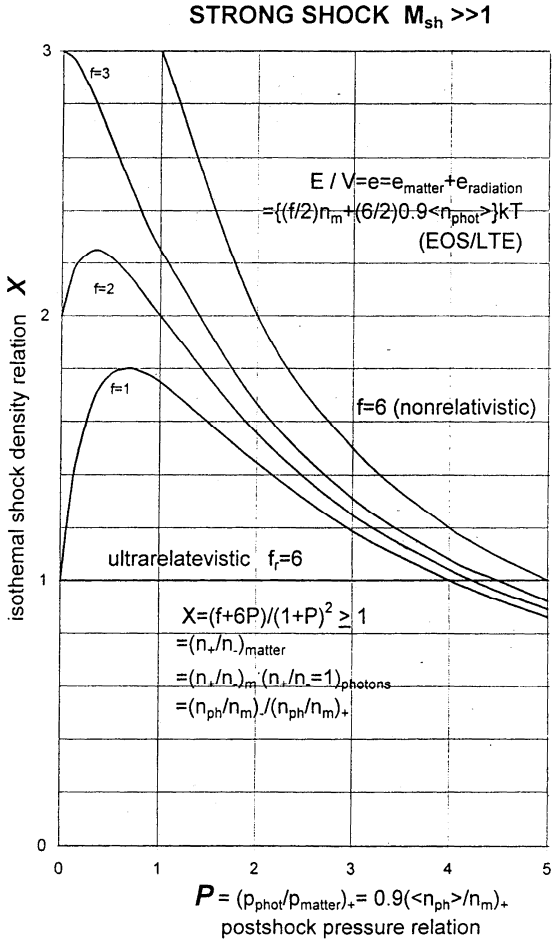

Fig. *The lower curve corresponds to the "PARADOXICAL" anew appearance of the isothermal shock initiated by the heat radiation in the two component substance (matter γ_m = 3 and photons $\gamma_{p/h}$ = 4/3).*

Selected publications

1910 Baron Rayleigh : Permanent aerial waves of finite amplitude, Cambridge.

1944 / 1986 L. Landau and E. Livshiz : Курс теоретической физики (гидродинамика).

1968 H.Brode: Ann.Rev.Nucl.Sci., v.18.

1968 Valentine A. Belokogne (В.А. Белоконь: Всесоюзный конгресс по механике, МГУ.

1972 Valentine A. Belokogne: Доклады АН СССР т. 202, № 3 (English translation by in APS was incorrect).

2008 Зельдович А.Я., Райзер Ю.П. Физика ударных волн и высокотемпературных гидродинамических явлений // Изд. 3. ISBN: 978-5-9221-0938-3, 656с.

2010 Крайко А. Н. Теоретическая газовая динамика: классика и современность / Издатель: ТОРУС ПРЕСС, ISBN: 978-5-94588-076-4, 440с.

2011 Крайко А. Н. Прикладная математика и механика, Российская академия наук, №6.

P11. ON HYPERSONIC FLOW OF RAREFIED HIGH BETA PLASMA FORMING ELECTROMAGNETIC STRUCTURES NEAR MAGNETIZED OBJECTS AND ON GOVERNING PARAMETERS DEFINED BY SHAPE OF THE FLOW VELOCITY DISTRIBUTION FUNCTION

Vladimir M. Gubchenko
Institute of Applied Physics, RAS, Nizhny Novgorod, Russia
(ua3thw@appl.sci-nnov.ru)

We consider 3D asymmetrical magnetized objects which are submerged in hypersonic plasma flows or these objects themselves are sources of the plasma flows. Plasma is hot and rarefied (collisionless), thermal pressure is much stronger in comparison with magnetic pressure (high plasma beta parameter), plasma particles are weakly magnetized and are characterized by shape of the velocity distribution function (VDF). These conditions are realized for the aerospace applications, for the Space physics - 3D magnetosphere-like magnetic structures formation and for physics of high energy density plasmas (HEDP) near magnetized inertial targets. The effect of electromagnetic (e.m.) interaction provides formation near the objects of the elongated 3D large-scale structures of electric currents and e.m. fields. The topology of these structures depends on shape of the VDF what means that effect can be considered only in kinetic approach via Maxwell and Vlasov equations and not via traditional MHD approach. With reshaping of the VDF we can get transition from the resistive state, when flow of plasma particles behaves as conductor, to the diamagnetic state, when flow of particles behaves as dielectric. These states of the flow are characterized by kinetic dimensionless parameter G which we call a "quality" of a flow. The parameter G can be considered as the e.m. analog of the Mach number M which was invented in the past for description of the pressure-wave topological structures formed by the longitudinal fields and for description of acoustic properties of the flows. The effect is described by a parameter G required of the kinetic reconsideration of the dimensionless parameters provided by the MHD theory. The parameter G is varied in wide range and can be negative, it is a governing e.m. parameter of interaction of the objects and flows. When $G<<1$ we get resistive (conductive) state of a flow and structures near the objects are elongated by the flow. When $|G|>>1$ we get diamagnetic state of a flow and we get compact quasi-symmetrical envelope-like structures near the objects. When $G\sim1$ diamagnetic and resistive currents are of the same order and are in the same direction, plasma flow has mixed diamagnetic and resistive properties. When $G\sim-1$ diamagnetic and resistive currents are of the same order but have the opposite directions; plasma behaves a quasi-current-free (QCF) media in relation to e.m. fields and a quasi-neutral (QN) media in relation to pressure (electrostatic) fields. The negative G is related with possibility of the e.m. instabilities in plasma. The parameter G is a ratio of the "energy" to the "momentum" anisotropy parameters of the VDF. These anisotropy parameters are characterized by shape of the VDF. There are two spatial dispersion scales for plasma flow which are related with two anisotropy parameters. Requirement of weak magnetization for these scales realization for e.m. structures description provides dimensionless nonlinear parameters based on plasma beta and the VDF anisotropy parameters.

The work is in frame of the Russian State contract № 02.740.11.0246, supported by the grants RFBR № 11-02-00103-a and № 11-02-97088, supported by Division of Physical Sciences of the RAS – the program №. VI. 15.

References

1. Gubchenko V.M., Sov. J. Plasma Phys., 14, No 3, 186-190. 1988.
2. Gubchenko V.M. et al., Proc. 2nd Workshop on Magnetoplasma Aerodynamics in Aerospace Applications, IVTAN, Moscow, 313-317, 2000.
3. Gubchenko V.M. On kinetic description of large scale current carrying electromagnetic structures excited in moving hot collisionless plasma. «Problems of high energy density (HED) physics». Proc. «XIIth Khariton scientific readings on topics», RFNC-VNIIF, Sarov, Russia, 239-246, 2010, ISBN 978-5-9515-0151-6,

P12. NUMERICAL SIMULATION OF MICROENGINE BASED ON THE CAPILLARY DISCHARGE SYSTEM

Kuzenov V.V., [1)]Ryzhkov S.V.
Moscow, Russia, IPMech RAS; Russia, Moscow, [1)]BMSTU
vik_kuzenov@mail.ru
svryzhkov@gmail.com

At present time, systems with a dense plasma are of high interest and relevant for plasma and aerodynamic research and possible for micromotors [1, 2]. The aim of this work is finding new types of thrusters with a minimum overall weight and dimensions characteristics and energy consumption, which create the smallest possible unit thrust vector for the efficient solution of the spacecraft control.

A mathematical and numerical model [3] to study the structure of plasma jets ejected from the channel of a capillary discharge with an evaporating wall was constructed. A computer program for the complex radiation gasdynamic calculations taking into account radiative transfer was developed [4]. It is proposed to create the new type of engine for small spacecrafts. The numerical calculation was performed for the parameters of the experiment [5], which was proposed to use laser pulses for initiation a capillary discharge at low voltages and at low pressures when the ignition of discharge is hindered. Combined scheme (laser pulse plus the capillary discharge) can reduce the weight and size characteristics of pulsed plasma engines which operate in the pulsed and repetitively pulsed regimes.

Specific calculations are performed for a capillary discharge (1 - 4) system. Variable parameters: step between single discharges, and power characteristics of the system – the energy of capacitor bank, power and discharge time. Environment is the air in the pressure range 10^{-3} to 1 atm. We demonstrate efficient properties of the capillary discharge system using high-current discharge channel in a magnetic field (high field pulsed solenoid magnets).

The paper presents the spatial distribution of basic thermodynamic parameters (density, temperature, radiation density and Mach number) in system of interacting plasma jets in a magnetic field. In the microengine based on the capillary discharge system depending on the pressure of the surrounding gas under the combined action of focused laser radiation and discharge the following characteristics of engine: thrust, specific impulse, size and mass of the system, the combustion temperature, etc, were obtained. The influence of various factors on the final construction of the system was analyzed. These studies were performed with the following values of electrical and thermal parameters of capillary discharge (capillary length ~ 30 mm, the jet length 2-3 mm, temperature 10 - 70 kK (1 - 6 eV), the density in the jet ~ 10^{20} m^{-3}).

Funding for this research was provided by the Russian Foundation for Basic Research (Grants # 09-08-00137, 09-08-92422), and Russian Academy of Sciences (RNPVSh 2.1.1/4693).

References

1. F.N. Lubchenko, A.V. Fedenev, A.N. Chumakov, N.A. Bosak, V.F. Tarasenko, A.N. Panchenko. Proc. VIII Int. Symposium on Radiation Plasma Dynamics. 2009. P. 262-265 (in Russian).
2. V.V. Kuzenov. Proc. XXXIV Academic Readings on Cosmonautics in memories of Academician Korolev S.P. M.: BMSTU. 2010. P. 198-199 (in Russian).
3. V.V. Kuzenov. Preprint A.Yu. Ishlinsky IPMech RAS № 864. M.: IPMech RAS. 2008. 53 p.
4. V.V. Kuzenov. Vestnik MGTU. Ser. «Mashinostroenie». 2009. № 4(77). P. 45–77 (in Russian).
5. A.P. Panchenko, V.F. Tarasenko, M.A. Shulepov, F.N. Lubchenko, A.V. Fedenev. Technical Physics Letters. 2009. V. 35, No. 3. P. 53–59 (in Russian).

Index of Autors

Afanas'ev S.A. *(Joint Institute for High Temperatures RAS, Moscow, Russia)* **64, 326**

Akishev Yu. *(SRC RF TRINITI, Moscow region, Russia)* **276**

Aleksandrov N.L. *(Moscow Institute of Physics and Technology, Dolgoprudny, Russia)* **81**

Alekseev Yu.V. *(Joint Institute for High Temperatures RAS, Moscow, Russia)* **302**

Anisimov Yu.I. *(St-Petersburg State University, Russia)* **250**

Anokhin E.M. *(Moscow Institute of Physics and Technology, Dolgoprudny, Russia)* **81**

Artem'ev K.V. *(A.M. Prokhorov General Physics Institute of RAS, Moscow, Russia)* **141**

Astafiev A.M. *(St. Petersburg State University, Russia)* **118**

Baranov D.S. *(Joint Institute for High Temperatures RAS, Moscow, Russia)* **349**

Baranova O.D. *(Joint Institute for High Temperatures RAS, Moscow, Russia)* **349**

Baryshnikov A.S. *(Ioffe Physico-Technical Institute, S.Petersburg, Russia)* **95**

Basargin I.V. *(Ioffe Physico-Technical Institute, S.Petersburg, Russia)* **95**

Belokogne Valentine A. *(Oceanology Institute (RAS), RANS, Academia Cosmonautica)* **354, 356, 357, 359**

Benard N. *(Institut Pprime, CNRS, Université de Poitiers, ENSMA Dpt Fluides, Thermique, Combustion Bld Marie et Pierre Curie, Téléport 2, 86962 Futuroscope Cedex, France)* **69**

Berezhetskaya N.K. *(A.M. Prokhorov General Physics Institute, of RAS, Moscow, Russia)* **141, 145**

Bityurin V.A. *(Joint Institute for High Temperatures RAS, Moscow, Russia)* **22, 64, 177, 193, 226, 277, 294, 306, 333**

Bobashev S.V. *(Ioffe Institute RAS, Saint Petersburg, Russia)* **249, 255**

Bocharov A.N. *(Joint Institute for High Temperatures RAS, Moscow, Russia)* **226**

Bolshov M.A. *(Institute for Spectroscopy RAS, Troitsk, Moscow region, Russia)* **135**

Borghi Carlo Angelo *(Department of Electrical Engineering, University of Bologna, Italy)* **217, 261, 270**

Borisov I.A. *(Joint Institute for High Temperatures RAS, Moscow, Russia)* **22**

Boytsov A. *(Joint Institute for High Temperatures RAS, Moscow, Russia)* **193**

Brovkin V.G. *(Joint Institute for High Temperatures RAS, Moscow, Russia)* **64, 250, 326**

Bychkov V.L. *(M.V.Lomonosov Moscow state university, Physical department. Moscow, Russia)* **110, 256**

Bykov A.A. *(Moscow Institute of Physics and Technology, Dolgoprudny, Russia)* **313**

Chernikov V.A. *(M.V. Lomonosov MSU, Physical department Moscow, Russia)* **256**

Chernyshev A.S. *(Ioffe Institute RAS, Saint Petersburg, Russia)* **255**

Chertov D.S. *(Joint Institute for High Temperatures RAS, Moscow, Russia)* **22**

Chinnov V.F. *(Joint Institute for High Temperatures RAS, Moscow, Russia)* **294, 277**

Chistyakova M.V. *(Ioffe Physico-Technical Institute, S.Petersburg, Russia)* **95**

Cordier L. *(Institut Pprime, CNRS, Université de Poitiers, ENSMA Dpt Fluides, Thermique, Combustion Bld Marie et Pierre Curie, Téléport 2, 86962 Futuroscope Cedex, France)* **69**

Cristofolini Andrea *(Department of Electrical Engineering, University of Bologna, Italy)* **217, 270, 261**

Davydov A.M. *(A.M. Prokhorov General Physics Institute, of RAS, Moscow, Russia)* **141, 145**

Devjatkov V.N. *(Institute of High Current Electronics SB RAS, Khristianovich Institute of Theoretical and Applied Mechanic RAS, Russia)* **51**

Dobrovolskaya A.S. *(Joint Institute for High Temperatures RAS, Moscow, Russia)* **302**

Dyrenkov V.V. *(Institute for Applied Mechanics RAS, Moscow, Russia)* **313**

Efimov A.V. *(Joint Institute for High Temperatures RAS, Moscow, Russia)* **277, 294**

Emelin S.E. *(St. Petersburg State University, Russia)* **118**

Erofeev A.V. *(Ioffe Physical Technical Institute RAS, Saint Petersburg, Russia)* **239, 249**

Filimonova E.A. *(Joint Institute for High Temperatures RAS, Moscow, Russia)* **177, 141, 302**

Firsov A. A. *(Joint Institute for High Temperature RAS, Moscow, Russia)* **135, 181**

Firsov K.N. *(A.M. Prokhorov General Physics Institute RAS, Moscow, Russia)* **141,145**

Fomichev V. P. *(Khristianovich's Institute of Theoretical and Applied Mechanics SB RAS, Novosibirsk, Russia)* **51, 237,245**

Fomin V.M. *(Khristianovich Institute of Theoretical and Applied Mechanics, Novosibirsk, Russia)* **92**

Fortov V.E. *(Joint Institute for High Temperatures RAS, Moscow, Russia)* **337**

Fureby C. *(Defense Security Systems Technology, The Swedish Defense Research Agency – FOI, Stockholm, Sweden)* **184**

Geert C. Dijkhuis *(Converton N.V., Netherlands)* **108**

Georgievsky P.Yu. *(Institute for Mechanics MSU, Moscow, Russia)* **88**

Golovachev Yu.P. *(Ioffe Institute RAS, Saint Petersburg, Russia)* **255**

Golub V.V. *(Joint Institute for High Temperatures RAS, Moscow, Russia)* **58**

Goncharov A.E. *(Institute Theoretical and Applied Mechanics SB RAS, Novosibirsk, Russia)* **247**

Gordeev A.N. *(IPMech RAS; Moscow, Russia)* **184**

Grigorenko A.V. *(Joint Institute for High Temperatures RAS, Moscow, Russia)* **277, 294**

Gritsinin S.I. *(A.M. Prokhorov General Physics Institute RAS, Moscow, Russia)* **145**

Grushin M. *(SRC RF TRINITI, Moscow region, Russia)* **276**

Gubanov E.V. *(Joint Institute for High Temperatures RAS, Moscow, Russia)* **342**

Gubchenko V.M. *(Institute of Applied Physics RAS, Nizhny Novgorod, Russia)* **361**

Gusev I.N. *(Faculty of Physics, Moscow State University, Moscow, Russia)* **142**

Ivanov I.E. *(Moscow state University, Molecular Physics Department, Moscow, Russia)* **75**

Karachev A.A. *(Faculty of Physics, Moscow State University, Moscow, Russia)* **142**

Kazansky P.N. *(Joint Institute for High Temperatures RAS, Moscow, Russia)* **22**

Kazantsev S.Yu. *(A.M. Prokhorov General Physics Institute RAS, Moscow, Russia)* **141**

Khodotaev Kirill V. *(Moscow Radiotechnical Institute RAS, Moscow, Russia)* **109**

Kindysheva S.V. *(Moscow Institute of Physics and Technology, Dolgoprudny, Russia)* **81**

Kirpichnikov A.A. *(Moscow Institute of Physics and Technology, Dolgoprudny, Russia)* **81**

Klementyeva I.B. *(Joint Institute for High Temperatures RAS, Moscow, Russia)* **333**

Klimov A.I. *(Joint Institute for High Temperatures RAS, Moscow, Russia)* **22, 126, 193, 277, 294, 333**

Kochetov V.I. *(State Research Center of Russian Federation Troitsk Institute for Innovation and Thermonuclear Research (TRINITI), Troitsk, Moscow region, Russia)* **29**

Kolesnichenko Yu. *(Joint Institute for High Temperatures RAS, Moscow)* **326, 250**

Kolesnikov A.F. *(IPMech RAS; Moscow, Russia)* **184**

Kononov I.G. *(A.M. Prokhorov General Physics Institute RAS, Moscow, Russia)* **141**

Konyukhov A.V. *(Joint Institute for High Temperatures RAS, Moscow, Russia)* **337**

Kopyl P.V. *(Faculty of Physics, Moscow State University, Moscow, Russia)* **142**

Korotaeva T. A. *(Institute Theoretical and Applied Mechanics SB RAS, Novosibirsk, Russia)* **247**

Koroteeva E.Yu. *(Moscow state University, Molecular Physics Department, Moscow, Russia)* **75**

Kosarev I.N. *(Moscow Institute of Physics and Technology, Dolgoprudny, Russia)* **81**

Kossyi I.A. *(A.M. Prokhorov General Physics Institute, Moscow, Russia)* **141, 145**

Kostiuk A.A. *(M.V. Lomonosov Moscow State University, Physical department Moscow, Russia)* **256**

Koval N.N. *(Institute of High Current Electronics SB RAS, Khristianovich Institute of Theoretical and Applied Mechanic RAS, Russia)* **51**

Kozlov P.V. *(Institute of Mechanics, Lomonosov Moscow State University, Moscow, Russia)* **172**

Krasovskaya I.V. *(Ioffe Physico-Technical Institute RAS, Saint Petersburg, Russia)* **249**

Krikunova A.I. *(Moscow Institute of Physics and Technology, Russia)* **313**

Kudryavtsev A.A. *(St. Petersburg State University, Dolgoprudny,Russia)* **118**

Kuritsyn Yu. A. *(Institute for Spectroscopy RAS, Troitsk, Moscow region, Russia)* **135**

Kutuzov D.S. *(Joint Institute for High Temperatures, Moscow, Russia)* **277, 294**

Kuzenov V.V. *(Moscow, Russia, IPMech RAS; Russia, Moscow)* **362**

Lapushkina T.A. *(Ioffe Physical Technical Institute Russian Academy of Sciences, Saint Petersburg, Russia)* **239**

Lashkov V.A. *(St-Petersburg State University, Russia)* **250**

Leonov S. B. *(Joint Institute for High Temperatures of RAS, Moscow, Russia)* **135, 181**

Levin V.A. *(Institute for Mechanics MSU, Moscow, Russia)* **88**

Liger V.V. *(Institute for Spectroscopy RAS, Troitsk, Moscow region, Russia)* **135**

Likhachev A.P. *(Joint Institute for High Temperatures RAS, Moscow, Russia)* **337, 342**

Lomanovich K.A. *(Khristianovich Institute of Theoretical and Applied Mechanics, Novosibirsk, Russia)* **92**

Losev S.A. *(Institute of Mechanics, Lomonosov Moscow State University, Moscow, Russia)* **172**

Makaryan V.G. *(Samara State Aerospace University, Samara, Russia)* **185**

Malykh N.I. *(A.M. Prokhorov General Physics Institute, RAS, Moscow, Russia)* **141**

Mashek I. *(St.-Petersburg State University, St.-Petersburg)* **326**

Mashek I.Ch. *(St-Petersburg State University, Russia)* **250**

Medin S.A. *(Joint Institute for High Temperatures RAS, Moscow, Russia)* **342**

Melnichenko D. *(MRTI RAS, Moscow, Russia)* **134**

Mironenko V.R. *(Institute for Spectroscopy RAS, Troitsk, Moscow region, Russia)* **135**

Molevich N.E. *(Samara State Aerospace University, Samara Branch of P.N. Lebedev Physical Institute of RAS, Samara, Russia)* **185**

Moralev I.A. *(Joint Institute for High Temperatures RAS, Moscow, Russia)* **22, 193, 333**

Moreau E. *(Institut Pprime, CNRS, Université de Poitiers, ENSMA Dpt Fluides, Thermique, Combustion Bld Marie et Pierre Curie, Téléport 2, 86962 Futuroscope Cedex, France)* **69**

Mursenkova I.V. *(Moscow state University, Molecular Physics Department, Moscow, Russia)* **75**

Naidis G.V. *(Joint Institute for High Temperatures RAS, Moscow, Russia)* **60**

Neretti Gabriele *(Department of Electrical Engineering, University of Bologna, Italy)* **217, 261, 270**

Nikitin A.I. *(Institute for Energy Problems of Chemical Physics of RAS, Moscow, Russia)* **315**

Nikolayeva V.I. *(Joint Stock Company "GSKB "Almaz-Antei", Moscow, Russia)* **76, 210**

Nudnova M.N. *(Moscow Institute of Physics and Technology, Dolgoprudny, Russia)* **81**

Orlov D.M. *(Moscow state University, Molecular Physics Department, Moscow, Russia)* **75**

Pashchina A.S. *(Joint Institute for High Temperature RAS, Moscow, Russia)* **76, 210**

Petryakov A. *(SRC RF TRINITI, Moscow region, Russia)* **276**

Podzin V. E. *(Khristianovich's Institute of Theoretical and Applied Mechanics SB RAS, Novosibirsk, Russia)* **237, 245**

Polyakov L.B. *(Joint Institute for High Temperatures of RAS, Moscow, Russia)* **126, 294**

Poniaev S.A. *(Ioffe Physical Technical Institute of RAS, Saint Petersburg, Russia)* **239**

Popov N. A. *(Skobel'tsyn Institute of Nuclear Physics, Moscow State University, Moscow, Russia)* **35, 141, 145**

Popov V.V. *(Institute for Applied Mechanics RAS, Moscow, Russia)* **313**

Porfiriev D.P. *(Samara State Aerospace University, Samara Branch of P.N. Lebedev Physical Institute of RAS, Samara, Russia)* **185**

Postnikov B.V. *(Khristianovich Institute of Theoretical and Applied Mechanics, Novosibirsk, Russia)* **92**

Romanenko Yu.V. *(Institute of Mechanics, Lomonosov Moscow State University, Moscow, Russia)* **172**

Romadanov I.V. *(IPMech RAS; Moscow, Russia)*..... **216**

Ryzhkov S.V. *(BMSTU, Moscow, Russia)*..... **216, 362**

Sabelnikov V. *(Fundamental and Applied Energetics Department, ONERA, Palaiseau Cedex, France)* **152**

Sakharov V.A. *(Ioffe Physico-Technical Institute of RAS, Saint Petersburg, Russia)* **249**

Sakhonchik A.N. *(Joint Stock Company "GSKB "Almaz-Antei, Moscow, Russia)* **76**

Saveliev A.S. *(Joint Institute for High Temperatures RAS, Moscow, Russia)*..... **58**

Schevchenko A.B. *(Khristianovich Institute of Theoretical and Applied Mechanic RAS, Russia)*..... **51**

Schmidt A. A. *(Ioffe Institute RAS, Saint Petersburg, Russia)* **255**

Schweigert I.V. *(Institute of Theoretical and Applied Mechanics, Novosibirsk 0, Russia)* **50**

Sechenov V.A. *(Moscow Institute of Physics and Technology, Dolgoprudny, Russia)* **58**

Serov Yu.L. *(Ioffe Institute RAS, St.-Petersburg, Russia)*..... **101**

Shakarov M.R. *(Moscow Institute of Electronic Technology, Moscow, Russia)*..... **141**

Shashkin A.P. *(Institute Theoretical and Applied Mechanics SB RAS, Novosibirsk, Russia)* **247**

Shevchenko A. B.. *(Khristianovich's Institute of Theoretical and Applied Mechanics SB RAS, Novosibirsk, Russia)* . **237,245**

Shibkov V.M. *(Faculty of Physics, Moscow State University, Moscow, Russia)* **142**

Shibkova L.V. *(Faculty of Physics, Moscow State University, Moscow, Russia)* **142**

Shugaev F.V. *(M.V.Lomonosov Moscow state university, Physical department. Moscow, Russia)* **189**

Shurupov M. A. *(Joint Institute for High Temperatures RAS, Moscow, Russia)*..... **135, 181**

Sidorenko M.K. *(Joint Institute for High Temperatures RAS, Moscow, Russia)* **210**

Solenaya O.A. *(M.V.Lomonosov Moscow state university, Physical department. Moscow, Russia)*..... **189**

Soloviev V.R. *(Moscow Institute of Physics and Technology, Dolgoprudny, Russia)* **13**

Son E.E. *(Joint Institute for High Temperatures RAS, Moscow, Russia)* **58, 71**

Starikovskaia S.M. *(Ecole Polytechnique, Palaiseau Cedex, France)*..... **81**

Starikovskiy A.Yu. *(Princeton University, Princeton, USA)* **81**

Starodubtsev M.A. *(Central Aerohydrodynamic Institute, Zhukovsky, Russia)*..... **100**

Stepanova Z.A. *(Ioffe Physico-Technical Institute RAS, Saint Petersburg, Russia)* **249**

Surkont O.S. *(Faculty of Physics, Moscow State University, Moscow, Russia)*..... **142**

Sutyrin O.G. *(Institute for Mechanics MSU, Moscow, Russia)*..... **88**

Taktakishvili M.I. *(D.V. Skobeltsyn Institute of Nuclear Physics, Moscow State University, Moscow, Russia)*..... **141**

Tarasova N.M. *(A.M. Prokhorov General Physics Institute, of RAS, Moscow, Russia)* **145, 141**

Tereshonok D.A. *(Joint Institute for High Temperatures of RAS, Moscow, Russia)*..... **71**

Tolkunov B.N. *(Joint Institute for High Temperatures RAS, Moscow, Russia)* **126, 193, 294, 313**

Trushkin A.N. *(State Research Center of Russian Federation Troitsk Institute for Innovation and Thermonuclear Research (TRINITI), Troitsk, Moscow region, Russia)*..... **29**

Tumakaev G.K. *(Ioffe Physico-Technical Institute of RAS, Saint Petersburg, Russia)* **249**

Vasilevskii S.A. *(IPMech RAS; Moscow, Russia)* **184**
Vedenin P.V. *(Joint Institute for High Temperatures RAS, Moscow, Russia)* **64**
Velikodny V.Yu. *(Moscow Institute of Physics and Technology)* **313, 354**
Vlasov A.N. *(The Ryazan State Radio Engineering University, Ryazan, Russia)* **282**
Volkov S.A. *(M.V. Lomonosov Moscow State University, Physical department Moscow, Russia)* **256**

Yadrenkin M. A. *(Khristianovich's Institute of Theoretical and Applied Mechanics SB RAS, Novosibirsk, Russia)* **237,245**
Yarantsev D. A. *(Joint Institute for High Temperature RAS, Moscow, Russia)* **135**

Zavershinsky I.P. *(Samara State Aerospace University, Samara, Russia)* **185**
Znamenskaya I.A. *(Moscow state University, Molecular Physics Department, Moscow, Russia)* **75**

НАУЧНЫЕ ТРУДЫ
Десятое Международное Совещание по Магнитоплазменной Аэродинамике

Подписано к печати 01.09.2011 Формат 60×84/8
Печать офсетная Усл.печ.л. 46
Тираж 100 экз. Заказ №

ООО «Печатный Салон «Шанс»». 125412, Москва, Ижорская ул., 13, стр.2
Материал отпечатан по оригинал-макетам